

Surveys in
FLUID MECHANICS

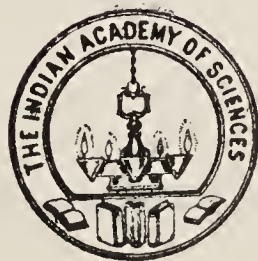
Edited by
R. NARASIMHA
S. M. DESHPANDE



INDIAN ACADEMY OF SCIENCES
BANGALORE 560 080

Surveys in **FLUID MECHANICS**

Edited by
R. NARASIMHA
S. M. DESHPANDE
Indian Institute of Science, Bangalore



1 9 8 2

INDIAN ACADEMY OF SCIENCES

Bangalore 560 080

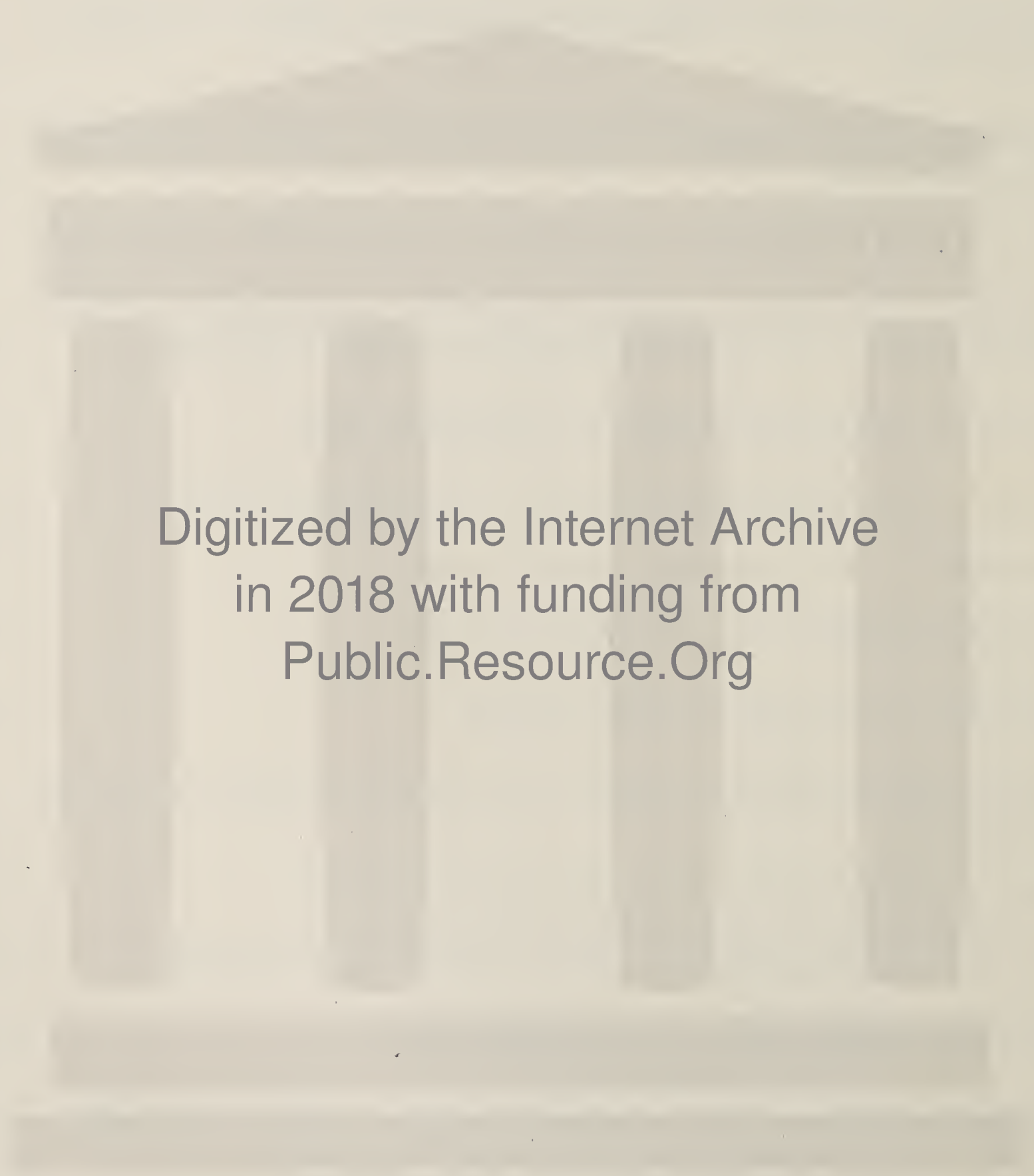
© 1982 by the Indian Academy of Sciences

Reprinted from the Proceedings of the Indian Academy of Sciences,
Engineering Sciences
Volume 4, pp 95-404, 1981

Edited by R. Narasimha and S. M. Deshpande and printed for the
Indian Academy of Sciences by Macmillan India Press,
Madras 600 002, India

CONTENTS

Foreword	(i)
SATISH DHAWAN: A glimpse of fluid mechanics research in Bangalore 25 years ago	1
DONALD COLES: Prospects for useful research on coherent structure in tur- bulent shear flow	17
A K M FAZLE HUSSAIN: Role of coherent structures in turbulent shear flows	35
HUANG YUNG-NIEN and CHOU PEI-YUAN: On the solutions of Navier- Stokes equations and the theory of homogeneous isotropic turbulence	83
M OHJI: Mathematical modelling of turbulent shear flows	105
ITIRO TANI: Three-dimensional aspects of boundary-layer transition	125
T MATSUI: Flow visualization studies of vortices	145
G B WHITHAM: On finite amplitude water waves	165
P K DAS: Storm surges in the Bay of Bengal	175
RUBY KRISHNAMURTI: Generation of large scale circulation in turbulent convection	183
SULOCHANA GADGIL: Fluid dynamics of the monsoon	201
T C LIN and JIA ZHENXUE: Inviscid transonic flow field analysis	221
PRADIP NIYOGI: Transonic flow past thin wings	253
KOICHI OSHIMA: Thermal and fluid mechanical problems in space flight	269
VIJAY H ARAKERI: Real-fluid effects in flow cavitation	287
S SIVASEGARAM: Wind tunnel tests on slow-running vertical-axis wind- rotors	301
Author Index	311
Subject Index	319



Digitized by the Internet Archive
in 2018 with funding from
Public.Resource.Org

<https://archive.org/details/surveysinfluidme00unse>

SURVEYS IN FLUID MECHANICS

Foreword

The motion of fluids is a subject of great interest to a wide variety of engineers and scientists. Apart from numerous applications in almost all branches of engineering, a variety of fascinating fluid dynamical problems arise in meteorology, oceanography and astrophysics. And there are aspects of fluid flow such as turbulence and separation that have to this day defied all attempts at understanding them, and have posed a fundamental challenge not only to engineers but to physicists and mathematicians as well.

This volume presents surveys of a variety of topics in fluid mechanics. The papers are extended versions of the invited lectures that were given at the First Asian Congress of Fluid Mechanics held in Bangalore during 8–13 December 1980. In bringing out the volume, it is our hope that they will provide useful surveys of some of the most recent advances in fluid mechanics, and, at the same time, offer a cross-section of work being done in Asian countries on fluid mechanical problems.

This issue begins with a brief account by Dhawan of how research in fluid mechanics began in Bangalore more than twenty five years ago. The turbulent spot, the subject of a few studies at that time, has attracted much attention in recent years again, in the search for coherent structure in the turbulent boundary layer. D E Coles examines the spot as well as five other flows involving coherent structures. Such discoveries as the presence of discrete vortices in the mixing layer, which 'is not the featureless wedge of turbulence which it had been thought for many years to be', have suddenly opened up many promising lines of enquiry. Coles draws up what he calls a personal manifesto, setting out strategies for formulating experiments as well as theoretical models. Fazlé Hussain presents an extensive survey of recent work in coherent structures, especially in free shear flows, where he finds that excitations of a certain type can *suppress* turbulence. He also concludes that coherent structures dominate transport in the early stages of their formation, but not further downstream.

Still in the area that Dhawan touched upon, namely transition from laminar to turbulent flow, progress has been steady if not spectacular. The development of three-dimensional structures (like a spot) in a basically two-dimensional flow is an intriguing phenomenon, of which a masterly survey is presented by that doyen of Asian fluid dynamicists, Itiro Tani, who for decades now has been contributing to and examining critically our understanding of the problem. A convincing theoretical treatment of transitional and fully turbulent flow remains of course the prize goal of much research in fluid mechanics. Chou describes an impressive attempt at unravelling the dynamics of homogeneous isotropic turbulence by considering it as a superposition of spherical vortices. While waiting for the 'final' theory of

turbulence, if there were ever going to be one such, however, engineers have to get on with the task of predicting how turbulent flows are going to behave in a variety of situations without the aid of a satisfying fundamental theory. Ohji has presented a very useful survey of the principles and strategies underlying the many methods now in use all over the world for making such flow predictions. He finds it unlikely that only one of these schemes—any one—will survive into the future, but expects that eventually there will be a dualism: one a handy, effective scheme of limited validity, and the other a supersize scheme of allround ability.

It is interesting how, time and again, progress in fluid mechanics has been achieved by a careful visual observation of the flow, aided often by the best assistance that technology can offer at the time. Matsui's survey shows some superb examples of such visualizations, especially of vortices in separated flow. We fear that the photographs as they appear in print here do not do full justice to the originals that Prof. Matsui displayed during the Congress.

These papers on some of the fundamental problems of fluid mechanics are followed by a series of four papers on problems of natural or geophysical interest. Whitham continues his distinguished studies on finite amplitude deep water waves using variational principles. The problem of storm surges, important for many Asian countries, has been studied by P K Das for many years now using linear theory; he presents here an analytical solution of the shallow water equations for a basin of uniform depth, bringing out the relative importance of the divergence and curl of the wind stress. Another striking geophysical phenomenon, crucially important to South Asia, is the monsoons; and Sulochana Gadgil outlines the fluid dynamical problems they pose, in terms of interactions on three different scales, namely cumulus, synoptic and planetary. Consideration of the organization of cumulus clouds leads one naturally to studies of natural convection; Ruby Krishnamurti summarizes the results of her illuminating laboratory experiments, and constructs a mathematical model whose solutions show qualitative similarity to the observed flows.

The rest of the papers are concerned with technological applications. Transonic aerodynamics has witnessed some spectacular theoretical and experimental discoveries in the last decade or two, and we have two papers describing very different approaches to problems in this area. Lin explores the full potential of the simple idea that the slope of the streamline at any point in a compressible flow is not vastly different from that in the incompressible flow past the same body at the same point; Niyogi considers the application of the integral equation method to solve the problem of supercritical flow past a thin symmetric wing at zero incidence. Space technology brings its own special problems in fluid dynamics and heat transfer—often quite different in character from those which aerodynamicists are used to handle. Oshima describes methods now being used to tackle these problems.

Cavitation is of great interest to designers of hydraulic machines, but as a problem in two-phase flows has implications in a variety of other fields. Arakeri discusses the strong connections that exist between phenomena observed in cavitation and those well known in real fluid flow past bodies. Sivasegaram considers work on windmill rotors, a subject that has attracted wide interest in recent years because of the possible potential of wind energy in easing the energy crisis.

Fluid mechanics however is too vast and rich a subject to be covered adequately within the pages of one volume, or during the week that is normally the duration of a scientific meeting. We are therefore under no illusion that these papers survey

all recent developments of interest in fluid mechanics. Nevertheless, we hope that these pages will provide interesting and stimulating reading, and serve to demonstrate—if there were any need to do it—what a wide variety of challenging problems still remain in the attempt to understand and control the diverse phenomena that are exhibited in the flow of even such simple fluids as air and water.

R. NARASIMHA
S. M. DESHPANDE
Special Editors

A glimpse of fluid mechanics research in Bangalore 25 years ago

SATISH DHAWAN

Indian Institute of Science, Bangalore 560 012

MS received 22 July 1981

Abstract. This paper gives a brief historical account of how fluid mechanics research began in the Aeronautical Engineering Department of the Indian Institute of Science. The motivation for the various investigations carried out in the 1950s and 1960s is recalled and some of the major results are summarized.

Keywords. Fluid mechanics; transition; base flows; separation bubbles; wall jets; turbulent spots.

1. Introduction

Fluid mechanics research at the Indian Institute of Science (IISc) has evolved over the years in a spectrum of directions in six different departments, namely, Aeronautical, Chemical, Civil and Mechanical Engineering, Applied Mathematics, and Centre for Theoretical Studies. I would like to recall here how fluid mechanics research began in the Aeronautical Engineering Department, which has the oldest traditions in the subject, and with which I was personally associated.

The Department came into being in 1942 towards the end of World War II, mainly in view of the requirements of the Indian aircraft industry, Hindustan Aeronautics (then called Aircraft) Limited (HAL). Early activities in the Department were chiefly confined to teaching postgraduate courses in aeronautical engineering to engineering graduates; the annual admission was around ten, and there were a few research students as well. The main facility in those days was the 5 ft \times 7 ft wind tunnel having a speed of about 250 ft/s. Dr. V. M. Ghatage who had designed the tunnel had moved on to HAL as chief designer. When I joined the Department in 1951, Prof. O. G. Tietjens was the head of the Department; faculty members included Prof. T. N. Krishnaswamy, Prof. C. V. Joga Rao, Prof. K. Karamcheti, Prof. G. V. Ramana Rao and a few others. Around that time, the Government granted Rs. 16 lakhs (US \$ 200,000 approx.) for developing new experimental facilities. In a period of about five years thereafter, four high speed wind tunnels (1 in. \times 3 in., $M = 2$; 1 in. \times 4 in. and 1 in. \times 2 in. transonic tunnels with ventilated walls; 5 in. \times 7 in. supersonic, $M = 4$), and three low speed wind tunnels (20 in. \times 20 in. boundary layer tunnel, 9 ft \times 12 ft open circuit tunnel and 15 ft diameter spinning tunnel) were established. Figure 1 (plate 1) showing a 1/4 in. blowdown supersonic tunnel is a good indication of how experimental research started in high speed aerodynamics. The compressed air storage for this tunnel consisted of two oxygen tanks from an aircraft. Some pictures of supersonic jet flow were taken in this tunnel using a simple Schlieren set-up (figure 2, plate 2).

Fluid mechanics research started around 1952–53 when the 1 in. \times 3 in. supersonic tunnel and the 20 in. \times 20 in. boundary layer tunnel went into operation (Badri-narayanan 1958, on base flows; Narasimha 1957, on transition). The base flow studies were made in the light of the Crocco-Lees mixing theory, and included investigation of the effect of small bleed on base pressure. The transition studies arose from tests in progress at that time in the 5 ft \times 7 ft tunnel for HAL on the Marut supersonic fighter (HF 24), the Kiran jet trainer (HJT 16), and an advanced double delta configuration. Typical Reynolds numbers in the tunnel were low (about $1.5 \times 10^6/\text{ft}$), and turbulence level was high (about 1–3%). Difficulties were experienced in extrapolating experimental data on these aircraft models, and led to a series of transition studies in the 20 in. \times 20 in. tunnel.

2. Studies in transition

These transition studies were greatly influenced by Emmons's modelling of the transition process. He stipulated that the process is characterised by a source density or spot production function which determines the probability of any point on a surface in the flow experiencing turbulence. This probability, called the intermittency γ , is then given in terms of the spot production function $g(x, z, t)$, x and z being longitudinal and spanwise coordinates, and t time, by

$$\gamma = 1 - \exp \int -g(x, z, t) dx dz dt. \quad (1)$$

Observations at IISc (Narasimha 1957) showed that the breakdown was pointlike and random in time but the events were confined spatially to a very narrow band across the flow; the location of this band also defines the transition 'point' x_t . Various passive disturbance agents were studied, including screens, trip wires, roughness elements, wakes of rods and plates, etc. It was found that the spot production function g could be approximated by a narrow Gaussian distribution centred at x_t . Approximation of this function by a Dirac delta function gives

$$\gamma = 1 - \exp(-A\xi^2), \quad A = 0.412, \quad \xi = (x - x_t)/\lambda, \quad (2)$$

where λ is a measure of the extent of the transition zone, being the distance between the points where $\gamma = 0.25$ and $\gamma = 0.75$. As shown in figure 3, this gives a very good approximation to the intermittency; regardless of the details of the transition agent.

It is possible to make a reasonably complete calculation of the mean flow during transition by using superposition of mean flow velocities in turbulent and laminar flow. In particular, the following two relations, for the velocity profile and skin friction, were found to be fairly satisfactory:

$$(u/U)_{\text{transition}} = \gamma(u/U)_{\text{turbulent}} + (1 - \gamma)(u/U)_{\text{laminar}}, \quad (3)$$

$$c_{f_{\text{transition}}} = \gamma c_{f_{\text{turbulent}}} + (1 - \gamma)c_{f_{\text{laminar}}}. \quad (4)$$

Detailed studies at the National Bureau of Standards (Schubauer & Klebanoff 1955) had just then shown that spot growth is virtually linear and that its shape is preserved as the spot moves downstream.

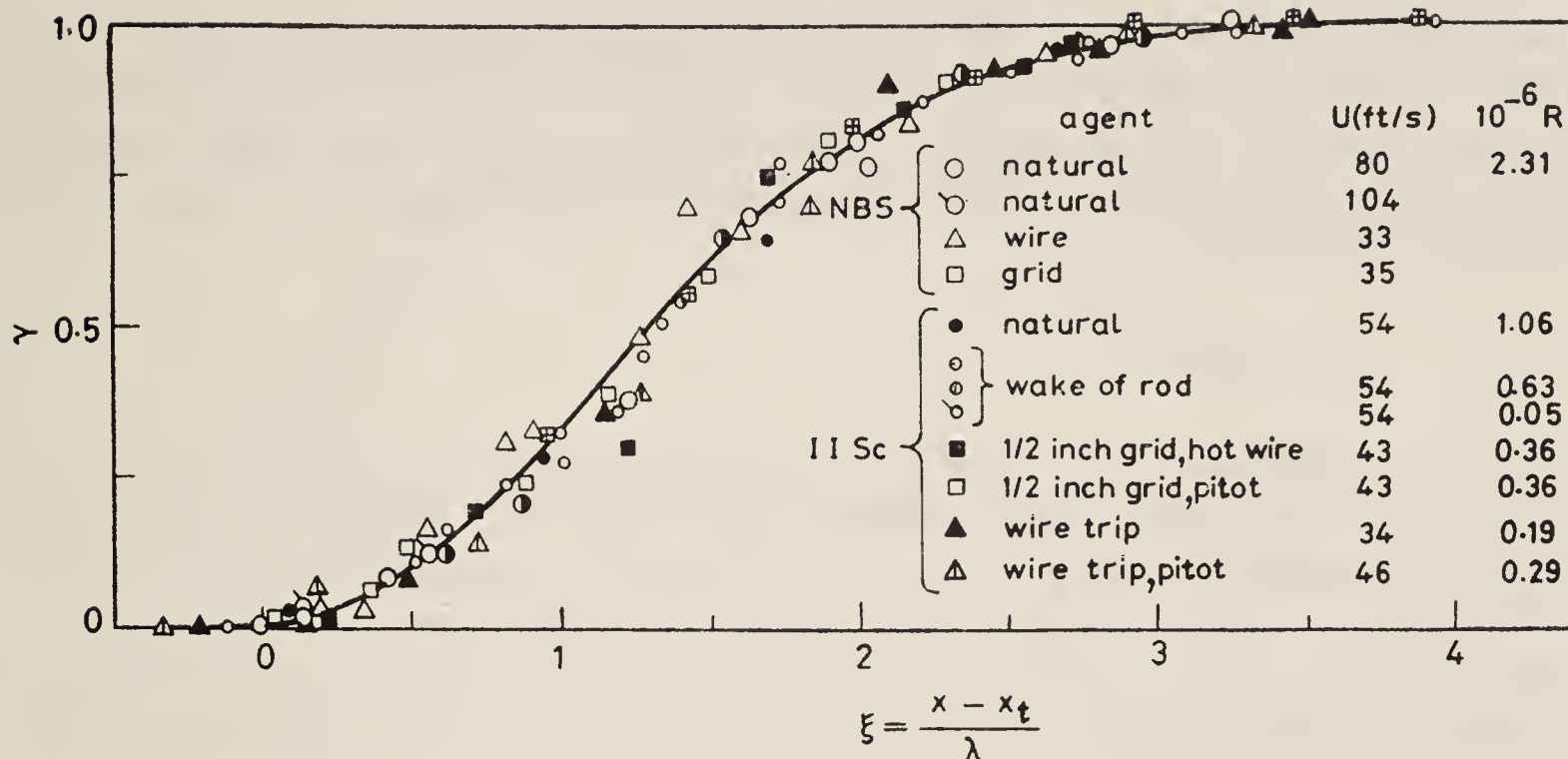


Figure 3. Universal intermittency distribution during transition on a flat plate, with a variety of agents causing transition.

These investigations were extended to the case of a pipe and an axial cylinder. Reynolds had observed that the classical pipe flow had turbulent “flashes”. At Reynolds numbers just above the critical value of about 2000, the flow becomes intermittent, spots grow rapidly into ‘plugs’ of turbulence, and a one-dimensional extension of the arguments underlying (2) explains observed intermittency distributions, which follow the relation (Pantulu 1962)

$$\gamma = 1 - \exp(-B\xi), \quad B = 1.1. \tag{5}$$

Figure 4 shows that the above description is a good approximation at relatively low Reynolds number for various ratios of pipe length to diameter. However, at Reynolds numbers greater than about 5,000, and length/diameter ratios greater than about 75, the turbulence plug production and growth strongly interact with the mean flow, causing reduction in the Reynolds number (for a given pressure drop along the pipe), and suspension of turbulence production, until the plugs are washed out.

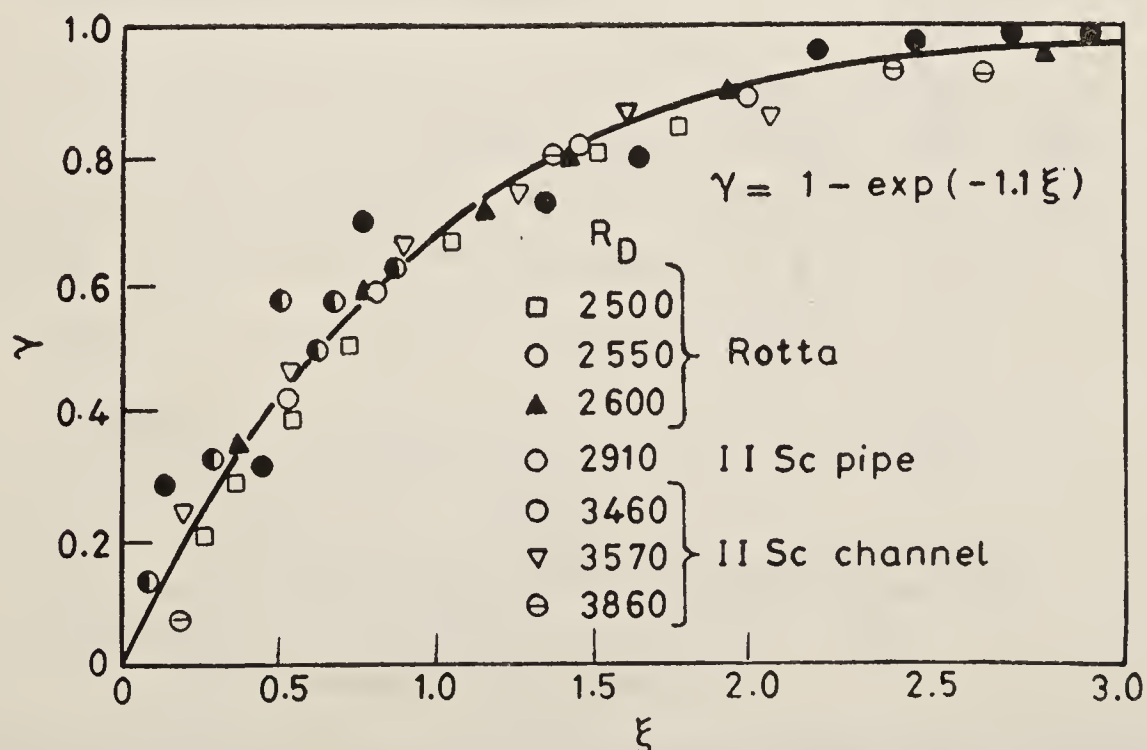


Figure 4. Universal intermittency distribution in duct flow.

The process becomes regular and periodic, and intermittency loses its significance. Figure 5 (plate 3) shows the events as Reynolds number and length-to-diameter ratio are increased. In the range of higher Reynolds number and higher length-to-diameter ratio, the rather regular and periodic turbulence production is characterised by a Strouhal number

$$S^* = nD/U^*,$$

where n = frequency, $U^* = (2\Delta p/\rho)^{1/2}$; S^* depends on the Reynolds number R^* (based on U^*) and the length-to-diameter ratio (figure 6). The propagation speeds of laminar-turbulence interfaces in ducts and boundary layers are shown in figure 7.

Transition on axial cylinders (Rao 1966) has some special features when the radius of the cylinder is comparable to or less than the boundary layer thickness. Stability is enhanced by the fuller profile characteristic of this axisymmetric flow. Except for short distances near the location of the transition agent, the turbulent spots wrap around the cylinder into sleeves and the intermittency distribution can be obtained from one-dimensional theory; so the distribution (5) is valid for this flow also. Furthermore, in fully turbulent flow, the form of the law of the wall has to be modified on account of transverse curvature.

3. Reverse transition

Transition from turbulence to laminar flow was also investigated in supersonic flow around a corner (Vivekanandan 1963), and in a channel with a sudden expansion (Badrinarayanan 1966). Figure 8 (plate 4) shows a Schlieren photograph of supersonic

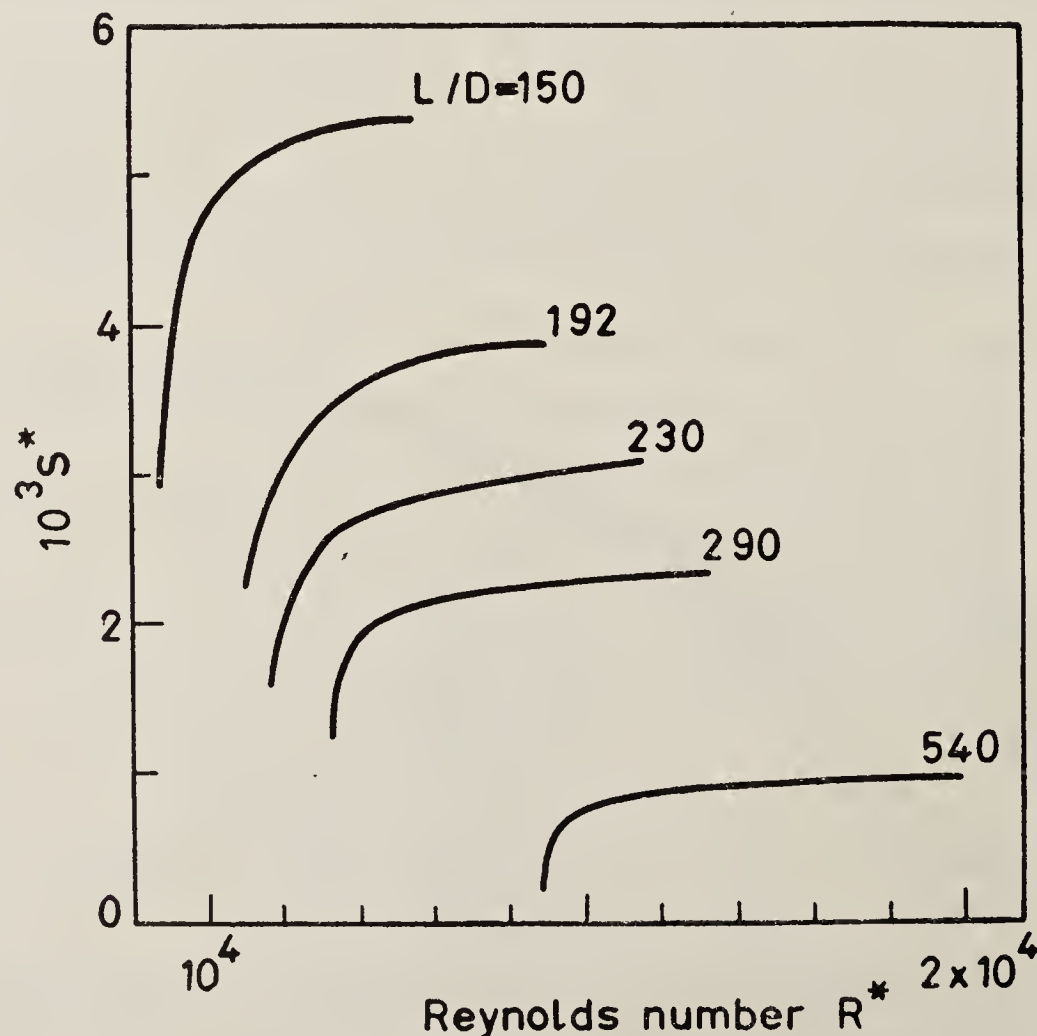


Figure 6. The frequency in the periodic turbulence production regime in pipe flow, as a function of pipe length and a pressure drop Reynolds number.

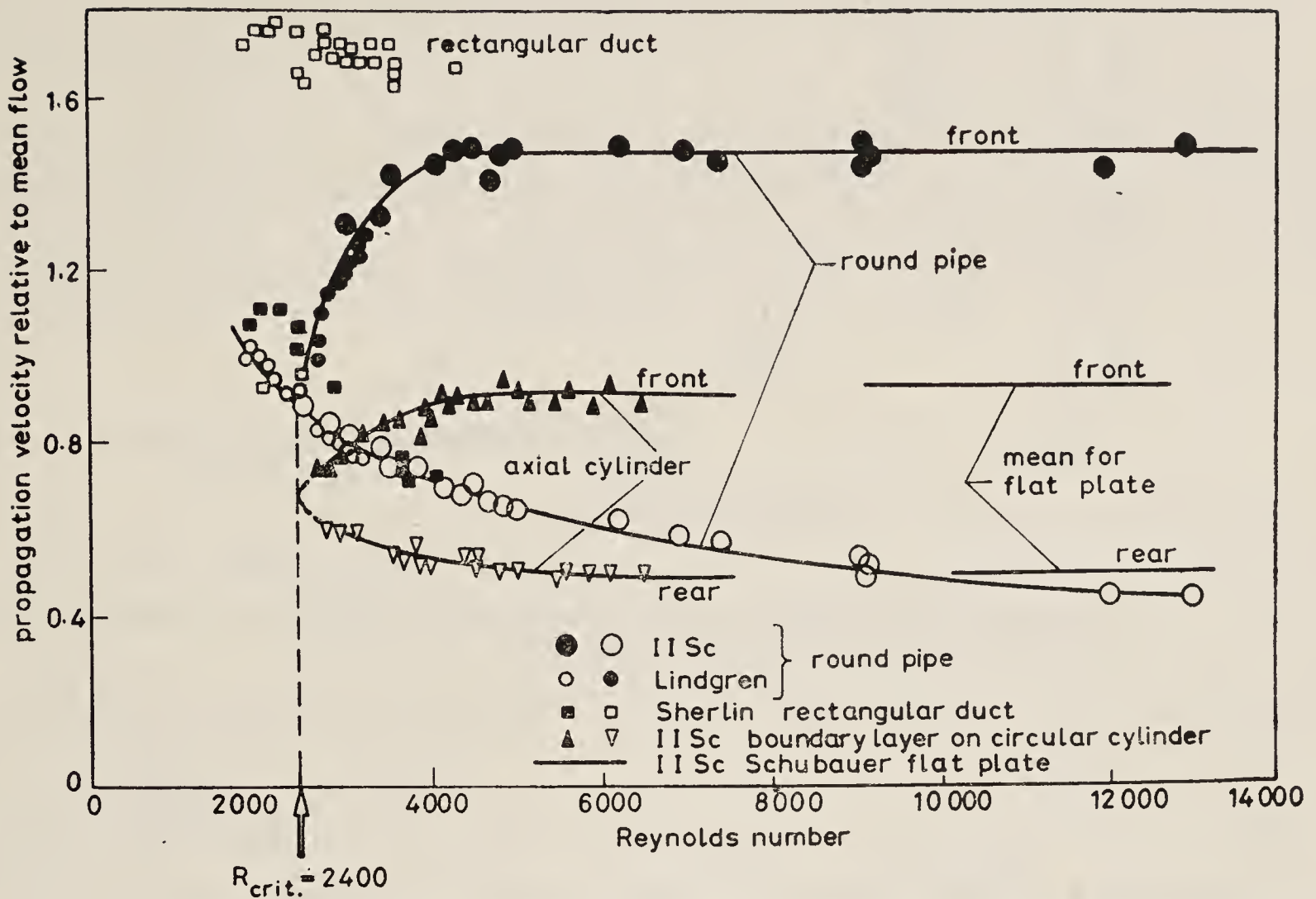


Figure 7. Propagation velocity of turbulent spots and plugs. Reynolds number based on section-average velocity and diameter or height for ducts, and on free-stream velocity and boundary layer thickness for flat plate.

expansion around a corner (Viswanath *et al* 1978). This flow was studied by Vivekanandan using the method of rotational characteristics, and an approximate calculation of the mean velocity profiles was found to be possible. Figure 9 shows the channel used for studying the reverse transition and figure 10 shows the behaviour of several related indicators of turbulence as Reynolds number is decreased.

Relaminarization has been subsequently studied extensively by Narasimha and his co-workers (Narasimha & Sreenivasan 1979).

4. Leading edge separation and laminar bubbles

The phenomenon of bursting of laminar bubbles has been observed on aerofoils with peaky pressure distribution. The adverse pressure gradient near the curved leading edge causes laminar separation and the laminar layer subsequently undergoes transition and reattaches forming a separation bubble. When the angle of attack is in-

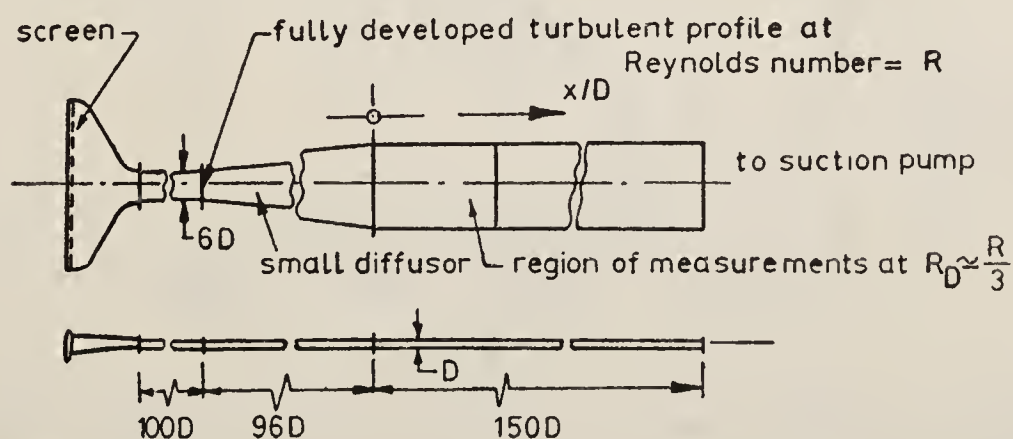


Figure 9. Channel in which the reverse transition from turbulent to laminar flow was studied.

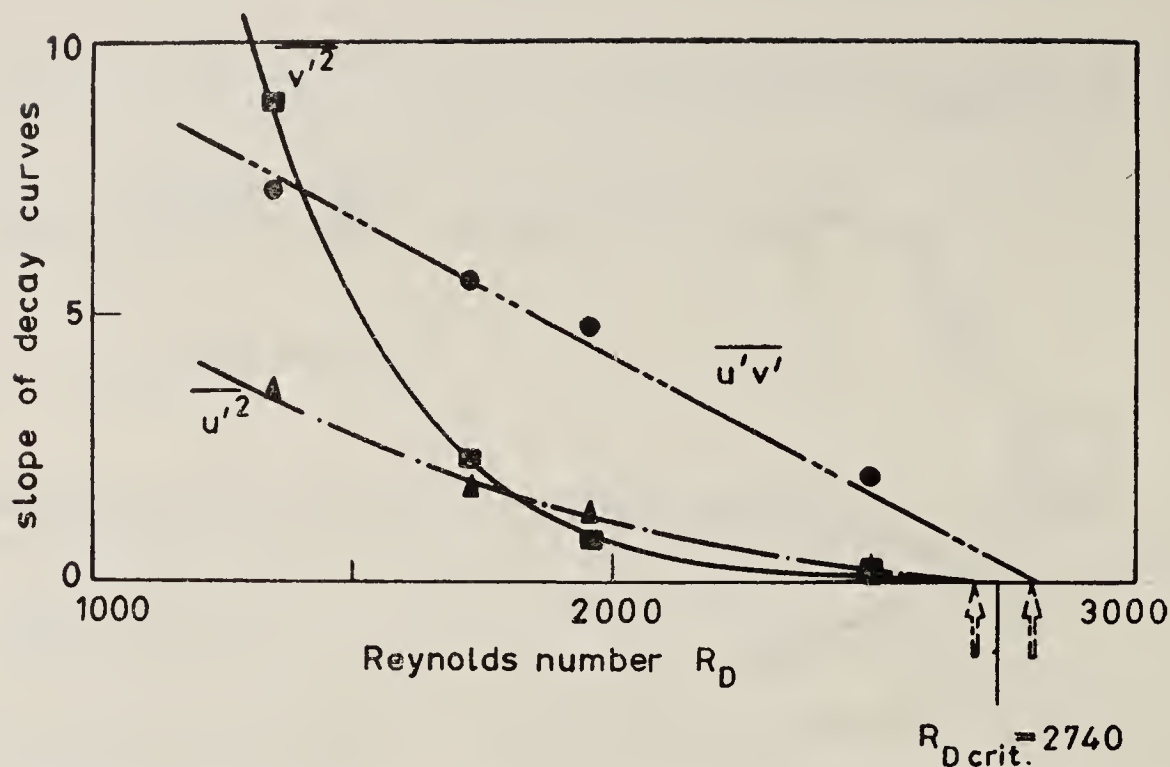


Figure 10. Decay of Reynolds stresses in two-dimensional channel, leading to the determination of the critical Reynolds number.

creased, the bubble length increases; finally the bubble bursts suddenly, which has adverse consequences on C_L vs α characteristics. The studies at IISc attempted to separate the effect of pressure gradient from that of curvature by producing laminar bubbles on a flat plate (figure 11, Ojha 1965). The curvature effects were studied by higher order boundary layer theory where not only the velocity but also velocity gradient at the edge of the boundary layer has to be matched. It was found that convex curvature tends to reduce the skin friction coefficient. An approximate method similar to Pohlhausen's was also developed.

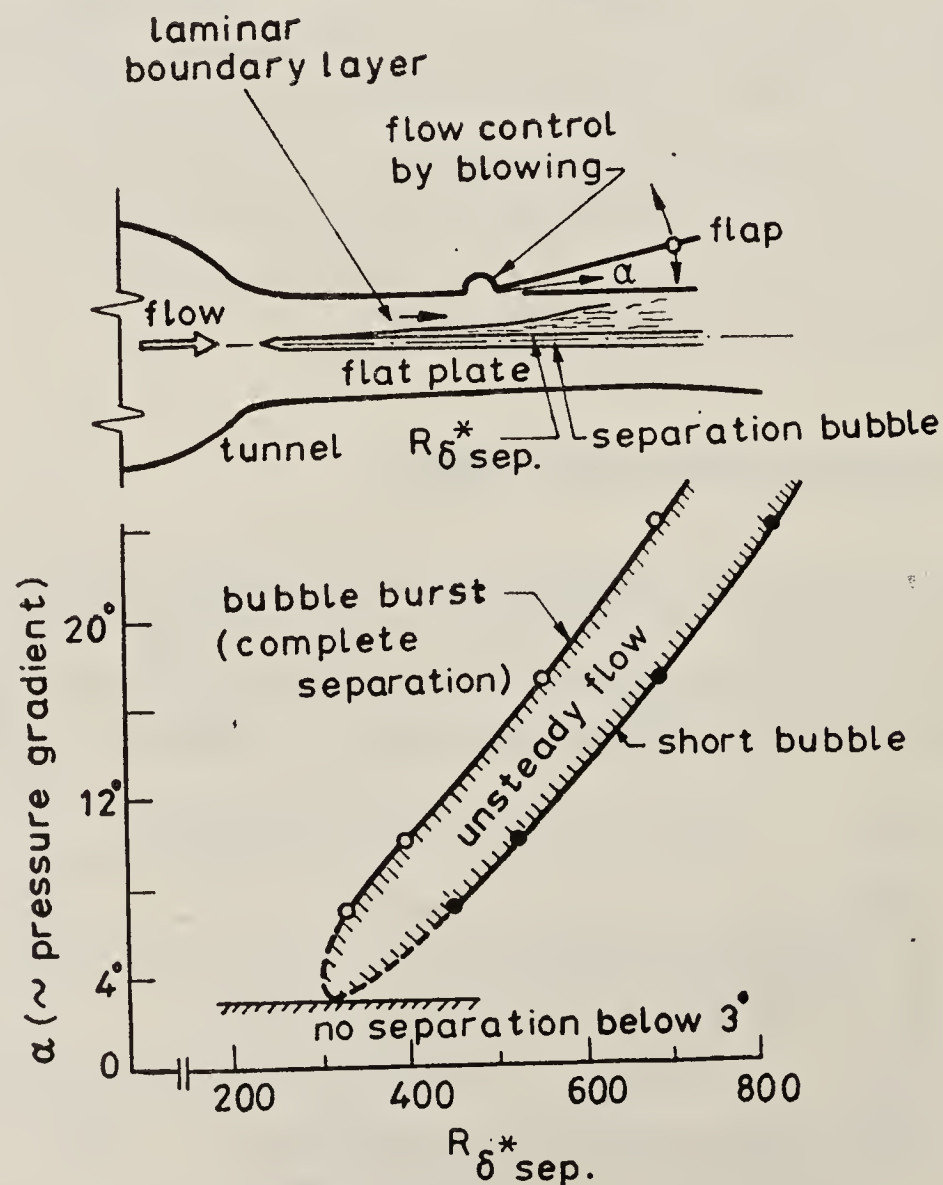


Figure 11. Different regimes of laminar separation bubbles. Also shown (above) is the schematic of the experimental arrangement used for producing separation bubbles on a flat plate.

5. Boundary layer flow control and wall jets

At this time there was significant interest in the intake tests for the Marut supersonic fighter (figure 12, plate 5). Slot blowing needed for velocity profile control in the duct led to interest in wall jets (Parthasarathy 1964). A skin friction balance was built (figure 13) and the effect of external flow on the wall jet was investigated on the basis of direct measurement of skin friction (figure 14).

6. Controlled production of turbulent spots

Although I moved away from active research from 1965, there was a short holiday from administration in 1972, when I was able to return to experimental studies in transition and large-scale turbulent structures. The ideas behind these studies originated from the Bangalore activities. Figure 15 shows the experimental set-up used by me at California Institute of Technology to generate controlled turbulent

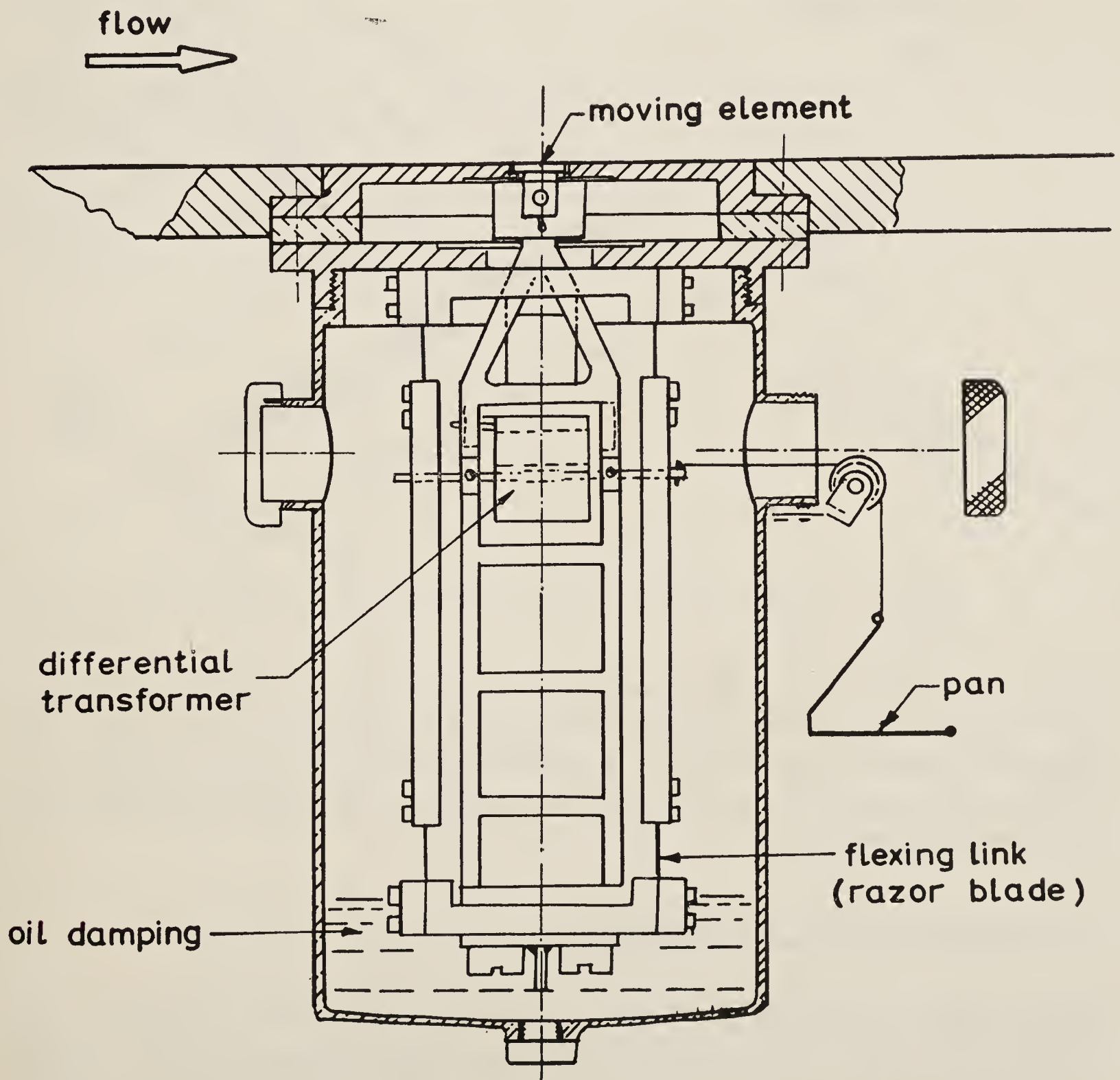


Figure 13. Skin friction balance, used for making wall stress measurements in a wall jet.

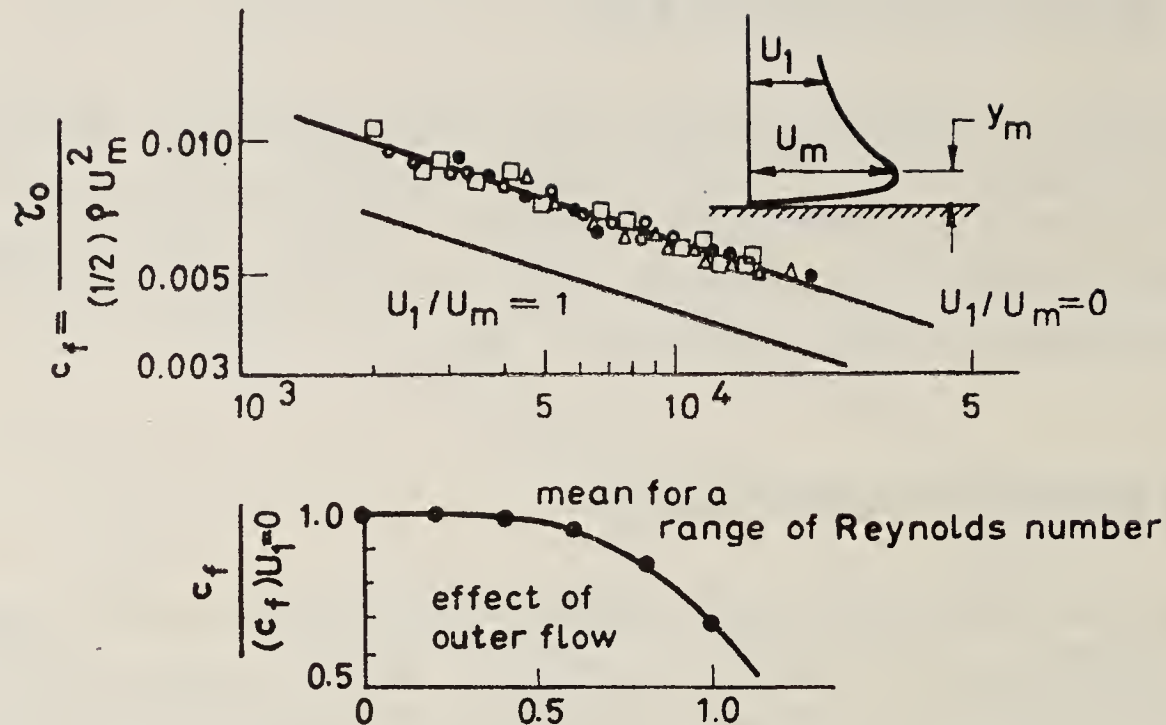


Figure 14. Skin friction in wall jets.

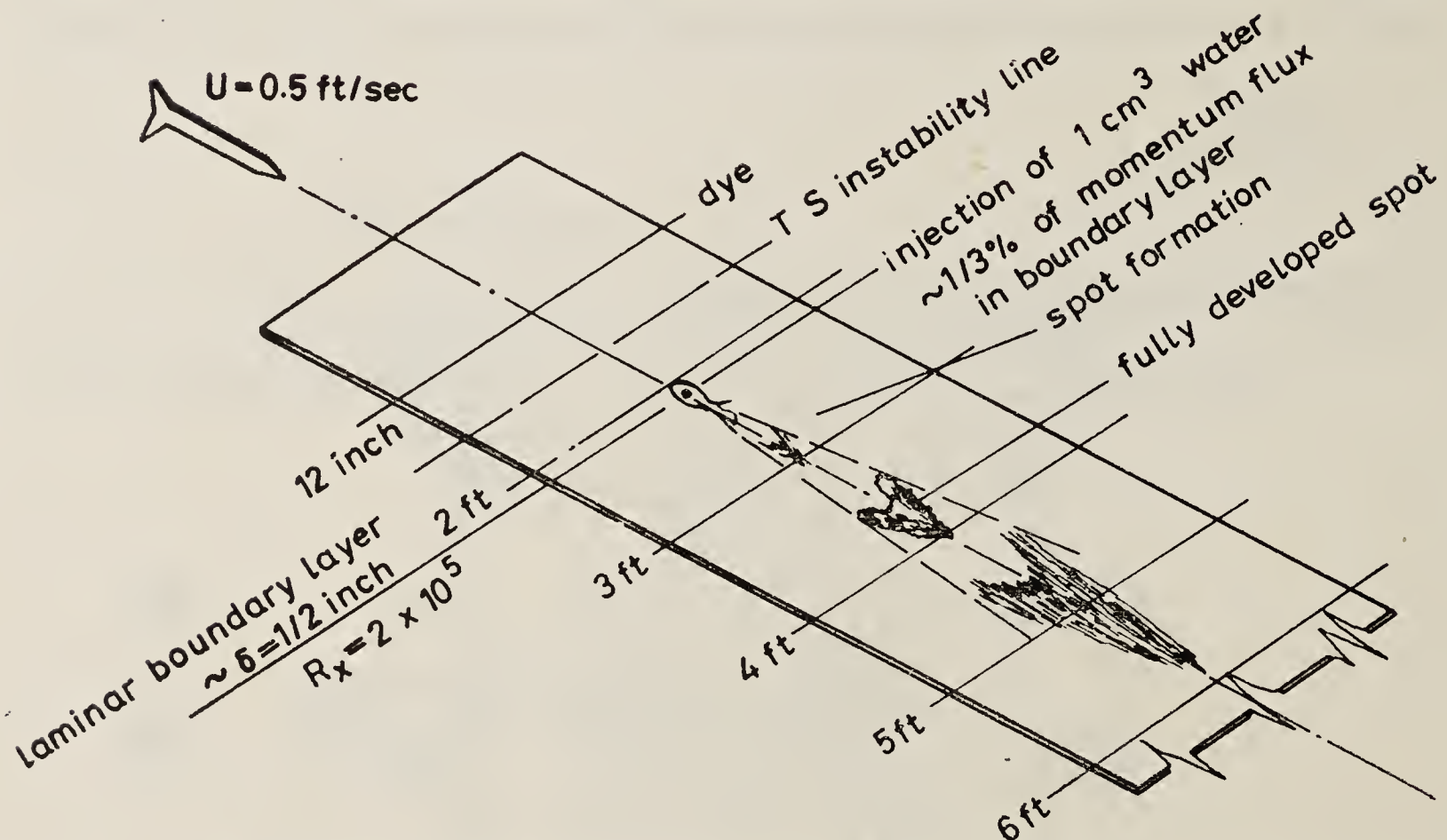


Figure 15. Experimental arrangement for production of turbulent spots by periodic injection of water.

spots by injecting dye in the boundary layer on a flat plate. Flow velocity was about 0.5 ft/s and injection frequency was once in 5 seconds and 2.5 seconds. The Reynolds number at injection was 2×10^5 and boundary layer thickness was 0.5 in. I made a short movie to show how the spots are formed and how they develop their typical arrow-head shape.

7. Concluding remarks and acknowledgements

Experimental work described here was carried out by many of my colleagues, some of whom were earlier students in the Aeronautical Engineering Department. It called for considerable ingenuity and dedication to work under adverse conditions, and the results reported in many papers in journals, not mentioned here, bear testimony to

the spirit of scientific investigation. I should also mention again that I have limited my remarks to investigations that I personally know about, and there were many, which are not mentioned here, which have also contributed significantly to the development of fluid mechanics research in India.

References

- Badrinarayanan M A 1958 *An experimental investigation of base flows at supersonic speeds*. AIISc thesis, Dept. Aero. Engg., IISc
- Badrinarayanan M A 1966 *Inverse transition from turbulent to laminar flow in a two-dimensional channel*. PhD thesis, Dept. Aero. Engg., IISc
- Narasimha R 1957 *A study of transition from laminar to turbulent flow in the boundary layer of a flat plate*. AIISc thesis, Dept. Aero. Engg., IISc
- Narasimha R & Sreenivasan K R 1979 *Adv. Appl. Mech.* **19** 221
- Ojha S K 1965 *A study of laminar boundary layers and separation bubbles near the leading edge of two-dimensional airfoils*. PhD thesis, Dept. Aero. Engg., IISc
- Pantulu P V 1962 *Studies on the transition from laminar to turbulent flow in a pipe*. MSc thesis, Dept. Aero. Engg., IISc
- Parthasarathy S P 1964 *Two-dimensional turbulent wall jets with and without a constant outside stream*. MSc thesis, Dept. Aero. Engg., IISc
- Rao G N V 1966 *Effect of convex transverse surface curvature on transition and other properties of incompressible boundary layer*. PhD thesis, Dept. Aero. Engg., IISc
- Schubauer G B & Klebanoff P S 1955 Contributions on the mechanics of boundary layer transition. NACA T.N. 3489
- Viswanath P R, Narasimha R & Prabhu A 1978 *J. Indian Inst. Sci.* **60** 159
- Vivekanandan R 1963 *A study of boundary layer expansion fan interactions near a sharp corner in supersonic flow*. MSc thesis, Dept. Aero. Engg., IISc

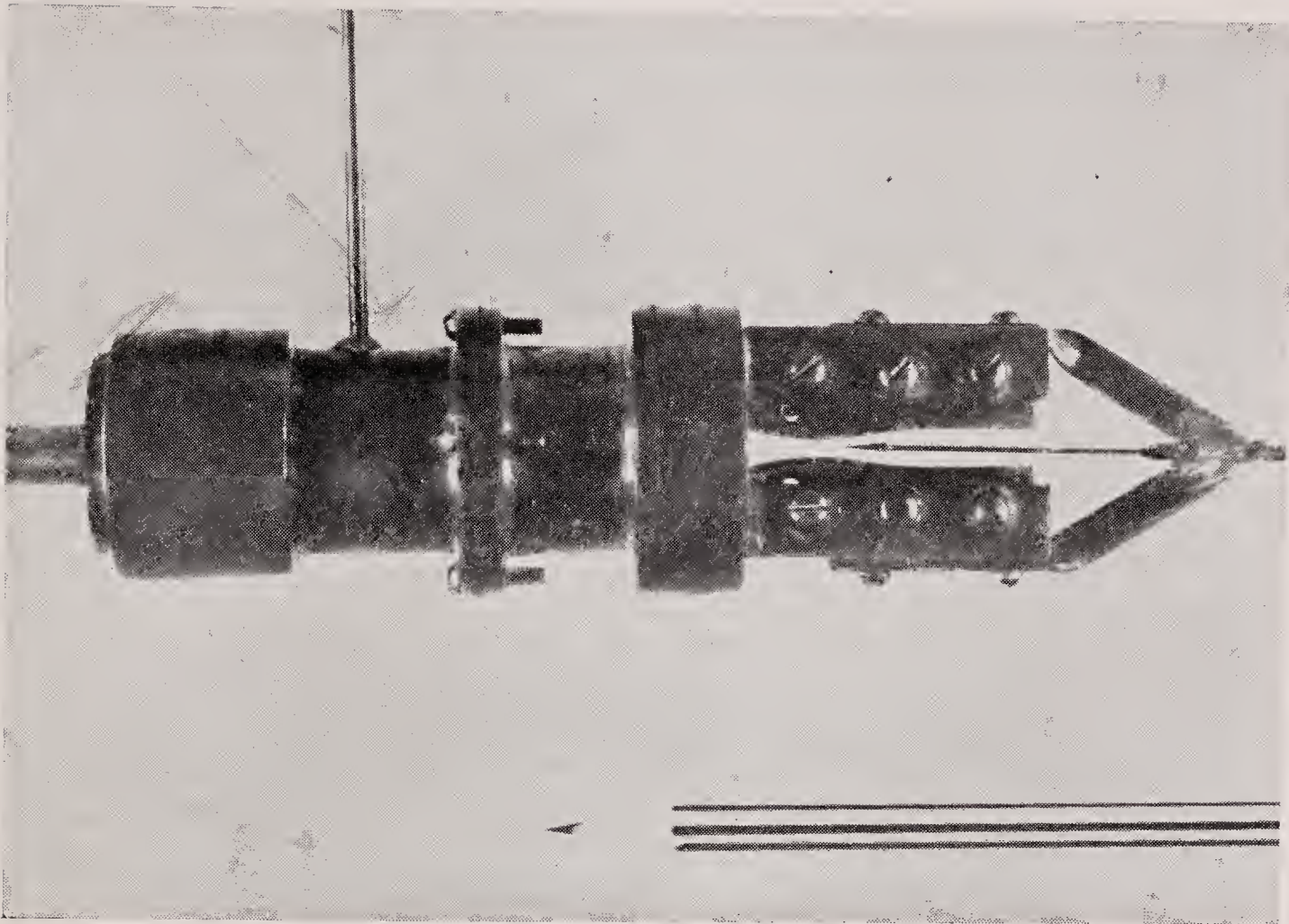


Figure 1. A 5×5 mm intermittent blow-down tunnel, built and operated in 1952 at the Indian Institute of Science (pencil in photograph indicates scale). The tunnel ran on compressed air stored in two oxygen tanks from an aircraft.

Plate 2



Figure 2. A Schlieren photograph taken in the tunnel of figure 1, at a Mach number of 2.3.

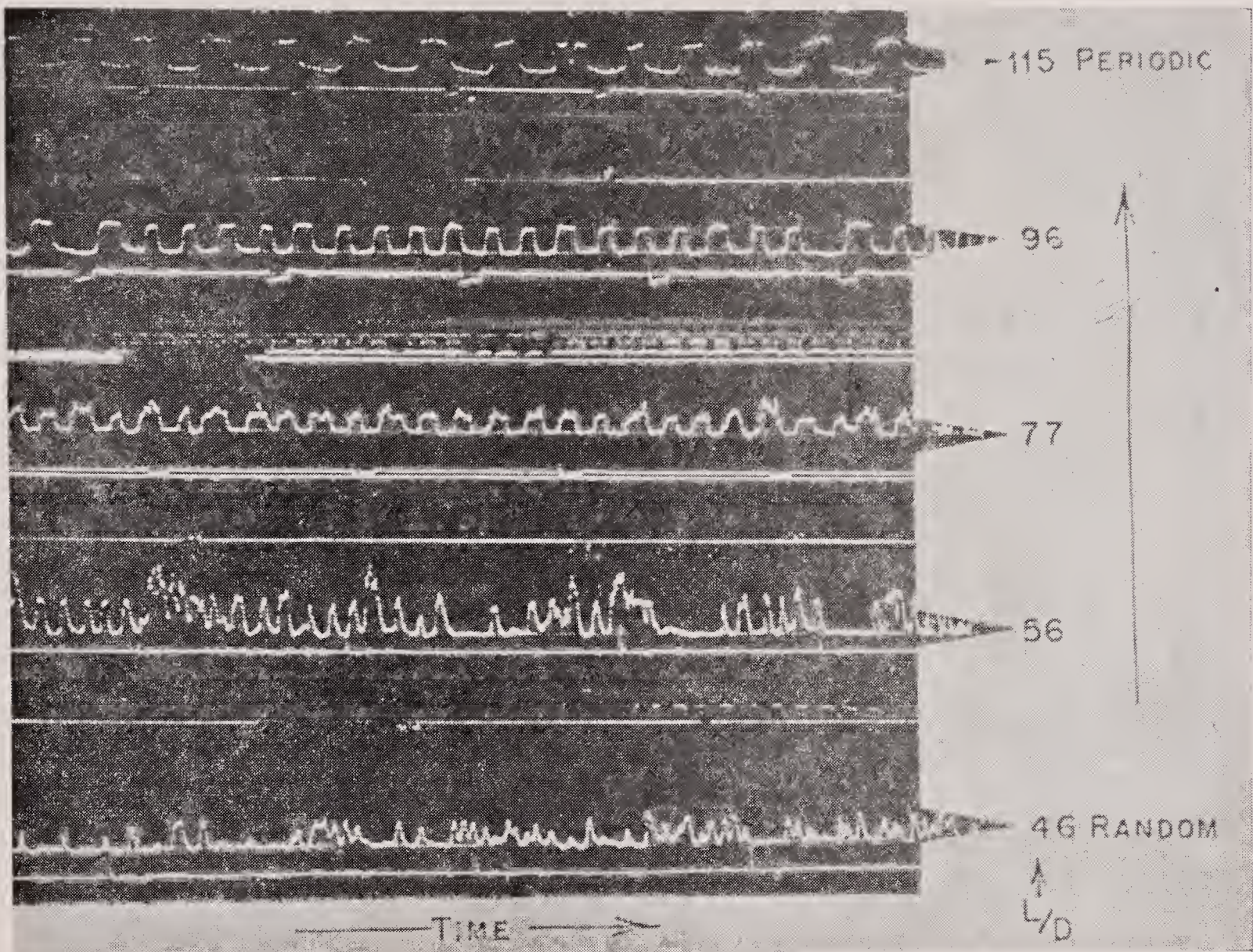


Figure 5. Hot wire traces taken in a pipe, at a Reynolds number $R_D \simeq 5500$, showing the change in character of velocity fluctuations from random to periodic as pipe length increases.

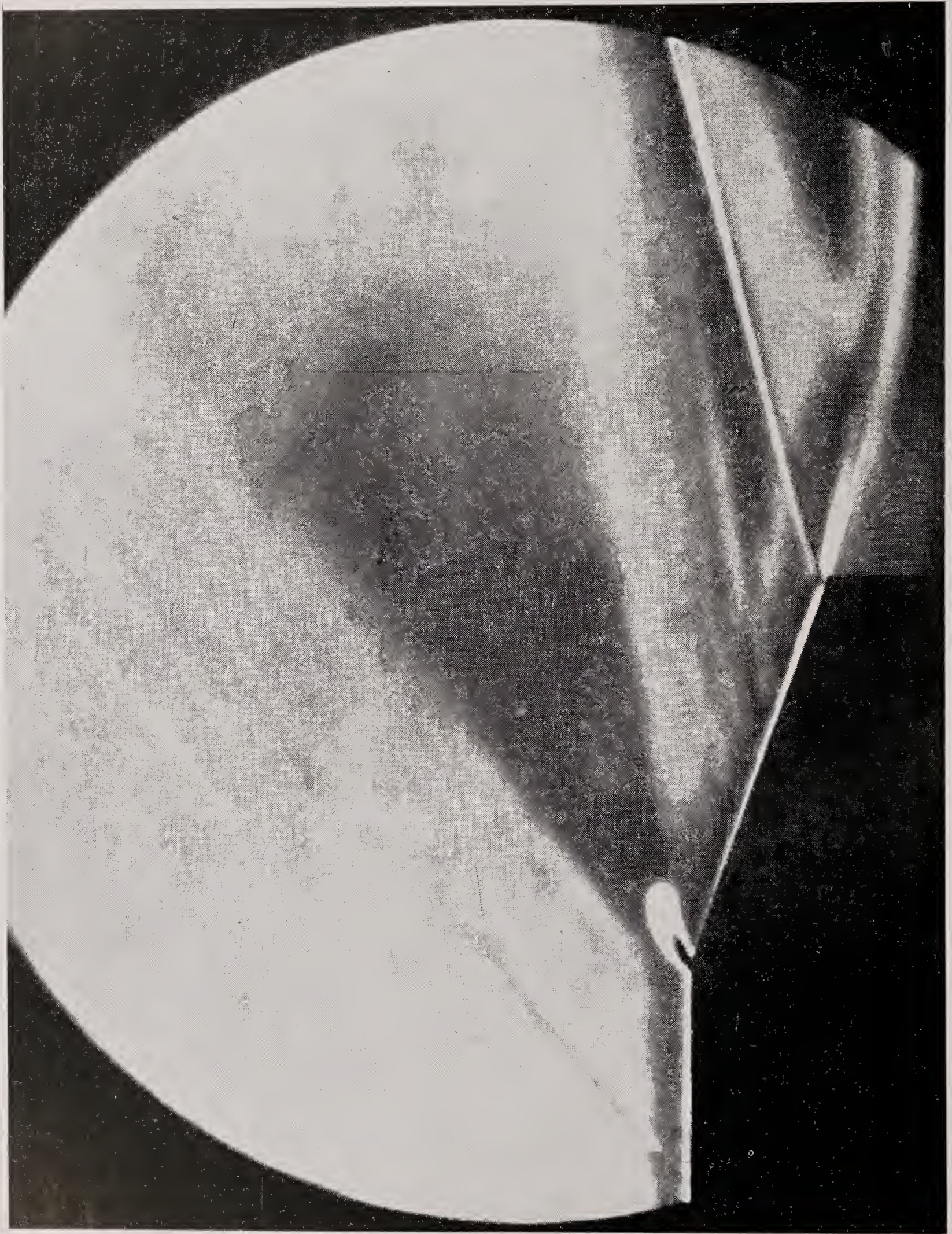


Figure 8. Schlieren photograph of flow past an expansion corner at a Mach number of 1.5. The model is actually a 'boat-tailed' step: a lip shock and the separating shear layer can also be seen.

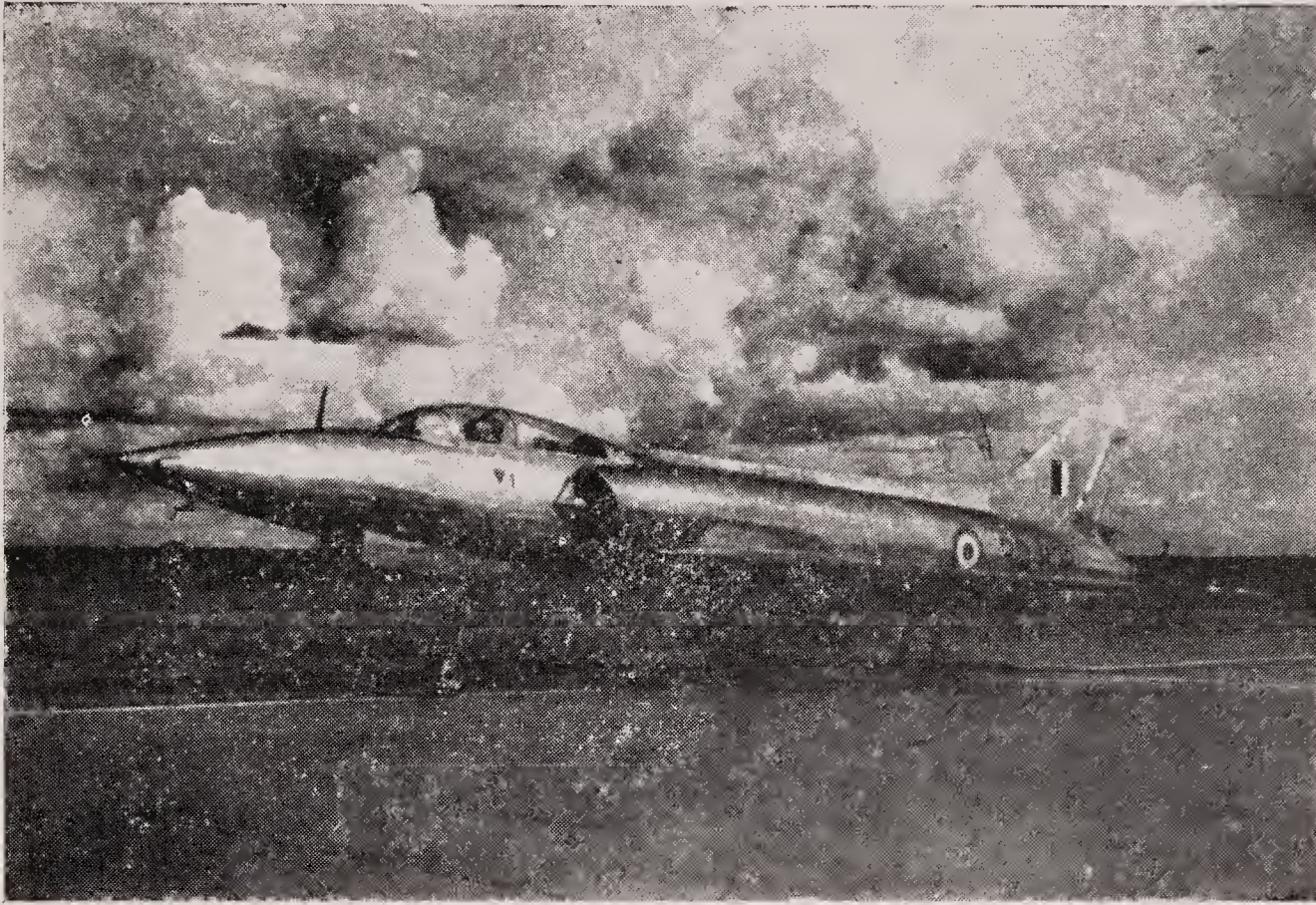


Figure 12. The *Marut* (HF 24) supersonic fighter, designed and manufactured at Hindustan Aeronautics.

Prospects for useful research on coherent structure in turbulent shear flow

DONALD COLES

Graduate Aeronautical Laboratories, California Institute of Technology, Pasadena, California 91125, USA

MS received 9 December 1980

Abstract. Six different flows involving coherent structures are discussed with varying amounts of detail. These are the puff in a pipe, the turbulent spot, the spiral turbulence, the vortex ring, the vortex street, and the mixing layer. One central theme is that non-steady similarity arguments and topology are of the essence of coherent structure. Another is that the Reynolds equations, which are sterile when applied to a structureless mean flow, may be quite productive when applied to a single structure. A third theme is the prospect for at least partial control of technically important flows by exploiting the concept of coherent structure.

Keywords. Boundary layer; coherent structure; Couette flow; mixing layer; pipe flow; transition; turbulence; vortex ring; vortex street.

1. Introduction

This paper is not intended to be either a report on my own research in progress or a review of recent contributions to the concept of coherent structure. It is a personal manifesto which sets out my own views about useful strategies for formulating experiments and for modelling of turbulence.

In the phrase "coherent structure", the word "coherent" means having an orderly and logical arrangement of parts such as to assist in comprehension or recognition. The meaning of the word "structure" is less transparent. At one level, coherent structure can be any feature which attracts attention in photographs of a flow. Flow visualization is always a powerful tool, and never so powerful as when it leads to new discoveries. Examples include the discovery by Kline *et al* (1967) that the sublayer of a turbulent boundary layer is full of streamwise vortices, and the discovery by Brown & Roshko (1971) that the mixing layer is not the featureless wedge of turbulence which it had been thought for many years to be.

At another level, coherent structure can be any flow pattern which survives the operation of ensemble averaging over realizations having a common phase reference. The mark of real commitment to the concept of coherent structure is therefore rejection of the concept of Reynolds averaging in the traditional or global sense. Instead, phase information is retained, at least at the largest local scale of the flow, and a celerity, or phase velocity, is sought which will make the mean flow stationary or nearly stationary in some suitable moving frame. In practice, the question of celerity is often approached initially in terms of interface geometry and eventually

in terms of topology, which is to say in terms of particle paths both outside and inside the structure. I should say that I was first persuaded of the power of this topological approach in its full generality by Brian Cantwell, who was persuaded by Tony Perry, who was persuaded by I know not whom.

Among flow configurations which qualify as coherent structures, some of the best-known examples occur in isolation in the regime of transition from laminar to turbulent flow. These include

the puff in a pipe,
the spot in a boundary layer, and
the spiral in circular Couette flow.

Two other flows which belong in this group but about which not much is known are the puff in a channel and the spot in a free-convection boundary layer. Other structures which occur in isolation but not as part of a transition process, because they appear in laminar as well as turbulent versions, include the line vortex, the thermal in two or three dimensions, the vortex pair, and

the vortex ring.

Finally, there are a number of cases in which laminar or turbulent structures occur naturally in train. The best-known examples are

the vortex street, and
the mixing layer.

In this paper I will discuss, at rather uneven levels of detail, the six coherent structures which are singled out in the last paragraph. My premise is that each structure is defined for practical purposes by its characteristic pattern of centres and saddles in an appropriate coordinate system. The most appropriate coordinate system is assumed to be one in which both the boundary of the structure and the particle paths are as nearly steady as they can be made.

The centres are points of concentration or accumulation of mean vorticity. The saddles are often points of large mean rate of strain, either in shear or in extension. Thus the saddles are likely to be associated with large rates of turbulence production, although the evidence on this point is at present mostly circumstantial.

The concept of celerity needs careful definition. Topology and celerity go together, because the pattern of instantaneous mean streamlines or particle paths is very sensitive to the speed of the observer. A coherent structure may not grow (puff, spiral); or it may grow according to certain essentially inviscid similarity laws (vortex ring, possibly spot); or it may undergo a slow distortion (vortex street, mixing layer, possibly spot) which limits the value of similarity arguments. However, each part of the average structure, including its boundary, presumably moves at a well-defined speed. A case in point is the mixing layer, for which $x-t$ diagrams have been constructed by various observers (Damms & Kuchemann 1972; Brown & Roshko 1974; Acton 1980). Each of these observers chose a particular local feature (not necessarily the same feature) in order to assign a value to the variable x , and to the celerity dx/dt , and each was successful in exposing the phenomenon of coalescence in the mixing

layer. The topological approach can also help to clarify the problem of celerity in cases where this problem does not have a trivial solution, as in the case of the turbulent spot. If particle paths are not known, celerity can sometimes be defined by following points of peak vorticity or centroids of vorticity, as in the case of the vortex street. In my opinion, direct measurements of phase velocity are very unreliable for this purpose (for a typical struggle with the case of vortex evolution in the near wake of a cylinder, see Simmons 1974), as are indirect measurements in terms of time-space correlations. It does not follow that early experimenters who used these techniques were in any doubt about the meaning of their work, as is evident from the fact that Favre and Kovasznyai chose the French word *celerité* to describe their findings quantitatively, rather than the more conventional word *vitesse*.

In this paper I will take up three different but related aspects of each flow, to the extent that I have so far been able to digest the available experimental evidence. One aspect is the topology of the standard structure. Another is the effect of off-design conditions; *i.e.*, the response of the structure to strain imposed by a change in the governing parameters or by the presence of neighbouring structures. The third aspect is the possible role played by the structure in the corresponding technical flow. Two of my six topological sketches (for the puff and the spot) have special elegance and authority because they are based directly on measured data, and thus represent nature. The other four sketches are of lesser quality because they are based at least in part on combinations of flow visualization and conjecture.

2. The puff in pipe flow

Although laminar pipe flow is stable to small disturbances, a well-defined transition regime is known to exist when the entrance flow is highly disturbed and the pipe is sufficiently long. For Reynolds numbers $Re = Ud/\nu$ between about 2000 and 2800 ($U =$ mean velocity, $d =$ diameter), the disturbed flow eventually relaxes far downstream to a statistically steady state of intermittent turbulence. The dimensionless frequency fd/U ($f =$ frequency of passage of turbulent regions) was first measured by Rotta (1956), using an ingenious mechanical method, and by Lindgren (1957), using an optical method. The consensus of these and later measurements by Vallerani (1964) and by Wygnanski & Champagne (1973) is that the frequency fd/U has a maximum value of about 0.025 at about $Re = 2450$, where the celerity is about $0.9 U$. The average interval between turbulent regions is thus about 35 diameters. Given an intermittency of 0.45, this interval can be divided into lengths of about $20 d$ and $15 d$, respectively, for laminar and turbulent regions. For Re between 2100 and 2400, according to Vallerani, the flow at the exit of a very long pipe tends to consist of standard regions of turbulent flow about 15 diameters long, separated by non-standard regions of laminar flow ranging upward in length from about 20 diameters. For Re between 2600 and 2800, the flow tends to consist of standard regions of laminar flow about 10 diameters long, separated by non-standard regions of turbulent flow ranging upward in length from about 10 diameters. In all of these estimates, the most uncertain quantity is intermittency, because the leading interface is not well defined in the lower transition region, and in any event the interfaces are not plane. The term "length" is therefore used very loosely.

A few measurements of celerity have been made in flow with disturbed entry by

Lindgren (1957), Stern (1970), and Wygnanski & Champagne (1973). Below the divide at $Re = 2450$, turbulent regions have approximately constant length and therefore essentially a single celerity, which is most easily measured at the trailing interface. Above the divide, the leading interface moves faster than the trailing one if space is available, as first noted by Lindgren. Hence celerity at these higher Reynolds numbers is usually measured in a different mode. Laminar flow is set up in a pipe with smooth entry, and the time interval is measured (for example) between a local artificial disturbance and the associated response at one or more downstream stations. Most such measurements suffer from deficiencies which raise the question of reproducibility among the various experiments. In some cases (Vallerani 1964, Meseth 1974), the response was observed at only one downstream station, so that the formation process for the turbulent region was not excluded from the measured time intervals. In other cases (Gilbrech & Hale 1965; Sarpkaya 1966), the duration of the disturbance was probably too long, at least in the lower transition region, where a sharp impulsive disturbance is called for. Measurements of celerity at high Reynolds numbers have a particularly *ad hoc* quality in short pipes when transition occurs spontaneously or is triggered artificially in the developing laminar boundary layer (Lindgren 1957; Wygnanski 1970; Wygnanski & Champagne 1973). In such cases it is relevant that the boundary layer in the pipe has thickness $\delta \sim (\nu x/u_\infty)^{1/2}$, from which $x/\delta \sim u_\infty \delta/\nu$. To assure a parabolic laminar profile, the condition to be met is $x/d \sim Ud/\nu$. Detailed calculations and/or measurements (Reshotko 1958; Wygnanski & Champagne 1973) give the constant of proportionality as about 0.1. When this condition is not met, the shape of the laminar-turbulent interfaces will imitate the shape of the laminar profile, and will depend on x/d (Wygnanski 1970; Wygnanski & Champagne 1973; *cf.* Teitgen 1975). Moreover, the proper reference velocity for celerity is no longer the theoretical maximum velocity $2U$ for the parabolic profile, but rather the actual maximum velocity at the station in question (Wygnanski & Champagne 1973). In a short pipe, this velocity may be closer to U than to $2U$, and may vary over the observation distance.

Finally, it is clear that close attention must be paid to flow regulation. If the mean velocity is not regulated by the experimenter (say by use of a sonic orifice, a positive-displacement pump, or a massive upstream flow restriction), it will be regulated by the experiment, and will vary with the relative fractions of laminar and turbulent flow at each instant. This transient effect is probably less important for intermittent flow with disturbed entry than for intermittent flow at higher Reynolds numbers. In cases where enough information is available to judge the matter, flow regulation has often been poor. Lindgren, for example, recognized that his flow circuit was unstable, and that the limit cycle described by Prandtl & Tietjens (1934) could occur in his apparatus.

Experiments with controlled disturbances provide direct access to the phenomenon of splitting discovered by Lindgren, a phenomenon which introduces complications in any study of celerity. In the lower transition regime, one turbulent region can become two, three, four... regions as the structures move downstream, provided again that space is available. Different observers do not agree about the site of this splitting; Lindgren (1957) seems to place the site at the front, while Wygnanski *et al* (1975) seem to place it at the rear. Quantitative information about splitting is rare and inconsistent. Wygnanski *et al* report up to four turbulent regions in train at a

station $450d$ downstream from a single disturbance. Vallerani reports the same number at a station almost an order of magnitude farther downstream in an apparatus having a better-developed laminar profile but having very poor flow regulation. Vallerani also noted substantial changes in the length of laminar regions created by splitting, depending on Reynolds number and on the number of turbulent regions in train. There are evidently several important unresolved issues involving the mechanisms which promote splitting and prevent coalescence of turbulent regions in pipe transition.

Wyganski & Champagne (1973) refer to the turbulent structure within the transition range as a puff, and to the structure above the transition range as a slug. They make the distinction strictly in terms of origin; disturbed entry for the puff, boundary-layer instability for the slug. A distinction is certainly desirable, but I do not think it ought to involve the conditions of origin. I prefer a distinction in terms of operational properties of the structures, based on the well-documented change in behaviour near $Re = 2450$. The only new feature at higher Reynolds numbers is the disappearance of laminar regions at about $Re = 2800$, a disappearance which occurs gradually and may mean only that relatively quiet regions are being classified as turbulent rather than laminar. In this paper the term "puff" always means the structure which is at home in the range of Reynolds numbers from 2000 to 2450.

The puff is a logical candidate for standard coherent structure in pipe flow. Mean streamlines have been measured by Wyganski *et al* (1975) for an ensemble of artificially generated puffs at $Re = 2230$ (a value chosen to avoid splitting), as shown in figure 1. The mean flow should be steady in a coordinate system moving with a celerity of about $0.90U$ to $0.95U$; the value used to construct the figure is not stated, but may be U itself. The puff has a long, rather vaguely defined nose of decaying low-frequency turbulence at the right which is visible in photographs (Lindgren 1959; Mattioli & Zito 1960; Yellin 1966; Wyganski & Champagne 1973) but is missing in the present figure because the interface is represented by the locus of a relatively high fluctuation level ($q'/U = 0.10$ in figure 12d of Wyganski *et al* 1975).

Figure 1 shows that the puff as coherent structure is a vortex ring, a property which I missed completely in my contribution to the 1961 colloquium in Marseille (Coles 1961). The term "vortex" implies here (as it does in the case of the Hill spherical vortex) only the existence of closed mean streamlines in a moving coordinate system, and not necessarily the existence of a local peak in mean vorticity. Given the present view, an explanation immediately presents itself for the strong stabilizing effect of

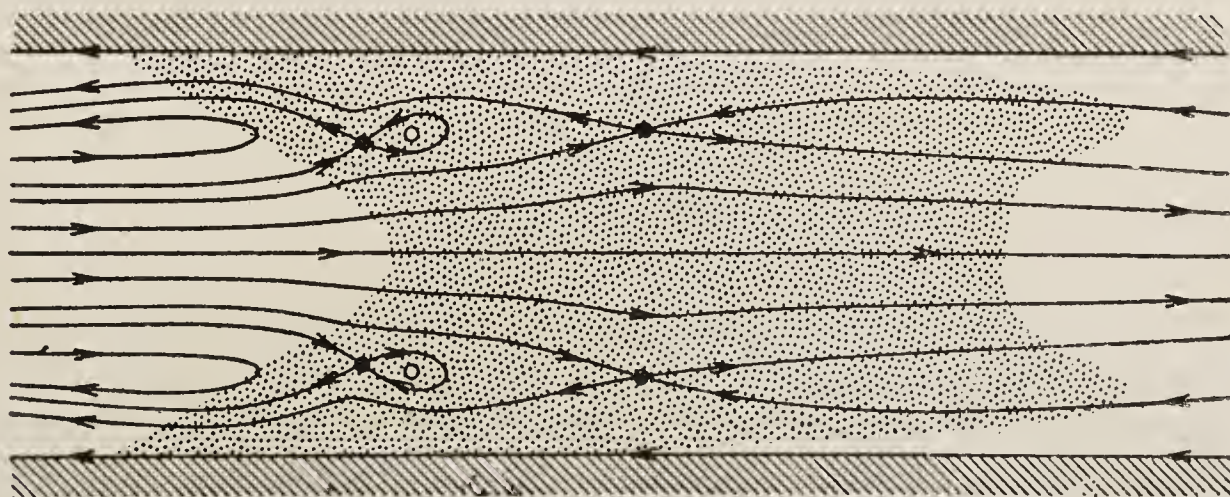


Figure 1. Mean streamlines in a puff, after Wyganski *et al* (1975). The presentation uses coordinates $(z - ct, r)$, where the celerity c is close to the mean velocity U measured over the pipe cross-section. The ratio of the vertical/horizontal scales is about $2.5/1$.

curvature noted by Taylor (1929). Puffs survive in a straight pipe for Re greater than about 2000; but puffs survive in a pipe coiled to a diameter of $100d$, say, only for Re greater than about 5000. In a puff the vortex ring must be the engine which makes the structure run. The secondary flow in the curved pipe presumably disables this engine by destroying the geometric and dynamic equilibrium between the puff and its environment.

Bits and pieces of circumstantial evidence can be found to suggest that the vortex ring is (or is not) the prototype large eddy in fully developed turbulent pipe flow. Lindgren (1969) thought he recognized puffs in flow at Reynolds numbers near 6000. Champagne (private communication) has verified the emergence of puffs when an initially turbulent flow was reduced in Reynolds number from 11300 to 2260 in a long diffuser, but no hard numbers are available. Rubin *et al* (1980) suggested that the length of a slug might be quantized in multiples of $25d$, but their evidence is not completely persuasive.

Several investigators have reported dimensionless frequencies associated with coherent events in fully developed pipe flow at quite high Reynolds numbers, far above the transition range. In the dimensionless form TU/d (T = mean period between events), these frequencies can be roughly interpreted as spacing in diameters, given the celerity of $1.0U$ to $1.1U$ implied by time-space correlations in figure 20 of Sabot & Comte-Bellot (1976) or figure 8 of Hassan *et al* (1980). This quantity TU/d tends to fall in the range from 10 to 20 if it is defined by a weak maximum in the auto-correlation of $u(t)$ (Mizushima *et al* 1973) or by intervals between bursts according to Blackwelder's burst-detection scheme (van Maanen 1980). On the other hand, the quantity TU/d tends to fall in the range from 1 to 2 if it is defined by a quadrant analysis of $u'v'$ (Sabot & Comte-Bellot 1976) or by bursts of high-frequency fluctuations in $\partial u/\partial r$ (Heidrick *et al* 1977). The smaller values for TU/d suggest that structural details are being observed on a scale one order of magnitude smaller than the scale of the main structure. If so, the corresponding structural details should also be encountered in other flows, and this may be so. However, the implication that a structural hierarchy may develop at high Reynolds numbers is far beyond the range of the present paper. In the case of pipe flow, a serious further difficulty is the finding by Sabot & Comte-Bellot (1976) that large excursions in $u'v'$ in both directions are common on the pipe axis. This finding is not consistent with a vision of coherent structure in fully developed pipe flow as an irregular train of vortex rings. The matter needs clarification, perhaps by use of conditions requiring simultaneous large-scale maxima in local wall shearing stress and/or local pressure gradient at several points along and around the pipe.

3. The turbulent spot in a laminar boundary layer

If it was ever supposed that boundary-layer transition might involve a continuous range of states from laminar to turbulent, this supposition should not have survived Dryden's observations of intermittency (Dryden 1936). A plausible but wrong explanation of these observations might have been that a continuous interface exists between laminar and turbulent regions and moves erratically back and forth like the interface between shore and ocean at a beach. Some experiments in another context, and a powerful stroke of intuition, led Emmons (1951) to the correct explanation in

terms of turbulent spots, and this explanation was promptly verified by Schubauer & Klebanoff (1955).

Except for one paper by Dhawan & Narasimha (1958) on the connection between spot formation and growth and boundary-layer transition, one paper by Elder (1960) on the question of spot origin, and some unpublished flow-visualization movies by Head, interest in the turbulent spot languished until the rise of the coherent-structure concept. Recent contributions by Coles and by Wygnanski and their co-workers (Coles & Barker 1975; Wygnanski *et al* 1976; Cantwell *et al* 1978; Zilberman *et al* 1977; Haritonidis *et al* 1978; Coles & Savas 1980) illustrate two quite different points of view toward the problem. Wygnanski invariably emphasizes the interaction between spot and ambient flow. For an isolated spot, for example, he consistently measures deviations from an undisturbed state which includes the laminar boundary layer. Coles, on the other hand, thinks in terms of an asymptotic state in which the laminar boundary layer is reduced to a vortex sheet on the surface. Since this sheet has no thickness (no viscous scale), it is permissible to force a conical approximation in order to gain easy access to the powerful machinery of non-steady similarity. These two points of view are not mutually exclusive; they are simply different.

Another difference on the question of structure is more fundamental. Coles & Barker (1975) concluded that the main feature of the spot was a single large Λ -shaped vortex, located under the ridge of maximum thickness. This conclusion was originally based on weak evidence for instantaneous mean streamlines and on the correctness of a plausible guess as to the characteristic celerity of the vortex in the plane of symmetry. Wygnanski *et al* (1976) did not endorse either the guess or the conclusion, although their own more extensive measurements, particularly of the mean velocity normal to the wall, might suggest to some the presence of just such a vortex and give some information about its spanwise strength and extent. Support for the large-vortex view is also provided by measurements by Handa (1976). Cantwell *et al* (1978) again made the point about the vortex, using the method of non-steady similarity, and proposed a celerity of $0.77 u_\infty$ in the plane of symmetry (subject to the influence of a small negative pressure gradient). Their main topological result is reproduced in figure 2. They also concluded that most of the entrainment in a spot occurs along the trailing interface as the spot is overtaken by faster-moving free-stream fluid. Much of this work was aimed at relatively primitive issues, and none of it includes enough detailed data about fluctuations (or about mean particle paths in three dimensions) to allow

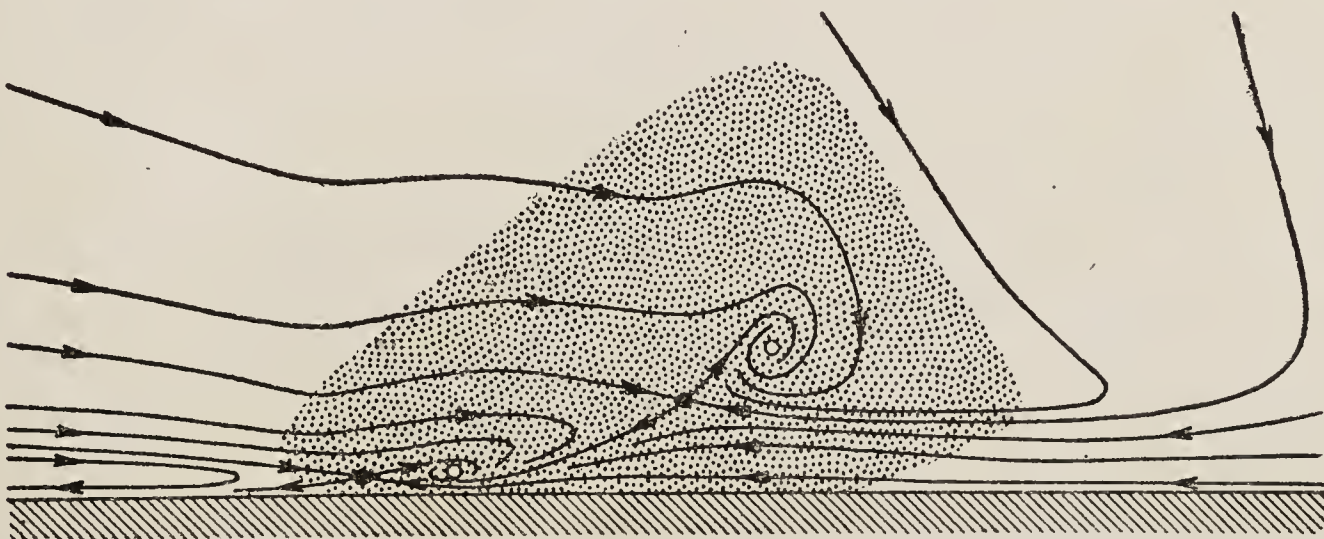


Figure 2. Mean particle paths in the plane of symmetry of a turbulent spot, after Cantwell *et al* (1978). The presentation uses non-steady similarity coordinates $(x/u_\infty t, y/u_\infty t)$. The ratio of the vertical/horizontal scales is about 14/1.

a complete quantitative analysis of structure. The spot therefore represents a formidable piece of unfinished business. In fact, the prospect of having to establish experimentally the effects of pressure gradient, longitudinal curvature, mass transfer, compressibility, etc., is more than formidable; it is mind-boggling.

One property attributed to the spot, for example by Schubauer & Klebanoff (1955), is that it can grow in size only if the Reynolds number in the ambient laminar boundary layer is large enough to support amplification of Tollmien-Schlichting waves. I have some reservations about this property, because two other structures, the puff and the spiral, occur in laminar flows which are confidently believed to be stable to infinitesimal disturbances. Although the puff and the spiral have fixed volumes, they both entrain (and de-entrain) fluid along part of their bounding interfaces, and must therefore share with the spot the property that they provoke some kind of strong local instability in the vorticity-bearing ambient flow.

A related and quite remarkable phenomenon reported by Wygnanski *et al* (1979) is the appearance of regular wave packets, bearing a strong family resemblance to Tollmien-Schlichting waves, near the wing tips of a spot. If these wave packets can break down into new turbulence, as they apparently do, it should be possible for the volume of a turbulent spot to change essentially discontinuously. However, there is no direct evidence of such behaviour in any of the available flow visualization. The phenomenon of eddy transposition reported for certain spot arrays by Coles & Savas (1980) is probably closely related to Wygnanski's discovery, and further suggests the possibility that the normal processes of entrainment and energy transfer can be modified when downstream structures are shielded by upstream ones.

Flow-visualization photographs of spots have been published by several investigators (Elder 1960; Cantwell *et al* 1978; Falco 1979; Gad-el-Hak *et al* 1980; Matsui 1980). When dye or smoke is used as a passive contaminant and is properly placed in the flow, the large Λ -vortex promptly materializes as a locus of accumulation for the contaminant. Heat has also been used as a passive contaminant, with a similar result, by Van Atta and Helland (1980). Other flow visualization using dye by Coles (see Cantwell *et al* 1978) and by Gad-el-Hak *et al* (1980) leaves no doubt that turbulent wedges and regions of turbulent transverse contamination contain spot-like structures. Some experiments on spots in train by Coles (unpublished) and by Wygnanski (1979) suggest that the main vortex structure is the last feature to be affected by interactions due to growth. Modulation of a periodic spot-generating disturbance by subharmonics of the fundamental frequency might therefore shed considerable light on coalescence processes for the spot without some of the problems which are caused by jitter when the same technique is applied to the mixing layer.

A central issue in much of this research is the role of the spot as prototype large eddy for the boundary layer. I cannot do justice to this issue here. It may be that the isolated spot, which can apparently grow indefinitely, should be viewed as an alternative flow to the boundary layer in the same way that the slug is an alternative flow to fully developed pipe flow. If so, a more complicated structure, almost indistinguishable from a boundary layer, might eventually develop. An artificial spot in a crowd behaves differently. It tends to be about 10δ long and 3δ wide, according to estimates from different sources (Zilberman *et al* 1977; Haritonidis *et al* 1977; Savas 1980), but little else is known about its structure. The main obstacle to progress at the moment is lack of a quantitative technique for observing velocity in three dimensions.

4. Spiral turbulence in circular Couette flow

Roughly speaking, spiral turbulence is characteristic of transition for flow between concentric rotating cylinders in the absence of Taylor instability. The spiral turbulence was discovered by Coles (1965), using flow visualization, during a general exploration of transition phenomena in circular Couette flow. One special case was studied quantitatively by Van Atta (1966) in an important early contribution to research on coherent structure, complete with use of digital techniques to define the flow at constant phase. The spiral structure apparently appears when the gap is narrow, but not too narrow. It has been observed for radius ratios of 0.80 and 0.89, for example, but not for radius ratios of 0.50 or 0.96, at least up to moderate speeds (Snyder 1970). For one case of opposite rotation at cylinder Reynolds numbers chosen to minimize dispersion, Van Atta found the spiral flow to be unequivocally stable for a radius ratio of 0.89 and an aspect ratio (length/gap ratio) of 28, but unstable, in the sense that the spiral occasionally changed hand, for an aspect ratio of 18.

The basic structure of the spiral turbulence is almost certainly a single helical vortex. The mean flow is three-dimensional but steady in a coordinate system rotating at approximately the mean angular velocity of the two cylindrical walls. A section through this steady flow is shown unwrapped in figure 3. The laminar-turbulent interfaces are accurately placed in the figure, but the mean streamline pattern is approximate.

The spiral flow seems to be a near relative of the puff in a pipe, except that the energy supply comes from moving walls rather than from the pressure field. The common property is that the mean volume of turbulent fluid is constant, so that entrainment is precisely balanced by de-entrainment. This property at one time seemed to me to be more mysterious than it actually is. Observations by Coles & Van Atta (1966) show that the spiral structure makes an angle of about 30 degrees with the plane of the paper, and that the mean flow has a strong axial component (having, of course, a mean value of zero over the annular cross-section). The phase of this axial component is such that the mean flow near the de-entrainment interfaces is nearly parallel to these interfaces. De-entrainment must therefore be essentially a decay process which proceeds until the fluctuation level is low enough to establish that an interface must exist. This decay process, in company with the nearby entrainment

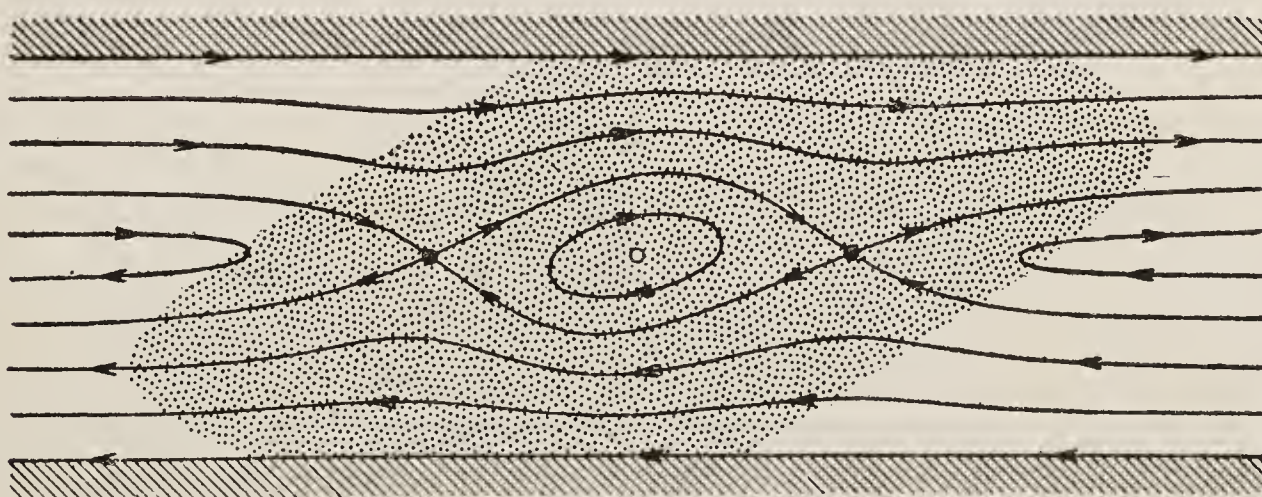


Figure 3. Conjecture for mean streamlines in spiral turbulence, based on measurements by Coles & Van Atta (1967). The presentation uses unwrapped coordinates $(r, \theta - \omega_c t)$, where the celerity ω_c is close to the arithmetic mean of the two wall velocities ω_0, ω_1 . The ratio of the vertical/horizontal scales is about 12/1.

process and whatever viscous and pressure forces turn the flow, presumably determines the spiral angle. A similar decay process, with mean flow nearly parallel to the interface, must determine the leading-edge angle for the spot (Coles 1961; Cantwell *et al* 1978) and the length of the long nose for the puff.

5. The turbulent vortex ring

Vortex rings come in laminar and turbulent versions, with an intervening transition. Much of the literature on vortex rings is naturally concerned with this transition, and specifically with an elegant instability in which azimuthal waves appear on the vortex core when the core is sufficiently thin. To describe the turbulent regime which is of interest in this paper, it is reasonable to ignore the viscosity of the fluid, leaving only the initial momentum ρJ (say) to characterize the motion at stations far from the orifice. Appropriate non-steady similarity coordinates are therefore $(r/J^{1/4} t^{1/4}, z/J^{1/4} t^{1/4})$. The local Reynolds number for the ring varies like $t^{-1/2}$ and hence decreases continuously. The motion must eventually decay. An important element in this decay process, according to dye flow visualization by several investigators (Johnson 1970; Maxworthy 1974; Schneider 1980; Glezer unpublished), is shedding of vorticity into the wake. One anomaly which has to be resolved is that photographs seem to show the direction of dye transport in the near wake to be opposite to the direction of fluid transport required for entrainment.

The similarity variables just described for the turbulent vortex ring have been invented and re-invented several times (Grigg & Stewart 1963; Richards 1965; Johnson 1970; Lugovtsov 1970; Kovasznay *et al* 1973). In no case have these variables been fully exploited, nor have sufficient experimental data been obtained to resolve important structural questions about entrainment and turbulence production. Even given suitable non-intrusive instrumentation, it is a major difficulty that the trajectory of successive rings is subject to considerable dispersion, so that statistical quantities are likely to be even less precisely defined than is usually the case in work on coherent structure.

The sketch in figure 4 is my present conjecture as to probable mean particle paths

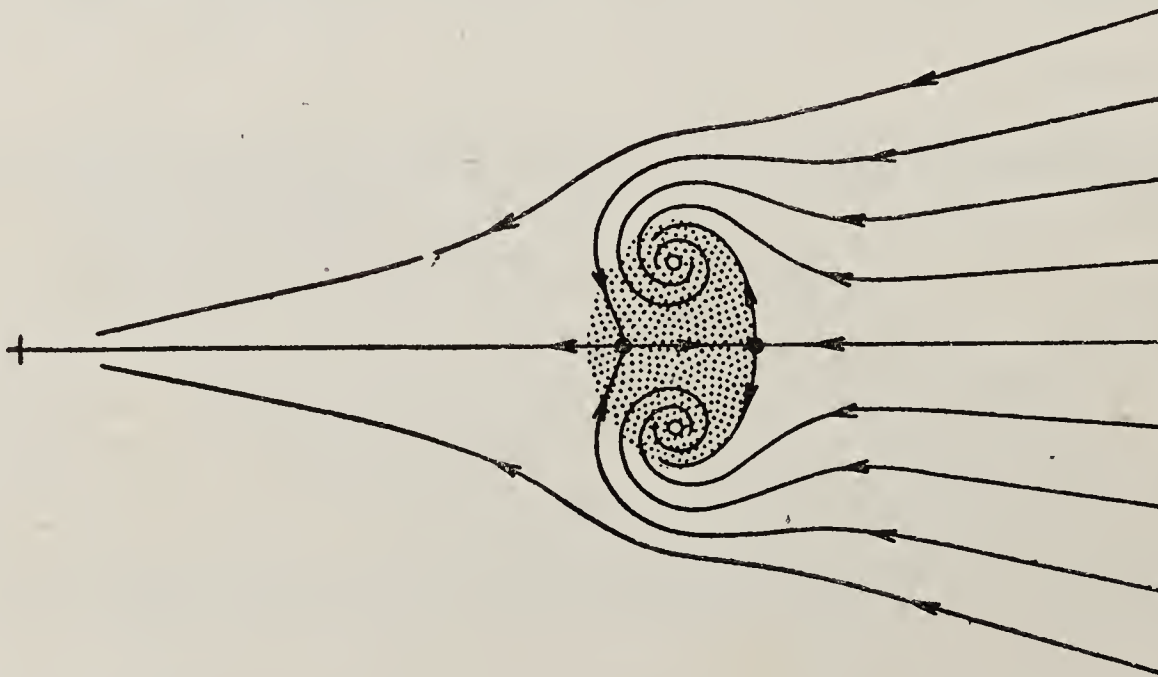


Figure 4. Conjecture for mean particle paths in a turbulent vortex ring based on computations by Turner (1964) and on experiments in progress at CIT by Glezer. The presentation uses non-steady similarity coordinates $(z/J^{1/4} t^{1/4}, r/J^{1/4} t^{1/4})$, where ρJ is the initial momentum. The proper scales are at present uncertain.

in non-steady similarity coordinates for a turbulent vortex ring with a thin core. However, the structure in the sketch is not a likely candidate for prototype large eddy for the circular jet. The growth rate is much too slow. In this respect the vortex ring is very like the line vortex in a mixing layer, and very unlike the spot in a boundary layer. Coalescence, if it occurs, must be a very complex phenomenon. Several fascinating studies of the behaviour of non-circular rings and of multiple-ring interactions have demonstrated the occurrence of ringing, fusion, fission, and various other processes which can be roughly described as excitations or as collisions (Kambe & Takao 1971; Oshima 1972; Viets & Sforza 1972; Fohl & Turner 1975; Oshima & Asaka 1975, 1976, 1977a, b).

Another large part of the literature on vortex rings deals with effects of buoyant forces. A thermal, whose momentum is continuously changing, is not the same as a vortex ring, whose momentum is fixed when it is formed. Nevertheless, these two motions are often considered together, and similarity arguments are in fact quite advanced for buoyant flows. The term puff is commonly used in this literature to denote a structure whose vorticity is distributed rather than concentrated in a thin core. Such distributed vorticity can be realized experimentally by use of a screen or other resistance at the nozzle exit, or analytically by use of an eddy viscosity. The structure which is obtained is turbulent by definition and intent, and in the absence of buoyant forces is completely consistent with the similarity variables already defined. The puff, because it has a growth rate very much larger than the growth rate for a vortex ring, may in fact be the proper prototype large eddy for the turbulent jet.

6. The turbulent vortex street

The vortex street is a train of two-dimensional vortex structures which are very closely linked. Excellent flow-visualization studies of the laminar case have been made, for example, by Taneda (1959), Zdravkovich (1969), Corke *et al* (1977), and Matsui & Okude (1980). Each vortex entrains fluid and grows in size. Vortex coalescence and doubling of scale are thought to occur, but only after a distance of many tens or hundreds of body diameters (Taneda; Matsui & Okude). The turbulent case is not qualitatively different from the laminar one, and I believe that the sketch in figure 5, which is based on experiments by Cantwell (1975 and unpublished) and Owen & Johnson (1980) and on flow visualization by Ryan (1951) and Thomann (1959), is topologically sound. In particular, the saddle points in the sketch are real and are properly placed. Each vortex entrains fluid mainly along its upstream-facing interface, and this fluid comes mainly from the opposite side of the wake.

The measurements by Cantwell were concerned with vortex formation and shedding close to the cylinder, and the measured celerity was far from constant. A major mystery in these data and in the earlier data of Nielsen (1970) is that the circulation of an individual vortex is found to decrease slowly as the vortex moves downstream in the wake. If this finding is real, the turbulent bridges between vortices must constitute very weak upstream jets which continuously transport small amounts of mean vorticity between vortices of opposite sign.

An important feature in figure 5 is the set of saddle points, near which there is a substantial strain field. It is almost certain that the rate of turbulence production

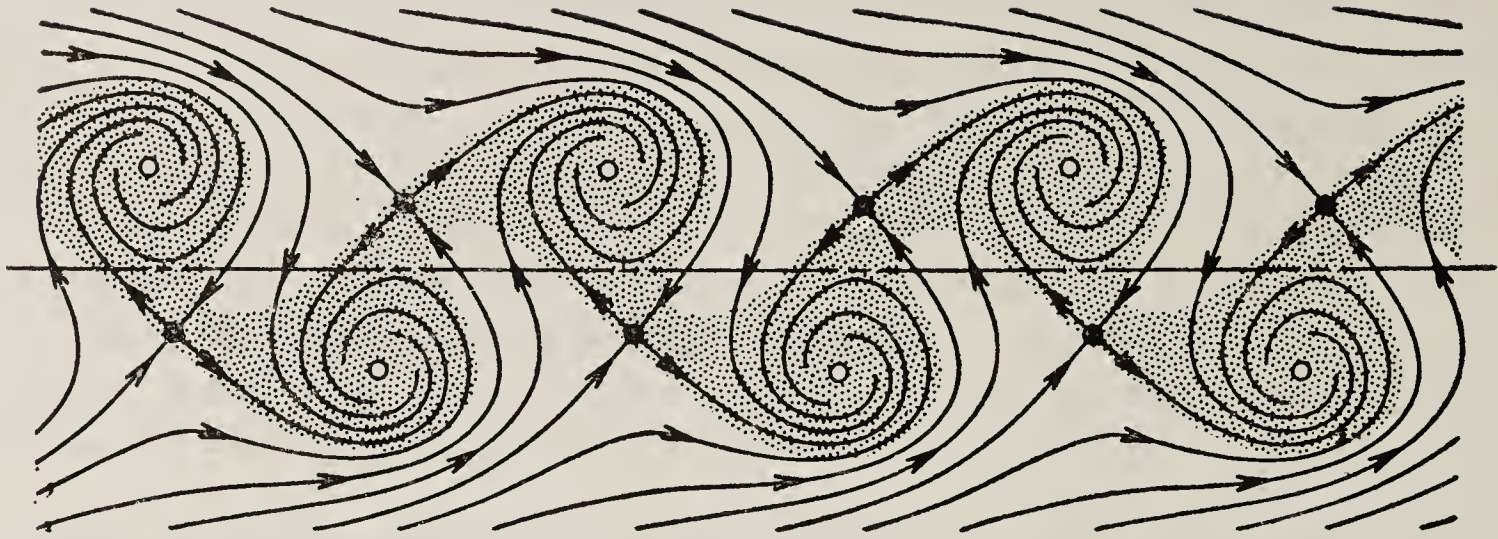


Figure 5. Conjecture for approximate mean particle paths in a turbulent vortex street, mostly after Cantwell (1975 and private communication). The presentation assumes quasi-steady flow in coordinates $(x - ct, y)$, where the celerity c is close to the mean of the centreline and free-stream velocities. There is no appreciable distortion of scale.

is large near these saddles, and that this turbulence is subsequently transported into the main vortex structures, where it accounts for the observed peaks in turbulent energy.

The real structure of a turbulent far wake is not known, although estimates of scale have been made by Barsoum *et al* (1978). My own conjecture, in view of the fact that vorticity of both signs is present in the flow, is that the characteristic structure is probably a vortex loop closed across the wake. Some evidence on this point can be found in the work on tapered cylinders, or cylinders having discontinuities in diameter, or uniform cylinders in shear flow, although I will not present the evidence here. It is characteristic of vortex shedding in the high subcritical range of Reynolds numbers that there is considerable dispersion in the strength and trajectory of successive turbulent vortices. No method was found in Cantwell's experiment to reduce this dispersion. The vortices grow slowly, and this growth must eventually cause interference and coalescence, probably with large three-dimensional effects. Future experiments on the turbulent vortex street might well take advantage of the fact that oscillation of a cylindrical body normal to the flow greatly increases the coherence of the shedding process.

7. The turbulent mixing layer

A seminal event in the development of coherent-structure concepts was the presentation of a paper on the turbulent mixing layer by Brown & Roshko at an AGARD conference in London in 1971. This paper is the basis for figure 6. The problem of the mixing layer has by now generated a very large literature, which I regret that I have not had time to examine with the care it deserves.

A part of this literature deals with the transition process, particularly the appearance of three-dimensional small-scale motions. Another part deals with eddy coalescence and its control. Numerical as well as experimental studies have contributed to both of these areas. One important result of this research certainly must be mentioned. The analysis by Hernan & Jimenez (1979) of motion pictures from the CIT apparatus, as well as numerical simulations by Takaki (1979), suggest that the

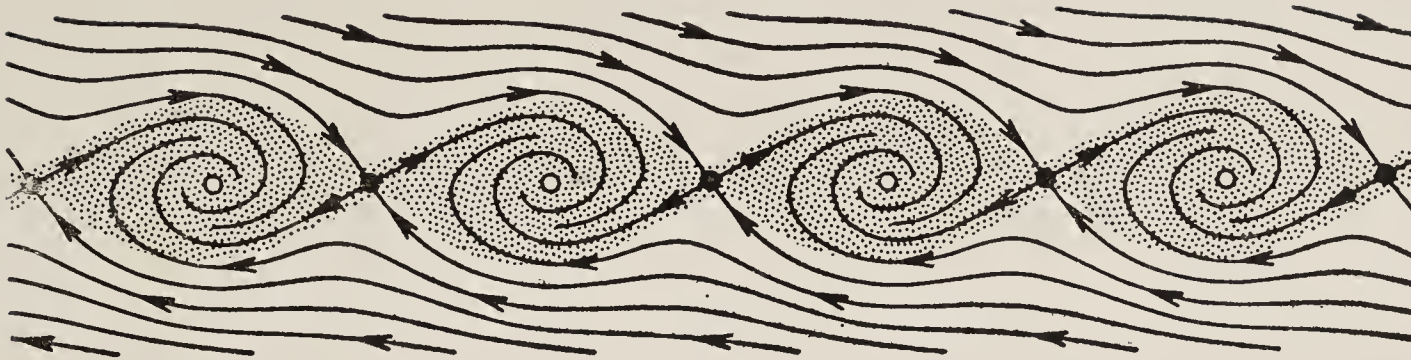


Figure 6. Conjecture for approximate mean particle paths in a turbulent mixing layer, mostly after Brown & Roshko (1971) and various numerical studies. The presentation uses coordinates $(x - ct, y)$, where the celerity c is close to the mean of the two stream velocities. There is no appreciable distortion of scale.

total volume of turbulent fluid is nearly constant during coalescence in the mixing layer. An immediate implication (which may be valid for other flows also) is that it is only the growth rate between interactions which determines the overall behaviour. Unfortunately, experiments in the mixing layer have so far not led to quantitative information on this growth rate, despite the fact that this information may be vitally necessary for understanding the interference and instability which lead to vortex coalescence.

8. Discussion

The six structures just described have in common that each involves a recognizable concentration of large-scale mean vorticity in two or three dimensions. To any approximation which leaves out effects of viscosity, these concentrations can be thought of as obeying the usual vortex laws. The vortices must close on themselves or go to infinity. In a viscous fluid, branching may occur.

Classification of these flows into a smaller number of species is an uncertain process. The transition structures—the puff, spot, and spiral—involve walls. Hence vorticity is present in the external environment, and propagation of turbulence may be governed by special rules. The transition structures also have in common that they may be thin enough to call for a boundary-layer approximation. The vortex ring is free to grow indefinitely, but because the vorticity is supplied impulsively the structure must eventually decay. The structures which occur in train—the mixing layer and the vortex street—are not free to grow indefinitely, because interference between adjacent structures must inevitably lead to interactions which change the pattern.

The idea of coherent structures as vortex concentrations obeying the vortex laws has to be taken seriously. One example is the case of vortex shedding from a cylinder in shear flow, where the expected and observed result is a cellular shedding pattern and the appearance of closed vortex loops. Among the structures considered here, the spot is special, because the skeleton vortex presumably ends on a wall and is therefore in contact with its image system. Nothing is known about the fate of this image system when such a structure leaves a surface at a trailing edge or at a corner.

An important element of classification for coherent structures is the mechanism of turbulence production. In the wall-dominated flows, the mechanism is probably shearing strain, perhaps within a boundary-layer approximation. In the free shear

flows, the mechanism is probably vortex stretching. The turbulence moves away from its source region mainly by transport (both along and across mean particle paths) by motions at intermediate scales. Eventually, there must be an interface. I think it likely that the propagation velocity of this interface can be described by a non-linear diffusion model of a kind first suggested to me by Julian Cole, and proposed independently by Les Kovaszny (see Kline *et al* 1969). In this model the diffusion coefficient is proportional to the turbulent energy, and the propagation velocity is therefore proportional to the gradient of turbulent energy near the interface. That the gradient in question is roughly constant is suggested by some of the data already cited; see for example Coles & Van Atta (1967) or Wygnanski *et al* (1975). This non-linear model can perhaps account also for nearly passive interfaces if it is the gradient of the small-scale energy which governs the propagation process.

Several analytical (including numerical) directions of attack suggest themselves for the problem of coherent structure. Various authors have studied numerically the kinematics of discrete vortices, usually stipulating finite cores to avoid singularities. The results often imitate nature closely, suggesting that a rotational but inviscid model for coherent structure has considerable value. Large-eddy simulation is conceptually closer to an experiment. One advantage is access to more information than can be readily extracted from an experiment, including perhaps the elusive pressure-strain covariance which is not experimentally accessible. A disadvantage is cost, since celerity and structure have to be extracted simultaneously by statistical methods which may require many realizations (or a single realization extending over a long time).

By any standard, the puff in a pipe is an attractive candidate for study by large-eddy simulation, or even by direct solution of the Navier-Stokes equations. The structure is axisymmetric and occurs naturally in train, thus bounding the numerical domain. Moreover, because of the low Reynolds number, widely different grid intervals in different parts of the flow should not be required. One prospect is that the phenomenon of splitting might be reproduced and something learned about its nature. Another is that a test might be made of the recent conjecture that sublayer vortices are produced and maintained by an instability of Taylor-Görtler type. Such sublayer vortices were in fact observed in pipe flow by Richardson & Beatty (1959) at about the same time that they were first attracting attention in boundary-layer flow.

A more technically oriented but still realistic goal on the analytical side is to lower the application of Reynolds averaging one level, to a description of the coherent structure itself. Details which might themselves qualify as coherent structures under either of the working definitions in the introduction would automatically be averaged out. Several risks are involved in attempts to model an average structure, by which I mean a deterministic average structure, in this way. The problem of a model for diffusion of turbulence near interfaces has already been mentioned. Energy production should be concentrated mainly near saddles, with energy intensity increasing in the direction of mean particle trajectories toward the associated centres. The computed distribution of turbulent energy must possess the appropriate spatial gradients so that interfaces with the correct propagation velocity appear in the correct locations. Rates associated with various flow processes of considerable technical importance, possibly including separation, might eventually be describable using estimates of characteristic transit times from saddle to centre.

Finally, an exciting prospect, developing rapidly on all sides, is the prospect of control of turbulent shear flows by manipulation of coherent structures. The first demonstration of this technique was the use by Roshko of a splitter plate to inhibit vortex shedding and thus to affect the drag of a bluff body. Examples of diagnostic attacks on various flows using essentially black-box methods include the work on the boundary layer by Stratford (1959), the work in pipe transition by Vallerani (1964), and the work on jets by Crow & Champagne (1971), Olivari (1974) and others. In the case of the boundary layer, operational control of surface friction in liquids, using high-molecular weight polymers, is within reach. In a recent survey paper, Bushnell (1978) has described the use of riblets, or small streamwise grooves on a wall, in an effort to interfere with the natural scale of sublayer vortices, and the use of screens or honeycombs, in an effort to modify the outer boundary layer. This research is at an early stage, but the future is bright.

Preparation of this paper was supported in part by the National Science Foundation under grant CME-7723541.

References

- Acton E 1980 *J. Fluid Mech.* **98** 1
 Barsoum M L, Kawall J G & Keffer J F 1978 *Phys. Fluids* **21** 157
 Brown G & Roshko A 1971 Turbulent shear flows, AGARD CP 93, London, paper 23
 Brown G & Roshko A 1974 *J. Fluid Mech.* **64** 775
 Bushnell D M 1978 Boundary layer effects, AFFDL TR 78-111, p. 71
 Cantwell B J 1975 *A flying hot wire study of the turbulent near wake of a circular cylinder at a Reynolds number of 140,000*, Thesis, California Institute of Technology, USA
 Cantwell B, Coles D & Dimotakis P 1978 *J. Fluid Mech.* **87** 641
 Coles D 1961 *Mécanique de la turbulence* (Marseille: CNRS) p. 229
 Coles D 1965 *J. Fluid Mech.* **21** 385
 Coles D & Van Atta C 1966 *AIAA J.* **4** 1969
 Coles D & Van Atta C 1967 *Phys. Fluids* **10** S120
 Coles D & Barker S J 1975 *Turbulent mixing in nonreactive and reactive flows* (New York: Plenum) p. 285
 Coles D & Savas O 1980 *Laminar-turbulent transition* (Berlin: Springer) p. 277
 Corke T, Koga D, Drubka R & Nagib H 1977 *Int. Congress on instrumentation in aerospace simulation facilities* (New York: Inst. Electrical & Electronic Engrs.) p. 74
 Crow S C & Champagne F H 1971 *J. Fluid Mech.* **48** 547
 Damms S M & Kuchemann D 1972 RAE Tech. Rep. 72139
 Dhawan S & Narasimha R 1958 *J. Fluid Mech.* **3** 418
 Dryden H L 1936 NACA Rep. 562
 Elder J W 1960 *J. Fluid Mech.* **9** 235
 Emmons H W 1951 *J. Aeronaut. Sci.* **18** 490
 Falco R E 1979 *Coherent structure of turbulent boundary layers* (Bethlehem P A: Dept. Mech. Eng., Lehigh Univ.) p. 448
 Fohl T & Turner J S 1975 *Phys. Fluids* **18** 433
 Gad-el-Hak M, Blackwelder R F & Riley J J 1980 *Laminar-turbulent transition* (Berlin: Springer) p. 297
 Gilbrech D A & Hale J C 1965 *Developments in mechanics* (London: Pergamon) Vol. 2, Part 1, p. 3
 Grigg H R & Stewart R W 1963 *J. Fluid Mech.* **15** 174
 Handa N 1976 *The structure of a turbulent spot* (in Japanese) Thesis, Nihon Univ.
 Haritonidis J H, Kaplan R E & Wygnanski I 1978 *Structure and mechanisms of turbulence I* (Berlin: Springer) p. 234

- Hassan Y A, Jones B G & Adrian R J 1980 *AIAA J.* **18** 914
- Heidrick T R, Banerjee S & Azad R S 1977 *J. Fluid Mech.* **82** 705
- Hernan M A & Jimenez J 1979 *2nd Symp. on turbulent shear flow* (London: Univ. London) p. 77
- Johnson G M 1970 Wright-Patterson AFB, Rep. ARL 70-0093
- Kambe T & Takao T 1971 *J. Phys. Soc. Jpn.* **31** 591
- Kline S J, Reynolds W C, Schraub F A & Runstadler P W 1967 *J. Fluid Mech.* **30** 741
- Kline S J, Morkovin M M, Sovran G & Cockrell D J (eds) 1969 *Computation of turbulent boundary layers* (Stanford: Stanford Univ.) Vol. 1, p. 327
- Kovaszny L S G, Fujita H & Lee R L 1973 *Adv. Geophys.* **B18** 253
- Lindgren E R 1957 *Ark. Fys.* **12** 1
- Lindgren E R 1959 *Ark. Fys.* **15** 97
- Lindgren E R 1969 *Phys. Fluids* **12** 418
- Lugovtsov B A 1970 *Nekotorye problemy v. matematiki i mekhaniki* (in Russian) (Leningrad) p. 182
- Matsui T & Okude M 1980 15th Int. Congr. Theor. Appl. Mech. Toronto (in press)
- Matsui T 1980 *Laminar-turbulent transition* (Berlin: Springer) p. 288
- Mattioli E & Zito G 1960 AGARD Rep. R-263
- Maxworthy T 1974 *J. Fluid Mech.* **64** 227
- Meseth J 1974 Mitt. MPI Göttingen No. 58
- Mizushina T, Maruyama T & Shiozaki Y 1973 *J. Chem. Eng. Jpn.* **6** 487
- Nielsen K T W 1970 *Vortex formation in a two-dimensional periodic wake*, Thesis, Oxford Univ. U.K.
- Olivari D 1974 von Karman Inst. Tech. Note 104
- Oshima Y 1972 *J. Phys. Soc. Jpn.* **32** 1125
- Oshima Y & Asaka S 1975 *Natl. Sci. Rep. Ochanomizu Univ.* **26** 31
- Oshima Y & Asaka S 1976 *4th Symp. on flow visualization* (in Japanese) (Tokyo: Inst. of Space & Aeronaut. Sci.) p. 79
- Oshima Y & Asaka S 1977a *J. Phys. Soc. Jpn.* **42** 708
- Oshima Y & Asaka S 1977b *J. Phys. Soc. Jpn.* **42** 1391
- Owen F K & Johnson D A 1980 *AIAA J.* **18** 1173
- Prandtl L & Tietjens O 1934 *Applied hydro-and aeromechanics* (New York: McGraw-Hill) p. 36
- Reshotko E 1958 Jet Propulsion Laboratory, Calif. Inst. Technol., Prog. Rep. 20-364
- Richards J M 1965 *J. Fluid Mech.* **21** 97
- Richardson F M & Beatty K O 1959 *Phys. Fluids* **2** 718
- Rotta J 1956 *Ing.-Arch.* **24** 258
- Rubin Y, Wagnanski I & Haritonidis J H 1980 *Laminar-turbulent transition* (Berlin: Springer) p. 17
- Ryan L F 1951 ETH Zürich, Inst. Aerodyn., Mitt. No. 18
- Sabot J & Comte-Bellot G 1976 *J. Fluid Mech.* **74** 767
- Sarpkaya T 1966 *Trans. ASME (J. Basic Eng.)* **D88** 589
- Savas O 1980 Turbulent boundary layers; experiments, theory and modelling, AGARD CP-271, Delft, Paper 23
- Schneider P 1980 *Z. Flugwiss. Weltraumforsch.* **4** 307
- Schubauer G B & Klebanoff P S 1955 NACA TN 3489
- Simmons J E L 1974 *J. Fluid Mech.* **64** 599
- Snyder H 1970 *Int. J. Nonlinear Mech.* **5** 659
- Stern E 1970 *Acta Mech.* **10** 67
- Stratford B S 1959 *J. Fluid Mech.* **5** 17
- Takaki R 1979 *Coherent structure of turbulent boundary layers* (Bethlehem PA: Dept. Mech. Eng., Lehigh Univ.) p. 410
- Taneda S 1959 *J. Phys. Soc. Jpn.* **14** 843
- Taylor G I 1929 *Proc. R. Soc. (London)* **A124** 243
- Teitgen R 1975 *The accuracy of flow measurements by laser Doppler methods* (Skovlunde, Denmark: Proc. LDA-Symp. (Copenhagen) p. 725
- Thomann H 1959 Aeronaut. Res. Inst. Sweden (FFA), Rep. 84
- Turner J S 1964 *J. Fluid Mech.* **18** 195
- Vallerani E 1964 Effect of single and periodic disturbances on intermittency in pipe flow, AE Thesis, Calif. Inst. of Technol.,
- Van Atta C W 1966 *J. Fluid Mech.* **25** 495
- Van Atta C W & Helland K N 1980 *J. Fluid Mech.* **100** 243

- Van Maanen H R E 1980 Turbulent boundary layers; experiments, theory and modelling, AGARD CP 271, Delft, Paper 3
- Viets H & Sforza P M 1972 *Phys. Fluids* **15** 230
- Wynanski I 1970 *Israel J. Technol.* **9** 105
- Wynanski I & Champagne F 1973 *J. Fluid Mech.* **59** 281
- Wynanski I, Sokolov M & Friedman D 1975 *J. Fluid Mech.* **69** 283
- Wynanski I, Sokolov M & Friedman D 1976 *J. Fluid Mech.* **78** 785
- Wynanski I 1979 *Coherent structure of turbulent boundary layers* (Bethlehem PA: Dept. Mech. Eng., Lehigh Univ.) p. 168
- Wynanski I, Haritonidis J H & Kaplan R E 1979 *J. Fluid Mech.* **92** 505
- Yellin E L 1966 *Circ. Res.* **19** 791
- Zdravkovich M M 1969 *J. Fluid Mech.* **37** 491
- Zilberman M, Wynanski I, Kaplan R E 1977 *Phys. Fluids Suppl.* **20** S258

Role of coherent structures in turbulent shear flows

A K M FAZLE HUSSAIN

Department of Mechanical Engineering, University of Houston, Houston, Texas 77004, USA

MS received 22 June 1981

Abstract. A definition for the large-scale coherent structure is presented, and the nature and role of coherent structures in turbulent shear flows are examined. The equations governing the coherent motions and the experimental considerations as well as constraints in the investigations of coherent structures in wall-bounded and free turbulent shear flows are discussed. Results from a few of our recent and on-going studies of coherent structures in excited and unexcited free turbulent shear flows are reviewed. These results show that coherent structures are dominant in transport in the early stages of their formation, but not in the self-preserving regions of turbulent shear flows.

Keywords. Coherent structures; turbulent shear flows; large scale organised motions; conditional sampling; importance of coherent structures; unsteady turbulent flows; axisymmetric jets; mixing layers; vortex pairing; Taylor hypothesis; effects of initial condition; phase average; eduction of large-scale structures.

1. Introduction

Turbulence research has undergone two revolutions in the seventies: one is at the conceptual frontier, the other in the measurement area.

The first revolution was the discovery of large-scale coherent structures. This revolution has rekindled interest in turbulence research which was gradually losing both excitement and momentum owing to the lack of any significant breakthroughs or optimism for a realistic turbulence theory. The profound impact of this revolution should be obvious from the vigorous contemporary pursuits of coherent structures in one form or another by essentially every turbulence researcher. Whether this new-found excitement is a passing fad fuelled by premature claims of some overzealous researchers or not warrants a careful scrutiny.

The second revolution is the integration of the high-speed digital computer as an active (even interactive) component of the turbulence measurement arsenal. This has enabled the researcher not only to relegate to the computer a variety of tedious chores (even decision-making) which would otherwise be either crude or impossible (owing to speed or multiplicity of event-dependent decisions) but also to measure quantities previously considered inconceivable (owing to either the prohibitive volume or the sophisticated nature of measurement). In fact, the second revolution has been principally spurred by the first as extensive (on-line) computerization of turbulence research has been necessary for eduction of coherent structure properties. [A facet of the second revolution is the instantaneous solution of the Navier-Stokes equation in

three dimensions; the computer requirements (both size and speed) in these numerical experiments, however, considerably exceed those in the laboratory experiments.]

This paper will review the physics of coherent structures in general and, unlike the paper by Coles (1981), will also review some detailed coherent structure investigations performed *via* computer-controlled experimentation. Thus, this paper will address both the revolutions just mentioned.

Even though the occurrence of large-scale eddying motions has been well-known for quite some time—perhaps for centuries—these were not recognized as characteristic features of fully-developed turbulent shear flows until the last decade. The prevalent notion of a turbulent flow being an assemblage of chaotic, random motions has undergone a re-examination, and in the opinion of many researchers, even a revision, after some recent investigations (principally Brown & Roshko 1974) demonstrated that the apparently fully-turbulent mixing layer consisted of a train of quasi-deterministic large-scale structures. The organized aspects of turbulence were first recognized by Townsend (1956) and investigated in a number of succeeding studies (for example, Grant 1958; Keffer 1965; Payne & Lumley 1967). However, neither the preponderance of these structures in turbulent shear flows in general nor their dominant role in transport was suggested by these earlier studies. One way those early studies differ from the current focus on coherent structures is that those mostly addressed fully-turbulent regions while most recent investigations have addressed the early stages of the post-transition flow. The dominant role of organized motions in aerodynamic noise generation was not recognized in Lighthill's (1952, 1961) theory, either. The occurrence of organized motions in the axisymmetric jet near field was apparent in the works of Bradshaw *et al* (1964) and Mollo-Christensen (1967), and strongly emphasized by Crow & Champagne (1971), even though a realization of their dominant role had to wait until later. The possible significance of these structures in fully-developed turbulent shear flows was raised by the mixing layer pictures of Brown & Roshko and was given a strong momentum by the experiments of Winant & Browand (1974) who claimed that the quasi-organized interaction (namely pairing) of the coherent structures was crucial for entrainment. Laufer (1974) further conjectured that the pairing event was critical in the production of jet noise, a claim supported by Ffowcs-Williams & Kempton (1978) but challenged by Hussain & Zaman (1981a, b). Dimotakis & Brown (1976) demonstrated the occurrence of coherent structures in a high Reynolds number mixing layer and suggested a feedback mechanism as the connecting link between the near- and far-field structures in the layer; see also Hussain & Zaman (1978).

In the case of the turbulent boundary layer, the understanding of the coherent structure is unfortunately much poorer. Successive investigations continue to raise many more questions than they answer. The counter-rotating vortices whose boundaries are marked by the wall layer streaks were observed a long time-ago; their universal nature as well as the nature and role of 'bursting' were established by Kline *et al* (1967). In spite of the rather extensive investigations of the boundary layer over the past decades, many first-level questions remain unanswered (briefly discussed later). The nature of the organized motion in a boundary layer is much more complex, as is to be expected, because, unlike simple free shear flows, it is not a flow of a single length scale and a single time scale; the existence of inner variables (U_* , ν) and the outer variables (U_∞ , δ) guarantees at least three regions of flow, the third being a region adjacent to the wall where viscous effects predominate. Even this apparently

simple region of flow is shrouded with amazing numbers of unresolved questions (Willmarth 1975; Dinkelacker *et al* 1977; Falco 1980). Because of these, the boundary layer is quite likely to have more than one kind of coherent structures ('hairpins,' 'typical eddies,' 'pockets,' 'folds,' 'streaks' etc!), and as such, it is not surprising that the understanding is not clearer.

Based on the accumulated information, there is a strong possibility that all turbulent shear flows are characterized by large-scale coherent structures (Roshko 1976; Townsend 1979). Less is known about the details of the structures in any particular flow. Still less known is whether each class of flows has a characteristic structure different from others and how dominant these structures are in the fully-developed states of the flows (see later).

An experimental approach that played a key role in both the revolutions mentioned earlier is flow-visualization, which appears to have found a kind of rebirth in recent years. Even though most early investigations of viscous flows relied on flow-visualization, the advent of the economic and simple (constant-temperature) anemometer system saw diminished uses of flow visualization owing to economy of effort and increased emphasis on quantitative data. However, it was indeed flow-visualization which brought about the first revolution (see Brown & Roshko 1974) as well as the second revolution. Flow-visualization is essential not only in obtaining a clear perception of the flow (for example, Winant & Browand 1974; Crow & Champagne 1971; Browand & Laufer 1975; Moore 1977; Chandrsuda *et al* 1978; Perry & Lim 1978; Offen & Kline 1974; Praturi & Brodkey 1978; Falco 1980; Head & Bandyopadhyay 1981) but also in planning sophisticated measurements (Browand & Wiedman 1976; Yule 1978; Liepmann 1978; Cantwell *et al* 1978; Wygnanski 1980; Hernan & Jimenez 1979; Fiedler *et al* 1980; Hussain & Zaman 1977) and planning as well as calibrating numerical experiments on the computer (Ashurst 1977; Acton 1980; Kim & Moin 1979; Couët *et al* 1979; Riley & Metcalfe 1980; Corcos 1980; Leonard 1980; Knight & Murray 1980; Aref & Siggia 1980; Cain *et al* 1981). Still another facet of the second revolution in which flow-visualization plays the central role is image processing (Hernan & Jimenez 1979, 1981; Schon *et al* 1979; J D Shlien, private communication).

Unfortunately, the description of the coherent motion is highly qualitative when based on flow-visualization but, on the other hand, quite speculative and crude when based on hot-wire (or LDA) data. The inherent constraints of the two approaches can be summarized as: "Flow-visualization presents excessive information but very little hard data, and hot-wires or LDAs give some hard data but very little flow physics." Consequently, efforts should be made to employ both flow-visualization and signal analysis in coherent structure investigations, a point well-emphasized by Hussain & Clark (1981b). The success of both the approaches, however, depends on some kind of conditional sampling directed by the imagination (hence the prejudices) of the experimenter. Here lies the dilemma: the same prejudices, which are essential for the success of a coherent structure study, can also mislead one as one can pretty much see in flow-visualization what one wants to see just as one can find different structures in the same signal. To quote Lumley (1980): "One can find in statistical data irrelevant structures with high probability; . . . they are formed by chance juxtaposition of other, relevant, structures and have no significance."

The flow-visualization itself has undergone not only evolutionary changes with technological progress but also breakthroughs (for example, shear stress from

birefringence, mixedness from reaction product colour, illumination with a scanning laser beam etc.).

1.1 *Why bother about coherent structures?*

Why is there so much excitement about the coherent structures? There have been persistent suggestions that the coherent structures dominate transport including mixing and entrainment as well as noise production in turbulent shear flows. Since these structures are quasi-deterministic, there is a high likelihood that the essence of a turbulent shear flow can be represented by an appropriate combination of these quasi-deterministic structures, whose evolution in space and time might be much more tractable than the solution of the complete Navier-Stokes equation or some statistically averaged form of this equation.

Large-scale coherent structures have been extensively investigated in our laboratory with three goals in mind: (i) understand the physics of shear flow turbulence; (ii) obtain detailed structure properties; and (iii) attain turbulence management through structure manipulation. If the coherent structures perform significant amounts of transport and if all turbulent shear flows are characterized by coherent structures, some understanding of their dynamics is crucial to an improved understanding of the physics of turbulence. Again, if the structures are both prevalent and dominant, a viable shear flow turbulence theory must incorporate these structures explicitly. In that case, the theory would most probably need model functions for the coherent structures; those functions must be inferred from the detailed contours of structure properties measured at some phases. The coherent structures and their interactions could be augmented or suppressed *via* some kind of interruption or excitation imposed on the flow, and the resulting modification (either enhancement or suppression) may have important technological implications regarding drag and heat transfer, mixing and entrainment as well as aerodynamic noise production.

A number of studies have been (and are being) carried out with the three above goals in mind, and a fair amount of success has been achieved in each of the three goals listed above. A limited demonstration of the effect of controlled excitation on turbulence management has already been achieved and further studies are in progress. Some of the key results will be briefly summarized later in this paper.

2. Definition of a coherent structure

In spite of extensive use of the term, there is no agreement among the researchers as to what is precisely meant by a 'coherent structure' (see Hussain 1979). The term has different meanings to different researchers; no two of them even agree with each other. It is not likely that a definition could be agreed upon without loud protests. However, I feel ill at ease to talk about a quantity unless I can define it. So, an attempt was made to provide a definition (Hussain 1980) at a coherent structure meeting in 1980. It should be noted that Professor Phil Saffman reacted to this definition by reminding the meeting that a sure way to ruin a turbulence meeting in the fifties and sixties was to ask for a definition of turbulence, and such would be the case if a definition for the coherent structure was asked for in that meeting. In the following I will reiterate my definition of the coherent structure.

A coherent structure is a turbulent fluid mass connected by a phase-correlated vorticity. That is, underlying the three-dimensional, random vorticity fluctuations characterizing the turbulence, there must be a *coherent vorticity* which is instantaneously correlated over the entire fluid mass. This fluid mass is singly-connected and the coherent vorticity must be instantaneously of the same sign in any plane; thus, a collection of vortices with phase-correlated vorticity is *not a* coherent structure.

In any turbulent flow, the motion at the Kolmogoroff scale is the most coherent, as no significant variation of velocity or vorticity smaller than this scale can be sustained. However, by coherent structures we do not mean motion at the Kolmogoroff scale but those with sizes comparable to the scale of the shear flow; *i.e.*, the Reynolds numbers associated with the structures are large. Consequently, the dynamics of the coherent structures is inherently inviscid. Consistent with this definition, a vortex ring near the end of the potential core of a jet or the Brown-Thomas structure in a boundary layer is a coherent structure, but the 'typical eddy', or the 'fold' or the 'hairpin vortex' in a turbulent boundary layer should perhaps be called a 'coherent substructure.'

The coherent structure is expected to be quite important in transport and in Reynolds stress production without itself being highly energetic. Thus, measurements based on linear momenta like velocity correlation (auto or space-time) and spectra do not uniquely identify a coherent structure. Clearly, a blob of irrotational fluid, somehow 'inserted' in a turbulent flow, will produce strong velocity correlation and broadband spectra as well as have significant kinetic energy. But this blob is neither turbulent nor performs any mixing. Bradshaw (1980) objected to this requirement by stating that it is impossible to have high Reynolds stress without high kinetic energy since $\bar{uv} < u'v'$ must always be satisfied. This requirement is not violated by my definition since it is suggested that the coherent structures contribute a major part of the total Reynolds stress while incoherent turbulence may account for the major part of the total turbulent kinetic energy. Thus, not only globally, but even spectrally, $\bar{uv} < u'v'$ is satisfied. It should be emphasized that in their pristine states soon after their formation, coherent structures are also highly energetic. As these structures evolve, and especially in the self-preserving region of the flow, these are not likely to be comparatively as energetic.

The key identifier of a coherent structure in my definition is the coherent vorticity, which must be the criterion for the detection of a coherent structure and eduction of any of its properties. Michalke (1980) has proposed to me a definition based on the coherence function,

$$C(x_i, \Delta x_i, \omega) = \frac{S(x_i, \Delta x_i, \omega)}{[S(x_i, 0, \omega) S(x_i + \Delta x_i, 0, \omega)]^{1/2}}, \quad (1a)$$

where S is the modulus of cross-spectral density, *i.e.*,

$$S(x_i, \Delta x_i, \omega) = \left| \int_{-\infty}^{\infty} R(x_i, \Delta x_i, \tau) \exp(i\omega\tau) d\tau \right|, \quad (1b)$$

and
$$R(x_i, \Delta x_i, \tau) \equiv (1/T) \int_0^T u(x_i, t) u(x_i + \Delta x_i, t + \tau) dt \quad (1c)$$

is the cross-correlation function of $u(x_i, t)$. For a value of C less than a threshold level, the boundary of the structure can be determined. Apart from the complexity in the measurement of C , a definition based on $C(x_i, \Delta x_i, \omega)$ is not acceptable for the reasons explained above.

If the typical vague notion of an eddy is considered, then, loosely speaking, a coherent structure is an eddy. However, if the more rigorous definition of an eddy (Lumley 1970; Tennekes & Lumley 1974) is accepted, a coherent structure is not an eddy. Eddies are (orthogonal) eigenmodes of a shear flow and exist in spatial superposition. Coherent structures are spatially mutually exclusive. It is perhaps because of this non-overlapping nature of the coherent structure that all coherent structure interactions (tearing and pairing) are inherently nonlinear. In this sense, there is no analogue of the cascade model for energy transfer between large-scale coherent structures. An eddy of a wavenumber k receives most of its energy from the next larger eddy (at the wavenumber $0.4k$) and transfers its energy mostly to the next smaller eddy (at the wavenumber $2.6k$). On the other hand, a coherent structure evolves under the balance of energy exchanges between the mean flow and incoherent turbulence. There is essentially no energy exchange between two coherent structures. Interactions like tearing and pairing result into new structures. This is quite different from two eddies which exchange energy while coexisting simultaneously.

Lumley (1980) has contended that the spatial superposition of eddies emphasized in my definition is not essential. Even though 'proper orthogonal decomposition' does not imply overlapping, it seems to me that spatial superposition of eddies of various scales is inherent to the cascade concept. The smaller eddies must be embedded within the larger eddies.

No suggestion is being made here that the cascade is not valid among the smaller to fine scales. However, when large-scale coherent structures are present, the cascade concept is not very helpful as there does not occur a continuous distribution of scales which co-exist and exchange energy. On the contrary, the coherent structure interaction is often of the anticascade type (such as pairing) even though tearing becomes important at higher Reynolds numbers (Hussain & Clark 1981b). Yule (1980) contends that long survival distance is a feature of coherent structures. This is clearly not true in the mixing layer where structures rapidly lose identity *via* pairing (Winant & Browand 1974) as well as tearing and fractional pairing (Hussain & Clark 1981b). The existence and nature of large-scale coherent structures in the self-preserving region of a turbulent shear flow is still an open question (Tso *et al* 1980; see also Hussain & Clark 1981a). It is expected that just like those in the boundary layer and the wake (Townsend 1979), the structures in the self-preserving regions of jets also undergo cycles of formation, growth and breakdown. Considering the motions in the axisymmetric mixing layer and the boundary layer, I feel that all the three criteria used by Yule (1980) for defining a coherent structure *viz.* (i) repetitive, (ii) survival distance much larger than the length scale, and (iii) contribute greatly to turbulent kinetic energy are both unrealistic and unnecessary.

3. Analytical treatment of coherent structures

Even if the coherent structures in a turbulent shear flow were identical, these would occur at random phases and their description must involve phase-dependent

information. Thus, similar to the time-average concept, an artifice like the *phase average* (Hussain 1970) needs to be introduced. This is the ensemble average of any property at a particular phase and a particular location with respect to the boundary of the structure. That is,

$$\langle f(x, y, z, \phi) \rangle = \lim_{N \rightarrow \infty} \frac{1}{N} \sum_{i=1}^N f_i[x, y, z, \phi + \phi_i(t)], \quad (2a)$$

where ϕ_i denotes the random phases of occurrence of the successive structures at the location (x, y, z) . When these structures occur at regular intervals, a situation that essentially occurs in vortex shedding, in flow resonances like the shear layer tone, or when structures are induced *via* controlled excitation, this definition reduces to the *periodic phase average*

$$\langle f(\mathbf{x}, t) \rangle = \lim_{N \rightarrow \infty} \frac{1}{N} \sum_{i=1}^N f_i(\mathbf{x}, t + iT), \quad (2b)$$

where T is the period of occurrence of the structure and t is the instant corresponding to the reference phase. Because the phase average provides time-dependent description, it gives more information than what is looked for in many engineering situations, where one is interested in the *time average*,

$$\bar{f}(\mathbf{x}) = \lim_{T \rightarrow \infty} \frac{1}{T} \int_{-T/2}^{T/2} f(\mathbf{x}, t') dt'. \quad (3)$$

Since f is considered to be a stationary function, the starting time is irrelevant. In practical measurements, neither the ensemble size in (2) nor the averaging period T in (3) is infinite. The adequacy of the ensemble size or the integration time is established when the measured average is found to be convergent.

The phase and time averages were used by Hussain & Reynolds (1970) and Reynolds & Hussain (1972) to analyze the behaviour of a periodic travelling wave in a turbulent channel flow. The same mathematical formulation can be applied to understand the dynamics of coherent structures and incoherent turbulence.

3.1 Triple decomposition

In the presence of coherent structures (considering one kind at a time when a variety of coherent structures are involved in the same flow), it is tempting to consider the instantaneous variable to consist of three components: the time-independent component, the coherent component, and the incoherent turbulence. That is, for any instantaneous variable $f(\mathbf{x}, t)$,

$$f(\mathbf{x}, t) = F(\mathbf{x}) + \tilde{f}_c(\mathbf{x}, t) + f_r(\mathbf{x}, t), \quad (4a)$$

where $\bar{f} = F$, $\langle f \rangle = F + \tilde{f}_c$. (4b)

Thus, at any given location, provided that the phase of the structure is also known, the three fields can be determined. To understand the interplay between the three

fields, it is necessary to write down the component equations which follow from the substitution of (4a) for each variable into the governing equations and carrying out first the phase average and then the time average. For incompressible flow, the corresponding continuity and momentum equations are:

$$\partial U_i / \partial x_i = \partial \tilde{u}_{ci} / \partial x_i = \partial u_{ri} / \partial x_i = 0, \quad (5a)$$

$$\frac{\overline{D}}{Dt} U_i = - \frac{\partial P}{\partial x_i} + \frac{1}{\text{Re}} \frac{\partial^2 U_i}{\partial x_j \partial x_j} + \frac{\partial}{\partial x_j} [-\overline{\tilde{u}_{ci} \tilde{u}_{cj}} - \overline{u_{ri} u_{rj}}], \quad (5b)$$

$$\begin{aligned} \frac{\overline{D}}{Dt} \tilde{u}_{ci} = & - \frac{\partial \tilde{p}_c}{\partial x_i} + \frac{1}{\text{Re}} \frac{\partial^2 \tilde{u}_{ci}}{\partial x_j \partial x_j} - \frac{\partial}{\partial x_j} (U_i \tilde{u}_{cj}) \\ & + \frac{\partial}{\partial x_j} [\overline{\tilde{u}_{ci} \tilde{u}_{cj}} - \tilde{u}_{ci} \tilde{u}_{cj}] + \frac{\partial}{\partial x_j} [\overline{u_{ri} u_{rj}} - \langle u_{ri} u_{rj} \rangle], \end{aligned} \quad (5c)$$

$$\begin{aligned} \frac{\overline{D}}{Dt} u_{ri} = & - \frac{\partial p_r}{\partial x_i} + \frac{1}{\text{Re}} \frac{\partial^2 u_{ri}}{\partial x_j \partial x_j} - \frac{\partial}{\partial x_j} [\tilde{u}_{cj} u_{ri} + U_i u_{rj} \\ & + \tilde{u}_{ci} u_{rj}] - \frac{\partial}{\partial x_j} [u_{ri} u_{rj} - \langle u_{ri} u_{rj} \rangle], \end{aligned} \quad (5d)$$

where
$$\frac{\overline{D}}{Dt} = \frac{\partial}{\partial t} + U_j \frac{\partial}{\partial x_j} \quad (5e)$$

is the material derivative following a fluid particle in the time-average flow field. Note that *summation* is *not* implied by the subscripts *c* and *r* which identify coherent and incoherent (random) components. In this derivation, use is made of the notions that phase average of the time average is just the time average, phase and time averages of the incoherent field have zero values, and coherent and incoherent motions are uncorrelated *i.e.*,

$$\overline{\tilde{f}_c g_r} = \langle \tilde{f}_c g_r \rangle = 0.$$

The interpretations of each term in equations (5b)–(5d) should be fairly obvious. Note that each of the three fields independently satisfy the equation for isochoric motion. In the momentum equations, the quadratic terms arise from the nonlinearity of the Navier-Stokes equation. There is a hierarchy of momentum transports involved:

$$-\overline{\tilde{u}_{ci} \tilde{u}_{cj}} \text{ and } -\overline{u_{ri} u_{rj}}$$

are the contributions of the coherent and incoherent motions to the mean momentum field. The modulations in these two terms due to the coherent motion contribute to the coherent field momentum. The interaction of the incoherent field with the time-average and coherent fields, in addition to self-interaction, instantaneously contributes to the incoherent field momentum. The instantaneous momentum

transport due to the incoherent field *i.e.*, $-u_{ri} u_{rj} = r_{ij}$ can be split into three components,

$$r_{ij} = \bar{R}_{ij} + \tilde{R}_{cij} + R_{rij}, \quad (6a)$$

where $\bar{R}_{ij} = -\overline{u_{ri} u_{rj}},$ (6b)

$$\tilde{R}_{cij} = -\langle u_{ri} u_{rj} \rangle + \overline{u_{ri} u_{rj}}, \quad (6c)$$

$$R_{rij} = -u_{ri} u_{rj} + \langle u_{ri} u_{rj} \rangle, \quad (6d)$$

i.e., $\bar{r}_{ij} = \bar{R}_{ij}; \langle r_{ij} \rangle = \bar{R}_{ij} + \tilde{R}_{cij}.$ (6e)

The contribution of incoherent turbulence to the mean momentum field is \bar{R}_{ij} , to the coherent structure field is \tilde{R}_{cij} and to the incoherent field itself is R_{rij} . It is clear that the three fields are strongly coupled and the unknowns like \bar{R}_{ij} , \tilde{R}_{cij} , R_{rij} , $\overline{\tilde{u}_{ci} \tilde{u}_{cj}}$ must be expressed in terms of other variables in order to solve the three velocity and the pressure fields. The corresponding vorticity equations are

$$\begin{aligned} \frac{\bar{D}}{Dt} \Omega_i &= \Omega_j \frac{\partial U_i}{\partial x_j} + \frac{1}{\text{Re}} \frac{\partial^2 \Omega_i}{\partial x_k \partial x_k} + \frac{\partial}{\partial x_j} [\overline{\tilde{u}_{ci} \tilde{\omega}_{cj}} - \overline{\tilde{u}_{cj} \tilde{\omega}_{ci}}] \\ &+ \frac{\partial}{\partial x_j} [\overline{u_{ri} \omega_{rj}} - \overline{u_{rj} \omega_{ri}}], \end{aligned} \quad (7a)$$

$$\begin{aligned} \frac{\bar{D}}{Dt} \tilde{\omega}_{ci} &= \tilde{\omega}_{cj} \frac{\partial U_i}{\partial x_j} + \Omega_j \frac{\partial \tilde{u}_{ci}}{\partial x_j} + \frac{1}{\text{Re}} \frac{\partial^2 \tilde{\omega}_{ci}}{\partial x_k \partial x_k} + \frac{\partial}{\partial x_j} [\tilde{u}_{ci} \tilde{\omega}_{cj} - \overline{\tilde{u}_{ci} \tilde{\omega}_{cj}}] \\ &- \frac{\partial}{\partial x_j} [\tilde{u}_{cj} \tilde{\omega}_{ci} - \overline{\tilde{u}_{cj} \tilde{\omega}_{ci}}] - \frac{\partial}{\partial x_j} (\tilde{u}_{cj} \Omega_i) \\ &+ \frac{\partial}{\partial x_j} [\langle u_{ri} \omega_{rj} \rangle - \overline{u_{ri} \omega_{rj}}] - \frac{\partial}{\partial x_j} [\langle u_{rj} \omega_{ri} \rangle - \overline{u_{rj} \omega_{ri}}], \end{aligned} \quad (7b)$$

$$\begin{aligned} \frac{\bar{D}}{Dt} \omega_{ri} &= (\Omega_j + \tilde{\omega}_{cj}) \frac{\partial u_{ri}}{\partial x_j} + \omega_{rj} \frac{\partial}{\partial x_j} (U_i + \tilde{u}_{ci}) + \frac{1}{\text{Re}} \frac{\partial^2 \omega_{ri}}{\partial x_k \partial x_k} \\ &- u_{rj} \frac{\partial}{\partial x_j} (\Omega_i + \tilde{\omega}_{ci}) - \tilde{u}_{cj} \frac{\partial \omega_{ri}}{\partial x_j} \\ &+ \frac{\partial}{\partial x_j} [u_{ri} \omega_{rj} - \langle u_{ri} \omega_{rj} \rangle] - \frac{\partial}{\partial x_j} [u_{rj} \omega_{ri} - \langle u_{rj} \omega_{ri} \rangle]. \end{aligned} \quad (7c)$$

These equations could be further simplified but are written down for completeness. Note that equations (5, 7) are nondimensionalized by appropriate velocity and length scales U_s, L_s so that $\text{Re} = U_s L_s / \nu$ is the appropriate Reynolds number.

The complexity of the equations (5) and (7) does not permit a direct appreciation of the interaction between the three fields. However, some further insight can be

obtained from a consideration of the energetics. Since total kinetic energy must be equal to the sum of the average kinetic energies of the three fields,

$$\frac{1}{2} \overline{u_i u_i} = \frac{1}{2} \overline{U_i U_i} + \frac{1}{2} \overline{\tilde{u}_{ci} \tilde{u}_{ci}} + \frac{1}{2} \overline{u_{ri} u_{ri}}, \quad (8)$$

$E \qquad \qquad \qquad \mathcal{E} \qquad \qquad \qquad e$

$$\begin{aligned} \frac{\overline{DE}}{Dt} = & - \frac{\partial P U_i}{\partial x_i} - \underbrace{\left(- \overline{\tilde{u}_{ci} \tilde{u}_{cj}} \right) \frac{\partial U_i}{\partial x_j}}_{\text{I}} - \underbrace{\left(- \overline{u_{ri} u_{rj}} \right) \frac{\partial U_i}{\partial x_j}}_{\text{II}} \\ & + \frac{\partial}{\partial x_j} \left[U_i \left(\overline{\tilde{u}_{ci} \tilde{u}_{cj}} + \overline{u_{ri} u_{rj}} \right) \right] + \frac{1}{\text{Re}} \frac{\partial}{\partial x_j} \left[U_i \bar{S}_{ij} \right] - \bar{\epsilon}, \end{aligned} \quad (9a)$$

$$\begin{aligned} \frac{\overline{D\mathcal{E}}}{Dt} = & - \frac{\partial}{\partial x_j} \left[\overline{\tilde{u}_{cj} \left(p_c + \frac{1}{2} \tilde{u}_{ci} \tilde{u}_{ci} \right)} \right] - \underbrace{\overline{\tilde{u}_{ci} \tilde{u}_{cj}} \frac{\partial U_i}{\partial x_j}}_{\text{I}} - \underbrace{\left[- \langle u_{ri} u_{rj} \rangle \frac{\partial \tilde{u}_{ci}}{\partial x_j} \right]}_{\text{III}} \\ & - \frac{\partial}{\partial x_j} \left[\overline{\tilde{u}_{ci} \langle u_{ri} u_{rj} \rangle} \right] + \frac{1}{\text{Re}} \frac{\partial}{\partial x_j} \left[\overline{\tilde{u}_{ci} \tilde{S}_{cij}} \right] - \tilde{\epsilon}_c, \end{aligned} \quad (9b)$$

$$\begin{aligned} \frac{\overline{De}}{Dt} = & - \frac{\partial}{\partial x_j} \left[\overline{u_{rj} \left(p_r + \frac{1}{2} u_{ri} u_{ri} \right)} \right] - \underbrace{\overline{u_{ri} u_{rj}} \frac{\partial U_i}{\partial x_j}}_{\text{II}} \\ & - \underbrace{\langle u_{ri} u_{rj} \rangle \frac{\partial \tilde{u}_{ci}}{\partial x_j}}_{\text{III}} + \overline{\tilde{u}_{cj} \frac{\partial}{\partial x_j} \langle \frac{1}{2} u_{ri} u_{ri} \rangle} + \frac{1}{\text{Re}} \frac{\partial}{\partial x_j} \left[\overline{u_{ri} S_{ri}} \right] - \epsilon_r, \end{aligned} \quad (9c)$$

where $\bar{S}_{ij} = \partial U_i / \partial x_j + \partial U_j / \partial x_i, \quad (9d)$

$$\tilde{S}_{cij} = \partial \tilde{u}_{ci} / \partial x_j + \partial \tilde{u}_{cj} / \partial x_i, \quad (9e)$$

$$S_{rij} = \partial u_{ri} / \partial x_j + \partial u_{rj} / \partial x_i, \quad (9f)$$

and $\bar{\epsilon} = \frac{1}{2\text{Re}} \overline{\bar{S}_{ij} \bar{S}_{ij}}, \quad (9g)$

$$\tilde{\epsilon}_c = \frac{1}{2\text{Re}} \overline{\tilde{S}_{cij} \tilde{S}_{cij}}, \quad (9h)$$

$$\epsilon_r = \frac{1}{2\text{Re}} \overline{S_{rij} S_{rij}}, \quad (9i)$$

are the dissipations in the three fields. Once again, *no summation* is implied by subscripts *c* and *r*. In each of the equations, the first, fourth and fifth terms represent the transport (redistribution) of energy within the flow as their integrals over the entire flow region are zeroes. The first represents the flow work and the fifth reversible viscous work. The term identified as I represents the production of coherent kinetic energy by the action of the average coherent Reynolds stress $-\overline{\tilde{u}_{ci} \tilde{u}_{cj}}$ against the

mean strain rate $\frac{1}{2}(\partial U_i/\partial x_j + \partial U_j/\partial x_i)$. The same term appears as a source term in the equation for coherent kinetic energy. Similarly, the term identified as II represents the production of incoherent turbulence by the action of the incoherent Reynolds stress against the mean strain rate. The same term appears as a source term in the incoherent kinetic energy equation. The coherent motion also can produce incoherent turbulence by the action of the phase-average incoherent Reynolds stress $-\langle u_{ri} u_{rj} \rangle$ against the coherent strain rate $\frac{1}{2}(\partial \tilde{u}_{ci}/\partial x_j + \partial U_{cj}/\partial x_i)$. Note that this term III appears as a source term in equation (9c). The energy flux terms are schematically depicted in figure 1. Note that the relative widths of the paths are qualitatively proportional to the energy fluxes. The dissipation from the time-average and coherent motion fields are expected to be much smaller than the incoherent turbulence dissipation ϵ_r ; that is, $\bar{\epsilon} < \tilde{\epsilon}_c \ll \epsilon_r$. Note that in the early stages of formation of the coherent structures, the term I is quite likely to be much larger than II, but in the fully developed regions, these two become comparable (see later).

Note that even though the coherent and incoherent turbulences are uncorrelated, *i.e.*, $\overline{\tilde{f}_c g_r} = \langle \tilde{f}_c g_r \rangle = 0$, these two are not independent. The incoherent turbulence is indeed both produced and organized by the coherent structures. However, these two are not mostly in strong interaction because of the differing time scales of the coherent and incoherent motions; the incoherent turbulence is typically of a time scale considerably smaller than that of the coherent structures.

The triple decomposition (4a) provides a formalism for discussing the physics of coherent structures *vis-a-vis* the time-mean flow and incoherent turbulence. However, it is basically an unrealistic artifice. Implicit in this decomposition is the assumption that the coherent structure is a perturbation of the time-mean flow. However, the time-mean flow is the result of many such structures and their interactions. In a region occupied by a structure, the entire nonrandom motion is the coherent structure. In that sense, the coherent structure is the flow and not a perturbation.

3.2 Double decomposition

It is then tempting to use the double decomposition

$$f(x, t) = f_c(x, t) + f_r(x, t) \quad (10)$$

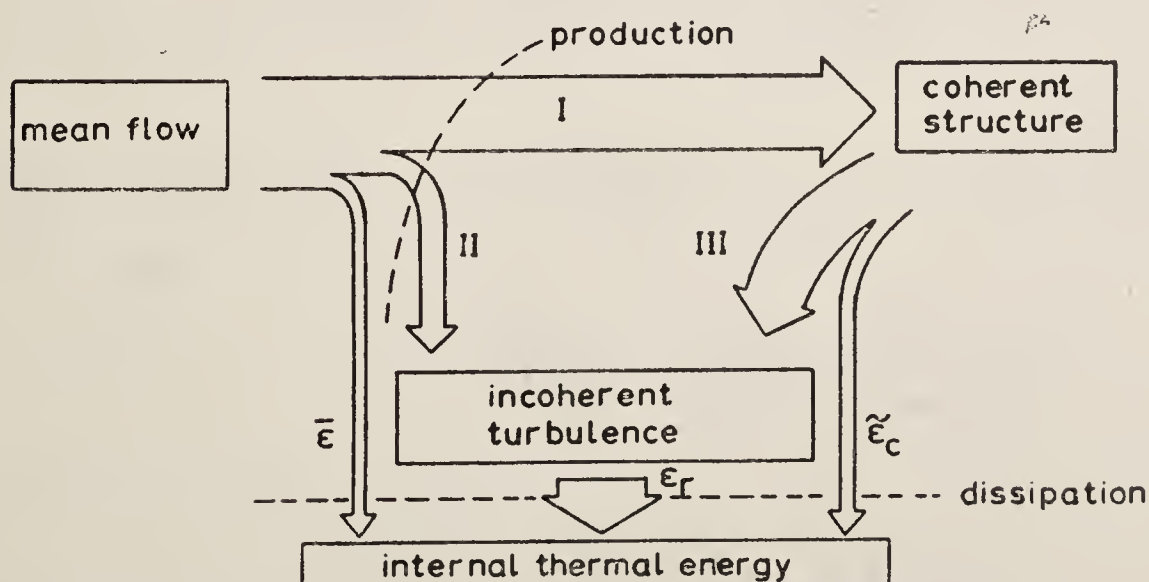


Figure 1. Energy exchanges between mean, coherent and incoherent fields.

introduced by Hussain (1977a). The corresponding motions must be described in a coordinate moving with a particle in the coherent flow field *i.e.*,

$$\partial u_{ci}/\partial x_i = \partial u_{ri}/\partial x_i = 0, \quad (11a)$$

$$\frac{\hat{D}}{Dt} u_{ci} = -\frac{\partial p_c}{\partial x_i} + \frac{1}{\text{Re}} \frac{\partial^2 u_{ci}}{\partial x_k \partial x_k} - \frac{\partial}{\partial x_j} \langle u_{ri} u_{rj} \rangle, \quad (11b)$$

$$\frac{\hat{D}}{Dt} u_{ri} = -\frac{\partial p_r}{\partial x_i} + \frac{1}{\text{Re}} \frac{\partial^2 u_{ri}}{\partial x_k \partial x_k} - u_{rj} \frac{\partial u_{ci}}{\partial x_j} - \frac{\partial}{\partial x_j} [u_{ri} u_{rj} - \langle u_{ri} u_{rj} \rangle], \quad (11c)$$

$$\frac{\hat{D}}{Dt} \omega_{ci} = \omega_{cj} \frac{\partial u_{ci}}{\partial x_j} + \frac{1}{\text{Re}} \frac{\partial^2 \omega_{ci}}{\partial x_k \partial x_k} + \frac{\partial}{\partial x_j} [\langle u_{ri} \omega_{rj} \rangle - \langle u_{rj} \omega_{ri} \rangle], \quad (11d)$$

$$\begin{aligned} \frac{\hat{D}}{Dt} \omega_{ri} = & \omega_{cj} \frac{\partial u_{ri}}{\partial x_j} + \omega_{rj} \frac{\partial u_{ci}}{\partial x_j} + \frac{1}{\text{Re}} \frac{\partial^2 \omega_{ri}}{\partial x_k \partial x_k} - u_{rj} \frac{\partial \omega_{ci}}{\partial x_j} \\ & - \frac{\partial}{\partial x_j} [\omega_{ri} u_{rj} - \langle \omega_{ri} u_{rj} \rangle] + \frac{\partial}{\partial x_j} [\omega_{rj} u_{ri} - \langle \omega_{rj} u_{ri} \rangle], \end{aligned} \quad (11e)$$

where
$$\frac{\hat{D}}{Dt} = \frac{\partial}{\partial t} + u_{cj} \frac{\partial}{\partial x_j} \quad (11f)$$

is the material derivative following a fluid particle in the coherent flow field.

Once again, *no summation* is implied by subscripts *c* and *r*. The corresponding kinetic energy and Reynolds stress equations are:

$$\begin{aligned} \frac{\hat{D}}{Dt} \frac{\langle u_{ci} u_{ci} \rangle}{2} = & - \frac{\partial}{\partial x_i} (p_c u_{ci}) + \langle u_{ri} u_{rj} \rangle \frac{\partial u_{ci}}{\partial x_j} - \frac{\partial}{\partial x_j} (u_{ci} \langle u_{ri} u_{rj} \rangle) \\ & + \frac{1}{\text{Re}} \frac{\partial}{\partial x_j} \left\langle u_{ci} \left(\frac{\partial u_{ci}}{\partial x_j} + \frac{\partial u_{cj}}{\partial x_i} \right) \right\rangle \\ & - \frac{1}{2\text{Re}} \left\langle \left\{ \frac{\partial u_{ci}}{\partial x_j} + \frac{\partial u_{cj}}{\partial x_i} \right\} \left\{ \frac{\partial u_{ci}}{\partial x_j} + \frac{\partial u_{cj}}{\partial x_i} \right\} \right\rangle, \end{aligned} \quad (12a)$$

$$\begin{aligned} \frac{\hat{D}}{Dt} \frac{\langle u_{ri} u_{ri} \rangle}{2} = & - \frac{\partial}{\partial x_j} \left\langle u_{rj} \left(p_r + \frac{1}{2} u_{ri} u_{ri} \right) \right\rangle - \langle u_{ri} u_{rj} \rangle \frac{\partial u_{ci}}{\partial x_j} \\ & + \frac{1}{\text{Re}} \frac{\partial}{\partial x_j} \left\langle u_{ri} \left(\frac{\partial u_{ri}}{\partial x_j} + \frac{\partial u_{rj}}{\partial x_i} \right) \right\rangle \\ & - \frac{1}{2\text{Re}} \left\langle \left(\frac{\partial u_{ri}}{\partial x_j} + \frac{\partial u_{rj}}{\partial x_i} \right) \left(\frac{\partial u_{ri}}{\partial x_j} + \frac{\partial u_{rj}}{\partial x_i} \right) \right\rangle, \end{aligned} \quad (12b)$$

$$\begin{aligned}
\frac{\hat{D}}{Dt} \langle u_{ri} u_{rj} \rangle = & - \left\langle \left(u_{ri} \frac{\partial p_r}{\partial x_j} + u_{rj} \frac{\partial p_r}{\partial x_i} \right) \right\rangle - \frac{\partial}{\partial x_k} \langle u_{ri} u_{rj} u_{rk} \rangle \\
& - \langle u_{rj} u_{rk} \rangle \frac{\partial u_{ci}}{\partial x_k} - \langle u_{ri} u_{rk} \rangle \frac{\partial u_{cj}}{\partial x_k} + \frac{1}{\text{Re}} \frac{\partial^2 \langle u_{ri} u_{rj} \rangle}{\partial x_k \partial x_k} \\
& - \frac{2}{\text{Re}} \left\langle \frac{\partial u_{ri}}{\partial x_k} \frac{\partial u_{rj}}{\partial x_k} \right\rangle.
\end{aligned} \tag{12c}$$

In equation (12a) the terms denote: I-coherent pressure work, II-coherent production of incoherent turbulence, III-coherent energy transport by incoherent turbulence, IV-reversible viscous work by coherent motion, and V-irreversible viscous work by coherent motion (*i.e.*, coherent dissipation). The terms in equation (12b), which results from contraction of equation (12c) denote: I'-incoherent turbulent kinetic energy transport by pressure and normal stresses, II'-coherent production, III'-reversible viscous work by incoherent turbulence, IV'-incoherent turbulence dissipation. For further discussion, see Hussain (1977a).

The double decomposition helps explain the interaction between coherent and incoherent motions. However, it cannot address the evolution of the coherent structures or extraction of energy by the coherent structures from the flow which drives the structures. Perhaps a quasi-Lagrangian description of the coherent structure in a frame moving with the convection velocity of the structure is a better approach. However, in any shear flow, the structure convection velocity has a large dispersion. Thus, either a totally Lagrangian formulation or a numerical solution of the Eulerian field is unavoidable.

3.3 Characterization of the coherent structures

What are the characteristic properties of the coherent structures? The key property identifying a coherent structure is the coherent vorticity $\Omega_{ci} = \epsilon_{ijk} \partial u_{ck} / \partial x_j$. For a better perception of the properties, these will be discussed in one plane only (say, the x - y plane). In many flows, the coherent structures are two-dimensional or axisymmetric. In such cases properties in one plane only are required. Depending on whether double decomposition or triple decomposition is used, the quantity carries different meanings. In the following, the properties are tabulated.

	Double decomposition	Triple decomposition
Coherent vorticity Ω_c	$\frac{\partial v_c}{\partial x} - \frac{\partial u_c}{\partial y}$	$\frac{\partial \tilde{v}_c}{\partial x} - \frac{\partial \tilde{u}_c}{\partial y}$
Coherent Reynolds stresses	$-\langle u_c v_c \rangle$	$-\langle \tilde{u}_c \tilde{v}_c \rangle$
Incoherent Reynolds stress time and phase averages		$-\overline{u_r v_r} - \langle u_r v_r \rangle$

	Double decomposition	Triple decomposition
Incoherent turbulence intensities	$\langle u_r^2 \rangle^{1/2}, \langle v_r^2 \rangle^{1/2}, \langle w_r^2 \rangle^{1/2}$	
Coherent strain rate	$\langle S \rangle = \frac{\partial u_c}{\partial y} + \frac{\partial v_c}{\partial x}$	$\langle \tilde{S} \rangle = \frac{\partial \tilde{u}_c}{\partial y} + \frac{\partial \tilde{v}_c}{\partial x}$
Time-average strain rate	$\bar{S} = \frac{\partial U}{\partial y} + \frac{\partial V}{\partial x}$	
Coherent structure shear production	$P_c = - \langle u_c v_c \rangle \bar{S}$	$\tilde{P}_c = - \langle \tilde{u}_c \tilde{v}_c \rangle \bar{S}$
Coherent shear production	$\langle P \rangle = - \langle u_r v_r \rangle \langle S \rangle$	$\langle \tilde{P} \rangle = - \langle u_r v_r \rangle \langle \tilde{S} \rangle$
Coherent normal production	$- \langle u_r^2 \rangle \frac{\partial u_c}{\partial x} - \langle v_r^2 \rangle \frac{\partial v_c}{\partial y}$	$- \langle u_r^2 \rangle \frac{\partial \tilde{u}_c}{\partial x} - \langle v_r^2 \rangle \frac{\partial \tilde{v}_c}{\partial y}$
Coherent structure normal production	$- \langle u_c^2 \rangle \frac{\partial U}{\partial x} - \langle v_c^2 \rangle \frac{\partial V}{\partial y}$	
Incoherent vorticity intensity	$\langle \omega_z^2 \rangle^{1/2}, \langle \omega_x^2 \rangle^{1/2}, \langle \omega_y^2 \rangle^{1/2}$	
Instantaneous vector patterns ψ_c	$\hat{\psi}_c = \langle u_c, v_c \rangle$	$\tilde{\psi}_c = \langle \tilde{u}_c, \tilde{v}_c \rangle$
Instantaneous streamlines	$dx/u_c = dy/v_c$	$dx/\tilde{u}_c = dy/\tilde{v}_c$
Pseudo-stream function	$\langle \psi \rangle = \int_0^Y r^* (u_c - U_0) dr^*$	
Coherent intermittency	$\langle \gamma_c \rangle$	

where $U_0 =$ structure convection velocity. Note that \bar{S} and $\langle S \rangle$ actually represent twice the strain rates. In a flow with significant heat and mass transport, the instantaneous temperature θ and species concentration s can be decomposed

as $\theta = \theta_c + \theta_r = \bar{\theta} + \tilde{\theta} + \theta_c$ and $s = s_c + s_r = \bar{s} + \tilde{s}_c + s_r$. Consequently, the following properties are of interest:

	Double composition	Triple composition
Transverse coherent heat transfer rate	$\langle v_c \theta_c \rangle$	$\langle \tilde{v}_c \tilde{\theta}_c \rangle$
Longitudinal coherent heat transfer rate	$\langle u_c \theta_c \rangle$	$\langle \tilde{u}_c \tilde{\theta}_c \rangle$
Transverse coherent mass transfer rate	$\langle v_c s_c \rangle$	$\langle \tilde{v}_c \tilde{s}_c \rangle$
Longitudinal coherent mass transfer rate	$\langle u_c s_c \rangle$	$\langle u_c \tilde{s}_c \rangle$
Transverse and longitudinal phase-average incoherent heat transfer rates		$\langle v_r \theta_r \rangle, \langle u_r \theta_r \rangle$
Transverse and longitudinal phase-average incoherent mass transfer rates		$\langle v_r s_r \rangle, \langle u_r s_r \rangle$
Incoherent temperature fluctuation intensity		$\langle \theta_r^2 \rangle^{1/2}$
Incoherent concentration fluctuation intensity		$\langle s_r^2 \rangle^{1/2}$

Since these properties vary over the cross-section of a structure, it is best to represent these as contour maps non-dimensionalized by appropriate parameters (Hussain *et al* 1980). Note that all properties are invariant under Galilean transformation except $\hat{\psi}_c$, $\tilde{\psi}_c$ and $\langle \psi \rangle$. Thus, streamlines or contours of \tilde{u}_c or \tilde{v}_c are not likely to be helpful for identifying the structure boundaries as these will depend on the reference frame used. Note that it is a rare coincidence that contours of \tilde{u}_c ($= 0.02U_\infty$) closely agree with the boundary of a 'spot' in a laminar boundary layer (Coles & Barker 1975; Wygnanski 1980). On the other hand, contours of vorticity, which are invariant under Galilean transformation, agree well with the instantaneous streaklines (Michalke 1972) and, therefore, constitute the primary identifiers of the coherent structure boundary and strength. The coherent intermittency contours can also be regarded as a reliable identifier of the structure. Use of ψ_c or $\langle \psi \rangle$ has some advantages, however, as these provide some details of

phase-average fluid motion. The function $\langle \psi \rangle$ would correspond to the stream-function if the flow were steady and the structure two-dimensional; hence the name pseudo-stream function (see Hussain *et al* 1980).

The above listed properties address those in flows with two-dimensional coherent structures. When the structures are three-dimensional, the other components of coherent vorticity, strain rate, production, etc. have to be considered. When the three-dimensional flows also involve heat and mass transfer, coherent transport terms like $\langle w_c \theta_c \rangle$, $\langle \tilde{w}_c \tilde{\theta}_c \rangle$, $\langle w_c s_c \rangle$, $\langle \tilde{w}_c \tilde{s}_c \rangle$ and the incoherent transport terms like $\langle w_r \theta_r \rangle$, $\langle w_r s_r \rangle$ are of importance. In most flows of interest, the coherent structures appear to be two-dimensional (Browand & Troutt 1980; Hussain & Zaman 1980) even though this is not necessarily well accepted (Chandrsuda *et al* 1978; Batt 1978; Pui & Gartshore 1979).

For both two-dimensional and three-dimensional motions, also important are the different phase-averaged energy flux terms over the spatial extent of the structure. These may include the advection terms like

$$u_c \frac{\partial}{\partial x} \langle u_r^2 \rangle, v_c \frac{\partial}{\partial y} \langle u_r^2 \rangle, \tilde{u}_c \frac{\partial}{\partial x} \langle v_r^2 \rangle, \tilde{v}_c \frac{\partial}{\partial y} \langle v_r^2 \rangle,$$

the incoherent transport of (coherent kinetic energies) terms like

$$\frac{\partial}{\partial y} (u_c \langle u_r v_r \rangle), \frac{\partial}{\partial x} (\tilde{v}_c \langle u_r v_r \rangle),$$

of turbulent heat and mass transport terms like

$$\frac{\partial}{\partial x} \langle \theta_r^2 u_r \rangle, \frac{\partial}{\partial y} \langle \theta_r^2 v_r \rangle, \frac{\partial}{\partial x} \langle s_r^2 u_r \rangle, \frac{\partial}{\partial y} \langle s_r^2 v_r \rangle$$

and gradient production terms like

$$\langle \theta_r u_r \rangle \frac{\partial \theta_c}{\partial x}, \langle s_r u_r \rangle \frac{\partial s_c}{\partial y}, \langle \theta_r v_r \rangle \frac{\partial \theta_c}{\partial y}, \langle s_r v_r \rangle \frac{\partial s_c}{\partial y} \text{ etc.}$$

Of special interest are the spatial distributions of phase-average incoherent dissipation terms like

$$\left\langle \left(\frac{\partial u_r}{\partial x} \right)^2 \right\rangle, \left\langle \left(\frac{\partial u_r}{\partial y} \right)^2 \right\rangle, \left\langle \frac{\partial u_r}{\partial z} \cdot \frac{\partial w_r}{\partial x} \right\rangle, \left\langle \frac{\partial u_r}{\partial y} \frac{\partial v_r}{\partial x} \right\rangle, \left\langle \left(\frac{\partial v_r}{\partial x} \right)^2 \right\rangle, \\ \left\langle \left(\frac{\partial v_r}{\partial y} \right)^2 \right\rangle, \left\langle \left(\frac{\partial w_r}{\partial x} \right)^2 \right\rangle, \left\langle \left(\frac{\partial w_r}{\partial y} \right)^2 \right\rangle, \left\langle \left(\frac{\partial \theta_r}{\partial x} \right)^2 \right\rangle, \left\langle \left(\frac{\partial s_r}{\partial x} \right)^2 \right\rangle, \text{ etc.}$$

Apart from revealing the roles of different zones of the coherent structures in turbulent dissipation, the dissipation terms will also show the accuracy of the assumption of local isotropy. However, because small-scale transverse gradients are not easy to measure, most convenient measurements will be the phase average of squares

of longitudinal derivatives (*i.e.* $\langle(\partial/\partial x)^2\rangle$ terms) only. These would, of course, require the use of the Taylor hypothesis, whose validity is also in serious question. The extent of error introduced by Taylor hypothesis remains undetermined, except for the large-scale structures (see later).

4. Origin of coherent structures

A coherent structure results from an instability of one kind or another. For an initially laminar free shear layer, the initial (Kelvin-Helmholtz) instability produces roll-up of the shear layer through nonlinear saturation. A row of vortical structures (of the same sign) is unstable because of perturbations in their spacing or strength, which result into amalgamations. This second (Lamb) instability appears to be the primary mechanism for entrainment (Winant & Browand 1974) even though Hernan & Jimenez (1979) suggest otherwise. In a plane mixing layer, this amalgamation can continue *ad infinitum*, the number of amalgamations will be determined by the length of the layer. Somewhere in this chain of amalgamations, the flow becomes turbulent. Integral to the instability is the evolution of spanwise or azimuthal structures *via* a third (Widnall) instability. The amalgamations of the turbulent coherent structures proceed essentially like those in the laminar situation. However, there is some controversy on whether the amalgamation process in a two-dimensional (or axisymmetric) flow is actually two-dimensional (Chandrasuda *et al* 1978).

Even though amalgamations would typically mean merging of two structures (Winant & Browand 1974; Hussain & Zaman 1980), a number of them could amalgamate together depending on the frequency of the perturbation. The merging of a number of structures simultaneously was first observed by Hussain & Zaman (1977) but was more conclusively demonstrated by Ho (1980) and called by him as ‘collective interaction.’ Hussain & Zaman (1977) also showed that depending on the phase of excitation, a large region of ‘negative production’ can be induced (see later).

A free shear layer emerging from a fully-developed turbulent boundary layer can also undergo an instability and roll up (Clark 1979; Clark & Hussain 1979). The evolution and interactions farther downstream are not different from that originating from an initially laminar boundary layer. The flow downstream from the potential core of a plane jet or a circular jet also probably becomes organized through some instability of the fully turbulent flow resulting from the merger of the mixing layers.

The initiation of coherent structures in the turbulent boundary layer is less certain. The transitional ‘spots’ may persist in the turbulent boundary layer. However, there has not yet been any evidence that would suggest that the prototype ‘spot’ (Coles & Barker 1975; Wignanski *et al* 1976) is a characteristic structure of the turbulent boundary layer. Whether the outer structure triggers the bursting or vice versa is still unknown (Brown & Thomas 1977). Both in the boundary layer and in the free turbulent shear flows, there is a strong suggestion that the structures form intermittently and undergo cyclical processes of formation, growth and decay (Townsend 1979; Tso *et al* 1980; Mumford 1981).

4.1 Role of the initial condition

The evolution of a single-phase, incompressible shear flow depends on the initial

(*i.e.* exit) condition, the boundary condition, the Reynolds number and the Strouhal number (of the natural and forced disturbances). Since no flow is disturbance-free, all flows are driven if the disturbance frequencies fall within the unstable band of the flow (Hussain 1980). We will, for the time being, ignore the effect of the Strouhal number. Even though conclusive evidence for Reynolds number similarity or asymptotic invariance is still lacking, we have no basis to suggest its invalidity except to suggest that the Reynolds number at which the invariance occurs is considerably higher than assumed previously (Hussain & Zaman 1981 a, b). If the dimension of the unobstructed space surrounding a free shear flow is at least an order of magnitude larger than the characteristic width of the shear flow, then the boundary condition is not likely to have a dominant effect on the flow. The evolution of the flow will then be a strong function of the initial condition (Hussain & Clark 1977; Hussain 1977b; Hussain & Zedan 1978a). This influence is quite likely to be longer for a free shear flow than in a boundary layer because the scales associated with the wall assume control of the flow, making it forget the initial condition faster.

For a free shear flow starting from a trailing edge, a large number of measures can be used to characterize the initial condition (Hussain & Zedan 1978a, b). This may include profiles of $U(y)$, $V(y)$, $u'(y)$, $v'(y)$, $w'(y)$, $\overline{uv}(y)$, spectra of u , v , uv , etc. However, in view of the finite size of the sensor (hot-wire or LDV), it is not realistic that V , v' , w' , or \overline{uv} can be measured with adequate transverse resolution. Consequently, one must be content with single-wire measurements only and use $U(y)$, ϕ_u , $u'(y)$ and higher moments of $u(t)$ to characterize the initial condition.

The initial condition can be grouped into four classes: (a) laminar; (b) nominally laminar; (c) highly disturbed; and (d) fully-developed turbulent. The laminar state (a) should be free from any fluctuations. The class (b) may have the average measures like the shape factor the same as that of (a) but may have noticeable fluctuations. The class (d) represents a fully-developed turbulent equilibrium boundary layer. The class (c) consists of all other cases not included in (a), (b) or (d). If the trailing edge contains a sufficient straight length, then the profile in (a) will agree with the Blasius profile with a shape factor of 2.59 and the profile in (d) will have a shape factor of about 1.4 depending on the local Re_θ (Hinze 1975 p. 633; Purtell *et al* 1981). It should be obvious that profiles other than the Blasius will occur if a straight portion is not included upstream of the trailing edge. In all our experiments, including those in the circular jet, we have included a straight portion preceding the trailing edge and advise its use in all free shear flow experiments.

Because of the nonunique nature of the classes (b) and (c), it is clear that experiments can be meaningful if performed for the asymptotic limiting cases *i.e.* (a) and (d). However, in many practical cases, the initial condition ends up falling in the category (b) when an attempt is made to achieve the category (a) and in (c) when the goal is (d).

The asymptotic limiting case (a) is essentially impossible to attain because of the presence of unavoidable disturbances originating from a variety of sources, including rotating stall, blade wake, resonance of the settling chamber as an organ pipe or a Helmholtz resonator, the presence of shear tone over cavities inside the tunnel or caused by sensor or other structures in the flow or by impingement downstream, laboratory acoustic modes, air-conditioning sound and room circulation, etc. These various disturbances dominate the 'free-stream turbulence' which is mostly potential fluctuations. In the presence of such fluctuations, the longitudinal turbulence inten-

sity would show a peak at $y/\delta^* \cong 1$ (Hussain & Clark 1977). Because of these, any flow is most likely 'driven'. The extent to which it is driven depends on the strengths of the disturbances within the unstable bandwidth of the flow. Because of these considerations, the spectral content of the 'free-stream turbulence' is far more important than the intensity. It is strongly urged that all future studies should report the 'free stream spectrum.' In recording the spectrum, the scale should be amplified enough to reveal the otherwise hidden spectral peaks. The peaks due to the electronic sources should also be identified as these are of no consequence to the flow.

The case (d) is the only unique initial condition that can be achieved practically. Typically, a trip should be used sufficiently upstream from the trailing edge. The distance between the trip and the trailing edge will depend on the nature of the trip. Trips enhancing three-dimensionality should be preferred. Our experience suggests that a trip, with a series of teeth so that the height, width, spacing and depth of the teeth, all equal to the local displacement thickness, and placed at least 100 displacement thicknesses upstream, is adequate to produce a fully-developed turbulent boundary layer at the trailing edge. We have used the following criterion to certify the achievement of the initial condition (d): (i) the profile must have at least one decade length of the logarithmic region in the universal coordinates; this length, of course, decreases with decreasing Re_θ ; (ii) the wake component must have an amplitude equal to that expected of an equilibrium flat plate boundary layer (Coles 1962), (iii) the fluctuation intensity profile should compare well with that in the boundary layer (Klebanoff 1955); (iv) the peak fluctuation intensity should occur at about $y^+ = 13$, (v) the peak value of u'/U_* should be around 2.4 — 2.6, (vi) the shape factor should be (around 1.4) consistent with the local Re_θ ; (vii) the u -spectrum should be broadband without any sharp peak and, (viii) the U_* value should be consistent with the flat plate data (Coles 1962). For convenience, the profile is measured about 0.5 mm downstream from the trailing edge. The U_* value is obtained from the Clauser plot technique by iteratively fitting the measured profile $U(y)$ with the universal profile $U^+ = 5.6 \log_{10} y^+ + 4.9$ over the range $14 \lesssim U^+ \lesssim 18$.

Unless care is taken to guarantee a fully-developed turbulent boundary layer through checks like those listed above, the achievement of the asymptotic limiting initial condition (d) cannot be assured. The typical use of a circular rod (without any notches) placed spanwise close to the trailing edges in the experiments of Wignanski & Fiedler (1970), Champagne *et al* (1976), Brown & Roshko (1974) and Batt (1975) not only could hardly have produced a turbulent boundary layer at the exit, but it is quite likely that the separated shear layers even never reattached (Chandrasuda *et al* 1977). Sufficient downstream separation of the trailing edge from the trip was not provided in these experiments.

5. Eduction of coherent structures

Characterization of the coherent structures requires measurement of the properties (listed earlier) over the spatial extent of the structure. Measurement of these properties involves ensemble-averaging these properties over a large number of realizations such that properties associated with only the same relative spatial location are ensemble averaged. So, care is necessary to trigger the eduction of the structure at the same selected phase. The detection of the structures, and consequently the eduction

of any phase-average property, is complicated by the large dispersion in the characteristic structure measures like the shape, size, orientation, strength, convection velocity and 'age' of the structures. Furthermore, the trajectory of a structure varies from one to the next. Thus, the problem in eduction of the coherent structure is considerably more complex than the effect of phase scrambling (Blackwelder 1977; Yule 1979). For any turbulent shear flow, the task is thus to capture structures in their three-dimensional forms, to concentrate on structures of a particular set of characteristic measures at a time, to shift and rotate these so that structures of the same class are properly aligned with respect to each other, and then ensemble average to obtain the phase-average properties of that class. The phase-average properties must be obtained for each possible class identified by a selected combination of the structure measures like shape, strength, etc. That is, for each point in the six-dimensional probability density distribution in the function space of the characteristic measures, a set of phase-average properties must be educed. This prohibitive effort can be drastically reduced if the probability density distribution function has a few isolated strong peaks.

The structures corresponding to the peaks are called the 'preferred-modes.' Eduction of these preferred modes may suffice on the expectation that these can essentially represent the total effects of the flow. Eduction of these few preferred modes of a flow is still a formidable task. The researcher's dream is thus to find a shear flow which has a 'unique preferred mode.' Fortunately, the near field of the axisymmetric jet is characterized by such a unique preferred mode (Crow & Champagne 1971; Hussain & Zaman 1975; Zaman & Hussain 1980). No other flow is yet known to be blessed as such. For this reason, the near-field of an axisymmetric jet occupies a unique position and has been the focus of extensive investigations in our laboratory.

Even in the axisymmetric jet, a variety of structures occur, the dominant one being the preferred mode. Eduction of this mode would require their detection and then alignment in the streamwise (x), transverse (y) and azimuthal (z) directions, after accepting structures of the same strength and the same 'age'. This is still a prohibitive task. The jitter in 'age' orientation as well as strength can be significantly reduced by inducing the structures *via* controlled excitation. When induced *via* controlled excitation at the Strouhal number corresponding to the preferred mode, the excitation does not produce an artificial structure but paces the formation of the natural structure. This not only reduces the phase scrambling but also reduces the variation between trajectories of successive structures. This is the reason why a majority of our effort has been devoted to the induced coherent structures. The unforced, natural structures are now being also investigated in a variety of turbulent shear flows.

A question faced in the eduction of natural structures is: How often should these structures occur to be significant? The answer depends on the flow and on the region of the flow. For the near field of a jet, structures are quite likely to occur frequently, while in the far field of the jet or in a boundary layer, the frequency is quite likely to be low. For the boundary layer, a structure would be significant if it occurs at a given location for even 5% of the time.

6. Coherent structures in the boundary layer

It is generally agreed that the 'bursting' process plays a dominant role in the tran-

sport of mass and momentum and in production in a turbulent boundary layer. In spite of numerous studies of this event, no one has yet been able to produce even a single contour of any property of the bursting coherent structure, presumably because of the random occurrence in location and time of this structure. Thus, the bursting coherent structure remains an unknown entity. The understanding regarding the 'turbulent spot' in a laminar boundary layer (Dhawan & Narasimha 1958; Kovaszny *et al* 1962; Wygnanski *et al* 1976; Cantwell *et al* 1978) is considerably more detailed, allowing adequate description of the flow. However, the recent realization prompted by Klebanoff (1980) and Perry *et al* (1981) that the spot is not a single structure, but an assemblage of hairpin-like vortices (Wygnanski 1980), suggests that reexamination and modification of the contours of the 'spot' properties are in order. There is as yet no evidence that the 'spot' is a characteristic structure of the turbulent boundary layer. It appears that studies of the 'spot' in a boundary layer, while extremely interesting on their own right, are not of any direct relevance to the turbulent boundary layer.

Even though the existence of hairpin vortices in a turbulent boundary layer has been mentioned previously (by, for example, Theodorsen 1952; Klebanoff *et al* 1962; Black 1968; Frenkiel & Klebanoff 1973; Offen & Kline 1975), there has never been any detailed study of these vortices until recently by Head & Bandyopadhyay (1981). However the connection of these hairpin vortices with the large-scale structures in the boundary layer (Grant 1958; Kovaszny *et al* 1970; Brown & Thomas 1977) is not known. The origin of the Brown-Thomas structure and its connection with bursting and the hairpin vortices is quite elusive. Bandyopadhyay's (1981) suggestion for a connection between this structure and the hairpin vortices is plausible but quite improbable as such ramps were found by Head & Bandyopadhyay very infrequently. Since Brown & Thomas (1977) suggest this structure to be responsible for triggering bursting, the Brown-Thomas structure is supposed to occur frequently. It is not clear how Falco's (1977) 'typical eddy', which is an order of magnitude smaller than the boundary layer thickness, can be as dominant as suggested by him and why the typical eddy, being a characteristic feature of the outer layer, scales on the inner variables. Falco (1979) disagrees with Head & Bandyopadhyay's (1981) suggestion that the 'typical eddy' is the tip of a hairpin vortex because these occur in isolation and have a rotation opposite to that of the hairpin vortex. The mechanisms for the formation of the counter-rotating vortices and the bursting structure are still not understood.

Apart from these questions regarding the coherent structures, a number of related questions remain unanswered. For example: Does the bursting frequency scale on the outer or wall variables and does it vary with R_θ (Rao *et al* 1971; Laufer & Badri Narayanan 1971; Sabot & Comte-Bellot 1976; Blackwelder & Haritonidis 1980; Sharma & Willmarth 1980)? Does the bursting result into outer structures or do the outer structures trigger bursting (Offen & Kline 1974; Praturi & Brodkey 1978; Smith 1978)? How does the bursting phenomenon vary with R_θ and pressure gradient (Kline *et al* 1967; Narasimha & Sreenivasan 1979)? What is the variation of the size and angle of inclination of the hairpin vortices with R_θ and pressure gradient? How are the statistics of large and small scales related (Badri Narayanan *et al* 1977; Rajagopalan & Antonia 1981)? In what way are the 'pockets' (Falco 1979) or folds (Perry *et al* 1981) related to the counter-rotating vortex rolls near the wall (Sirkar & Hanratty 1970; Blackwelder & Eckelmann 1979)? What is the mechanism of low-speed streak

formation? What happens to the longitudinal vortices when 'sweep' occurs? Is the sublayer motion decoupled from that in the rest of the boundary layer (Dinkelacker *et al* 1977; Willmarth & Bogar 1977)? Does a turbulent pipe flow consist of axisymmetric structures? What are the relative roles of coherent structures and incoherent turbulence to production and transport?

It should be clear that not only are there a variety of coherent structures in the turbulent boundary layers, very little is known about these structures. It seems that it should be possible to induce bursting at a fixed location at regular intervals and thus deduce contours of its properties at different phases in its evolution. It should also be possible to modulate/control the natural bursting structure through controlled pulsation of the boundary layer. Since bursting is more energetic and less frequent in the presence of a polymer additive (Oldaker & Tiederman 1977), it seems that a boundary layer with polymer additive provides a better opportunity for the investigation of the bursting structure.

If the coherent structure plays a key role in the transport phenomena in a boundary layer, then excitation at the bursting frequency should greatly alter the bursting event and thus the overall characteristics of the boundary layer. However, all experiments of periodic modulation of the boundary layer show no influence of the excitation in the time-average measures like $U(y)$, $u'(y)$ except very close to the wall *i.e.*, $y^+ < 50$ (Carr 1981; Parikh *et al* 1981; Simpson *et al* 1981), even though experiments of Mizushima *et al* (1973) showed some significant effects.

Modification or destruction of coherent structures may produce drag reduction. Yajnik & Acharya (1977) showed that a screen inserted in the boundary layer reduces the skin friction downstream; this is to be expected even naively because of the reduction of the wall slope of the velocity profile by the screen. Their results spawned extensive investigations at the NASA Langley Research Centre involving more effective devices (Hefner *et al* 1980). However, both these studies have not yet succeeded in producing net drag reduction because of the device drag penalty. Hefner *et al* claim that skin friction reduction is associated with reduction of the outer turbulence scale, an observation also supported by flow-visualization (Nagib *et al* 1978; Corke *et al* 1980). However, there have not yet been any cause-and-effect relationships established between coherent structure modification and drag reduction. Careful hot-wire and flow-visualization studies are necessary to show the effect of the devices on the sublayer structure, which must be altered in order to reduce drag.

Boundary layer studies are underway in our laboratory addressing some of the questions raised above. The rest of this paper discusses our studies of coherent structures in free turbulent shear flows.

7. Coherent structures in free turbulent shear flows

Large-scale coherent structures have been a major thrust of our recent research activity. These studies address the dynamics of coherent structures in a variety of turbulent shear flows *via* on-line computer-controlled experimentation and education of the coherent structure physics. To our knowledge, ours is the most active effort representing both the revolutions mentioned at the beginning of this paper. In the

following, we briefly review some of the studies of coherent structures and a few related matters.

7.1 Bimodal nature of coherent structures in a jet

In an attempt to understand the nature of organized motions in the near field of an axisymmetric jet, three air jets were subjected to controlled excitation *via* cavity resonance induced with a loudspeaker attached to the first of the two settling chambers of the facility (Hussain & Zaman 1975, 1977; Zaman & Hussain 1977, 1981b). These measurements showed that the receptivity of the jet as measured by the total centreline longitudinal fluctuation intensity, was the highest, not at $St_D (\equiv f_p D/U_e) = 0.3$ as suggested by Crow & Champagne (1971), but at the St_D value of about 0.85, which is twice the 'preferred-mode' of our facility. However $St_D = 0.3$ is still the preferred mode when it is redefined to represent the situation when the fundamental receives the maximum amplification.

It was shown that the jet near field consists of two distinct kinds of coherent structures: one results from the roll-up of the initial shear layer (when laminar) and scales on the characteristic thickness of the shear layer, say the exit momentum thickness θ_e ; the other forms farther downstream, say $x/D \gtrsim 1$, independent of whether the initial shear layer is laminar or turbulent and scales on the jet diameter (figure 2). Since the jet near field is a flow with two length scales, it is not surprising that these two distinct structures occur. We named these 'the shear layer mode' and 'the jet column mode', which now appear to have found general acceptance (see for example, Kibens 1980). If the frequencies associated with these two modes are denoted as f_s and f_j , then we found that the jet centreline fluctuation intensity was the maximum when $f_s \theta_e / U_e \cong 0.012$ and $f_j D / U_e \cong 0.85$, the large fluctuations being associated with intense large-scale activity during the 'shear layer mode of pairing' and the 'jet column mode of pairing'. As many as three successive stages of pairing have been found to occur in the shear layer mode while only one stage of jet column of pairing is found to occur. Thus, the final jet column mode structure forms at $f_p = f_j/2$. In an unforced

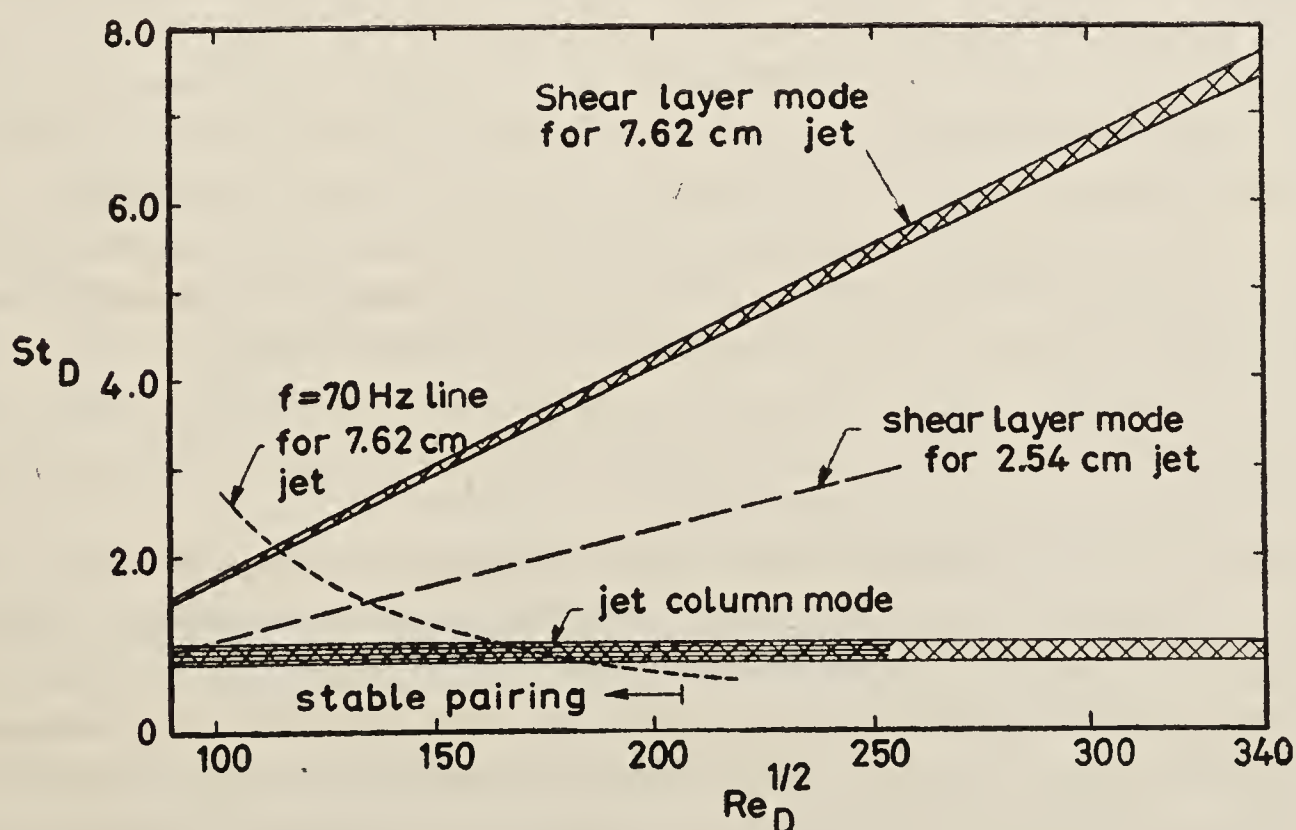


Figure 2. The jet-column and shear-layer modes.

jet, the frequency measured on the centreline progressively decreases until at $x/D \cong 3$ to the value f_p . Clearly, if U_e and D are such that $f_s > f_p$ as is typically the case, and if $f_s/f_p = 2^N$, then the terminal frequency f_p is reached through successive stages of pairings of the shear layer mode coherent structures. Even though N can have any value approaching infinity, it is not likely to be greater than 4; we have found N to be as high as 3. Thus, the coherent structures reach the terminal frequency f_p and achieve independence from the initial rolled up structures through successive pairings, not always as suggested by Browand & Laufer (1975), but only if f_s and f_p are in appropriate ratios. On the other hand, if excitation at f_p is very strong, an arbitrary number of the initially rolled-up vortices wrap up around each other (Hussain & Zaman 1977). It was also found that the vortex pairing in an initially laminar jet can be induced to be stable—so that successive pairings occur at the same location at periodic intervals—when the jet is excited at $f_s \theta_e / U_e = 0.012$ to induce the shear layer mode of pairing, or at $f_j D / U_e = 0.85$ to induce the jet column mode of pairing. However, for $Re_D \lesssim 5 \times 10^4$ or with increasing fluctuation intensity in the initial boundary layer, the pairing becomes progressively more random.

The trajectories of vortex centres and their convection velocities have also been recorded through phase-locked measurements. During pairing, two merging vortices undergo intense relative motions. The one ‘leapfrogging’ through has a velocity 25% higher than the centreline velocity U_e , while the other one slows down to $0.35U_e$. In measurements which involve the Taylor hypothesis or in others which are dependent on the structure convection velocity, the pairing stage poses a special problem because of the largely different convection velocities of the merging vortices. Vortex pairing is also found to produce large excursions of the instantaneous $uv(t)$ signal, suggesting that only certain phases of the pairing process may be important in turbulence and noise production as well as in entrainment.

7.2 Coherent structure dynamics during vortex pairing

The dynamics of the coherent structures in the near field of an initially laminar axisymmetric jet has been investigated by inducing stable vortex pairing in the ‘jet column mode’ (at $x/D \cong 1.75$). The structure properties have been studied in the region of stable vortex pairing, in a region preceding the pairing, and in a region downstream to the pairing location—all at the same phase. These are denoted as regions II, I and III, respectively. In the region II of pairing, the structure properties have been studied at four different phases of the pairing process. The studied properties include contours of phase-average longitudinal and lateral velocities u_c, v_c , coherent vorticity Ω_c , velocity vector pattern, instantaneous streamlines and pseudo-stream function $\langle \psi \rangle$, coherent Reynolds stress $\langle \tilde{u}_c \tilde{v}_c \rangle$ and incoherent turbulence Reynolds stress $\langle u_r v_r \rangle$ and intensities $\langle u_r^2 \rangle^{1/2}, \langle v_r^2 \rangle^{1/2}$.

Contours of the azimuthal vorticity Ω_c nondimensionalized by the excitation frequency f_p are shown in figures 3(a)–(c) for the three regions, respectively. The lowest vorticity contours are denoted by a dotted line in view of the relatively large uncertainty at this level. Note that the peak coherent vorticity continually decreases with increasing downstream locations of the structures from the jet exit, and that pairing of two vortices of the same sign does not produce an increase of the core vorticity. The braids connecting adjacent vortices are marked by very low vorticity. While

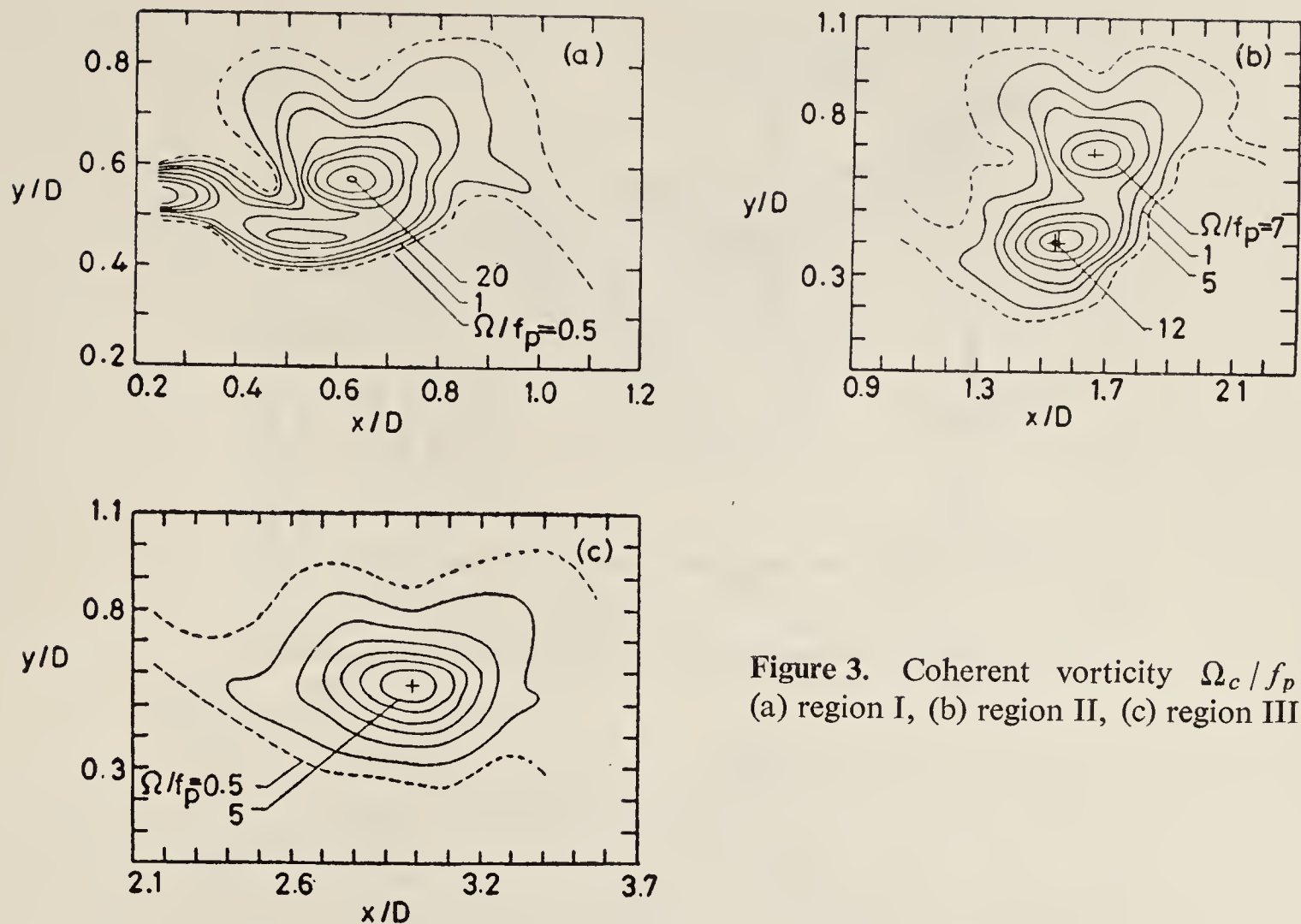
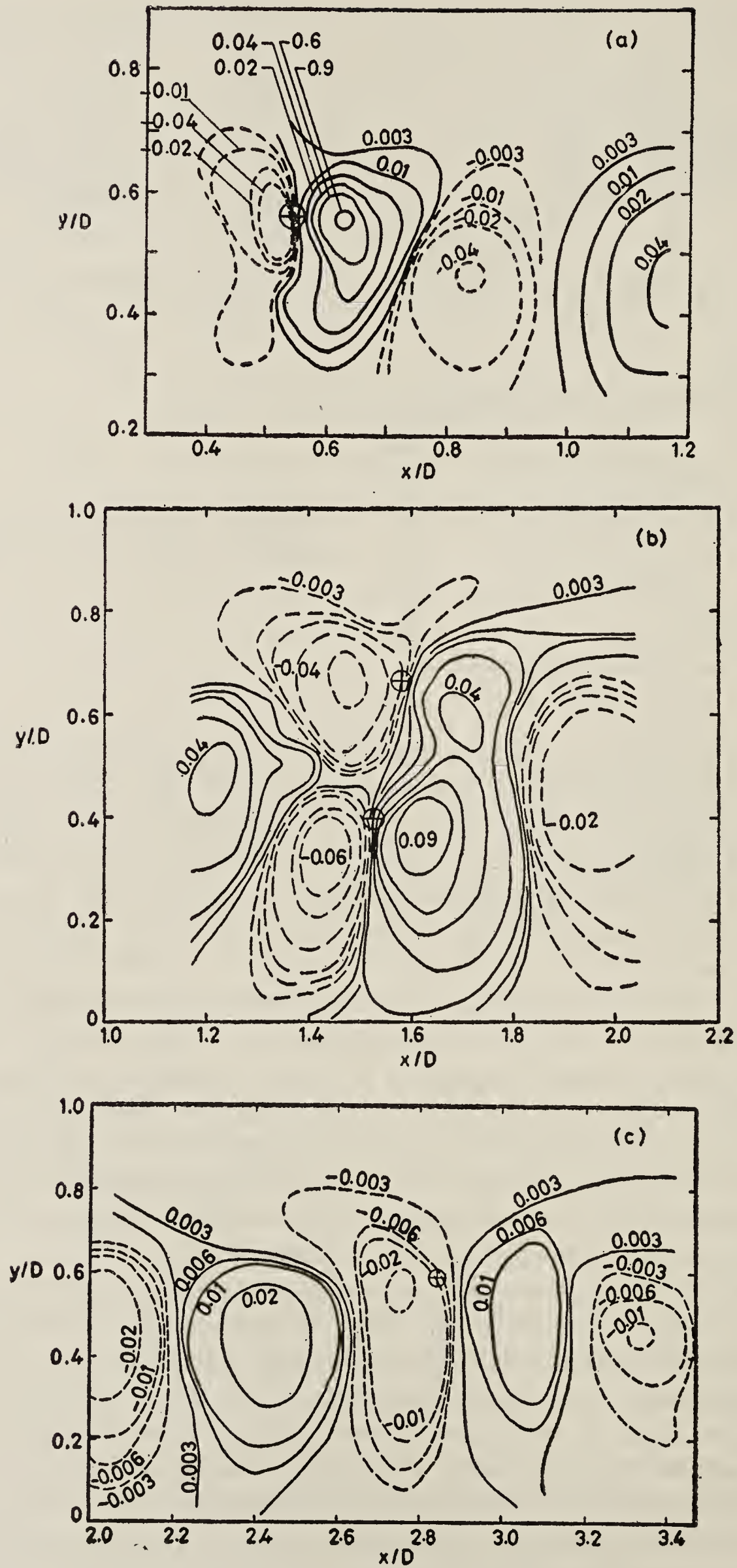


Figure 3. Coherent vorticity Ω_c/f_p :
 (a) region I, (b) region II, (c) region III.

jitter can partly contribute to the low measured vorticity in the braid, the vorticity is indeed low because the vortical fluid is continually advected away from the braid under the induced motions of the coherent structures and deposited at the structure cores (Corcos & Sherman 1976). The dips in the vorticity contours on the low-speed side are due to two artefacts of measurement: flow reversal and jitter. Associated with the passage of each vortical structure, the flow on the outer edge of the structure has an upstream velocity in the laboratory frame (Antonia *et al* 1980b; Hussain & Zaman 1980). Because the hot-wire rectifies the corresponding velocity signal, it produces a distortion in the contours of vorticity, streamlines etc. on the low-speed side. With progressive increases of spatial separation between the detection and measurement probes, the effects of jitter on ensemble averages increase, producing a progressive smearing in the deduced contours. Because the structure detection probe is located in region II, the low-speed side dip due to jitter is the largest in region I. The effects of flow reversal and jitter have been conclusively demonstrated to produce the low-speed side dips shown in figures 3(a)–(c) (Hussain & Zaman 1980).

The coherent Reynolds stress distributions corresponding to figures 3(a)–(c) are shown in figures 4(a)–(c), respectively. Since the time average Reynolds stress \overline{uv} consists of contributions from alternate positive and negative regions, and the positive contribution exceeds the negative contribution, the net contribution is positive on a time-average basis. In the region of pairing, the relative positive and negative contributions depend on the frequency of excitation and the phase of pairing. Thus, depending on the frequency of excitation, the zone-average coherent Reynolds stress can be either of the co-gradient or counter-gradient type. The zone-average coherent Reynolds stress for the phase selected for figures 3(a)–(c) is much higher for the pairing region II than in either of regions I and III or even further downstream. Even in the pairing region II, the zone-average coherent Reynolds stress is much higher only at an early phase of the pairing event. Thus, depending on the phase—which repeats



Figures 4(a)-(c). Coherent Reynolds stress $\langle \tilde{u}_c \tilde{v}_c \rangle / U_e^2$ corresponding to (a), (b), and (c) in figure 3.

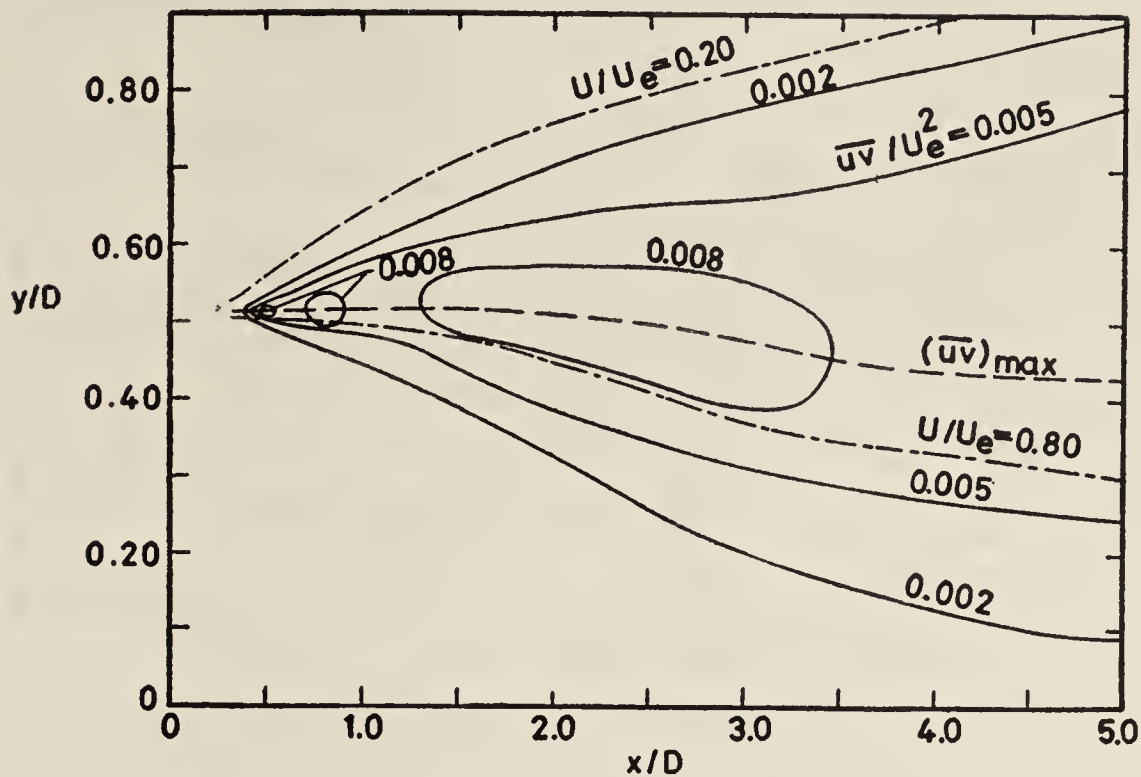


Figure 5. (a) \overline{uv}/U_e^2 contours.

at regular intervals at the same measurement location—the sign of the time-average Reynolds stress can be such as to make the production positive or negative. Figure 5b shows the contours of time-average Reynolds stress for the composite of the regions I–III and farther downstream. The corresponding contours without forcing are shown in figure 5a. Note the large region of ‘negative production’ induced by the stable pairing (first demonstrated and explained by Hussain & Zaman 1977). When pairing occurs at random locations, as is the case in forcing at Strouhal numbers other than $St_D \simeq 0.85$ or $St_\theta \simeq 0.012$, negative production would not be measured. That is, for the mixing layer, negative production will occur when excitation forces the pairing event to repeat itself at the same location. Wygnanski & Oster (1980) also reported ‘negative production’ in a strongly forced plane mixing layer, but have not explained it.

Associated with the localization of the positive and negative peaks of the Reynolds stress, there is a large displacement of the location where maximum \overline{uv} occurs. Note that at the x -location where ‘negative production’ occurs, the \overline{uv} -peak is far away from the y -location of maximum mean strain rate, located essentially at $U/U_e = 0.5$ and that the negative production occurs between these two maxima. The width of the mixing layer, denoted by the transverse separation between the $U/U_e = 0.8$ and $U/U_e = 0.2$ lines, shows an abrupt increase followed by an abrupt decrease. The increase is associated with the start of the pairing event when the two structures move radially away from the $U/U_e = 0.5$ line. The decrease is associated with a slightly later phase when the two radially displaced structures return to the $U/U_e = 0.5$ line after the rear structure has moved ahead of the other through the ‘leapfrogging’ motion. Note that the decrease in the width is associated with the ‘negative production’ as the $\langle \tilde{u}_c \tilde{v}_c \rangle$ contours at this concluding phase of pairing was found to be negative over a much larger area (Zaman 1978).

The time-average Reynolds stress is dominated by the zone-average coherent Reynolds stress $\langle \tilde{u}_c \tilde{v}_c \rangle$ in region II. However, in region III and further downstream, $\langle \tilde{u}_c \tilde{v}_c \rangle$ progressively decreases and becomes comparable to the incoherent Reynolds stress $\langle u_r v_r \rangle$. Figure 5c shows the contours of $\langle u_r v_r \rangle$ for the range $0 < x/D < 5$; the plus signs indicate the locations of peak vorticity. Note that

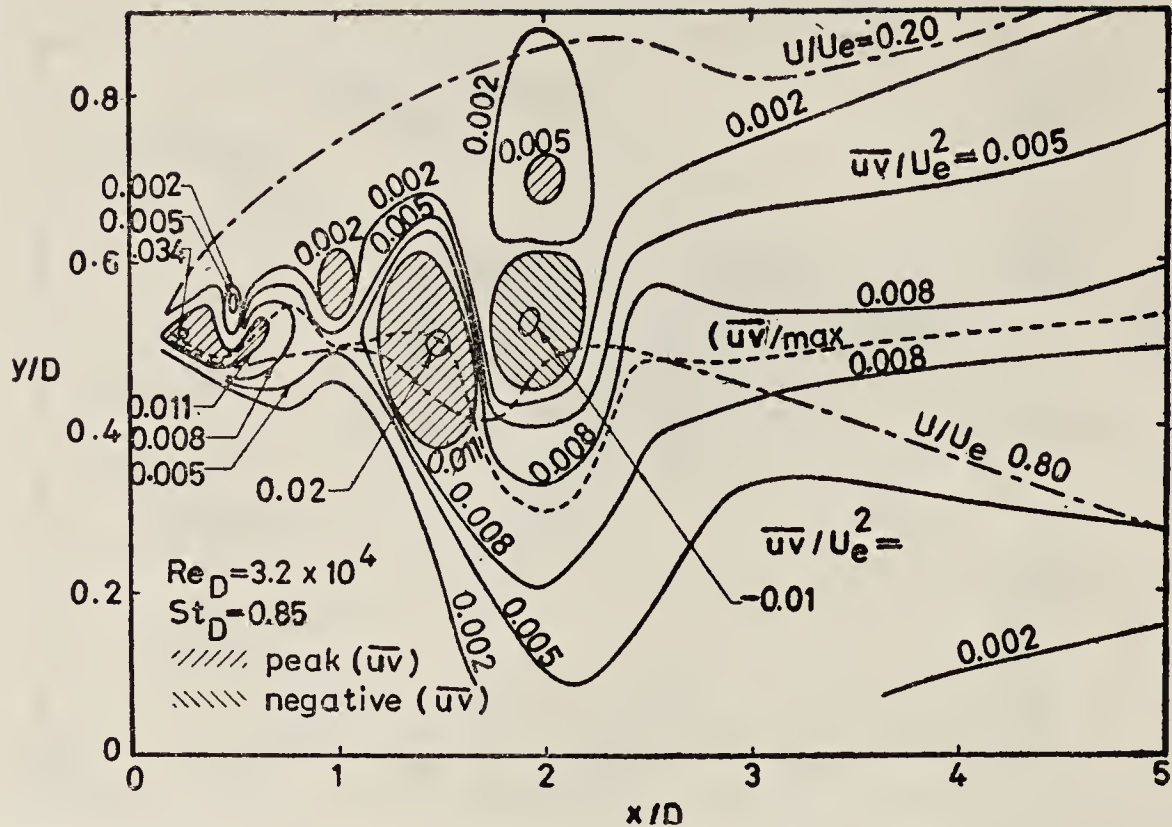


Figure 5(b) \overline{uv}/U_e^2 contours when excited at $St_D = 0.85$;

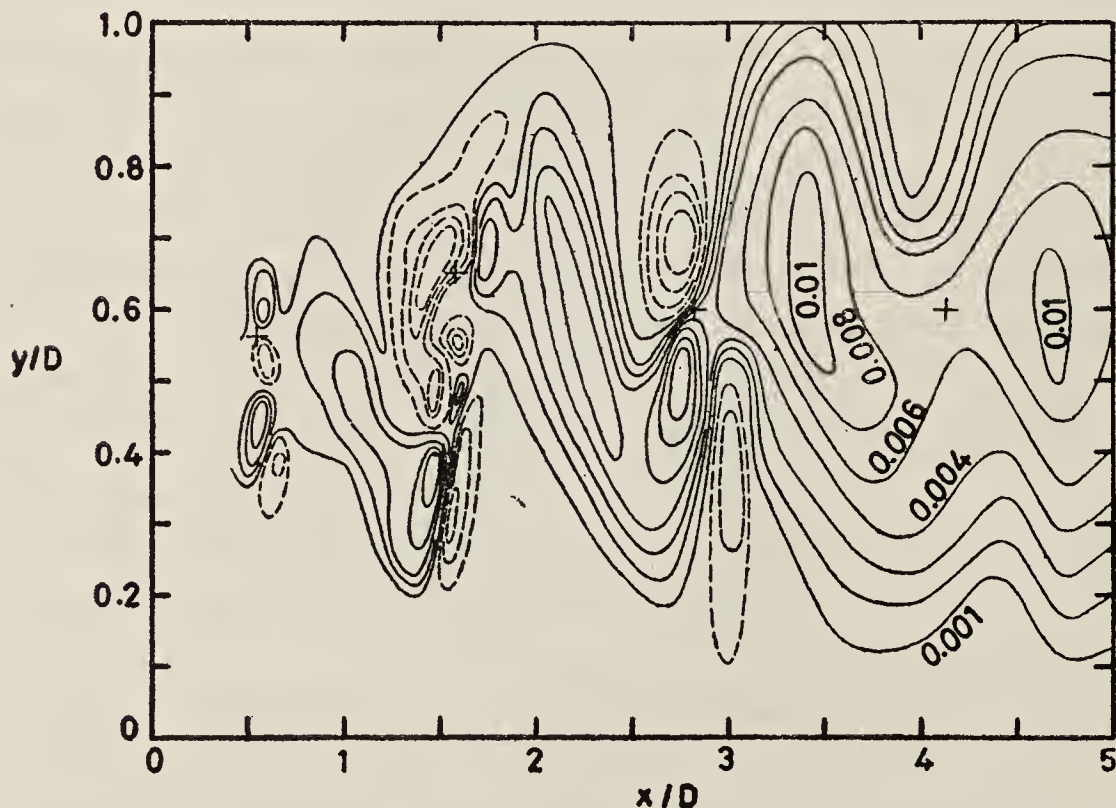


Figure 5 (c) $\langle u_r v_r \rangle / U_e^2$ contours corresponding to (b), dashed contours are in sequence: -0.001 , -0.002 , -0.003 , -0.004 , -0.006 , -0.008 , -0.01 .

$\langle u_r v_r \rangle$ distributions have 'saddle points' at the locations of structure centres as can be predicted from the coherent vorticity equation (Hussain & Zaman 1980). Physically, incoherent turbulence production is the maximum at the braid (see later) due to large strain rates, although vorticity is low there. The continual rotation of the structures drains the turbulent fluid away from the braids and deposits in the structure centres and thus produces the dilution of coherent vorticity there.

The azimuthal extent of the coherent structures was investigated by both time-average and phase-average circumferential correlations; the latter was obtained by sampling the hot-wire signal at the phase at which the coherent structure was at the measurement probe location. These data show that in the absence of excitation, the circumferential correlation is lost by $x/D \cong 2.8$. Excitation enhances the initial azimuthal organization of the structures but fails to prevent their breakdown near the end of the potential core. The breakdown of the initially toroidal structure occurs through evolution of azimuthal lobes (Widnall 1975; Saffman 1978; Davies & Baxter 1977).

7.3 The preferred mode with and without excitation

Even though the near field of an axisymmetric jet is known to be dominated by a structure convected at a Strouhal number $St_D \cong 0.3$ (Crow & Champagne 1971; Hussain & Zaman 1975), the details of these structures were not explored previously. In particular, contours of properties over the spatial extent of the structure and the dynamical role of these structures were never elucidated. Additional questions that were never addressed are: To what extent are the structure details dependent on the Reynolds number and the initial condition? Do the induced structures resemble the naturally occurring structures? What should be the most effective criterion for the education of the natural structures?

The preferred-mode coherent structure has been elucidated for both excited and unexcited situations at a few Reynolds numbers and for the two asymptotic initial conditions (*i.e.* laminar and fully-developed turbulent).

The excited preferred-mode coherent structure was studied by inducing it with controlled excitation at $St_D \cong 0.3$. The resulting coherent structure properties were documented *via* phase-locked hot-wire measurements with the help of the on-line laboratory computer over the spatial extent of the structure and thus without invoking the Taylor hypothesis (figure 6). In order to reduce the effect of jitter, the education was triggered by a reference signal from a detection probe located on the jet centreline at $x/D = 3$. The triggering condition was selected by simultaneous examination of the reference signal and flow visualization of the coherent structure. Note that since the structure is induced at the 'terminal Strouhal number', it does not undergo pairing.

Figures 7(a)–(d) show the contours of azimuthal component of coherent vorticity Ω_c nondimensionalized by the excitation frequency f_p ; (a), (b), (c) are for the Reynolds numbers $Re_D = 25,000$, $55,000$ and $110,000$ —all with fully-developed turbulent exit condition (see § 4.1); (d) is for $Re_D = 55,000$ but with a laminar initial condition. The excitation frequencies f_p are: 178 Hz, 44 Hz, and 87 Hz for $Re_D = 25,000$, $55,000$, and $110,000$, respectively. Note that in spite of large variations in the diameter (3 times), the frequency (4 times) and the jet speed (2 times), the nondimensional peak value of the coherent vorticity is essentially the same; there is no significant difference with the initial condition either. However, with increasing Re_D , the structures become more rounded and thus should become more efficient in momentum transport. The

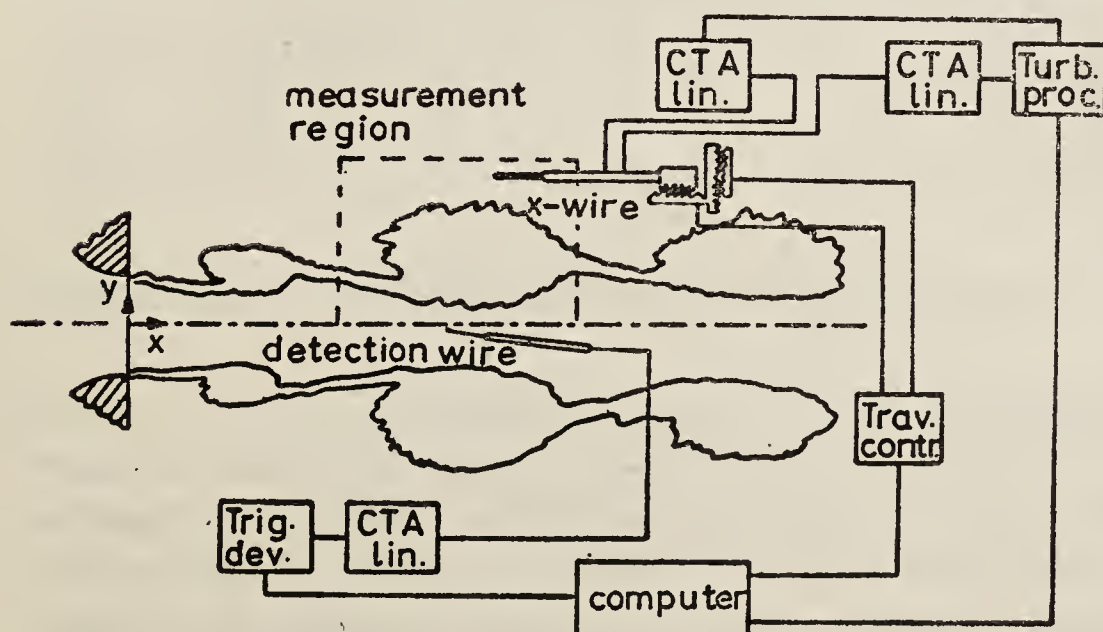


Figure 6. Schematic of education of the preferred-mode coherent structure.

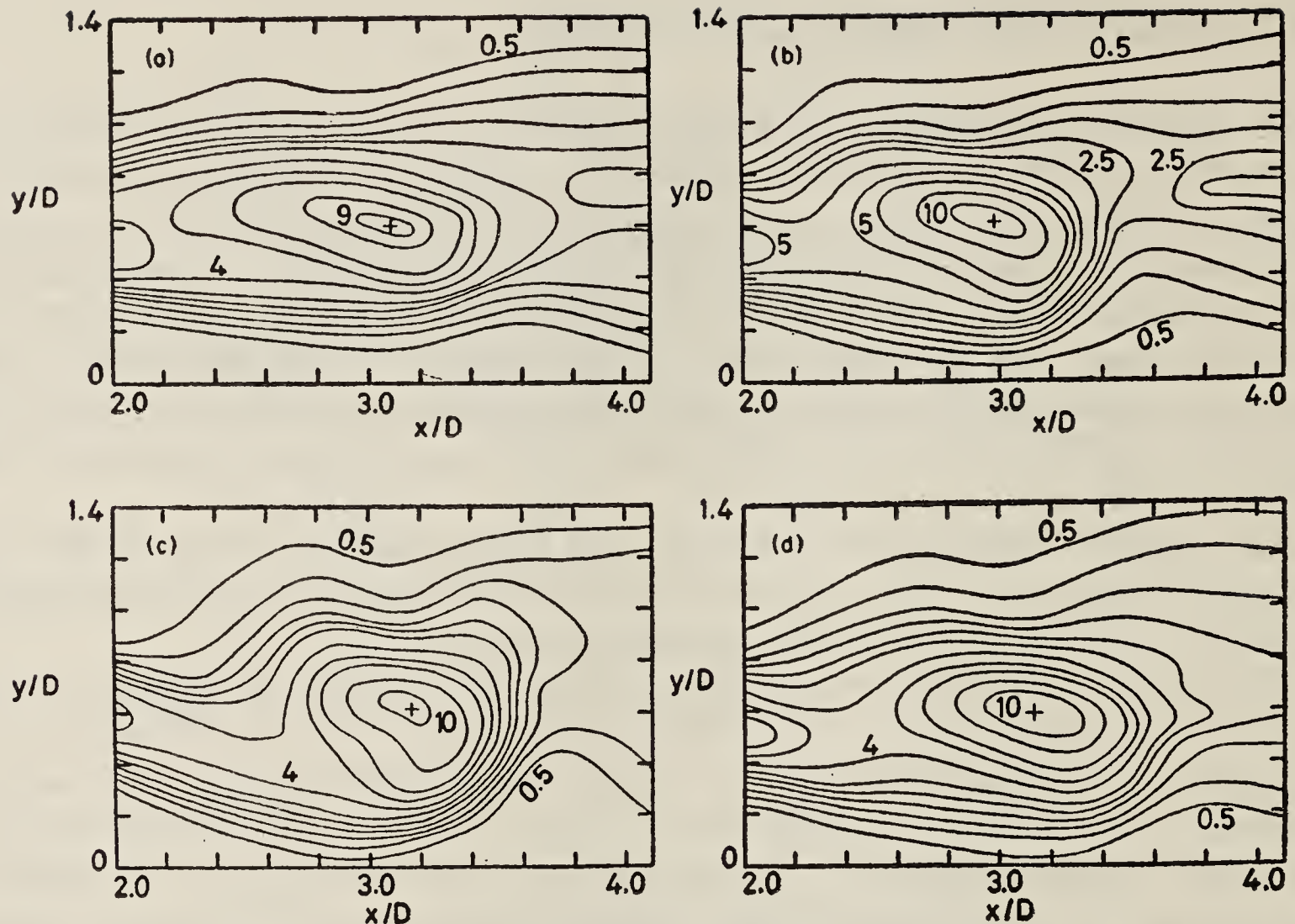
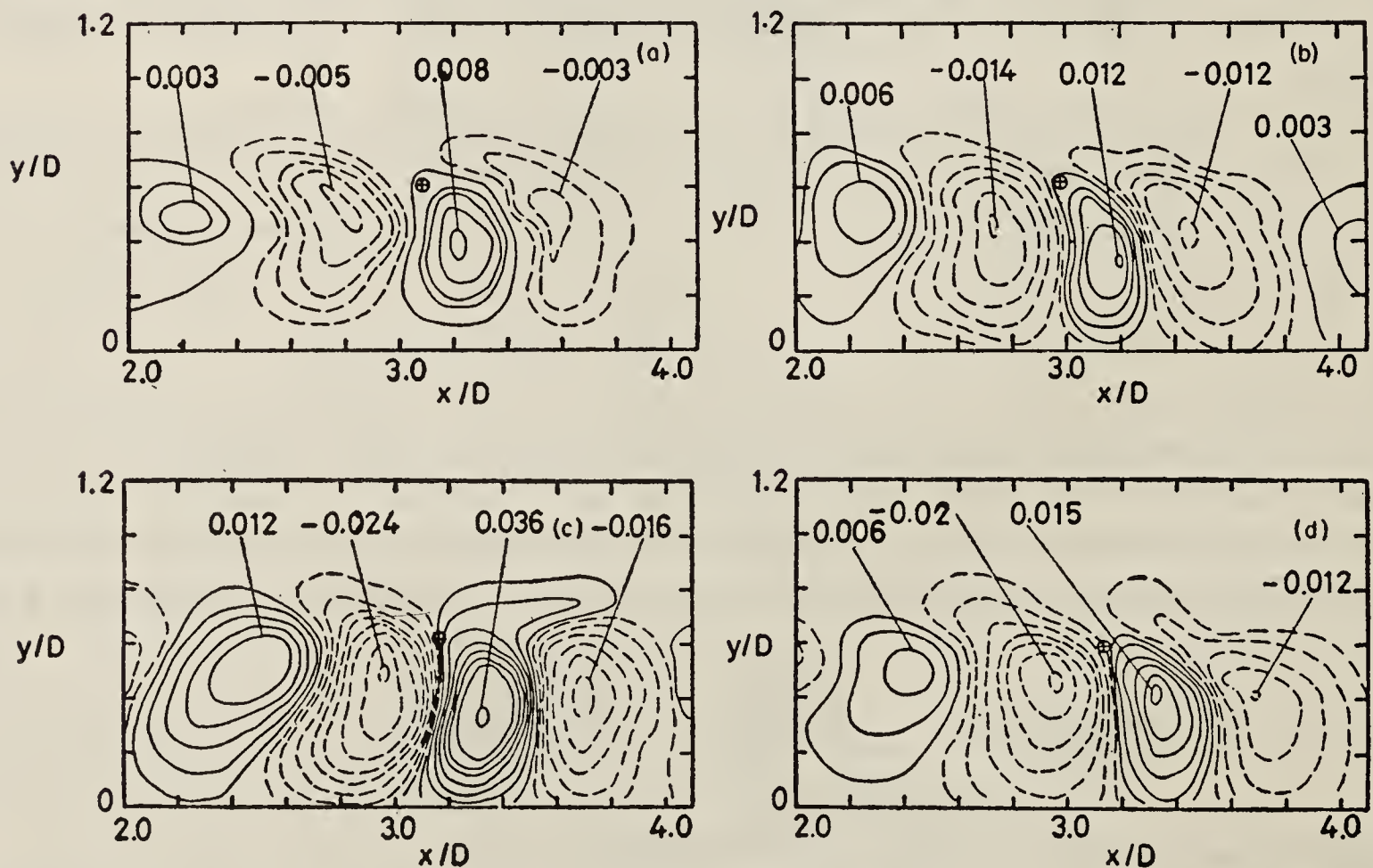


Figure 7. Contours of Ω_c/f_D : (a) $Re_D = 25,000$ tripped; (b) $Re_D = 55,000$ tripped; (c) $Re_D = 110,000$ tripped; (d) $Re_D = 55,000$ laminar.



Figures 8(a)-(d). Contours of coherent Reynolds stress $\langle \tilde{u}_c \tilde{v}_c \rangle / U_e^2$ corresponding to figures 7(a)-(d).

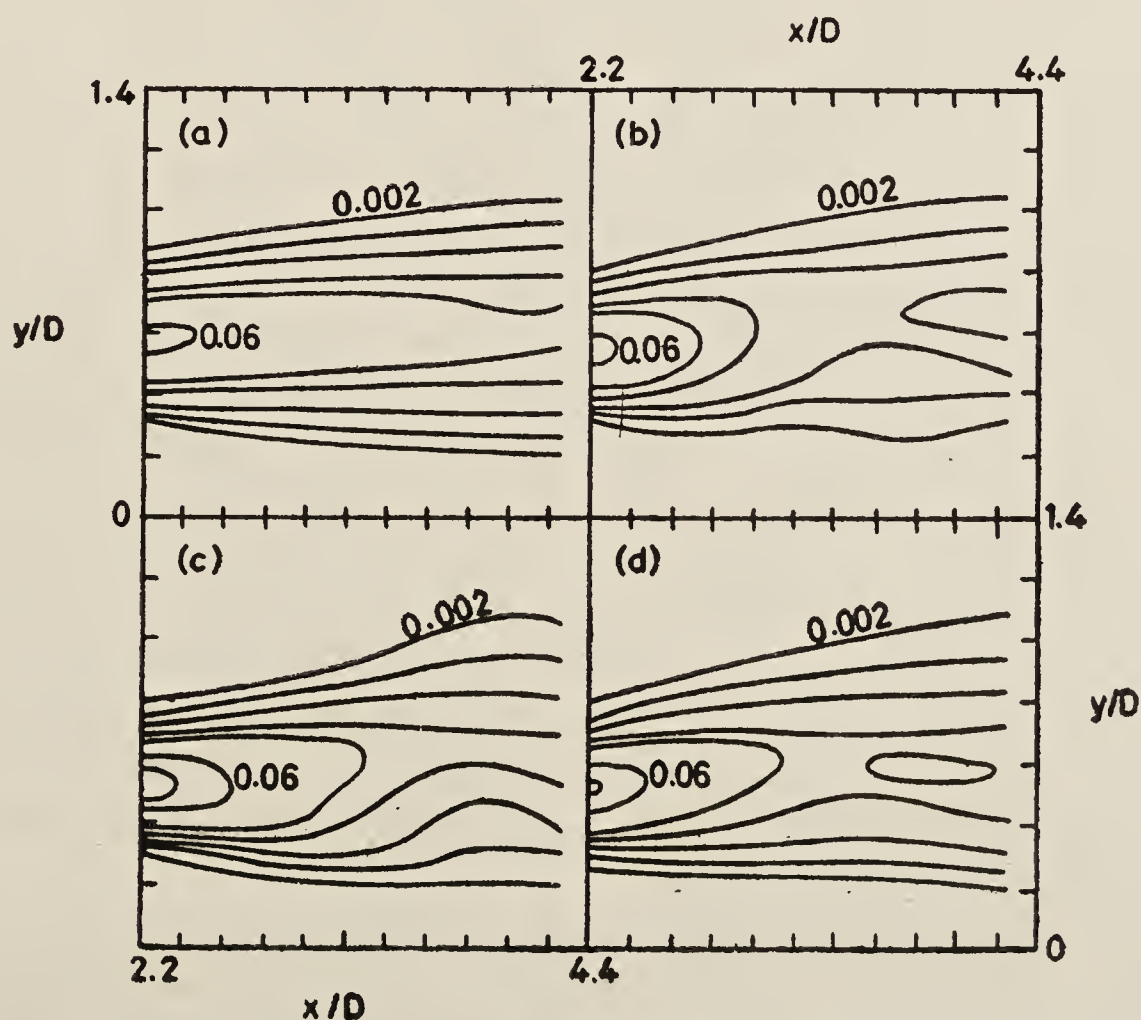
contours of coherent Reynolds stress $\langle \tilde{u}_c \tilde{v}_c \rangle$, corresponding to the figures 7(a)-(d) are shown in figures 8(a)-(d). Note that the structures carry with them alternate regions of positive and negative $\langle \tilde{u}_c \tilde{v}_c \rangle$, as to be expected. Both positive and negative peaks increase with Re_D , so that their difference, which is a measure of the structure contribution to the time-average Reynolds stress, also increases with Re_D . Note that

even $\langle \tilde{u}_c \tilde{v}_c \rangle$, which is a higher order measure than Ω_c , shows no clear dependence on the initial condition.

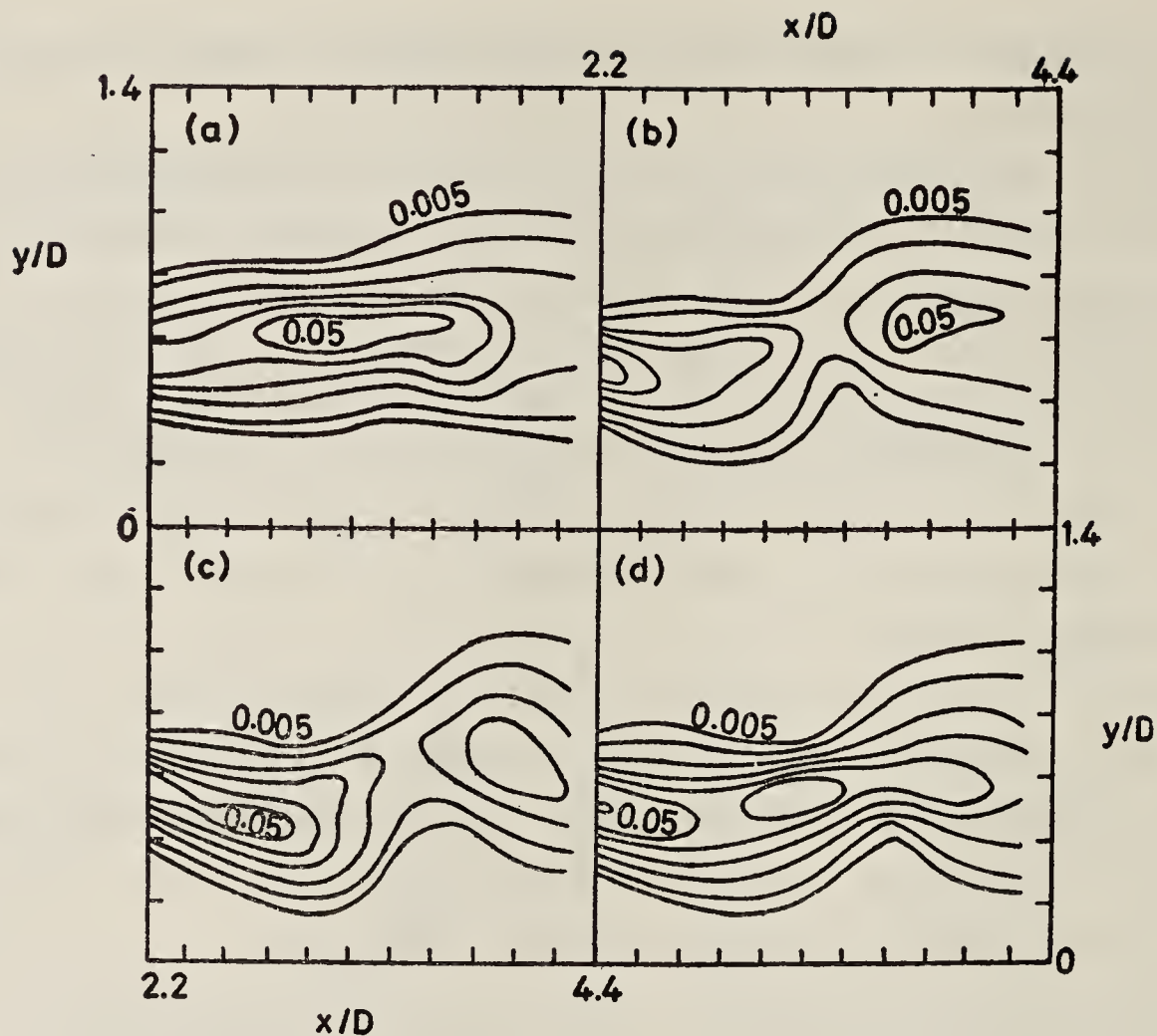
Do the increasing coherent Reynolds stress peaks with increasing Re_D suggest that the nondimensional time-average Reynolds stress increases indefinitely with Re_D ? Even though the Reynolds number similarity or asymptotic invariance has lacked adequate scrutiny and is yet to be proven to be true, we do not intend to suggest a violation of this invariance. Thus, the above results would then suggest that in the unforced jet, the organized structure occurs less frequently at higher Re_D . The flow-visualization studies of Hussain & Clark (1981b) support this. Furthermore, the experiments suggest that the preferred-mode St_D decreases with increasing Re_D (Hussain & Zaman 1981a).

While Ω_c and $\langle \tilde{u}_c \tilde{v}_c \rangle$ have been found to vary with Re_D up to 10^5 , it is not expected that this trend will be manifest for still higher Re_D . In fact, Crighton's (1980) observation and Hasan & Hussain's (1981) data suggest invariance for $Re_D > 10^5$. These results also strongly suggest that high Re_D jet behaviour cannot be extrapolated from data obtained at Re_D significantly below 10^5 .

The contours of time-average and phase-average shear productions \bar{P} and $\langle P \rangle$ are shown in figures 9 and 10, respectively. Note that the phase average reveals that the production is more non-uniform in space with increasing Re_D and that production is the maximum at the braids. The contours of incoherent turbulence intensities, however, show maxima at the structure centres. Thus, turbulence produced in the braids is advected and deposited at the structure core. This also produces dilution of the core vorticity due to the enhanced turbulent diffusion (Hussain & Zaman 1981a, b).



Figures 9(a)-(d). Contours of $\bar{P}/(f_p U_e^2)$ corresponding to figures 7(a)-(d).



Figures 10(a)–(d). Contours of $\langle P \rangle / (f_p U_0^2)$ corresponding to figures 7(a)–(d).

In order to compare the educed structure, which is induced *via* controlled excitation, with the naturally-occurring structure, an optimum conditional sampling technique was developed (Zaman & Hussain 1981c). The optimization was based on the vorticity contours measured by an X-wire while the data sampling by the laboratory computer was triggered by characteristic features of the reference signals obtained from triggering probes located at the same station. After considering the $u(t)$ and $v(t)$ signals at different transverse locations across the width of the mixing layer, it was found that the eduction of the coherent structure was the best when triggered on the positive peaks on the high-speed side. Furthermore, the sensitivity of the eduction to the threshold amplitude was also determined; with increasing threshold levels, the eduction improved, as to be expected. If the peaks are associated with passages of large-scale structures, the higher positive peaks or the lower negative peaks are due to either stronger structures or structures which are closer to the triggering probe as they travel past the triggering probe. Because these structures are detected near the jet exit ($x/D = 3$), the lateral wandering (which increases with increasing x) should be minimal. Thus at $x/D = 3$, the variations in the peak can be mostly attributed to different strengths. At lower detection threshold levels, structures of a variety of strengths are accepted by the triggering criterion, thus producing a smearing of the educed structures. At higher threshold levels, only the strongest, and thus the more select structures are accepted. It was found that a threshold level equal to twice the r.m.s. of the signal produced the best eduction when triggered on the positive peaks in the u -signal. Higher threshold levels and selection of a narrow window for the signal peak values improved the eduction marginally, but at the penalty of prohibitively increasing the experiment time.

The eduction scheme was calibrated by first educing the preferred-mode coherent structures when induced *via* controlled excitation. Then, the forcing was turned off, and the structure properties, educed by the conditional sampling technique, were compared with those of the excitation-induced structures educed by the same

technique. The similarity between the two contours confirm our contention that the excitation, especially when small-amplitude, does not produce artificial structures (as suggested by many, for example, see Lau 1979) but merely paces the formation times of the natural structures. Educated vorticity contours for the unforced preferred-mode coherent structures at $Re_D = 327,000$ and $800,000$ show no difference with those at $Re_D = 110,000$. We conclude that the structure details, which depended on Re_D at lower values, are independent of Re_D larger than 10^5 . The same conditional sampling technique educed essentially the same structure for both laminar and fully turbulent initial conditions (Hussain & Zaman 1981c). At the higher values of Re_D , we could not obtain a laminar exit condition and thus the independence of the initial condition is based on data up to $Re_D \simeq 10^5$.

7.4 Turbulent 'spots' in axisymmetric and plane mixing layers

The evolution of a highly localized impulsive disturbance in a mixing layer was investigated by producing an electrical spark in the boundary layer upstream of the trailing edge. Unlike the sinusoidal excitation inducing periodic structures discussed in §§ 7.1 and 7.2, where all adjacent structures are excitation-induced, the induced structures in this case are separated by natural structures. The induced structures occupy about 4% of the time between two sparks. Using the sparks as phase reference and considering the structure convection velocity, 200 realizations of each spark were captured with an X-wire, the data sampling being controlled by the on-line laboratory computer. Data were recorded for small time spans capturing the 'spot' signature at different radial and azimuthal locations—all triggered at the same phase.

Because of the turbulence-induced jitter, a straightforward ensemble average smears out the spot signature; the smearing increases with increasing downstream distances and also with increasing radial distances. These factors necessitated alignment of the signals at each location. However, due to the absence of any distinguishable characteristic feature in the signal associated with the 'spot', the alignment was done *via* a method of iterative alignment by optimizing the cross-correlation of each realization with the ensemble average. This elaborate process was hastened by low-pass filtering each record since the signature of the 'spot', which is a large-scale structure, was assumed to be associated with lower frequencies. However, after the final alignment, the unfiltered signals were ensemble-averaged to educe structure properties. The education was further refined by rejecting realizations which required excessive time shifts and thus considered 'freak'. The criterion used was that time shifts larger than three times the r.m.s. of all time shifts for that ensemble were 'excessive.' The rationale was that those structures have strayed away too far in time and they have been subjected to unusual distortions. The rejection was the least on the high-speed side but the most on the low-speed side, as to be expected (Bruun 1977; Yule 1978; Hussain & Clark 1981b), but in no case the rejection exceeded 50% of the realizations. Since more realizations are accepted on the high-speed side, the high-speed side contours are more reliable. Note that further refinement is possible by rejecting realizations that produce very low peak correlations after final alignment. This was not done, as this should be accompanied by a lesser stringent criterion for rejection due to time-alignment. Otherwise, there will be locations where more than 50% of the realization will be discarded, and the resulting ensemble average,

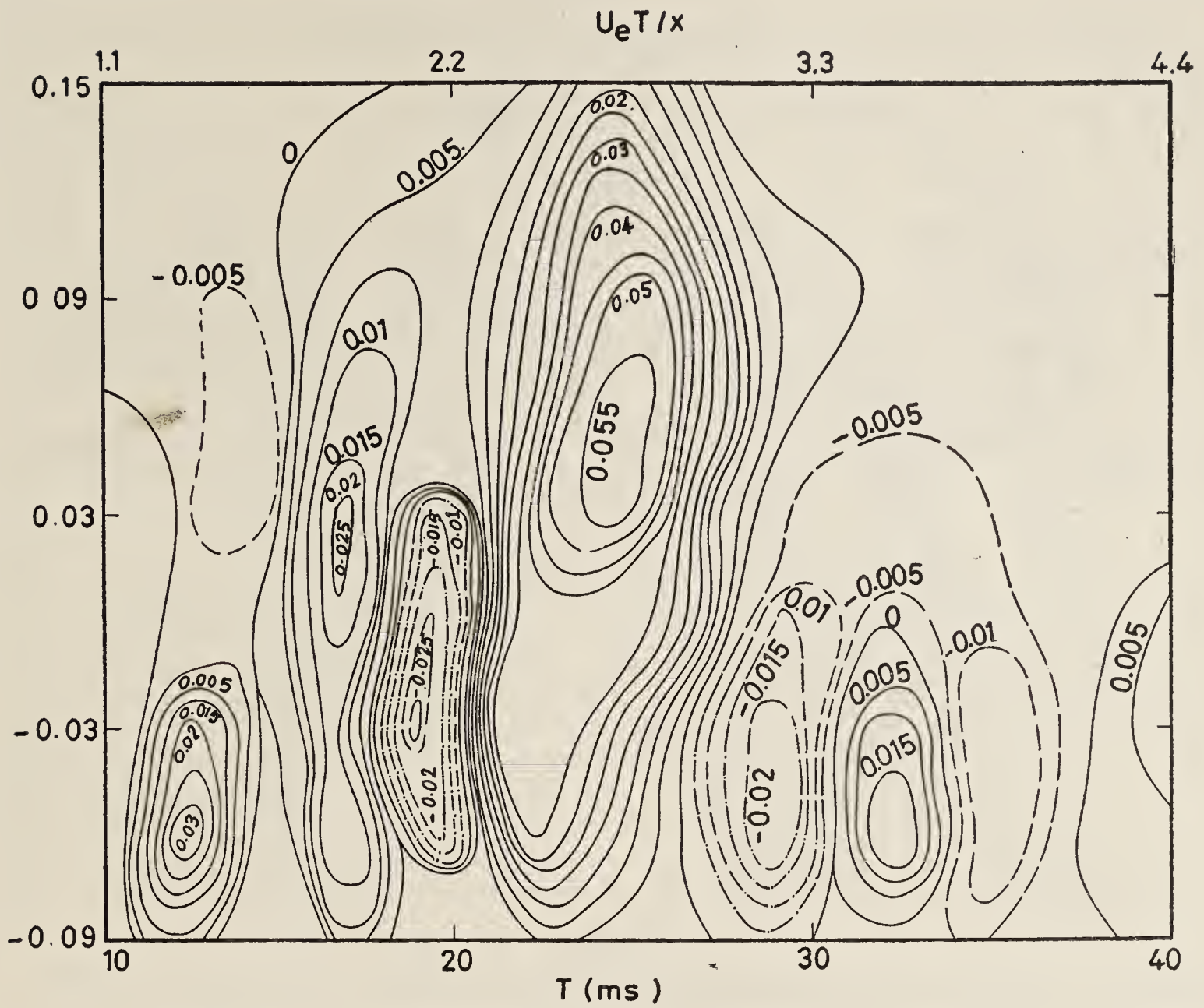


Figure 11c. Contours of phase-average spot properties at $x/D=1.5$; $\eta=(y-0.5D)/x$. $\langle u_c v_c \rangle / U_e^2$.

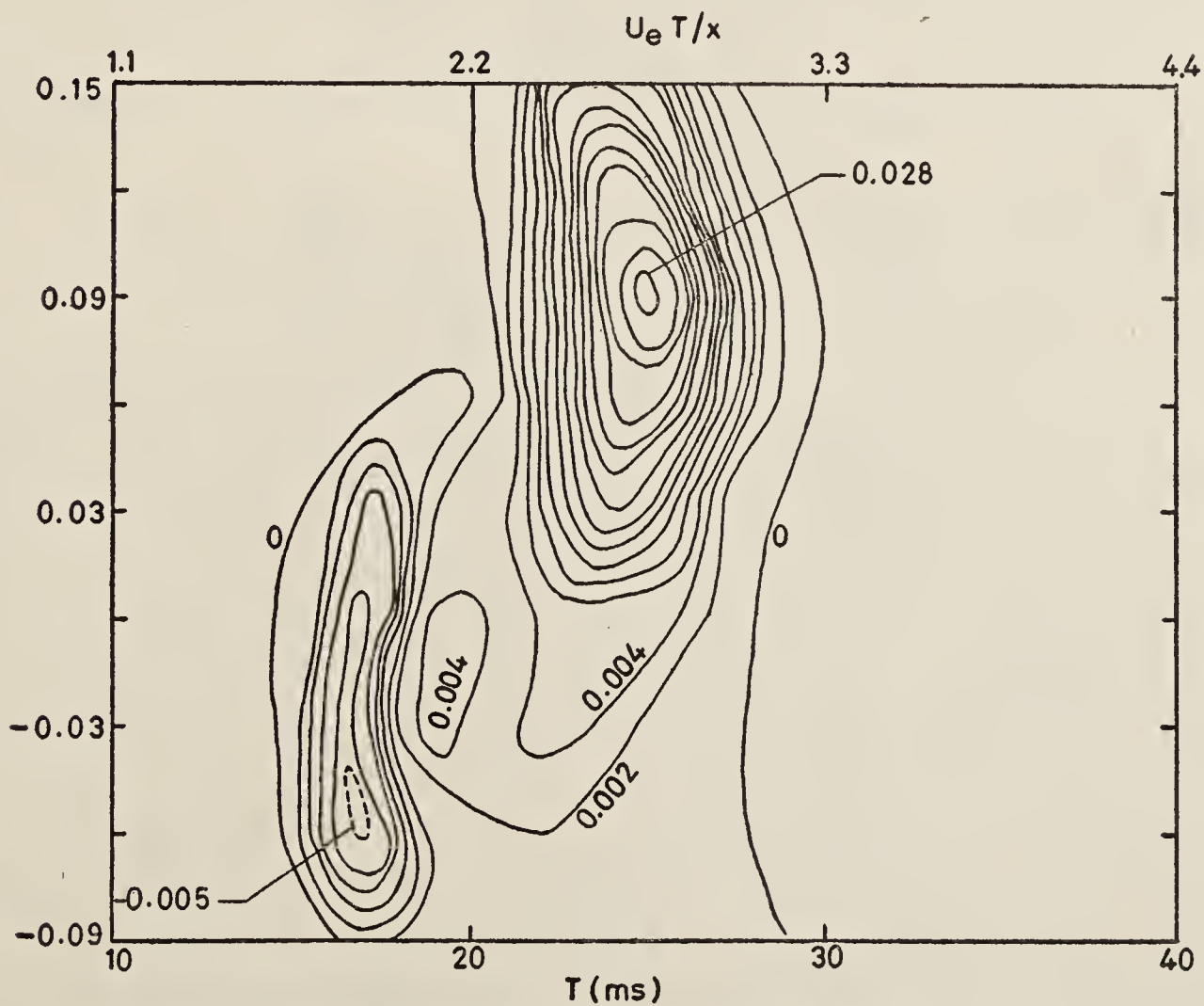


Figure 11d. Contours of phase-average spot properties at $x/D=1.5$; $\eta=(y-0.5D)/x$. $\langle \tilde{u}_c \tilde{v}_c \rangle / U_e^2$.

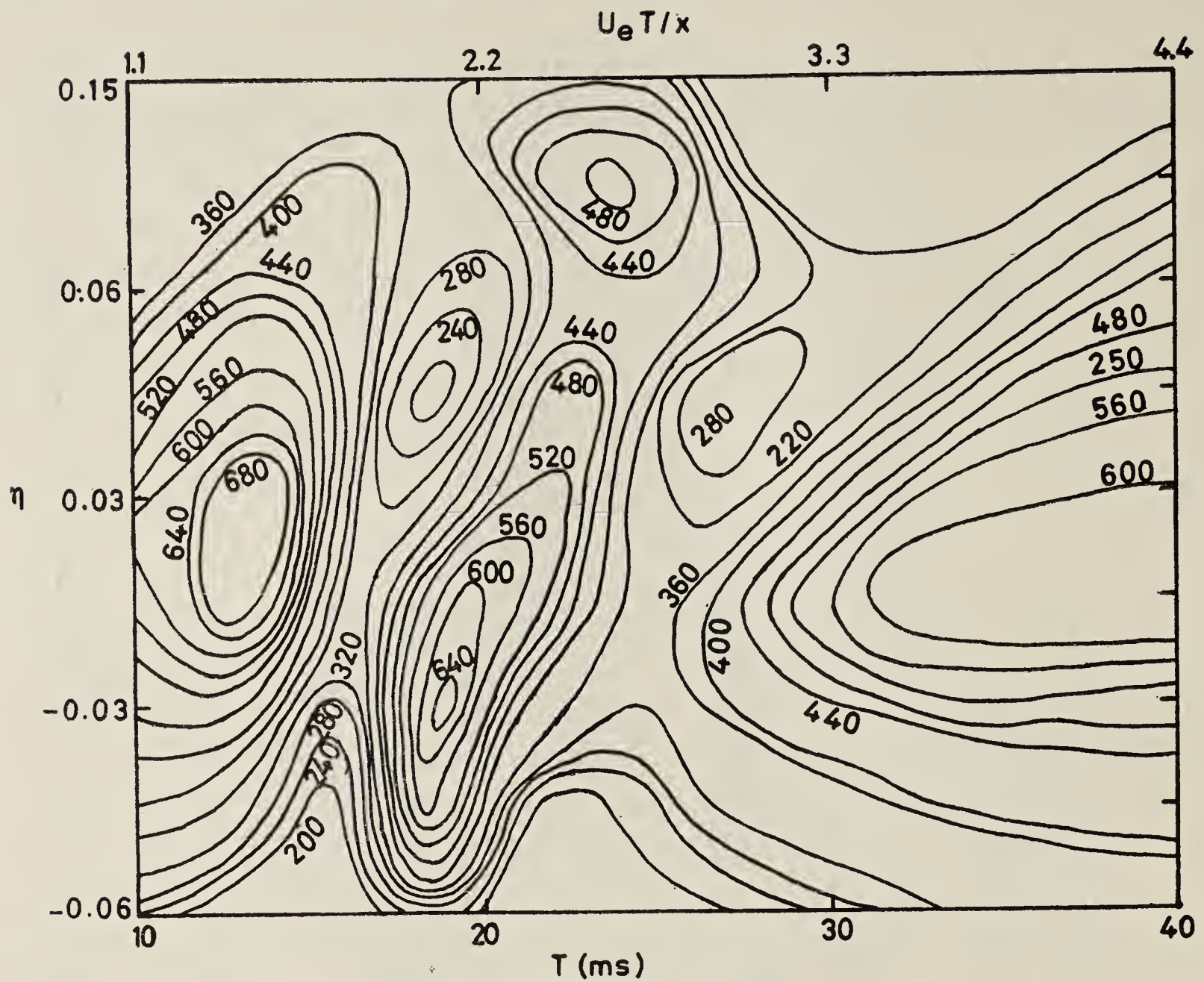


Figure 11e. Contours of phase-average spot properties at $x/D=1.5$; $\eta=(y-0.5D)/x$. Ω_c/f_p .

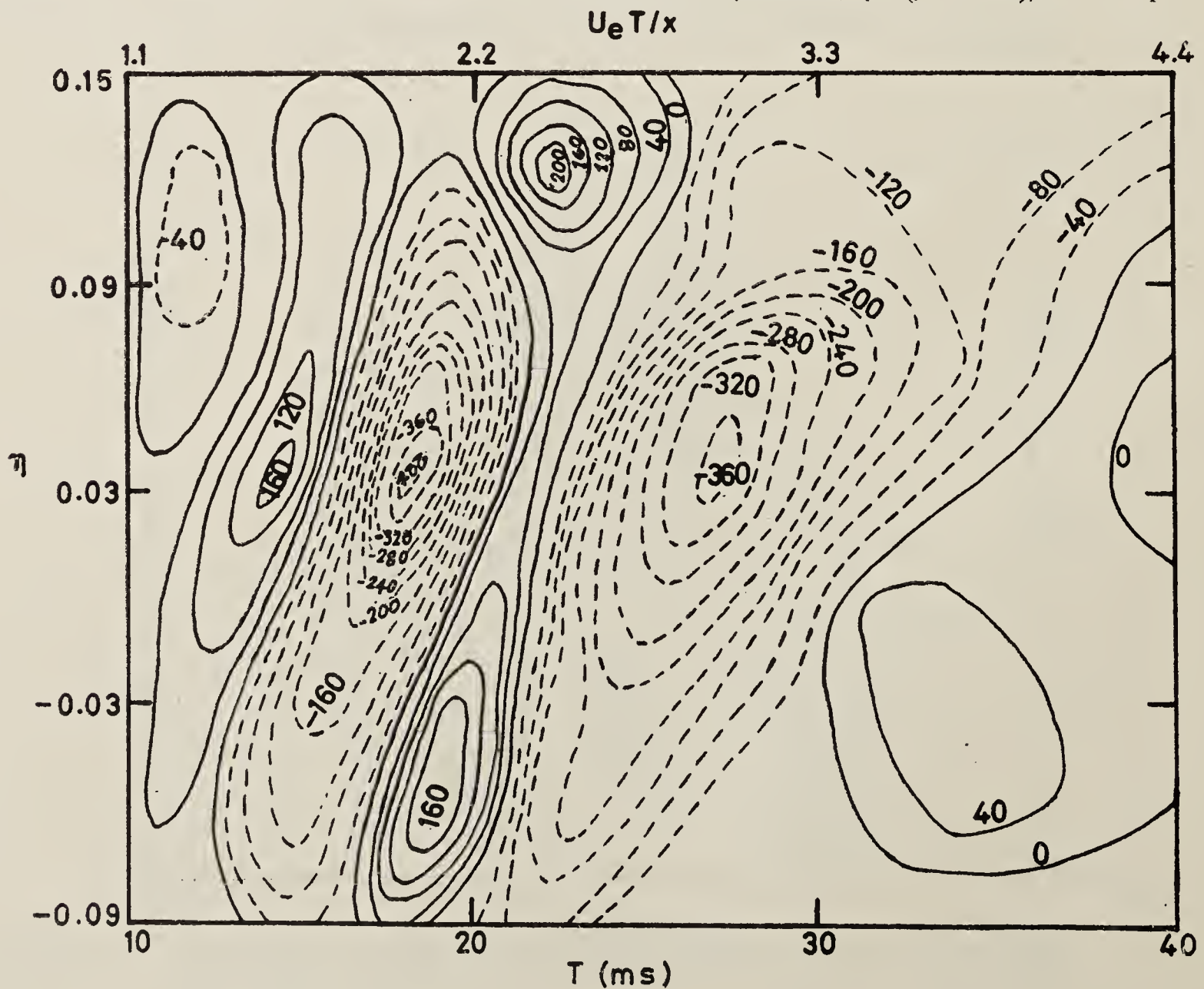


Figure 11f. Contours of phase-average spot properties at $x/D=1.5$; $\eta=(y-0.5D)/x$. $\tilde{\Omega}_c/f_p$.

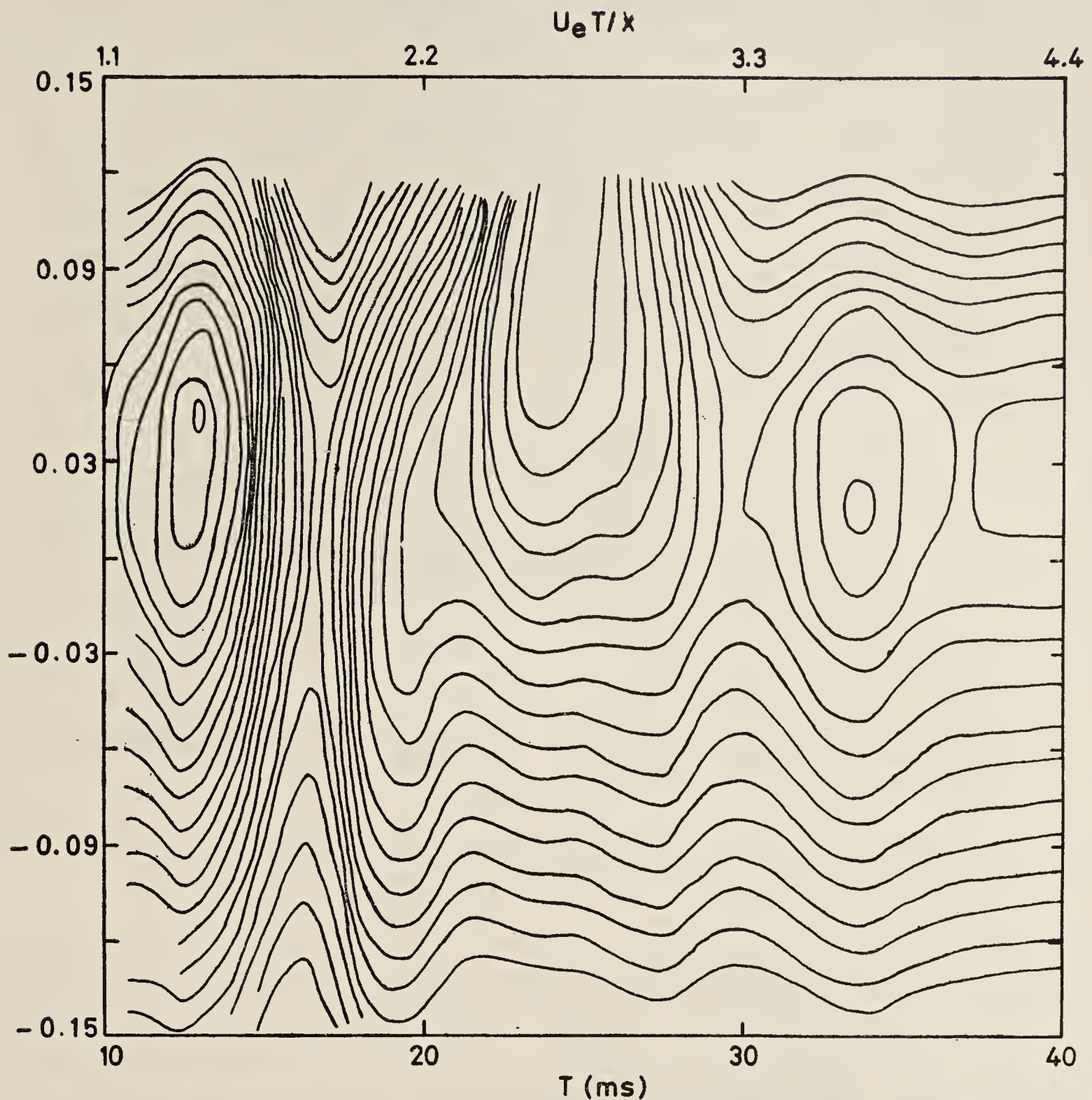


Figure 11g. Contours of phase-average spot properties at $x/D = 1.5; \eta = (y - 0.5D)/x$
 $\langle \psi \rangle = \int_0^y y' [(\langle u \rangle - 0.5U_e) dy'] / (D^2 U_e)$

In an attempt to understand the interaction of two 'spots', two sparks located at diametrically opposite points were fired simultaneously. The resulting structure properties were deduced at different azimuthal planes. The variation of the properties with the azimuthal angle was found to be marginal (Sokolov *et al* 1981). This suggested to us that perhaps even a single spark induces an axisymmetric structure also. With a single spark the structure properties were then deduced at different azimuthal planes at $x/D = 1.5, 3.0$, and 4.5 , and these showed that the highly localized spark induces a structure which is essentially axisymmetric and travels downstream at a velocity equal to 60% of the centreline velocity (Kleis *et al* 1981). To show that this is not an artifact of the alignment process, the unaligned ensemble average \tilde{v}_c at different values of the azimuthal angle α at $x/D = 4.5$ are shown in figure 12. Except for some variation of the peak strength with the azimuthal angle, the structure axisymmetry is clear.

It was then considered interesting to explore if the instability induced by the spark was instantaneously axisymmetric. For this, seven single wires were placed equally spaced in the azimuthal direction at the radius where $U/U_e = 0.8$. The signals are

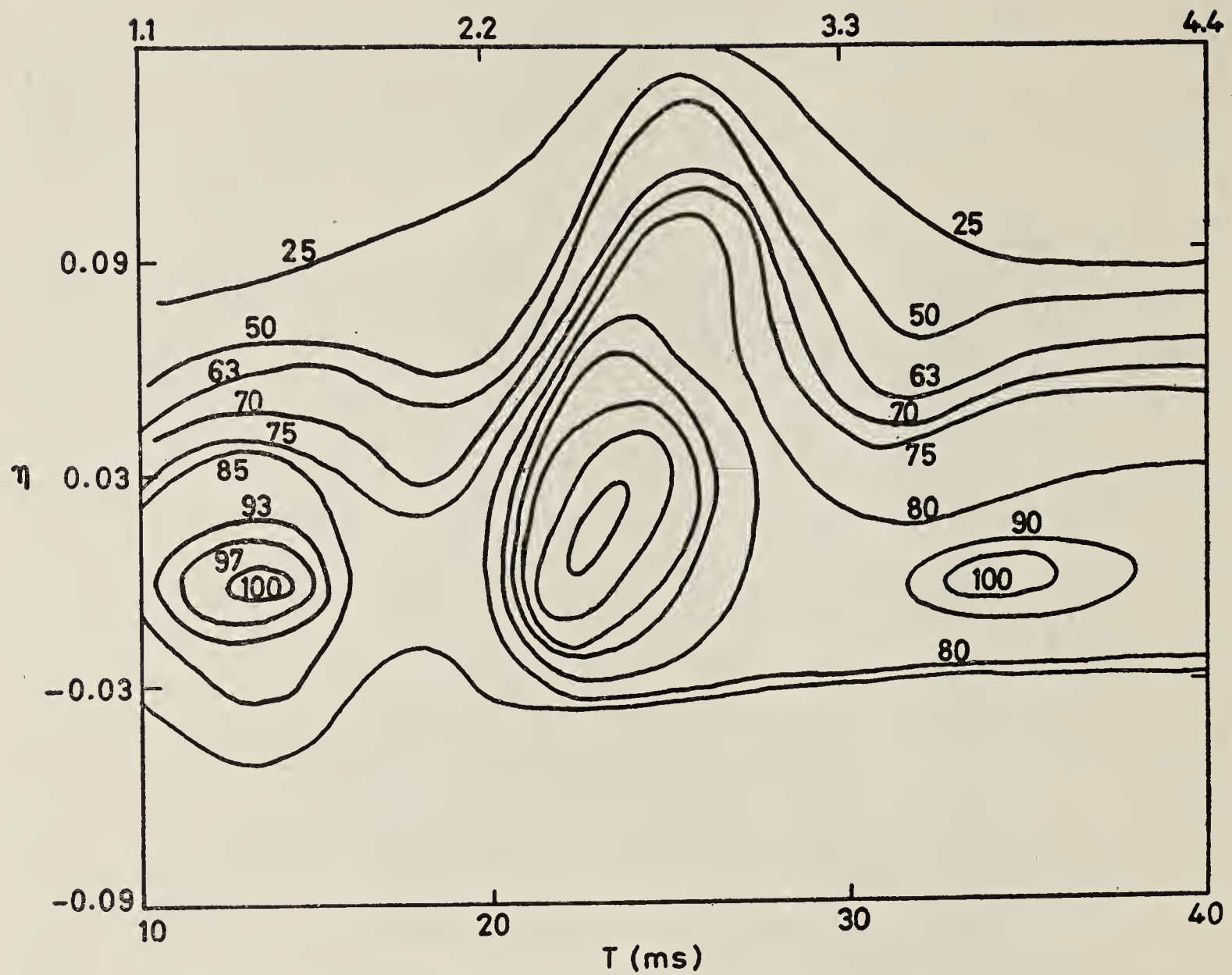


Figure 11h. Contours of phase-average spot properties at $x/D=1.5$; $\eta=(y-0.5D)/x$. $\langle \gamma_c \rangle$ in per cent.

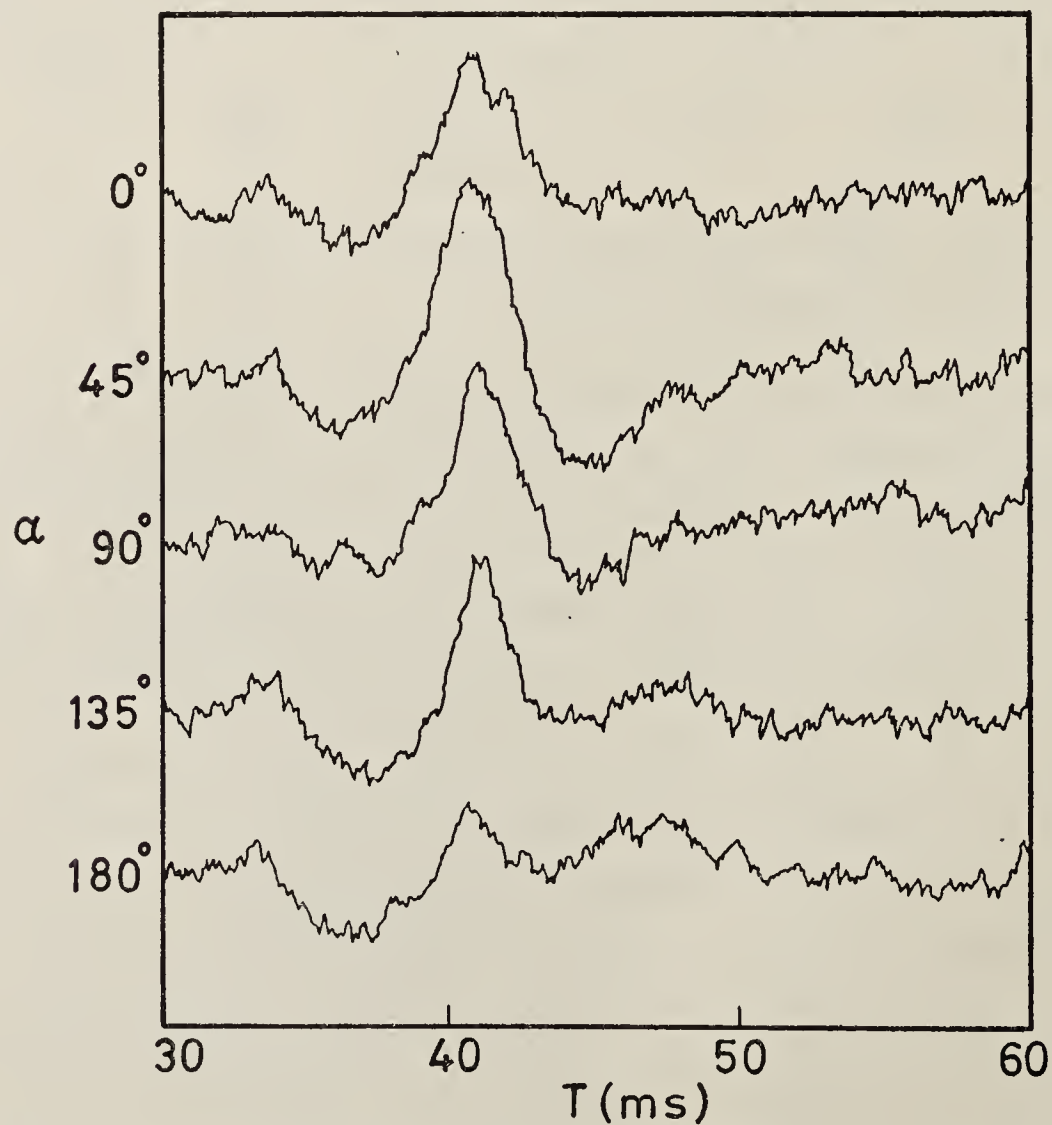


Figure 12. Unaligned ensemble averages of \tilde{v}_c at various α at $x/D=4.5$ and $y=D/2$.

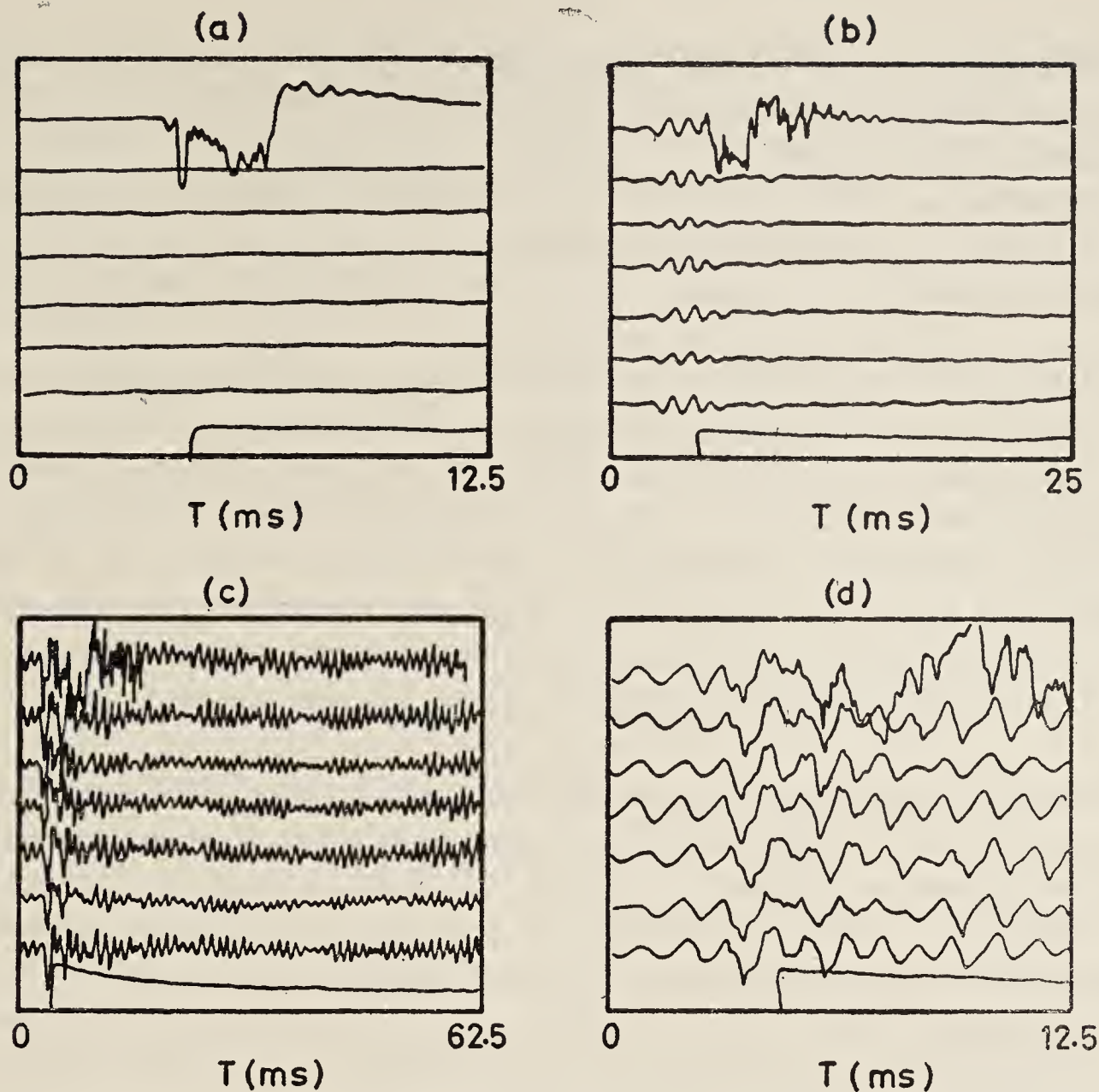


Figure 13. $u(t)$ signals at different x : (a) $x/D = 0.04$; (b) $x/D = 0.12$; (c) $x/D = 0.20$; (d) an expanded segment of (c).

shown in figures 13(a)–(c) for $x/D = 0.04$, 0.12 , and 0.20 respectively; figure 13(d) shows an expanded segment of figure 13(c). In each, the top trace corresponds to the hot-wire in the plane of the spark. The bottom trace is on the centreline and has a superimposed negative pulse for triggering data acquisition by the computer. The top trace depicts the legacy of the boundary layer spot (figure 13a). Note that the shear layer instability, triggered by the spark, is instantaneously axisymmetric (figure 13b) and that the front of the mixing layer spot is also aligned azimuthally (figure 13c). It is interesting to note that all instantaneous undulations are in phase around the periphery of the jet (figure 13d). Note that sufficiently away from the spot signature, the natural instability is amplitude modulated and this modulation is instantaneously axisymmetric (figure 13c). The variations among the amplitudes of the various traces may be more due to slight variations in the radial positions of the wires than due to azimuthal variations of the instability.

Similar study with a spark in a planemixing layer shows that the spot grows in a self-similar fashion in the downstream direction but the strength falls off in the spanwise direction (Kleis & Hussain 1981). A spark was fired in an initially fully turbulent mixing layer, and the eduction technique as described above, failed to educe any ‘spot’.

7.5 Natural structures in the self-preserving regions of the axisymmetric and plane jets

The organized nature of the near field of the circular jet has been documented in detail for both excited and unexcited situations (for example, Zaman & Hussain

1980, 1981c; Kleis *et al* 1981; Hussain & Clark 1981b). The near-field of the plane jet has been studied under excitation (for example, Sato 1960; Rockwell 1972; Hussain & Thompson 1980); detailed flow-visualization study is in progress in unforced plane jets in our laboratory (by J D Shlien and H S Hussain). We have been simultaneously pursuing studies to see if the self-preserving region of the axisymmetric jet consists of large-scale coherent structures. From the wavenumber-celerity spectra data, we inferred some characteristics of the dominant structure in the far fields of axisymmetric and plane jets (Hussain & Clark 1981a). Detailed correlation measurements (Tso *et al* 1980) suggested existence of such structures. It was decided to pursue this further by examining the instantaneous signal patterns from a rake of hot-wires (Tso & Hussain 1980). Figure 14 shows a sample of the instantaneous (smoothed by short-time averaging) velocity vector pattern in a plane passing through the jet axis. The existence of large-scale vortical structures is quite clear. Further efforts are now in progress to educe ensemble-average contours of structure properties in the self-preserving regions of the circular jet and the planemixing layer.

Visualization of the plane jet *via* smoke wires reveals that the self-preserving region of the plane jet is also characterized by large-scale coherent structures which have both spanwise and streamwise vorticities. Detailed characterization must await completion of our studies now in progress involving visualization in air and water plane jets and data analysis with a rake of hot-wires similar to those in the axisymmetric jet discussed above. The structure of the plane jet has also been investigated by Oler & Goldschmidt (1981) and Mumford (1981), but our observations suggest structures different from those found by them.

8. Some concluding comments

Spurred by the expectation that large-scale coherent structures are inherent to all turbulent shear flows and that these dominate the transport processes and noise

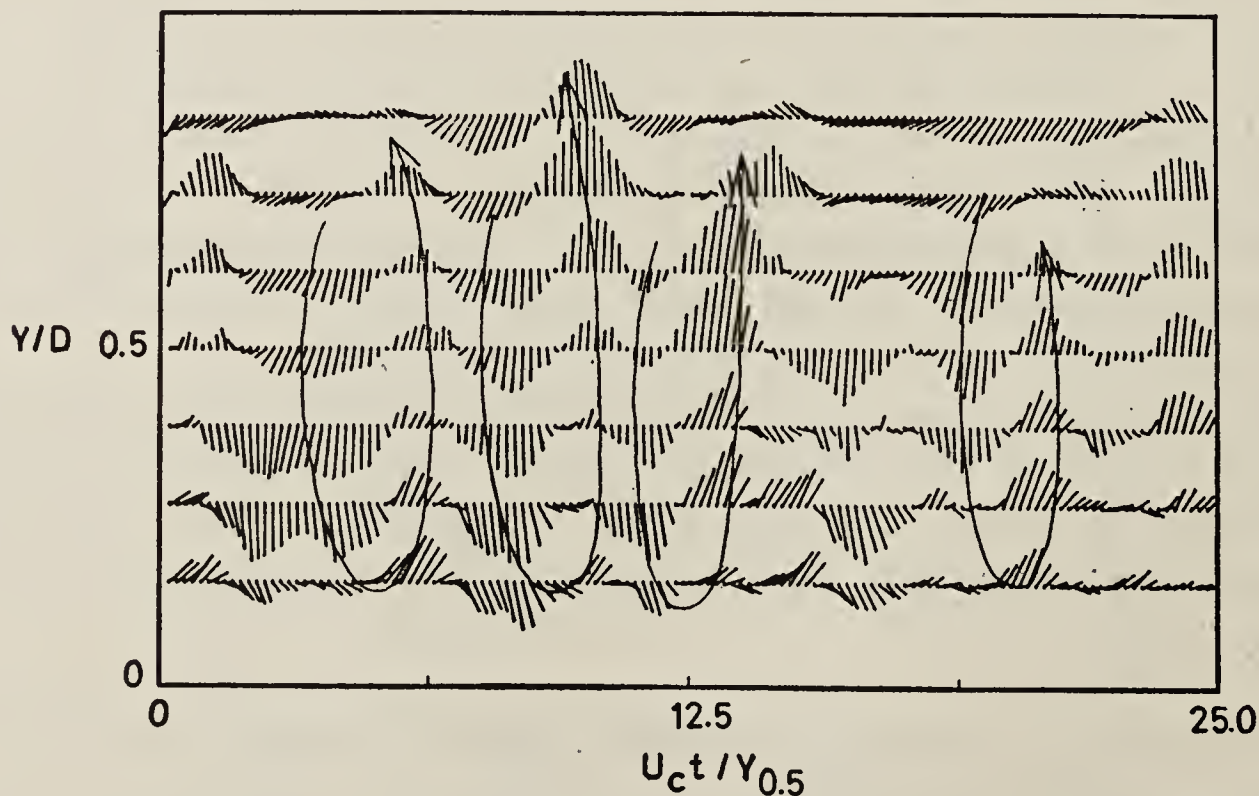


Figure 14. Instantaneous velocity vector pattern as a function of time and radius in the self-preserving region ($x/D = 50$, $Re_D = 65,000$).

production in turbulent shear flows, these structures have been and are still being vigorously investigated in our laboratory. This paper has primarily addressed the definition, the general analytical and experimental considerations in the investigations of these structures and brief summaries of a few of our results. A number of other studies of coherent structures and related topics in our laboratory cannot be reviewed here because of the obvious space constraint. But the more critical ones will be summarized below.

Likewise in many aspects of turbulence research, economy and convenience dictate the use of a limited few sensors which are typically held stationary in the laboratory frame. While these sensors provide time records of flow variables at fixed spatial points, the interest is often in the spatial description of the flow field and the time-evolution of a realization of a spatial description. The researcher thus has to endeavour to deduce spatial description from temporal information from a few stationary sensors. The classic example is the deduction of the wavenumber spectrum $E(k)$ from the measured frequency spectrum $E(f)$. Taylor (1938) hypothesized that the time-history of the flow signal from a stationary sensor can be regarded as that due to advection of a 'frozen' spatial pattern of turbulence past the sensor with the mean speed U , *i.e.*, $u(x, t) = u(x - Ut, 0)$, and Favre *et al* (1952) were the first to experimentally demonstrate its validity for grid turbulence. The factors contributing to errors in the Taylor hypothesis (*i.e.*, $\partial/\partial t = -U_T \partial/\partial x$) have been well explained (Lin 1953; Fisher & Davies 1964). The error due to the hypothesis is expected to be quite large at the smallest scales (Lumley 1965; Heskestad 1965; Wyngaard & Clifford 1977; Antonia *et al* 1980b) even though the error has never been determined as the 'true spectrum' can only be estimated on the basis of local isotropy (Lumley 1965; Champagne 1978).

The unavoidable use of the Taylor hypothesis in the studies of coherent structures (Zilberman *et al* 1977; Cantwell *et al* 1978; Sokolov *et al* 1980) introduces errors which appear in the computation of coherent vorticity Ω_c at two levels; first, in the computation of $\Omega_c(t, y)$ as a function of time; and second, in converting $\Omega_c(t, y)$ to spatial distributions $\Omega_c(x, y)$. Both levels are also involved in the measurements of $\langle S(x, y) \rangle$, $\langle P(x, y) \rangle$ etc. The second error occurs in the deduction of spatial description of any property, say, $\langle u_c, v_c \rangle \langle u_r^2 \rangle^{1/2}$, etc. The errors introduced by the different choices of U_T in the hypothesis have been quantitatively evaluated by first obtaining the actual spatial distributions through phase-locked measurements without using the hypothesis (§ 7.2) and then obtaining the spatial distributions through the Taylor hypothesis. Furthermore, the spatial distributions of the terms neglected by the hypothesis have also been evaluated (Zaman & Hussain 1981b).

To summarize, contrary to the widespread belief, the Taylor hypothesis works quite well when advection of single structures is involved, provided that the advection velocity of the structure centre is used for U_T everywhere across the structure. When pairing or tearing is involved, no choice of U_T is satisfactory. The popular use of the local time-average velocity U introduces unacceptably large distortions. For a typical shear flow, use of a constant value of U_T , equal to the average of the velocities across the shear region, everywhere across the shear region, is the least objectionable choice. It is shown that terms associated with the coherent motion but neglected by the hypothesis are significant; in particular, the pressure term cannot be neglected.

Turbulence suppression in a jet due to excitation, observed by Hussain & Zaman (1975), remained a mystery for quite some time because Crow & Champagne (1971) did not report this unavoidable phenomenon. Even though it was subsequently learnt that Vlasov & Ginevskiy (1974) and Petersen *et al* (1974) had also observed a similar phenomenon, they neither suggested an explanation nor even emphasized this observation. However, the fact that the St_D values at which the three studies found the suppression effect were different, suggested to us that this was not a 'tail-pipe' effect of the axisymmetric jet and must occur in plane jets and mixing layers also. Data in four axisymmetric jets, a plane jet and a plane mixing layer enabled us to establish that the phenomenon, which can produce turbulence suppression by as much as 80%, is related to the interaction of the excitation with the instability mechanism (Zaman & Hussain 1981a), in a way quite different from the simple superposition explanation of Pfizenmaier (1973) and Rockwell & Schachemann (1981). The suppression effect is shown to be the maximum when excited at a $St_\theta (= f_p \theta_e / U_e)$ value of about 0.017 in all configurations. Suppression occurs for $0.75 < x/D < 8$ in the jets and up to as much as $x = 6000 \theta_e$ in the plane mixing layer; the maximum relative suppression occurs at $x \simeq 400 \theta_e$ downstream from the trailing edge. Studies of coherent structures with and without suppression reveal that the breakdown of the rolled-up laminar structures, which naturally form at $St_\theta \simeq 0.012$ (Hussain & Hussain 1979) and grow to larger sizes, occurs earlier in x under excitation at $St_\theta \simeq 0.017$. Excitation at $St_\theta \simeq 0.017$ also reduces the number of pairings before breakdown. Thus, the breakdown of the structures earlier in x due to excitation at $St_\theta \simeq 0.017$, which prevents structure growth to larger sizes as well as energetic pairings, is the explanation for the suppression effect.

Some interesting results of relevance to the coherent structures are those of the effects of the initial condition. These studies were motivated by our speculation that the differences between the shear layer data from different investigations must be due to different initial conditions (Hussain & Zedan 1978a) and different natural excitations (Hussain & Zedan 1978b), and that given sufficient length of the flow, the effects of the initial condition must disappear (Hussain 1977b). The first support for the initial condition effect came from the plane jet showing that the jet spread, mean velocity decay, turbulence intensity, the mass and momentum fluxes and the entrainment rate varied strongly depending on the initial condition (Clark 1974). The most striking result was that the momentum flux in a jet can increase by as much as 60% depending on the initial condition (Clark & Hussain 1975). This violation of the universally accepted momentum flux invariance was so incredible that the publication of the results was withheld until the data were repeated and an explanation was provided in terms of the negative pressure in the turbulent flow due to the transverse turbulence (Hussain & Clark 1977; Hussain 1977b). It is to be noted that George & Baker (1980) suggests an opposite trend of the momentum flux, *i.e.*, decreasing momentum flux below the exit value with increasing x , and verified the measurements of Wagnanski & Fiedler (1969) to show momentum flux decrease. It is gratifying to learn that the LDA measurements of Ramaprian (1981)—which are free from the effects of high fluctuation intensity and flow reversal—have confirmed our finding of large increases in the momentum flux.

Noting the significant dependence of the mixing layer average measures on the initial fluctuation level, Hussain & Zedan (1978b) speculated that the spectral content

of the disturbance must be important because of the possible influence on coherent structure interactions. This has been confirmed and further explored by Hussain & Zaman (1980, 1981a), Kita *et al* (1980), Wygnanski & Oster (1980).

While the jet near- and far-field flows are unaffected by the addition of an end plate in the axisymmetric jet (Husain & Hussain 1979; Husain 1981), the effect of the initial condition (*i.e.*, laminar or turbulent exit boundary layers) persists in the axisymmetric mixing layer until the end of the potential core; this has been confirmed in jets up to 27 cm in diameter. However, the plane mixing layer is shown to achieve independence of the initial condition at large downstream distances (Kleis & Hussain 1979; Kita *et al* 1980); Wygnanski & Oster's (1980) results are to the contrary perhaps because their mixing layer is considerably shorter. Thus, given sufficient length, the plane mixing layer does reach a universal asymptotic state as suggested by Birch (1977), Foss (1977), Fiedler & Thies (1977) and Hussain (1977).

The axisymmetric mixing layer is indeed highly complex because of the geometry. For $x/D < 1$, the behaviour of the layer must be similar to the plane layer provided that $\theta_e/D \ll 1$. However, the diameter becomes a length scale, in addition to x , for $x/D > 1$. With increasing Re_D , this layer is found to be progressively more infrequently and intermittently organized and the survival times of the structures become smaller. Tearing is as frequent a mode of interaction as pairing, and pairing is quite often of the 'fractional' and 'partial' type rather than of the complete type (Hussain & Clark 1981b). These features, rather than Lau's (1979) hypothesis, explain the large frequency variation across the mixing layer and are the reasons why the motions across the axisymmetric layer are poorly correlated (Zaman & Hussain 1981c). The inherent differences between the coherent structures due to geometry, in addition to tearing and fractional pairing, must be the causes for the difference found in the plane mixing layer whose high- and low-speed sides are much better correlated (Browand & Wiedman 1976; Zaman & Hussain 1981d).

Do all turbulent shear flows consist of the same coherent structure module? Or, does each flow have its own unique module? Even though the answer must await further studies, it appears that a universal module is unlikely. For example, the hair-pin vortex would appear to be a basic module in the boundary layer while free shear flows may have structures like rollers, vortex rings or Hill's spherical vortices.

How important are the coherent structures? Our data in a number of studies show that $\langle \tilde{u}_c \tilde{v}_c \rangle$ is much larger than $\langle u_r v_r \rangle$ in the initial stages following the formation of the structures. However, with increasing downstream distances, these two become comparable. Thus, in the self-preserving regions of turbulent shear flows, while the structures are important, their dominance has been exaggerated. It is not clear at all whether a theory based on deterministic large-scale coherent structures alone would satisfactorily model fully-developed turbulent shear flows.

Some of the results briefly summarized are the outcomes of collaborative works with Dr K B M Q Zaman, Dr S J Kleis, Dr A R Clark, Dr M Sokolov, Dr L S G Kovasznay, Mr J Tso, Mr Z D Husain, and others whose specific involvements should be obvious from the cited references. The author has benefitted from extensive discussions with these and other colleagues. He is also grateful to Dr P Bandyopadhyay and Mr S K Ali for reviewing the manuscript, and making valuable suggestions. Our research has been funded by the NSF, ONR, NASA Langley, NASA Ames, and NASA Lewis Research Centres and the AFOSR.

References

- Acton E 1980 *J. Fluid Mech.* **98** 1
- Antonia R A, Chambers A J & Hussain A K M F 1980a *Phys. Fluids* **23** 695
- Antonia R A, Chambers A J & Phan-Thien N 1980b *J. Fluid Mech.* **100** 193
- Aref H & Siggia E D 1980 *J. Fluid Mech.* **100** 705
- Ashurst W T 1977 *Turbulent shear flows* (Pennsylvania State University) p. 11. 43
- Badri Narayanan M A, Rajagopalan S & Narasimha R 1977 *J. Fluid Mech.* **80** 237
- Bandyopadhyay P 1980 *Phys. Fluids* **23** 2326
- Batt R G 1975 *AIAA J.* **13** 245
- Batt R G 1978 *J. Fluid Mech.* **82** 53
- Birch S F 1977 *Turbulent shear flows* (Pennsylvania State University) p. 16. 10
- Black T J 1968 NASA CR-888
- Blackwelder R F 1977 *Phys. Fluids Suppl.* **20** S232
- Blackwelder R F & Eckelmann H 1979 *J. Fluid Mech.* **94** 577
- Blackwelder R F & Haritonidis J H 1980 *Bull. Am. Phys. Soc. Ser. II* **25** 1094
- Bradshaw P 1980 private communication
- Bradshaw P, Ferriss D H & Johnson R F 1964 *J. Fluid Mech.* **19** 591
- Browand F K & Laufer J 1975 *Turbulence in liquids* (Rolla : University of Missouri) 5, p. 333
- Browand F K & Troutt T R 1980 *J. Fluid Mech.* **97** 771
- Browand F K & Wiedman P D 1976 *J. Fluid Mech.* **76** 127
- Brown G L & Roshko A 1974 *J. Fluid Mech.* **64** 775
- Brown G L & Thomas A S W 1977 *Phys. Fluids Suppl.* **20** S243
- Bruun H H 1977 *J. Fluid Mech.* **64** 775
- Cain A B, Reynolds W C & Ferziger J H 1981 *Turbulent shear flows* (Davis: University of California) (to appear)
- Cantwell F J, Coles D & Dimotakis P 1978 *J. Fluid Mech.* **87** 641
- Carr L W 1981 *Lecture Notes in Physics* (Berlin: Springer-Verlag) (to appear)
- Champagne F H 1978 *J. Fluid Mech.* **86** 67
- Champagne F H, Pao Y H & Wygnanski I 1976 *J. Fluid Mech.* **74** 209
- Chandrsuda C, Mehta R D, Weir R A D & Bradshaw P 1978 *J. Fluid Mech.* **85** 693
- Clark A R 1974 *Effects of initial conditions on the development of a plane turbulent jet*, M.S. Thesis, University of Houston
- Clark A R 1979 *An experimental study of the coherent motions in an axisymmetric mixing layer*, Ph. D. Thesis, University of Houston
- Clark A R & Hussain A K M F 1975 *Proc. Soc. Engr, Sci.* University of Texas, Austin, p. 1149
- Clark A R & Hussain A K M F 1979 *Turbulent shear flows* (London) p. 2.30
- Coles D E 1962 Rand Corporation Rep. R-403-PR
- Coles D E & Barker S J 1975 in *Turbulent mixing in nonreactive and reactive flows* (ed. S N B Murthy) (New York: Plenum Press) p. 285
- Coles D E 1981 *Proc. Indian Acad. Sci. (Engg. Sci.)* **4** 111
- Corcos G M 1980 *Lecture Notes in Physics* (ed. J. Jimenez) **136** 10
- Corcos G M & Sherman F S 1976 *J. Fluid Mech.* **73** 241
- Corke T C, Guezennec Y & Nagib H M 1980 in *Viscous flow drag reduction* (ed. G R Hough) (New York: AIAA) p. 128
- Couët, B, Buneman O & Leonard A 1979 *Turbulent shear flows* (London) p. 14.29
- Crighton D G 1980 *Lecture Notes in Physics* (ed. J. Jimenez) **136** 340
- Crow S C & Champagne F H 1971 *J. Fluid Mech.* **48** 547
- Davies P O A L & Baxter D R J 1977 *Lecture Notes in Physics* (ed. H. Fiedler) (Berlin: Springer Verlag) **75** p. 125
- Dhawan S & Narasimha R 1958 *J. Fluid Mech.* **3** 414
- Dimotakis PF & Brown GL 1976 *J. Fluid Mech.* **78** 535
- Dinkelacker A, Hessel M, Meier G A E & Schewe G 1977 *Phys. Fluids Suppl.* **20** S 216
- Falco R 1977 *Phys. Fluids Suppl.* **20** S 214
- Falco R 1979 *Symposium on Turbulence* (Rolla: University of Missouri) (in press)
- Falco R 1980 AIAA Paper No. 80-1356

- Favre A, Gaviglio J & Dumas R 1952 *Proc. 8th Int. Congr. Appl. Mech.*, Istanbul, p. 304
- Ffowcs-Williams J E & Kempton A J 1978 *J. Fluid Mech.* **84** 673
- Fiedler H E, Dziomba B, Mensing P & Rosgen T 1980 *Lecture Notes in Physics* (ed. J. Jimenez) **136** 219
- Fiedler H & Thies H J 1977 *Lecture Notes in Physics* (ed. H Fiedler) **75** 108
- Fisher M J & Davies P O A L 1964 *J. Fluid Mech.* **18** 97
- Foss J F 1977 *Turbulent shear flows* (Pennsylvania State University) p. 11. 33
- Frenkiel F N & Klebanoff P S 1973 *Phys. Fluids* **16** 725
- George W K & Baker C B 1980 *Bull. Am. Phys. Soc. Ser. II* **25** 1074
- Grant H L 1958 *J. Fluid Mech.* **4** 149
- Hasan M A Z & Hussain A K M F 1981 *J. Fluid Mech.* (in press)
- Head M R & Bandyopadhyay P 1981 *J. Fluid Mech.* (in press)
- Hefner J N, Weinstein L M & Bushnell D M 1980 in *Viscous flow drag reduction* (ed. G R Hough) (New York: AIAA) p. 110
- Hernan M A & Jimenez J 1979 *Turbulent shear flows* (London) p. 7.7
- Hernan M A & Jimenez J 1981 *J. Fluid Mech.* (submitted)
- Heskestad G 1965 *J. Appl. Mech.* **87** 735
- Hinze J O 1975 *Turbulence*, 2nd ed. (New York: McGraw Hill)
- Ho C M 1980 private communication
- Husain Z D 1981 Ph. D. Thesis, University of Houston (in preparation)
- Husain Z D & Hussain A K M F 1979 *AIAA J.* **17** 48
- Hussain A K M F 1979 *The mechanics of a perturbation wave in turbulent shear flow* Ph. D. Thesis, Stanford University
- Hussain A K M F 1977a *Cardiovascular flow dynamics and measurements* (eds. N H C Hwang & N Norman) (Baltimore: University Park Press) p. 541
- Hussain A K M F 1977b *Lecture Notes in Physics* (ed. H. Fiedler) **75** 103
- Hussain A K M F 1979 *Symposium on Turbulence* (Rolla: University of Missouri) p. 207
- Hussain A K M F 1980 *Lecture Notes in Physics* (ed. J. Jimenez) **136** 252
- Hussain A K M F & Clark A R 1977 *Phys. Fluids* **20** 1416
- Hussain A K M F & Clark A R 1981a *AIAA J.* **19** 51
- Hussain A K M F & Clark A R 1981b *J. Fluid Mech.* **104** 263
- Hussain A K M F, Kleis S J & Sokolov M 1980 *J. Fluid Mech.* **98** 97
- Hussain A K M F & Reynolds W C 1970 *J. Fluid Mech.* **41** 241
- Hussain A K M F & Thompson C A 1980 *J. Fluid Mech.* **100** 397
- Hussain A K M F & Zaman K B M Q 1975 *Proc. Third Interagency Symposium, University Res. Transportation Noise*, University of Utah, p. 314
- Hussain A K M F & Zaman K B M Q 1977 *Lecture Notes in Physics* (ed. H. Fiedler) (Berlin: Springer-Verlag) **75** 31
- Hussain A K M F & Zaman K B M Q 1978 *J. Fluid Mech.* **87** 349
- Hussain A K M F & Zaman K B M Q 1980 *J. Fluid Mech.* **101** 493
- Hussain A K M F & Zaman K B M Q 1981a *J. Fluid Mech.* **110** 39
- Hussain A K M F & Zaman K B M Q 1981b *Lecture Notes in Physics* (in press)
- Hussain A K M F & Zedan M F 1978a *Phys. Fluids* **21** 1100
- Hussain A K M F & Zedan M F 1978b *Phys. Fluids* **21** 1475
- Keffer J F 1965 *J. Fluid Mech.* **22** 135
- Kibens V 1980 *AIAA J.* **18** 434
- Kim J & Moin P 1979 *Turbulent boundary layers—Experiment, theory and modelling*, Proc. AGARD Symp., The Hague, Netherlands
- Kita Y, Hussain A K M F & Kleis J 1980 *Bull. Am. Phys. Soc. Ser. II* **25** 1070
- Klebanoff P S 1955 Characteristics of turbulence in a boundary layer with zero pressure gradient, NACA. Rep. 1247
- Klebanoff P S 1980 private communication
- Klebanoff P S, Tidstrom K D & Sargent L M 1962 *J. Fluid Mech.* **12** 1
- Kleis S J & Hussain A K M F 1979 *Bull. Am. Phys. Soc. Ser. II* **24** 1132
- Kleis S J & Hussain A K M F 1981 (in preparation)
- Kleis S J, Hussain A K M F & Sokolov M 1981 *J. Fluid Mech.* (in press)
- Kline S J, Reynolds W C, Schraub F A & Rundstadler P W 1967 *J. Fluid Mech.* **30** 741

- Knight D D & Murray B T 1980 *Lecture Notes in Physics* (ed. J. Jimenez) **136** 62
- Kovaszny L S G, Kibens V & Blackwelder R F 1970 *J. Fluid Mech.* **41** 283
- Kovaszny L S G, Komoda H & Vasudeva B R 1962 *Proc. Heat Transfer Fluid Mechanics Institute* (Stanford University Press) p. 1
- Lau J C 1979 *Proc. R. Soc. London* **A368** 547
- Laufer J 1974 in *Omaggio A. Carlo Ferrari* p. 451
- Laufer J & Badri Narayanan M A 1971 *Phys. Fluids* **14** 182
- Leonard A 1980 *Lecture Notes in Physics* (ed. J. Jimenez) **136** 119
- Liepmann H W 1978 Lecture at the 8th US National Congress of *Appl. Mech.*, UCLA
- Lighthill M J 1952 *Proc. R. Soc. London* **A211** 364
- Lighthill M J 1961 *Proc. R. Soc. London* **A222** 1
- Lin CC 1953 *Q. Appl. Math.* **18** 295
- Lumley J L 1965 *Phys. Fluids* **8** 1056
- Lumley J L 1970 *Stochastic tools in turbulence* (New York: Academic Press)
- Lumley J L 1980 Coherent structures in turbulence, Cornell University Rep. FDA 80-08
- Michalke A 1972 *Progr. Aeronaut. Sci.* **12** 213
- Michalke A 1980 private communication
- Mizushima T, Maruyama T & Shiozaki Y 1973 *J. Chem. Engg. Jpn* **6** 487
- Mollo-Christensen E 1967 *Trans. ASME E, J. Appl. Mech.* **89** 1
- Moore C J 1977 *J. Fluid Mech.* **80** 321
- Mumford J C 1981 *J. Fluid Mech.* (to be published)
- Nagib H M, Guezenc Y & Corke T C 1978 in *Coherent structure of turbulent boundary layers* (eds C R Smith & D E Abbott) (Bethlehem: Lehigh University) p. 372
- Narasimha R & Sreenivasan K R 1979 *Adv. Appl. Mech.* **19** 221
- Offen G R & Kline S J 1974 *J. Fluid Mech.* **62** 223
- Offen G R & Kline S J 1975 *J. Fluid Mech.* **70** 209
- Oldaker D K & Tiederman W G 1977 *Phys. Fluids Suppl.* **20** S133
- Oler J W & Goldschmidt V W 1981 *Turbulent shear flows* (Davis: University of California) (to appear)
- Parikh P G, Reynolds W C, Jayaraman R & Carr L W 1981 *Lecture Notes in Physics* (Berlin Springer-Verlag) (to appear)
- Payne F R & Lumley J L 1967 *Phys. Fluids Suppl.* **10** S194
- Perry A E & Lim T T 1978 *J. Fluid Mech.* **88** 451
- Perry A E, Lim T T & Teh E W 1981 *J. Fluid Mech.* **104** 387
- Petersen R A, Kaplan R E & Laufer J 1974 NASA Contractor Rep. No. 134733
- Pfizenmaier E 1973 *Zur Instabilitaet des schallbee in flussten Freistrahls* Doktor-Ingenieur thesis, Technische Universitaet, Berlin
- Praturi A K & Brodkey R S 1978 *J. Fluid Mech.* **89** 251
- Pui N K & Gartshore I S 1978 *J. Fluid Mech.* **91** 111
- Purtell L P, Klebanoff P S & Buckley F T 1981 *Phys. Fluids* **24** 802
- Rajagopalan S & Antonia R A 1980 *Phys. Fluids* **23** 1101
- Ramaprian B R 1981 private communication
- Rao K N, Narasimha R & Badri Narayanan M A 1971 *J. Fluid Mech.* **48** 339
- Reynolds W C & Hussain A K M F 1972 *J. Fluid Mech.* **54** 263
- Riley J & Metcalfe R 1980 *AIAA Paper No.* 80-0274
- Rockwell D O 1972 *Trans. ASME D J. Appl. Mech.* **39** 883
- Rockwell D & Schachenmann A 1981 *J. Fluid Mech.* (submitted)
- Roshko A 1976 *AIAA J.* **10** 1349
- Sabot J & Comte-Bellot G 1976 *J. Fluid Mech.* **74** 767
- Saffman P G 1978 *J. Fluid Mech.* **84** 625
- Sato H 1960 *J. Fluid Mech.* **7** 53
- Schon J P, Danel F, Melinand J P, Rey C & Charnay G 1979 *Symposium on Turbulence*, Rolla University of Missouri, (in press)
- Sharma L K & Willmarth W W 1980 *Bull. Am. Phys. Soc. Ser. II* **25** 1075
- Simpson R L, Shivaprasad B G & Chew Y T 1981 *Lecture Notes in Physics* (Berlin: Springer-Verlag) (to appear)

- Sirkar K K & Hanratty T J 1970 *J. Fluid Mech.* **44** 605
- Smith C R 1978 in *Coherent structures of turbulent boundary layers* (eds. C R Smith & D E Abbott) (Bethlehem: Lehigh University), p. 48
- Sokolov M, Hussain A K M F, Kleis S J & Husain Z D 1980 *J. Fluid Mech.* **98** 65
- Sokolov M, Kleis S J & Hussain A K M F 1981 *AIAA J.* **19** 1000
- Taylor G I 1938 *Proc. R. Soc. London* **A164** 476
- Tennekes H & Lumley J L 1974 *A. First course in turbulence* (Mass. : MIT Press)
- Theodorsen T 1952 *Proc. Second Midwestern Mechanics Conference* (Ohio State University) p. 1
- Townsend A A 1956 *The structure of turbulent shear flow* (Cambridge: University Press)
- Townsend A A 1979 *J. Fluid Mech.* **95** 515
- Tso J & Hussain A K M F 1980 *Bull. Am. Phys. Soc. Ser. II* **25** 1082
- Tso J, Kovaszny L S G & Hussain A K M F 1980 AIAA Paper No. 80-1355
- Vlasov Y V & Ginevskiy A S 1974 Structure of turbulence in boundary layers, NASA TTF-15, 721
- Widnall S 1975 *Annu. Rev. Fluid Mech.* **7** 141
- Willmarth W W 1975 *Advances in applied mechanics* (New York: Academic Press) **15** 159
- Willmarth W W & Bogar T J 1977 *Phys. Fluids Suppl.* **20** S9
- Winant C D & Browand F K 1974 *J. Fluid Mech.* **63** 237
- Wynanski I 1980 *Lecture Notes in Physics* (ed. J. Jimenez) **136** 304
- Wynanski I & Fiedler H E 1969 *J. Fluid Mech.* **38** 577
- Wynanski I & Fiedler H E 1970 *J. Fluid Mech.* **41** 327
- Wynanski I & Oster D 1980 *J. Fluid Mech.* (submitted)
- Wynanski I, Sokolov M & Friedman D 1976 *J. Fluid Mech.* **78** 785
- Wyngaard J C & Clifford S F 1977 *J. Atmos. Sci.* **34** 922
- Yajnik K & Acharya M 1977 *Lecture Notes in Physics* (ed. H Fiedler) **75** 249
- Yule A J 1978 *J. Fluid Mech.* **89** 413
- Yule A J 1979 *Turbulent shear flows* (London) p. 7.1
- Yule A J 1980 *Lecture Notes in Physics* (ed. J. Jimenez) **136** 188
- Zaman K B M Q 1978 *An experimental investigation of vortex pairing in a circular jet under controlled excitation* Ph. D. Thesis, University of Houston
- Zaman K B M Q & Hussain A K M F 1977 *Turbulent shear flows* (Pennsylvania State University) p. 11.23
- Zaman K B M Q & Hussain A K M F 1980 *J. Fluid Mech.* **101** 449
- Zaman K B M Q & Hussain A K M F 1981a *J. Fluid Mech.* **103** 133
- Zaman K B M Q & Hussain A K M F 1981b. *J. Fluid Mech.* (in press)
- Zaman K B M Q & Hussain A K M F 1981c *J. Fluid Mech.* (submitted)
- Zaman K B M Q & Hussain A K M F 1981d (in preparation)
- Zilberman M, Wynanski I & Kaplan R E 1977 *Phys. Fluids Suppl.* **20** S258

On the solutions of Navier-Stokes equations and the theory of homogeneous isotropic turbulence

HUANG YUNG-NIEN* and CHOU PEI-YUAN†

*Department of Mechanics Beijing University, Beijing, China

†Academia Sinica, Beijing, China; (visiting) Massachusetts Institute of Technology, Cambridge, Massachusetts, USA.

MS received 10 February 1981

Abstract. This paper is an extension of our earlier work of solving the whole problem of homogeneous isotropic turbulence from the initial period to the final period of decay. An expansion method has been developed to obtain an axially symmetrical solution of the Navier-Stokes equations of motion in the form of an infinite set of nonlinear partial differential equations of the second order. For the present we solve the zeroth order approximation. By using the method of the Fourier transform, we get a nonlinear integro-differential equation for the amplitude function in the wave number space. It is also the dynamical equation for the energy spectrum.

By choosing a suitable initial condition, we solve this equation numerically. The energy spectrum function and the energy transfer spectrum function thus calculated satisfy the spectrum form of the Kármán-Howarth equation exactly. We have computed the energy spectrum function, the energy transfer function, the decay of turbulent energy, the integral scale, the Taylor microscale, the double and triple velocity correlations on the whole range from the initial period to the final period of decay. On the whole all these calculated statistical physical quantities agree with experiments very well except for a few cases of small discrepancies at large separations.

Keywords. Navier-Stokes equations; homogeneous isotropic turbulence; energy spectrum.

1. Introduction

In our statistical vorticity structure theory of homogeneous isotropic turbulence (Chou Pei-Yuan & Huang Yung-nien 1975*) the element of turbulence is considered to be an axially symmetric vortex, which is a solution of the Navier-Stokes equations of motion; and turbulent motions of fluids are considered to be the statistical average effects of the stochastic motions of those numerous identical eddies, both the orientations of their axes of symmetry and their positions being randomly distributed in space. Since the Navier-Stokes equations are partial differential equations of the second order and since we are dealing with a statistical and not merely a boundary value problem, we have to assume conditions to determine the solutions of these equations in order to find the particular type of vortex which is the element of turbulence. We define a vortex Reynolds number,

$$R_a = Ua/\nu, \quad (1)$$

*Chou Pei-yuan & Huang Yung-nien 1975 will be referred to as I in the present paper. We use the notations of I unless otherwise specified.

in which U and a represent respectively the characteristic velocity and characteristic length of the vortex. They are related to each other by the condition of the conservation of angular momentum of the vortex,

$$Ua^4 = c_0. \quad (2)$$

We then assume a condition of pseudo-similarity which is the relation between the vortex Reynolds number R_a and the characteristic length a expressed in the form**

$$\frac{a}{\nu} \frac{da}{dt} = R_a + 1. \quad (3)$$

In the present paper we further introduce the condition upon the turbulent energy

$$\overline{u^2} = \text{const } U^2 a^3, \quad (4)$$

which can be called the "energy condition" and which was regarded as an approximation in I. From the above four relations and Taylor's equation of the decay of turbulent energy we have found respectively the relations of the decay of turbulent energy and Taylor's microscale of turbulence with time from the initial period to the final period of decay. The theoretical results agree well with Batchelor & Townsend's experiments.

In I, we have given the solution of the nonlinear vorticity equation by expanding the vorticity and stream functions in power series of R_a and solved the equation of the zeroth order approximation which is linear. The solution is only good for low Reynolds number flows, so the theoretical double velocity correlation functions computed are lower than the experimental curves.

In the present paper, we shall solve the nonlinear Navier-Stokes equations by expanding the vorticity and stream functions of the vortex in series of derivatives of the Legendre polynomial. The variables of these equations can be separated and we obtain a set of infinitely many nonlinear partial differential equations involving an infinite number of functions of different orders of approximation with time t and radial coordinate R as independent variables. This set of equations can be truncated and solved by the method of successive approximation.

We solve the zeroth order approximation for the time being. The nonlinear partial differential equations in the physical space are transformed into the spectrum space by Fourier transforms. This nonlinear integro-differential equation in the spectrum space (see (26) below) is then solved numerically by computers. We have computed the energy spectrum, the energy transfer function, the decay of turbulent energy, the integral scale L , the microscale of turbulence λ , the double and triple velocity correlations on the whole range from the initial period to the final period of decay. These theoretical results have been compared with the available experimental data. With the exception of the triple velocity correlation which has discrepancies with the experiments at large separations, all the other measured physical quantities agree with experiment very well.

We have also shown the relations of our present work with the Kármán-Howarth equation and the Loitsianskii's integral, compared our theory with the existing hypo-

**In I (4.1) there appeared two constants γ and β which can be absorbed into U and a without the loss of generality.

theses of the energy transfer functions and pointed out the limitations of the present zeroth order approximation.

2. Methods of solving the equations of vortex motion—the equation for the energy spectrum

In this section, we shall obtain an equation for the evolution of the energy spectrum. This is expressed in the form (26) where the amplitude function defined in (25) is used. It is an integro-differential equation which will be solved numerically in § 3, where the results will also be compared with experimental data.

As in I, let Ψ and η represent the stream and vorticity functions respectively defined by

$$\Psi = \frac{1}{2} U a^2 \xi^2 \sin \theta G(\xi, \mu, t), \quad \eta = \frac{15U}{2a} \xi \sin \theta F(\xi, \mu, t), \quad (5)$$

where $\xi = R/a, \mu = \cos \theta.$ (6)

The functions F and G satisfy the following equations of motion (equation 3.5 in I):

$$\begin{aligned} \left(\frac{\partial F}{\partial t} \right)_{\xi} - \frac{1}{a} \frac{da}{dt} \xi \frac{\partial F}{\partial \xi} + \frac{a^2}{U} \frac{d}{dt} \left(\frac{U}{a^2} \right) F + \\ \frac{U}{2a} \left\{ \frac{\partial}{\partial \mu} [(1 - \mu^2)G] \frac{\partial F}{\partial \xi} - \frac{1}{\xi^2} \frac{\partial}{\partial \xi} [\xi^2(1 - \mu^2)G] \frac{\partial F}{\partial \mu} \right\} \\ = \frac{\nu}{a^2} \left[\frac{\partial^2 F}{\partial \xi^2} + \frac{4}{\xi} \frac{\partial F}{\partial \xi} - \frac{4}{\xi^2} \mu \frac{\partial F}{\partial \mu} + \frac{1}{\xi^2} (1 - \mu^2) \frac{\partial^2 F}{\partial \mu^2} \right], \quad (7) \\ F = \frac{1}{15} \left[\frac{\partial^2 G}{\partial \xi^2} + \frac{4}{\xi} \frac{\partial G}{\partial \xi} - \frac{4}{\xi^2} \mu \frac{\partial G}{\partial \mu} + \frac{1}{\xi^2} (1 - \mu^2) \frac{\partial^2 G}{\partial \mu^2} \right]. \end{aligned}$$

We now expand the functions F and G as follows:

$$\begin{aligned} F &= \sum_{n=0}^{\infty} F_n(\xi, t) H_n(\mu), \quad (8) \\ G &= \sum_{n=0}^{\infty} G_n(\xi, t) H_n(\mu), \end{aligned}$$

where $H_n(\mu)$ is defined as

$$H_n(\mu) = \frac{(2n+1)!}{(4n+3)!!} \frac{d P_{2n+2}(\mu)}{d\mu}, \quad (9)$$

and $P_{2n+2}(\mu)$ is the Legendre polynomial defined by

$$P_m(\mu) = \frac{(-1)^m}{2^m m!} \frac{d^m}{d\mu^m} (1-\mu^2)^m, \quad (10)$$

Obviously $H_n(\mu)$ is a polynomial of degree $2n+1$ in μ .

Polynomials $P_m(\mu)$ and $H_n(\mu)$ satisfy the following differential equations respectively:

$$(1-\mu^2) \frac{d^2 P_m}{d\mu^2} - 2\mu \frac{d P_m}{d\mu} + m(m+1) P_m = 0, \quad (11)$$

$$(1-\mu^2) \frac{d^2 H_n}{d\mu^2} - 4\mu \frac{d H_n}{d\mu} + (2n+1)(2n+4) H_n = 0. \quad (12)$$

The set of polynomials $H_n(\mu)$ is orthogonal on the interval $-1 \leq \mu \leq 1$, with respect to the weight function $1 - \mu^2$, (Gradshteyn & Ryzhik 1965) namely

$$\int_{-1}^1 (1-\mu^2) H_m(\mu) H_n(\mu) d\mu = 0, \text{ for } m \neq n \quad (13)$$

and
$$\int_{-1}^1 (1-\mu^2) H_n^2(\mu) d\mu = \frac{2(2n+1)!(2n+3)!}{(4n+3)!!(4n+5)!!}. \quad (14)$$

Before inserting expansions (8) into (7) we expand the expressions

$$\frac{d}{d\mu} [(1-\mu^2) H_m] H_s \text{ and } (1-\mu^2) H_m \frac{d H_s}{d\mu}$$

in series of $H_n(\mu)$ as follows:

$$\frac{d}{d\mu} [(1-\mu^2) H_m] H_s = \sum_{n=0}^{\infty} d_{nms} H_n, \quad (15)$$

$$(1-\mu^2) H_m \frac{d H_s}{d\mu} = \sum_{n=0}^{\infty} h_{nms} H_n, \quad (16)$$

and use the integral formulae (Gradshteyn & Ryzhik 1965)

$$\begin{aligned} e_{nms} &= \int_{-1}^1 P_{2n+2}(\mu) P_{2m+2}(\mu) P_{2s+2}(\mu) d\mu \\ &= \frac{(m+n+s+3)! \Gamma(n+s-m+\frac{3}{2}) \Gamma(m+s-n+\frac{3}{2}) \Gamma(m+n-s+\frac{3}{2})}{\pi(n+s-m+1)! (m+s-n+1)! (m+n-s+1)! \Gamma(m+n+s+\frac{9}{2})}, \end{aligned}$$

$$\text{for } m+s+1 \geq n \geq |m-s|-1; \quad (17)$$

$$e_{nms} = 0 \text{ otherwise.}$$

We give the coefficients d_{nms} and h_{nms} below. Their derivations are given in Appendix A.

$$\begin{aligned}
 d_{nms} &= -\frac{(2m+3)!(2s+1)!(4n+5)!!}{2(4m+3)!!(4s+3)!!(2n+3)!} [(n+1)(2n+3) \\
 &\quad + (s+1)(2s+3) - (m+1)(2m+3)] e_{nms}, \\
 h_{nms} &= \frac{(2m+1)!(2s+1)!(4n+5)!!}{(4m+3)!!(4s+3)!!(2n+3)!} \{[(m+1)(2m+3) \\
 &\quad + (n+1)(2n+3)](s+1)(2s+3) \\
 &\quad - [(m+1)(2m+3) - (n+1)(2n+3)]^2\} e_{nms}, \tag{18}
 \end{aligned}$$

both for $m+s+1 \geq n \geq |m-s|-1$;

otherwise, $d_{nms} = h_{nms} = 0$.

Substituting functions F and G from (8) into (7) and using the results in (13), (14) and (18), we obtain the equations which determine F_n and G_n as follows:

$$\begin{aligned}
 &\left(\frac{\partial F_n}{\partial t}\right)_\xi - \frac{1}{a} \frac{da}{dt} \xi \frac{\partial F_n}{\partial \xi} + \frac{a^2}{U} \frac{d}{dt} \left(\frac{U}{a^2}\right) F_n \\
 &\quad + \frac{U}{2a} \sum_{s=0}^{\infty} \sum_{m=|s-n|}^{s+n+1} -1 \left[d_{nms} G_m \frac{\partial F_s}{\partial \xi} - h_{nms} \frac{1}{\xi^2} \frac{d}{d\xi} (\xi^2 G_m) F_s \right] \\
 &= \frac{\nu}{a^2} \left[\frac{\partial^2 F_n}{\partial \xi^2} + \frac{4}{\xi} \frac{\partial F_n}{\partial \xi} - \frac{(2n+1)(2n+4)}{\xi^2} F_n \right], \tag{19}
 \end{aligned}$$

$$F_n = \frac{1}{15} \left[\frac{\partial^2 G_n}{\partial \xi^2} + \frac{4}{\xi} \frac{\partial G_n}{\partial \xi} - \frac{(2n+1)(2n+4)}{\xi^2} G_n \right] (n = 0, 1, 2, 3, \dots).$$

Here we note that we have obtained a set of infinitely many nonlinear partial differential equations involving an infinite number of unknown functions. If we truncate this set of equations and consider the n th order approximation involving the first n equations, the sums of the nonlinear cross-product terms of $H_m(\mu)$ in (7), which can again be expressed in sums of $H_n(\mu)$, include the polynomials from $H_{n+1}(\mu)$, to $H_{2n+1}(\mu)$ also. But we know that the Legendre polynomial $P_{2n+2}(\mu)$ has $2n+2$ zeros on the range $-1 \leq \mu \leq 1$ (Abramovitz & Stegun 1964), and its derivative has $2n+1$ zeros on the same range, including $\mu = 0$. Hence the function

$$S_n(\mu) = \frac{H_{n+1}(\mu)}{H_0(\mu)}$$

has $2n$ zeros on this range. Owing to

$$\left| \frac{d}{d\mu} P_{2n+2}(\mu) \right| \leq \frac{1}{2} (2n+2)(2n+3),$$

we have $|H_n(\mu)| \leq (2n+3)! / [2(4n+3)!!]$.

It is easy to prove that the absolute value of $S_n(\mu)$ decreases to zero as n increases indefinitely. Therefore when we consider the n th order approximation, we may neglect the terms involving $H_{n+1}(\mu)$ to $H_{2n+1}(\mu)$.

Now we have $2n$ partial differential equations which determine $2n$ unknown functions from (19). Furthermore, in view of the orthogonality property of $H_n(\mu)$, all the neglected terms do not make any contribution to the average values of the correlation functions of n th order approximation, as for example, in the calculations of the double and triple correlations, except that they may have some small influences on the forms of the first $2n$ functions $F_n(\xi)$ and $G_n(\xi)$.

In the present paper we consider the zeroth order approximation from (19) with $n = 0$ and retain only the terms in F_0, G_0 . The resulting equations are

$$\begin{aligned} \frac{\partial F_0}{\partial t} - \frac{1}{a} \frac{da}{dt} \xi \frac{\partial F_0}{\partial \xi} + \frac{a^2}{U} \frac{d}{dt} \left(\frac{U}{a^2} \right) F_0 - \frac{U}{7a} \left[G_0 \frac{\partial F_0}{\partial \xi} + \frac{2}{\xi^2} \frac{\partial}{\partial \xi} (\xi^2 G_0) F_0 \right] \\ = \frac{\nu}{a^2} \left(\frac{\partial^2 F_0}{\partial \xi^2} + \frac{4}{\xi} \frac{\partial F_0}{\partial \xi} - \frac{4}{\xi^2} F_0 \right), \\ F_0 = \frac{1}{15} \left(\frac{\partial^2 G_0}{\partial \xi^2} + \frac{4}{\xi} \frac{\partial G_0}{\partial \xi} - \frac{4}{\xi^2} G_0 \right). \end{aligned} \quad (20)$$

Define a function B_0 by

$$B_0 = \frac{\partial G_0}{\partial \xi} + \frac{4}{\xi} G_0. \quad (21)$$

Then equations (20) become

$$\begin{aligned} \frac{\partial B_0}{\partial t} - \frac{1}{a} \frac{da}{dt} \xi \frac{\partial B_0}{\partial \xi} + \frac{a}{U} \frac{d}{dt} \left(\frac{U}{a} \right) B_0 - \frac{U}{7a} \left(G_0 \frac{\partial B_0}{\partial \xi} + \frac{1}{2} B_0^2 \right) \\ = \frac{\nu}{a^2} \left(\frac{\partial^2 B_0}{\partial \xi^2} + \frac{4}{\xi} \frac{\partial B_0}{\partial \xi} \right), \\ F_0 = \frac{1}{15} \frac{\partial B_0}{\partial \xi}. \end{aligned} \quad (22)$$

From the physical point of view, the expansions (8) can be interpreted to mean that the turbulent flow field is the cumulation of an infinite number of vortices with different structures interacting with each other due to the nonlinearity of the equations

of motion. The zeroth order approximation corresponds to the assumption that the element of turbulence is an eddy of the same structure. This is, of course, a crude picture of turbulence. But it reveals the essential property of homogeneous isotropic turbulence and by means of it many physical measurements can be interpreted as shown below.

In order to simplify our calculation we transform equations (21) and (22) of the physical space into their corresponding equations in the spectrum space by using the method of their Fourier transform. Let

$$\Pi_0(k, t) = -\frac{U}{2\pi^2 a k^3} \int_0^\infty R B_0(R, t) (\sin kR - kR \cos kR) dR. \quad (23)$$

which can be defined as an amplitude function and related to $\Gamma_0(k, t)$ in equation (5.18) of I as

$$\Pi_0(k, t) = U k^2 \Gamma_0(k, t). \quad (24)$$

Then the energy spectrum function $E_0(k, t)$ in equation (5.24) of I becomes

$$E_0(k, t) = \frac{8}{15} \pi^4 \frac{N}{V} k^4 \Pi_0^2(k, t). \quad (25)$$

In the spectrum space the partial differential equation (22) becomes the following integro-differential equation satisfied by the amplitude function

$$\begin{aligned} \frac{\partial \Pi_0(k, t)}{\partial t} + \nu k^2 \Pi_0(k, t) + \frac{1}{112} \int \int \int \frac{Q(k'^2 - k^2)}{k^2 k''^2} \Pi_0(k', t) \Pi_0(k'', t) dk' \\ = 0, \end{aligned} \quad (26)$$

where $\mathbf{k} + \mathbf{k}' + \mathbf{k}'' = 0$, $Q = k^4 + k'^4 + k''^4 - 2k^2 k'^2 - 2k'^2 k''^2 - 2k''^2 k^2$.

The proof is given in Appendix B.

As we pointed out in the introduction, in order to get the solution representing the element of turbulence, we have to assume some conditions upon the amplitude function $\Pi_0(k, t)$. For example, from the energy condition (4) and the definition of turbulent energy

$$\bar{u}^2 = \frac{2}{3} \int_0^\infty E_0(k, t) dk, \quad (27)$$

and the formula of $E_0(k, t)$ in (25), we obtain an integral condition

$$\int_0^\infty k^4 \Pi_0^2(k, t) dk = \text{const} \frac{1}{a^5}. \quad (28)$$

The constant is determined from the solution of the final period of decay. According to I this solution is

$$\Pi_0(k, t) = -c_0 \exp(-\frac{1}{2} a^2 k^2), \text{ as } R_a \rightarrow 0, \quad (29)$$

in which c_0 is given in (2). Hence the integral condition (28) reads

$$\int_0^\infty k^4 \Pi_0^2(k, t) dk = \frac{3}{8} \pi^{1/2} \frac{c_0^2}{a^5}. \quad (30)$$

Then from (26) by taking the limit $k \rightarrow 0$ and using (1), (2), (3) and (29) we obtain a boundary condition for $\Pi_0(k, t)$ [see Appendix B],

$$\lim_{k \rightarrow 0} \Pi_0(k, t) = -c_0 \left[1 + \frac{1}{84} \pi^{3/2} \ln(1 + R_a) \right]. \quad (31)$$

The condition (30) is consistent with the condition (29) only if the amplitude function $\Pi_0(k, t)$ satisfies (26).

3. Numerical calculations and comparisons with experiments

For convenience in numerical calculations we introduce the non-dimensional variables like the wave number k^* , time t^* and amplitude function $\Pi_0^*(k^*, t^*)$ in terms of two constants: a representative wave number k_0 and the constant angular momentum c_0 defined in (2) as follows:

$$k^* = k/k_0, \quad t^* = c_0 k_0^5 t, \quad \Pi_0^*(k^*, t^*) = -\frac{1}{c_0} \Pi_0(k, t), \quad (32)$$

with the Reynolds number $R_0^* = c_0 k_0^3/\nu$. Then the integro-differential equation (26) can be expressed in non-dimensional form as

$$\begin{aligned} \frac{\partial}{\partial t^*} \Pi_0^*(k^*, t^*) + \frac{k^{*2}}{R_0^*} \Pi_0^*(k^*, t^*) + \frac{\pi}{14} \int_0^\infty \int_{-1}^1 (1 - \mu^{*2}) \frac{k^{*4}}{k^{*''2}} \\ \times (k^{*'2} - k^{*2}) \Pi_0^*(k^{*'}, t^*) \Pi_0^*(k^{*''}, t^*) d\mu^* dk^{*'} = 0. \end{aligned} \quad (33)$$

where $k^{*''2} = k^{*2} + k^{*'2} + 2\mu^* k^* k^{*'}$.

The integral condition in (30) becomes

$$\int_0^\infty k^{*4} \Pi_0^{*2}(k^*, t^*) dk^* = \frac{3}{8} \pi^{1/2} \left(\frac{R_a}{R^*} \right)^{5/3}, \quad (34)$$

and the boundary condition in (31) reads

$$\Pi_0^*(0, t^*) = 1 + \frac{1}{84} \pi^{3/2} \ln(1 + R_a). \quad (35)$$

The relation between time t^* and vortex Reynolds number R_a is given by equation (4.2) in I:

$$t^* = \frac{1}{2} R_0^{*5/3} \left[R_a^{-2/3} + \frac{1}{3} \ln \frac{(1 + R_a^{1/3})^3}{1 + R_a} - \frac{2\sqrt{3}}{3} \tan^{-1} \frac{\sqrt{3}}{2R_a^{1/3} - 1} \right]. \quad (36)$$

Theoretically we can use the known solution (29) in the final period of decay for very large t^* as the initial condition and solve (33) numerically by satisfying the integral condition (34) at the same time. But due to inaccuracy in the very lengthy calculation, this method of solution is not practical. Hence we choose an alternative course by assuming an initial condition for $\Pi_0^*(k^*, t^*)$ at very small t^* and carry out the numerical calculation. The integral condition (34) or the boundary condition (35) is then used as a check whether the initial condition chosen is correct.

We choose the initial condition for the calculation to be

$$\Pi_0^*(k^*, t_0^*) = \frac{(1+C_1)}{2} \left[\frac{1}{(1+B_1 k^{*2})^{1.7}} + \frac{1+4.75k^*}{(1+B_2 k^*)^{4.75}} \right], \quad (37)$$

with $R_{a0} = 28$, $R_0^* = 1,067$, $C_1 = \frac{1}{84} \pi^{3/2} \ln(1 + R_{a0})$, $B_1 = 2.91$, $B_2 = 8.82$.

Our method of numerical calculations is similar to that used by Tatsumi *et al* (1978). Here instead of t^* we introduce a new variable τ by

$$\tau = \ln \left(\frac{R_{a0} + 1}{R_a + 1} \right),$$

and use a two-step scheme to approximate the derivative ($\partial/\partial\tau$). First, we use the forward difference quotient, then we use the centre difference quotient once again.

Computations are carried out for the physical quantities mentioned in §1 on the whole range from the initial period to the final period of decay. But up to the present no complete experimental data have been published for these quantities over such a range. Stewart & Townsend (1951) have measured a number of them at different positions behind the grid in the initial period of decay. Hence most of the following discussions are concerned with a comparison of their experiments with our theoretical results.

It is well known that in the decay of turbulence, which is generated by the grid in a wind tunnel, the relative distance x/M from the grid is proportional to the time of decay. Here M is the mesh size of the grid. In order to compare with Stewart & Townsend experiments we take

$$t^* = 8x/M. \quad (38)$$

We have calculated the numerical solutions from $R_{a0} = 28$ to $R_a = 1.6$. According to the relation (36) the corresponding values of t^* vary from 84.4 to 7222.4 with the values of x/M ranging from 10.55 to 902.8. This range includes most of the existing experimental data.

3.1 The energy spectrum and energy transfer function

According to (25) the energy spectrum $E_0(k, t)$ can be calculated from the amplitude function. It is obvious that the energy spectrum function is positive definite and behaves like k^4 at small k , namely,

$$\lim_{k \rightarrow 0} E(k, t) = \frac{8}{15} \pi^4 \frac{N}{V} c_0^2 \left[1 + \frac{\pi^{3/2}}{84} \ln(1 + R_a) \right]^2 k. \quad (39)$$

The numerically calculated results of $E_0(k, t)$ are shown in figure 1 and compared with Stewart & Townsend's experiments. The theoretical curves of the decay of $E_0(k, t)$ are in general agreement with their experiments.

The energy spectrum transfer function $W_0(k, t)$ given in the Appendix of I becomes, in terms of the amplitude function $\Pi_0(k, t)$,

$$W_0(k, t) = \frac{1}{105} \frac{N}{V} \pi^4 k^2 \Pi_0(k, t) \iiint Q \frac{k'^2 - k^2}{k'^2} \Pi_0(k', t) \Pi_0(k'', t) dk'. \quad (40)$$

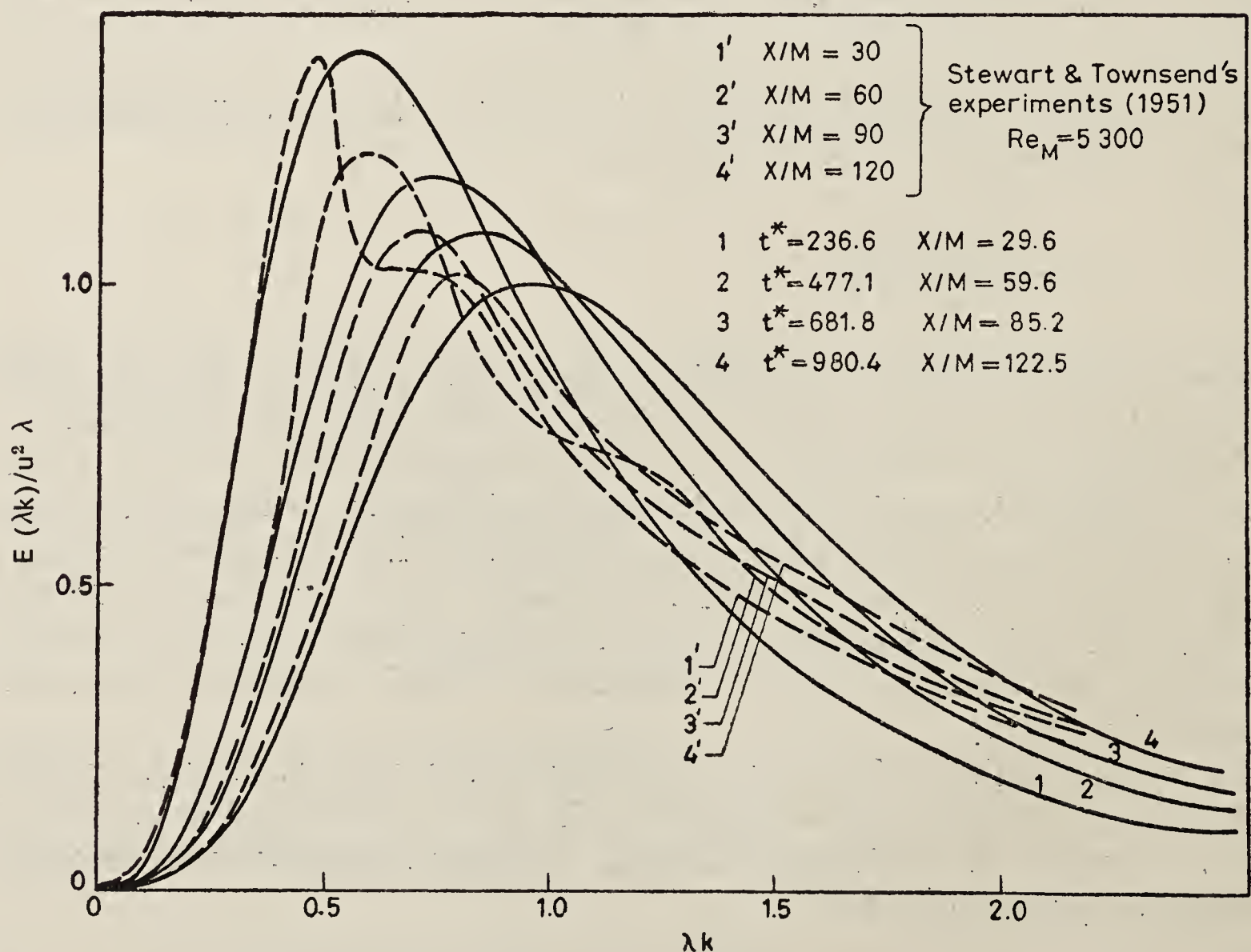


Figure 1. Three-dimensional energy spectrum function.

Using (B. 9) and (B. 10) in Appendix B and (30) and (31) we obtain

$$\lim_{k \rightarrow 0} W_0(k, t) = \frac{4}{105} \pi^{11/2} \frac{N}{V} c_0^3 \left[1 + \frac{\pi^{3/2}}{84} \ln(1 + R_a) \right] \frac{1}{a^5} k^4, \quad (41)$$

namely, $W_0(k, t)$ is also proportional to k^4 at small k .

Since Stewart & Townsend's experiments do not include the energy transfer function $W(k, t)$, we compare our theoretical curve with the experiments of Van Atta & Chen (1969) and Yeh & Van Atta (1973) in figure 2. The agreement is quite satisfactory.

In figure 3 we also plot the one-dimensional energy spectrum $E_1(k_1)$ determined by the formula,

$$E_1(k_1) = \int_{k_1}^{\infty} \left(1 - \frac{k_1^2}{k^2} \right) \frac{E(k, t)}{k} dk, \quad (42)$$

as compared with Favre's experiments (Favre *et al* 1953). The theoretical results decrease faster than the experimental ones presumably because the initial vortex Reynolds number R_{a0} chosen might not be high enough for comparison with Favre's experiments.

3.2 The energy decay, integral scale L and microscale λ

From formula (27) and (25) we obtain the turbulent energy

$$\overline{u^2} = \frac{16}{45} \pi^4 \frac{N}{V} c_0^2 k_0^5 \int_0^{\infty} k^{*4} \Pi_0^{*2}(k^*, t^*) dk^*. \quad (43)$$

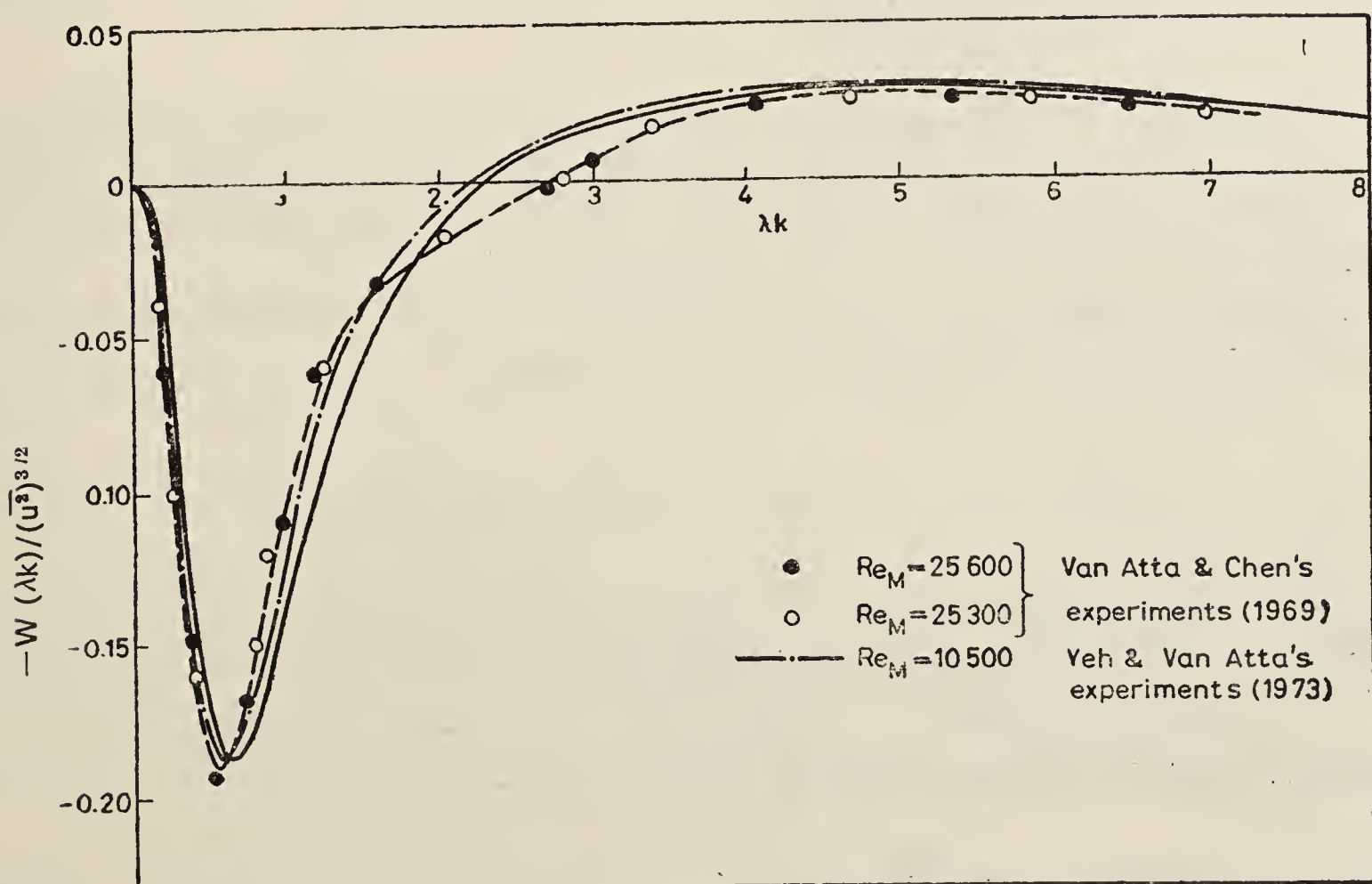


Figure 2. Energy transfer spectrum function

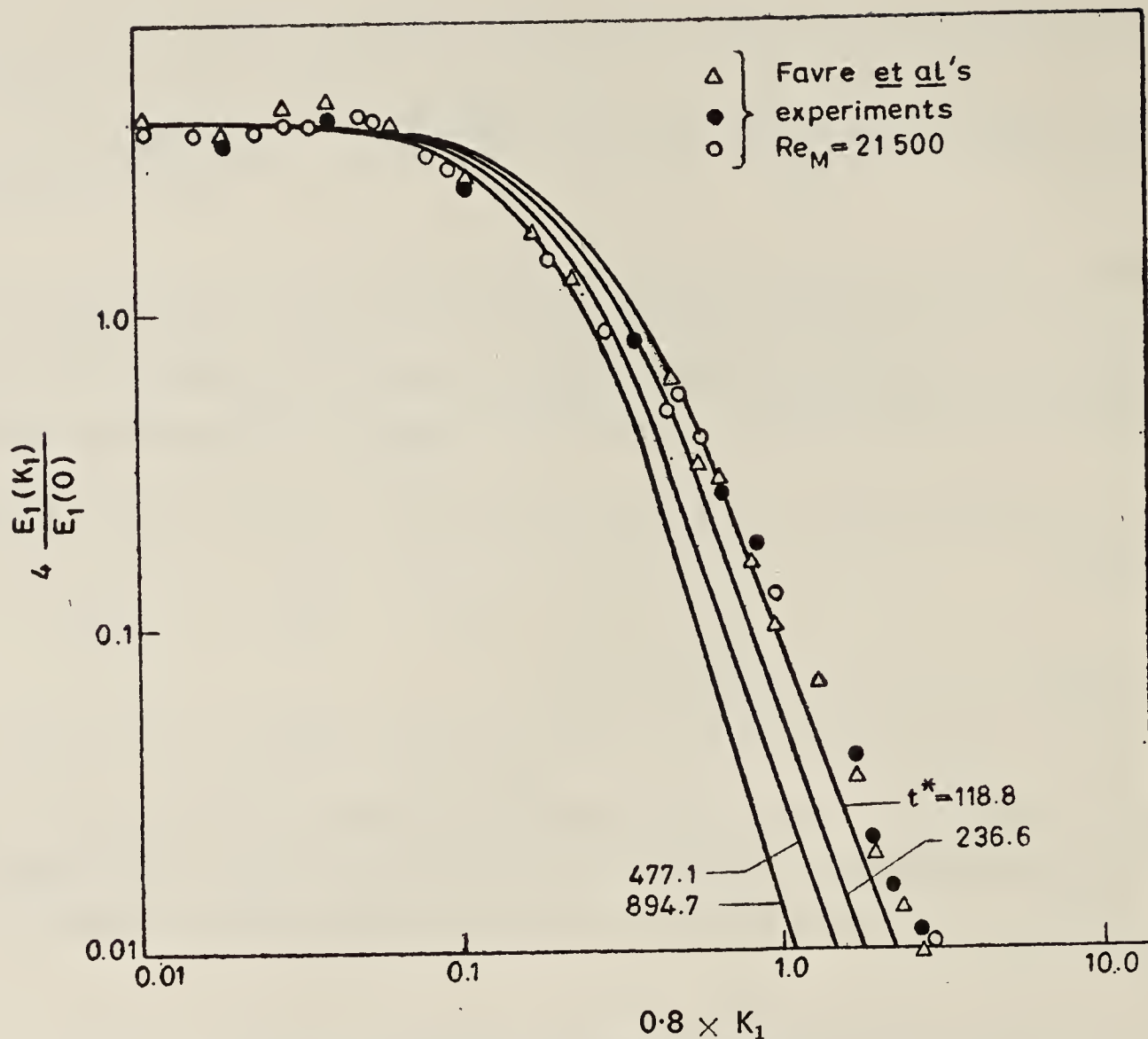


Figure 3. One-dimensional energy spectrum function

Using (34), it reads

$$\overline{u^2} = \frac{2}{15} \pi^{9/2} \frac{N}{V} c_0^2 k_0^5 \left(\frac{R_a}{R_0^*} \right)^{5/3}. \quad (44)$$

As we mentioned in I, this expression represents the law of decay of the turbulent energy from the initial period to the final period of decay. The numerical results of the energy decay by (43) shown in figure 4 agree with the linear law of decay measured by Stewart & Townsend in the initial period.

The integral scale L and the Taylor microscale λ of the turbulence are defined respectively in terms of the energy spectrum function by

$$L = \int_0^\infty f(r, t) dr = \frac{3\pi}{4} \int_0^\infty \frac{E(k, t)}{k} dk \Big/ \int_0^\infty E(k, t) dk, \quad (45)$$

and

$$\lambda^2 = - \left(\frac{\partial^2 f(r, t)}{\partial r^2} \right)_{r=0}^{-1} = 5 \int_0^\infty E(k, t) dk \Big/ \int_0^\infty k^2 E(k, t) dk. \quad (46)$$

From the energy condition (4) and the Taylor formula

$$d\overline{u^2}/dt = -10\nu \frac{\overline{u^2}}{\lambda^2}, \quad (47)$$

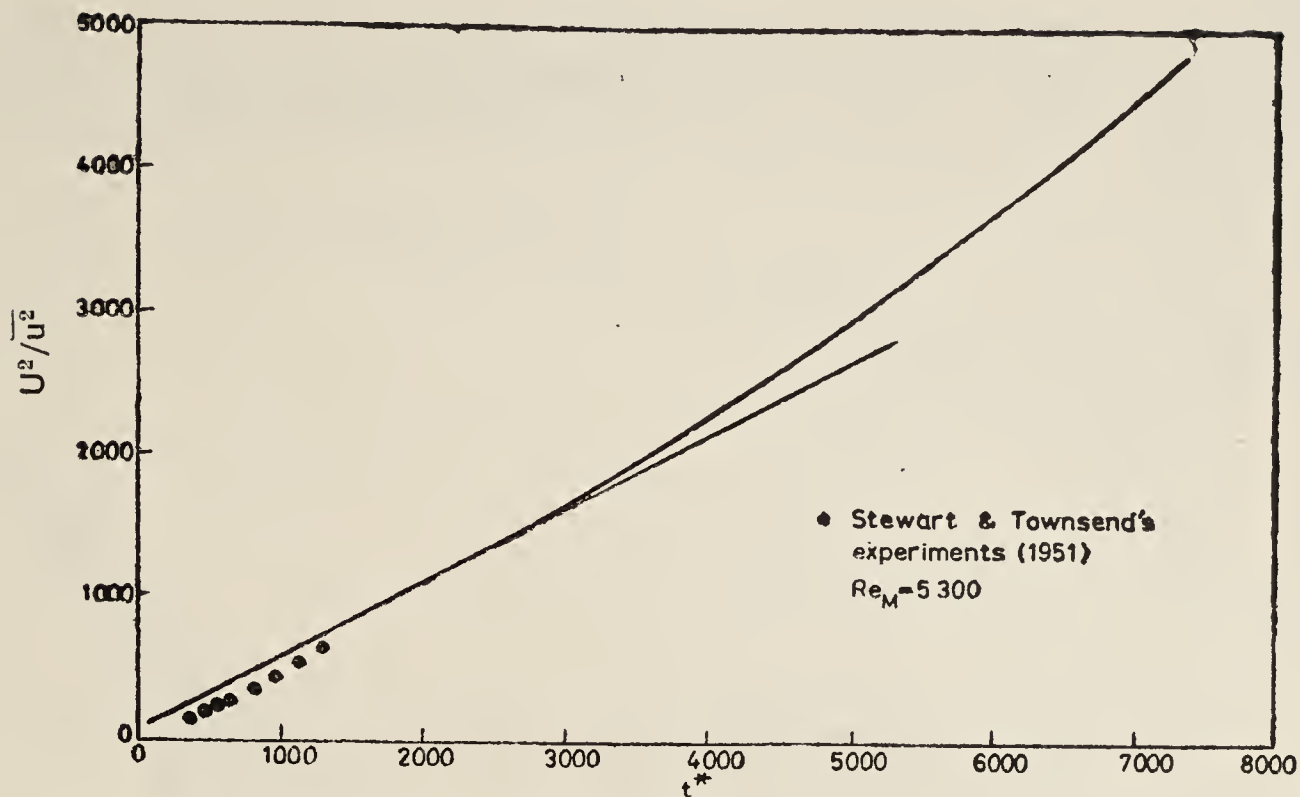


Figure 4. The decay of turbulent energy

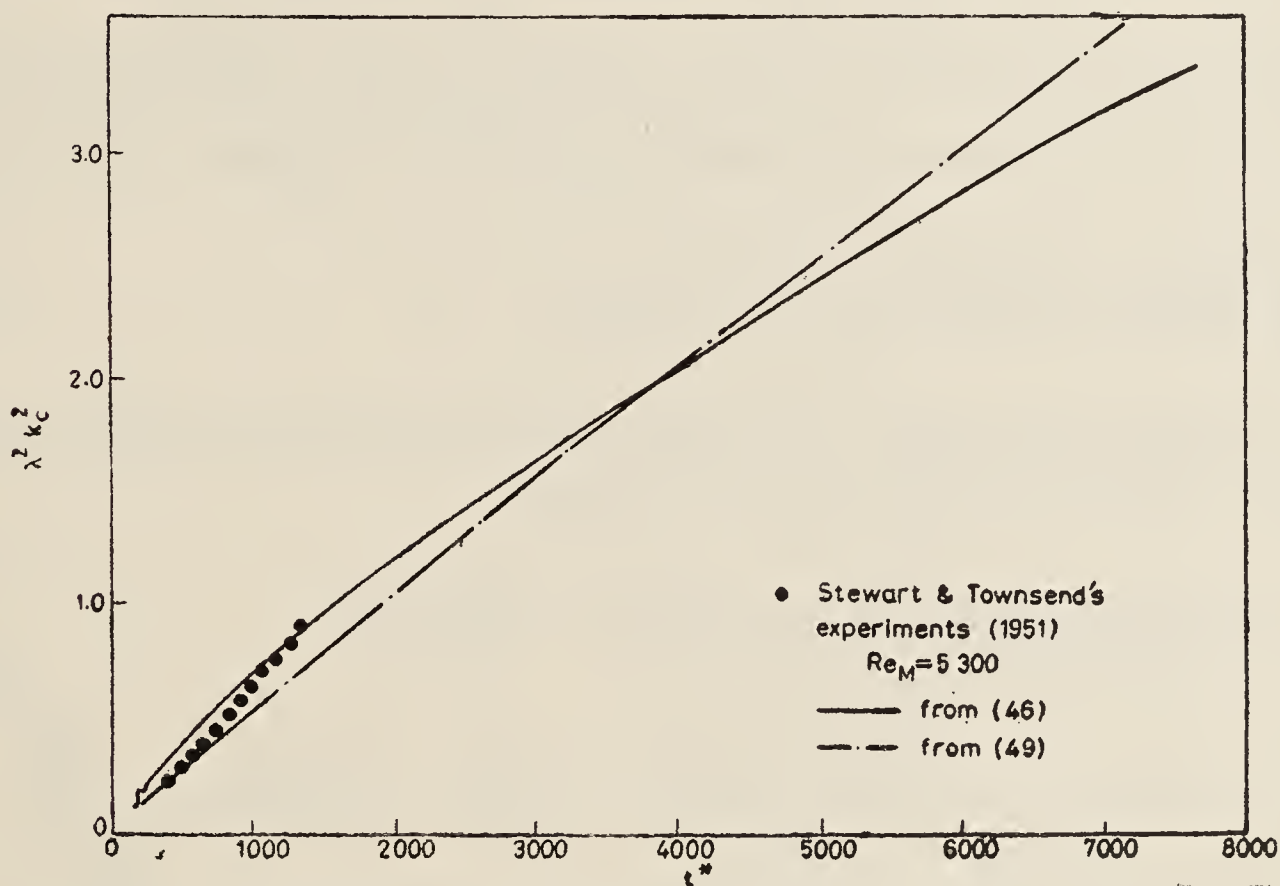


Figure 5. The microscale of turbulence

we obtain a relation between the microscale λ and the eddy scale a as follows,

$$\lambda^2 = 2a^2/(R_a + 1). \quad (48)$$

This relation has been obtained in I (5.29) before. The numerical results which are shown in figures 5 and 6 also agree with those of Stewart & Townsend (1951) and Batchelor & Townsend (1948). But the values of the numerical calculation according to (46) of the microscale λ are a little different from the values of the theoretical prediction (48), which can be written as

$$\lambda^2 = \frac{2}{R_a + 1} \left(\frac{R_0^*}{R_a} \right)^{2/3} \frac{1}{k_0^2}. \quad (49)$$

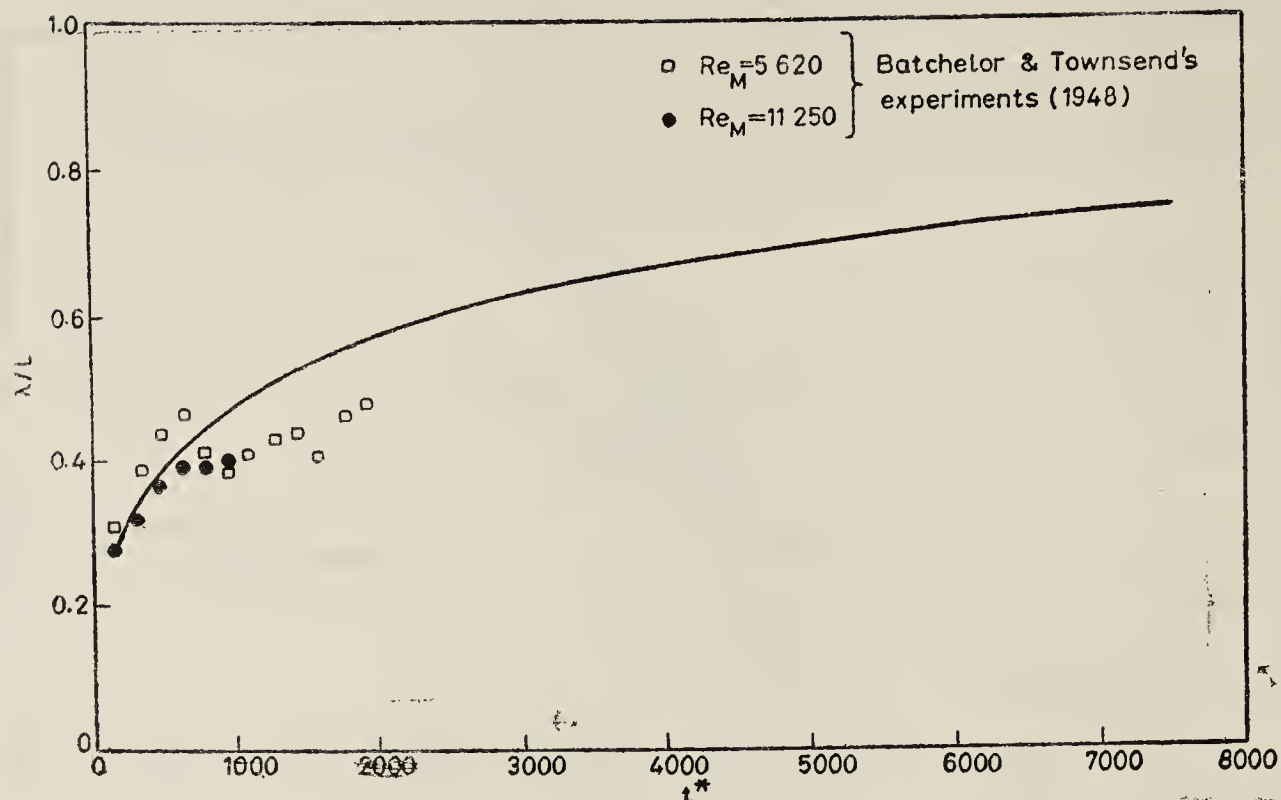


Figure 6. The integral scale.

One reason is that the initial condition (37) which we have chosen makes the denominator of (46) divergent. It means that this initial condition (37) obviously is not the exact form of the solution of the integro-differential equation (33) at the initial instant.

3.3 The double and triple velocity correlations

The double and triple velocity correlations can be calculated from the formulas of the Fourier transforms of the spectrum functions

$$\overline{u^2} f(r, t) = 2 \int_0^\infty E(k, t) \left(\frac{\sin kr}{k^3 r^3} - \frac{\cos kr}{k^2 r^2} \right) dk, \quad (50)$$

$$\overline{u^2} g(r, t) = \int_0^\infty E(k, t) \left(\frac{\sin kr}{kr} + \frac{\cos kr}{k^2 r^2} - \frac{\sin kr}{k^3 r^3} \right) dk, \quad (51)$$

$$\overline{(u^2)^{3/2}} k(r, t) = 2 \int_0^\infty W(k, t) \left(\frac{\sin kr}{k^3 r^2} + 3 \frac{\cos kr}{k^4 r^3} - 3 \frac{\sin kr}{k^5 r^4} \right) dk. \quad (52)$$

As pointed out previously, there are no complete sets of experiments on the double and triple velocity correlations from the initial period to the final period of decay. Hence in figures 7, 8 and 9, we compare the theoretical calculations with the experiments of Stewart & Townsend and Batchelor & Townsend respectively. All the theoretical curves agree with the measurements except at large separations between the two points measured. One reason is that we have only considered the zeroth order approximation of the nonlinear effects. Owing to the much greater influence of the latter on the triple velocity correlation than on the double velocity correlation, the discrepancies between theory and experiment for triple correlations at such separations are more pronounced. On the other hand, as Mills *et al* (1958) pointed out, there are some differences between the measured values of the triple velocity

correlation and the values computed from the Kármán-Howarth equation through the measured values of the double-velocity correlation. Hence the disagreement may also be attributed to the inaccuracy of the measurements at large separations.

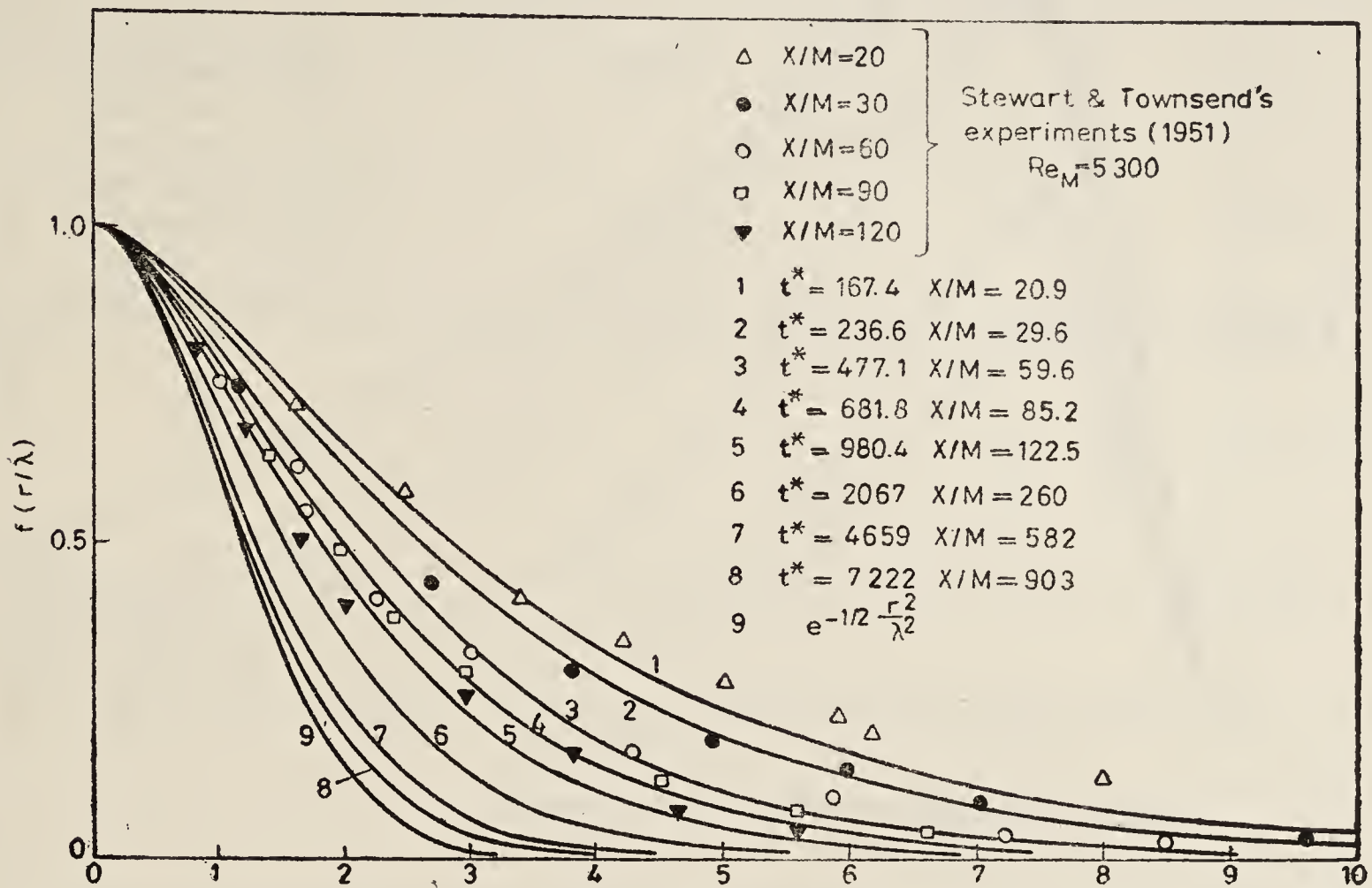


Figure 7. Longitudinal double velocity correlation

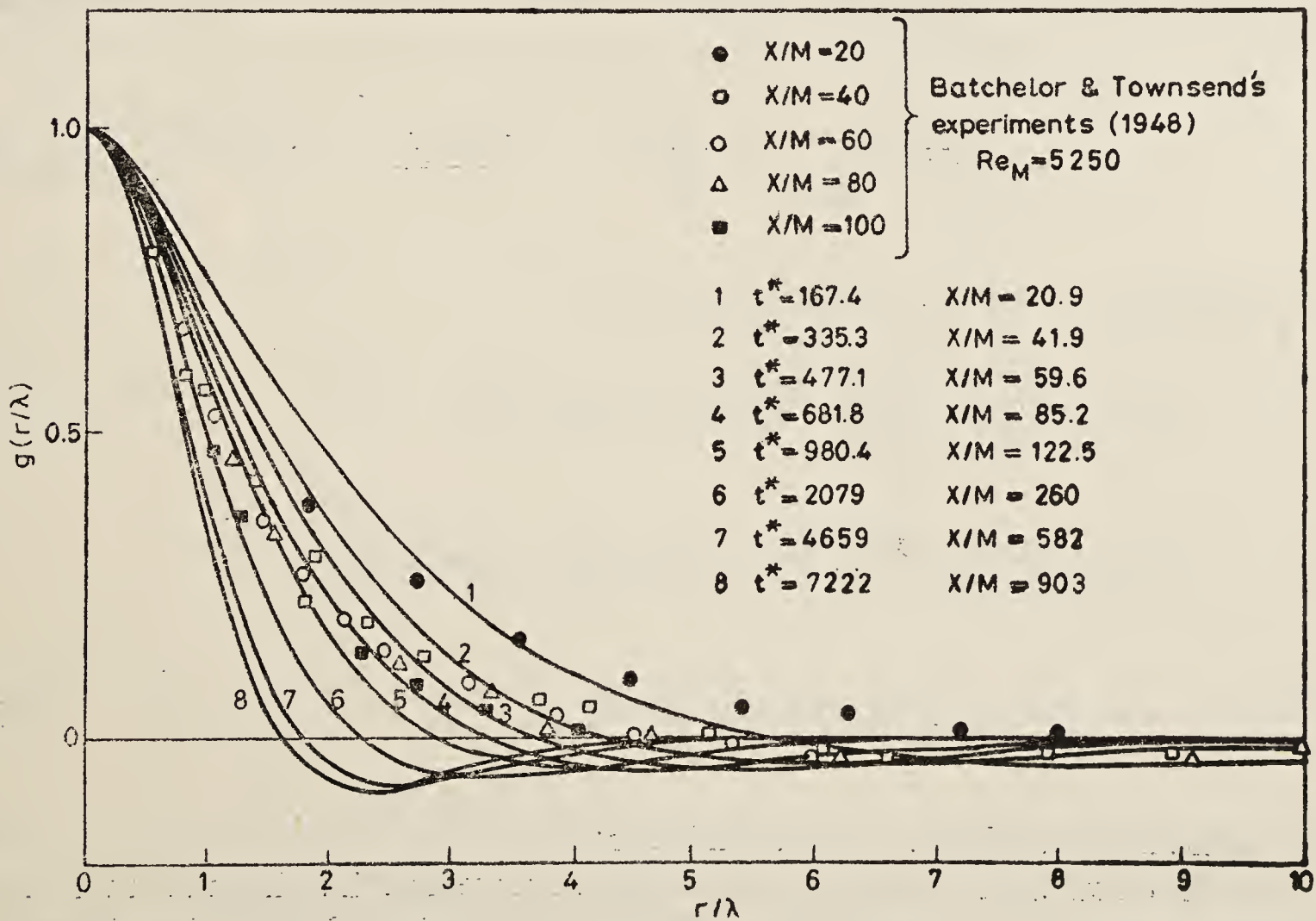


Figure 8. Transverse double velocity correlation

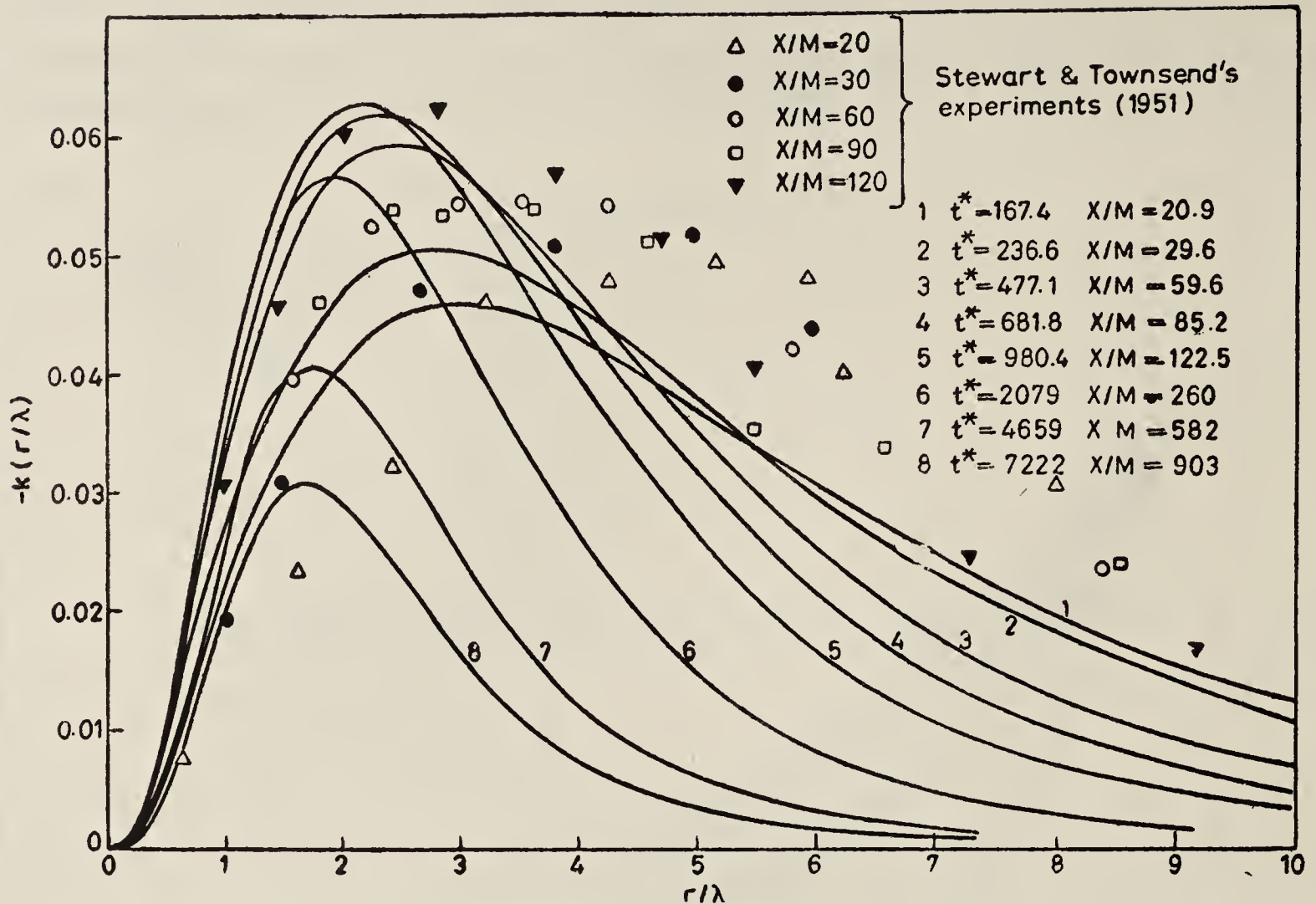


Figure 9. Longitudinal triple velocity correlation

According to our theory we can also prove that at large separations the triple velocity correlation $k(r, t)$ behaves like r^{-4} , which was also shown by Batchelor & Proudman (1956). By using the Fourier transform of triple velocity correlation $k(r, t)$,

$$W(k, t) = \frac{1}{\pi} (\overline{u^2})^{3/2} \int_0^\infty \left[r \frac{\partial^2 k(r, t)}{\partial r^2} + 7 \frac{\partial k(r, t)}{\partial r} + 8 \frac{k(r, t)}{r} \right] kr \sin kr \, dr,$$

and expanding it at small k , with (41), we obtain

$$\lim_{r \rightarrow \infty} (\overline{u^2})^{3/2} \left[r^3 \frac{\partial k(r, t)}{\partial r} + 4r^2 k(r, t) \right] = 0,$$

$$\lim_{r \rightarrow \infty} (\overline{u^2})^{3/2} \left[r^5 \frac{\partial k(r, t)}{\partial r} + 2r^4 k(r, t) \right] = \frac{8}{35} \pi^{3/2} \frac{N}{V}$$

$$\times \left[1 + \frac{\pi^{3/2}}{84} \ln(1 + R_a) \right] \frac{c_0^2}{a^5}. \quad (53)$$

The second limit in (53) was not known before.

From the calculation of triple velocity correlation we find that the maximum value of the magnitude of $k(r, t)$ increases during the initial period of decay, then decreases after the initial period. This phenomenon has yet to be verified by experiments.

4. Discussion

First of all, we wish to point out an important conclusion that the energy spectrum function $E_0(k, t)$ and the energy transfer function $W_0(k, t)$ thus calculated in the present zeroth order approximation satisfy the exact Kármán-Howarth equation in the spectrum space. By multiplying with

$$\frac{16}{15} \pi^4 \frac{N}{V} k^4 \Pi_0(k, t)$$

on both sides of the equation (26) and using (25) and (40) we obtain the equation

$$\frac{\partial E_0}{\partial t} + W_0 = -2\nu k^2 E_0 \quad (54)$$

which is the spectral form of the Kármán-Howarth equation. In another paper to be published elsewhere, we shall prove that in the n th order approximation this conclusion still holds.

It is well known that there are many assumptions about the spectral energy transfer function in the theories of homogeneous isotropic turbulence. For example, there are the hypotheses proposed by Heisenberg and others (see Hinze 1975). Comparing (40) with these hypotheses we can see that all these theories, like ours, indicate that the spectral energy transfer function is proportional to the $3/2$ power of the energy spectrum or to the cube of the amplitude function. But they only consider the interaction of two wave numbers k, k' in the spectral energy transfer function, while our theory has considered the interaction among the three wave numbers k, k', k'' which form a vector triangle, and is therefore more comprehensive.

From our theory we can determine the property of the Loitsianskii's integral Λ , which is defined by

$$\Lambda = \bar{u}^2 \int_0^\infty f(r, t) r^4 dr. \quad (55)$$

With the Fourier transform of the double velocity correlation, which form a vector triangle

$$E(k, t) = \bar{u}^2 \frac{1}{\pi} \int_0^\infty f(r, t) kr (\sin kr - kr \cos kr) dr, \quad (56)$$

we have $\lim_{k \rightarrow \infty} E(k, t) = \frac{1}{3\pi} \bar{u}^2 \int_0^\infty f(r, t) r^4 dr k^4.$ (57)

Hence comparing with (39) we obtain

$$\Lambda = \frac{8}{5} \frac{N}{V} \pi^5 c_0^2 \left[1 + \frac{1}{84} \pi^{3/2} \ln(1 + R_a) \right]^2. \quad (58)$$

From (58) we can conclude that the Loitsianskii integral exists but it is not a constant. It decreases during the decay process as R_a decreases and becomes a constant in the final period of decay, when the vortex Reynolds number R_a is negligible. This conclusion has also been obtained by Batchelor & Proudman (1956) and Proudman & Reid (1954) before.

The relation between the turbulent scale λ and the eddy scale a can be determined from the formula (48). It shows that when the eddy Reynolds number is very large in the initial period of decay, a is much greater than λ ; when the eddy Reynolds number is very small in the final period of decay, a is of the same order of λ . This indicates that the elements of turbulence in the high Reynolds number flow are large-scale eddies, and they become small-scale eddies in the final period of decay.

According to the definition of the turbulent Reynolds number R_λ and the definition of the vortex Reynolds number R_a (equation (1)), we can obtain the relation between R_λ and R_a by using (44) and (49):

$$R_\lambda = \frac{2}{\sqrt{15}} \pi^{9/4} \left(\frac{N}{V} \frac{c_0}{\nu} \frac{R_a}{R_a + 1} \right)^{1/2}. \quad (59)$$

when R_a is very large. R_λ is equal to a constant which agrees with the experiments of initial decay. In our present case $R_{a0} = 28$, and we have

$$R_{\lambda_0} \approx 27.22. \quad (60)$$

It is near to the values given by Stewart & Townsend and Batchelor & Townsend.

According to our calculation, we find that the choice of the initial condition of the amplitude function (37) is very important. Especially in the high vortex-Reynolds number flows the solution is very sensitive to the initial condition and the errors of the calculation in view of the strong effects of the nonlinear term in the Navier-Stokes equations of motion. Further we wish to point out that the influence of the higher approximations upon the present zeroth order approximation has to be investigated. The present investigation was started in Peking after 1975 and continued at M.I.T. since 1979. The numerical computations were made on the HP-7700 computer of the Department of Mathematics of M.I.T. We wish to express our hearty gratitude to Professor C.C. Lin for his concern and the advice that he gave us during this work, and to M.I.T. for the facilities of research put at our disposal. We are also grateful to the National Science Foundation of USA for the financial assistance given to our investigation.

This paper was also presented at the International Congress of Theoretical and Applied Mechanics at Toronto, Canada, August 1980.

Appendix A: The coefficients d_{nms} and h_{nms}

From equation (11) we have

$$\frac{d}{d\mu} \left[(1 - \mu^2) \frac{dP_m}{d\mu} \right] = -m(m+1)P_m. \quad (A.1)$$

Integrating the following integral by parts three times and using (A.1) we obtain a formula

$$\int_{-1}^1 (1 - \mu^2) \frac{dP_{2n+2}}{d\mu} \frac{dP_{2s+2}}{d\mu} P_{2m+2} d\mu = [(s+1)(2s+3) + (n+1)(2n+3) - (m+1)(2m+3)] e_{nms}. \quad (\text{A.2})$$

By multiplying with $(1 - \mu^2)H_l$ on both sides of (15) and (16) and integrating μ from -1 to 1 , then using (13) and (14), we get the following expressions:

$$\begin{aligned} d_{nms} &= \frac{(4n+5)!! (2m+1)! (2s+1)!}{2(2n+3)! (4m+3)!! (4s+3)!!} \\ &\quad \times \int_{-1}^1 (1 - \mu^2) \frac{dP_{2n+2}}{d\mu} \frac{d_{2s+2}}{d\mu} \frac{d}{d\mu} \left[(1 - \mu^2) \frac{dP_{2m+2}}{d\mu} \right] d\mu, \\ h_{nms} &= \frac{(4n+5)!! (2m+1)! (2s+1)!}{2(2n+3)! (4m+3)!! (4s+3)!!} \\ &\quad \times \int_{-1}^1 (1 - \mu^2) \frac{dP_{2n+2}}{d\mu} \frac{dP_{2m+2}}{d\mu} \frac{d^2 P_{2s+2}}{d\mu} d\mu. \end{aligned} \quad (\text{A.3})$$

Then using (A.1) and (A.2) and integrating by parts we obtain the formulas (18).

Appendix B: Derivation of the integro-differential equation (26) and the boundary condition

In the zeroth-order approximation, from I (5.15) we know that the velocity components U_{0i} can be expressed in tensor form

$$U_{0i} = \frac{1}{2} U \beta_{mni} l_m l_n, \quad (\text{B.1})$$

where

$$\begin{aligned} \beta_{mni} &= \left(R \frac{\partial G_0}{\partial R} + G_0 \right) \frac{R_m R_n R_i}{R^3} + G_0 \frac{R_i}{R} \delta_{mn} - \frac{1}{2} \left(2G_0 + R \frac{\partial G_0}{\partial R} \right) \\ &\quad \times \left(\frac{R_m}{R} \delta_{in} + \frac{R_n}{R} \delta_{im} \right). \end{aligned} \quad (\text{B.2})$$

The Fourier transform Γ_{mni} of β_{mni} is given by I (5.17)

$$\Gamma_{mni} = {}_t \Gamma_0(k, t) (k_m k_n k_i - \frac{1}{2} k^2 k_m \delta_{in} - \frac{1}{2} k^2 k_n \delta_{im}). \quad (\text{B.3})$$

Now we consider the Fourier transform

$$\Omega = U^2 k_n \int \int \int \beta_{mni} \frac{\partial \beta_{mjj}}{\partial R_i} \exp({}_t \mathbf{k} \cdot \mathbf{R}) d\mathbf{R}. \quad (\text{B.4})$$

Inserting (B.2) into (B.4) and using (21) we have

$$\Omega = i 8\pi \frac{U^2}{a^2 k} \int_0^\infty R \left(G_0 \frac{\partial B_0}{\partial \xi} + \frac{1}{2} B_0^2 \right) (\sin kR - kR \cos kR) dR. \quad (\text{B.5})$$

On the other hand substituting

$$\beta_{mni} = \iiint \Gamma_{mni} \exp(i \mathbf{k} \cdot \mathbf{R}) d\mathbf{k} \quad (\text{B.6})$$

into (B.4) and changing the order of integration, we obtain

$$\Omega = i (2\pi)^3 \iiint k_n k'_i \Gamma_{mni}(\mathbf{k}'', t) \Gamma_{mji}(\mathbf{k}', t) d\mathbf{k}'. \quad (\text{B.7})$$

Using the cosine formulas,

$$k''^2 = k^2 + k'^2 + 2\mu' k k', \quad k'^2 = k^2 + k''^2 + 2\mu'' k k'',$$

we have

$$\begin{aligned} Q &= -4 k^2 k'^2 (1 - \mu'^2) = -4 k^2 k''^2 (1 - \mu''^2) \\ &= -4 k''^2 k_i k_a \Delta_i^a(\mathbf{k}''). \end{aligned} \quad (\text{B.8})$$

After direct calculation and in terms of $\Pi_0(k, t)$ (B.7) reads

$$\Omega = i\pi^3 \iiint Q \frac{(k'^2 - k^2)}{k''^2} \Gamma_0(k', t) \Pi_0(k'', t) d\mathbf{k}'. \quad (\text{B.9})$$

Then with (23) (B.5) and (B.9) we can transform the differential equation (22) into the integro-differential equation (26).

Inserting (B.8) into (B.9) and taking the limit $k \rightarrow 0$, we obtain

$$\lim_{k \rightarrow 0} \Omega = -i \frac{32}{3} \pi^4 \int_0^\infty k'^4 \Pi_0'(k', t) dk k^2. \quad (\text{B.10})$$

Then from (26) and (30) we get

$$\frac{d\Pi_0(0, t)}{dt} = \frac{2\pi}{21} \int_0^\infty k'^4 \Pi_0^2(k', t) dk' = \frac{1}{28} \pi^{3/2} \frac{c_0^2}{a^5}. \quad (\text{B.11})$$

According to (1) to (3) we have

$$\frac{dR_a}{dt} = -\frac{3c_0}{a^5} (1 + R_a). \quad (\text{B.12})$$

Hence (B.11) becomes

$$\frac{d\Pi_0(0, t)}{dR_a} = -\frac{\pi^{3/2} c_0}{84(1 + R_a)}. \quad (\text{B.13})$$

Integrating (B.13) and using (29) to determine the integral constant we obtain the boundary condition (31).

References

- Abramowitz M & Stegun I A 1964 *Handbook of mathematical functions with formulas, graphs and mathematical tables* (New York: Dover)
- Batchelor G K & Proudman I 1956 *Philos. Trans. R. Soc. (London)* **A248** 369
- Batchelor G K & Townsend A A 1948 *Proc. R. Soc. London* **A193** 539
- Chou Pei-yuan & Huang Yung-nien 1975 *Sci. Sin.* **18** 199
- Favre A, Gaviglio J & Dumas R 1953 *Recherche Aeronaut.* **32** 21
- Gradshteyn I S & Ryzhik I M 1965 *Table of integrals, series and products* (New York: Academic Press) p. 796
- Hinze J O 1975 *Turbulence* (New York: McGraw Hill)
- Mills R R, Kistler A L, Obrien V & Corrsin S 1958 NACA TN 4288 pp. 1-67
- Proudman I & Reid W I 1954 *Philos. Trans. R. Soc. (London)* **A247** 163
- Stewart R W & Townsend A A 1951 *Philos. Trans. R. Soc. (London)* **A243** 359
- Tatsumi T, Kida S & Mizushima J 1978 *J. Fluid Mech.* **85** 97
- Van Atta C W & Chen W Y 1969 *J. Fluid Mech.* **38** 743
- Yeh T T & Van Atta C W 1973 *J. Fluid Mech.* **58** 233

Mathematical modelling of turbulent shear flows

M OHJI

Fluid Engineering Laboratory, The University of Electro-Communications,
Chofu, Tokyo 182, Japan

MS received 27 May 1981

Abstract. A critical review of the current methods of mathematical modelling for quantitative predictions of turbulent shear flows is presented. Emphasis is laid on the basic principles and general strategy rather than on computational or bibliographical details. Three major groups of modelling, *viz.* the integral methods, the differential methods and the numerical simulations are described in the simplest forms. These methods are compared and their future prospects are discussed.

Keywords. Modelling; prediction; shear; transport; turbulence.

1. Introduction

In spite of the seemingly chaotic nature of violent eddy mixing, it is a common understanding that the turbulent motions of an ordinary Newtonian fluid are governed by the Navier-Stokes (NS in short, hereafter) equations just as laminar motions are. To speak more cautiously, NS turbulence is expected to be a sufficiently close copy of real turbulence under the usual conditions. However, since the NS equations for turbulent state are very difficult to solve even approximately, a fully reliable theory of turbulence remains unestablished as yet. From the practical point of view, however, the need for quantitative prediction of turbulent flows is increasing greatly in diverse fields of application: for instance, aero- and astronautics, fluid machinery, chemical plants, reactor designs, weather forecasts, oil- and water resources, environmental problems, and so on. Thus, to bridge the wide gap between theory and practice, some drastic assumptions and/or simplifications to make the mathematical computations tractable are unavoidable. Such procedures may be referred to as 'mathematical modelling', procedures which play an important role in engineering applications. This paper reviews the principles and modern trends in the mathematical modelling of turbulent shear flows in their simplified context. It is not intended here to give computational details or a complete list of the available literature.

For the sake of conciseness, let us now consider an incompressible fluid of constant properties under no external forces. Then, the NS equations are written, in a non-dimensional form, as

$$\nabla \cdot \mathbf{u} = 0, \tag{1a}$$

$$\partial \mathbf{u} / \partial t = - \mathbf{u} \cdot \nabla \mathbf{u} - \nabla p + R^{-1} \nabla^2 \mathbf{u}, \tag{1b}$$

where \mathbf{u} is the velocity vector, p the pressure, and R stands for the Reynolds number. The notorious difficulty of the turbulence problem comes essentially from the fact that the non-linear term $\mathbf{u} \cdot \nabla \mathbf{u}$ (NL in short) of equation (1b) counteracts in a sense the viscous dissipative term $R^{-1} \nabla^2 \mathbf{u}$ (VD). As a result of subtle competition between these two effects, the system of partial differential equations (1) ceases to be a well-posed one at high values of $R \sim (\text{NL}) / (\text{VD})$ in general. Namely, a very small perturbation would then cause a drastic deviation of the solution in an unpredictable way. This peculiar nature of the solutions is the first primary obstacle to numerical computation of NS turbulence. What is worse, the turbulent chaos is known to be excited over a wide range of the spectrum. In fact, if the length- and time-scales of the energetic eddies are L and T while those of the smallest eddies are l_d and t_d , we have, in the limit of $R \rightarrow \infty$, the Kolmogorov scaling

$$l_d \sim (\nu^3/\epsilon)^{1/4}, \quad t_d \sim (\nu/\epsilon)^{1/2}, \quad (2)$$

together with

$$L \sim q^3/\epsilon, \quad T \sim L/q, \quad (3)$$

from dimensional considerations, where q denotes the r.m.s. of velocity fluctuations, ν the kinematic viscosity, and ϵ the mean rate of energy dissipation. On eliminating ϵ , it follows, with $R \sim qL/\nu$,

$$L/l_d \sim R^{3/4}, \quad T/t_d \sim R^{1/2}, \quad (4)$$

and hence these scale-ratios would be as large in order as of 10^3 and 10^2 respectively at $R = 10^4$, for example. When R is large, therefore, direct numerical integration of equation (1) requires a very high resolving power far beyond the capacity of even the largest computers.

In most practical applications, however, we are not concerned with every detail of turbulent fluctuations but only with a few statistical quantities such as the mean velocity, the mean flux of turbulent transport, and so on. This is the very reason why we can develop mathematical modelling of turbulent flows without solving the NS equations themselves.

2. General background of the subject

To begin with, it should be noted that in the present context modelling is not simply an 'approximation'. Figure 1 illustrates the difference conceptually. That is, approximation (left) retains the full information contained in the original equations as much as possible, so that an approximate solution is expected to approach the exact solution when improved. In contrast with this, by 'modelling' (right) we mean an artefact on a different mathematical level obtained at the sacrifice of a vast amount of information contained in the original equations; the exact solution would never be approached by modelling. It is thus most important to pick out the essential part

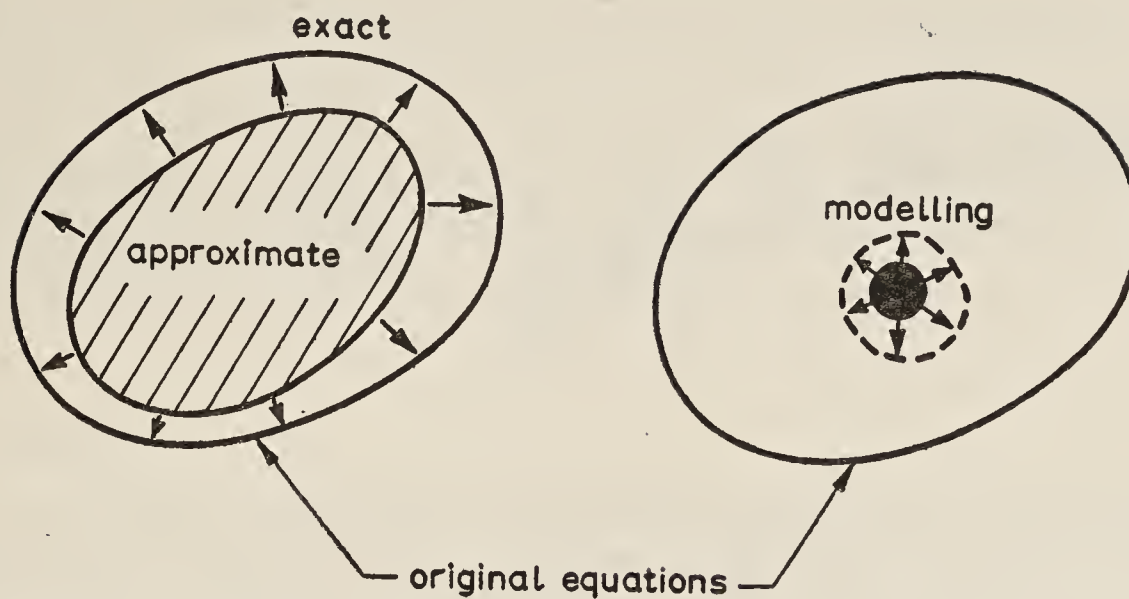


Figure 1. Approximation and modelling.

of the information effectively. Now among various criteria to evaluate the utility of modelling, we shall mention here the following three in particular:

- (i) accuracy (to make reliable predictions),
- (ii) economy (to lower the cost of computation),
- (iii) universality (to secure a wide range of applicability),

as shown in figure 2. However, since these attributes conflict with one another as a rule, we cannot avoid a compromise in practice, and the optimum choice will depend on the type of flow as well as on the purpose of computation.

In this connection a turbulent shear layer may be qualified as 'simple', if it is incompressible with uniform properties, two-dimensional or axisymmetric, steady and fully-developed, thin in the cross-stream direction (s), free from body forces.

If even one of these conditions does not apply, then we are concerned with 'complex flows'. Figure 3 is a schematic drawing of a typical simple flow on a solid wall. Even in this type of flow, it is not uncommon for the transition to turbulence and separation of the shear layer to complicate the matter considerably.

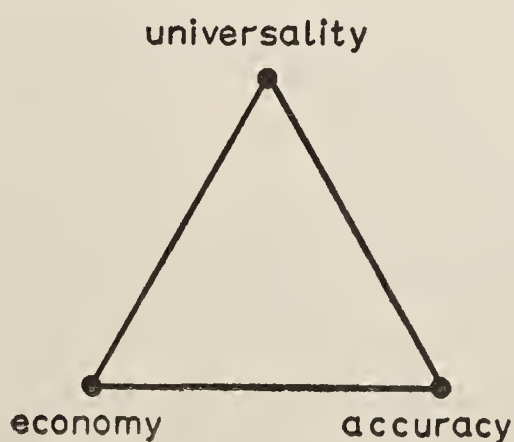


Figure 2. Criteria of modelling.

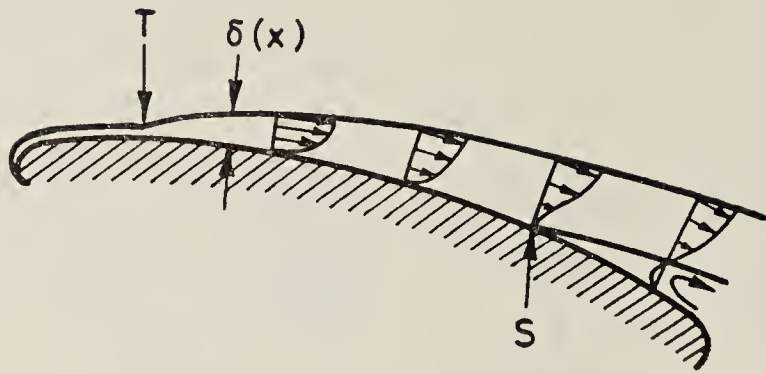


Figure 3. 'Simple flow' along a solid wall. T: transition point, S: separation point, $\delta(x)$: boundary layer thickness.

At any rate, the first step in the mathematical modelling of turbulence in the sense of figure 1 is to smooth out the chaotic nature of the problem by averaging the NS equations. If we divide any turbulent quantity f into the mean value F or \bar{f} and the fluctuation part f' in such a way that

$$f = F + f'; \quad \bar{f} = F, \bar{f}' = 0, \quad (5)$$

the averaged equations then obtained are called the Reynolds equations, which of course retain only a very small part of the information contained in the NS equations. For simple flows defined above, the Reynolds equations reduce to, in the dimensional form,

$$\frac{\partial U}{\partial x} + \frac{\partial V}{\partial y} = 0, \quad (6a)$$

$$U \frac{\partial U}{\partial x} + V \frac{\partial U}{\partial y} = -\frac{1}{\rho} \frac{dP}{dx} + \frac{\partial}{\partial y} \left(\nu \frac{\partial U}{\partial y} - \overline{u'v'} \right), \quad (6b)$$

by virtue of the 'thin shear layer approximation', where (U, u') and (V, v') are the streamwise (x) and the normal (y) components of the velocity, ρ the density, and an extra term $-\partial(\overline{u'^2} - \overline{v'^2}) / \partial x$ has been neglected on the r.h.s. of (6b). As is well-known, the pressure gradient dP/dx is a prescribed function of x , but $-\rho \overline{u'v'}$ is the Reynolds shear stress which needs further modelling. Moreover, since any kind of stress modelling will inevitably introduce new unknowns, we are confronted with the 'closure problem' from the outset. In the absence of a rigorous theory of turbulent transport, the task of model-developers is to devise effective schemes of closure on a more or less semi-empirical basis.

Most of the current schemes of closure may be classified into two groups: the 'integral methods' and the 'differential methods'. The former originate from the Kármán integral form of the momentum equation, the latter from the eddy viscosity concept usually connected with the mixing length hypothesis. In spite of many efforts at their refinement, the predicting power of those methods remained rather poor during the pre-computer age before the 1960s. An important event in the subsequent period was the Stanford Conference on Computation of Turbulent Boundary Layers in 1968, where twenty varieties of the integral methods and ten of the differential methods mainly concerning simple flows were presented for competition (Kline *et al*

1969; Coles & Hirst 1969). After that the remarkable growth of high-speed computers has greatly encouraged a rapid development of advanced versions of the differential methods on the one hand, and introduced novel methods of numerical simulations on the other. In fact, the next 'Stanford Conference' being held in 1981–82 is expected to focus on the computation of complex flows. An outline of these methods of modelling will be presented in the following three sections.

3. Integral methods

The integral methods are based on the principle that we can reduce the number of space variables by integration of the Reynolds equations over the corresponding directions. In fact, for simple flows as shown in figure 1, equation (6b) is integrated in the y -direction to give an ordinary differential equation

$$\frac{d\theta}{dx} + (H + 2) \theta \frac{d \ln U_1}{dx} = \frac{1}{2} c_f; \quad H \equiv \frac{\delta^*}{\theta}, \quad (7)$$

where θ is the momentum thickness, δ^* the displacement thickness, c_f the wall-friction coefficient, and $U_1 \equiv (U)_{y=\delta(x)}$ (figure 3) is a given function of x

$$(\rho U_1 dU_1/dx = - dP/dx).$$

Although (7) is much more tractable than (6), it contains three unknowns θ , H and c_f , so that we need two extra relations to get a solution. The integral form (7) of the mean momentum equation looks exactly identical to that for laminar flows, but the choice of those extra relations is not so well-established as in the laminar case; there are two major subgroups in this context.

3.1 Integral parameter closures

First, we regard the shear layer as a 'black box', and use empirical correlations among several integral parameters to close (7). No information is obtained on the inside of the shear layer. A typical example of this approach is the 'entrainment method' due to Head (1958), where one extra relation is Ludwig-Tillmann's friction formula for a smooth wall

$$c_f = 0.246 \times 10^{-0.678H} (U_1 \theta / \nu)^{-0.268}, \quad (8)$$

and the second relation correlates H to θ via another integral parameter H_E called the 'entrainment factor' in such a way as

$$\frac{d(U_1 H_E \theta)}{dx} = U_1 \phi(H_E); \quad H_E = \frac{1}{\theta} \left(\frac{1}{U_1} \int_0^\delta U dy \right) = \psi(H). \quad (9)$$

Here $\phi(H_E)$ and $\psi(H)$ are algebraic functions to be determined by experiment, and thus (7), (8) and (9) constitute a closed set of equations.

3.2 Weighted residual closures

Contrary to the above, we assume a suitable 'test function' including a few adjustable parameters to approximate the mean velocity profile. For instance, the composite function of Coles (1956)

$$\frac{U}{U_1} = \left(\frac{c_f}{2}\right)^{\frac{1}{2}} \left[\underbrace{2.5 \ln \left\{ \left(\frac{c_f}{2}\right)^{\frac{1}{2}} \frac{U, y}{\nu} \right\}}_{\text{wall law}} + 5 + \underbrace{5 \Pi \sin^2 \left(\frac{\pi y}{2\delta} \right)}_{\text{wake law}} \right] \quad (10)$$

with three parameters c_f , δ and Π is often used as such. Then, by requiring that the residual r of (6b) resulting from the assumed profile should satisfy the weighted integral conditions

$$J_{m,n}(x) \equiv \int_0^\delta U^m y^n r dy = 0, \quad (11)$$

say, we can derive as many extra relations as we please. In particular, $J_{0,0} = 0$ recovers (7), $J_{1,0} = 0$ corresponds to the integral energy equation, and $J_{0,1} = 0$ to the moment of momentum equation. Various combinations of these equations have been worked out, where the contributions to (11) from the Reynolds stress terms must be correlated empirically to close the system of equations (Kline *et al* 1969). Unlike the integral parameter closures, the present schemes can predict the mean velocity profile also.

3.3 Refinement and resume of the integral methods

In order to improve their accuracy and universality, the schemes outlined above have been modified or refined in many respects. For rapidly changing shear layers far from equilibrium, the use of 'lag equations' is found to be fairly successful to reflect the effect of upstream history on the Reynolds stresses; figure 4 reproduces a recent result

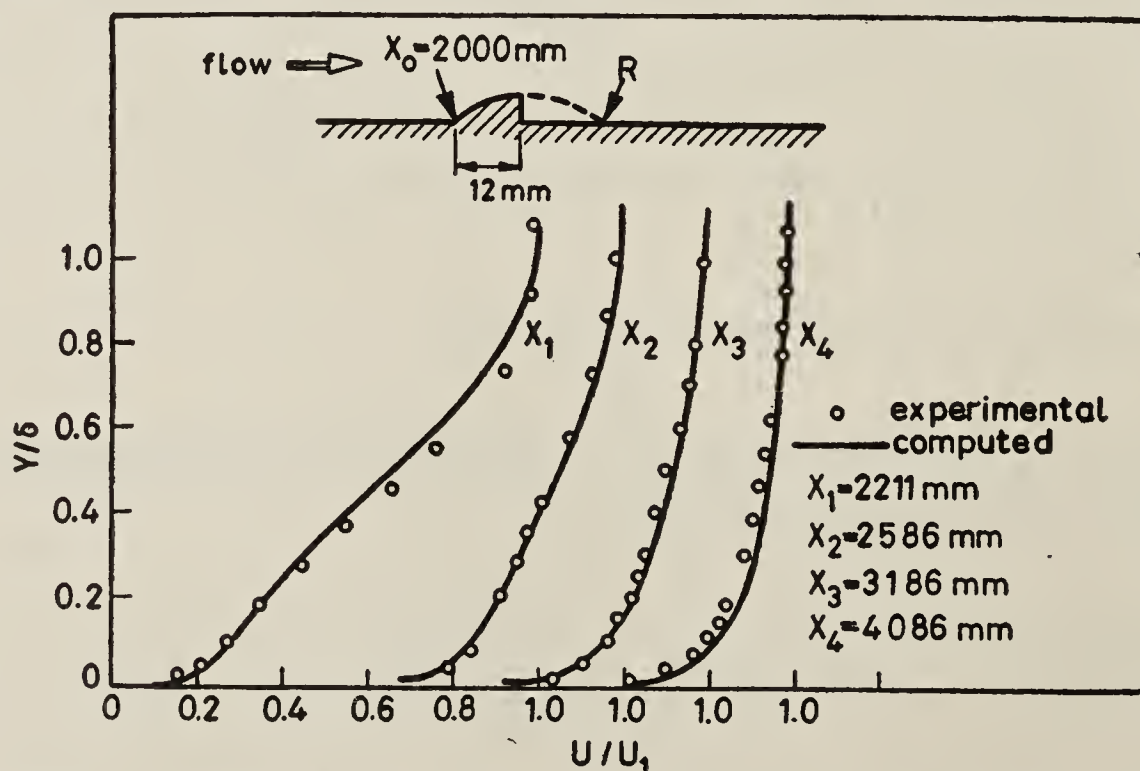


Figure 4. Experimental and computed U -profiles in the Tillmann ledge flow ($\# 1500$, Coles & Hirst 1969, p. 124). The moment of momentum method with a lag equation (Ishida 1978). R: reattachment point.

computed by Ishida (1978) for such a case. Mathematical transformations for compressible flows, and non-Cartesian formulations for three-dimensional flows are other examples of refinement (Cebeci and Bradshaw 1977).

Nevertheless, the primary merit of the integral methods lies in their economy. As they are easier for programming and faster for processing, the integral methods are especially suited for routine computation of a series of similar simple flows for which a lot of good experimental data are available. Highly sophisticated refinement of these methods to complicate the analysis seems to be of little benefit in practical use.

4. Differential methods

The differential methods embrace those attempts to solve the Reynolds equations from point to point, and hence they are much superior to the integral methods conceptually, but their practical success must depend on how the Reynolds stresses can be modelled. Suppose a simple flow again, and for later convenience rewrite (6b) as

$$\frac{\bar{D}U}{Dt} = U_1 \frac{dU_1}{dx} + \frac{\partial}{\partial y} \left(\nu \frac{\partial U}{\partial y} + \tau \right), \quad (12)$$

where $\bar{D}/Dt \equiv U\partial/\partial x + V\partial/\partial y$, and the abbreviations

$$\tau \equiv -\overline{u'v'}, \quad 2k \equiv \overline{u'^2} + \overline{v'^2} + \overline{w'^2}, \quad (13)$$

will be used throughout. Since the Reynolds stress $\rho\tau$ represents the mean momentum flux due to turbulence, the crux of the problem is to estimate the effective rates of turbulent transport across the shear layer. In this connection, the 'gradient diffusion' assumption of the form

$$\overline{\theta'v'} = -K \frac{\partial \Theta}{\partial y}, \quad (14)$$

for the mean flux of any transportable quantity $\theta = \Theta + \theta'$ has been well-known, and from dimensional considerations the transport coefficient K may be expressed most simply as

$$K \sim qL, \quad (15)$$

where q and L are velocity- and length-scales typical of the eddies responsible for transport. Starting from these elementary ideas, the differential methods have grown up to higher levels of closure which are mentioned below in due order.

4.1 Mean velocity field closures (MVF)

These are classical tactics of closing equation (12) at the level of the mean velocity

field (U -level, say). Namely, the gradient diffusion assumption (14) is applied to the Reynolds stress to give

$$\tau = \nu_T \frac{\partial U}{\partial y}, \quad (16)$$

and the eddy (kinematic) viscosity ν_T is correlated with U by phenomenological relations. In particular, according to the mixing length hypothesis, we have

$$\nu_T = L^2 \left| \frac{\partial U}{\partial y} \right|, \quad (17)$$

implying $q \sim L \left| \frac{\partial U}{\partial y} \right|$ in (15). If L (or sometimes ν_T itself) is given as an empirical function of y , this completes the closure called the 'zero-equation models', where we need no other equations than (12). Though by no means up-to-date, these models are still in successful use for a number of simple flows (Cebeci & Smith 1974).

As a variation, Nee & Kovaszny (1969) proposed a one-equation model at the U -level by extending the algebraic relation (17) to a kind of lag equation of the form

$$\frac{\overline{D} \nu_T}{Dt} = A \nu_T \left| \frac{\partial U}{\partial y} \right| - B \frac{\nu_T^2}{L^2} + \frac{\partial}{\partial y} \left(\nu_T \frac{\partial \nu_T}{\partial y} \right), \quad (18)$$

or the like, where A , B are empirical constants, and $L(y)$ is an empirical function as above.

4.2 Mean turbulent field closures (MTF)—one-equation models

At the next level of closures, reference is made to the unaveraged fluctuation equations

$$\nabla \cdot \mathbf{u}' = 0, \quad (19a)$$

$$\frac{\partial \mathbf{u}'}{\partial t} = -\mathbf{U} \cdot \nabla \mathbf{u}' - \mathbf{u}' \cdot \nabla \mathbf{U} - \nabla \cdot (\mathbf{u}' \mathbf{u}' - \overline{\mathbf{u}' \mathbf{u}'}) - \frac{1}{\rho} \nabla p' + \nu \nabla^2 \mathbf{u}' \quad (19b)$$

to connect the rate of transport with the mean turbulent field. The fastest way to do so is to derive from (19) the mean turbulent energy equation, which reduces, in the present context, to

$$\frac{Dk}{Dt} = \underbrace{\tau \frac{\partial U}{\partial y}}_{\text{production}} - \underbrace{\epsilon}_{\text{dissipation}} + \underbrace{\frac{\partial \Gamma}{\partial y}}_{\text{transport}}; \quad \Gamma = -\overline{k'v'}, \quad (20)$$

to the first order, where $k' \equiv \mathbf{u}' \cdot \mathbf{u}' / 2$, $k \equiv \overline{k'}$ and the viscosity terms are omitted. Now, on assuming $q \sim k^{1/2}$, equation (3) gives

$$\epsilon \sim k^{3/2} / L, \quad (21)$$

but there are two different ways of further modelling to close the equations at the level of (20) (k -level, say). [A] After Prandtl (1945) τ and Γ are modelled in the gradient diffusion form (14) with $K \sim k^{1/2} L$. Thus (20) becomes

$$\frac{\overline{Dk}}{Dt} = \beta_1 k^{1/2} L \left(\frac{\partial U}{\partial y} \right)^2 - \gamma_1 \frac{k^{3/2}}{L} + \beta_2 \frac{\partial}{\partial y} \left(k^{1/2} L \frac{\partial k}{\partial y} \right), \quad (22)$$

where β_1 , β_2 and γ_1 are empirical constants, and we have then a couple of equations (12) and (22) for U and k , $L(y)$ being an empirical function here (Beckwith & Bushnell 1968). [B] Alternatively, Bradshaw *et al* (1967) abandoned the concept of gradient diffusion, and instead assumed

$$\tau = a_1 k, \quad L = -a_2 k V^* \quad (23)$$

with constants a_1 , a_2 and another empirical function V^* which represents the effective velocity of transport. This kind of modelling is called the 'bulk convection' assumption, and has the merit of reducing the rank of differential equations, making the analysis easier. In fact, so long as the viscous effects are omitted, the modelled version of (20)

$$\frac{\overline{Dk}}{Dt} = a_1 k \left| \frac{\partial U}{\partial y} \right| - \gamma_1 \frac{k^{3/2}}{L} - a_2 \frac{\partial}{\partial y} (k V^*), \quad (24)$$

as well as that of (12) are of the hyperbolic type to be solved by the method of characteristics. 'Diffusive transport *vs* conductive transport' may deserve further studies, but the possibility of a hybrid mode of transport would not be excluded in real turbulent flows.

4.3 Mean turbulent field closures—two-equation models

For model-developers it might seem somewhat unfair that at the k -level the length-scale L remains an empirical function, while the velocity scale $k^{1/2}$ is determined by a differential equation. This was the motivation for developing the two-equation models at a still higher level of closures (L -level, say). Although the derivation and modelling of the second equation is less obvious than that of the k -equation, we have now several schemes for practical purposes. According to a nice summary by Launder & Spalding (1972, lecture 5), the second variable containing L is generally written as

$$Z_{m,n} = k^m L^n, \quad (25)$$

and dropping the subscript m , n for brevity, we can express the modelled transport equation for $Z_{m,n}$ in a common form,

$$\frac{\overline{DZ}}{Dt} = \underbrace{\alpha_Z \frac{LZ}{k^{1/2}} \left(\frac{\partial U}{\partial y} \right)^2}_{\text{production}} - \underbrace{\gamma_Z \frac{k^{1/2} Z}{L}}_{\text{destruction}} + \underbrace{\beta_Z \frac{\partial}{\partial y} \left(k^{1/2} L \frac{\partial Z}{\partial y} \right)}_{\text{diffusion}} + \text{c.t.}, \quad (26)$$

on the basis of the gradient diffusion assumption, where α_Z , β_Z , γ_Z are constants, and c.t. stands for correction terms. Given below are a few examples of the second equation in current use.

[A] k — kL model ($kL \equiv Z_{1,1}$)

$$\frac{\overline{DkL}}{Dt} = \alpha_L k^{1/2} L^2 \left(\frac{\partial U}{\partial y} \right)^2 - \gamma_L k^{3/2} + \beta_L \frac{\partial}{\partial y} \left(k^{1/2} L \frac{\partial kL}{\partial y} \right) + \text{c.t.} \quad (27a)$$

(Rodi & Spalding 1970; Ng & Spalding 1972).

[B] k — ϵ model ($\epsilon \equiv Z_{3/2,-1}$)

$$\frac{\overline{D\epsilon}}{Dt} = \alpha_\epsilon k \left(\frac{\partial U}{\partial y} \right)^2 - \gamma_\epsilon \frac{\epsilon^2}{k} + \beta_\epsilon \frac{\partial}{\partial y} \left(\frac{k^2}{\epsilon} \frac{\partial \epsilon}{\partial y} \right) + \text{c.t.} \quad (27b)$$

(Harlow & Nakayama 1967; Jones & Launder 1972).

[C] k — W model ($W \equiv Z_{1/2,-1}$)

$$\frac{\overline{DW^2}}{Dt} = \alpha_W W^2 \left| \frac{\partial U}{\partial y} \right| - \gamma_W W^3 + \beta_W \frac{\partial}{\partial y} \left(\frac{k}{W} \frac{\partial W^2}{\partial y} \right) + \text{c.t.} \quad (27c)$$

(Saffman 1970; Wilcox & Traci 1976), where the bulk convection assumption is used to get the production term $\alpha_\epsilon W \left| \partial U / \partial y \right|$ with a similar modification in the k -equation.

Figure 5 shows a result obtained by Kawamura (1979) for pipe flows in comparison with Laufer's experiment. The fact that we are freed from empirical functions at the L -level implies a remarkable progress in modelling, and paves the way to the computation of complex flows. Actually, some successful predictions have been made by these methods in various cases such as internal jets, recirculating flows, reverse transition to laminar flows, and so on, with or without heat transfer. Furthermore, two-equation models are now being built into computer programs for engineering design work. Thus, it would be very urgent to establish the numerical values of a set of empirical constants on a firm experimental basis to improve the accuracy further.

4.4 Reynolds stress field closures (RSF)

Most of the closures cited above use the eddy viscosity concept (16), according to which τ should vanish with $\partial U / \partial y$. However, as illustrated in figure 6, it is sometimes not the case in reality, especially when the mean velocity profile has an asymmetric shape. This is a typical drawback of (16), suggesting the need of modelling the equations for the Reynolds stress field themselves, and Chou (1945) was the first who discussed the full Reynolds tensor equations

$$\left(\frac{\partial}{\partial t} + U_i \frac{\partial}{\partial x_i} \right) \overline{u'_i u'_j} = \underbrace{P_{ij}}_{\text{production}} - \underbrace{2\epsilon_{ij}}_{\text{destruction}} + \underbrace{D_{ij}}_{\text{diffusion}} + \underbrace{\Pi_{ij}}_{\text{redistribution}}, \quad (28)$$

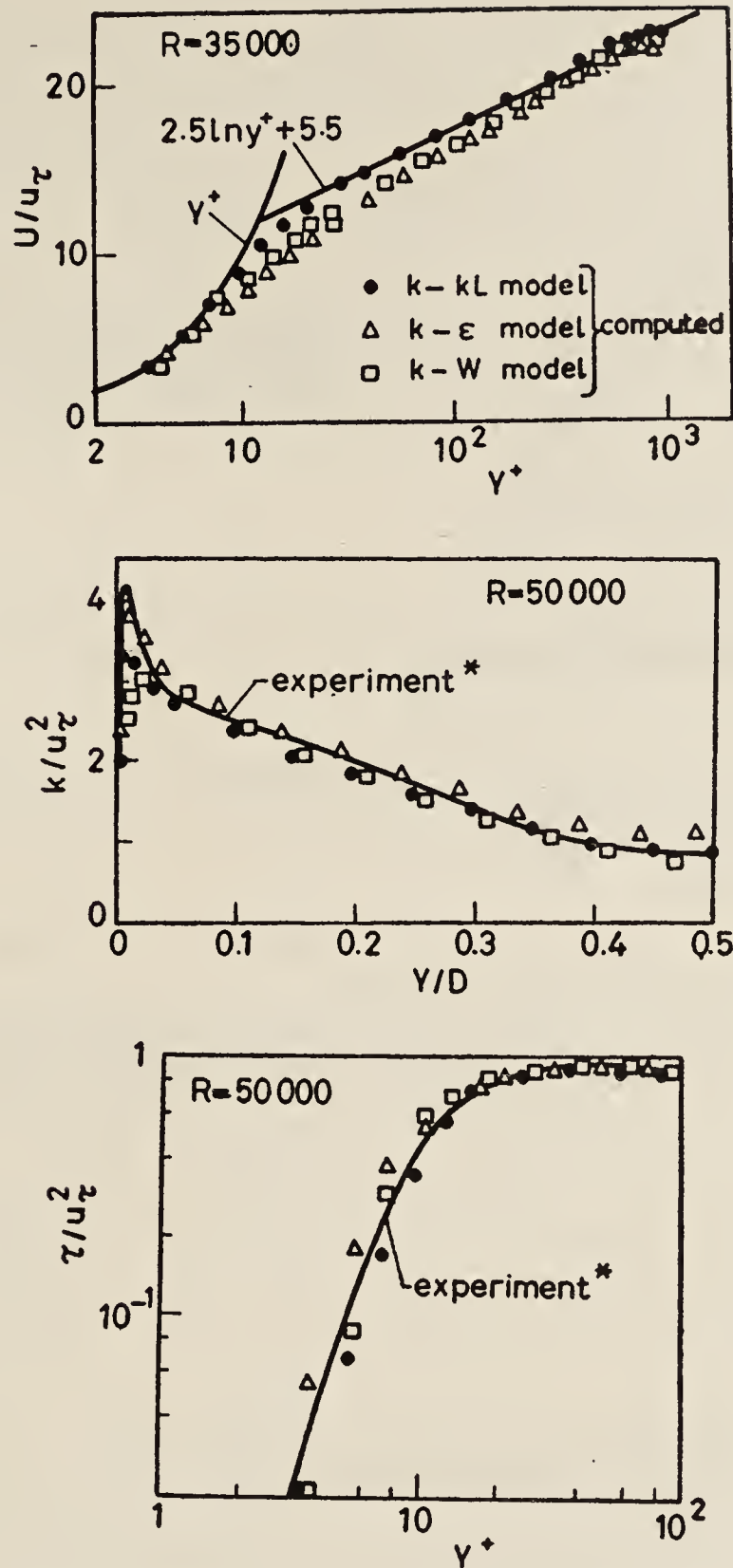


Figure 5. Experimental and computed U -, k - and τ -profiles in circular pipe flows. MTF, two-equation models (Kawamura 1979). u_τ : friction velocity, $y^+ = u_\tau y/\nu$, D : pipe diameter * J Laufer 1954 *NACA TR 1174*

to this end. Here, in the usual index notation we have

$$P_{ij} = Q_{ij} + Q_{ji}; \quad Q_{ij} = -\overline{u'_i u'_i} \frac{\partial U_j}{\partial x_i}, \quad (29a)$$

$$2\epsilon_{ij} = 2\nu \overline{\left(\frac{\partial u'_i}{\partial x_l}\right) \left(\frac{\partial u'_j}{\partial x_l}\right)}, \quad (29b)$$

$$D_{ij} = 2 \frac{\partial \Gamma_{ijl}}{\partial x_l};$$

$$2\Gamma_{ijl} = -\overline{u'_i u'_j u'_l} - \frac{1}{\rho} (\overline{p' u'_i} \delta_{jl} + \overline{p' u'_j} \delta_{il}) + \nu \frac{\partial u'_i u'_j}{\partial x_l}, \quad (29c)$$

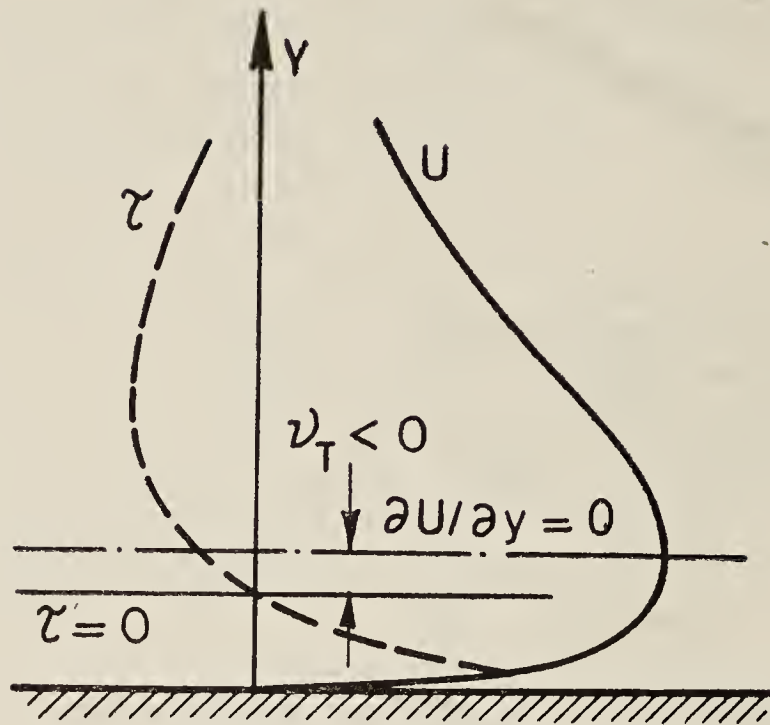


Figure 6. Wall jet showing a failure of the eddy viscosity (gradient diffusion) concept.

$$\Pi_{ij} = \frac{1}{\rho} p' \left(\frac{\partial u'_i}{\partial x_j} + \frac{\partial u'_j}{\partial x_i} \right), \quad (29d)$$

respectively, without any *ad hoc* assumptions.

At this level of closures (τ -level, say) each of these terms except P_{ij} may be modelled in diverse ways, among which we shall mention below the simplest ones simply as examples.

[1] For destruction,

$$\epsilon_{ij} = \frac{1}{3} \epsilon \delta_{ij} \quad (30a)$$

on assuming locally isotropic energy dissipation ($\epsilon_{ii} = \epsilon$).

[2] For diffusion,

$$D_{ij} = \beta_D \frac{\partial}{\partial x_l} \left(\frac{k^2}{\epsilon} \frac{\partial \overline{u'_i u'_j}}{\partial x_l} \right) \quad (30b)$$

with a constant β_D , or the like, on neglecting the pressure- and the viscosity-diffusions.

[3] For redistribution of the energy ($\Pi_{ii} = 0$),

$$\Pi_{ij} = \Pi_{ij}^{(1)} + \Pi_{ij}^{(2)}; \quad (30c)$$

$$\Pi_{ij}^{(1)} = -c_1 \frac{\epsilon}{k} \left(\overline{u'_i u'_j} - \frac{2}{3} k \delta_{ij} \right), \quad (30c')$$

$$\Pi_{ij}^{(2)} = c_2 \left(P_{ij} - \frac{1}{3} P_{ii} \delta_{ij} \right), \quad (30c'')$$

c_1 and c_2 being constants, where $\Pi_{ij}^{(1)}$ is the rate of the relaxation of energy anisotropy due to the eddy-interactions, while $\Pi_{ij}^{(2)}$ is that of the intensification of anisotropy due to the mean rate of strains.

Equation (28) has six components one of which is equivalent to the k -equation. In two-dimensional flows, since $\overline{u'w'} = \overline{v'w'} = 0$, we have four equations for $\overline{u'^2}$, $\overline{v'^2}$, $\overline{w'^2}$ and $\overline{u'v'}$. Thus, supplementing them with the ϵ -equation, say, we are led to five-equation models (Daly & Harlow 1970; Launder *et al* 1975), but here is shown only a simplified form of the stress equation in the three-equation version of Hanjalic & Launder (1972),

$$\frac{\overline{D\tau}}{Dt} = \alpha_\tau k \frac{\partial U}{\partial y} - \gamma_\tau \frac{\epsilon}{k} \tau + \beta_\tau \frac{\partial}{\partial y} \left(\frac{k^2}{\epsilon} \frac{\partial \tau}{\partial y} \right) \quad (31)$$

to be coupled with the k - and ϵ -equations. A striking success of this type of model applied to an asymmetric flow is seen in Launder & Spalding (1972, p. 120).

4.5 Resume of the differential methods

As a comparative illustration, figure 7 shows some results of the differential methods to compute a turbulent boundary layer disturbed by a circular cylinder placed near the wall (Suzuki *et al* 1980). Agreement with experiment is fairly good, the agreement not being much dependent on the level of closures in this example. However, it seems still premature to draw any definite conclusion on their predicting power at present, since various kinds of refinement, especially those at the τ -level, are being proposed in succession from the theoretical as well as practical points of view (Launder 1979).

Of course, as we proceed to higher order closures, more terms must be modelled with increasing numbers of adjustable constants and boundary conditions. Moreover, mathematical or physical consistency of tangled sets of modelled differential equations then would be less and less guaranteed (Schumann 1977). We cannot, therefore, simply imagine that higher order closures are always superior to lower order ones. Actually, for simple flows the MVFs are often useful; even for complex flows the level of RSF is likely to be the upper bound in practice, where the good 'physics' of (28) will be of vital importance.

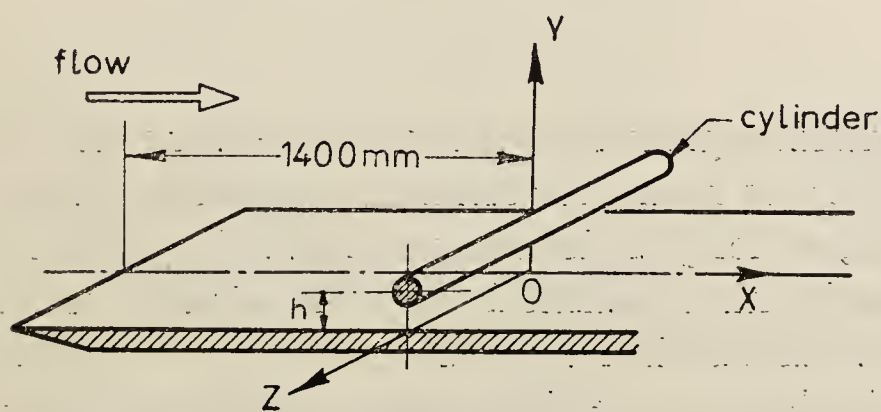


Figure 7a. Experimental and computed U -, k -, τ - and ϵ - profiles in a disturbed boundary layer flow (Suzuki *et al* 1980).

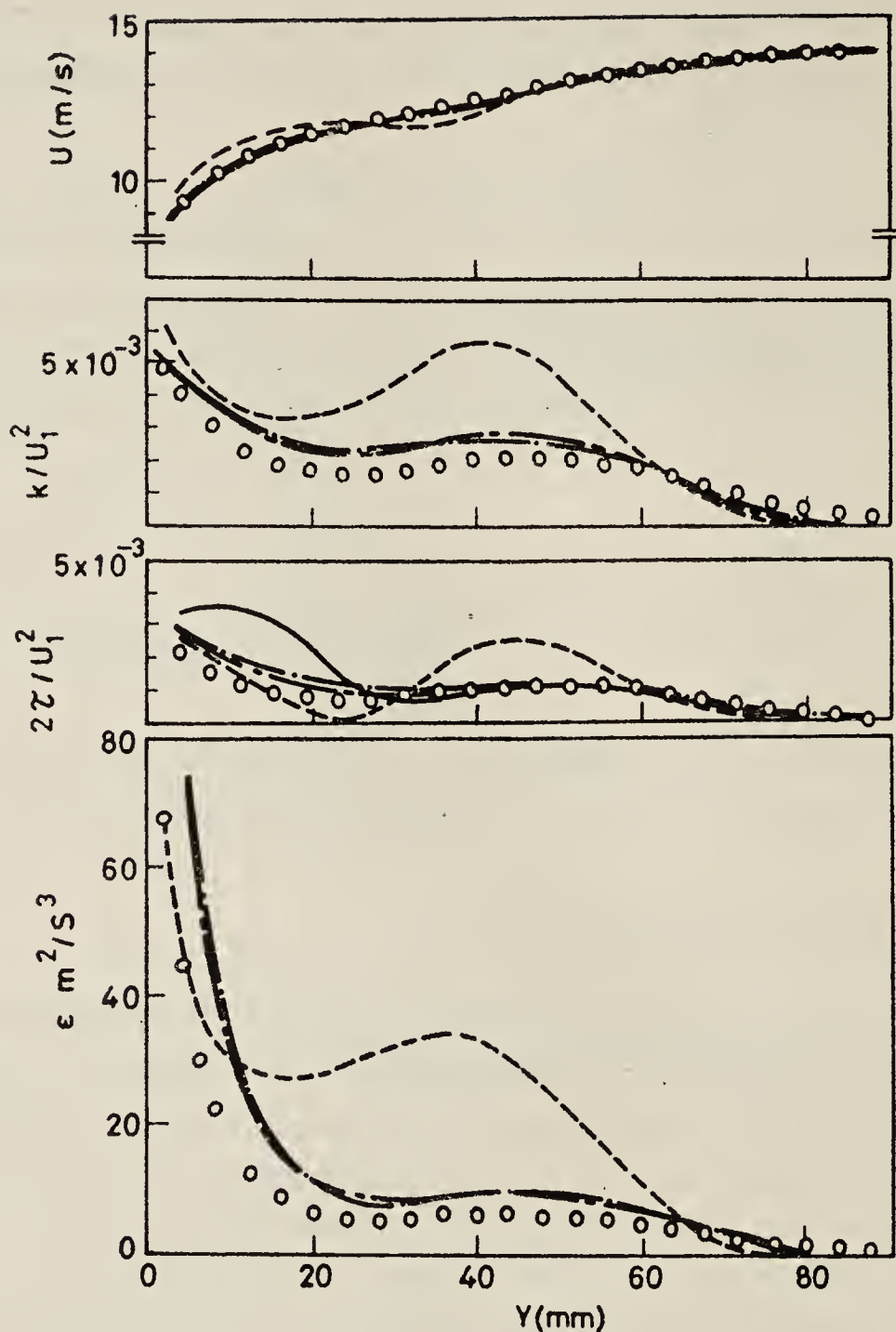


Figure 7b. Experimental and computed U^- , k^- , τ^- and ϵ^- profiles in a disturbed boundary layer flow (Suzuki *et al* 1980). (o) experimental; $h=33.5$ mm, $x=836$ mm; (---) measured profiles at $x=0$. (—) MVF, mixing length hypothesis; (-.-) MTF, two-equation model (k - ϵ model); (— — —) RSF, three-equation model, [equation (31)]

5. Numerical simulations

In the new approaches to turbulence prediction, some basically computer-oriented methods of 'numerical simulations' are attracting special attention. They are more closely related to the unaveraged NS equations so as to get a maximum of universality with a minimum of modelling, while the differential methods are essentially based on multiple modelling. Regarding these, a brief survey will be made below.

5.1 Large eddy simulations (LES)

So far we have started from the Reynolds equations obtained by averaging the NS equations in the sense of (5), but they are of no use for simulating turbulent fluctuations themselves. On the other hand, so long as the energy cascade hypothesis is accepted, small eddies may be replaced with a statistical ensemble of more or less universal character, and thus we could simulate the large-scale components of fluctuations at least to some extent. This idea leads to the 'large eddy simulations' which are most significant among the current schemes of numerical simulations.

Now, in order to eliminate the small-scale fluctuations effectively, we introduce a local weighted mean such that

$$\langle f(\mathbf{x}, t) \rangle = \int G(\mathbf{x}, \mathbf{y}; \Delta) f(\mathbf{y}, t) d^3\mathbf{y}, \quad (32)$$

for any field variable f , where the integration extends over the whole field of \mathbf{y} . This procedure is called 'filtering' as distinct from the usual averaging, where G is the grid filter function characterized by the 'width' Δ ; it may be a box-filter (figure 8) or a Gaussian filter

$$G(\mathbf{x}, \mathbf{y}; \Delta) \equiv (6/\pi)^{3/2} \Delta^{-3} \exp \left[-\frac{6(\mathbf{x} - \mathbf{y})^2}{\Delta^2} \right], \quad (33)$$

or the like at our disposal. Then, we can divide f into the filtered variable F' or $\langle f \rangle$, and the subgrid variable f'' as

$$f = F' + f''; \quad F' = \langle f \rangle, \quad (34)$$

but we have to note here that, unlike the case of (5),

$$\langle f'' \rangle = F' - \langle F' \rangle \neq 0, \quad (35)$$

in general. Thus filtering of the NS equations gives

$$\frac{\partial U'_i}{\partial x_i} = 0, \quad (36a)$$

$$\frac{\partial U'_i}{\partial t} + U'_j \frac{\partial U'_i}{\partial x_j} = -\frac{1}{\rho} \frac{\partial P'}{\partial x_i} + \frac{\partial}{\partial x_j} \left(\nu \frac{\partial U'_i}{\partial x_j} + S_{ij} + \Lambda_{ij} \right), \quad (36b)$$

in the index notation, where the 'subgrid stress' term

$$S_{ij} = -\langle u''_i u''_j \rangle - \langle u'_i U'_j \rangle - \langle U'_i u''_j \rangle, \quad (37a)$$

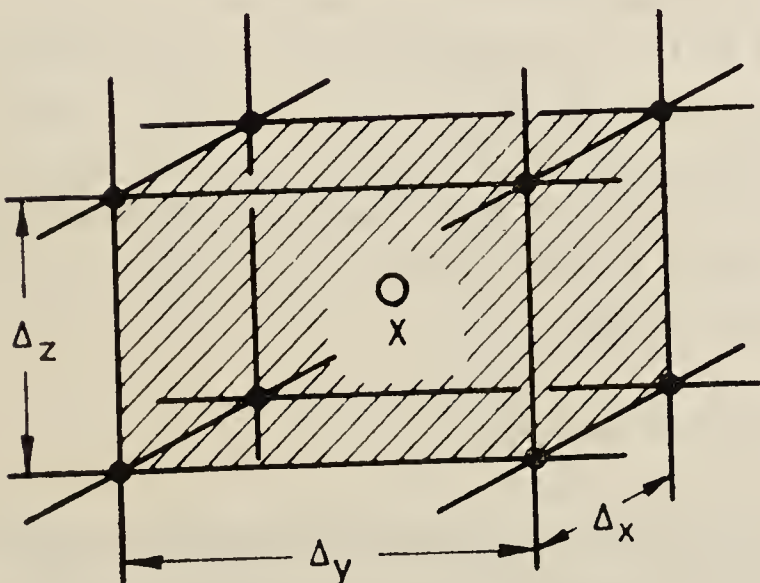


Figure 8. Box filter function. $G = 1$ inside the elementary box around \mathbf{x} , and $= 0$ outside. $\Delta = (\Delta_x \Delta_y \Delta_z)^{1/3}$, say.

is an analogue of the Reynolds stresses, and the unusual term

$$\Lambda_{ij} = U'_i U'_j - \langle U'_i U'_j \rangle, \quad (37b)$$

comes from the particular nature of (35). The 'filtered equations' (36), which describe large-scale motions, are intermediate between the NS and the Reynolds equations. In fact, they are intrinsically time-dependent and three-dimensional, still they need modelling of small-scale subgrid motions.

The tactics of subgrid modelling to close (36) are conveniently grouped into two categories:

[A] The filtered velocity field closures (FVF), say, are the subgrid versions of MVF at the U' -level; namely, for the subgrid stresses a gradient diffusion assumption of the form

$$S_{ij} - \frac{1}{3} S_{ii} \delta_{ij} = \nu_S \left(\frac{\partial U'_i}{\partial x_j} + \frac{\partial U'_j}{\partial x_i} \right), \quad (38)$$

is made, where the 'subgrid eddy viscosity' ν_S is given by

$$\nu_S = (c \Delta)^2 \left[\frac{\partial U'_i}{\partial x_j} \left(\frac{\partial U'_i}{\partial x_j} + \frac{\partial U'_j}{\partial x_i} \right) \right]^{1/2}, \quad (39)$$

for example (Smagorinsky 1963). Here the only empirical coefficient c is expected to be a universal constant provided that Δ falls within Kolmogorov's inertial sub-range. Further, by the Taylor series expansion of G in (32) about \mathbf{x} we have

$$\Lambda_{ij} = -\frac{\Delta}{24} \nabla^2 (U'_i U'_j), \quad (40)$$

approximately, which completes the closure (Leonard 1974).

[B] The subgrid stress field closures (SSF), say, are higher-order schemes of modelling the transport equations for S_{ij} term by term in an analogous way to the RSF (Lilly 1967), the general formulation being too lengthy to reproduce here. Conceptually the FVF's are preferable because of simplicity, but the SSF's may be recommended when a coarse grid is used.

Since Deardorff (1970) used an early form of the FVF for channel flows to demonstrate the real utility of the method, a good deal of experience has been accumulated in recent years with considerable refinement such as the use of modified grids, Fourier transforms, vorticity variables, and so on (Herring 1979). Though not readily applicable to engineering analysis, yet, large eddy simulations have been proved to be on the right track as a whole, and may be useful for the purpose of testing various models in the integral and the differential methods.

5.2 Direct integration and prospects for numerical methods

As the grid scale Δ decreases, the filtered equations (36) would contain more and more information. In particular, when the filter G tends to the delta-function $\delta(\mathbf{x} - \mathbf{y})$,

the NS equations are recovered, and we get back to the very beginning again. Nevertheless, the fact that a challenge to direct numerical integrations is being attempted should not be overlooked; actually Orszag & Patterson (1972) succeeded in simulating homogeneous isotropic turbulent motions at lower Reynolds numbers by means of the 'spectral methods', where the instantaneous field variables were expanded in Fourier series without any modelling other than suitable high wave-number truncations. Encouraged by their striking results, subsequent studies are now in continual progress (Orszag 1977), but since extensions to shear flow turbulence and/or the case of higher Reynolds numbers seem still formidable at present, we do not enter into the details here.

Generally speaking, the numerical simulations are concerned with 'turbulence' generated in computers rather than in real flows. Such an idea was first inspired by von Neumann (1949) in the early days of the historic machine ENIAC, and his prophecy was partly realized about twenty years later. As to the future prospects, table 1 predicts the general trends of increase in computer speeds which hold the essential key to the practical utility of these novel methods. It is seen beyond doubt that within the next several years we could have some machines at least ten times faster than the existing ones. Thus, combined with possible development of software, numerical simulations would be a powerful tool of turbulence predictions in the not too distant future.

6. Concluding remarks

For clarity and brevity of exposition, we have confined ourselves mainly to mathematical modelling of 'simple flows' in the present paper. In practical applications to engineering or geophysical flows, however, we are confronted with various complicating factors among which typical important examples are listed in table 2. Moreover, it is not seldom in actual situations for several of those factors are coexistent. Still being in the course of rapid development, these 'complex flow problems' will need many separate reviews which could be compiled into a thick

Table 1. Effective speed of typical modern and future computers

Machine	MFLOPS ^a	Year
(existing)		
CDC 6600	1	1965
HITAC 8800	6	1968
CDC 7600	10	1970
CRAY-1	60	1977
(to appear)		
CRAY-2	100	1984
NAS	1000	1987
J-J ^b	~10 ⁵	1990?

^aMFLOPS = Mega floating operations per second.

^bThe Josephson junction which is expected to be used as switching element in the next generation.

Table 2. Examples of complicating factors in practical applications

(a) Wall properties	(b) Fluid properties
rough curved porous flexible	compressible electro-conductive reactive multi-phase non-Newtonian baroclinic
(c) Flow conditions	(d) Additional forces
externally turbulent viscosity-dependent recirculating three-dimensional unsteady non-isothermal polluted	normal stress terms buoyancy centrifugal force Coriolis force Lorentz force

Table 3. Comparative summary of the existing methods of mathematical modelling

	Integral methods	Differential methods	Numerical simulations
Feature	Economy	Accuracy	Universality
Generation	Past	Present	Future
Equations	Ordinary differential equations	Partial differential equations	Unsteady difference equations
Assumptions	Empirical functions	Empirical constants	Universal constants
Application	Simple flows	Complex flows	Large-scale flows
Utilization	Routine design work	Advanced design work	Numerical forecast
Example ^a	Entrainment method (3.1)	RSF (4.4)	LES (5.1)

^aThe most typical one is cited, where () refers to the sub-section of the text.

book. A fully universal model could unify all complications on a common basis, but we have not arrived at such an ideal model as yet.

To recapitulate, table 3 compares the three major groups of modelling in a concise way; it should not be forgotten that the table is more or less oversimplified in order to make the essential contrast striking. At any rate, mathematical modelling of turbulent shear flows is indispensable for quantitative prediction of real turbulence, and it is now in more and more frequent use in wider fields of applications. The basic understanding of the 'physics' as well as good experimental data will refine our tactics further but it is not likely that any one scheme would survive in the future. The existing methods are expected to be converging to a 'dualism'; one aspect of which is a handy but effective scheme with a limited range of validity, and the other aspect is a supersized scheme of all-round capacity. In these respects, close co-operation among engineers, physicists and mathematicians is particularly desired.

The author is very grateful to the National Scientific Committee of the First Asian Congress of Fluid Mechanics, Bangalore 1980, for affording him an opportunity to publish the present survey in these Proceedings. The work was partially supported by a grant-in-aid for scientific research from the Japanese Ministry of Education, Science and Culture.

References

- Beckwith I E & Bushnell D M 1968 Detailed description and results of a method for computing mean and fluctuating quantities in turbulent boundary layers NASA TN D4815
- Bradshaw P, Ferriss D H & Atwell N P 1967 *J. Fluid Mech.* **28** 593
- Cebeci T & Bradshaw P 1977 *Momentum transfer in boundary layers* (Washington, London: Hemisphere Publishing Corp.)
- Cebeci T & Smith A M O 1974 *Analysis of turbulent boundary layers* (New York: Academic Press)
- Chou P Y 1945 *Q. Appl. Math.* **3** 38
- Coles D 1956 *J. Fluid Mech.* **1** 191
- Coles D & Hirst E A (eds.) 1969 *Computation of turbulent boundary layers Proc. AFOSR-IFP-STANFORD Conf. 1968* (Stanford: Stanford Univ.) Vol. 2
- Daly B & Harlow F H 1970 *Phys. Fluids* **13** 2634
- Deardorff J W 1970 *J. Fluid Mech.* **41** 453
- Hanjalic K & Launder B E 1972 *J. Fluid Mech.* **52** 609
- Harlow F H & Nakayama P I 1967 *Phys. Fluids* **10** 2323
- Head M R 1958 Aero. Res. Council R & M # 3152
- Herring H J 1979 *Turbulent shear flows I* eds. F Dirst, B E Launder, F W Schmidt & J H Whitelaw (Berlin, Heidelberg, New York: Springer Verlag) p. 347
- Ishida Y 1978 A method for calculating incompressible two-dimensional turbulent boundary layers NAL Tech. Rep., Japan TR-524 (in Japanese)
- Jones W P & Launder B E 1972 *Int. J. Heat Mass Transfer* **15** 301
- Kawamura H 1979 *Trans. Jpn. Soc. Mech. Eng.* **45** 1038 (in Japanese)
- Kline S J, Morkovin M, Sovran G & Cockrell D J (eds.) 1969 *Computation of turbulent boundary layers Proc. AFOSR-IFP-STANFORD Conf. 1968* (Stanford: Stanford Univ.) Vol. 1
- Launder B E 1979 *Turbulent shear flows I* eds. F Dirst, B E Launder, F W Schmidt & J H Whitelaw (Berlin, Heidelberg, New York: Springer Verlag) p. 259
- Launder B E, Reece G J & Rodi W 1975 *J. Fluid Mech.* **68** 537
- Launder B E & Spalding D B 1972 *Mathematical models of turbulence* (New York: Academic Press)
- Leonard A 1974 *Adv. Geophys.* **A18** 237
- Lilly D K 1967 *Proc. IBM Scientific Computing Symp. on Environmental Science* (Yorktown Heights: T J Watson Res. Center) p. 195
- Nee V W & Kovaszny L S G 1969 *Phys. Fluids* **12** 473
- Ng K H & Spalding D B 1972 *Phys. Fluids* **15** 20
- Orszag S A 1977 *Handbook of turbulence* Vol. 1 eds. W Frost & T H Moulden (New York: Plenum Press) p. 281
- Orszag S A & Patterson G S Jr 1972 *Phys. Rev. Lett.* **28** 76
- Prandtl L 1945 *Nachr. Akad. Wiss. Göttingen, Math. Phys. Klasse* **6**
- Rodi W & Spalding D B 1970 *Wärme u. Stoffübertragung* **3** 85
- Saffman P G 1970 *Proc. R. Soc. London* **A317** 417
- Schumann U 1977 *Phys. Fluids* **20** 721
- Smagorinsky J 1963 *Mon. Weather Rev.* **91** 99
- Suzuki K, Tanaka J, Marumo E & Sato T 1980 *Trans. Jpn. Soc. Mech. Eng.* **46** 1447 (in Japanese)
- von Neumann J 1949 *John von Neumann collected works* Vol. 6 ed. A H Taub (New York, Oxford, London, Paris: Pergamon Press 1961) p. 437
- Wilcox D C and Traci R M 1976 *AIAA Paper* # 76-531

Three-dimensional aspects of boundary-layer transition

ITIRO TANI

National Aerospace Laboratory, 1880 Jindaiji, Chofu, Tokyo, 182 Japan
Also Professor Emeritus, University of Tokyo.

MS received 13 December 1980

Abstract. A review is made in this paper of the three-dimensional nature of instability leading to transition in a two-dimensional flow on a flat plate (Blasius boundary layer) or between parallel plates (plane Poiseuille flow), with additional reference to the flow on a concave wall. Instability and transition in a three-dimensional boundary layer are then reviewed, with particular attention to the flow due to a rotating disk and the flow perturbed by a three-dimensional roughness element on a flat plate. The growth of a turbulent spot is discussed as a phenomenon exhibiting a similar feature of instability. Only the flow of an incompressible fluid is considered.

Keywords. Boundary-layer transition; three-dimensional aspects; wave motion; roughness element; turbulent spot.

1. Introduction

The subject of boundary-layer transition is a vast and long-pending one, but in the present paper it is intended to confine the consideration to the three-dimensional aspects of the problem, with a view to affording a correct understanding of the basic features of transition. A review is first made of the three-dimensional nature of instability leading to transition in a two-dimensional flow on a flat plate or between parallel plates, with additional reference to the flow on a concave wall. Instability and transition in a three-dimensional boundary layer are then considered, with particular attention to the flow due to a rotating disk and the flow perturbed by a three-dimensional roughness element on a flat plate. The growth of a turbulent spot is discussed as a phenomenon exhibiting a similar feature of instability. Only the flow of an incompressible fluid is considered.

2. Transition in two-dimensional boundary layers

2.1 *Formation of peaks and valleys*

It is now established that the transition in a Blasius boundary layer as well as a plane Poiseuille flow is preceded by the appearance of two-dimensional vorticity waves of the type predicted by the linear stability theory, the so-called Tollmien-Schlichting waves, provided all sources of disturbance are sufficiently small. When the vorticity wave becomes too large in amplitude, however, the nonlinear effect manifests itself in the form of a nearly periodic variation of wave amplitude in the spanwise direc-

tion, with maxima and minima along certain streets parallel to the stream (Schubauer 1958; Klebanoff & Tidstrom 1959). Regions of maximum and minimum amplitude are referred to as 'peaks' and 'valleys' respectively. Associated with the variation in wave amplitude, there is also a spanwise variation in local mean velocity, with its maxima and minima occurring at valleys and peaks respectively (Klebanoff *et al* 1962). This indicates the generation of a system of alternating streamwise vortices, as accounted for by the theory of Benney & Lin (1960) and Benney (1961, 1964), which is centred on the nonlinear interaction between the two-dimensional wave and the three-dimensional wave with spanwise periodicity.

Figure 1 shows the streamwise growth of the wave amplitude at a distance of 1.2 mm from the wall at peak and valley for different initial amplitudes, x being the distance from the leading edge of the flat plate (Klebanoff & Tidstrom 1959). An artificial wave is created by a ribbon vibrating at a frequency of 145 Hz in the boundary layer at $x = 89$ cm. The low-amplitude wave amplifies and then damps in accordance with linear theory, exhibiting the same behaviour both at peak and valley. No breakdown ensues. At the higher amplitude, however, the wave at peak and valley at first follows the linear amplification but then exhibits a characteristically different behaviour, namely a very rapid growth at peak and an initially weak and followed by a rapid growth at valley, until eventually breakdown occurs. Increasing the initial amplitude has no significant effect except to move the position of departure from linear amplification and breakdown further upstream. This experimental result is really worthy of note for it suggests the existence of a threshold amplitude above which the formation of peaks and valleys eventually leads to breakdown of wave motion (Tani 1973).

The theory of Benney & Lin accounts for the development of a pronounced three-dimensional pattern from an initially weak spanwise variation, but offers no explanation whatever of the mechanism by which the three-dimensional effects predominate in the nonlinear evolution of wave disturbance. No attempt had been made to predict theoretically the threshold amplitude for the formation of peaks and valleys. The weakly nonlinear stability theory, due primarily to Stuart (1960) and Watson (1960, 1962) for two-dimensional disturbances, had been extended by Stuart (1962b) to include three-dimensional effects, but the numerical calculation

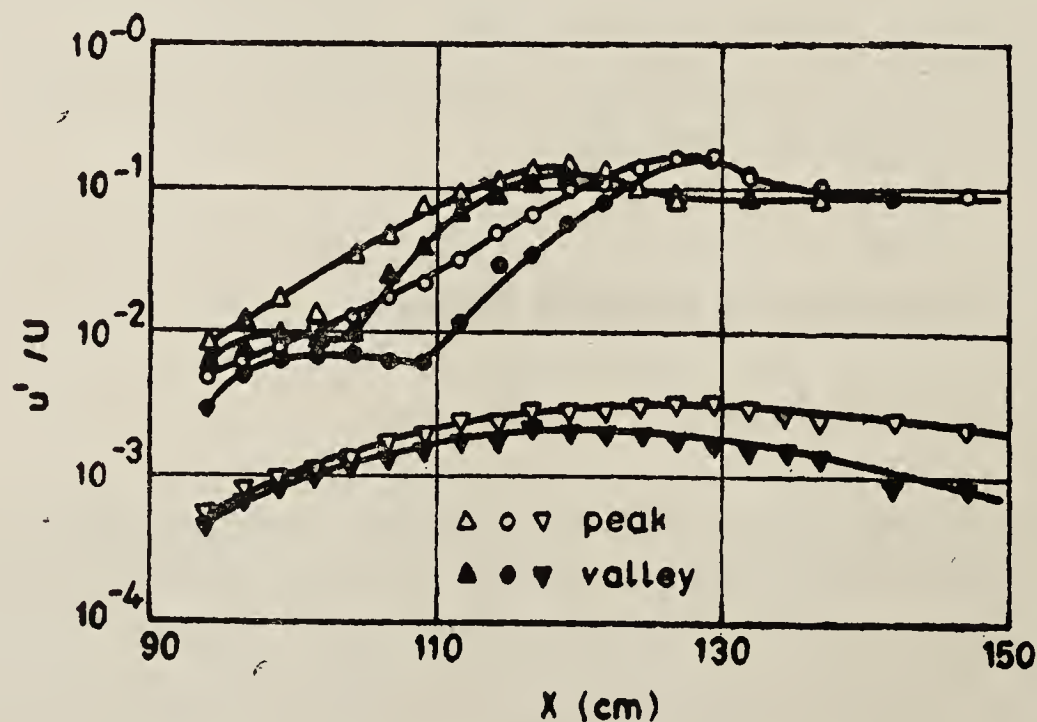


Figure 1. Streamwise growth of wave amplitude at peak and valley in Blasius boundary layer. Composed from figures 8 and 9 of Klebanoff & Tidstrom (1959)

along this line was only recently carried out by Itoh (1980) for plane Poiseuille flow. Assuming the disturbance to be so small in amplitude that its dominant part consists of a two-dimensional wave and a three-dimensional wave of spanwise periodicity, Itoh obtained the equations for determining the maximum amplitudes of two-dimensional and three dimensional waves, A and B , and the phase difference, $\frac{1}{2} \sigma$, between them of the form

$$A^{-2} dA^2/dt = C + DA^2 + \{E + F \sin(\sigma + \alpha)\} B^2,$$

$$B^{-2} dB^2/dt = G + \{H + J \sin(\sigma + \beta)\} A^2 + KB^2,$$

$$d\sigma/dt = L + \{M + N \cos(\sigma + \beta)\} A^2 + \{P + Q \cos(\sigma + \alpha)\} B^2,$$

where t is the time, and $C, D, E, F, G, H, J, K, L, M, N, P, Q, \alpha$ and β are constants depending on the Reynolds number and wavenumbers in streamwise and spanwise directions. A detailed discussion of stability may be made by following the trajectories in space with A, B and σ as coordinates, but consideration is confined to the simplest case when only two-dimensional disturbance exists. In order for the disturbance to remain two-dimensional with the passage of time, it is necessary that the right-hand side of the second equation with $B=0$, when averaged over a period of σ , vanishes, namely, $A^2 = -G/H$. This gives a threshold amplitude for two-dimensional disturbance above which three-dimensional disturbances are continuously amplified. It is seen from figure 2 that the value is lower than the threshold amplitude, $A^2 = -C/D$, predicted by two-dimensional stability theory, indicating clearly that the generation of three-dimensional disturbances is the result of subcritical threshold instability. Another point to note is indicated by the third equation with $B=0$, which gives the trajectories in the $(d\sigma/dt, \sigma)$ -plane as shown in figure 2. When the amplitude A becomes large, the curve intersects with the horizontal axis $d\sigma/dt = 0$ at two points during a cycle of σ , one of which is stable but the other unstable. The stable equilibrium is interpreted as providing a synchronization in phase between the two-dimensional and three-dimensional waves, which has been assumed in the theory of Benney & Lin. For such a large amplitude, however, some modification might be introduced by the terms neglected in the analysis, so that the result is to be occupied with all reserve until attempts at incorporating higher-order perturbations are made.

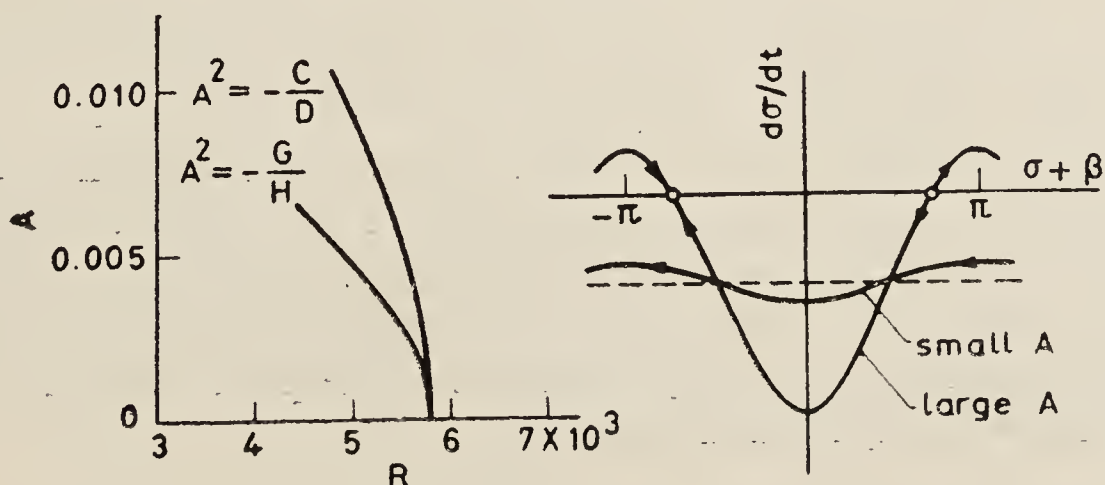


Figure 2. Theoretical predictions by weakly nonlinear stability theory for plane Poiseuille flow. Streamwise wavenumber 1 (wavelength = 2π times half depth), spanwise wavenumber chosen so as to give the lowest threshold amplitude (Itoh 1980)

Reference may also be made here to a numerical solution by Orszag & Kells (1980) of the Navier-Stokes equations for the evolution of finite-amplitude disturbances of plane Poiseuille flow. It is found that while there exists threshold instability at subcritical Reynolds numbers, there is apparently no sign of explosive breakdown when only two-dimensional disturbances are allowed. In three dimensions, however, the flow develops into a state of randomness with appreciable small-scale fluctuations. Because of the limited resolution of the numerical calculation, no claim can be laid to the minute accuracy of the result, but there is no room for doubt that the numerical solution has demonstrated the major role of three-dimensional disturbances in producing transition.

As regards the preferred wavenumber in spanwise direction, an attempt was made by Raetz to find a possible explanation in the resonant interactions among a triad of three-dimensional Tollmien-Schlichting waves (Stuart 1962a). The idea was elaborated by Craik (1971) to concentrate on the nonlinear interactions among two-dimensional and three-dimensional waves with two frequencies, the one half of the other. Another attempt was made by Maseev (1968) to explore the instability of the Blasius flow superimposed by a two-dimensional Tollmien-Schlichting wave against three-dimensional disturbances. However, comparison of the theoretical prediction with existing experiments remains inconclusive. In the numerical solution of Orszag & Kells, the values of the streamwise and spanwise wavenumbers appear to have been chosen so as to give approximately the most strongly unstable results.

Frequent mention has been made of the failure of the stable finite-amplitude equilibrium to appear in experiments on boundary layer flows. It is the author's view (Tani 1980), however, that the formation of peaks and valleys might be interpreted as displaying a stable equilibrium flow. In support of this view it is adequate to recapitulate the experimental result (Klebanoff & Tidstrom 1959) that increasing the initial wave amplitude beyond a threshold value has no significant effect on the structure of peaks and valleys. Furthermore, the maximum of the wave amplitude distribution, located at a distance of about one-fifth of the boundary layer thickness from the wall in the linear amplification, moves out to about two-fifths of the thickness at the peak position in the nonlinear development. Associated with this shift in amplitude distribution, there exists a marked increase in vorticity on the outside of the position of the maximum amplitude. The succession of these processes is fairly gradual and suggestive of the mechanism through which the spanwise vorticity is convected away from the wall by the induced velocity due to the streamwise vortices. Upon reaching the outer part of the boundary layer, where the streamlines of induced flow are divergent and the velocity of the basic boundary-layer flow is greater, the vortex tubes constituting the spanwise vorticity are stretched out, until high concentration of vorticity is formed in a thin layer called the high-shear layer (Kovaszny *et al* 1962), bringing about a prerequisite to a new type of instability. These considerations are consistent with the interpretation that the stable finite-amplitude equilibrium manifests itself as the formation of peaks and valleys, in which the tendency toward instability is gradually developed at the peak position as the vorticity maximum is moved away from the wall.

1.2 Breakdown of wave motion

The nonlinear development of wave disturbances terminates with 'breakdown', a

term used by Klebanoff & Tidstrom (1959) to describe an abrupt change in the character of the wave motion. Immediately prior to breakdown there is a high-shear layer as already mentioned, which makes the instantaneous velocity profile at the peak position take on an inflexional profile for a certain fraction of each cycle of the primary wave (figure 3). The experiment of Klebanoff *et al* (1962) indicates that breakdown is associated with a rapid, almost explosive increase in wave amplitude, followed by intense velocity fluctuations exhibiting a definite frequency one order of magnitude higher than that of the primary wave. This is interpreted as the onset of a secondary instability (or more exactly, high-frequency secondary instability) of the boundary layer perturbed by the primary wave. The difference in the scale between the primary and secondary waves warrants the validity of the approximation of quasi-steadiness, on the basis of which there is good reason to believe that the appearance of an instantaneous inflexional velocity profile would give rise to a secondary instability. Besides, the location of the maximum velocity gradient away from the wall is responsible for generating high-frequency disturbances. On the other hand, the sequence of instantaneous velocity profiles may also be looked upon as representing a bulge of displacement thickness which moves downstream with the phase velocity of the primary wave. The secondary instability is then identified with the shedding of vortices from the bulge as viewed by an observer moving with the phase velocity. Klebanoff *et al* call these vortices 'hairpin eddies' and point out the similarity between the bulge and a three-dimensional roughness element on a wall. Discrete vortices are clearly observed in the hydrogen-bubble picture of Hama & Nutant (1963). However, detailed experimental observation by Nishioka *et al* (1980) of plane Poiseuille flow provides the phase velocity varying with the distance from the wall, suggesting the underlying mechanism to be the rolling up of the high-shear layer rather than the vortex shedding from the solid-natured bulge.

The secondary instability of the inflexionally-profiled flow was long ago assumed by Prandtl (1933) as being directly responsible for inducing the breakdown of wave motion. Betchov (1960) renewed the concept for elucidating the earlier observation of Klebanoff & Tidstrom (1959) on high-frequency oscillations. Later Greenspan & Benney (1963) applied a linearized, two-dimensional inviscid analysis to calculate the growth of disturbances in a boundary layer with a time-dependent velocity

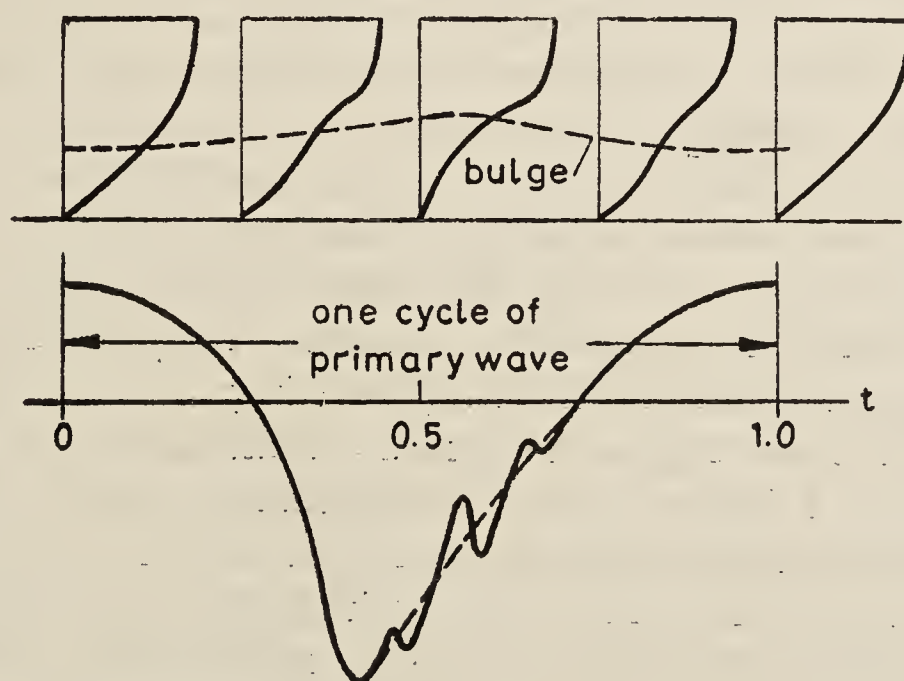


Figure 3. Sequence of instantaneous velocity profiles in a cycle of the primary wave. Blasius boundary layer.

profile composed of straight lines, which simulates that observed in experiments. In spite of crude approximations, the analysis is successful in predicting the extreme rapidity of the growth of secondary instability. Landahl (1972) then made a more ambitious approach on the basis of the kinematic wave theory developed by Whitham (1974) for conservative systems. The kinematic wave theory is concerned with the propagation of wave trains in a slightly inhomogeneous medium, the spatial and temporal variations in the medium being small over a distance of one wavelength and a time of one cycle of the wave, respectively. In the application, the small-scale secondary wave corresponds to the disturbance generated by the secondary instability, while the medium with large-scale inhomogeneity corresponds to the basic flow modified by the primary instability. The characteristics of wave propagation are described approximately by the local dispersion relation, which is real for conservative systems, but becomes complex for dissipative systems under consideration. As regards temporally growing disturbances, the wavenumber is real but the frequency is complex, its real and imaginary parts representing the temporal frequency and temporal rate of amplification, respectively. Landahl has extended the ideas of the kinematic wave theory to slightly dissipative systems somewhat unconvincingly, essentially following the equation of phase conservation and adding a linear correction to the equation of wave action conservation, with assuming that the wavenumber remains real but the amplification rate is sufficiently small. He then proceeds to develop a theory, according to which, in particular, breakdown occurs when the group velocity of the secondary wave at its crest for neutral stability is equal to the phase velocity of the primary wave. The validity of the breakdown condition is confirmed by calculating by linear theory the group velocity for the instantaneous velocity profile at the crest and the phase velocity for the mean velocity profile, all the velocity profiles being taken from the measurements of Klebanoff *et al* (1962). Unfortunately, however, the present author has been unable to follow Landahl's analysis without meeting with inconsistencies. Applying Landahl's analysis to the region close to the critical Reynolds number, Stewartson (1975) also observed some inconsistencies. At present the author is reluctantly obliged to comment on the analysis of Landahl as unjustifiable in a mathematical sense, although the critical condition for breakdown appears to be attractive in a physical sense. Recently Itoh (1981) made a new approach by treating both wavenumber and frequency as complex and introducing the complex space coordinates, with the real coordinate corresponding to the Galilean coordinate moving with the phase velocity of the primary wave, thus pursuing a way out of the difficulties encountered in Landahl's attempt. It is found that the secondary instability occurs by way of continuous evolution of wave trains when the group velocity of the spectral component coincides with the phase velocity of the primary wave, a condition in accord with that deduced by Landahl. A numerical calculation based on the two-dimensional Tollmien-Schlichting wave in plane Poiseuille flow provides a wave amplitude of about 8% at the critical condition, but the frequency of the secondary wave being of the same order of magnitude as that of the primary wave. The failure in predicting higher frequency is attributed to the simple use of the Tollmien-Schlichting wave as the primary wave, which gives rise to the instantaneous velocity profiles so different from those observed experimentally prior to breakdown. The use of complex coordinates presents additional difficulty in the physical interpretation of the imaginary coordinate, but the author looks with favour on it seeing

that the complex coordinates are introduced simply as mathematical means for making the equation a hyperbolic one.

2.3 *Boundary layer on a concave wall*

For the boundary layer on a concave wall the destabilizing effect due to the centrifugal force generates a system of alternating streamwise vortices, the so-called Görtler vortices, at Reynolds numbers much lower than the critical value for the Tollmien-Schlichting waves. The role of the Görtler vortices is similar to that of the streamwise vortices produced by nonlinear wave interactions on a flat plate, bringing about velocity profiles that are highly inflexional and unstable at the spanwise positions where the induced velocity is directed away from the wall. The smoke photographs reproduced in figure 4 (plate 1) from Ito's paper (Ito 1980) illustrate the process of amalgamation of neighbouring vortices, followed by the breakdown into hairpin eddies. The Reynolds number based on the displacement thickness is about 7×10^2 at $x = 85$ cm (from the leading edge), where Ito observed a high-frequency fluctuation of 140 Hz superposed on a low-frequency wave of 8 Hz at the spanwise position mentioned above. The high frequency appears to be close to that of the most unstable mode of disturbance due to the inflexional velocity profile, while the low frequency is found to be within the unstable frequency range of the Tollmien-Schlichting wave. In the experiments of Bippes & Görtler (1972), a velocity fluctuation of 12 Hz was observed at displacement thickness Reynolds number of 5.5×10^2 . The frequency of 12 Hz appears to originate from the inflexional velocity profile, but not due to the unperturbed Blasius profile, which is estimated to exhibit instability for the frequency of 1 to 2 Hz under the conditions of the experiment.

3. Transition in three-dimensional boundary layers

In a three-dimensional boundary layer such as that which occurs on a rotating disk or on a swept wing, the velocity vectors along the solid wall at a particular station are not in a plane and possess components both parallel and normal to the inviscid streamline outside the boundary layer. The parallel or streamwise component is of the ordinary boundary-layer profile, whereas the normal or cross-flow component is zero both at the wall and at the edge of the boundary layer. For any other direction, the velocity profile is a combination of these two extreme cases. It has been made clear by the pioneering investigation of Gregory *et al* (1955) that the equations of stability, with certain approximations, resemble formally those for the two-dimensional flow, in which the basic flow is represented by the velocity profile in the direction of propagation of the disturbance at that station. In view of this local two-dimensional nature of instability, there is a certain range of directions, in which the velocity profile is unstable and the disturbance is amplified.

The theory was applied by Gregory *et al* to explain the vortex system observed in the region upstream of transition to turbulent flow on a rotating disk. Examination of stability at infinite Reynolds number for the corresponding velocity profiles indicates that neutral disturbances of zero phase velocity are generated by a particular velocity profile (the so-called *J* profile), which changes sign from positive to negative as the distance from the wall increases and has a point of inflexion at the

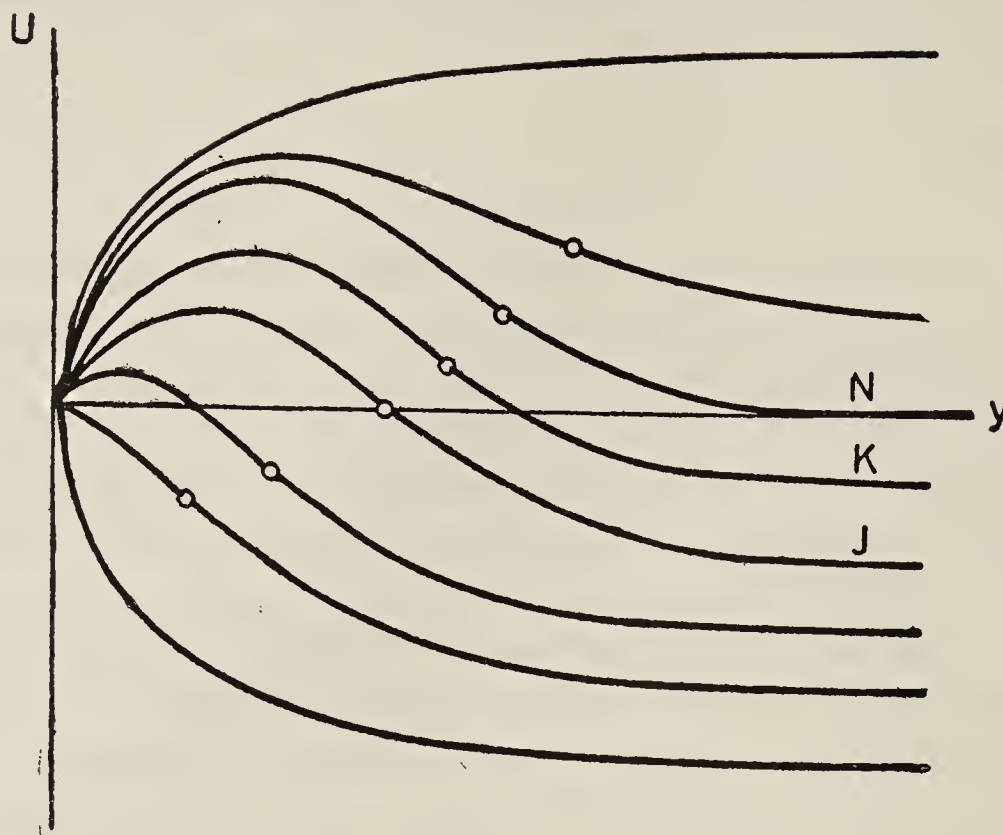


Figure 5. Velocity profiles in different directions of disturbance propagation (Gregory *et al* 1955)

point of zero velocity (figure 5). The stationary (zero phase velocity) disturbances predicted by theory have their axes in the form of equiangular spirals, the normal to a spiral making an angle of 13° with the radial direction, in good agreement with the vortex patterns visualized by the china-clay evaporation technique. However, the theoretical wavenumber $1.5/\delta^*$ (where $\delta^* = 1.271 (\nu/\omega)^{1/2}$ is the displacement thickness of the circumferential velocity profile, ω the angular velocity of the disk, and ν the kinematic viscosity) in the direction normal to the spiral gives rise to a number of vortices attached to the disk surface as 113 to 140, which is about four times too large compared to the experimentally observed value of 30. The discrepancy has been simply attributed to the effect of viscosity.

On the other hand, however, it is generally known that the stability characteristics of inflexional velocity profiles are modified only slightly by the effect of viscosity. A doubt has therefore been cast upon the explanation of the discrepancy in the wavenumber. By numerically integrating the inviscid stability equation, Yamashita & Takematsu (1974) obtained two distinct modes of stationary disturbance for *J* profile of velocity distribution: the one is a neutral disturbance with a wavenumber of $1.5/\delta^*$, corresponding to that mentioned above, whereas the other is an amplified disturbance with a wavenumber of about $0.2/\delta^*$, which seems to have been overlooked by the preceding investigations (Gregory *et al* 1955; Tobak 1973). The latter mode of amplified stationary disturbance deserves special attention because of its smaller wavenumber and greater likelihood of being observed in experiment as compared to the neutral mode of disturbance. Yamashita & Takematsu extended the numerical solution to finite Reynolds numbers, where two distinct modes of stationary disturbance were obtained as at infinite Reynolds number (figure 6). Calculations were also repeated for other neighbouring profiles. Similar but more or less sporadic calculations at finite Reynolds numbers were made independently by Tobak (1973) and subsequently by Kobayashi *et al* (1980). In view of these calculations it is suggested that a more satisfactory explanation for the observed vortex system be offered

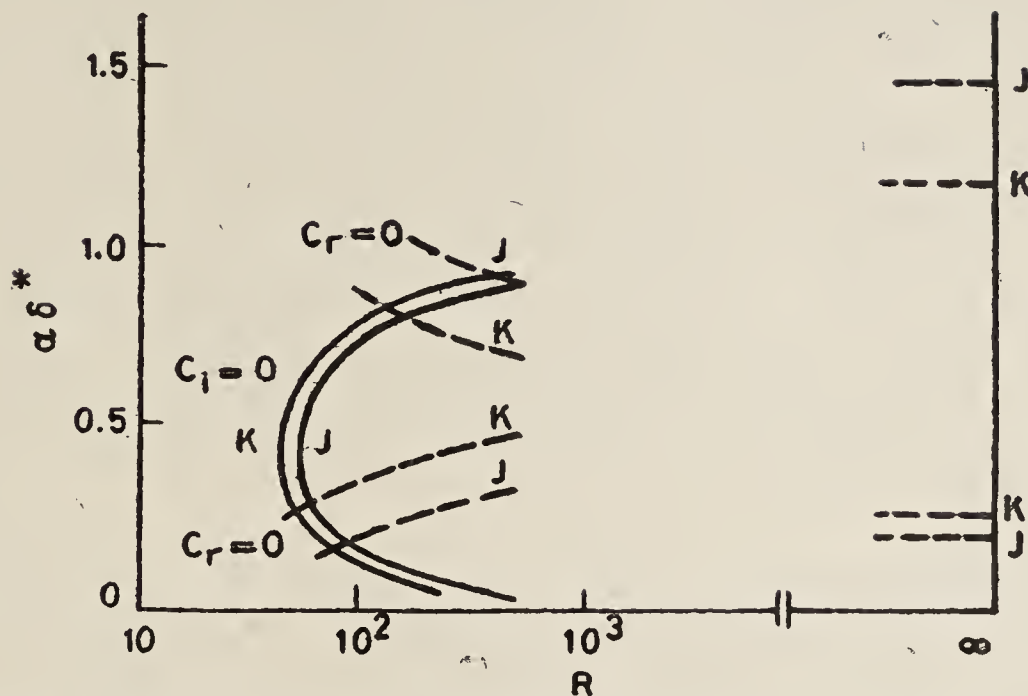


Figure 6. Curves of neutral stability ($c_i = 0$) and zero phase velocity ($c_r = 0$) for J and K profiles (Yamashita & Takematsu 1974)

by the small-wavenumber mode of stationary disturbance of the maximum amplification rate generated by one of the neighbouring velocity profiles, in which the point of inflexion is located at the point of slightly positive velocity. In this connection it is mentioned that the characteristic feature of the J profile, that the point of inflexion occurs at the point of zero velocity, is required only for generating stationary mode of neutral disturbance at infinite Reynolds number. If the requirement for neutral disturbance is removed, no reason remains for adhering to this particular profile.

The two-dimensional stability theory is limited in relevance to the process of transition on a rotating disk or on a swept wing, since the velocity profile in the direction of propagation of the disturbance is not invariant with that direction. The two-dimensional analysis is thus useful only for predicting the appearance of the amplified disturbance at a particular station. An attempt has been made by Tobak (1973) to lift the restriction for affording a qualitative insight into the subsequent development of the disturbance. It is highly desirable that a more quantitative prediction be made by the multi-scale analysis, which has been successful in estimating the non-parallel flow effects on the stability of boundary layer flows (Bouthier 1972, 1973; Saric & Nayfeh 1975). Another natural approach is to investigate the evolution of linear perturbations about the flow due to a rotating disk, as has been attempted with some success by Cebeci & Keller (1977) and Cebeci & Stewartson (1980).

On the experimental side, some measurements were made on the flow due to a rotating disk in recent years (Chin & Litt 1972; Kitamura 1973; Clarkson *et al* 1980; Kobayashi *et al* 1980). Most of them are sketchy, amounting to no more than a reconfirmation of what had been observed by Gregory *et al* (1955). Only worthy of special mention is Kitamura's observation with a hot-wire sensing the fluctuation of a circumferential velocity component at a fixed distance of $1.3 (\nu/\omega)^{1/2}$ from the disk surface. A sinusoidal fluctuation is observed when the Reynolds number, $R = r(\omega/\nu)^{1/2}$, based on the length $(\nu/\omega)^{1/2}$ and the disk velocity ωr , exceeds a value of about 4×10^2 , where r is the radial distance. The frequency of the velocity fluctuation, when divided by the revolution per second $\omega/2\pi$, yields a value of 30 as the number of vortices on the disk. The amplitude of the

fluctuation is slightly modulated, indicating that the vortices are not exactly regularly spaced. The root-mean-square of velocity fluctuation, v' , made non-dimensional by ωr , is plotted semi-logarithmically against the Reynolds number R in figure 7. It is to be noted that the location of the hot-wire, $1.3(v/\omega)^{1/2}$ from the surface, corresponds to the location of a maximum of v' -distribution across the boundary layer. The nearly straight-line dependence of $\log(v'/\omega r)$ on R visualized in the range of R from 4.3×10^2 to 4.9×10^2 is associated with the linear amplification of disturbance in the radial direction. Nevertheless, the mean velocity components in the circumferential and radial directions remain unaffected by the fluctuations, in good agreement with the theoretical prediction of Cochran (1934) for R up to 5×10^2 .

When the Reynolds number exceeds 5×10^2 , the mean velocity distributions deviate from the theoretical result, and the sinusoidal fluctuation is distorted by the appearance of the second harmonics, and then the third and higher harmonics, until eventually it is interspersed with random fluctuations characteristic of turbulence at $R = 5.5 \times 10^2$. Fully developed turbulent flow exists beyond $R = 6 \times 10^2$. These observations suggest that the nonlinear development of the disturbance takes the course of the so-called 'spectral evolution' prior to transition to turbulent flow, as is common to the flow between rotating cylinders when the rotation of the inner cylinder predominates. However, the experimental data are too meagre to draw any definite conclusion at the present moment.

4. Transition induced by roughness element

A typical example of subcritical transition is offered by that induced by roughness on the surface. Transition occurs upstream of the position where it would without the roughness. For a two-dimensional roughness element on a flat plate, for example,

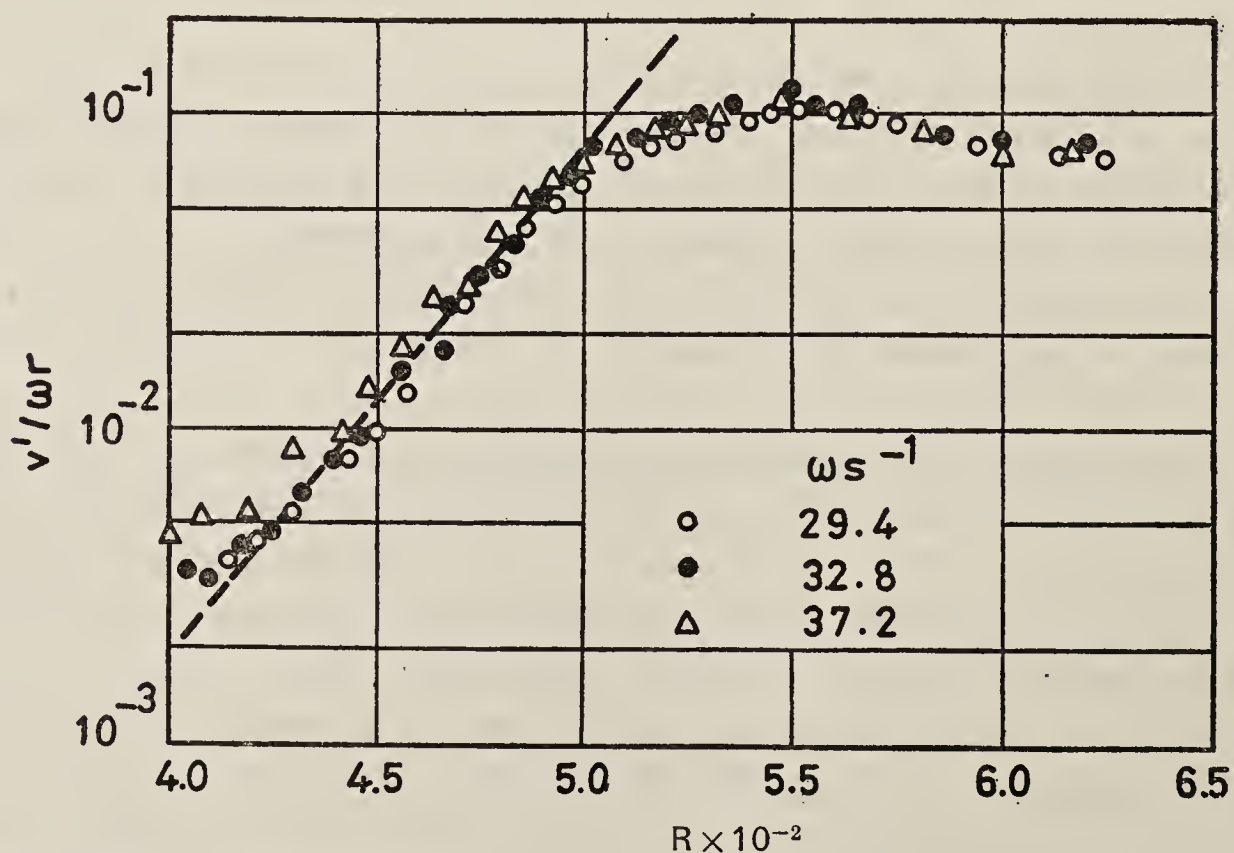


Figure 7. Root-mean-square fluctuating circumferential velocity at $z = 1.3(v/\omega)^{1/2}$ plotted against Reynolds number $R = r(\omega/\nu)^{1/2}$ (Kitamura 1973) Legend in figure quotes ω in units of s^{-1} .

the flow separated at the roughness reattaches to the surface as a laminar boundary layer provided the free-stream velocity is sufficiently small. Transition occurs in the reattached boundary layer, and the dominant frequency observed prior to transition is that characteristic of the Blasius velocity profile. As the velocity is increased, transition moves gradually upstream. The frequency observed prior to transition close enough to the roughness is peculiar to separated flow with inflexional profile (Tani & Sato 1956), suggesting a modification by roughness of the stability characteristics of the flow. However, this view of the matter had not been pursued further until Klebanoff (1966) and Klebanoff & Tidstrom (1972) traced the development of the disturbance spectra from the separated inflexional profile to the reattached Blasius profile. It was disclosed from the measurements that the destabilizing influence of the flow in the recovery region immediately downstream of the roughness is directly responsible for inducing earlier transition. Particularly, the range of selective amplification spreads to higher frequencies by the unstable behaviour of the recovery region. At a free-stream velocity small enough for transition to occur at some distance downstream, this gives rise to an increase in overall amplitude with dominant frequency centred all through around the value characteristic of the Blasius profile. At a higher velocity with transition close to the roughness, the same behaviour is observed except that some high-frequency disturbances no longer damp but amplify by nonlinear effects, until an amplitude comparable with that characteristic of the Blasius profile is reached.

As contrasted with the behaviour of a two-dimensional roughness element, the effect of a three-dimensional roughness element is more critical in nature (Gregory & Walker 1951; Klebanoff *et al* 1955). For a given three-dimensional roughness element, transition is unaffected up to a certain free-stream velocity, but moves rapidly upstream to the roughness when the critical velocity is reached, a wedge-shaped region of turbulent flow originating at the roughness and extending downstream. No satisfactory explanation has yet been offered for this critical behaviour. Supposing that the effect of a three-dimensional roughness is also stability-dominated, close attention is to be directed to the flow immediately downstream of the roughness element.

The visual observations of Gregory & Walker (1951) and Mochizuki (1961a, b) have disclosed the existence of two sets of streamwise vortices downstream of a three-dimensional roughness element at a subcritical free-stream velocity (figure 8). One is a closely-spaced pair of spiral filaments rising from the wall close behind the roughness until they trail downstream at a level of the top of the roughness, and the other is a horseshoe-shaped vortex filament wrapped round the front of the roughness and trailing downstream at a level closer to the wall. The sense of rotation is such that the momentum is to be transported upward (away from the wall) by the former pair and downward (toward the wall) by the latter pair. These vortices generate not only a spanwise corrugation of the boundary-layer flow, but also bring about a three-dimensional boundary layer possessing both streamwise and spanwise (cross-flow) velocity components somewhere away from the centre of the wake. The effect of the spanwise corrugation has been considered to some extent by Tani *et al* (1962), but the creation of the cross-flow velocity component appears to have escaped the attention it deserved. There is a fair possibility that the presence of cross-flow velocity produces instability, similar to that occurring on a rotating disk or on a swept wing. A single experimental evidence (Tani *et al* 1962) suggests the

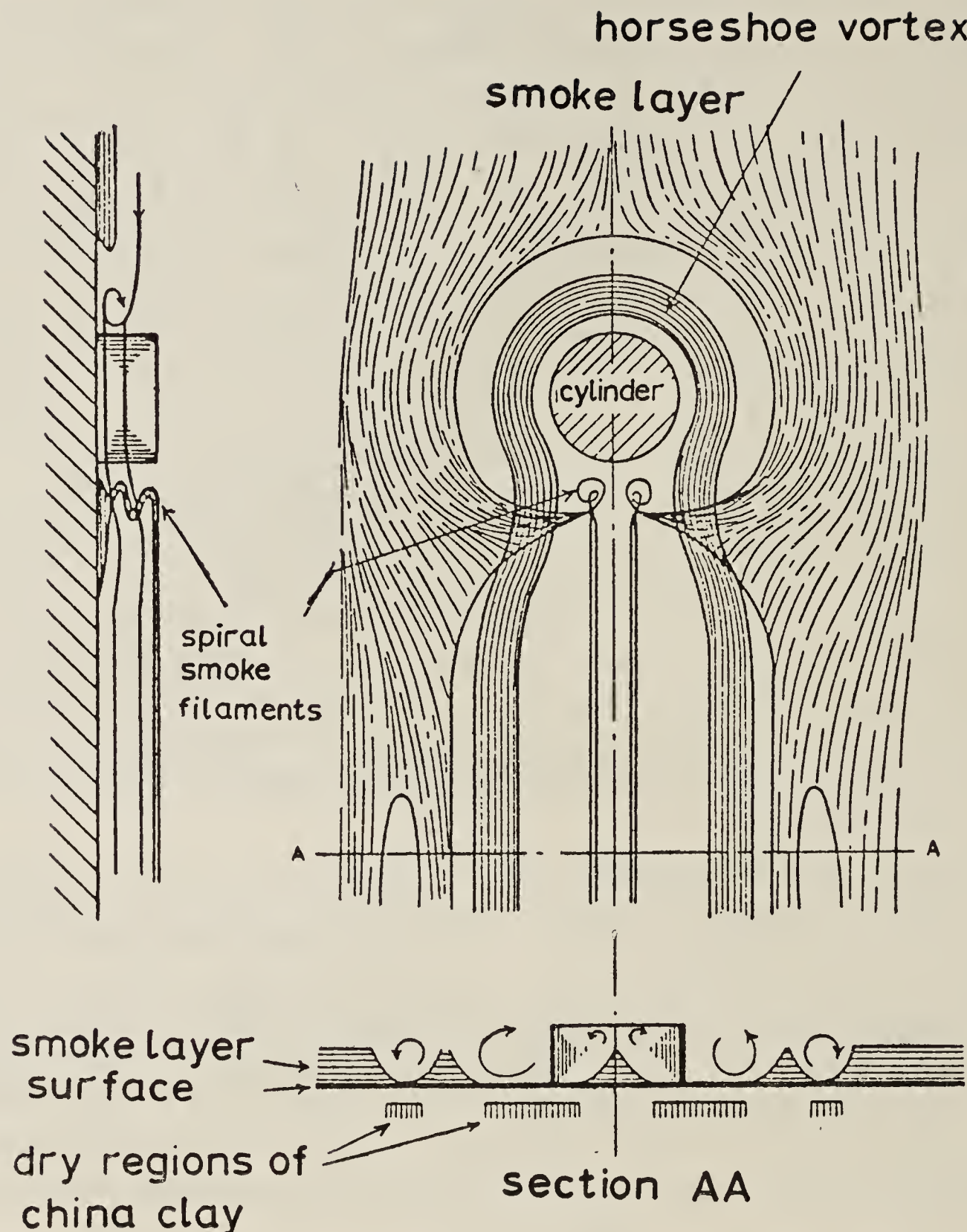


Figure 8. Diagrammatic representation of flow past a cylindrical roughness element on a flat plate. Not to scale (figure 6 of Gregory & Walker 1951)

cross-flow velocity to be of the same order of magnitude as that responsible for inducing transition on a swept wing.

The observations of Mochizuki (figure 9, plate 2) indicate that weak waviness appears on the closely-spaced trailing vortex filaments when the free-stream velocity is slightly increased. The waviness grows in amplitude with further increase in velocity, until the vortex filaments break up into a series of hairpin eddies, somewhat similar in appearance to those observed in the later stage of transition in Blasius flow on a flat plate. Unlike the Blasius flow, however, breakup into hairpin eddies does not result in turbulence. No explanation has been given for this phenomenon, but it appears to the author that the growth of disturbances leading to the generation of eddies is caused by the unstable behaviour of the inflexional velocity profile, which prevails along the centre line of the near wake of the roughness element. Further downstream, the influence of the closely-spaced trailing vortices declines so much

that the velocity profile regains Blasius form, assisted by the downward momentum imparted by the still persistent horseshoe-shaped vortex filament. As a result, the disturbance ceases to grow, and no turbulence ensues. It is to be remembered, however, that Mochizuki's observations were made at relatively low values of the boundary-layer thickness Reynolds number at roughness location. It remains uncertain whether the mechanism of transition for higher Reynolds numbers is basically the same as that so far conjectured.

Recent measurements of Gupta (1980) in the wake of a roughness element indicate laminar disturbances decaying on the centre line of the wake away from the wall but growing on either side close to the wall (figure 10). This appears to corroborate the above interpretation and also the possibility of breakdown of laminar flow by cross-flow instability. It is also probable that the stationary vortices generated by the cross-flow instability manifest themselves in the form of a new pair of nearly streamwise vortices, appearing some distance downstream and spanwise outside of the original pairs of streamwise vortices. The process repeats itself until a wedge-shaped region of turbulence is formed by the successively induced pairs of vortices, as first conjectured by Taylor (Gregory *et al* 1955) and later speculated on in more detail by Tobak (1973). The existence of a fine structure in the turbulent wedge has been recorded by the china-clay evaporation technique by Gregory & Walker (1951) and also by the long-exposure smoke photograph by Mochizuki (1961a).

5. Growth of a turbulent spot

The formation of a turbulent wedge behind a three-dimensional roughness element presents a typical example of the spanwise growth of a turbulent region embedded in a laminar boundary layer, a process first noted by Charters (1943) for its significantly rapid spread as compared to the usual turbulent entrainment. He called the process 'transverse contamination'. Both entrainment and contamination share in incorporating originally non-turbulent fluid, although the underlying mechanism is entirely different. The entrainment is the process in which random vorticity is transmitted by viscous action, while the contamination is now interpreted as due to destabilization by induction of the surrounding fluid. In order to shed further light on this problem, attention is directed to the growth of a turbulent spot, in which the growth

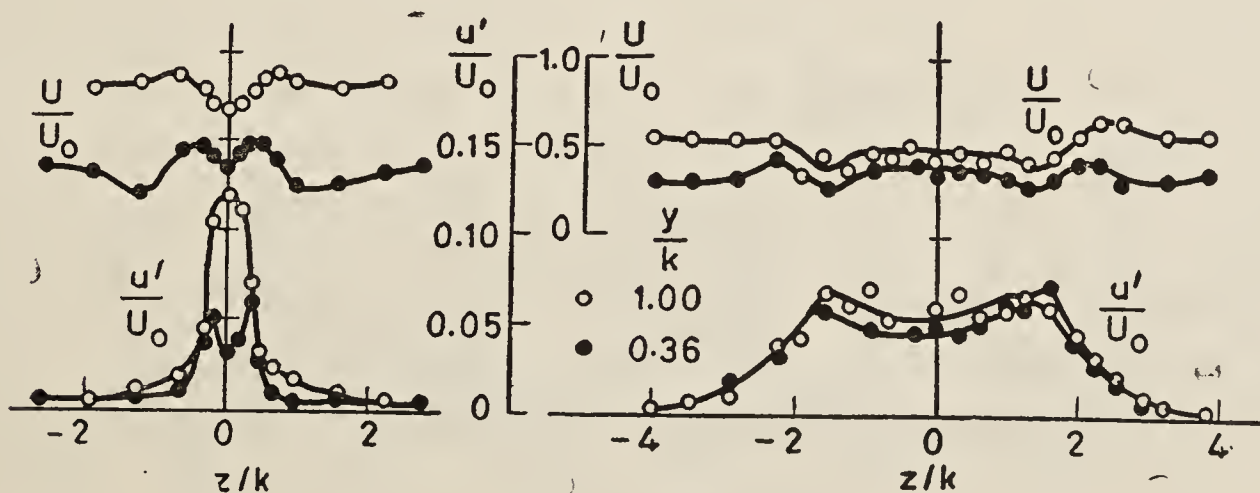


Figure 10. Spanwise distributions of streamwise mean velocity and its fluctuation intensity in the wake of a cylindrical roughness element. $(x - x_k)/k = 8$ (left), $(x - x_k)/k = 40$ (right), $k = 0.31$ cm, $x_k = 30$ cm, $U_0 x_k / \nu = 8 \times 10^4$ (Gupta 1980)

normal to the wall is governed by entrainment, while the growth in the spanwise direction is just the process of contamination.

Figure 11 shows the profiles of mean streamwise velocity U in the plane of symmetry of a turbulent spot, generated artificially every quarter second by a jet disturbance at 75 cm from the leading edge of a flat plate, the free-stream velocity being $U_0 = 10$ m/s, and the hot-wire probe being placed at a distance $x = 40$ cm downstream of the jet orifice and a distance y normal to the flat plate (Handa 1976). The mean velocity U is the ensemble average of the data recorded by the hot-wire after a time interval t from the jet discharge. The abscissa is the similarity variable $\xi = x/U_0 t$. Included also in the figure are the cross-section $ABCD$ of the spot interface, defined as the region inside which turbulent fluctuation is observed, a broken line connecting the points for which $U/U_0 = \xi$ (the stream velocity U is equal to the velocity of propagation x/t), and the region of high shear in which $\partial U/\partial y \geq 0.8(U_0/\delta^*)$, δ^* being the displacement thickness. Of great importance to note is that the leading (downstream) edge of the spot is characterized by the broken line $U/U_0 = \xi$ passing through the region of high shear. It is also seen that the value of $|\partial^2 U/\partial y^2|$ attains a maximum in the close vicinity of the point where $U/U_0 = \xi$. Seeing that the production of turbulent energy is most active in the vicinity of the location of the maximum $|\partial^2 U/\partial y^2|$ for a fully developed turbulent flow in a parallel channel or on a flat plate, it seems reasonable to conjecture that the same fluid particle remains in a high state of turbulence production in the region close to the leading edge of a spot, at least in the plane of symmetry. The turbulence generated there is then transferred in both directions, toward and away from the wall, resulting in a growth normal to the wall as visualized by the sloping segments AB and AD of the spot interface. The deceleration close to the wall increases the shear stress at the wall with the decrease in ξ as far as $\xi = 0.72$, but the high shear stress cannot be sustained because of the decline in turbulence production, as indicated by the broken line $U/U_0 = \xi$ located away from the wall. It is only when the broken line approaches the wall that the turbulence production recovers and the shear stress attains a maximum at $\xi = 0.52$. In line with this activity, there exists appreciable amount of entrainment along the rear segment CD of the spot interface. According to Cantwell *et al* (1978) most of the entrainment occurs along the segment CD , the remainder occurring along the segment AB .

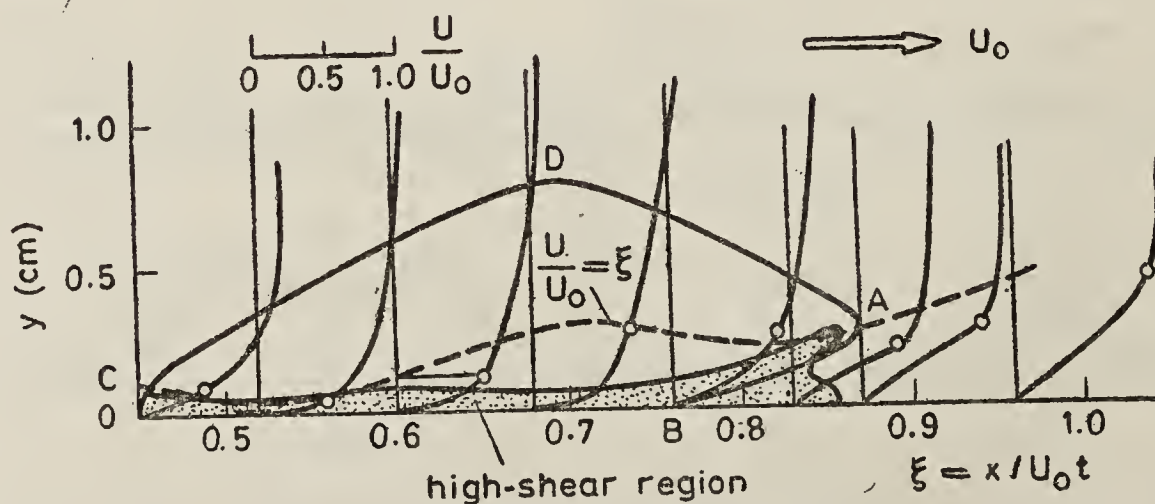


Figure 11. Profiles of mean streamwise velocity in the plane of symmetry of a turbulent spot (Handa 1976)

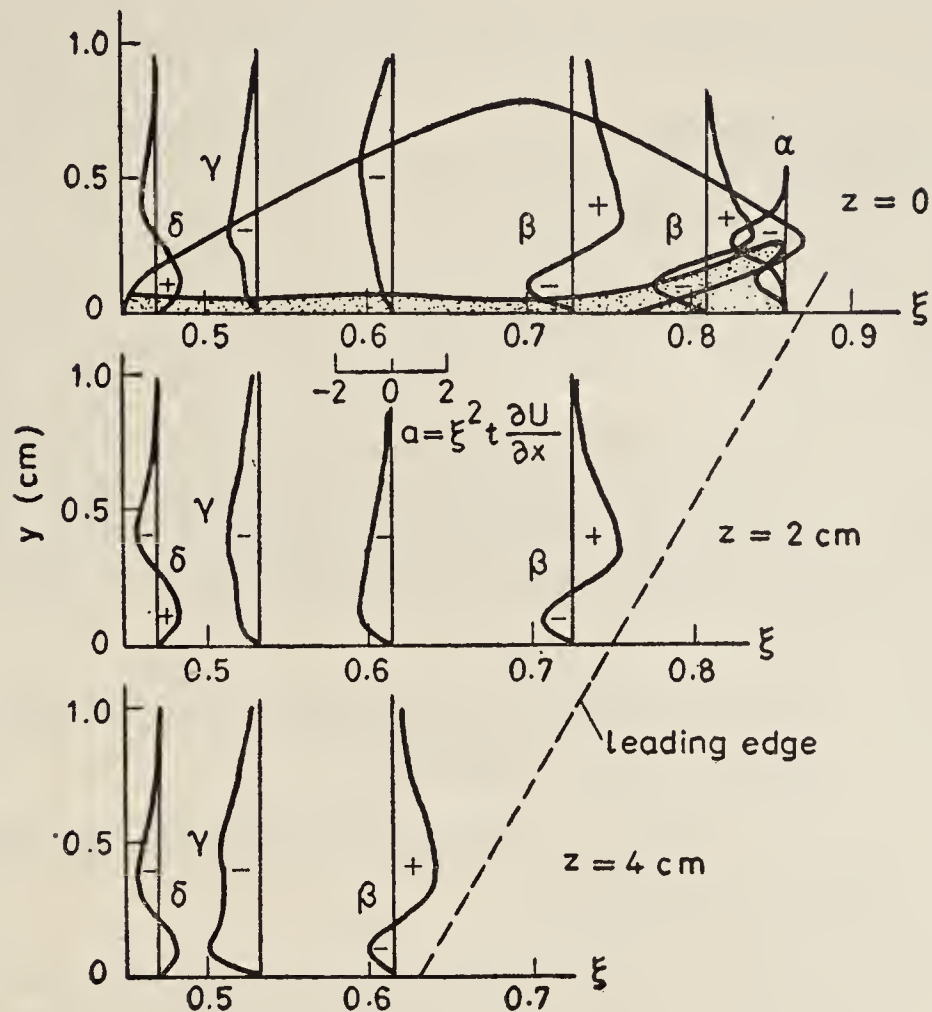


Figure 12. Profiles of mean streamwise acceleration in the plane of symmetry and in two spanwise sections of a turbulent spot (Handa 1976)

Figure 12 shows the profiles of non-dimensional acceleration $a = t\xi^2 (\partial U/\partial x)$, with ξ as abscissa, in the plane of symmetry ($z = 0$) as well as in two spanwise sections, $z = 2$ cm and $z = 4$ cm. Included in the figure is the region of high shear in the plane $z = 0$ as in figure 11. It is seen that the profile of type α , altogether negative but confined to a certain height, exists only close to the leading edge in the plane $z = 0$, while the profile of type β , changing from negative to positive as y increases, appears a little beyond (upstream) the leading edge in all spanwise sections. The profiles of type γ and δ are also common to all spanwise sections.

These observations suggest that the spanwise growth of a turbulent spot is governed by a mechanism different from that which accounts for the growth normal to the wall. With the aid of the continuity equation $\partial V/\partial y + \partial W/\partial z = -a/t\xi^2$, the profile of type α is interpreted as representing the field of flow due to a distributed source in the yz -plane. The normal velocity is then negative close to the wall and positive away from the wall, and is responsible for transferring turbulence generated in the high-shear layer in both directions, as mentioned above. The acceleration profile of type β represents a field of flow due to the distributed source close to the wall and the distributed sink away from the wall. The field of flow due to this system of singularities is approximately equivalent to that due to a pair of vortices located some distance from the wall, thus producing a situation similar to that already observed behind a three-dimensional roughness element. This again corroborates the view that spanwise contamination is due to destabilization by induction of the surrounding fluid. The view has also been recently shared by Gad-el-Hak *et al* (1980).

References

- Benney D J 1961 *J Fluid Mech.* **10** 209
 Benney D J 1964 *Phys. Fluids* **7** 319
 Benney D J & Lin C C 1960 *Phys. Fluids* **3** 656
 Betchov R 1960 *Phys. Fluids* **3** 1026
 Bippes H & Görtler H 1972 *Acta Mech.* **14** 251
 Bouthier M 1972 *J. Méc.* **11** 599
 Bouthier M 1973 *J. Méc.* **12** 75
 Cantwell B, Coles D & Dimotakis P 1978 *J. Fluid Mech.* **87** 641
 Cebeci T & Keller H B 1977 Stability calculations for a rotating disk, AGARD CP No. 224 7.1
 Cebeci T & Stewartson K 1980 *Am. Inst. Aeronaut. Astronaut. J.* **18** 395
 Charters A C 1943 Transition between laminar and turbulent flow by transverse contamination, NACA Tech. Note No. 891
 Chin D T & Litt M 1972 *J. Fluid Mech.* **54** 613
 Clarkson M H, Chin S C & Shacter P 1980 *Am. Inst. Aeronaut. Astronaut. Paper* 80 0279
 Cochran W G 1934 *Proc. Cambridge Philos. Soc.* **30** 365
 Craik A D D 1971 *J. Fluid Mech.* **50** 393
 Gad-el-Hak M, Blackwelder R F & Riley J J 1980 in *Laminar-turbulent transition*, eds R Eppler and H Fasel (Berlin: Springer Verlag) p. 297
 Greenspan H P & Benney D J 1963 *J. Fluid Mech.* **15** 133
 Gregory N, Stuart J T & Walker W S 1955 *Philos. Trans. R. Soc. London* **A248** 155
 Gregory N & Walker W S 1951 The effect on transition of isolated surface excrescences in the boundary layer. ARC R and M No. 2779 Pt. 1
 Gupta A K 1980 *Phys. Fluids* **23** 221
 Hama F R & Nutant J 1963 *Proc. 1963 Heat Transfer and Fluid Mech. Inst.* (Stanford: University Press) p. 77
 Handa N 1976 *Structure of a turbulent spot* (in Japanese), Doctor Thesis, Dept. Mech. Engg., Nihon Univ., Tokyo
 Ito A 1980 *J. Jpn Soc. Aeronaut. Space Sci.* **28** 327
 Itoh N 1980 *Trans. Jpn Soc. Aeronaut. Space Sci.* **23** 91
 Itoh N 1981 *Proc. R. Soc. London* **A375** 565
 Kitamura O 1973 *Experimental investigation on transition of the boundary layer formed on a rotating disk* (in Japanese), Master Thesis, Dept. Mech. Eng., Hokkaido University, Sapparo
 Klebanoff P S 1966 The effect of a two-dimensional roughness element on boundary layer transition. *Proc. 11th Int. Congr. Appl. Mech. Munich* (Berlin: Springer-Verlag) p. 803
 Klebanoff P S, Schubauer G B & Tidstrom K D 1955 *J. Aeronaut. Sci.* **22** 803
 Klebanoff P S & Tidstrom K D 1959 Evolution of amplified waves leading to transition in a boundary layer with zero pressure gradient, NASA Tech. Note D-195
 Klebanoff P S & Tidstrom K D 1972 *Phys. Fluids.* **15** 1173
 Klebanoff P S, Tidstrom K D & Sargent L M 1962 *J. Fluid Mech.* **12** 1
 Kobayashi R, Kohama Y & Takamadate Ch. 1980 *Acta Mech.* **35** 71
 Kovaszny L S G, Komoda H & Vasudeva B R 1962 *Proc. 1962 Heat Transfer and Fluid Mech. Inst.* (Stanford: University Press) p. 1
 Landahl M T 1972 *J. Fluid Mech.* **56** 775
 Maseev L M 1968 *Fluid Dyn.* **3** 23
 Mochizuki M 1961a *J. Phys. Soc. Jpn* **16** 995
 Mochizuki M 1961b *Natur. Sci. Rep. Ochanomizu Univ.* **12** 87
 Nishioka M, Asai M & Iida S 1980 in *Laminar-turbulent transition* ed R Eppler and H Fasel) (Berlin: Springer Verlag) p. 37
 Orszag S A & Kells L C 1980 *J. Fluid Mech.* **96** 159
 Prandtl L 1933 *Z. Ver. Dtsch. Ing.* **77** 105
 Saric W S & Nayfeh A H 1975 *Phys. Fluids* **18** 945
 Schubauer G B 1958 in *Grenzschichtforschung*. Symposium, Freiburg (Berlin: Springer Verlag) p. 110
 Stewartson K 1975 *Fluid Dyn. Trans.* **7** 101
 Stuart J T 1960 *J. Fluid Mech.* **9** 353

- Stuart J T 1962a *Proc. 10th Int. Congr. Appl. Mech. Stresa* (Amsterdam: Elsevier) p. 63
Stuart J T 1962b *Adv. Aeronaut. Sci.* **3** 121
Tani I 1973 *Z. Angew Math. Mech.* **53** T25
Tani I 1960 in *Laminar-turbulent transition* eds. R Eppler and H Fasel (Berlin: Springer Verlag)
p. 263
Tani I, Komoda H, Komatsu Y & Iuchi M 1962 *Aeronaut. Res. Inst., Tokyo University, Report*
No. 375
Tani I & Sato H 1956 *J. Phys. Soc. Jpn* **11** 1284
Tobak M 1973 *Z Angew Math. Phys.* **24** 330
Watson J 1960 *J. Fluid Mech.* **9** 371
Watson J 1962 *J. Fluid Mech.* **14** 211
Whitham G B 1974 *Linear and nonlinear waves* (New York: John Wiley)
Yamashita I & Takematsu M 1974 *Res. Inst. Appl. Mech., Kyushu University, Report. No. 69*

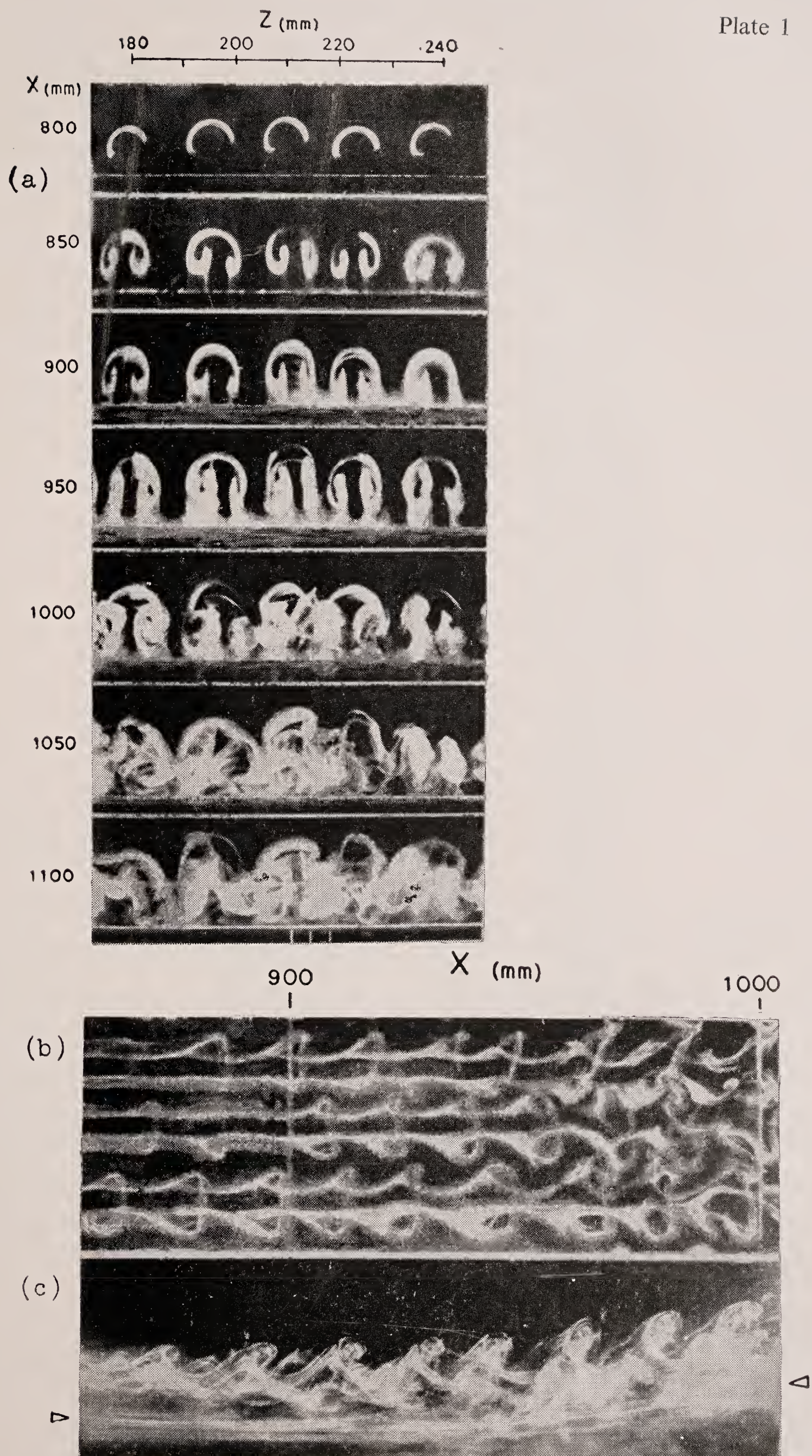


Figure 4. Amalgamation and breakdown of streamwise vortices on a concave wall (a) end view, (b) plan view, (c) side view. Figures 7 and 8 from Ito (1980)

Plate 2

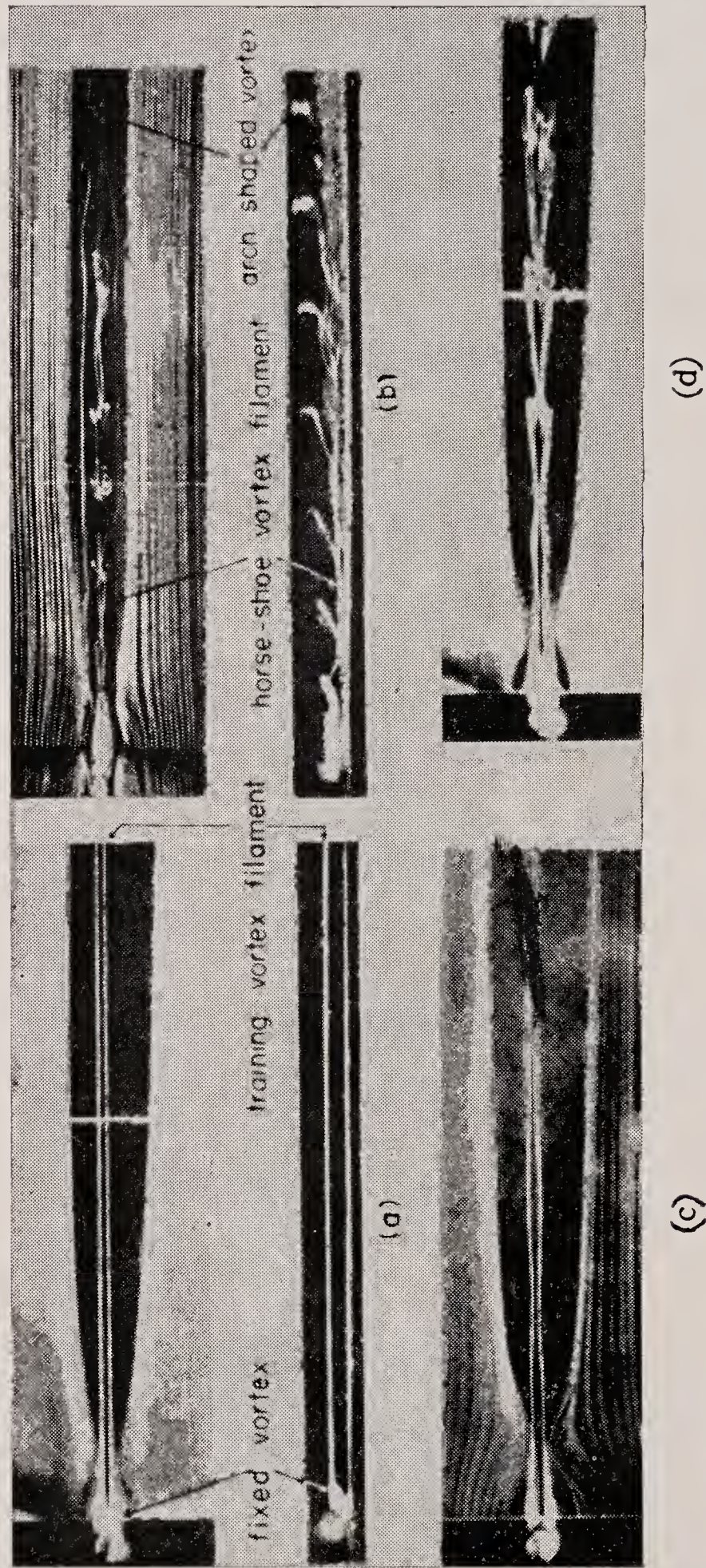


Figure 9. Flow patterns due to a spherical roughness element on a flat plate. Freestream velocity increases in the order of (a) (c), (d) and (b) (figure 3 of Mochizuki 1961a)

Flow visualization studies of vortices

T MATSUI

Department of Mechanical Engineering, Meijo University, Yagoto, Tenpaku-cho, Tenpaku-ku, Nagoya 468, Japan

MS received 16 May 1981

Abstract. An actual vortex in the Kármán vortex street downstream of a circular cylinder has a core of finite dimension which increases downstream. The circulation of the vortex is nearly constant. The ratio b/a which is 0.281 according to the theory of Kármán, grows from 0.2 to 0.4 in the near wake.

In the flow about a circular cylinder rotating in a uniform flow, a Kármán vortex street, Görtler-type vortices and Taylor vortices are generated at the same time.

In the flow about a circular cylinder impulsively started with a constant velocity, the primary twin vortices behind the cylinder induce secondary twin vortices near the separation point. At the beginning of the motion, the separation does not occur even though a reverse flow is observed in the boundary layer.

Mutual slip-through of a pair of vortex rings was achieved by increasing the Reynolds number. A vortex ring rebounds from a plane surface due to the separation of the flow on the surface induced by the vortex ring, and the secondary vortex ring is formed from the separated shear layer.

Keywords. Circulation of a vortex; core of a vortex; electrolysis method; flow visualization; Görtler vortex; hydrogen bubble technique; Kármán vortex street; rebound of a vortex ring; separation; slip-through of a pair of vortex rings; smoke-wire technique; Taylor vortex; time line; twin vortices; vortex ring; wall vortex.

1. Introduction

In former days, turbulent flows were considered to have random velocity fluctuations owing to superposed "eddies" of varying scale and strength in the flow. Nowadays, velocity fluctuations in turbulent shear flows are considered not to be perfectly random, but to possess some kind of regularity, owing to "vortices" of large scale; in other words, turbulent shear flows have "coherent structures". In these descriptions, the definition of "eddy" or "vortex" is not clear, but there is no doubt that the concept of eddy or vortex "in a flow", which is not stationary as a whole, is based on the Lagrangian standpoint. What appears from the Eulerian standpoint, however, is the idea of velocity fluctuations. As the Navier-Stokes equations are based on the Eulerian viewpoint, what we need is velocity fluctuations, not vortices. However, it seems that we are not satisfied with velocity fluctuations alone. This is presumably due to the fact that the concept of velocity fluctuation is not so intuitively satisfying as the concept of eddy or vortex. The concept of eddy or vortex is intuitively accepted and seems to be so clear that a definition is not necessary. Thus, we have no clear definition of eddy or vortex in fluid mechanics. Nevertheless, the concept of a vortex is frequently employed and appears to be useful. This is the justification for studying those characteristics of a vortex which have not so far been studied.

This paper summarises studies by the present author and his colleagues on the characteristics of vortices, in particular in the Kármán vortex street and in the flow around a circular cylinder, and also the characteristics of vortex rings.

2. Vortices in the flow around a circular cylinder

2.1 Kármán vortex street

The velocity fluctuations in the wake of a circular cylinder have wave forms like those shown in figure 1; these traces were obtained by the hot-wire technique. In this case, the cylinder diameter was 3 mm, the wind velocity was 73 cm/s, so that the Reynolds number based on the diameter was about 140. In the figure, y denotes the transverse distance from the wake centre, and d denotes the cylinder diameter. The wave forms were measured at the section $x/d = 20$, that is, twenty diameters downstream from the centre of the cylinder.

If the vortex street of Kármán's theory were realized in the actual wake, the velocity fluctuations in the wake would have quite different wave forms from those in figure 1. For example, the velocity fluctuations would be extremely large at the transverse location corresponding to the centre line of the vortex rows, because the Kármán vortex street consists of point vortices. In the actual flow, however, the wave forms in figure 1 do not show such large velocity fluctuations at any section measured. Then, we have the question how different the actual vortex street is from the Kármán vortex street.

For this purpose, the photographs of both the flow patterns and the hot-wire probe in it were taken at the same time as when the output of the hot-wire was being

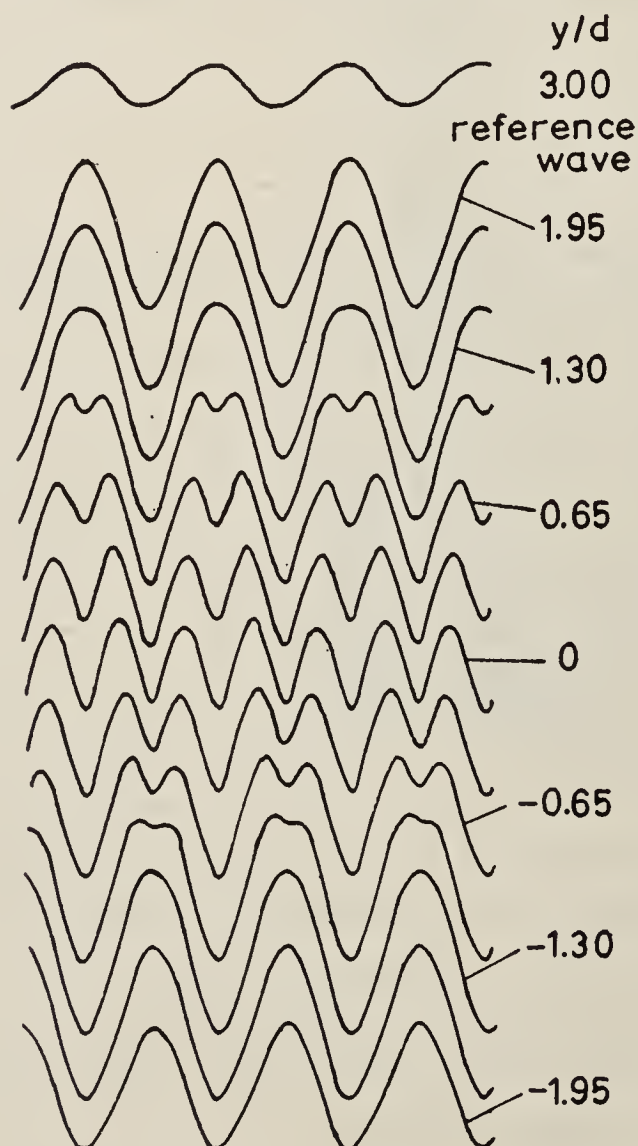


Figure 1. Transverse variation of velocity fluctuations. $U = 73$ cm/s, $d = 3$ mm, $Re = 140$, $x/d = 20$.

recorded, which indicated the wave forms of velocity fluctuations. The time mark of illumination for photography was also recorded under the wave form of velocity fluctuations. Thus, the output of the hot-wire on a wave form at an instant could be identified with the location of the probe in the flow pattern, as shown in figures 2, 3 and 4 (plates 1-3) at $Re = 140$ and at the section $x/d = 20$. The wave forms and the flow patterns at the transverse location of $y/d = 2.0$ are shown in figure 2 (plate 1), where two small triangles indicate the location of the hot-wire probe. In the figure, it is seen that the output of the hot-wire is maximum when it comes just above the centre of a vortex in the upper row (a), and minimum when it comes just above the centre of a vortex in the lower row (b). In figure 3 (plate 2) a similar comparison is shown at the location of $y/d = 0.67$, which corresponds to about the centre line of the upper vortex row. The wave forms have two similar peaks and two valleys, one of which is shallow, the other deep, in a wave length. It is seen in the figure that the two peaks correspond to both edges, downstream (a) and upstream (c) of a vortex in the upper row, and that the shallow valley corresponds to the centre of a vortex in the upper row (b) and the deep valley corresponds to the location just above the centre of a vortex in the lower row (d). In figure 4 (plate 3) on the centre line of a wake, it is seen that the wavelength is half of the wavelength in the outer part of the wake and that the peak corresponds to the midpoint between two consecutive vortices (a) and the valley corresponds to the centre of the vortices (b). From those figures, it is suggested that the vortices are not point vortices, but have cores of finite dimensions.

To observe the existence of vortex cores more directly, two smoke wires were used, the upstream one to visualize the vortex street as a whole, the downstream one to visualize a vortex core, as shown in figure 5 (plate 3). The time line of white smoke from the downstream smoke wire clearly shows the core of a vortex, which in turn is shown by the swirling white streak lines from the upstream smoke wire. The velocity distribution at the section through the vortex centre of the upper row can be measured by using the time line in the figure. The velocity distribution can also be measured by using a hot-wire if the conditional sampling method is applied. In other words, if the output of the hot-wire is sampled during the traverse at a specified x -section, only when the monitoring hot-wire in the outer part of a wake indicates the maximum output, then the result shows the velocity distribution in the section through a vortex centre of the upper row, because the reproducibility of the vortex street is as good as is shown in figure 6 (plate 4). This figure is a photograph taken by the multi-exposure of about 130 times synchronized by a monitoring hot-wire with the maximum velocity fluctuations and looks like a photograph taken by single exposure, showing the reproducibility of the vortex street. The velocity distributions in figure 7 at the section of $x/d = 20$ through the centre of a vortex in the upper row were obtained by the photograph of the time line and by the conditional sampling of the hot-wire output; and the velocity distribution of a Rankine vortex is also shown in the figure. The diameter of the core of a vortex can be measured in the figure. The downstream growth of vortex cores thus obtained is shown in figure 8 at several Reynolds numbers. The core diameter, D , decreases with increase in Reynolds number.

The circulation Γ , of a vortex can also be estimated by the velocity distribution in figure 8. It is seen in figure 9 that the non-dimensionalized circulation is nearly constant in a vortex street, independent of Reynolds numbers, the value being about 1.4.

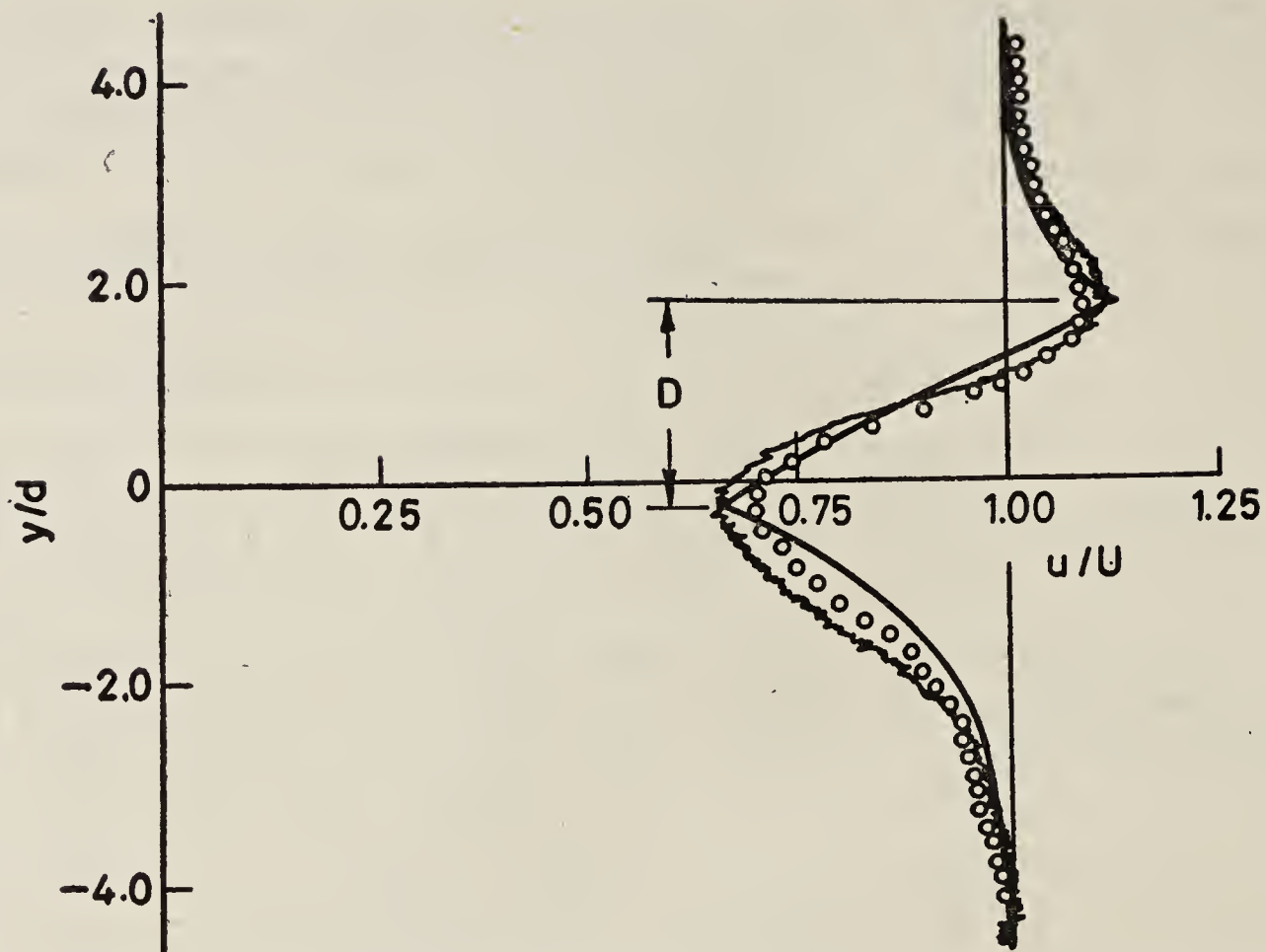


Figure 7. Velocity distribution through the centre of a vortex in the upper row at $x/d = 20$.

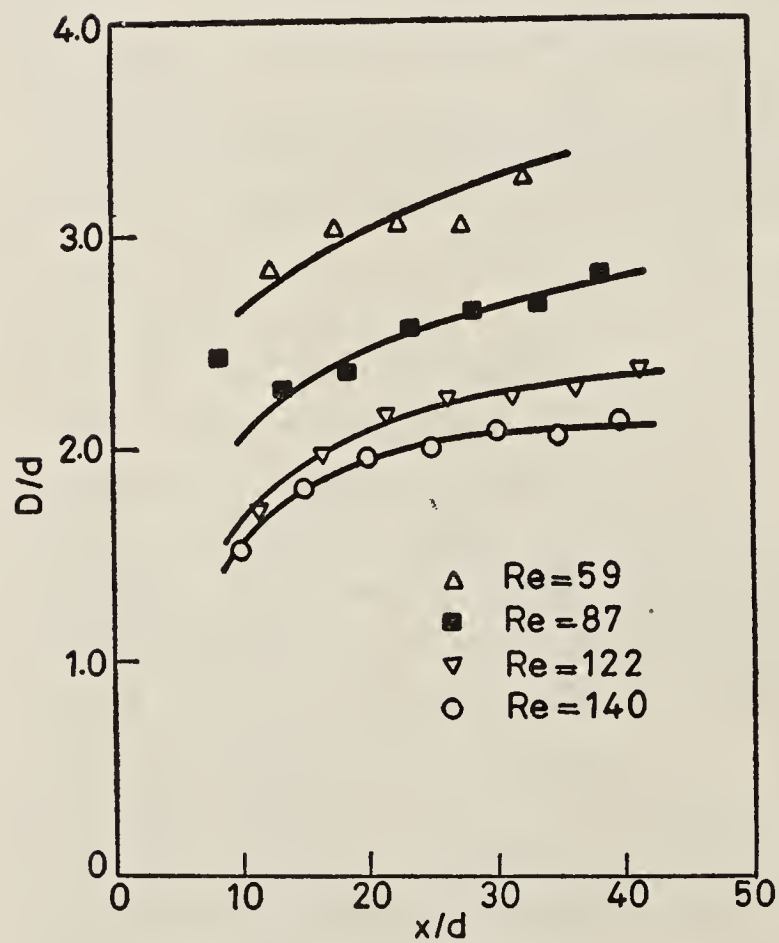


Figure 8. Downstream growth of vortex cores.

The location of the centre of a vortex can be measured in figure 6 (plate 4) and also from the velocity distribution shown in figure 7. When the flow is illuminated by a stroboscope synchronized by a monitoring hot-wire with the velocity fluctuation, the visualized flow pattern can be made stationary as shown in figure 6 (plate 4). Then, we can measure the location of the centre of a vortex directly by a telescope. When the streamwise distance between consecutive vortices measured by these methods is denoted by a and the transverse distance between two vortex rows is denoted by b , the downstream variation of the ratio b/a is shown in figure 10 where

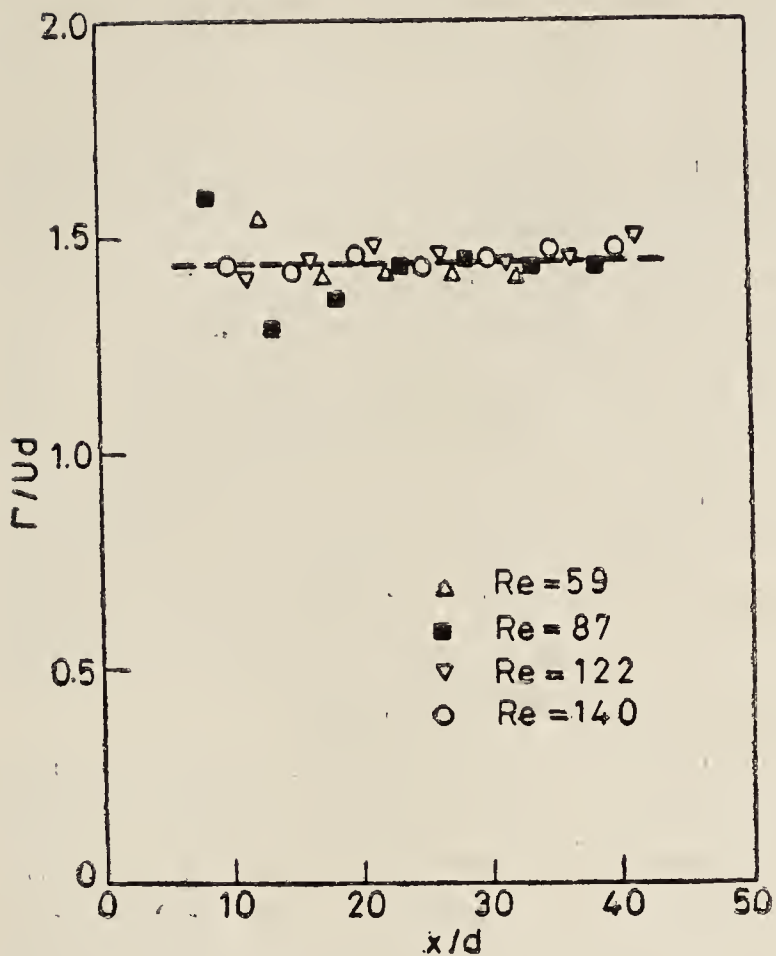


Figure 9. Circulation of vortices in a vortex street.

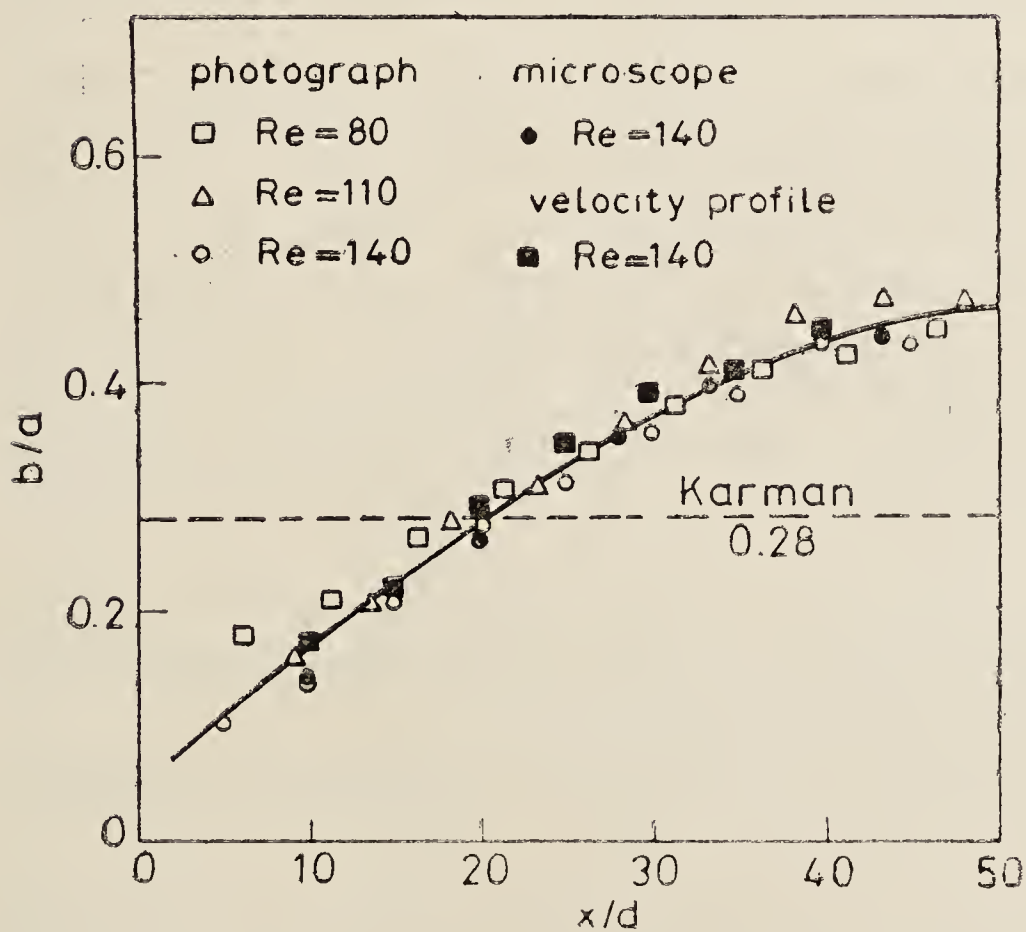


Figure 10. Downstream variation of the ratio b/a .

the value of 0.281 given by Kármán's theory is shown. The ratio increases with the streamwise distance from a value smaller than 0.2 in the near wake to a value greater than 0.4 at the section fifty cylinder diameters downstream.

Thus, we can see the discrepancies between Kármán's theory and the experimental results of the vortex street in the wake of a circular cylinder.

These experiments were carried out by Matsui & Okude (1980) at the Department of Transport Machine Engineering, Meijo University.

2.2 *Taylor vortex and Görtler vortex around a circular cylinder rotating in a uniform flow*

When the Reynolds number based on the cylinder diameter is in the pure Kármán vortex range and the peripheral speed of a rotating cylinder is greater than twice the velocity of a uniform flow, a remarkable transverse periodicity appears in every vortex of the Kármán vortex street in the wake, as shown in figure 11 (plate 4). The flow pattern was visualized by the hydrogen bubble technique in a water flow. The Kármán vortex street is considered to be formed as a result of the separation of the boundary layer from the cylinder surface. In this case, however, the fluid in the layer adjacent to the cylinder surface circulates around the rotating cylinder with it so that the fluid layer cannot separate from the cylinder surface. The outer layer outside the circulating layer may separate from the inner circulating layer at a point further away from the cylinder surface, as will be shown later in this paper.

The inner circulating layer has an instability identical to the Taylor instability in the flow between two concentric cylinders, the outer cylinder being at rest and the inner one rotating. When a hydrogen bubble-generating wire was set in the circulating layer, the flow pattern shown in figure 12 (plate 5) was obtained. In this picture, pairs of vortex rings around the cylinder can be observed to have a wavelength in the axial direction. These vortex rings are Taylor vortices. The wavelength is much smaller than the transverse wavelength appearing in the Kármán vortex street in figure 11 (plate 4).

Vortices with axes in the streamwise direction were observed by Colac-Antic & Hassler (1971) in the flow around a circular cylinder at rest in a uniform flow. The longitudinal vortices are generated from the same kind of instability in the flow near the front stagnation point as the Görtler instability in the boundary layer along a concave wall. In the present case, longitudinal vortices of the same kind were observed as shown in figure 13 (plate 5). The flow pattern was visualized by a bubble generating wire set in the outer layer in the region where the peripheral speed is in the same direction as the uniform flow velocity. The wavelength in the axial direction is almost the same as the transverse wavelength in the Kármán vortex street in figure 11 (plate 4).

Thus, it is seen that the outer layer with Görtler vortices separates from the inner layer circulating with the rotating cylinder, so that the Kármán vortex street is formed with the transverse periodicity due to the Görtler vortices.

These experiments were carried out at the Department of Precision Engineering, Gifu University, Japan (Matsui 1977).

2.3 *Twin vortices, the secondary twin vortices and wall vortex in the flow around an impulsively started circular cylinder*

When a circular cylinder suddenly began to move with a constant velocity between two parallel flat plates, the flow around the cylinder was visualized in water by the electrolysis method and the aluminium powder method at the same time. The flow pattern at $Re = 780$ is shown in figure 14 (plate 6) when the blockage ratio, d/h , is 0.07, d denoting the cylinder diameter and h the distance between the two flat plates. In this case, a ring of babbitt metal (tin alloy for bearings) of 2 mm width was set flush to the cylinder surface, and worked as an anode generating a white streak of

metallic ion. At the first stage of motion, twin vortices can be seen behind the cylinder. In the figure, the non-dimensional time, Ut/d , is denoted by τ . At later stages of motion, the secondary twin vortices appear near the stagnation points. The secondary twin vortices cannot be observed at Reynolds numbers lower than 500.

At Reynolds numbers higher than 500, the circulation of the primary twin vortices is stronger than that at lower Reynolds numbers so that the reverse flow to the separation point occurs at the second separation point downstream of the original one due to the increased pressure gradient on the surface. This results in the generation of a separation vortex, which induces another vortex of counter rotation. Thus, the secondary twin vortices are formed near but downstream of the original separation point, and a stagnation point on the surface appears between the original separation point and the second one. Another stagnation point in the fluid is at the intersecting point of two dividing streamlines, each emanating from the separation points.

The white streak line separating from the cylinder surface was continuous at Reynolds numbers lower than 1000. At $Re = 1220$, however, the shedding of the streak line was not continuous, but intermittent as seen in figure 15 (plate 6). Shedding of the streak line is completely stopped as seen in figure 15 b (plate 6) and began again as seen in figure 15c (plate 6). During the break in shedding, the streak lines both from the upstream boundary layer and the reverse flow go into the secondary twin vortices. Several intermittent breaks in shedding were observed at Reynolds numbers higher than 1500. The mechanism of this phenomenon is not clear for the present; however, a possible explanation is given below.

White streak lines come from the upstream boundary layer and from the reverse flow boundary layer, and carry the vorticity in the boundary layers with them. At Reynolds numbers lower than 1000, the intensity of the vortex formed by the reverse flow separation is rather weak. In compensation, therefore, the vorticity carried from the upstream boundary layer is excessively strong so as to make the secondary twin vortices of equal strength. The excess vorticity in the separated shear layer is continuously shed to the primary twin vortices. At higher Reynolds numbers, however, there is no excess vorticity, as the intensity of the vortex formed by the reverse flow separation is increased. Then, the vorticity in the separated shear layer from the upstream boundary layer is necessary to be supplied to the secondary twin vortices until they are established. During this period, the shedding of the streak line is stopped. After the secondary twin vortices are established, the streak line is shed again.

When the distance between two parallel flat plates decreases or the blockage ratio d/h increases, the separation of the flow along the plate was observed as shown in figure 16 (plate 7) where $Re = 1000$ and $d/h = 0.63$. In this case, the twin vortices behind the cylinder have a greater influence on the pressure distribution on the flat plate walls than in the case of a small blockage ratio. The increased adverse pressure gradient causes the separation of the flow along the wall, resulting in the formation of a vortex on the wall, which is called a "wall vortex". The cylinder advances further, and the wall vortex is left behind. Thus, the secondary wall vortex is formed between the cylinder and the primary wall vortex. In figure 16 (plate 7) the secondary vortex can be seen in front of the primary one. These wall vortices, in turn, influence the flow around the cylinder, which can be seen when figure 16 is compared with figures 14 and 15.

In a steady flow, the separation of a boundary layer occurs at the point on a solid surface where the velocity gradient normal to the surface is zero, and a reverse flow

takes place downstream of the separation point, the boundary layer flow breaking away from the surface. Thus, "separation causes the vorticity to 'penetrate' from the boundary layer into the fluid," as described by Landau & Lifshitz (1950, p. 151).

In the present case of a circular cylinder which is impulsively started, a different phenomenon was observed as shown in figure 17 (plate 7). In this figure, the flow pattern near the so-called separation point was visualized both by the hydrogen bubble method and by the electrolysis method. In the flow pattern shown by the time lines of hydrogen bubbles, a reverse flow can be clearly observed in the boundary layer on the rear surface of the cylinder. Nevertheless, in the flow pattern obtained by the electrolysis method, penetration of the vorticity from the boundary layer into the fluid cannot be observed, because the white streak line does not break away from the surface. In this case, in spite of the occurrence of a reverse flow in the boundary layer, we can say that the separation does not occur. In other words, a reverse flow does not always accompany separation in an unsteady flow. Here the description by Batchelor (1967, p. 327) should be cited: "despite the ubiquity of boundary layer separation, and the great importance of its consequences for the flow as a whole, a proper understanding of the phenomena and an analytical description of it have not yet been achieved".

These experiments were carried out by Nagata *et al* (1975, 1978) at the Department of Precision Engineering, Gifu University, Japan.

3. Vortex ring

3.1 *Mutual slip-through of a pair of vortex rings*

It is stated in many textbooks that when two nearly identical vortex rings move along a common axis of symmetry, owing to their mutual interaction, the rearward ring can pass through the forward ring. Recently, experimental results, which did not agree with textbook description, were published, and since then the possibility of the mutual slip-through of vortex rings has been doubted.

On inspection of the experimental results published so far, it was found that the Reynolds numbers in the reported experiments were lower than 600, based on the initial velocity of translation of the vortex ring and the diameter of the orifice. It is suspected that in those experiments the cores of ring vortices contact with each other during slip-through due to the small Reynolds numbers. At higher Reynolds numbers, it may be expected that the cores would not contact with each other but the two vortex rings could touch in the potential flow region so that they may accomplish their mutual slip-through without the effect of viscosity. Therefore, an experiment was carried out at $Re = 1600$ by using air as a working fluid and the flow pattern was visualized by the smoke-wire technique. The result is shown in figure 18 (plate 8). As seen in the figure, the mutual slip-through is accomplished once, but the two vortex rings coalesce during the second slip-through. Recently, slips-through of several times were successfully achieved in by Claus (1978).

3.2 *Interference of a vortex ring and a plane boundary*

When a vortex ring comes into the vicinity of a plane boundary perpendicular to the axis of the vortex ring, two interesting phenomena can be observed. One is the

rebound of the vortex ring from the plane boundary, and the other is the generation of the secondary vortex ring. As seen in figure 19 (plate 9), a vortex ring travels upward to a plane boundary. On the plane surface, an outward flow is induced by the vortex ring, and it experiences an adverse pressure gradient caused by the vortex ring. When the vortex ring approaches the plane surface, the outward flow separates from the surface due to the increased adverse pressure gradient. The separated shear layer prevents the vortex ring from increasing its diameter due to the image of the vortex ring with respect to the plane surface. The vortex ring almost stops increase in its diameter and goes down away from the surface. This is the phenomenon of rebound.

At the same time, concentration of vorticity in the separated shear layer generates a secondary vortex ring circulating in a direction opposite that of the main ring. The secondary ring goes around and comes inside the main ring as seen in the figure.

It is interesting to note that the separation of the flow along a plane boundary, the generation of the secondary twin vortices near the upstream separation point on a circular cylinder impulsively started, and the generation of a wall vortex, share the same cause, namely, the pressure gradient induced by the primary vortex on a solid surface.

The experiments on vortex rings were carried out by Yamada & Matsui (1978, 1979, 1980) at the Nagoya Institute of Technology.

4. Conclusion

4.1 *Kármán vortex street*

The actual vortices in a Kármán vortex street have cores of finite dimension, increasing downstream, due to viscosity. The distance between two vortex rows increases downstream. The circulation of a vortex is nearly constant.

4.2 *The flow around a rotating cylinder*

In the flow around a circular cylinder rotating with a peripheral velocity greater than twice the velocity of a uniform flow in the pure Kármán vortex range of Reynolds number, (i) Taylor vortices appear in the layer circulating with the cylinder, (ii) Görtler vortices appear in the layer outside the circulating layer, which separates from the circulating layer, at a separation point in the fluid, not on the cylinder surface, and results in the Kármán vortex street, (iii) the Görtler vortices make a transverse periodicity in the Kármán vortex street.

4.3 *The flow around a circular cylinder impulsively started*

In the unsteady flow around a circular cylinder impulsively started, twin vortices appear behind the flow, and they induce the secondary twin vortices near the separation point. They also induce wall vortices on the side walls of a channel.

At the beginning of this unsteady flow, separation does not always occur even when a reverse flow occurs in the boundary layer.

4.4 Vortex rings

Mutual slip-through of a pair of vortex rings was successfully achieved by increasing the Reynolds number. When a vortex ring approaches a plane boundary, the separation of the boundary layer flow on the plane surface causes the rebound of the vortex ring and generation of a secondary vortex ring.

The vortex phenomena mentioned above can be easily observed by flow visualization, but may be rather difficult to see by using the hot-wire technique.

References

- Batchelor G K 1967 *An introduction to fluid dynamics* (Cambridge: University Press)
- Claus H H 1978 Max-Planck-Institut für Strömungsforschung Bericht 26, Göttingen
- Colak-Antic P & Hassler H 1971 Deutsche Forschungs-und Versuchsanstalt für Luft-und Raumfahrt (DFVLR) Nachrichten Heft 5, p. 184
- Landau L D & Lifshitz E M 1950 *Fluid mechanics* (Oxford, New York : Pergamon Press)
- Matsui T 1977 *Proc. EUROMECH 90 Colloquium on techniques of wall measurements in fluid mechanics* (Laboratoire D'Energetique et de Mechanique theorique et Applique, Institut National Polytechnique de Lorraine, Nancy, France) VI b-2
- Nagata H, Kakehi Y, Tsunekawa M & Hasegawa K 1975 *Trans. Jpn Soc. Mech. Eng.* **41** 161
- Nagata H, Minami K & Murata Y 1978 *Trans. Jpn Soc. Mech. Eng.* **44** 2672
- Yamada H & Matsui T 1978 *Phys. Fluids* **21** 292
- Yamada H & Matsui T 1979 *Phys. Fluids* **22** 1245
- Yamada H & Matsui T 1980 *Preprints 2nd Int. Symp. Flow. Visualization* (Ruhr Universität, Institut für Thermo-und Fluidodynamik, Bochum) p. 518
- Matsui T & Okude M 1980 *Abstracts 15th ICTAM* (Toronto: University of Toronto) p. 73

Plate 1

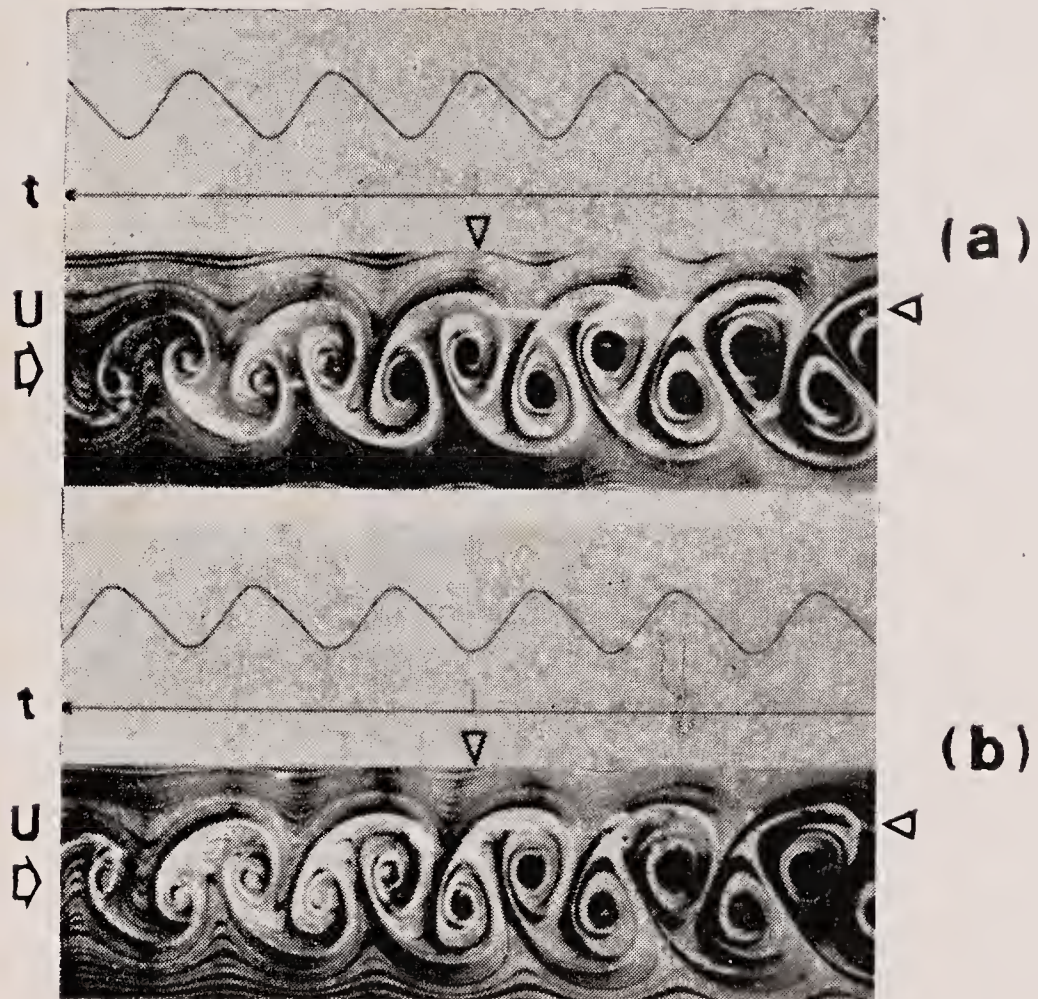


Figure 2. Comparison of the hot-wire signals with its location in the flow pattern at $x/d = 20$ and $Re = 140$. $y/d = 2.0$, in the outer part of a wake.

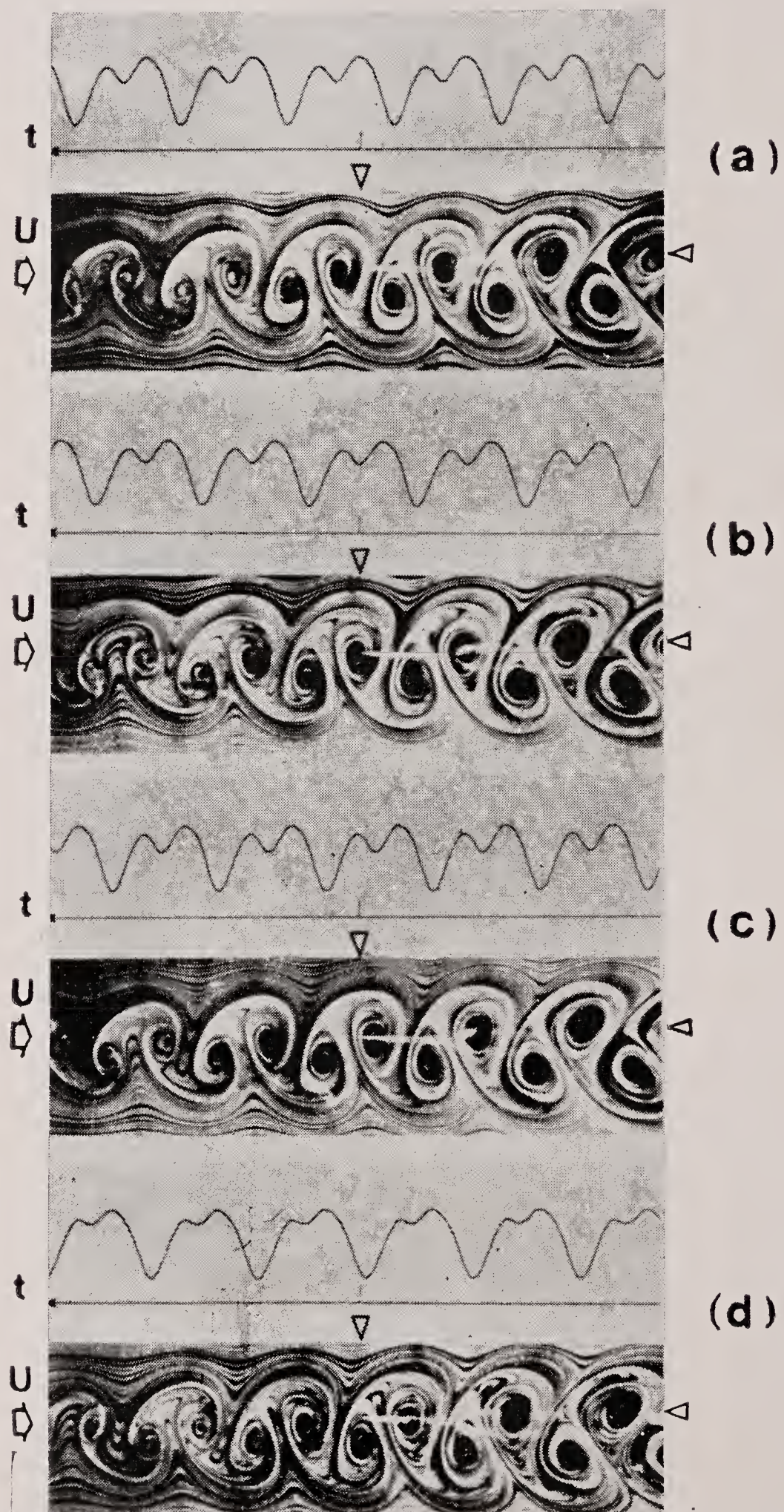


Figure 3. Comparison of the hot-wire signals with its location in the flow pattern at $x/d = 20$ and $Re = 140$, $y/d = 0.67$ on the centre line of the upper vortex row.

Plate 3

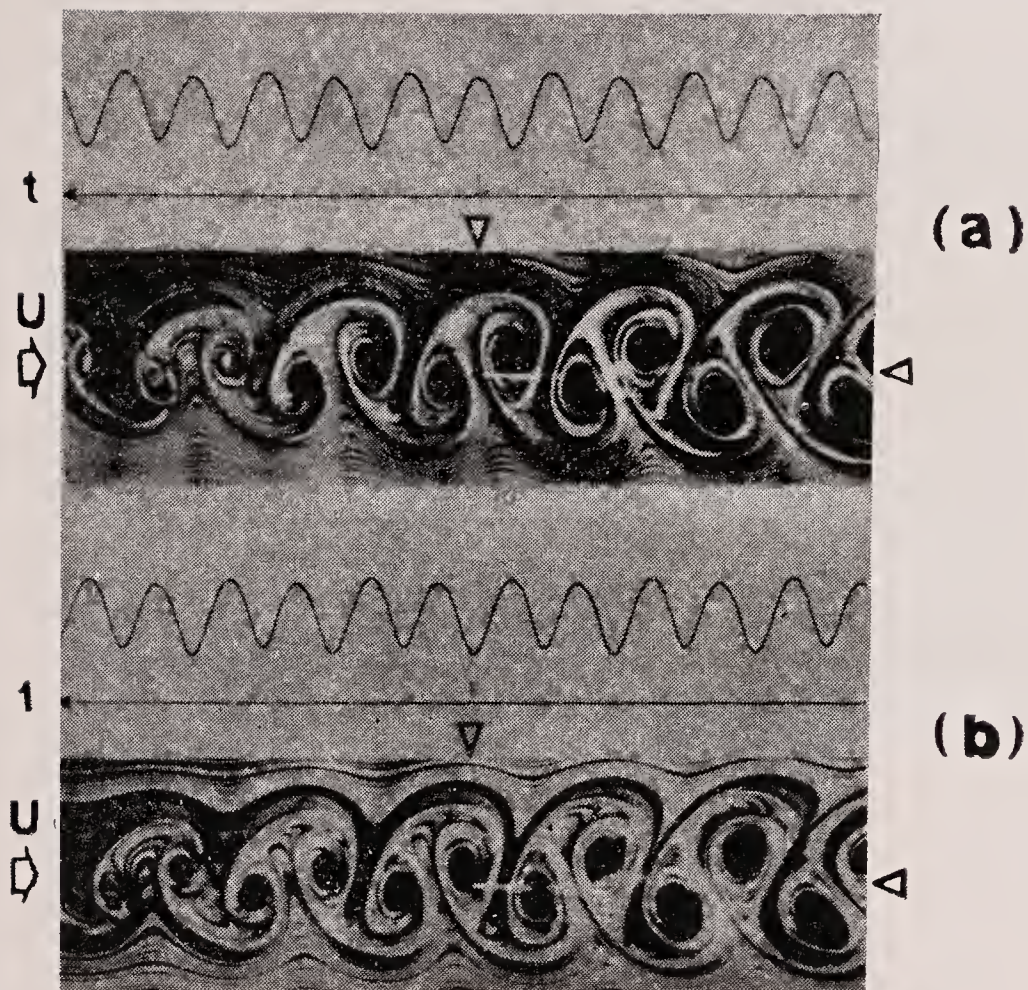


Figure 4. Comparison of the hot-wire signals with its location in the flow pattern at $x/d = 20$ and $Re = 140$. $y/d = 0$ on the centre line of a wake.

2nd smoke wire
 ↓
 ($x/d = 20$)

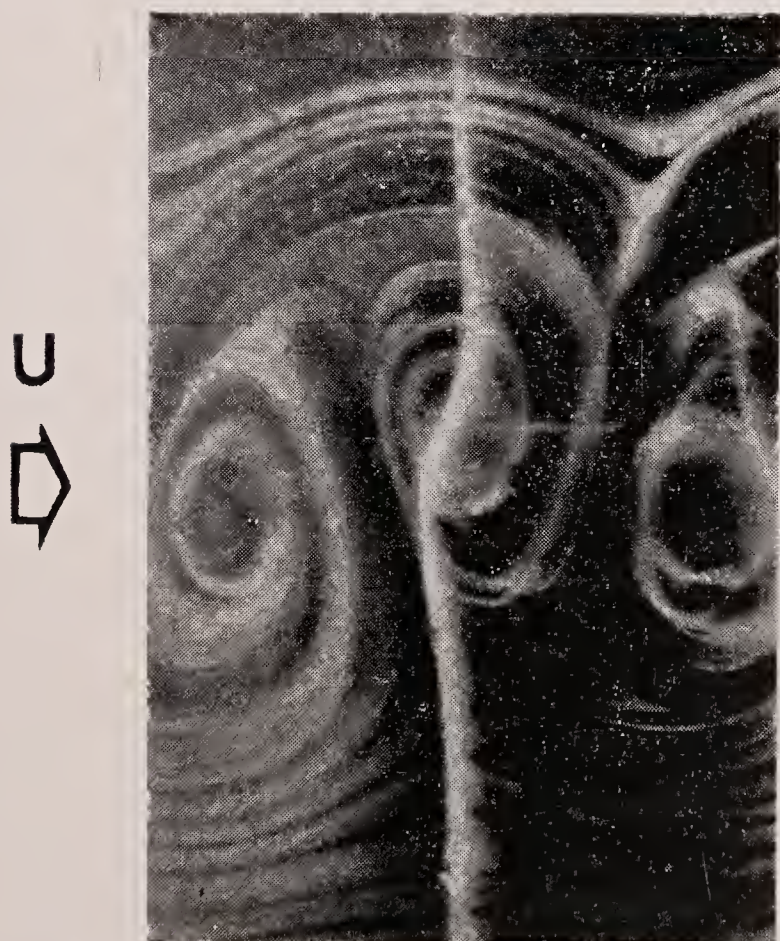


Figure 5. Vortex core.

Plate 4

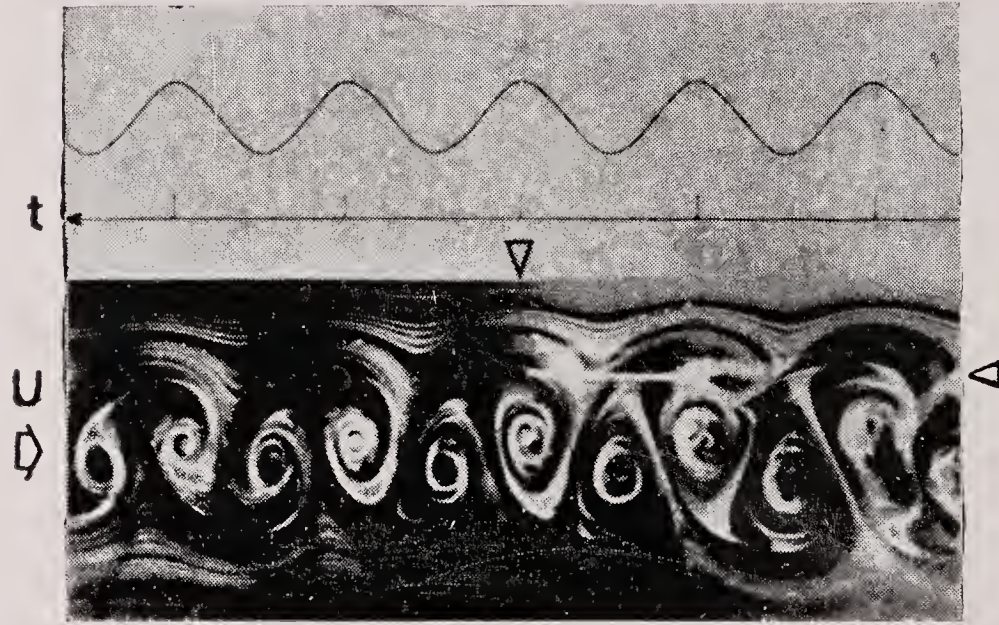


Figure 6. Flow pattern by multi-exposure at $Re = 140$.

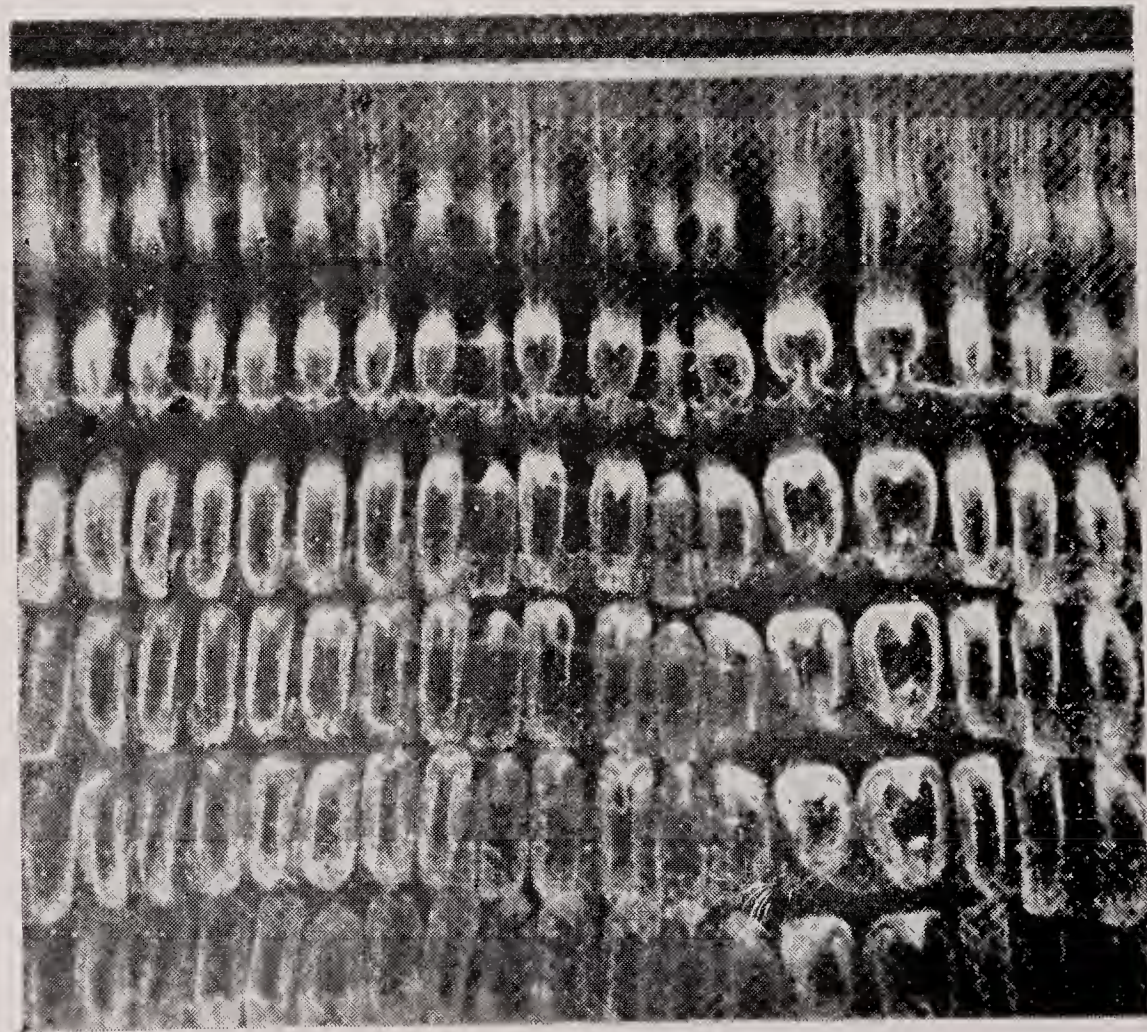


Figure 11. Wake of a circular cylinder rotating in a uniform flow, $d = 10$ mm
 $U = 2.78$ cm/s, $U_p/U = 2.4$ and $Re = 214$.

Plate 5

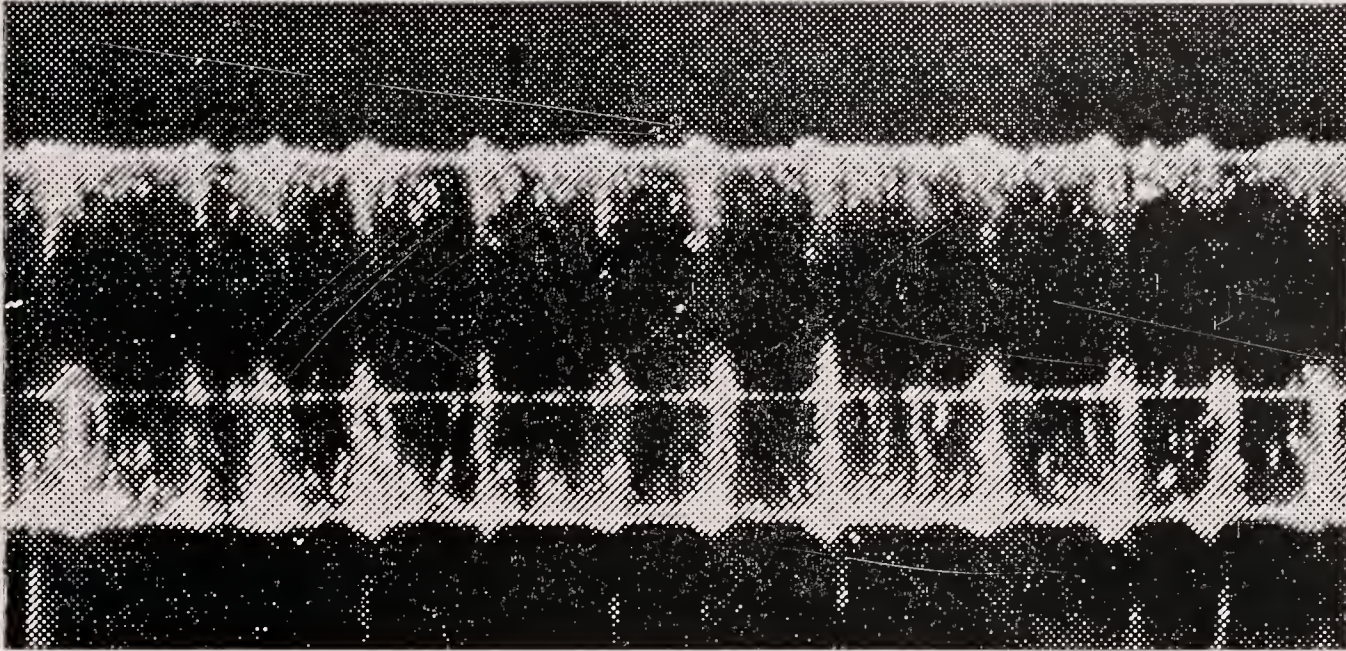


Figure 12. Taylor vortices in the circulating layer. $d = 10$ mm, $U = 3.1$ cm/s, $U_p/U = 2.2$, $Re = 238$.

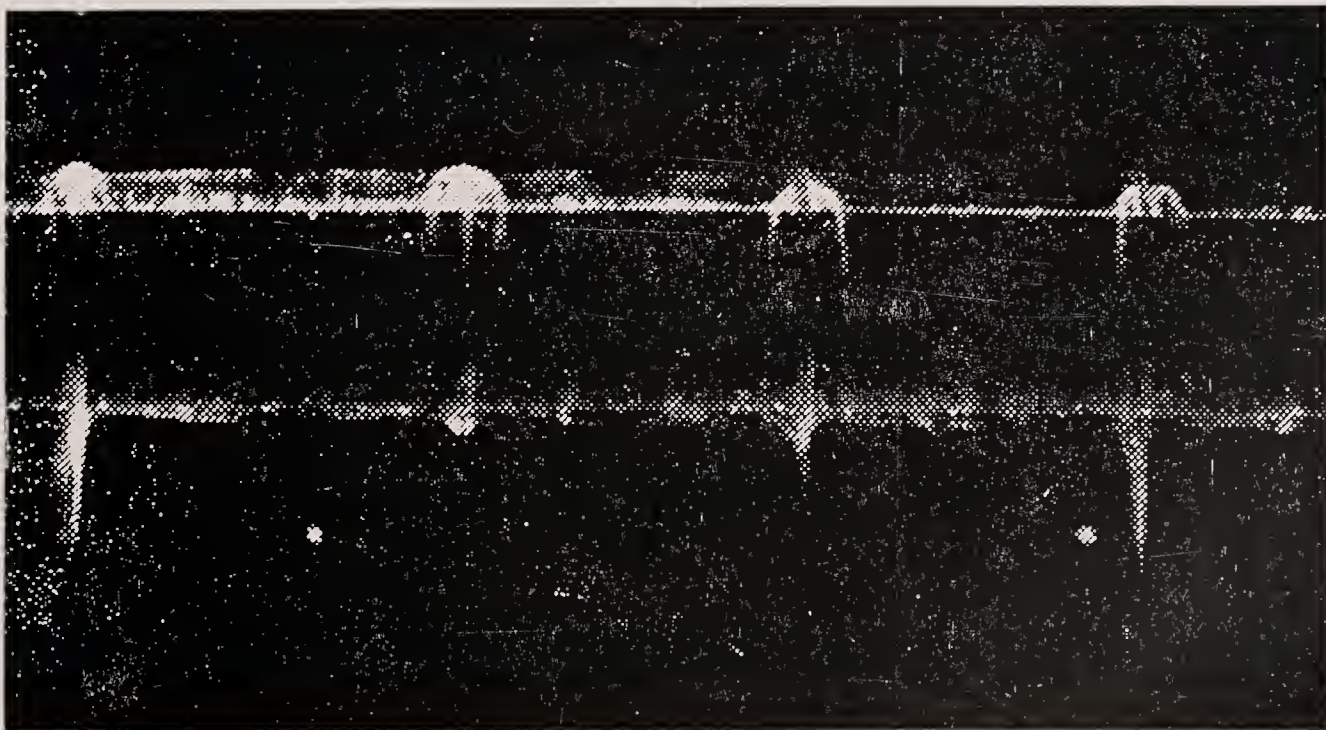


Figure 13. Görtler vortices in the outer layer. $d = 10$ mm, $U = 3.1$ cm/s, $U_p/U = 2.2$, $Re = 238$.

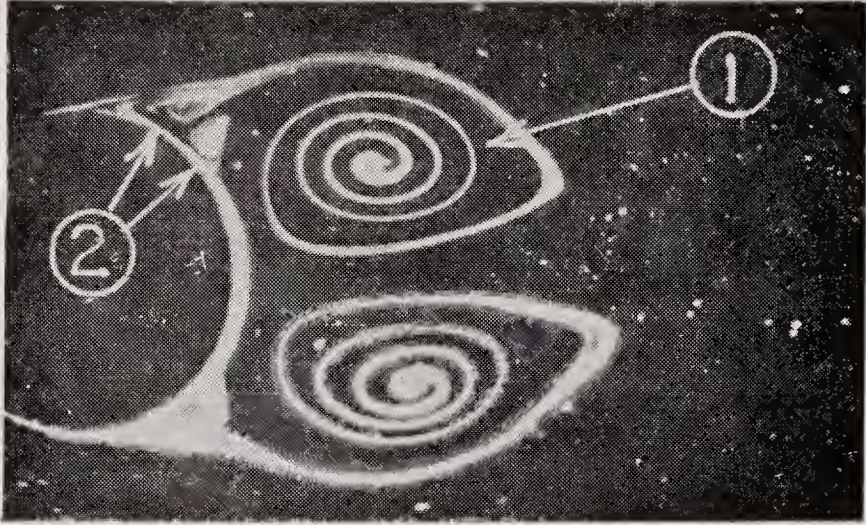


Figure 14. Secondary twin vortices
 $Re = 780$, $d/h = 0.07$, $\tau = 4.6$.

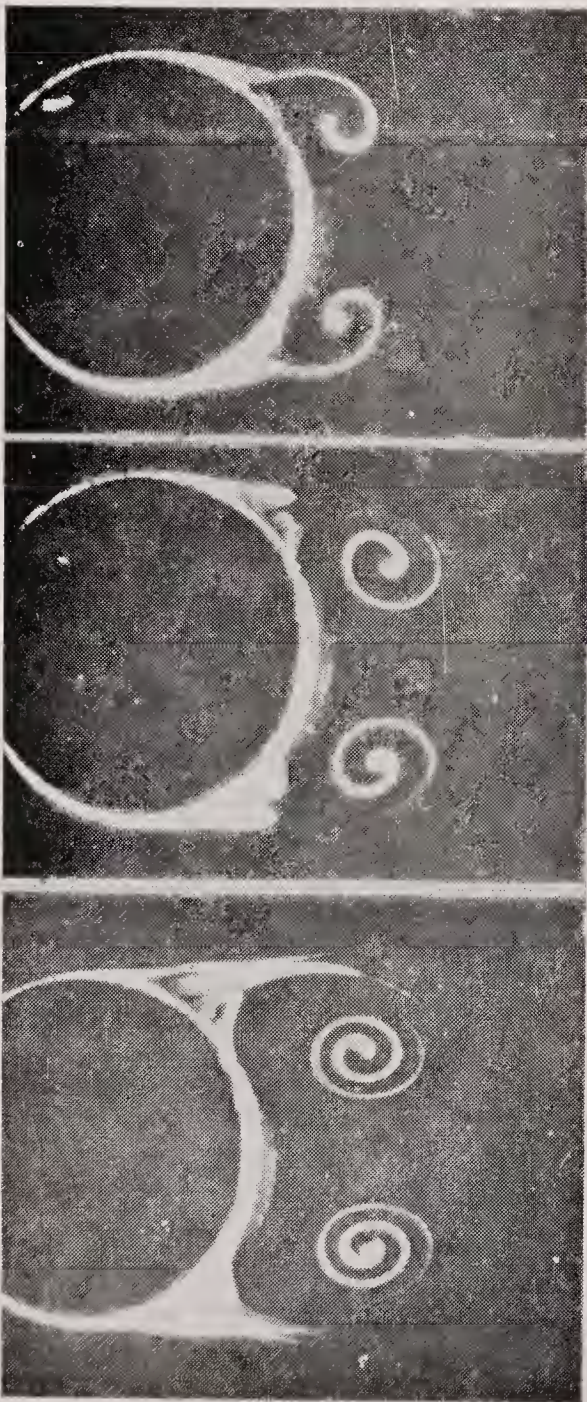


Figure 15. Intermittent shedding of streak lines.
 $Re = 1220$, $d/h = 0.07$.

Plate 7

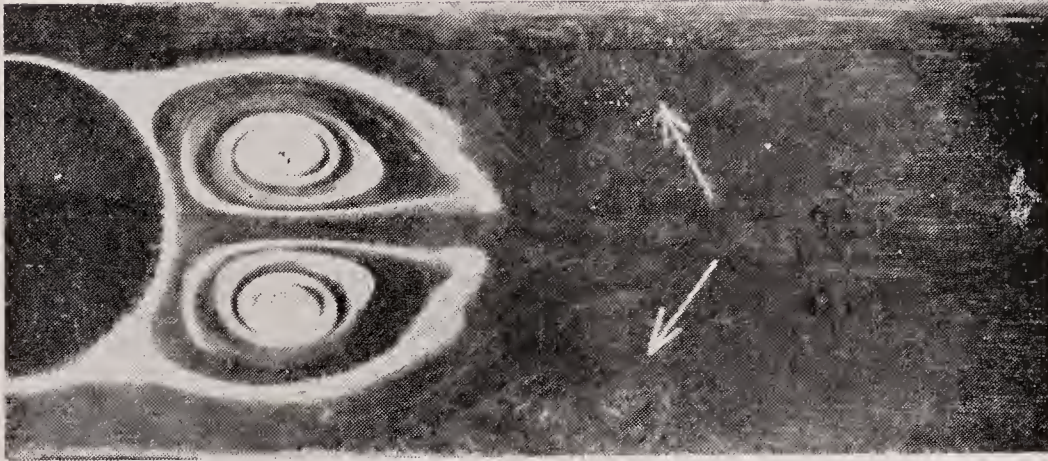


Figure 16. Development of wall vortex. $Re = 1000$, $d/h = 0.63$.

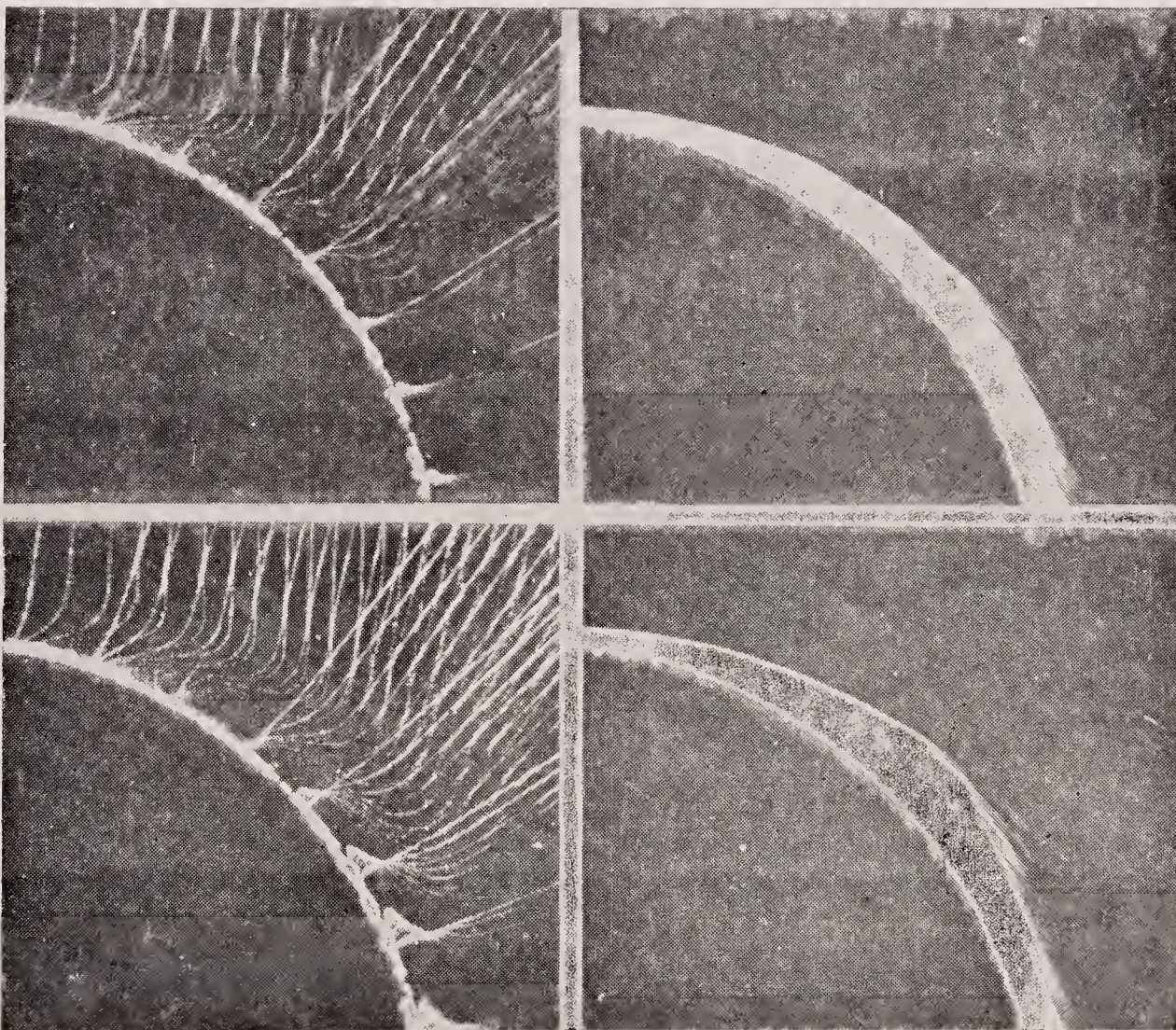


Figure 17. Reverse flow in the boundary layer. $Re = 1000$.

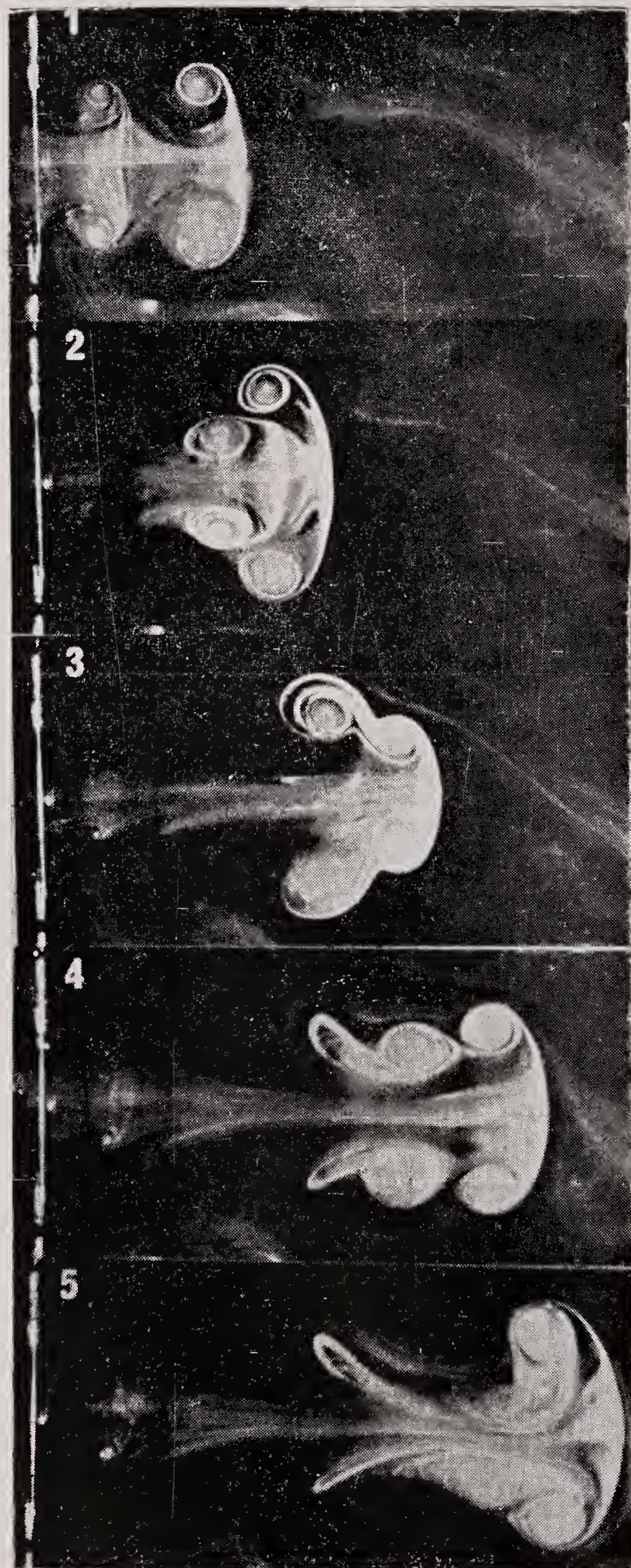


Figure 18. Mutual slip-through of a pair of vortex rings.

Plate 9

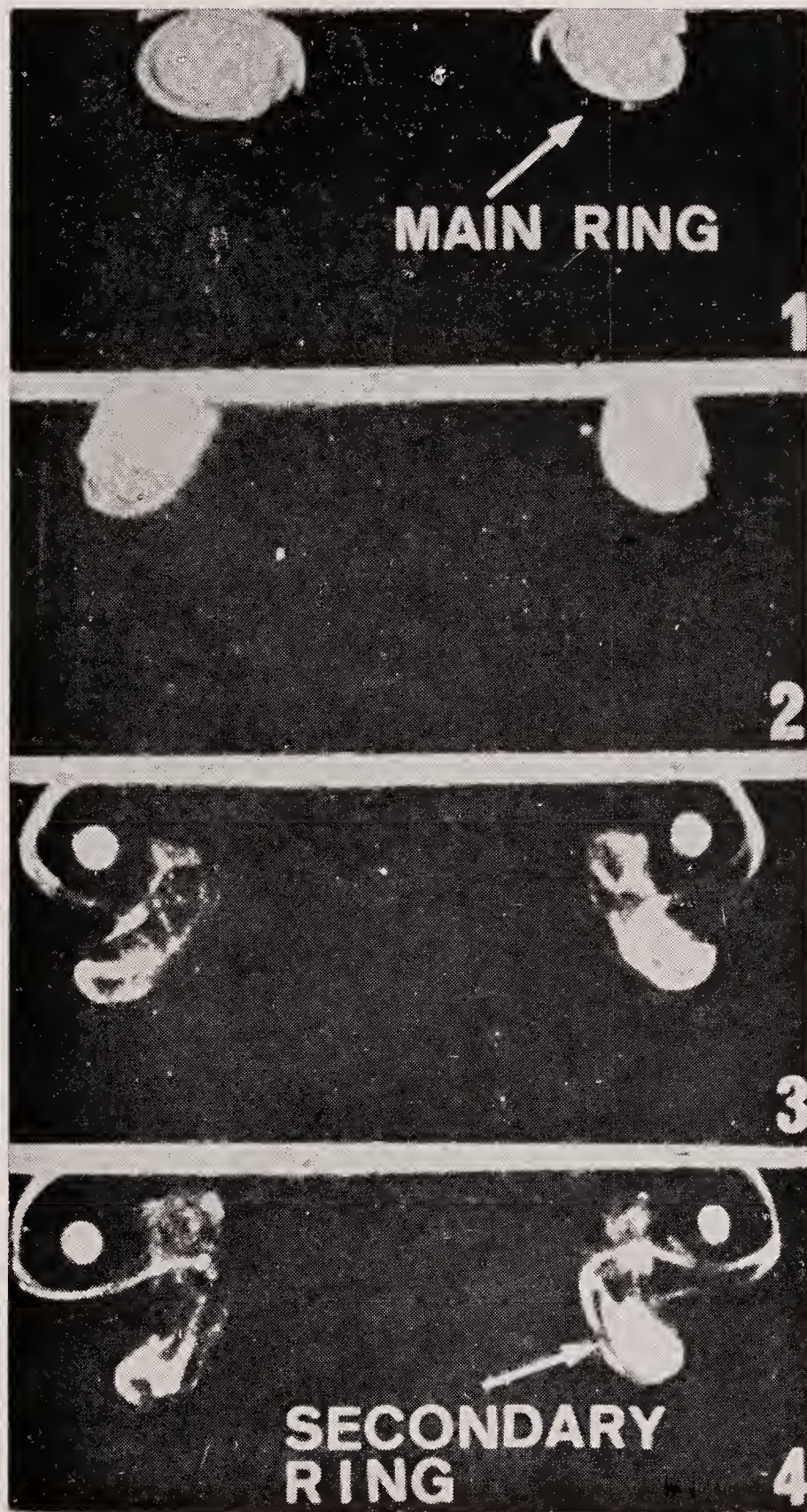


Figure 19. Interaction of a vortex ring and a plane boundary.

On finite amplitude water waves

G B WHITHAM

Department of Applied Mathematics, California Institute of Technology, Pasadena, California 91125, USA

MS received 3 February 1981

Abstract. The modulation theory for finite amplitude water waves is developed using the variational technique. It is shown how Levi-Civita's relation, Starr's relation and the conservation equations all follow very simply and naturally from this approach. The present paper is limited to deep water waves, but the results can be extended to arbitrary depth. For deep water, the appropriate Lagrangian can be reduced to a single function, which can be taken from recent numerical calculations on periodic waves. This is used to discuss the stability of wavetrains to long modulations.

Keywords. Water waves; nonlinear waves; variational methods.

1. Introduction

In water waves, due to the complexity of the problem, the modulation theory of wave-trains has usually been applied only to the small amplitude, nearly linear case. In this paper the full finite amplitude theory is formulated and used to study various questions. We shall restrict the discussion to deep water waves, but extensions to arbitrary depth can be made.

The modulation theory can be derived in concise form *via* an appropriate variational principle, and the equations are then found in terms of the corresponding Lagrangian (see Whitham 1974). In outline the method is as follows.

If $L\{\phi\}$ is the Lagrangian for a dependent variable $\phi(x, t)$, and the system admits periodic solutions in which ϕ is a periodic function f of a phase $\theta(x, t)$ and an amplitude parameter a , *i.e.*

$$\phi = f(\theta; a), \quad (1)$$

then the modulation equations for

$$k = \theta_x, \quad \omega = -\theta_t, \quad a \quad (2)$$

can be derived from the variational principle

$$\delta \iint \mathcal{L}(\omega, k, a) dx dt = 0, \quad (3)$$

where
$$\mathcal{L}(\omega, k, a) = \frac{1}{2\pi} \int_0^{2\pi} L\{\phi\} d\theta. \quad (4)$$

The Euler equations for variations δa and $\delta\theta$ respectively are

$$\delta a : \mathcal{L}_a = 0, \quad (5)$$

$$\delta\theta : \frac{\partial}{\partial t} \mathcal{L}_\omega - \frac{\partial}{\partial x} \mathcal{L}_k = 0, \quad (6)$$

and we add the equation between k and ω , obtained by eliminating θ :

$$\frac{\partial k}{\partial t} + \frac{\partial \omega}{\partial x} = 0. \quad (7)$$

Equation (5) gives the dispersion relation

$$\omega = \omega(k, a); \quad (8)$$

then (6) and (7) can be viewed as a pair of equations for a and k .

We shall be interested in conservation equations, so we note here that the energy equation is

$$\frac{\partial}{\partial t} (\omega \mathcal{L}_\omega - \mathcal{L}) + \frac{\partial}{\partial x} (-\omega \mathcal{L}_k) = 0, \quad (9)$$

and the momentum equation is

$$\frac{\partial}{\partial t} (k \mathcal{L}_\omega) + \frac{\partial}{\partial x} (\mathcal{L} - k \mathcal{L}_k) = 0. \quad (10)$$

These can be verified directly from (5)–(7), but may be obtained more significantly from Noether's theorem applied to (3).

2. The average Lagrangian for deep water waves

For water waves the Lagrangian involves two functions: the velocity potential $\phi(x, y, t)$, and the height of the free surface $y = \eta(x, t)$. The Lagrangian is

$$L = - \int_{-\infty}^{\eta} (\phi_t + \frac{1}{2} \phi_x^2 + \frac{1}{2} \phi_y^2) dy - \frac{1}{2} g \eta^2. \quad (11)$$

For waves periodic in x and t , with a phase function $\theta(x, t)$, we write

$$\phi = \Phi(\theta, y), \quad \eta = \eta(\theta). \quad (12)$$

These are to be substituted in (11), with wave number $k = \theta_x$ and frequency $\omega = -\theta_t$, as before, then (11) is integrated from $\theta = 0$ to $\theta = 2\pi$, in accordance with (4). We shall use the notation

$$\langle F \rangle = \frac{1}{2\pi} \int_0^{2\pi} F d\theta \quad (13)$$

for any quantity F .

We have

$$\bar{L} = \langle L \rangle = \omega I - T - V, \quad (14)$$

where
$$I = \left\langle \int_{-\infty}^{\eta} \Phi_{\theta} dy \right\rangle, \quad (15)$$

$$T = \frac{1}{2} k^2 \left\langle \int_{-\infty}^{\eta} \Phi_{\theta}^2 dy \right\rangle + \frac{1}{2} \left\langle \int_{-\infty}^{\eta} \Phi_y^2 dy \right\rangle, \quad (16)$$

$$V = \frac{1}{2} g \langle \eta^2 \rangle. \quad (17)$$

This gives one form of the average Lagrangian, but no amplitude parameters have been introduced as yet, so we denote it by \bar{L} and reserve the symbol \mathcal{L} for later forms.

Clearly T and V are the kinetic and potential energies. As regards the quantity I , we note that in the Euler equation (6), which still applies to \bar{L} ,

$$\bar{L}_{\omega} = I. \quad (18)$$

This identifies it as the wave action density, the analogue of the adiabatic invariant in mechanics. We also note that its companion flux is

$$-\bar{L}_k = k \left\langle \int_{-\infty}^{\eta} \Phi_{\theta}^2 dy \right\rangle. \quad (19)$$

From (14)–(16), the energy density in (9) is

$$\omega \bar{L}_{\omega} - \bar{L} = T + V, \quad (20)$$

so this checks. The momentum density in (10) is

$$k \bar{L}_{\omega} = k I. \quad (21)$$

This can also be seen directly, since the momentum density is

$$\left\langle \int_{-\infty}^{\eta} \phi_x dy \right\rangle; \quad (22)$$

the result follows from (15) and $\theta_x = k$. In the water wave problem then, I is also proportional to the momentum density.

3. Solution of Laplace's equation and the Lagrangian

Since $\phi(x, y, t)$ satisfies Laplace's equation, and therefore $\Phi(\theta, y)$ satisfies

$$k^2 \Phi_{\theta\theta} + \Phi_{yy} = 0, \quad (23)$$

we can specialize the above expressions to solutions of this equation. To do this, we take Fourier series

$$\Phi(\theta, y) = \frac{\omega}{k^2} \sum_1^{\infty} \frac{A_n}{n} \exp(nky) \sin n\theta, \quad (24)$$

$$\eta(\theta) = \frac{1}{k} \sum_1^{\infty} a_j \cos j\theta. \quad (25)$$

The coefficients A_n , a_n are left arbitrary in this choice. The only restriction introduced is that the class of Φ 's considered in the variational principle are all solutions of Laplace's equation (23); the variations of $\Phi(\theta, y)$ and $\eta(\theta)$ will now be made through variations of the coefficients \mathbf{A} and α .

The placing of the k and ω in the choice of parameters is intriguing, since in applying the variational arguments, different forms of the same quantity can be obtained. In at least one instance, this leads to a nontrivial identity (see Starr's identity in § 5 below).

When (24) and (25) are substituted in (14)–(17), the Lagrangian becomes

$$\mathcal{L}(\omega, k, \mathbf{A}, \alpha) = \frac{\omega^2}{k^3} \mathcal{J} - \frac{\omega^2}{k^3} \mathcal{T} - \frac{g}{k^2} \mathcal{V}, \quad (26)$$

where* $\mathcal{J} = v_n A_n$, $\mathcal{T} = \frac{1}{2} \mu_{mn} A_m A_n$, $\mathcal{V} = \frac{1}{4} a_j^2$, (27)

and v_n , μ_{mn} are functions of α only, given by

$$v_n = \left\langle \frac{\exp [nP(\theta)]}{n} \cos n\theta \right\rangle, \quad (28)$$

$$\mu_{mn} = \left\langle \frac{\exp [(m+n)P(\theta)]}{m+n} \cos (m-n)\theta \right\rangle, \quad (29)$$

with $P(\theta) \equiv k\eta(\theta) = \sum_1^{\infty} a_j \cos j\theta$. (30)

Although the functions of α in v_n and μ_{mn} are complicated, the dependence on ω , k and \mathbf{A} in (26)–(27) is extremely simple. It is noted that

$$I = \frac{\omega}{k^3} \mathcal{J}, \quad T = \frac{\omega^2}{k^3} \mathcal{T}, \quad V = \frac{g}{k^2} \mathcal{V}, \quad (31)$$

where \mathcal{J} , \mathcal{T} , \mathcal{V} are functions of \mathbf{A} and α only.

*Here and elsewhere, the summation convention is used. It should be clear where summation is intended and where not. For example, in (28) and (29), it is not.

4. The I, T identity

The variational equations deduced from (26) include

$$\mathcal{L}_{A_n} = 0. \quad (32)$$

From (27), this gives

$$v_n = A_m \mu_{mn}. \quad (33)$$

Re-substituting this relation in \mathcal{J} and \mathcal{T} , we have

$$\mathcal{J} = 2\mathcal{T}, \quad (34)$$

and therefore

$$I = 2T/\omega. \quad (35)$$

This identity, in the form momentum density $kI = 2T/c$, is attributed to Levi-Civita. It is usually established by manipulating the various relations in the boundary value problem for ϕ and η . It is interesting that it drops out here immediately and just reflects the fact that I is linear in the A 's and T is quadratic.

The relation (34) may be inserted back in (26) to obtain

$$\mathcal{L}(\omega, k, \alpha) = \frac{\omega^2}{k^3} \mathcal{T}(\alpha) - \frac{g}{k^2} \mathcal{V}(\alpha), \quad (36)$$

where now it is to be understood that (33) is used to eliminate the A 's. This form of the Lagrangian is the familiar $T - V$ of classical mechanics.

5. Starr's identity

A second identity is obtained merely from the different forms of \bar{L} and \mathcal{L} . Since \bar{L}_k and \mathcal{L}_k must be the same quantity, the expression (19) for $-\bar{L}_k$ must be equal to

$$-\mathcal{L}_k = \frac{3\omega^2}{k^4} \mathcal{T} - \frac{2g}{k^3} \mathcal{V}. \quad (37)$$

If C and S denote the horizontal and vertical contributions to the kinetic energy, (19) is $2C/k$ and the identity is

$$2C = 3T - 2V; \quad (38)$$

this can also be written

$$C + 3S = 2V. \quad (39)$$

This was obtained by Starr (1947), again by manipulating the expressions in the boundary value formulation.

In terms of the forms (27), the relation would read

$$\frac{\omega^2}{gk} (\mathcal{C} + 3\mathcal{S}) = 2\mathcal{V}, \quad (40)$$

where $\mathcal{C} = \frac{1}{2} \gamma_{mn} A_m A_n$, $\mathcal{S} = \frac{1}{2} \sigma_{mn} A_m A_n$, (41)

$$\gamma_{mn} = \left\langle \frac{\exp [(m+n)P(\theta)]}{m+n} \cos m\theta \cos n\theta \right\rangle, \quad (42)$$

$$\sigma_{mn} = \left\langle \frac{\exp [(m+n)P(\theta)]}{m+n} \sin m\theta \sin n\theta \right\rangle, \quad (43)$$

$$\mu_{mn} = \gamma_{mn} + \sigma_{mn}. \quad (44)$$

Just as the I, T relation comes from the A variations of \mathcal{L} , one might expect an analogous relation from the α variations. In the form (36),

$$\mathcal{L}_{\alpha_j} = 0 \quad (45)$$

implies $\frac{\omega^2}{k^3} \frac{\partial \mathcal{J}}{\partial \alpha_j} = \frac{1}{2} \frac{g}{k^2} \alpha_j$. (46)

Therefore, $\frac{\omega^2}{gk} \alpha_j \frac{\partial \mathcal{J}}{\partial \alpha_j} = 2\mathcal{V}$. (47)

Clearly, this must be another form of Starr's relation. The equivalence of (40) and (47) would require

$$\alpha_j \frac{\partial \mathcal{J}}{\partial \alpha_j} = \mathcal{C} + 3\mathcal{S}. \quad (48)$$

This may also be written, perhaps more suggestively, as

$$\alpha_j \frac{\partial \mathcal{J}}{\partial \alpha_j} - \mathcal{J} = 2\mathcal{S}. \quad (49)$$

A direct proof of this identity, using only the quadratic forms defined in (27) and (41), and the relation (33), has not yet been found.

6. Energy, momentum, action

The conservation equations of energy and momentum have been much discussed in the recent literature. Here we note that they follow immediately from the

Lagrangian (36). The energy equation is given in (9), the momentum equation in (10), and we note also the wave action quantities in (6). In the list, we add the usual form of the corresponding quantities for linear theory. In both cases $c = \omega/k$ denotes the phase velocity; in the linear results, $C = \frac{1}{2}c$ denotes the group velocity.

	<i>Nonlinear</i>	<i>Linear</i>
<i>Energy</i>		
Density	$\omega \mathcal{L}_\omega - \mathcal{L} = T + V$	$T + V = E$
Flux	$-\omega \mathcal{L}_k = c(3T - 2V)$	CE
<i>Momentum</i>		
Density	$k \mathcal{L}_\omega = 2T/c$	E/c
Flux	$\mathcal{L} - k \mathcal{L}_k = 4T - 3V$	$C(E/c)$
<i>Action</i>		
Density	$\mathcal{L}_\omega = 2T/\omega$	E/ω
Flux	$-\mathcal{L}_k = (3T - 2V)/k$	$C(E/\omega)$

In linear theory, \mathfrak{T} and \mathfrak{V} are just proportional to α_1^2 . Therefore, from $\mathcal{L}_{\alpha_1} = 0$, the stationary value of \mathcal{L} is zero. Hence,

$$T = V. \quad (50)$$

This relation and the relation $C = \frac{1}{2}c$ show how the nonlinear results reduce to the linear ones in the limit.

It is interesting that the odd combinations of T and V , especially in the expressions for the fluxes, merely reflect the powers of ω and k in (36). Those powers in turn come from little more than dimensional analysis.

It may also be noted that in any system, where

$$\mathcal{L} = T - V, \quad \omega \mathcal{L}_\omega - \mathcal{L} = T + V, \quad (51)$$

we always have

$$\mathcal{L}_\omega = 2T/\omega, \quad k \mathcal{L}_\omega = 2T/c; \quad (52)$$

These are independent of the k dependence in (36).

7. A reduced form for the Lagrangian

In principle, all but one of the variational equations

$$\mathcal{L}_{\alpha_j} = 0$$

could be solved to express \mathcal{L} in terms of ω , k and a single amplitude variable. One useful choice is to use the wave action I itself as the amplitude variable and work with $\mathcal{L}(\omega, k, I)$. Then, going through the reduction process, it is seen that \mathcal{L} may be put in the form

$$\mathcal{L}(\omega, k, I) = \omega I - E(k, I). \quad (53)$$

The identification of \mathcal{L}_ω as I and $\omega \mathcal{L}_\omega - \mathcal{L}$ as E shows this directly. Indeed this form may be used for any system where ω , k and a single amplitude parameter are the only variables in the problem; it is not restricted to deep water waves. Now, the variational equation, $\mathcal{L}_I = 0$, gives

$$\omega = E_I(k, I), \quad (54)$$

and the flux term in the action equation (6) has

$$J = -\mathcal{L}_k = E_k(k, I). \quad (55)$$

Equations (6) and (7) then provide the two equations

$$\frac{\partial I}{\partial t} + \frac{\partial J(k, I)}{\partial x} = 0, \quad (56)$$

$$\frac{\partial k}{\partial t} + \frac{\partial \omega(k, I)}{\partial x} = 0, \quad (57)$$

for k and I .

8. Type of the equations and stability

We now consider whether the equations for k and I are hyperbolic or elliptic. This follows the standard procedure for finding the characteristic form, and it is found that

$$dI \pm (J_k/\omega_I)^{1/2} dk = 0 \quad (58)$$

on characteristics

$$dx/dt = \omega_k \pm (\omega_I J_k)^{1/2}. \quad (59)$$

(Here the identity

$$\omega_k = J_I, \quad (60)$$

which follows from (54) and (55), has been used.) Thus when $\omega_I J_k > 0$ we have stability and modulations *propagate* with the group velocities in (59). When $\omega_I J_k < 0$, we have instability and small modulations will grow.

9. Small amplitude theory

For small amplitudes the functions E , ω and k may be expanded in the series

$$E = \omega_0(k) I + \frac{1}{2} \omega_2(k) I^2 + \dots,$$

$$\omega = E_I = \omega_0(k) + \omega_2(k) I + \dots,$$

$$J = E_k = \omega'_0(k) I + \dots$$

Therefore, the characteristic velocities are

$$dx/dt = \omega'_0 \pm (\omega_2 \omega''_0 I)^{1/2} + O(I).$$

For deep water waves $\omega_2 > 0$, but $\omega_0 = (gk)^{1/2}$ so that $\omega''_0 < 0$. Therefore the modulations are unstable.

10. Finite amplitude theory

For deep water waves, one can argue on dimensional grounds that the function E in (53) must take the form

$$E(k, I) = \frac{g}{k^2} W(\zeta), \quad \zeta = \frac{k^{5/2} I}{g^{1/2}}. \quad (61)$$

This is confirmed in considering the reduction process outlined at the beginning of § 7. While the function $W(\zeta)$ is contained implicitly in that analysis, it is not known explicitly. However, Longuet-Higgins (1975) and co-workers have accurate numerical results for the variations of E with I for fixed k . They do not calculate J or J_k , for example, but these can be deduced from the functional form in (61) once we take $W(\zeta)$ from their tables.

The significant quantities for our purposes are

$$\omega = E_I = g^{1/2} k^{1/2} W'(\zeta), \quad (62)$$

$$\omega_k = g^{1/2} k^{-1/2} \left\{ \frac{5}{2} \zeta W'' + \frac{1}{2} W' \right\}, \quad (63)$$

$$\omega_I = k^3 W'', \quad (64)$$

$$J = E_k = \frac{g}{k^3} \left\{ \frac{5}{2} \zeta W' - 2W \right\}, \quad (65)$$

$$J_k = \frac{g}{4k^4} \{ 25 \zeta^2 W'' - 25 \zeta W' + 24 W \}. \quad (66)$$

The stability is controlled by the sign of $\omega_I J_k$.

In Longuet-Higgins's tables (1975, p. 170), the amplitude to wavelength ratio H/λ varies from 0 to 0.141, the value for the wave of greatest height (H is the difference in levels at crest and trough). For small values of H/λ , we infer from the tables that $\omega_I > 0$ and $J_k < 0$, as in the small amplitude theory. At $H/\lambda = 0.109$ approximately, J_k changes sign and becomes positive. Thus the wavetrain becomes stable to the modulations considered here. The corresponding values of ζ and W are

$$\zeta = 0.053, \quad W = 0.055.$$

At $H/\lambda \simeq 0.137$ (close to breaking) I and E have maximum values as functions of H/λ , whereas ω is still increasing. Hence $\omega_I \rightarrow \infty$ at this value. Since $\omega_I \propto W''(\zeta)$, it follows that ω_k and J_k also tend to infinity. The further significance of this result and its relation to other stability investigations have not yet been assessed.

11. Oblique modulations

If the modulations are in a direction making an angle χ with the direction of the waves, the appropriate propagation velocities are modified to

$$\omega_k \cos \chi \pm \left\{ \omega_I \left(J_k \cos^2 \chi + \frac{J}{k} \sin^2 \chi \right) \right\}^{1/2}. \quad (67)$$

This checks with (59) when $\chi = 0$. In the extreme case of $\chi = \pi/2$, when the modulations are along the crest, we have

$$\pm (\omega_I J/k)^{1/2}. \quad (68)$$

These are stable up to the value $H/\lambda = 0.137$ where $\omega_I \rightarrow \infty$.

12. Arbitrary depth

Most of the results discussed here can be extended to the case of finite depth. The extra feature is that changes in mean flow and mean height become coupled to the wave motion. Appropriate extra variables appear in the Lagrangian \mathcal{L} . The details will be given in later papers.

This research was supported by the Office of Naval Research, U.S. Navy.

References

- Longuet-Higgins M S 1975 *Proc. R. Soc. (London)* **A342** 157
 Starr V P 1947 *J. Mar. Res.* **6** 175
 Whitham G B 1974 *Linear and nonlinear waves* (New York: Wiley-Interscience)

Storm surges in the Bay of Bengal

P K DAS

Meteorological Office, New Delhi 110 003

MS received 14 February 1981

Abstract. In this paper, the scaling of the shallow water equations in terms of the speed of a cyclone moving over a basin, and another velocity related to basin characteristics is reported. The zero-order equations for which numerical solutions were obtained earlier are described. For a basin of uniform depth, an analytical solution has been obtained for the zero-order equations. The solution suggests that, in the initial stages, the divergence of the wind stress is more important than the curl of the wind stress. In subsequent stages, the curl becomes more important. It is also shown that the basin does not respond to a cyclone until a certain time has elapsed. The adjustment time depends on the storm speed, and is inversely proportional to the square-root of the basin depth.

Keywords. Surges; basin response; Bay of Bengal

1. Introduction

Storm surges represent an accumulation of water in shallow seas. This is brought about by the wind stress, and a reduction in atmospheric pressure due to a tropical cyclone. They are known to cause devastating floods in the coastal regions of India, Bangladesh, Burma and Thailand. Wherever there is danger of floods, it is useful to construct a design surge, which will be generated by a storm with specified characteristics. Mathematical models often provide useful insight.

This paper examines how a basin responds to a sudden impulse of the kind provided by a tropical cyclone.

2. Basic equations

The shallow water equations given below are used:

$$u_t + (uu_x + vu_y) - fv = -\frac{\partial}{\partial x} \left(g\zeta + \frac{p_a}{\rho} \right) + \frac{1}{\zeta + h} \left(\frac{\Delta F}{\rho} \right), \quad (1)$$

$$v_t + (uv_x + vv_y) + fu = -\frac{\partial}{\partial y} \left(g\zeta + \frac{p_a}{\rho} \right) + \frac{1}{\zeta + h} \left(\frac{\Delta G}{\rho} \right), \quad (2)$$

$$\zeta_t + [(\zeta + h)u]_x + [(\zeta + h)v]_y = 0. \quad (3)$$

A list of symbols appears at the end of the paper.

Suffixes have been used to denote partial derivatives. In deriving (1) to (3) quantities such as $\overline{u^2} - \bar{u}^2 \simeq 0$ have been assumed. This assumption is generally valid save in exceptionally shallow waters. The basic equations reduce a three-dimensional problem into a two-dimensional one by using depth-averaged velocities. Although this does not provide information on the vertical structure of the surge, the equations are useful for examining the response of a basin.

For scaling the equations, we say

$$L = \text{characteristic length (500 km),}$$

$$T = \text{characteristic time (24 hr),}$$

$$Z = 2 \text{ m,}$$

$$H = 10 \text{ m,}$$

$$V_s = \text{average speed of storm propagation (6 ms}^{-1}\text{),}$$

$$C = \text{characteristic velocity of surge.}$$

The vertical velocity at the free surface (W) is of the order of (Z/T) but, from the equation of continuity, we find

$$W/H \sim C/L,$$

whence $C \sim (L/H)(Z/T)$.

Thus, the magnitude of C is 1–2 ms^{-1} , which is about a third of the storm speed (V_s).

The speed of the storm may be used to define a Froude Number Fr . We assume

$$Fr = V_s/(gH)^{1/2}. \quad (4)$$

Considering average values we find $Fr \simeq 0.6$.

It is convenient to make the equations non-dimensional. Let

$$\begin{aligned} f_* &= fT, & \zeta_* &= \zeta/Z, & P_* &= p_a/\rho gH, \\ u_*, v_* &= u, v/C, & h_* &= h/H, & \Delta F_* &= \Delta F/\rho u_*^2, \\ x_*, y_* &= x, y/L, & t_* &= t/T & \Delta G_* &= \Delta G/\rho u_*^2. \end{aligned}$$

We have scaled the differential friction terms ($\Delta F/\rho$) and ($\Delta G/\rho$) by a characteristic friction velocity (u_*). For strong winds, the magnitude of the friction velocity u_* is approximately $10^{-3} \text{ m}^2 \text{ s}^{-2}$. The non-dimensional variables are of order unity.

On dropping the asterisks, the non-dimensional equations are

$$u_t + \epsilon (uu_x + vv_y) - fv = -\frac{1}{Fr^2} \left[\zeta + \frac{V_s}{C} P \right]_x + \left(\frac{u_*^2 T}{CH} \right) \frac{\Delta F}{h + \epsilon \zeta}, \quad (5)$$

$$v_t + \epsilon (uv_x + vv_y) + fu = -\frac{1}{\text{Fr}^2} \left[\zeta + \frac{V_s P}{C} \right]_y + \left(\frac{u_*^2 T}{CH} \right) \frac{\Delta G}{h + \epsilon \zeta}, \quad (6)$$

$$\zeta_t + [(\epsilon \zeta + h)u]_x + [(\epsilon \zeta + h)v]_y = 0, \quad (7)$$

where $\epsilon = Z/H = CT/L$. (8)

3. Zero-order equations

If we expand the dependent variables in (5), (6) and (7) in powers of ϵ , we may derive systems of increasingly higher order. The zero-order equations, when $\epsilon \ll 1$, are

$$u_t - fv = -\frac{1}{\text{Fr}^2} \left[\zeta + \frac{V_s P}{C} \right]_x + \left(\frac{u_*^2 T}{CH} \right) \frac{\Delta F}{h}, \quad (9)$$

$$v_t + fu = -\frac{1}{\text{Fr}^2} \left[\zeta + \frac{V_s P}{C} \right]_y + \left(\frac{u_*^2 T}{CH} \right) \frac{\Delta G}{h}, \quad (10)$$

$$\zeta_t + (hu)_x + (hv)_y = 0. \quad (11)$$

Numerical solutions of the zero-order equations, or their equivalents, have been obtained for the northern sectors of the Bay of Bengal (Das *et al* 1974). We assume an idealized storm, with a specified distribution of pressure and winds, which moves along a straight track with constant speed. This hits a given sector of the coast. By changing the storm characteristics, it is possible to relate the surge amplitude with the intensity and speed of the storm. An extension of this method for the Gulf of Thailand by Sinha (1981) is shown in figures 1 and 2. The interesting fact emerges that for the same storm characteristics the response of the Gulf of Thailand is different from the Bay of Bengal. Both basins have a narrow concave configuration on their northern sectors, but the bottom topography is different. In the northern part of the Bay of Bengal, there is a comparatively large area where the sea is extremely shallow. This feature is not observed in the Gulf of Thailand; consequently, the amplitude of the surge is smaller for a storm of the same intensity. The correct formulation of sea-bed friction and wind stress and boundary conditions on the open sea boundary are some of the difficulties encountered in numerical models. In general, quadratic friction laws are assumed, but it is not yet clear whether the same friction law should be valid for both the storm surge and the astronomical tide. Tide-surge interactions are important, but difficult to estimate in shallow seas. The tidal cycle, often imposed as an initial state, cannot be determined with much accuracy due to lack of observations on the open sea. Despite these limitations, the zero-order equations provide a useful base for modelling a storm surge. Reliable observations of the storm surge are difficult to come by, but the available data suggest that models based on the zero order equations provide fairly good

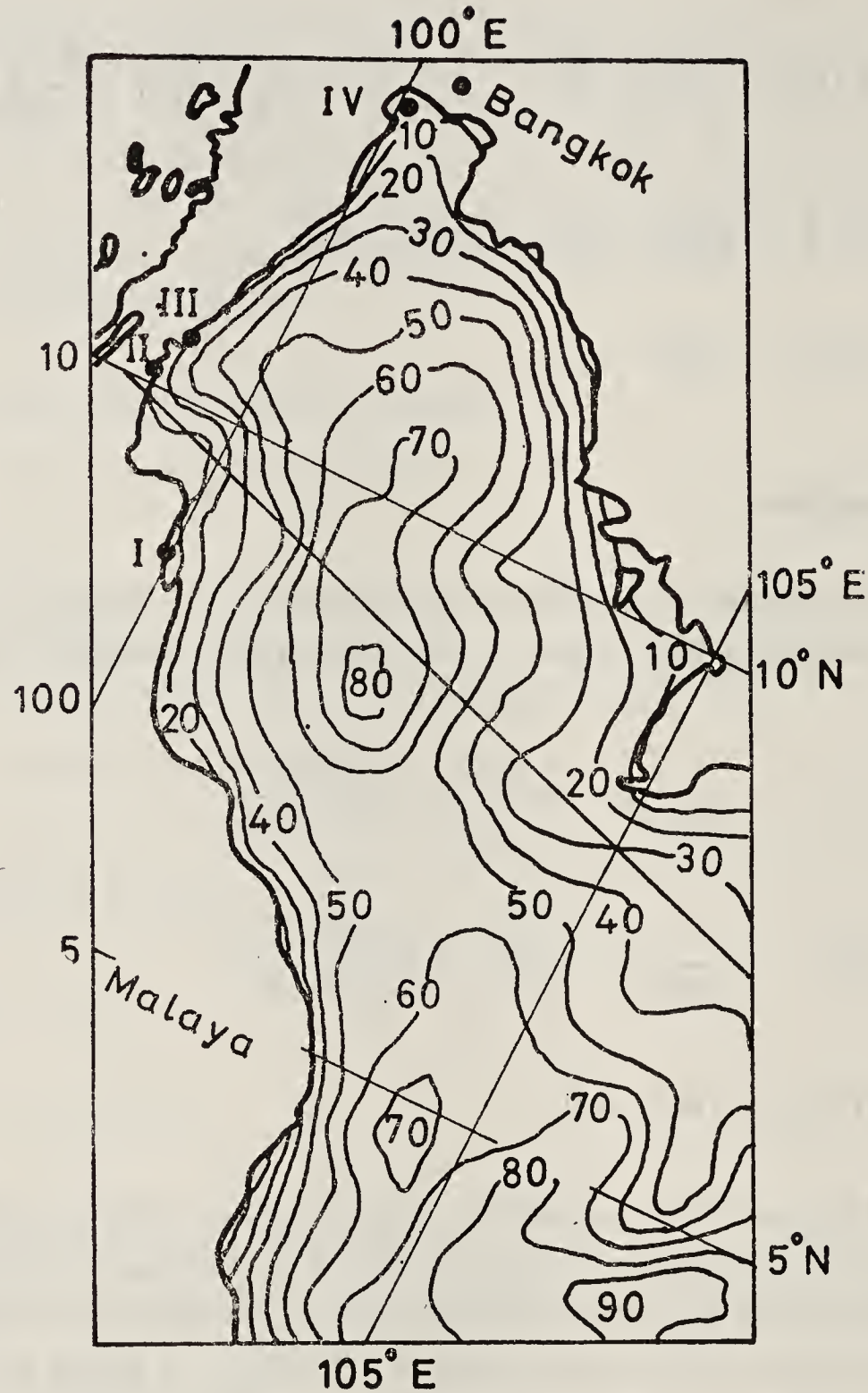


Figure 1. Gulf of Thailand. Sea-bed topography (m). The storm track is shown by full line with arrow. Surge amplitudes were computed at four points along coast marked I, II, III and IV (after Sinha 1981)

estimates of the storm surge, except in very shallow waters where ϵ is of the order of unity.

4. Basin response to winds

The zero-order equations could be used to estimate how quickly a basin will respond to the cyclonic winds of a tropical cyclone.

We may eliminate u, v from (5), (6) and (7) by computing the vorticity and divergence of the water. If we assume a basin with constant depth (h) we find

$$\zeta_{ttt} + \left[f^2 - \frac{h}{Fr^2} \nabla^2 \right] \zeta_t = \frac{h}{Fr^2} \left(\frac{V_s}{C} \right) \nabla^2 P_t + \left(\frac{u_*^2 T}{CH} \right) \left[\nabla \cdot \left(\frac{\Delta \tau}{\rho} \right) \right]_t + f \left(\frac{u_*^2 T}{CH} \right) \left[\mathbf{k} \cdot \nabla \times \frac{\Delta \tau}{\rho} \right] \quad (12)$$

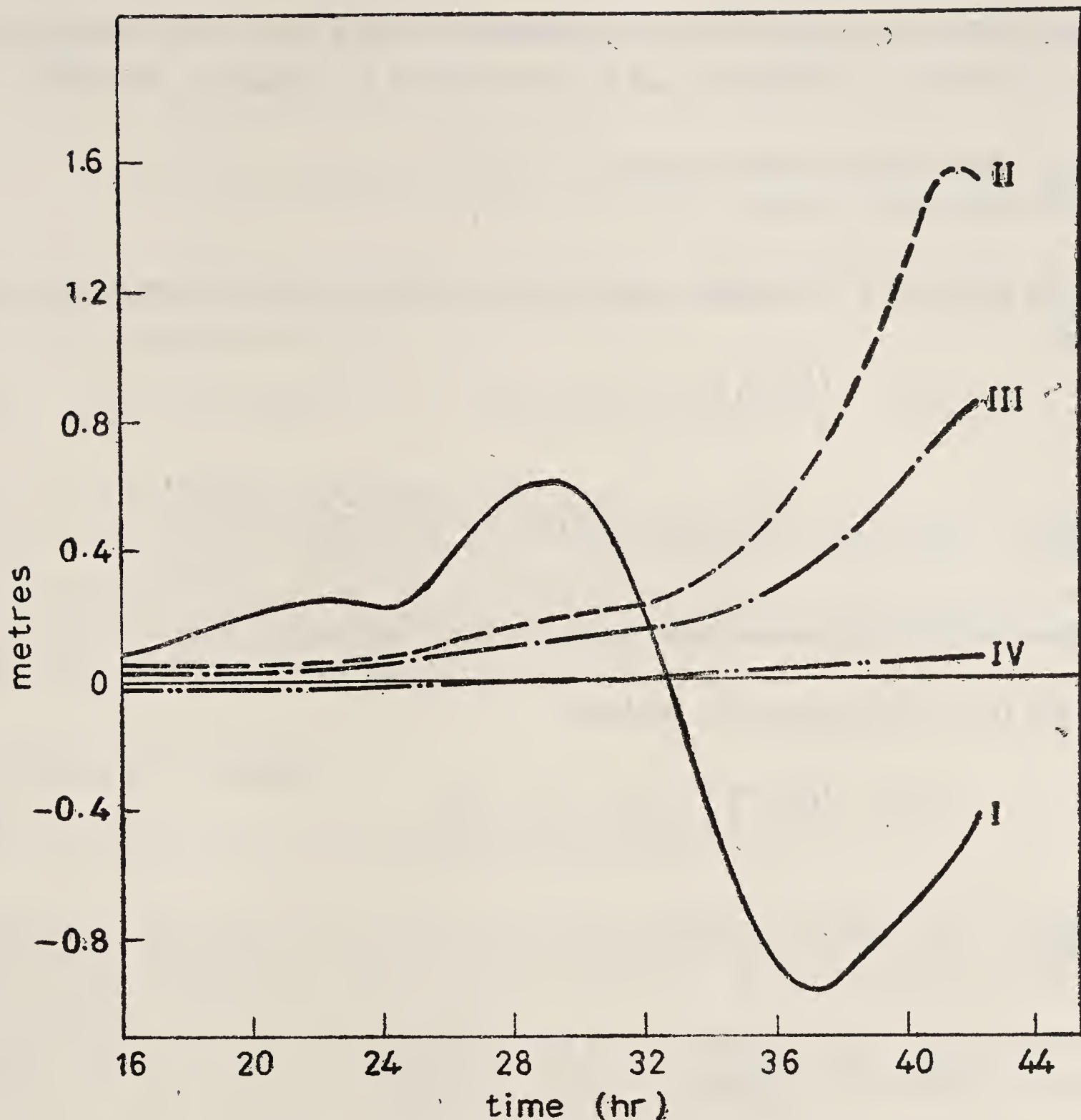


Figure 2. Surge amplitudes at I, II, III and IV (after Sinha 1981)

where $\Delta\tau = \mathbf{i} \Delta F + \mathbf{j} \Delta G$

and \mathbf{i} , \mathbf{j} , \mathbf{k} are unit vectors in cartesian coordinates.

As we can now see, the surge is generated by three forcing functions, namely,

- (i) the pressure tendency in the field of the cyclone,
- (ii) the rate of change of divergence of $\Delta\tau$ and
- (iii) the curl of differential friction.

As sea-bed friction is a small fraction of the wind stress, the second and third forcing terms in (12) represent (i) the rate of change of divergence and (ii) the curl of the wind stress. We note the interesting fact that it is only the curl of the wind stress that has no time dependency.

Let us represent the Laplace transform of ζ by

$$\hat{\zeta} = \int_0^{\infty} \zeta \exp(-st) dt, \quad (13)$$

with similar expressions for the transforms of P and $\Delta\tau/\rho$. We represent them by \hat{P} and $\Delta\hat{\tau}/\rho$. A distinction can be made between two situations. We have

- (a) small values of time (t) when $s \rightarrow \infty$, and
- (b) large time (t) when $s \rightarrow 0$.

We find, after a little algebra, that for (a) or small time, the relevant equation for $\hat{\zeta}$ is

$$\nabla^2 \hat{\zeta} - \left(\frac{\text{Fr}^2 s^2}{h}\right) \hat{\zeta} = -\phi(x, y, s), \quad (14)$$

where
$$\phi(x, y, s) = \frac{\text{Fr}^2}{h} (s \zeta_0) + \left(\frac{V_s}{C}\right) \nabla^2 \hat{P} + \frac{\text{Fr}^2}{h} \left(\frac{u_*^2 T}{CH}\right) \nabla \cdot \left(\frac{\Delta\hat{\tau}}{\rho}\right).$$

The subscript 0 denotes the initial value of ζ at the beginning ($t = 0$).

For (b), or large values of t , we have

$$\nabla^2 \hat{\zeta} - \left(\frac{\text{Fr}^2 f^2}{h}\right) \hat{\zeta} = \frac{1}{s} [\phi_1 + \phi_2 - \phi_3], \quad (15)$$

where
$$\phi_1 = \nabla^2 \zeta_0 + \frac{V_s}{C} \nabla^2 P_0, \quad (16a)$$

$$\phi_2 = \left(\frac{\text{Fr}^2}{h}\right) \left(\frac{u_*^2 T}{CH}\right) \mathbf{k} \cdot \nabla \times \left[\frac{\Delta\hat{\tau}}{\rho} + \left(\frac{\Delta\tau}{\rho}\right)_0\right], \quad (16b)$$

$$\phi_3 = f^2 \zeta_0 + \zeta_0''. \quad (16c)$$

A comparison between (14) and (15) suggests that for small values of t , that is, at the beginning, the surge is influenced by (i) the divergence of the wind stress, (ii) the pressure gradient weighted by the ratio (V_s/C) and (iii) the initial value of ζ weighted by Fr^2/h . The curl of the wind stress does not come into play initially. But, after a certain length of time the divergence is no longer important, and the curl takes over as in (15). At longer times the gradients of the initial values of ζ and P appear to assert themselves, while in the beginning only ζ_0 is important. These inferences are physically reasonable, because the initial response of a basin would be to drive away the water from the disturbance source. This is measured by the divergence of the wind stress. Subsequently, the rotational character of the wind will become more important. This is the curl of the wind stress.

We may express the solution of (14) in terms of a Green's function when we consider an infinite domain. If

$$R = [(x - x_0)^2 + (y - y_0)^2]^{1/2} \quad (17)$$

is the distance between an observation point (x, y) and a source (x_0, y_0) , then, for small R , we have

$$\hat{\zeta} = \int_{-\infty}^{\infty} \int_{-\infty}^{\infty} K_0 [FrR/\sqrt{h}] \phi(x_0, y_0) dx_0 dy_0, \quad (18)$$

where $K_0[FrR/\sqrt{h}]$ represents a modified Bessel function of the second kind. This is the Laplace transform of

$$[t^2 - Fr^2 R^2/h]^{-1/2},$$

for $t > FrR/\sqrt{h}$ (Morse & Feshbach 1953).

As $\hat{\zeta}$ is the Laplace transform of ζ , we infer that the basin does not respond to the impulsive force of the cyclone until a time FrR/\sqrt{h} is reached. This time, as we can see, depends on the storm speed represented by the Froude Number (Fr) and is inversely proportional to \sqrt{h} where h is the basin depth.

5. Summary and conclusions

The main conclusions of this study are the following:

(i) Scaling the shallow water equations in terms of the storm speed (V_s) and the characteristic surge velocity leads to a small parameter ϵ which enables us to expand the dependent variables in powers of ϵ .

(ii) The zero-order equations may be solved numerically for a basin with specified depth contours, coastal geometry and storm characteristics. The equations are sensitive to rapid changes in depth and coastal configuration.

(iii) An analytical solution for a basin of constant depth suggests that, in the initial stages, the divergence of the wind stress plays the dominant role. In the later stages, the curl of the wind stress becomes more important.

(iv) The rate of change of cyclone pressure is more important in the initial stages.

(v) The basin does not respond to a cyclone until a certain time (FrR/\sqrt{h}) has elapsed. This time depends on the storm speed, and is inversely proportional to \sqrt{h} where h is the basin depth.

List of symbols

f	Coriolis parameter ($2\Omega \sin \phi$)
F_s, F_b	eastward component of the wind stress at the surface (F_s) and sea-bed friction (F_b)
G_s, G_b	northward component of surface stress (G_s) and bottom stress (G_b)
h	depth of water
H	mean depth of water (10 m)

p_a	atmospheric pressure
u, v	depth-averaged velocities in rectangular cartesian co-ordinates ($0 x y z$), where the x and y axes point to the east and north respectively and z is the vertical axis
Z	mean surge amplitude (2 m)
ΔF	$F_s - F_b$
ΔG	$G_s - G_b$
ρ	density of water
ζ	amplitude of the surge

Figure 3 provides a physical representation of the above symbols.

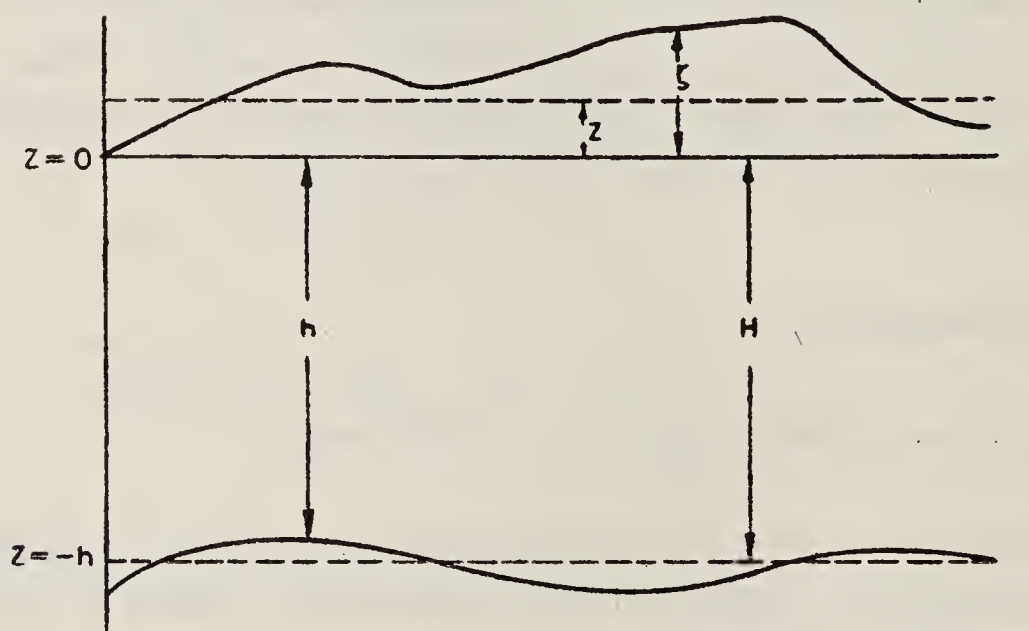


Figure 3. The storm surge. Bottom thick line indicates sea-bed topography.

References

- Das P K, Sinha M C & Balasubramanyam 1974 *Q.J.R. Meteorol. Soc.* **100** 437
 Morse P M & Feshbach H 1953 *Methods of theoretical physics*, Int. Student Ed., (New York: McGraw Hill) p. 1360
 Sinha M C 1981 *Mausam* **32** 4

Generation of large scale circulation in turbulent convection

RUBY KRISHNAMURTI

Department of Oceanography, Florida State University, Tallahassee, Florida 32306, USA

MS received 13 June 1981

Abstract. In a horizontal layer of fluid heated below and cooled above, cellular convection with horizontal length scale comparable to the layer depth occurs in a certain range of Rayleigh numbers. As the Rayleigh number is increased, cellular flow disappears and is replaced by a random array of transient plumes. Upon further increase, these plumes drift in one direction near the bottom and in the opposite direction near the top of the layer with the axes of the plumes tilted in such a way that horizontal momentum is transported upwards *via* the Reynolds stress. With the onset of this large-scale horizontal flow, the largest scale of motion increases from a scale comparable to the layer depth to a scale comparable to the layer width. The conditions for the occurrence and the determination of the direction of this large-scale circulation are described in this paper.

A simple mathematical model is also described which, like the experiment, has the feature of spontaneous generation of a large-scale horizontal flow, \bar{u} . A truncated Fourier representation of the streamfunction and temperature field is taken, which allows the possibility of a large-scale flow. The bifurcations of the resulting equations have been studied. The first bifurcation is from the conduction state to steady cellular convection. The second is from steady cellular convection to a steady tilted cell convection which has an Eulerian (but not Lagrangian) horizontal mean velocity, \bar{u} . The third bifurcation is from steady tilted cells to an oscillatory flow, which may be described as consisting of transient, drifting, tilted plumes. The flow in this regime does have a net Lagrangian horizontal mean velocity. Embedded in this regime are also regions of hysteretic and other regions of chaotic flow. A qualitative similarity to the observed flows is noted.

Keywords. Instability; transition; turbulence; large-scale order.

1. Introduction

Consider a horizontal layer of fluid that is being uniformly heated from below and cooled from above. This is the arrangement which leads to cellular convection for a range of Rayleigh numbers (the dimensionless measure of temperature difference, defined below), exceeding a critical value. The horizontal scale of these cells is comparable to the depth d of the layer. At successively larger values of the parameter, a number of transitions in the flow pattern as well as in the heat flux are observed (Malkus 1954; Willis & Deardorff 1967ab; Krishnamurti 1970ab; Busse & Whitehead 1971). Most of these changes are within the regime of cellular flows. However, there is a further transition which leads to a very different scale of motion and very different transport properties. In this regime the flow is no longer cellular. It is a flow with primarily two scales of motion. The smaller scale flow, with a horizontal scale comparable to the layer depth d , is best described as transient bubbles or plumes that have an organized tilt away from the vertical. The larger scale flow,

having scale L , is a horizontal flow with vertical shear such that the flow is in opposite directions near the bottom and the top. L is usually the container width which in these experiments is an order of magnitude larger than d . The large-scale flow is apparently maintained against viscous dissipation by the Reynolds stress divergence of the tilted plume motions.

The details of the laboratory experiments can be found in Krishnamurti & Howard (1981). The observations can be summarised as follows.

2. Laboratory observations

Figure 1 summarizes some observations of the flow found in the various ranges of the parameters. These parameters are the Rayleigh number R and the Prandtl number P defined as follows:

$$R = \frac{g\alpha}{\kappa\nu} \Delta T d^3, \quad P = \nu/\kappa,$$

where g is the acceleration of gravity, α the thermal expansion coefficient, κ the thermal diffusivity, ν the kinematic viscosity, d the depth of the fluid layer, and ΔT the temperature difference between bottom and top boundaries. The new observations refer to flows found to the upper left of the curve labelled V in figure 1. To the lower right of this curve the flows are cellular: as labelled, the flow is steady, two-dimensional in the parameter range between curves I and II. It is steady, three-dimensional,

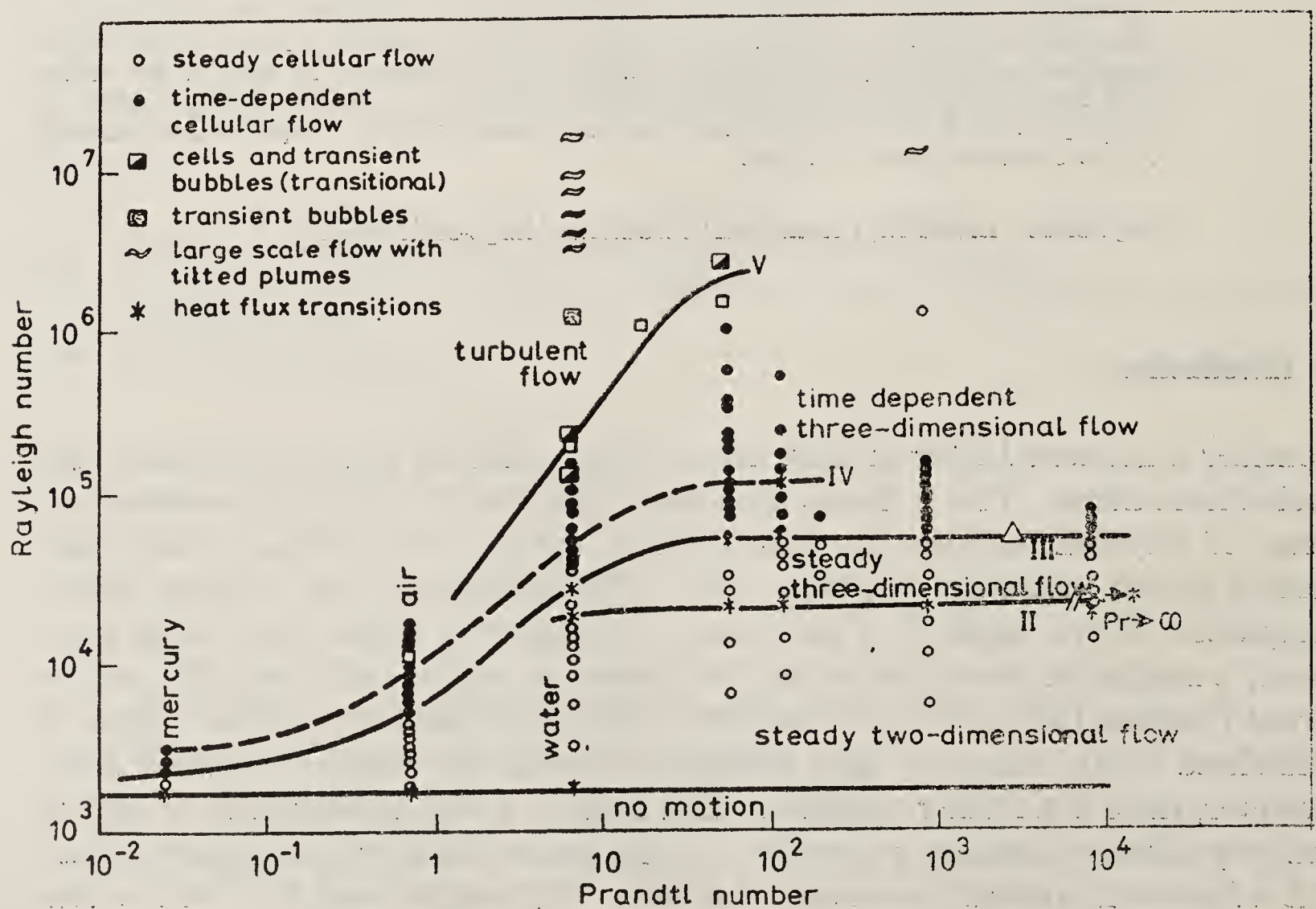


Figure 1. Regime diagram. See text and Krishnamurti (1970b) for further explanation.

cellular between curves II and III, and time-dependent (quasi-periodic), three-dimensional, and cellular between curves III and V. By 'cellular', we mean that a fluid parcel initially at some horizontal location is always confined to the vicinity of that location, horizontal excursions being limited to lie between cell boundaries which have horizontal separation comparable to the layer depth. (This is certainly so between curves I and III and at least largely so between III and V.) Since most of these states are history-dependent, the actual transition point varies depending upon how it was attained. Figure 1 obtains when the state of the system was reached from lower values of Rayleigh number, by small increments in R . Further explanation can be found in Krishnamurti (1970b).

Curve V was defined in Willis & Deardorff (1967a) as the Rayleigh number above which irregular fluctuations in temperature at a point mid-depth in the fluid layer were nearly always present. Although somewhat subjective, it is a useful criterion.

One of the major differences between the flows occurring to the upper left of V and that to the lower right is seen in the (x, t) photographs of figure 2 (plate 1). Here x refers to the horizontal coordinate along a fixed line within the fluid, and t refers to the time. Also let y be the coordinate along the line of sight and z the vertical coordinate. The fluid contains suspended tracer particles which are small light-reflecting flakes that become aligned by the shear of the flow. The illuminated region is 2 to 3 mm in diameter, 48 cm long along x , and was chosen to lie either near the bottom or the top of the fluid layer. The (x, t) photographs thus shows the time-evolution of a linear region in the fluid layer. Both 2b and 2c show a line in the fluid layer 0.2 cm above the bottom boundary. Figure 2b (plate 1), at $R = 10^6$, $P = 0.86 \times 10^3$ is for parameter values to the right of curve V. Figure 2c, at the same Rayleigh number, $R = 10^6$, but $P = 7$, is to the left of V. In 2b there are cell boundaries which, while they may oscillate laterally, are always identifiable. In 2c *there are no cell boundaries*. The former is a cellular flow with bright or dark regions moving repeatedly from one cell boundary to a neighbouring one. These regions have been shown in Krishnamurti (1970b) to correspond to hot or cold spots convected around the cell. In 2c, hot bubbles or plumes off the bottom, randomly spaced in position and time, form and vanish. Cold bubbles off the top likewise form and vanish, much as described by the bubble model (Howard 1966). At any instant of time, their horizontal spacing is approximately d or somewhat less. It should be pointed out also that figure 2c is not an initial transient state; it is the statistically steady state that is observed one hour or 100 hours after starting convection.

At $P = 7$, $R = 5 \times 10^4$ the flow is similar to 2b, so that increasing R at fixed P also leads to the change of flow depicted when going from figure 2b to 2c.

The other major difference—the one to which we particularly wish to call attention—is seen in figure 2d which shows an (x, t) photograph for $P = 7$, $R = 2.4 \times 10^6$, taken 0.2 cm above the bottom boundary. It shows that the *plumes have a net drift* from left to right with an average speed of 7×10^{-2} cm s $^{-1}$. A similar photograph taken 0.2 cm below the top showed plumes drifting from right to left with the same average speed.

From the (x, t) photos it is not known if this apparent motion is a wave propagation, or if there is an associated mass flux. Therefore, thymol blue was added to the water so that neutrally buoyant dye could be produced at an electrode, and the dyed fluid was followed with time. Figure 3 (plate 2) shows a sequence at 30 second intervals, of a vertical slice (x, z) view of the fluid. In this case the layer depth was

10 cm. The dye front along the bottom progressed at an averaged speed \bar{u} of 3×10^{-2} cm s $^{-1}$ from left to right, and actually reached the opposite wall, by which time it was quite diffuse. These magnitudes are not easily compared from case to case since only the x -component, u , is measured, whereas in some repetitions of the experiment there was a velocity component v in the y -direction as well. Maximum values of \bar{u} on the order of 10^{-1} cm s $^{-1}$ have been observed. In figure 3 (plate 2), as the dyed fluid becomes buoyant, it rises into the interior of the layer where it is seen to become entangled in the motion of the plume. It often rises to become caught in the leftward drift at the top of the layer. In figure 3 (plate 2), a general tilt of the plumes from lower right to upper left can be discerned even though the flow is quite turbulent. Thus we conclude that there is not only a (time- and/or horizontal) mean Eulerian velocity $\bar{u}(z)$, but a net horizontal Lagrangian transport, extending the entire width of the tank. Observations of the occurrence of cells, plumes, and large-scale flow in various regions of parameter space are summarized in figure 1.

When this large-scale flow was first discovered, various tests were made to see if it were inadvertently being driven directly by horizontal asymmetries. The levelling of the apparatus was checked. Horizontal temperature gradients in the boundaries were measured to check the possibility of malfunction of the cooling or heating system. The observed magnitude of horizontal gradient would drive, in water, a horizontal velocity $u \simeq 10^{-3}$ cm s $^{-1}$ which is two orders of magnitude smaller than observed. Although horizontal asymmetries must certainly be present, due to errors in levelling the apparatus, or due to small differences in temperature of the Plexiglas side walls, these had no observable effect at a lower Rayleigh number, or even at the same Rayleigh number (with the same ratio of side wall area to horizontal area), when a higher Prandtl number fluid was used and no large-scale flow was observed.

Convinced that the large-scale flow *was not externally driven*, we attempted to check, as to order of magnitude, that the large scale flow and the tilt of the plumes were consistent with the Reynolds equations relating a (time- and horizontal-) mean flow with the Reynolds stress associated with fluctuations. The principal equation here is the mean horizontal momentum equation, which if the tank were horizontally unbounded (or in the case of the cylindrical annulus) is

$$\overline{(u'w')}_z = \nu \bar{u}_{zz}. \quad (1)$$

The overbar indicates a horizontal and time average, u' and w' are the fluctuations from the mean and ν is the kinematic viscosity. (With the finite horizontal extent there could conceivably also be a non-zero mean horizontal pressure gradient term in this equation—which indeed might well be important were there external driving—but we omit this here.) Integrating vertically from the bottom wall we obtain,

$$\overline{u'w'} = \nu(\bar{u}_z - \bar{u}_z^0),$$

\bar{u}_z^0 being the mean shear at the wall. Detailed measurements of the fluctuating velocity components u' and w' , and of their correlation are planned but have not yet been made. However visual observation and photographs like figure 3 (plate 2), together with the (x, t) photographs, indicate that

- (i) the fluctuations are on the whole associated with the motions in the tilting plumes,
- (ii) the latter tilt in such a way (about 45 degrees from lower right to upper left in cases like figure 3) that $\overline{u'w'}$ has the opposite sign to that of \bar{u} in the lower half, and w' is characteristically about the same magnitude as u' ,
- (iii) the maximum magnitudes of u' , w' , and \bar{u} are all about 0.1 cm s^{-1} in our experiments in which the large-scale flow is observed.

Estimates of the terms in equation (1) show that the two terms are comparable, so there does not appear to be any clear inconsistency with the Reynolds equation (1). One may regard the mean flow as being “driven” by the Reynolds stress associated with the tilting plumes. We emphasize that such a statement is a *description*, and not an *explanation*, of the large scale flow. The Reynolds equation would also be consistent with the absence of mean flow, and no tilting of the plumes—and in fact this appears to be what occurs below a Rayleigh number of about 2×10^6 in water. The theoretical understanding of why this transition occurs, and why at $R = 2 \times 10^6$, remains a challenge. The phenomenon seems to resemble the onset of steady convection in that the physically realized “state” changes to one of a set, each member of which individually has less symmetry than the equations and boundary conditions describing the motion. Such symmetry-breaking occurs in many mathematical models involving changes of stability of stationary or periodic solutions and associated bifurcations, and Rayleigh’s explanation of the onset of cellular convection in such terms has been followed in spirit by essentially all of the many subsequent explorations of other aspects of cellular convection. Whether such concepts as stability and bifurcation can usefully contribute to an understanding of a transition entirely in the turbulent range seems less clear; this report, in any case, is about the observation of the transition, not its theoretical interpretation.

The large-scale flow was also observed in a cylindrical annulus of fluid (heated below and cooled above) showing that a pressure difference between two lateral boundaries is not necessary to produce this flow. The small scale plumes are considerably narrower than the depth d of the layer, but they tilt approximately 45 degrees and in this sense they occupy a horizontal distance of about d . The large scale flow was observed to continue around the annulus, in one direction near the bottom, and in the opposite direction near the top. With the geometry thus unbounded in x , the large scale flow has horizontal wave number zero.

Movies of the flow in the annulus and of an (x, z) slice in the square tank were shown.

The heat flux, non-dimensionalized to equal the Nusselt number times Rayleigh number, is plotted against Rayleigh number in figure 4. (The Nusselt number is the ratio of total to conductive heat flux.) A number of discrete changes in slope were seen, the last three of which are shown in figure 4. Some of these are in good agreement with the Malkus heat flux transitions. It appears that the onset of the large scale circulation might be associated with the slope change at $R_{VII} = 1.1 \times 10^6$.

3. Summary of the observations

As the Rayleigh number is increased, cellular flow vanishes and is replaced by a flow that has no permanent cell boundaries. It consists of hot rising and cold sinking

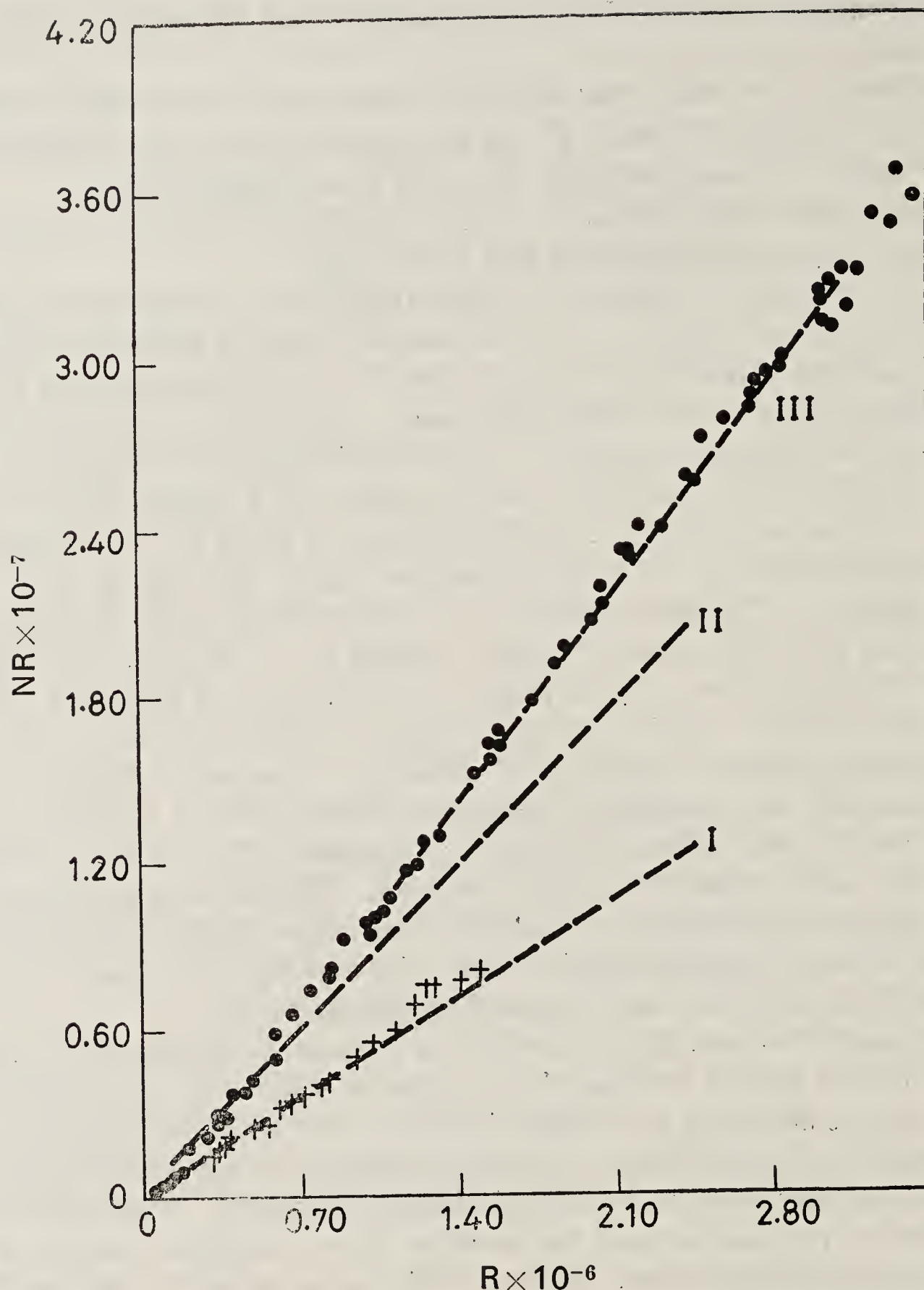


Figure 4. Heat flux H vs Rayleigh number R . H has been non-dimensionalized to equal NR where N is the Nusselt number. The coordinate scale is appropriate for the data shown by dots. For the crosses, the scale should be decreased by a factor 10. A least squares fit of segments of data to a straight line $NR = aR + b$ gave $a = 5.05$ for the line labelled I, $a = 8.40$ for II, $a = 10.7$ for III. The change in slope at $R = 1.1 \times 10^6$ may be associated with the onset of the large scale circulation which is seen at $R = 2 \times 10^6$.

transient bubbles or plumes. At still higher R , the plumes drift in one direction near the bottom, in the opposite direction near the top of the layer, while tilting from the vertical and thereby transporting mean horizontal momentum in the vertical direction. The transition when viewed in the (x, t) representation, is reminiscent of a phase transition. When there are cell boundaries as in figure 2a, fluid parcels are forever confined to circulate in the lattice-like confines of the cell walls. In 2b, plumes appear but are constrained by the cell walls to circulate within the cell. In 2c, the cell boundaries have vanished and as R is increased further in 2d, the "melt" begins to

flow. The largest scale of motion which was previously equal to the depth d , has suddenly changed to the layer width L . The appearance of this new large scale has many implications. Turbulent horizontal transport of a passive tracer is completely changed when this large scale flow sets in. Continental drift and sea floor spreading which have generally been thought to require deep convection in the mantle to explain the large scales observed at the crust, might perhaps be viewed in terms of a large-scale convective flow in the much shallower but more plastic asthenosphere.

4. The mathematical model

A mathematical model was formulated which would allow the simplest convective flow having the possibility of a large-scale circulation. Although such a large-scale flow (or a horizontally averaged Lagrangian velocity \bar{u}) was not imposed, the model incorporates the possibility for it to occur. And indeed such a flow did arise spontaneously after the third bifurcation.

The dimensionless vorticity equation and the heat equation, in the Boussinesq approximation are written as follows

$$\frac{\partial}{\partial t} \nabla^2 \psi = \sigma \nabla^4 \psi + \sigma \frac{\partial \theta}{\partial x} + \frac{\partial(\psi, \nabla^2 \psi)}{\partial(x, z)}, \quad (2)$$

$$\frac{\partial \theta}{\partial t} = \nabla^2 \theta + R \frac{\partial \psi}{\partial x} + \frac{\partial(\psi, \theta)}{\partial(x, z)}, \quad (3)$$

where ψ is the streamfunction, $\partial\psi/\partial x = -w$, $\partial\psi/\partial z = u$, and θ is the (negative) temperature perturbation. Here we have used σ to represent the Prandtl number. We use the following truncated representation for the ψ and θ .

$$\psi = A \sin \alpha x \sin z + B \sin z + C \cos \alpha x \sin 2z,$$

$$\theta = D \cos \alpha x \sin z + E \sin 2z + F \sin \alpha x \sin 2z. \quad (4)$$

Note that the term $B \sin z$ represents an x -independent horizontal velocity, if B is non-zero. Substituting (4) into the governing equations (2) and (3) and using the orthogonality of the trigonometric functions leads to the following set of equations governing the time evolution of the coefficients A, B, C, D, E, F .

$$\dot{A} + \sigma(1 + \alpha^2) A - \frac{\sigma\alpha}{(1 + \alpha^2)} D - \frac{\alpha}{2} \frac{(3 + \alpha^2)}{(1 + \alpha^2)} BC = 0, \quad (5)$$

$$\dot{B} + \sigma B + \frac{3}{4} \alpha AC = 0, \quad (6)$$

$$\dot{C} + \sigma(4 + \alpha^2) C + \frac{\sigma\alpha}{(4 + \alpha^2)} F + \frac{\alpha^3}{2(4 + \alpha^2)} AB = 0, \quad (7)$$

$$\dot{D} + (1 + \alpha^2) D - R\alpha A + \alpha AE + \frac{\alpha}{2} BF = 0, \quad (8)$$

$$\dot{E} + 4E - \frac{\alpha}{2} AD = 0, \quad (9)$$

$$\dot{F} + (4 + \alpha^2) F + RaC - \frac{\alpha}{2} BD = 0. \quad (10)$$

The Lorenz model, consisting of the three components with coefficients A , D , E , (Lorenz 1963) is recovered when we set $B = C = F = 0$. Other generalizations of the Lorenz equations (e.g. Curry 1978) have not included an x -independent term, such as $B \sin z$, in the streamfunction. Without the observation that a large-scale flow can occur, there would seem to be little point in doing so.

We have determined several interesting properties of the equations (5)–(10). These are summarized in the bifurcation diagram in figure 5, which will now be described:

- (i) The conduction state with $A = B = C = D = E = F = 0$ is stable below the critical Rayleigh number $R_c = 27/4$.
- (ii) At $R = R_c$ the conduction solution becomes unstable and two solutions with $A, D, E \neq 0$ (corresponding to the two possible directions of circulation within a cell) branch off in the A - R plane. These are the two Lorenz solutions. For $R_c < R < R^*$, the Lorenz solution $(A, 0, 0, D, E, 0)$ representing steady finite amplitude convection is the stable solution. R^* has been determined to be

$$R^* = \frac{\sigma^2 (4 + \alpha^2) + 3\sigma \frac{(1 + \alpha^2)^3}{(4 + \alpha^2)} + 3\alpha^2 (1 + \alpha^2)}{\frac{\sigma^2 \alpha^2}{(4 + \alpha^2)} + \frac{3\sigma \alpha^2}{(4 + \alpha^2)} + \frac{3\alpha^4}{(1 + \alpha^2)^2}}.$$

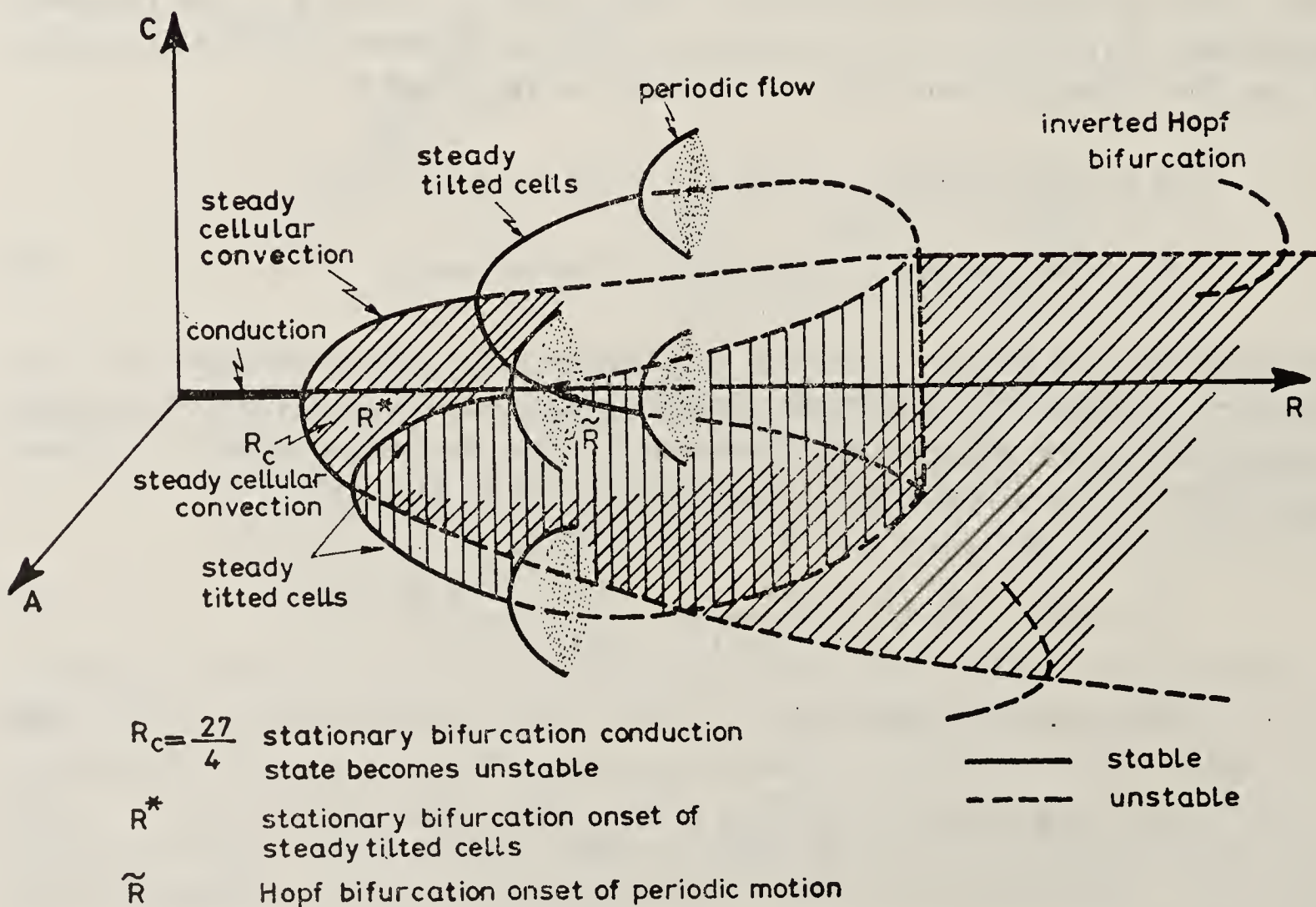


Figure 5. Bifurcation diagram.

- (iii) At $R = R^*$ the Lorenz solution becomes unstable and two solutions branch off from each of the two branches described above. These are the steady tilted cells, tilting either from lower left to upper right or from lower right to upper left. An example is shown in figure 6a. The horizontal average of the horizontal velocity component u is nonzero. Yet it is clear that a fluid parcel in one cell remains in that cell. There is an Eulerian, but not a Lagrangian average \bar{u} . The wavenumber dependence of the onset of such tilted cells is shown in figure 7.

Although *steady* convection with all cells tilted in one direction is not observed in laboratory fluid layers, it is observed in a Hele-Shaw cell. An example of this flow is seen in figure 6b (plate 3).

Steady convection restricted to the Lorenz sub-manifold is always stable if

$$\sigma < \frac{4}{(1 + \alpha^2/\pi^2)} + 1.$$

For example, if $\alpha = 1.2$, steady convection is stable if $\sigma < 4.49$. However, when embedded in the six-dimensional space, the Lorenz solution becomes unstable to steady tilted cells, even with $\sigma = 1$, (and $\alpha = 1.2$) at a Rayleigh number $\tilde{R} \simeq 23$. For other values of σ and α , the Lorenz system becomes unstable *via* an inverted Hopf bifurcation and unstable periodic flows result. However, embedded in the six-dimensional space, it becomes unstable before this, as other bifurcations occur at lower Rayleigh numbers.

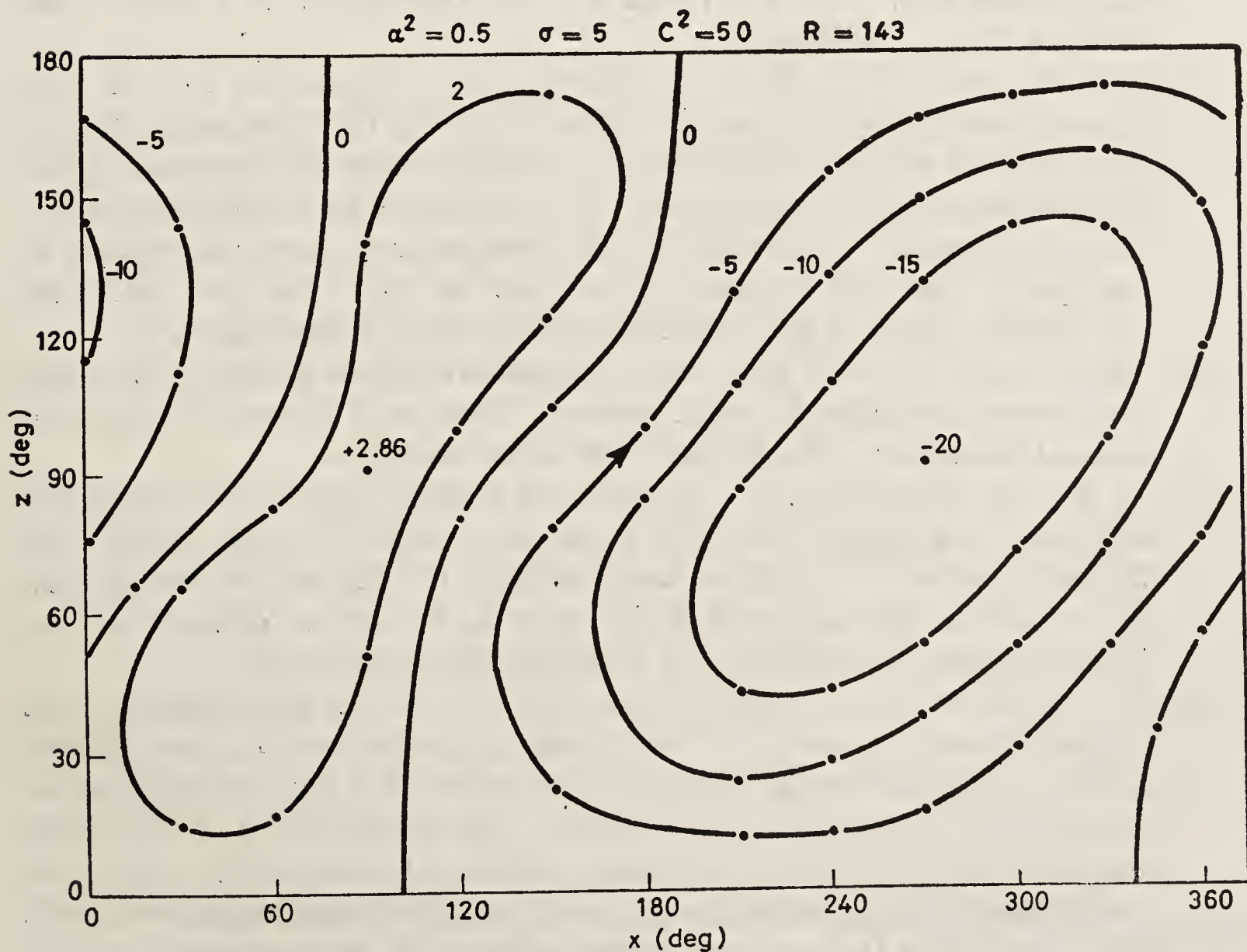


Figure 6a. Streamlines showing steady tilted cellular flow that occurs after the second bifurcation. $\sigma = 5.0$, $\alpha^2 = 0.5$, $R = 143$.

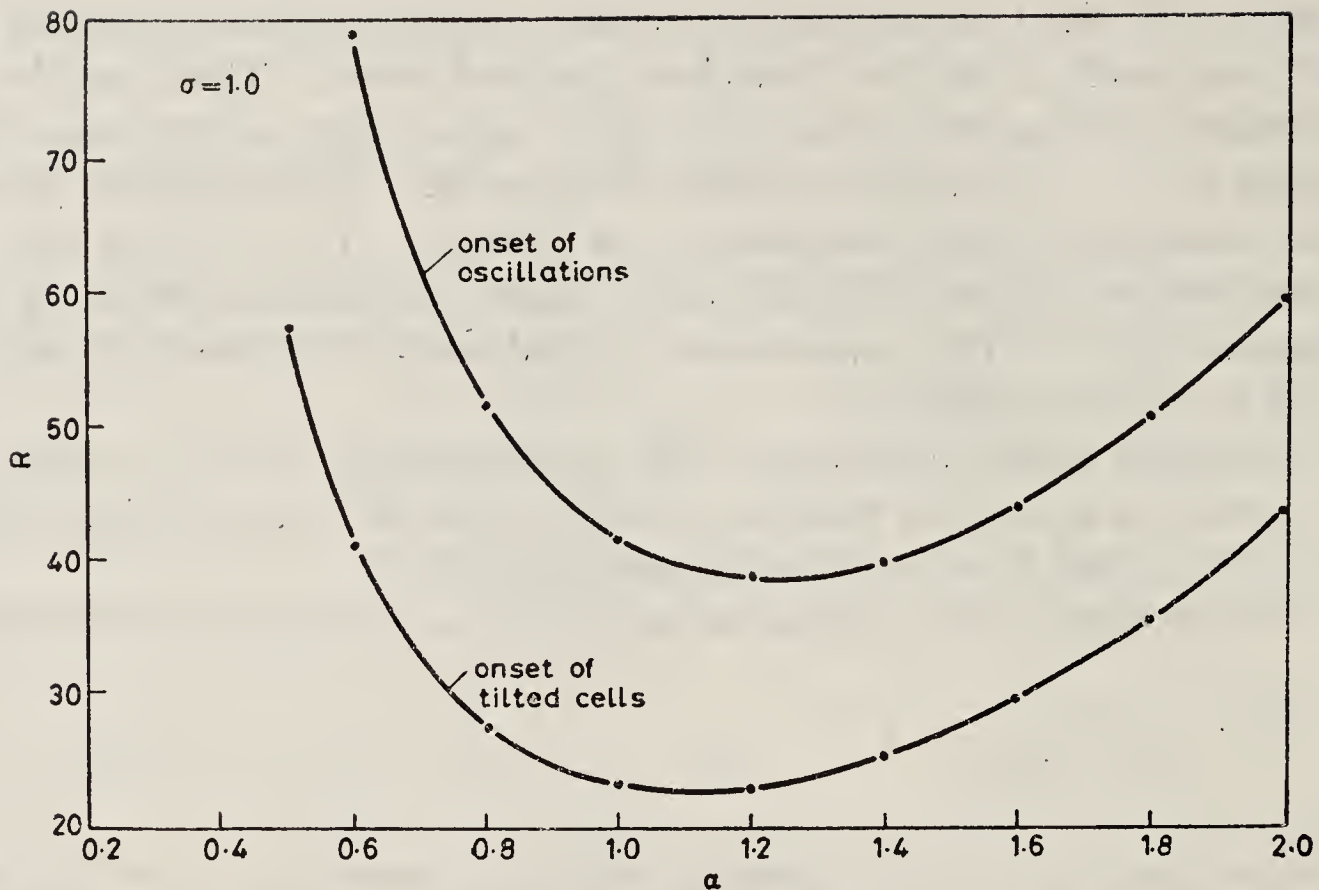


Figure 7. Marginal stability diagram for onset of steady tilted cells, and oscillatory flow.

- (iv) The steady tilted cells become unstable if R is increased to some value \tilde{R} , depending upon σ . At $R = \tilde{R}$ there is a Hopf bifurcation as a complex conjugate pair of eigenvalues crosses the imaginary axis and acquires a positive real growth rate. For $\sigma = 1$ and $\alpha = 1.2$, this occurs at $R \simeq 39$. The resulting flow is oscillatory.
- (v) Nonlinear periodic solutions were obtained for $\sigma = 1$ and for $40 < R < 90$ by numerically integrating the equations (5) to (10). The values of A , A , --- F were obtained as they varied with time, and from them the temperature and streamfunction can be constructed. One example of the temperature field is shown in figure 8. It shows a leftward propagating wave near the bottom of the layer, a rightward propagating wave near the top of the layer, while the zero isotherm near the mid-depth appears to vary as a standing wave.
- (vi) The periods of the limit cycles thus obtained are plotted in figure 9 as it was found to vary with the Rayleigh number. There are a number of regions of unusual behaviour. The following are some examples.
- (vii) At $R \simeq 45$, as well as at $R = 44$ there was a strong dependence upon initial condition, and multiple solutions at the same value of R were found. The hysteresis curve for $R \simeq 45$ is shown in figure 10. The arrows indicate that the solution at the value of R at the tip of the arrow was obtained using as initial condition the solution at R at the tail end of the arrow.
- (viii) Two spikes are seen in figure 9, one near $R = 44$, the other near $R = 51$. Actually, there is a gap near $R \simeq 51$ where periodic solutions were difficult to find. Approaching the gap from lower values of R , the last simple periodic solution was found for $R = 50.214$. The solution at $R = 50.215$ was chaotic in the sense that a particular sequence of states of the system was never found to be repeated after any long integration time that we attempted. However, approaching the gap from higher values of R , the last simple periodic solution was found at $R = 51.30$, with period $T_0 = 7$. At the slightly lower value of



Figure 8a.

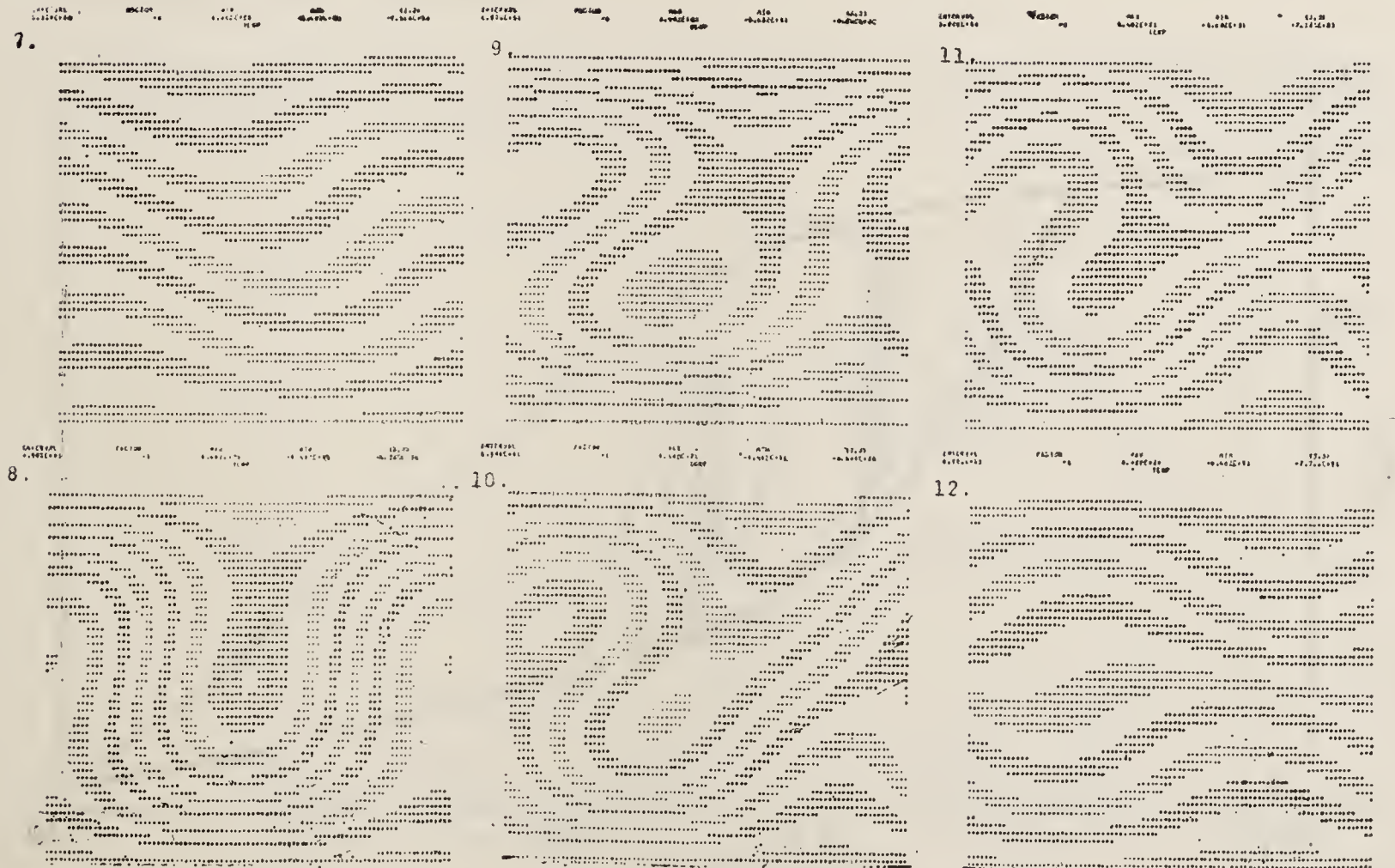


Figure 8 a & b. Temperature field at successive time intervals within one oscillation period. $\sigma = 1.0$, $\alpha = 1.2$, $R = 55$.

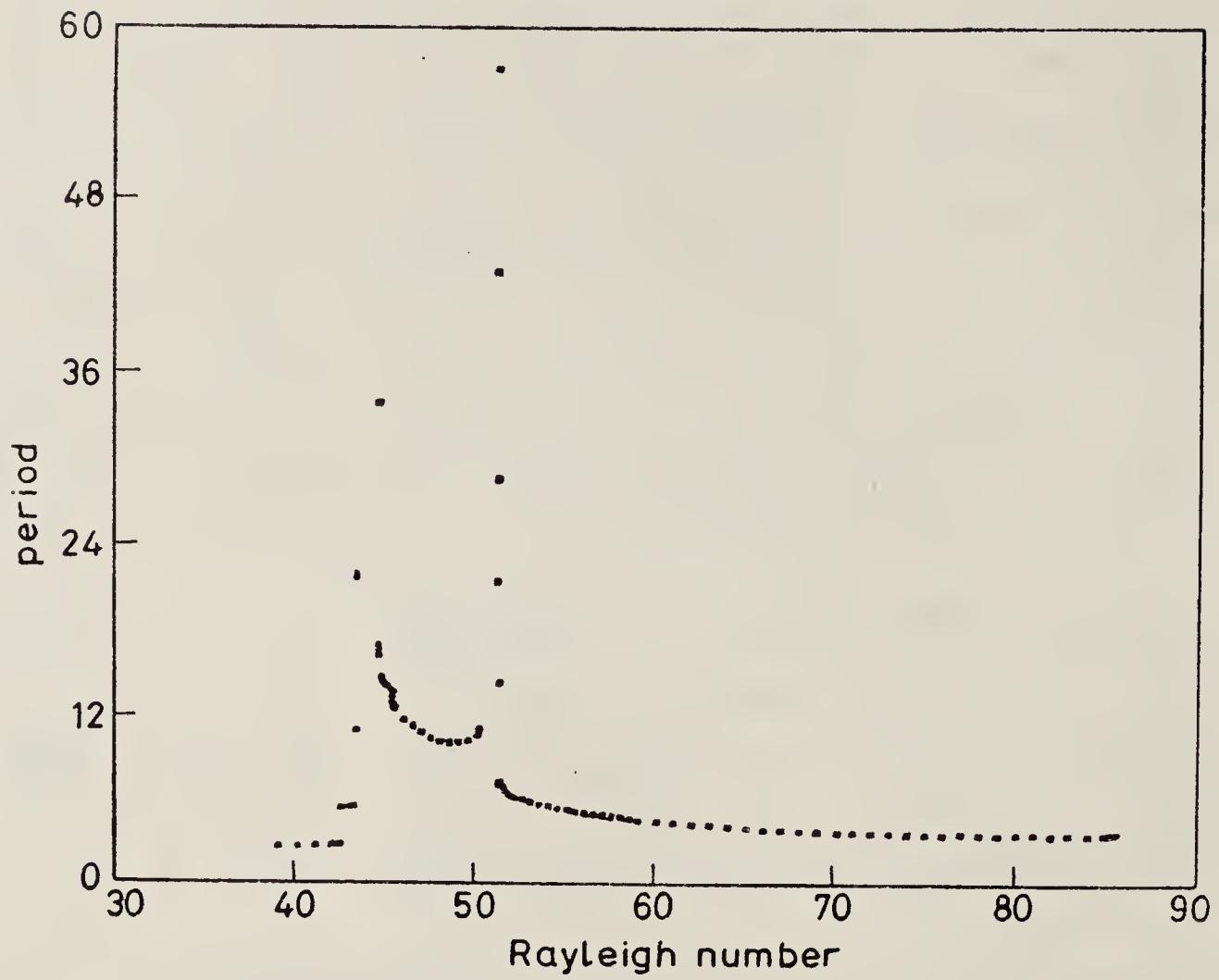


Figure 9. Period of the oscillatory solution as it varies with Rayleigh number beyond the third bifurcation.

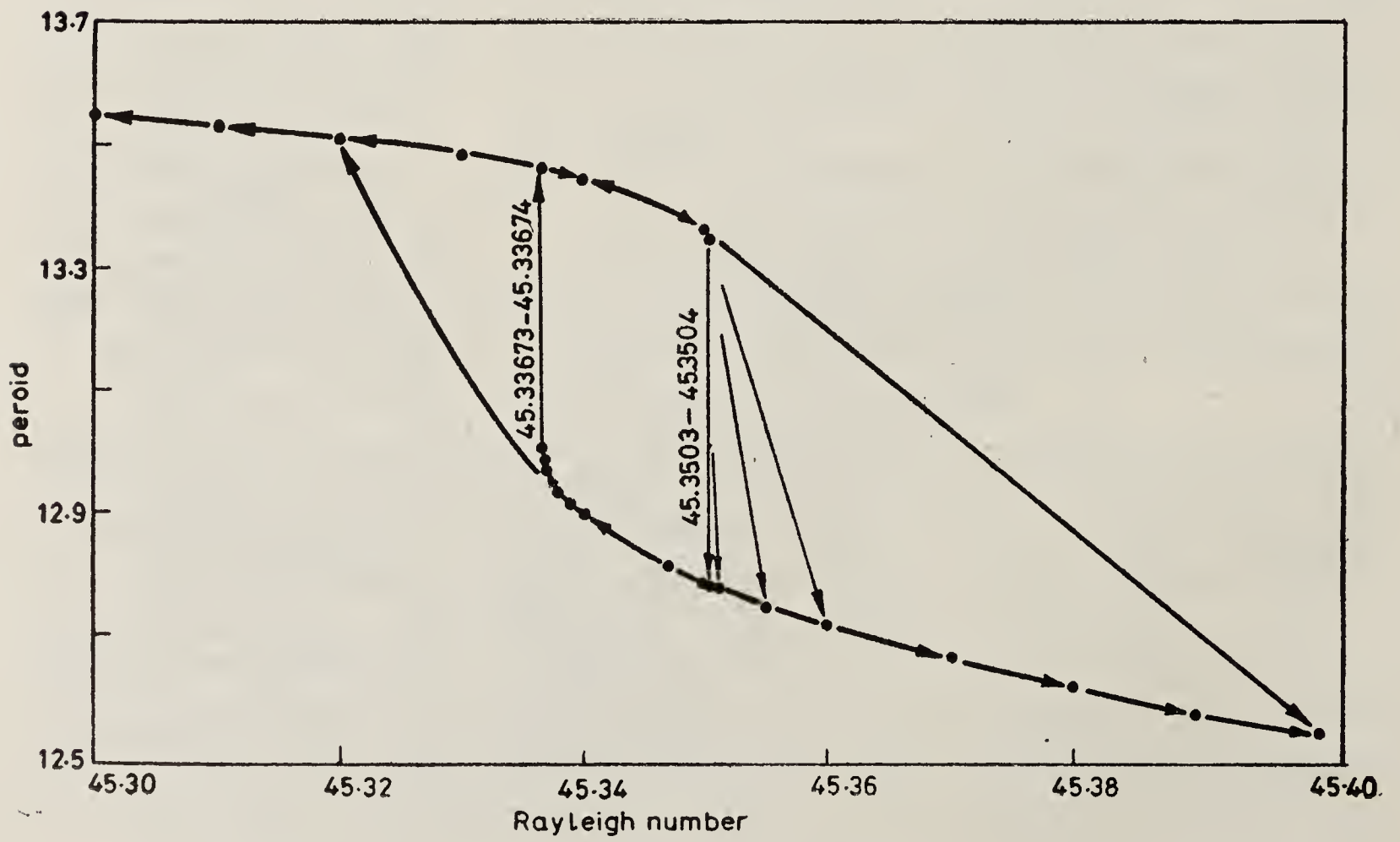


Figure 10. Period vs Rayleigh number showing hysteresis. $R \simeq 45$, $\sigma = 1.0$, $\alpha = 1.2$

$R = 51.25$, the period was found to be very nearly doubled; $T = 14 = 2T_0$. At $R = 51.24$, the period was quadrupled; $T = 28 = 4T_0$. In fact as R was decreased, the periods found were (in multiples of T_0) 1, 2, 4, 8, 16, 12, 6, 3. A similar sequence of period multiplying occurs also at the spike near $R = 44$. Within this spike is a narrow Rayleigh number range of chaotic flow. This period-multiplying follows the same sequence that is known to occur for a large class of one-dimensional maps of the unit interval (Sharkovsky 1964; Guckenheimer 1977; Feigenbaum 1978).

The orbit in the six-dimensional phase space, when projected onto the A - C plane appears at low R to be a roughly elliptical curve in the upper right quadrant ($A > 0$, $C > 0$). In figure 5, the orbit would be around one of the four paraboloidal curves resembling a "poppy head." (curves entirely in the other quadrants are also possible.) Such a curve is found in figure 11, labelled 1. Curves 1 and 2 are for R below the spike at $R \simeq 44$. Curve 3 is for $R > 44$. The orbit in this case goes around one "poppy head" then passes near the origin and goes around another "poppy head" before returning to the first. It is this passage near the origin (where the velocity goes to zero) that accounts for the lengthening of the period near $R = 44$.

Other quantities of interest such as the Reynolds stress \overline{uw} and the convective heat flux $\overline{w\theta}$ have been compiled from the computed values of A , --- F . The Lagrangian displacement of a particle can be computed also. For a particle on the boundary, $w = 0$, and its horizontal coordinate $G(t)$ can be determined as a function of time by integrating $u = dG/dt$, where $u(t)$ is known in terms of $A(t)$, $B(t)$ and $C(t)$. An example is shown in figure 12.

5. Summary of the model results

The highly truncated representation of ψ and θ given in equation (4) cannot be expected to give a quantitatively adequate description of turbulent flow. However,

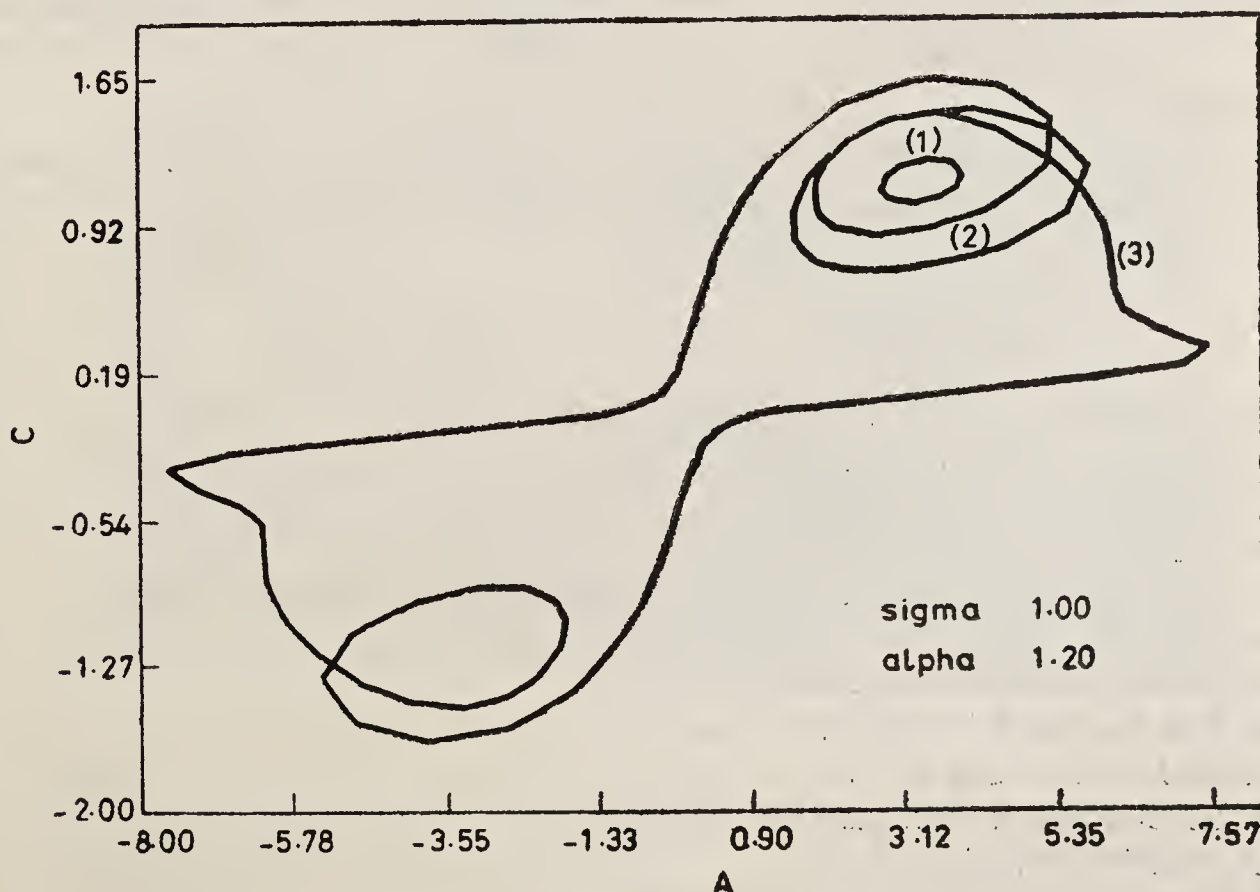


Figure 11. Projections of periodic orbits in phase space onto the A - C plane. $\sigma = 1$, $\alpha = 1.2$, (1): $R = 38.9$, (2): $R = 42.5$, (3): $R = 44.601$.

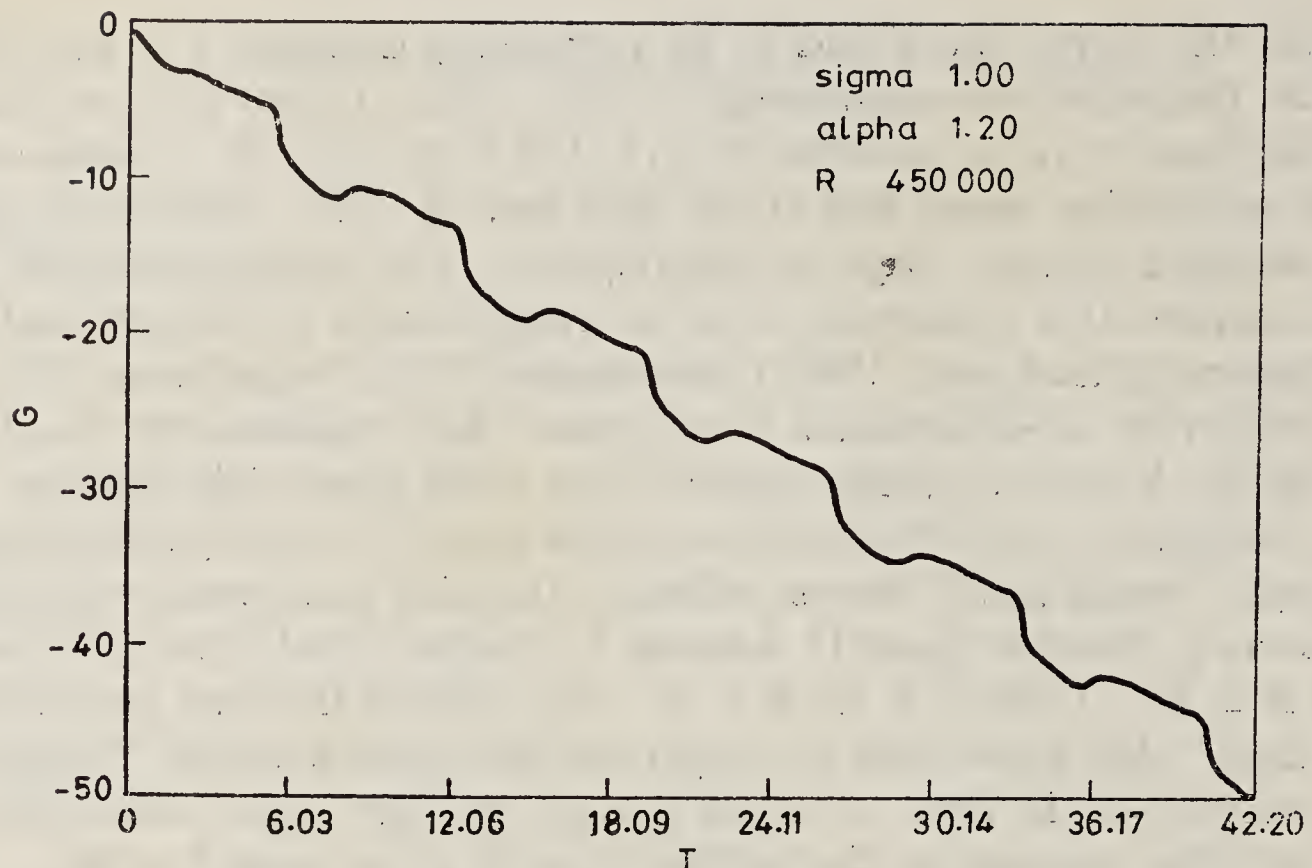


Figure 12. Horizontal coordinate G of a particle on the boundary, as it changes with time t .

terms such as $B \sin z$ in ψ were chosen so as to be able to describe some features of turbulent convection such as the spontaneous generation of large scale flow. The following qualitative features of the laboratory flow occur also in the present model.

- (i) Steady tilted cells appear in the laboratory (Hele-Shaw cell) and in the model after the second bifurcation.
- (ii) Tilting transient plumes occur in the laboratory flow at high R and in the model after the third bifurcation.
- (iii) Both the laboratory flow and the model have a net Lagrangian transport.

The new laboratory observations of convection and the related mathematical model described in this paper are the result of work done by Professor L N Howard of MIT and the author.

This work was supported by the Office of Naval Research, Fluid Dynamics Division and the National Science Foundation, through Grant Number OCE-772-7939.

References

- Busse F H & Whitehead J A 1971 *J. Fluid Mech.* **47** 305.
 Curry J H 1978 *Commun. Math. Phys.* **60** 193
 Feigenbaum M J 1978 *J. Stat. Phys.* **19** 25
 Guckenheimer J 1977 *Mathematicae* **39** 165
 Howard L N 1966 *Proc. 11th Int. Cong. Appl. Mech.* (Berlin: Springer Verlag) p. 1109
 Krishnamurti R 1970a *J. Fluid Mech.* **42** 295
 Krishnamurti R 1970b *J. Fluid Mech.* **42** 309
 Krishnamurti R & Howard L N 1981 *Proc. Natl. Acad. Sci. USA* **78** 1981
 Lorenz E N 1963 *J. Atmos. Sci.* **20** 130
 Malkus W V R 1954 *Proc. R. Soc. (London)* **A225** 185
 Sharkovsky A N 1964 *Ukr. Math. J.* **16** 61
 Willis G E & Deardorff J W 1967a *Phys. Fluids* **10** 931,
 Willis G E & Deardorff J W 1967b *Phys. Fluids* **10** 1861

Plate 1

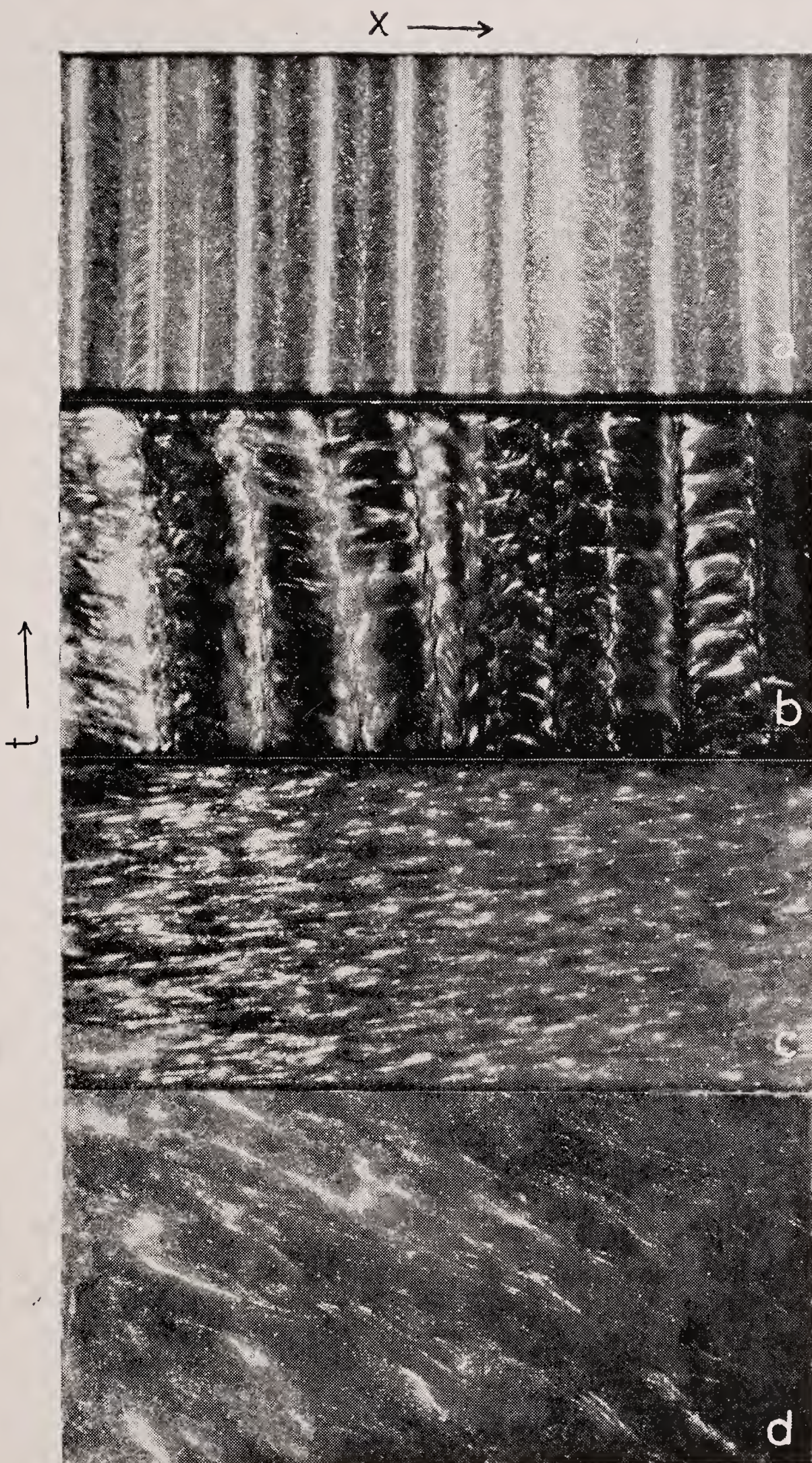


Figure 2. (x, t) representations of the flow 0.2 cm above bottom boundary. The range in x along the abscissa is 0 to 45 cm, t increases downward, range in time is 0 to τ : (a) $R = 7.5 \times 10^4$, $P = 0.86 \times 10^3$, $\tau = 17$ minutes. (b) $R = 10^6$, $P = 0.86 \times 10^3$, $\tau = 22$ minutes. (c) $R = 10^6$, $P = 7$, $\tau = 22$ minutes. (d) $R = 2.4 \times 10^6$, $P = 7$, $\tau = 9$ minutes.



Figure 3. Sequence of views of (x, z) slice through convecting fluid, showing rightward progress of dye along bottom and lower-right to upper-left tilt of plumes.

Plate 3

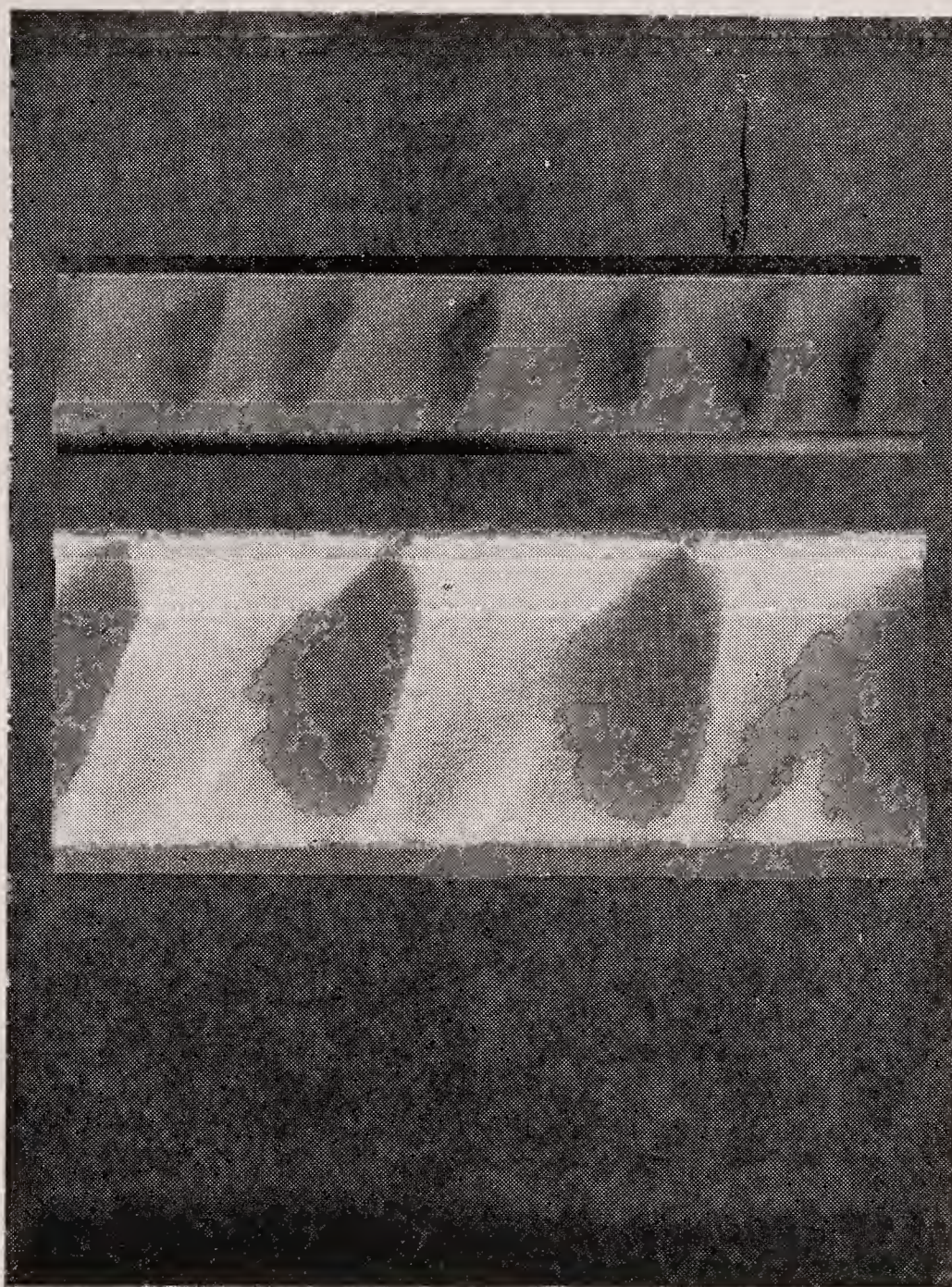


Figure 6b. Steady tilted cellular flow in a Hele-Shaw cell.

Fluid dynamics of the monsoon

SULOCHANA GADGIL

Centre for Theoretical Studies, Indian Institute of Science, Bangalore 560 012

MS received 15 January 1981

Abstract. The monsoonal regions of the world are characterized by a seasonal reversal in the direction of winds associated with the excursion of the equatorial trough (or the ITCZ) in response to the variation in the latitude of maximum insolation. This monsoonal circulation is a planetary scale phenomenon. However, the associated precipitation is critically dependent on the organization of the cumulus clouds (typically a few kilometers in horizontal extent) over the scale of synoptic vortices (typically a few hundred kilometers in horizontal extent). Thus modelling of the seasonal transitions and intraseasonal fluctuations requires an understanding of the fluid mechanics of these three scales of organizations and their interactions. The present paper is an attempt to outline the current state of understanding of these phenomena.

Keywords. Monsoon; tropical circulation; intertropical convergence zone; atmospheric instabilities.

1. Introduction

Over certain regions of the tropics, the wind blows in opposite directions in summer and winter. For instance, over the Arabian Sea, the wind at low levels blows from the southwest in the summer and from the northeast in the winter. Such a seasonal reversal in the direction of the wind is traditionally known as the monsoon. The Arabs first discovered the monsoon over the Arabian sea. In fact the word monsoon is derived from the Arabic word *mausam* for a season. Thus the essence of monsoon is seasonality.

Around the first century B.C. when India moved from pre-history to history, other traders from the Mediterranean world became aware of these winds and used this knowledge in planning their voyages. Ships travelling from Alexandria, which was then the entrepot of the Mediterranean world, would wait for the southwest monsoon to be established and then set sail for the west coast port of Bharukachchha (modern Broach). The northeast monsoon of the winter season would take these ships back. At this time Indians were involved in extensive trade with the Golden Isles of Jawa, Sumatra and Bali, which supplied the spices which were then sold to the Romans at enormous profits (Thaper 1966). Thus it is likely that they were also aware of the monsoon over the Bay of Bengal.

The monsoon is by no means restricted to the Indian region and the surrounding oceans. Ramage's (1971) delineation of the monsoonal regions of the world using a criterion based on the seasonality of winds shows the monsoon to be a planetary scale phenomenon (figure 1). As the famous astronomer Edmond Halley observed

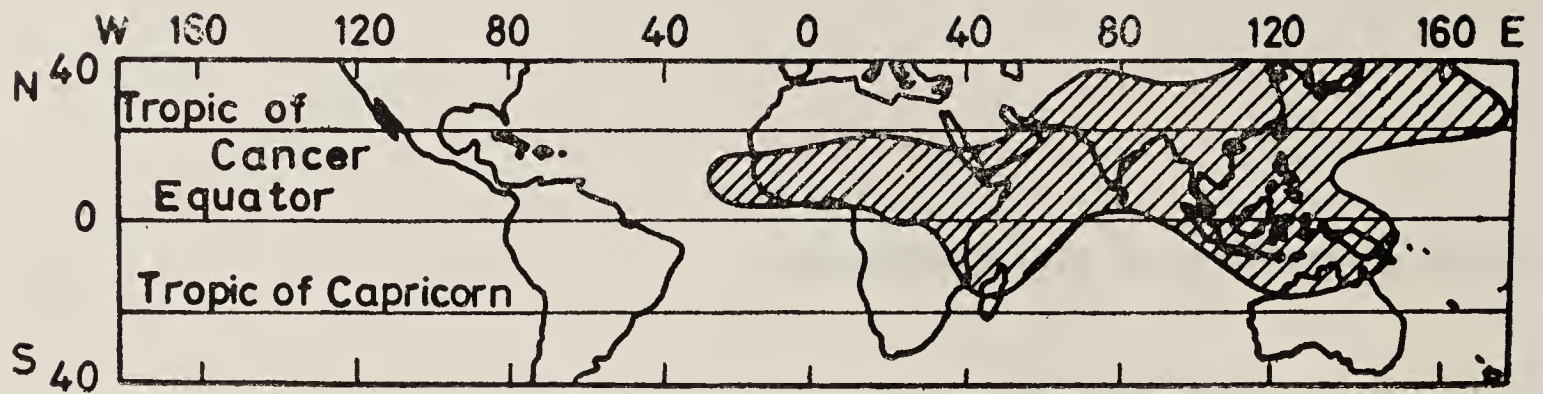


Figure 1. Monsoonal regions of the world (Ramage 1971)

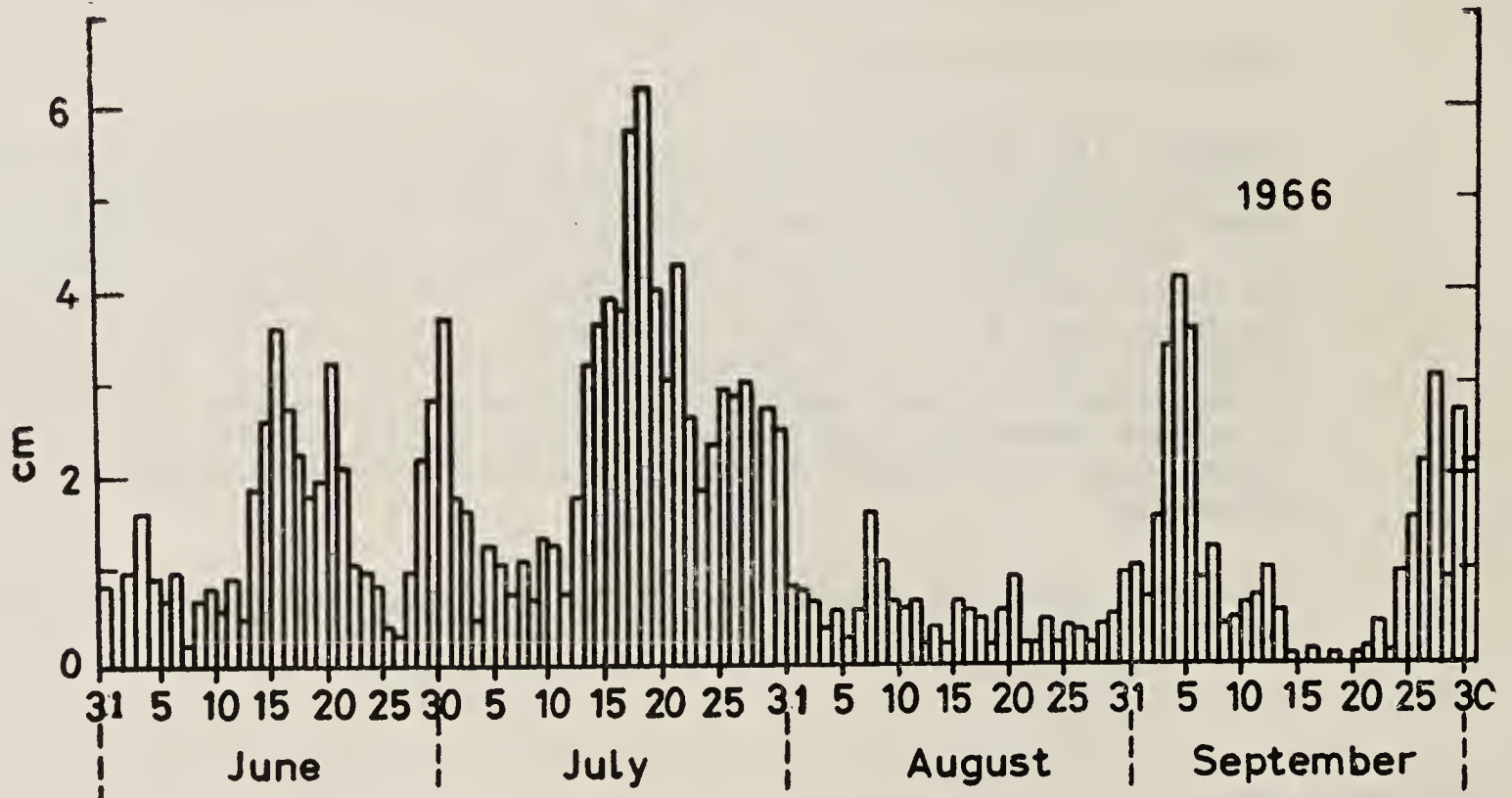


Figure 2. Average daily rainfall along the west coast of peninsular India (Anantha-krishnan 1966)

in 1686, in the monsoon 'are contained several problems that merit well the consideration of the acutest naturalists both by reason of constancy of effect and its vast extent'.

The seasonality of the wind is but one aspect of the variation of the tropical circulation. Of far greater concern to the large populations living in the monsoonal regions of the world is the variation of the rainfall associated with the monsoon. The rainfall along the west coast during one summer season is shown in figure 2. Two scales appear prominently in the variation: (i) the synoptic scale of 2-5 days associated with coherent structures of a few hundred kilometers in the horizontal extent, called tropical disturbances, and (ii) the longer period fluctuation (with a time-scale of two weeks or more) between active spells and weak spells, associated with the planetary scale.

The synoptic-scale disturbances organize the cumulus clouds (figure 3, plate 1), which are typically a few kilometers in horizontal extent, over the synoptic scale. This organization for the most intense tropical disturbance *viz.*, a typhoon or hurricane is shown in figure 4 (plate 2). These synoptic-scale disturbances are embedded in the planetary scale. Interactions between these three scales play a crucial role in the dynamics of the monsoon and its fluctuations. In this paper, an attempt is made to summarize what is known about the fluid mechanics of each of these scales of organization and their interaction.

2. Planetary-scale monsoon: the problem

As a first approximation, the general circulation of the atmosphere can be represented as in figure 5 (after Ferrel 1856). The major features of the longitudinally and temporally averaged tropical circulation at the surface of the earth are seen to be:

(i) The trade winds blowing from the subtropical high pressure belts towards the equatorial region in the northeasterly (southeasterly) direction in the northern (southern) hemisphere.

(ii) A zone of low pressure in the equatorial region called the equatorial trough or the intertropical convergence zone (ITCZ) in which the trades from the two hemispheres converge. Note that although the pressure field is axisymmetric, the trades have a westward component of velocity due to the action of the Coriolis force which is significant for these planetary scales. In fact, above the atmospheric boundary layer, the cross-isobar component becomes insignificant and the geostrophic component dominates.

The air converging in the ITCZ rises and moves poleward in the upper troposphere. The vertical circulation comprises ascent over the ITCZ and descent everywhere else. This meridional cell, called the Hadley cell, is depicted in figure 6.

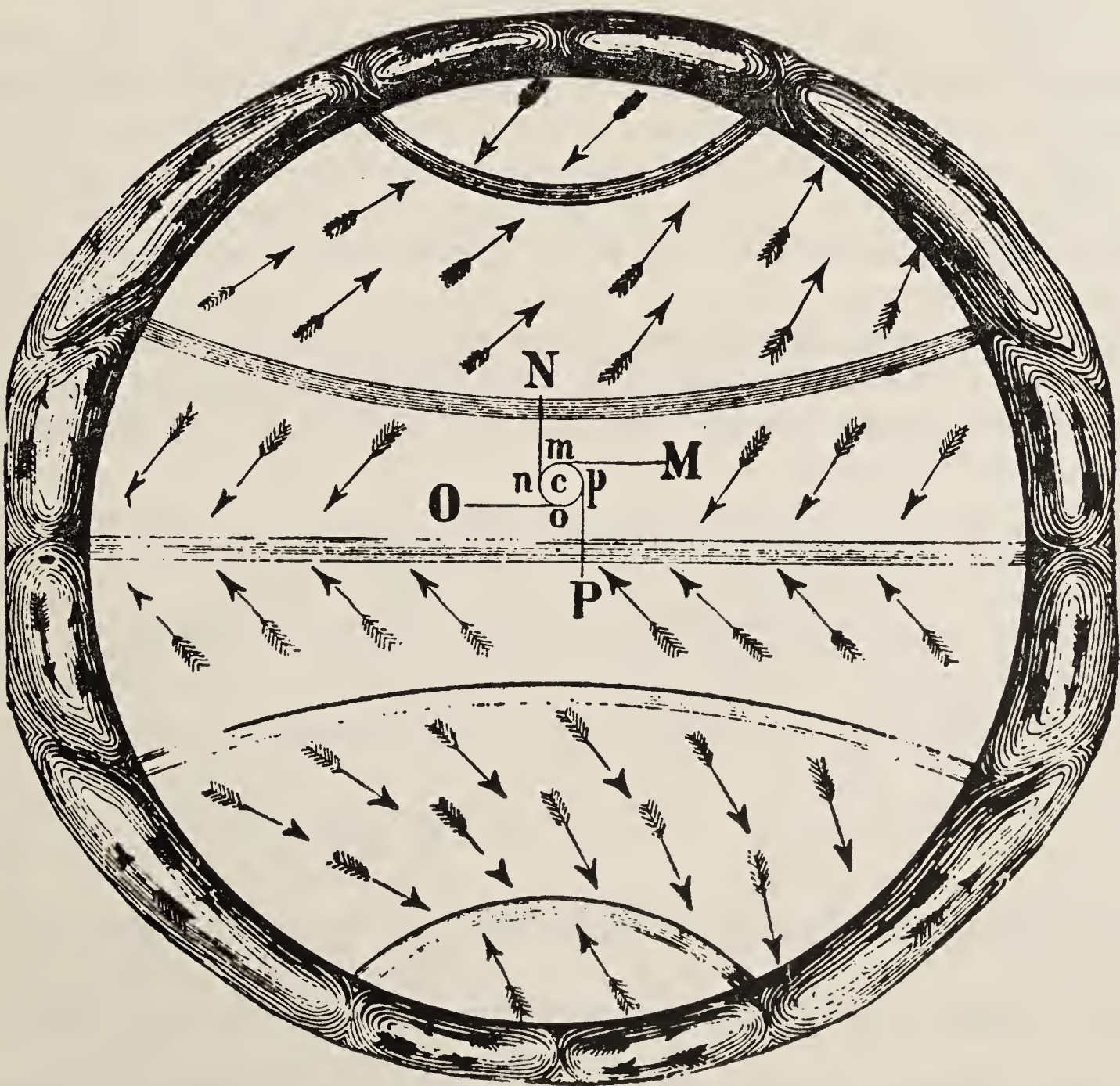


Figure 5. The general circulation of the atmosphere according to Ferrel (1856).

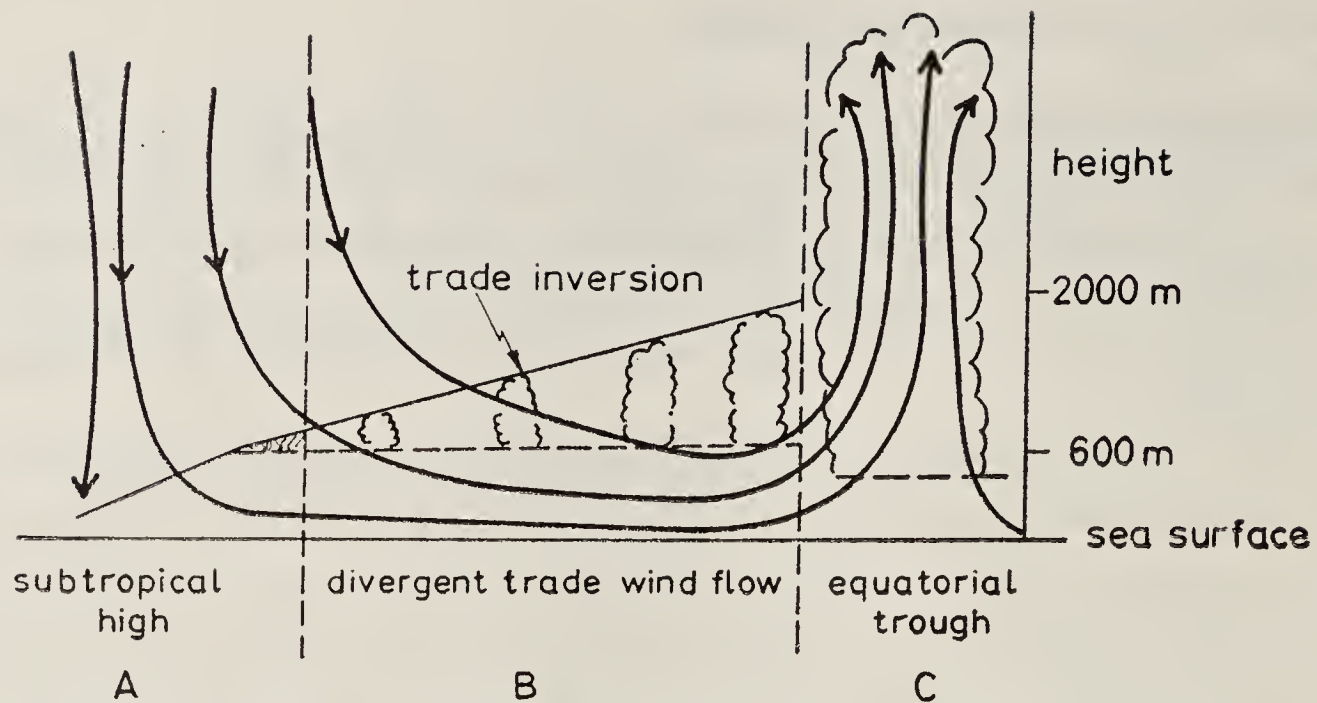


Figure 6. Schematic picture of the Hadley circulation (Augstein 1978).

The updraft in the ITCZ which occurs throughout the troposphere is associated with intense moist convection and hence the ITCZ is seen as a prominent feature of satellite cloud imagery (*e.g.* figure 7, plate 3). It is seen that the latitudinal extent of this cloud band, which stretches almost continuously around the earth in the tropics, is much smaller than the surrounding cloud-free region over which the air is descending.

The location of the ITCZ varies with the season (figure 8) in association with the variation of the sea-level trough (figure 9). It is seen that the amplitude of the seasonal variation is maximum in the monsoonal regions. The monsoonal change in the wind direction is merely a manifestation of this migration of the equatorial trough. When the trough is located in the northern hemisphere, the southeasterly trades from the southern hemisphere cross over into the northern hemisphere and blow towards this trough in a southwesterly direction. The zonal component changes from easterly to westerly upon crossing the equator because of the change in sign of the local vertical component of the rotation of the earth. Poleward of the trough, the northeasterly trades prevail. Thus a seasonal reversal in the direction of the wind occurs over the

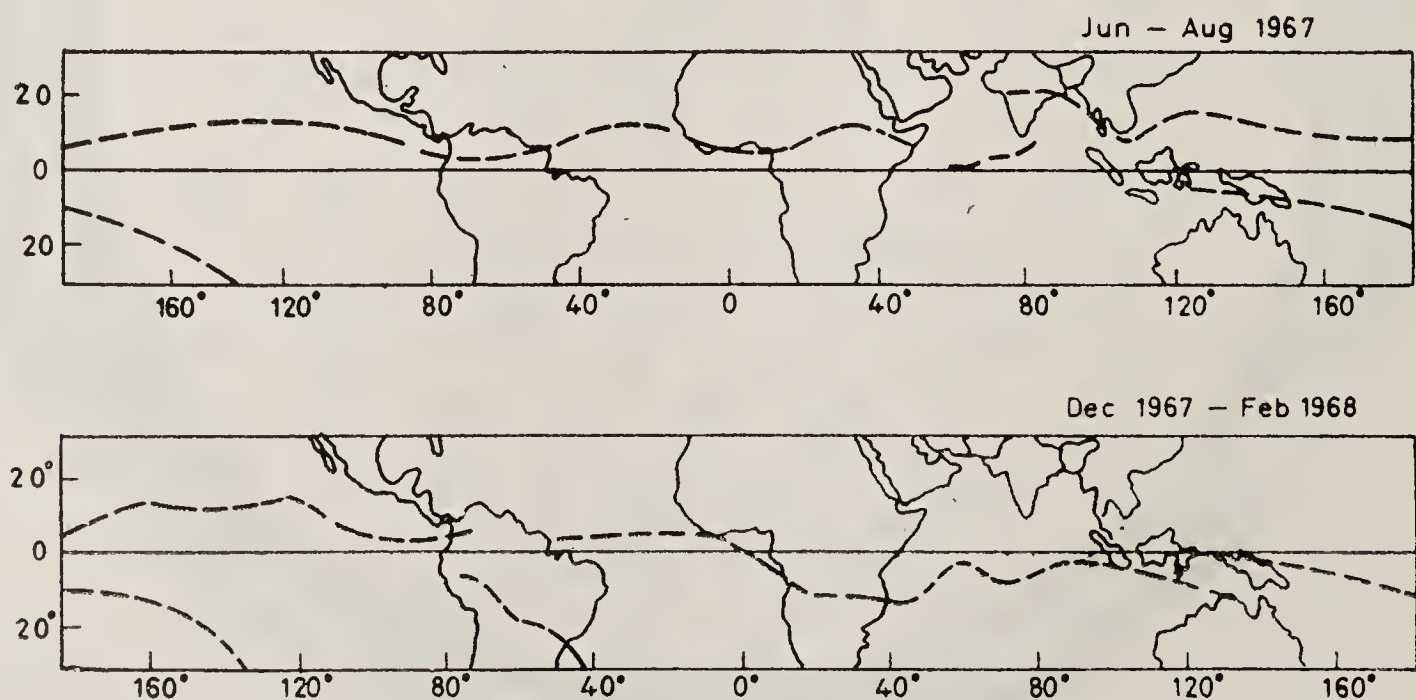


Figure 8. Seasonal distribution of axes of maximum brightness (cloudiness) from ESSA 3 and 5 digitized pictures over the tropics for March 1967–February 1968 (Hubert *et al* 1969)

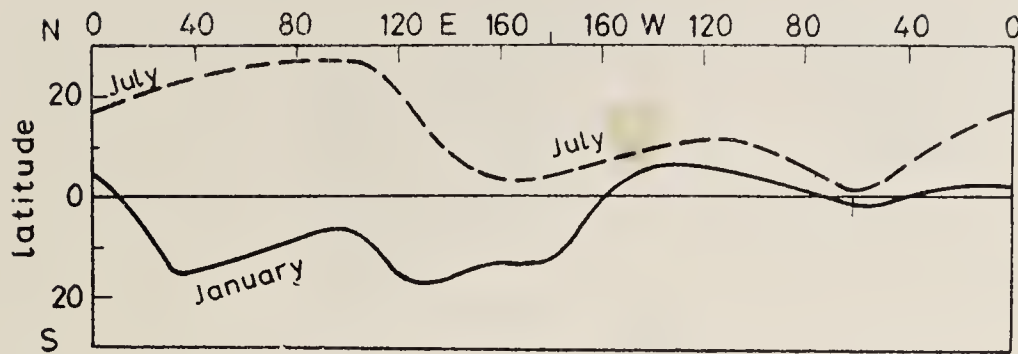


Figure 9. Mean location of the equatorial trough (Riehl 1954)

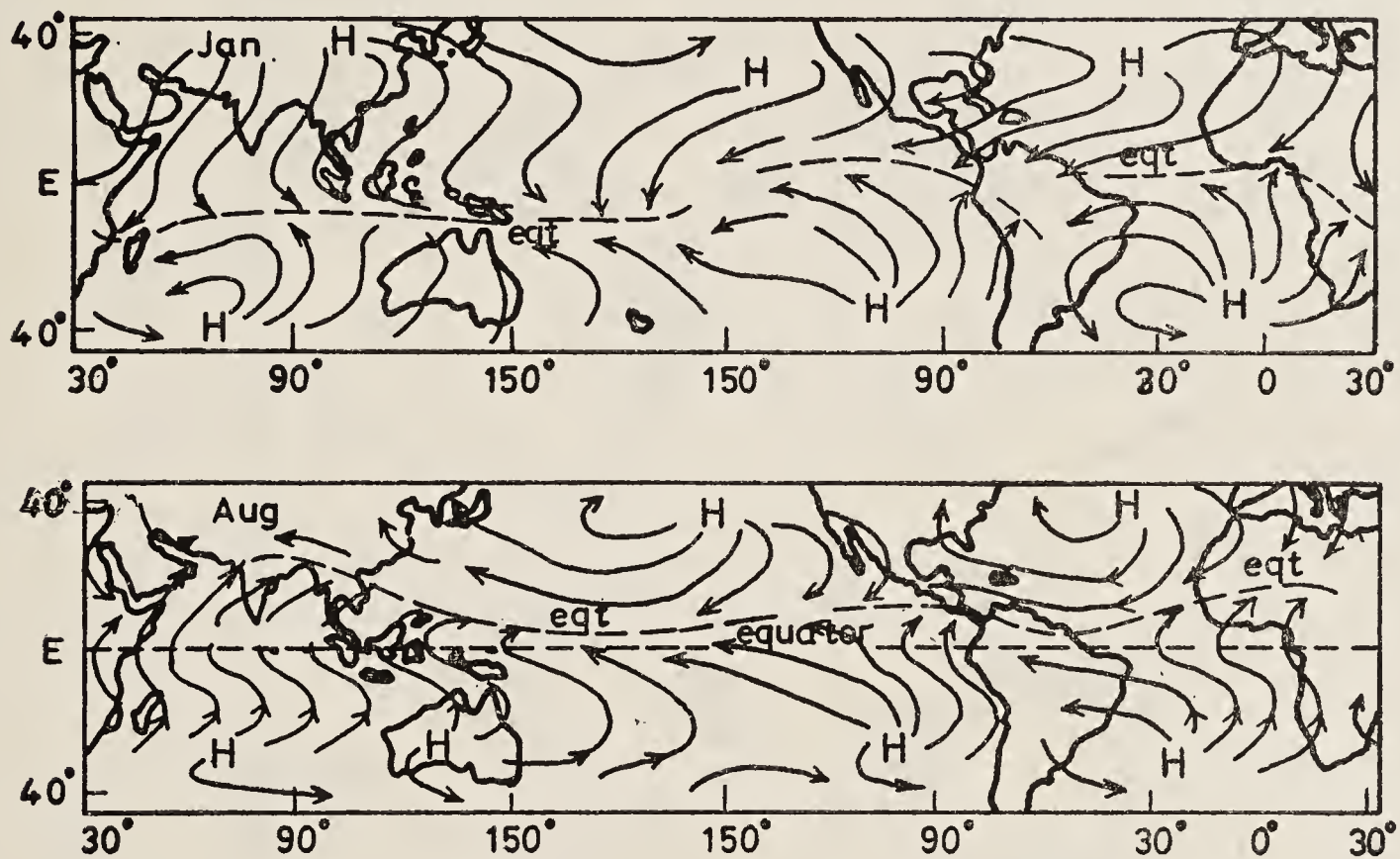


Figure 10. Idealized surface mean flow for January (top) and August (bottom) (Gray 1968)

region lying between the two latitudes corresponding to the extreme locations of the equatorial trough (figure 10).

Over the Indian longitudes, the northward shift of the ITCZ occurs during the onset phase of the monsoon in May and June. Towards the beginning of July the ITCZ gets established near the mean summer location of about 20°N (figure 11, plate 4). It persists over this region through August, with fluctuations in its location and in the intensity of the associated clouding and rainfall. The ITCZ migrates southwards in October and November during the withdrawal phase of the monsoon. The seasonal migrations and midseason fluctuations of the clouding and rainfall associated with the ITCZ are extremely complex (figure 12), and deciphering the role of the various mechanisms which drive or influence these variations is a rather difficult task. On the planetary scale, the major questions to which we need to address ourselves are the following.

- (i) How does the Hadley cell arise? Why is the vertical circulation asymmetric with a narrow rising limb?
- (ii) What determines the location and intensity of the ITCZ when the external forcing and boundary conditions are steady?
- (iii) How do the ITCZ and the rest of the Hadley cell respond to seasonally variable forcing?

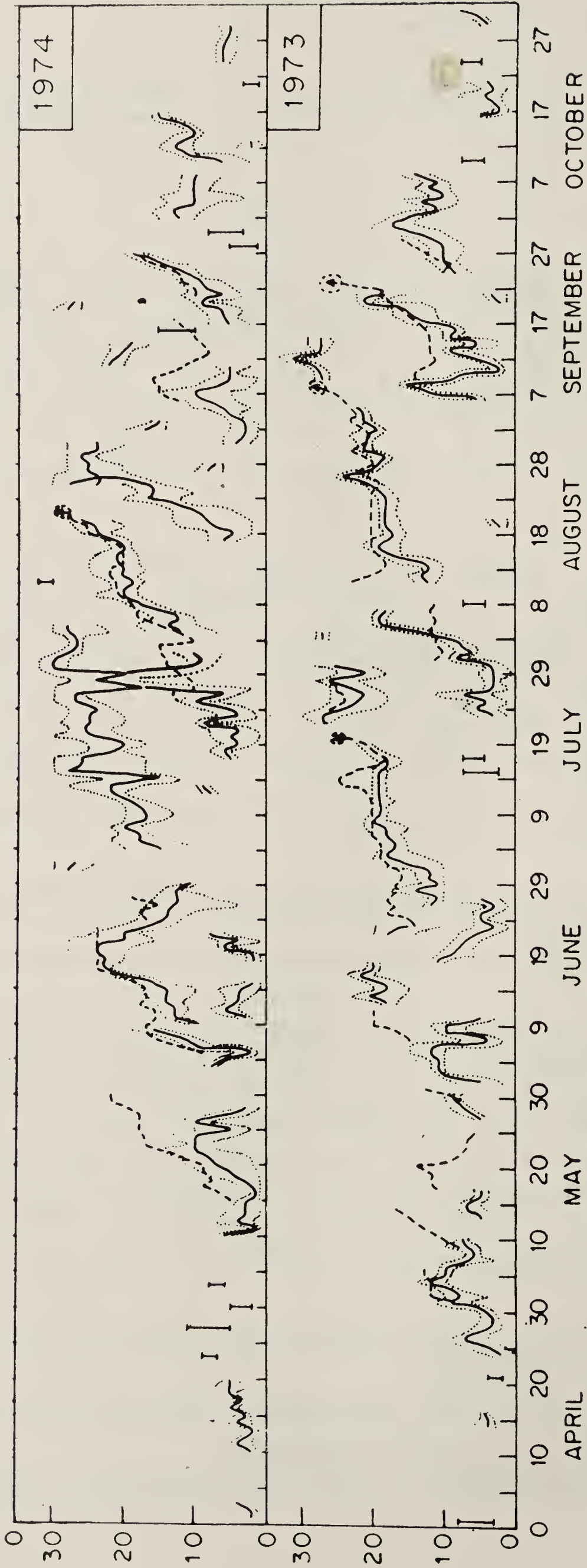


Figure 12a. Daily variation of the latitude of the zone of maximum brightness at 90° E for 1973-74. (See caption figure 12b for explanation).

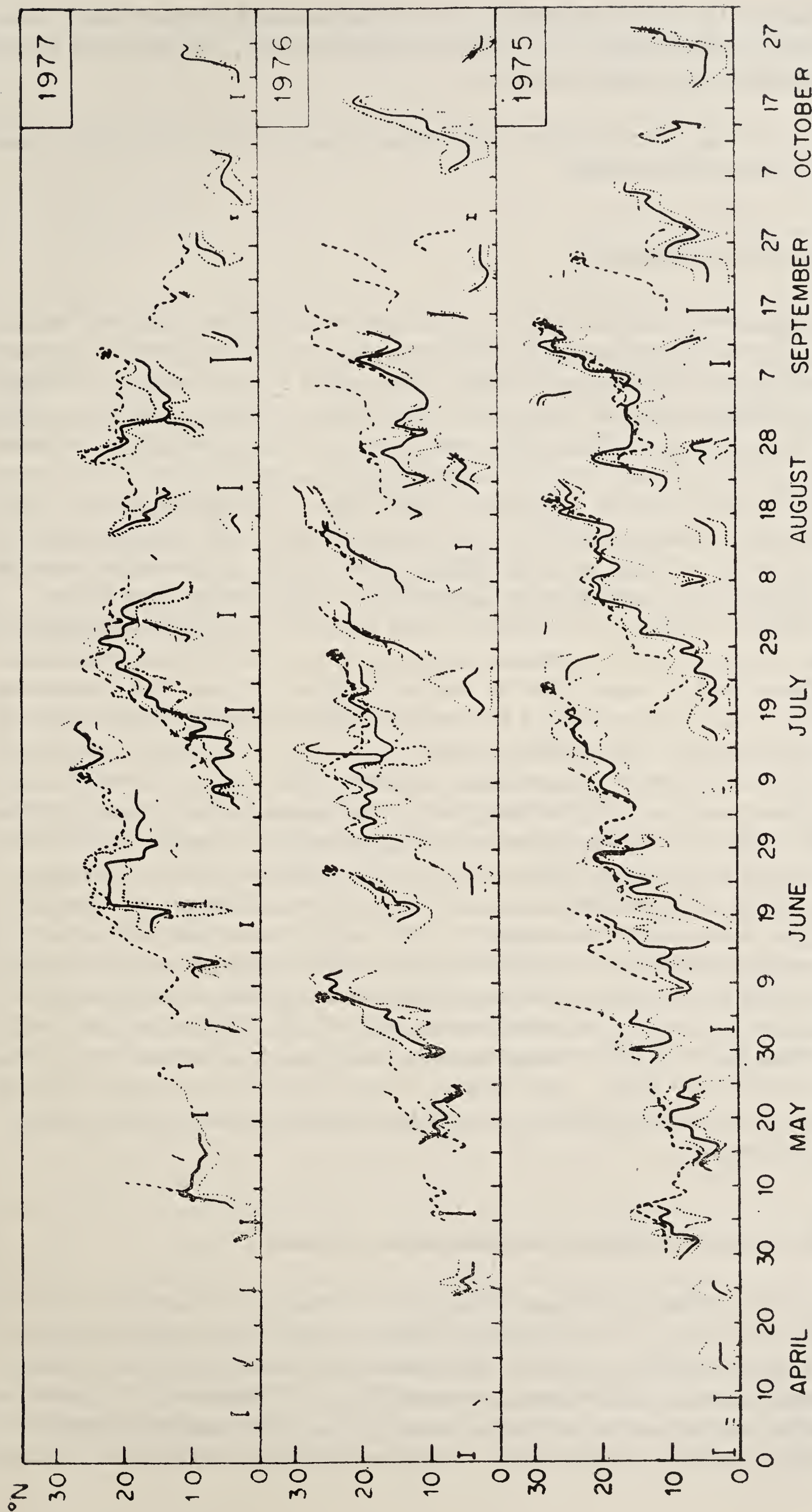


Figure 12b. Daily variation of the latitude of the zone of maximum brightness at 90°E for 1975-77. The solid line represents the axis, the dotted line northern and southern limits and the dashed line the location of the 700 mb trough (Sikka & Gadgil 1980).

- (iv) What are the factors responsible for (a) mid-season fluctuations such as the long dry spells known as breaks in the monsoon, and (b) inter-annual variability and climatic change?

I consider next what is known about each of these aspects on the basis of the existing theoretical and empirical studies.

3. Hadley cell: a simple model

The ultimate source of energy for the atmospheric motions is the radiation from the sun. As a first approximation, the earth's atmosphere may be considered to be transparent to the solar radiation and 'black' with respect to the terrestrial radiation. Hence the atmosphere is heated at its bottom boundary, *i.e.*, at the surface of the earth. The heat balance at the surface of the earth determines the nature of the boundary condition. For an ocean-covered earth, the large heat capacity of the ocean implies a prescription of the surface temperature with latitude. On the other hand, since the heat capacity of land is negligible, at its surface the heat flux has to be prescribed, again as a function of latitude. The Hadley cell is then the axisymmetric response of a rotating planetary atmosphere to latitudinally varying heating from below.

This problem of sideways convection has been studied by analytical and numerical models, in the linear as well as nonlinear regime (*e.g.* Stone 1968; Schneider & Lindzen 1977). These models assume that the vertical transport of heat and momentum by turbulence can be parametrized in terms of eddy-coefficients, which vary with height in some studies. More complex models also assume a similar parametrization for the horizontal transport of momentum and heat. The important results emerging from these models are: (i) the rising limb of the convective cell is located at the latitude at which the specified surface temperature or heat flux is maximum. (ii) When the Rayleigh numbers are high, the ascending limb is much narrower than the descending one. (iii) The cell driven by the boundary heating is rather shallow, the circulation being more or less restricted to a depth of about one kilometer from the surface for parameters appropriate to the earth's atmosphere. The circulation extends throughout the troposphere only when a mid-tropospheric heat source representing the latent-heat released by the convective clouds associated with the ITCZ is included in the model. Thus the interaction with the cumulus clouds has to be included even in the simplest model for the ITCZ. This leads us to the question: How do these cumulus clouds arise in the tropical atmosphere and how do they interact with the synoptic and planetary scales?

4. Cumulus dynamics: conditional instability of the first kind

In the lower part of the tropical atmosphere, the temperature is observed to decrease with height at a rate of about $5.5^{\circ}\text{C}/\text{km}$. Since a parcel of air rising adiabatically cools at a rate of $10^{\circ}\text{C}/\text{km}$, it finds itself colder and denser than its environment and is acted upon by a restoring buoyancy force. If, however, the parcel is saturated, the moisture condenses with a release of the latent heat of condensation and thereby prevents the parcel from cooling as rapidly as a dry one. Thus a

saturated parcel of air rising above the level at which condensation takes place cools at a rate of about $4.5^{\circ}\text{C}/\text{km}$. Such a parcel finds itself warmer than the surrounding air and is accelerated upward by the buoyancy force. The tropical atmosphere is therefore gravitationally stable for unsaturated air and unstable for saturated air. Such an atmosphere is said to be conditionally unstable.

If the moist air near the surface of the earth can be lifted upto the level at which condensation begins to occur (0.5 to 1 km), conditional instability triggers the formation of cumulus clouds. In the cumulus cloud, the air rises due to the buoyancy forces and the condensed moisture is lost through precipitation. This air descends in the region surrounding the cloud. Since the atmosphere is stable for dry air, work has to be done to transport the air downward against gravity. It can be shown that the ratio of the work done by the buoyancy forces in the upward displacement within the cumulus to that done against gravity in the downward displacement, increases with decreasing horizontal extent of the cloud. In other words, the thinner the cloud, the faster it grows in this simple inviscid model. If friction and entrainment of dry air in the cumulus are included in the model, the fastest growing scale is no longer zero, but depends on the horizontal mixing. It is known from the theory of Benard convection that these limitations will not be effective till the width approaches the depth of the troposphere. For parameters appropriate for our atmosphere, the favoured scale turns out to be about 5 km which is close to the observed width of a cumulus cloud.

5. Conditional instability of the second kind

In a conditionally unstable atmosphere, a cumulus scale perturbation is favoured over the synoptic scale perturbation, and hence if the two were to compete, the cumulus would surely win. The synoptic-scale disturbances can occur in this situation only because these two scales can cooperate with each other. We have seen that cumulus clouds can form only if the moist air at the surface is lifted upto the level at which condensation begins. The synoptic-scale disturbance triggers the formation of clouds by providing the required updraft. Charney & Eliassen (1964) first suggested the possibility of such a cooperative interaction. In their model the synoptic scale updraft arises due to boundary friction. Qualitatively, the nature of the interaction between the cumulus and synoptic scales they postulated is as follows.

A tropical disturbance is a cyclonic vortex (*i.e.* with anticlockwise rotation in the northern hemisphere) which is associated with a well-marked low pressure area in the weather maps of the lower troposphere. The air in the frictional boundary layer in a rotating system converges when the vorticity above the boundary layer is cyclonic. This results in an updraft from the surface boundary layer into the interior whose magnitude is proportional to that of the vorticity above the boundary layer. Thus the frictionally-generated updraft of the tropical disturbance leads to the generation of cumulus clouds throughout the disturbance (figure 13).

The air ascending within the cumulus cloud gains heat because the latent heat released exceeds the cooling due to adiabatic expansion. The air descending between the clouds also gains heat due to adiabatic compression. Thus once cumulus clouds are generated, the entire region comprising the clouds and their downdrafts heats up.

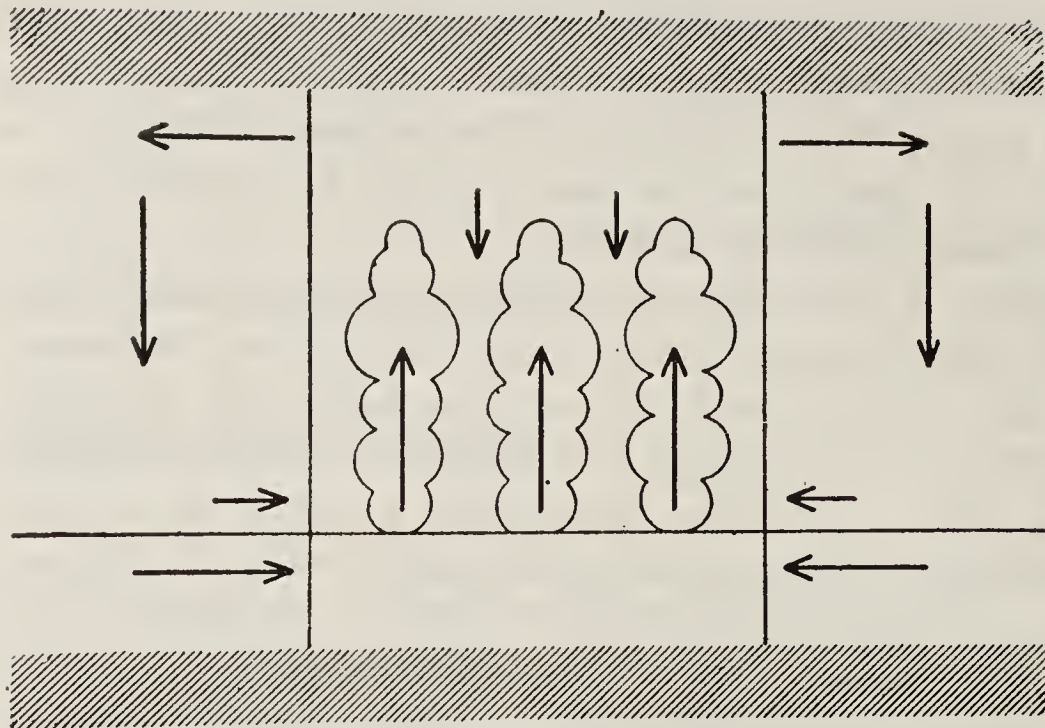


Figure 13. Schematic representation of interaction between cumulus cells and a synoptic scale cyclonic disturbance (Charney 1967)

This heating lowers the pressure and intensifies the synoptic scale vortex. This in turn increases the updraft and hence the cloud formation. Thus there is a positive feedback which allows the clouds and the disturbance to cooperate with each other and leads to the intensification of the latter. This instability, which leads to the intensification of tropical disturbances, is called conditional instability of the second kind (CISK).

6. Interactions between planetary and synoptic scales

The synoptic-scale disturbances are generated by the instability of the planetary-scale flow. It is believed that tropical disturbances are a manifestation of the barotropic instability (shear flow instability) of the planetary-scale circulation.

Over the Indian Ocean, during the summer, most of the cross-equatorial flow occurs in a low-level jet near the east coast of Africa (figure 14). This jet traverses the Arabian sea and the Indian landmass. The nature of the variation of the wind in this jet is rather favourable for the development of barotropic instability. Krishnamurthy *et al* (1980) have shown that the formation of the onset vortex for the season of 1979 could be attributed to barotropic instability. However, although barotropic instability of the planetary scale wind field may be a necessary condition for genesis it is by no means sufficient. On many occasions, the disturbances do not form even when instability criteria are satisfied. We do not as yet have a complete theory which yields all the necessary and sufficient conditions for the formation of the disturbances. Once formed, they intensify if they can trigger cumulus developments *via* CISK.

The synoptic-scale vortices seem to play a major role in maintaining the planetary scale. A study of the daily weather charts over the Indian area for two summer seasons showed that on a vast majority of occasions when the ITCZ was active there were one or more synoptic-scale vortices embedded in it. Only on very few occasions was convection uniformly organized on the scale of the ITCZ. Sikka (1980) has also shown that the total rainfall in a season is directly related to the number of disturbances generated in the season. In fact even in the mean monthly streamline

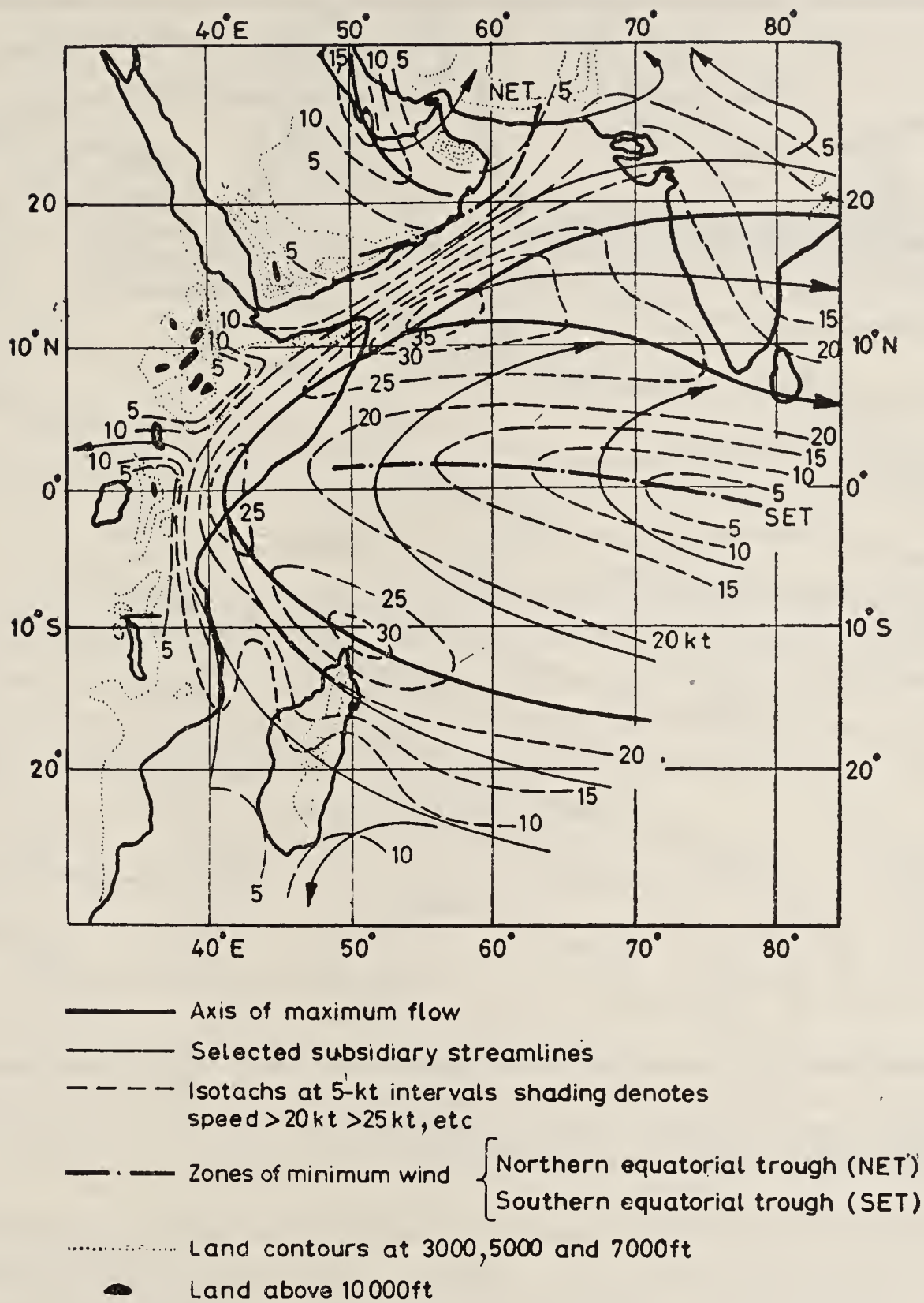


Figure 14. Mean monthly airflow at 1 km in July (Findlater 1977).

chart for July at a level just above the boundary layer the synoptic vortices are prominent (figure 15). All these observations suggest that the synoptic scale disturbances are crucial for the very existence of the ITCZ.

7. Seasonal variation of the ITCZ

Averaged over the globe, the location of the equatorial trough shows a seasonal oscillation with a phase lag of about two months (figure 16). It is seen from figure 8 that the amplitude of this seasonal variation is maximum over the Indian longitudes (about 30° latitude), is significant over the eastern parts of Africa and South America and negligible over the eastern and central Pacific and Atlantic Oceans. The phase lag over the continents is about one month whereas that over the oceans is two months. The difference in the amplitude of the response over land and ocean arises mainly because the ocean provides an interactive boundary at which the temperatures

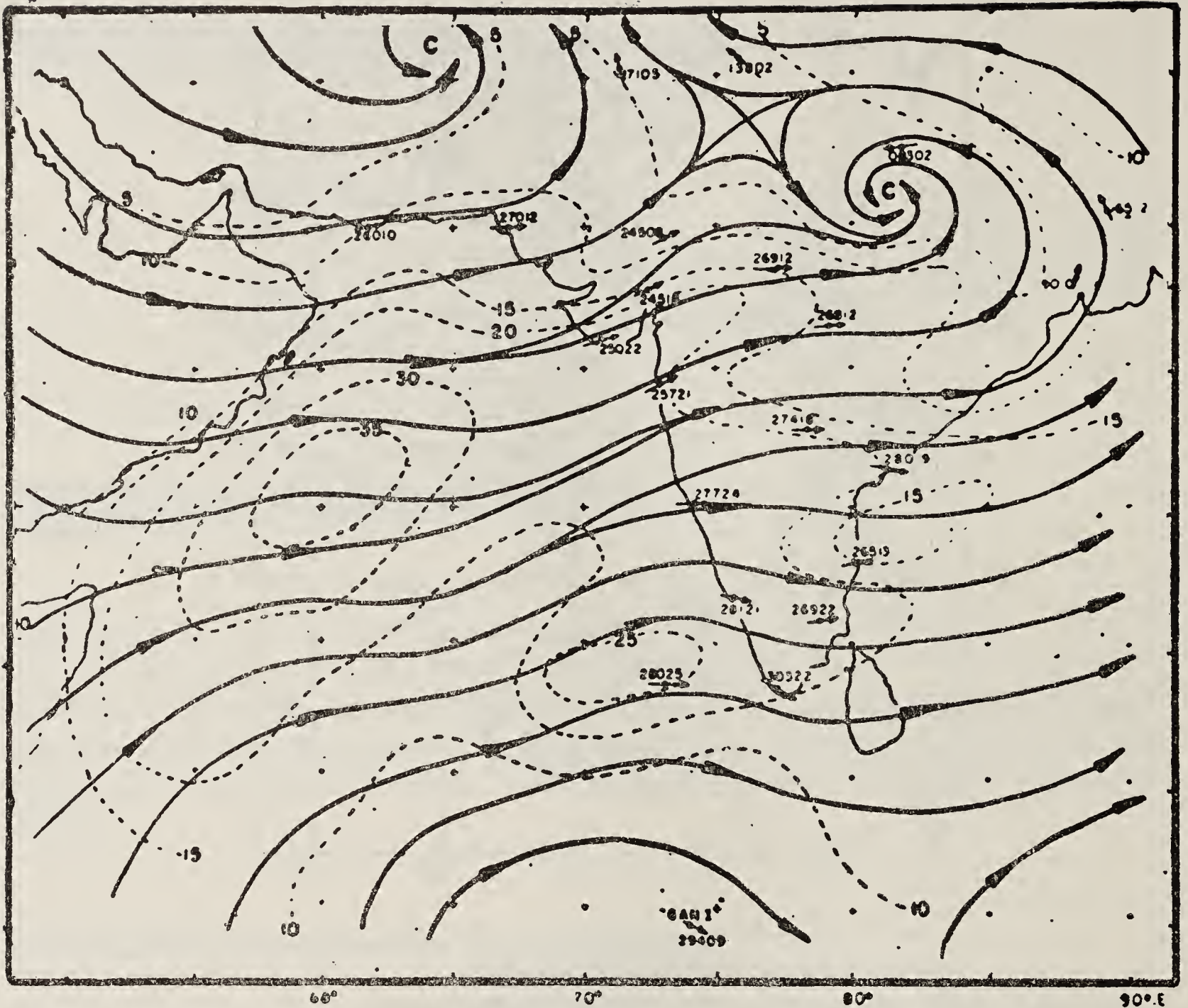


Figure 15. Kinematic analysis of mean resultant wind for July at 900 m. Isotachs are labelled in knots (Ramage 1971)

are determined not only by the insolation but by other factors such as the wind-driven ocean currents, up-welling etc. Thus the wind regime, consisting of easterlies equatorward of the subtropical highs and westerlies poleward of them, drives anticyclonic gyres in the oceans with poleward currents near the western boundaries and equatorward currents near the eastern boundaries of the oceans. Such strong equatorward currents occur along the west coasts of Southern Africa and America. They depress the sea-surface temperature of the equatorial region by advection of the cold water from the high latitudes. This seems to constrain the oscillation of the ITCZ in these oceanic areas to the northern hemisphere.

The location of the radiative heat source over the continental areas corresponds rather closely to that of the maximum insolation and hence the amplitude of the oscillation over the eastern hemisphere is larger. Further, the Tibetan plateau which extends to half the troposphere, acts as an elevated heat source so the amplitude is even larger over the Indian longitudes than over other continental areas.

8. Transitions, fluctuations and climatic changes

The seasonal transitions over any given longitudinal belt differ markedly from the mean picture of figure 16, in being rather abrupt. For example, the northward

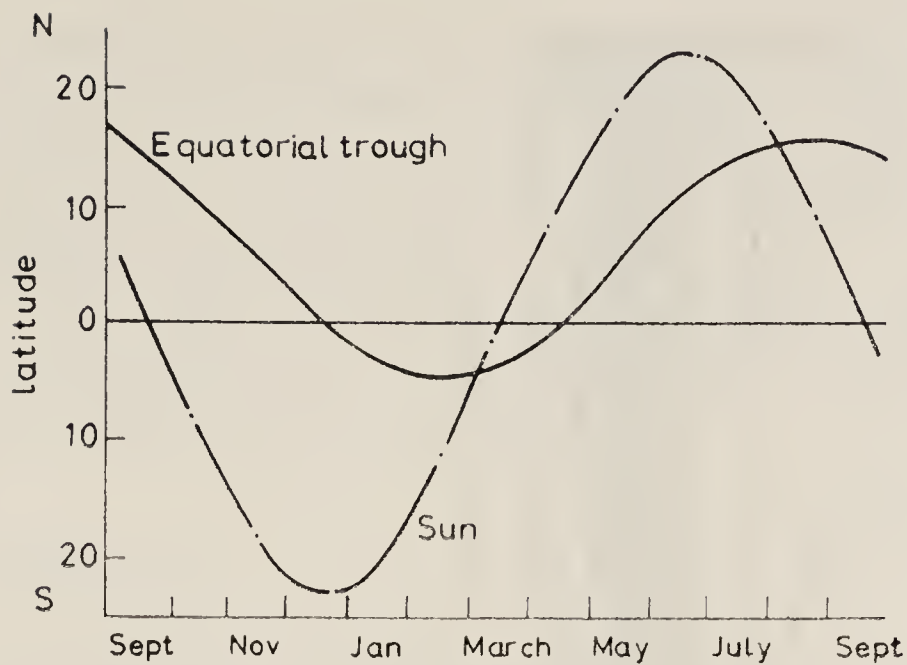


Figure 16. Seasonal variation in the latitude of the equatorial trough and sun averaged over the globe (Riehl 1978).

movement of ITCZ over the Indian longitudes during the onset phase of the monsoon, *i.e.* in the spring-to-summer transition, occurs in a series of northward surges, each successive surge taking the ITCZ farther northward. These surges arise from the poleward movement of the synoptic-scale vortices generated in the ITCZ (Sikka & Gadgil 1980). Hence the prediction of the transition phase involves the prediction of the generation and movement of the disturbances.

The fluctuations in the precipitation over the time-scale of 2–4 weeks between the active and the weak phases of the ITCZ probably arise from the clouds and the hydrological cycle associated with them. A relatively simple model of the monsoon including important features such as the presence of a continental as well as oceanic areas with the latter being an interactive boundary (Webster *et al* 1977) brings out clearly the important role played by the clouds (figure 17). Note that with the incorporation of the clouds, the synoptic-scale fluctuations become more prominent and the larger time-scale fluctuation also appears with a 'break' in the monsoon every four weeks. This suggests that the decrease in the strength of the radiative source brought about by the clouds in the ITCZ may act as a negative feedback and generate intraseasonal fluctuations.

The interannual variability of the ITCZ arises from the interaction between the various components of the tropical atmospheric and oceanic circulation. There is evidence for strong coupling between trade winds and the underlying ocean (Barnett 1977). Reiter (1978 a, b) has shown that there is a positive feedback between the ITCZ, the trades and the sea-surface temperature (SST). Studies of predictabilities of SST (Davies 1976) suggest that the observed variation in SST is largely a result of the atmosphere driving the ocean, although earlier Bjerknes (1966) and Namias (1959) had suggested that the strength of the ITCZ is determined by the SST. Whether the oceanic or the atmospheric conditions play a determining role in the interaction depends upon the time-scale considered. It is likely that the low-frequency variabilities in the seasonal thermocline arise from stochastic forcings by short-period atmospheric disturbances (Frankignoul & Hasselmann 1977). The oceanic conditions so produced may in turn determine the intensity of the ITCZ in a given season. Such interactions are likely to be important in determining climatic changes occurring over longer time-scales.

A steady decrease in the precipitation leading to climatic change can occur due to a biogeophysical feedback in which precipitation decreases with the introduction of

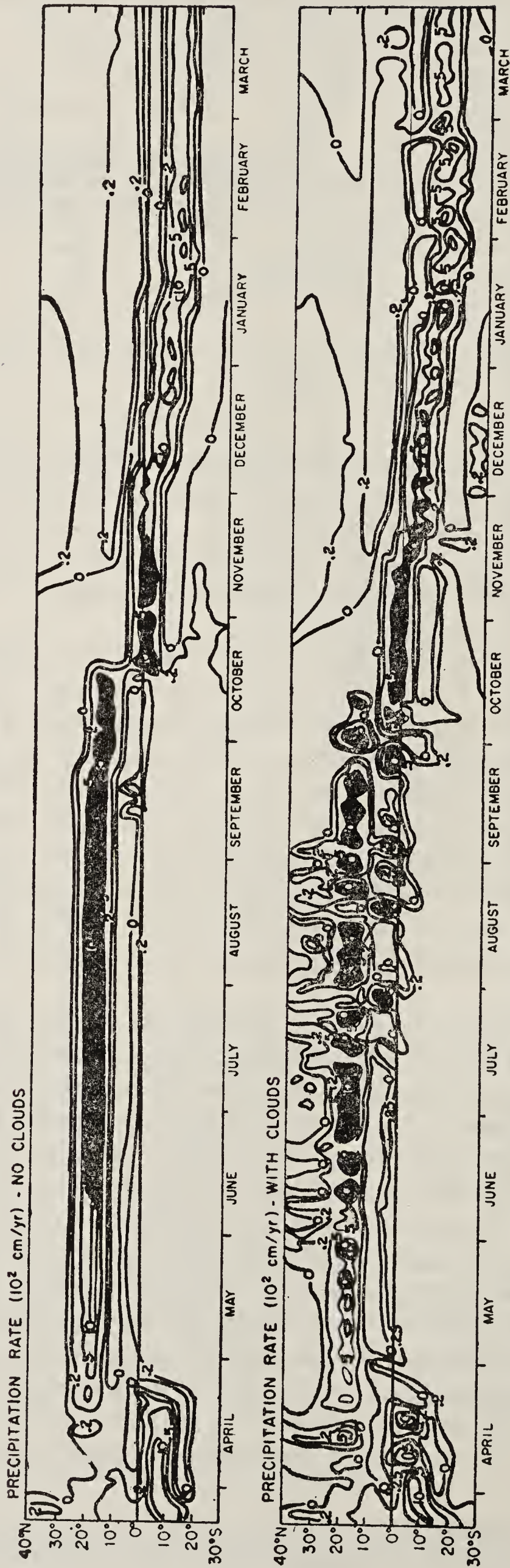


Figure 17. Precipitation rates of a model for monsoons with clouds (bottom) and without clouds (top) (Webster *et al* 1977)

desert-like conditions (with higher albedo at the surface) and this decrease of precipitation in turn triggers an intensification of desert conditions (Charney *et al* 1977). Changes in the evapotranspiration rates can also produce similar effects. Whether these or other mechanisms bring about the observed climatic change has to be ascertained by further studies.

All in all, it is clear that despite the progress in our understanding of the monsoon since Halley's time, it remains to this day one of the most exciting and challenging problems in fluid dynamics.

References

- Ananthakrishnan R 1966 *Monsoon rainfall summary, June to September* (Poona: India Met. Dept.)
- Augstein E 1978 in *Meteorology over the tropical oceans*, Proc. of Conf. (Bracknell, UK: Royal Met. Soc.) p. 73
- Barnett T P 1977 *J. Atmos. Sci.* **34** 221
- Bjerknes J 1966 *Tellus* **18** 820
- Charney J G 1967 in *Advances in numerical weather prediction* (Connecticut: Travellers Res. Centre)
- Charney J G, Quirk W J, Chow S & Kornfield J 1977 *J. Atmos. Sci.* **34** 1366
- Charney J G & Eliassen A 1964 *J. Atmos. Sci.* **21** 68
- Davis R E 1976 *J. Phys. Oceanogr.* **3** 249
- Ferrel W 1856 *Nashville J. Med. Surgery* **11** 287 (Reprinted: 1882 Prof. Pap. Signal Serv. No. 12, Washington 7-19, 64)
- Findlater J 1977 *Pageoph.* **115** 1251
- Frankignoul C & Hasselmann K 1977 *Tellus* **29** 289
- Gray W M 1968 *Mon. Weather Rev.* **96** 669
- Halley E 1686 *Philos. Trans.* **26** 153
- Hubert L F, Krueger A F & Winston J S 1969 *J. Atmos. Sci.* **26** 771
- Krishnamurthi T N, Ardanuy P, Ramanathan Y & Pasch R 1980 On the onset-vortex of the summer monsoon, Rep. No. 80-3 Dept of Meteorology, Florida State Univ., Tallahassee
- Namias J 1959 *J. Geophys. Res.* **64** 631
- Ramage C S 1971 *Monsoon meteorology* (New York: Academic Press)
- Reiter E R 1978a *J. Atmos. Sci.* **35** 349
- Reiter E R 1978b *Mon. Weather Rev.* **106** 324
- Riehl H 1954 *Tropical meteorology* (New York: McGraw Hill)
- Riehl H 1978 *Introduction to the atmosphere* (New York: McGraw Hill)
- Schneider E K & Lindzen R S 1977 *J. Atmos. Sci.* **34** 263
- Sikka D R 1980 *Proc. Indian Acad. Sci. (Earth Planet. Sci.)* **89** 179
- Sikka D R & Gadgil S 1980 *Mon. Weather Rev.* (in press)
- Stone P H 1968 *J. Atmos. Sci.* **25** 644
- Thaper R 1966 *A history of India* (Harmondsworth, UK: Penguin)
- Webster P J, Chou L & Lan K M W 1977 *Pure Appl. Geophys.* **115** 1463

Plate 1

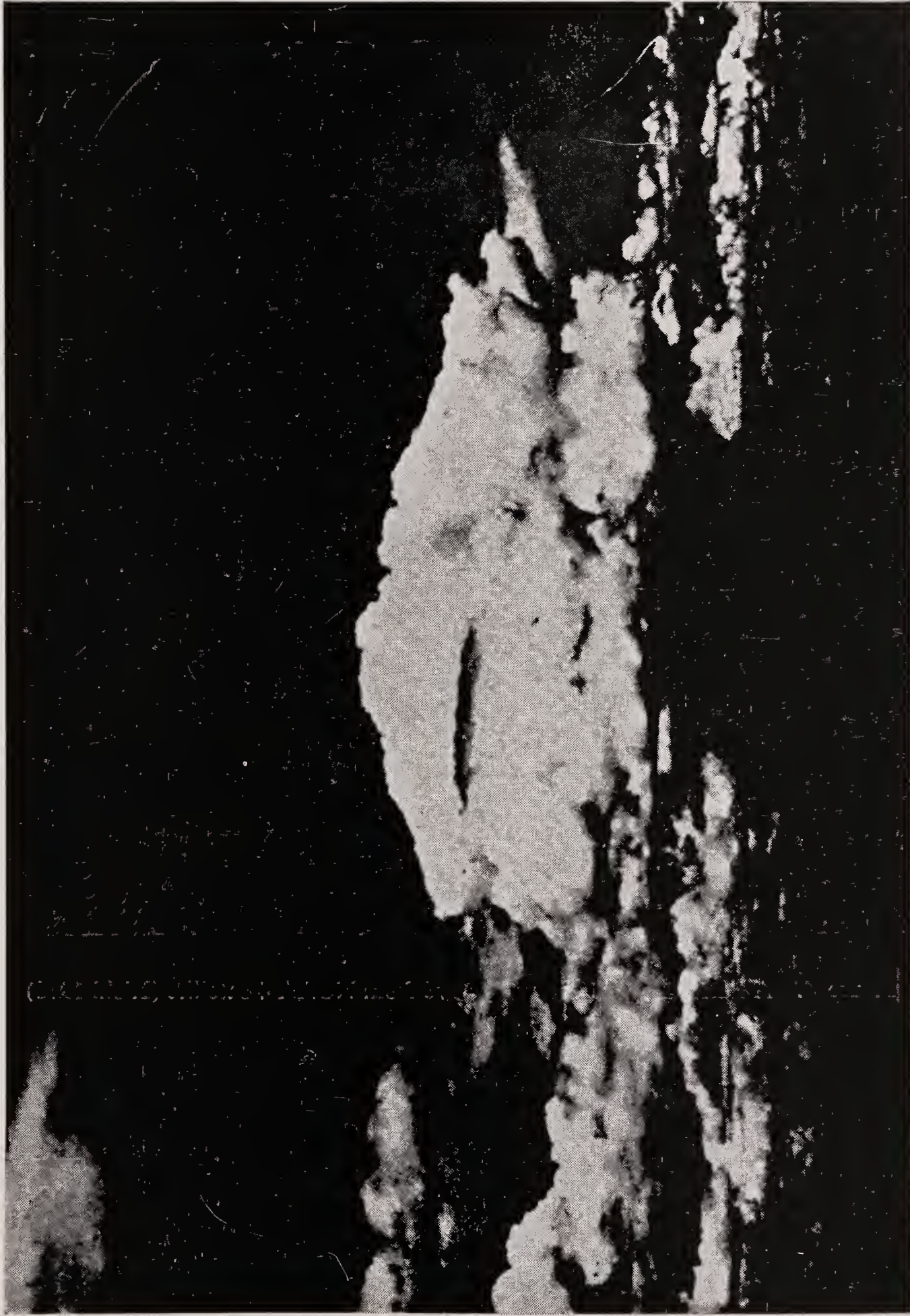


Figure 3. A cumulus cloud (Riehl 1978)

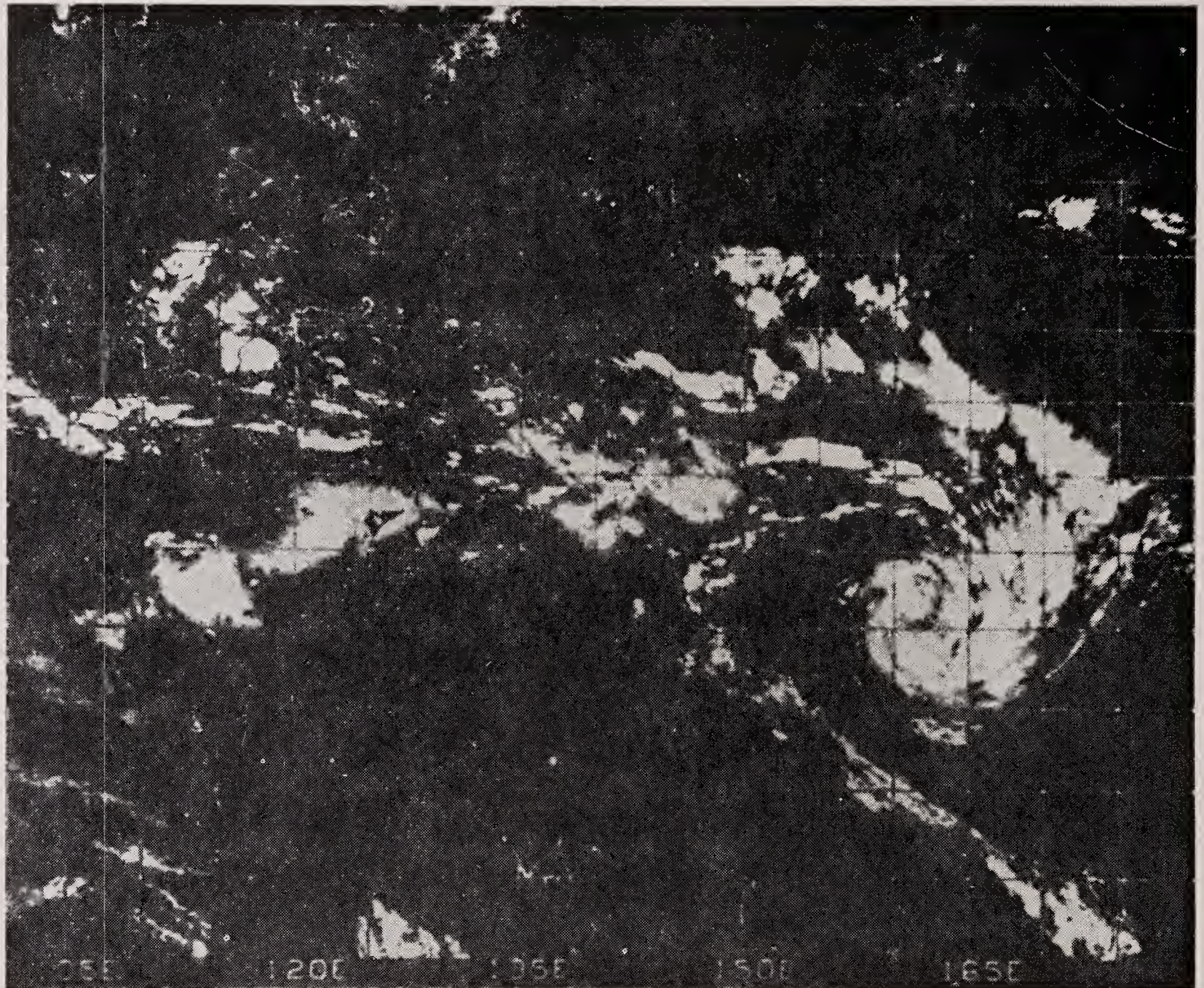


Figure 4. A hurricane on 17 January 1976 from NOAA 4 satellite (Riehl 1978)

Plate 3



Figure 7. The ITCZ over the Pacific Ocean on 22 August 1972 by satellite ATS 1 (Riehl 1978)

Plate 4



Figure 11. The ITCZ on 8 July 1973 (Sikka & Gadgil 1980).

Inviscid transonic flow field analysis

T C LIN & JIA ZHENXUE

Institute of Mechanics, Academia Sinica, Beijing, People's Republic of China

MS received 26 August 1981.

Abstract. This paper describes a method for analysing inviscid transonic flow. This method is based on the fact that the angle made by the streamline of the transonic flow and of the corresponding incompressible flow is usually small. By using curvilinear coordinates, the differential equation of the stream function of an inviscid compressible flow is simplified and a general solution of the equation obtained.

As examples of the method, transonic solutions are given for flow through two-dimensional and axisymmetric Laval nozzles of different throat wall radii together with sonic lines and iso-Mach lines. To determine the discharge coefficients of Laval nozzles, an integral relation is developed. The general behaviour of the transonic flow in the throat region is presented, and the effect of the mass discharge on the Mach number distribution in the nozzle analysed. The effects of the ratio of the specific heats on the characteristics of the flow in the throat region are discussed. For transonic flow around a circular cylinder and a sphere, sonic lines and iso-Mach lines are presented for free-stream Mach number varying from the subcritical to the supercritical, including a free-stream Mach number of one.

Part of the results obtained are compared with those available in current literature. For the two-dimensional hyperbolic Laval nozzles, the iso-Mach lines are compared with those given by Cherry (1959) and Serra (1972). For axisymmetric Laval nozzles, the discharge coefficient and the Mach number at the throat section for various throat wall radii are compared with those given by Sauer (1944), Hall (1962), Kliegel & Levine (1969), and Klopfer & Holt (1975). The theoretical discharge coefficients are compared with the experimental results by Back *et al* (1975), Durham (1955), Norton & Shelton (1969) etc. For the transonic flow around a circular cylinder, the iso-Mach lines are compared with Cherry's exact solution for the quasi-circular cylinder for M_∞ equal to 0.51. The Mach number distributions on the surface of the circular cylinder are compared with those given by Imai (1941) for M_∞ equal to 0.4, by Cherry (1947) for M_∞ equal to 0.51, by Dorodnicyn (1956) for M_∞ equal to 1, and by Hafez, South & Murman (1979) for M_∞ equal to 0.51.

The present method has a much wider scope of application, requires simpler computation and gives results with good accuracy. It is being used to analyse supercritical wings and cascades, and we expect to extend its application to the field of transonic unsteady flow.

Keywords. Transonic flow; Laval nozzles; flow field computations; flow past circular cylinder.

1. Introduction

A century has passed since De Laval (1883) invented the convergent-divergent nozzle, and Reynolds (1886) developed the one-dimensional subsonic-supersonic nozzle flow theory. An investigation of the representative works of the past century shows that the developments in this field may be roughly divided into three periods (see figure 1).

For the first sixty years, *i.e.*, from the early 1880s to the late 1930s, the problem of transonic flow was for the first time proposed and some fundamental investigations

essential to the founding of this branch of science were made. Notable contributors of this period include Chaplygin (1904), Meyer (1908), Tricomi (1923), Taylor (1930), and Görtler (1939). The hodograph method (Chaplygin 1904), the series expansion method (Meyer 1908; Taylor 1930; Görtler 1939), and the simplified transonic flow equation (Tricomi 1923) were introduced, and a number of transonic flow solutions obtained. However, the development was slow relative to the time span involved, as is the case with most of the virgin fields of study.

In the early forties, the speed of the aeroplane increased rapidly and approached that of sound. Owing to the so-called 'sonic barrier', growing attention was accorded to transonic flow research. Many aerodynamicists and mathematicians took part in this work, and remarkable progress was made. However, with the overcoming of the 'sonic barrier' through engine thrust, the next 15 years witnessed an obvious decrease in the research, followed by a state of low activity. These 25 years might be considered as the second period of transonic flow research. This notable upsurge and subsequent decrease in the activities of research is graphically shown in figure 1.

In this period the analytic methods of the early days, such as the hodograph method (Von Ringleb 1940; Frankl 1945; Lightill 1947; Goldstein *et al* 1948; Cherry 1947, 1949a, b, 1950, 1959; Tsien & Kuo 1946, Kuo 1948, 1951; Tomotika & Tamada 1950) and the series expansion method (Sauer 1944) were taken over and further developed. In addition, a number of distinct approaches were proposed, such as the small parameter expansion method (Imai 1941; Simasalsi 1956; Hall 1962; Kliegel & Levine 1969), the relaxation method (Green & Southwell 1944; Emmons 1946, 1948) the law of transonic similarity (Von Karman 1947; Lin *et al* 1948), the integral equation method (Oswatitsch 1950; Gullstrand 1951a, b; Spreiter & Alksne 1955), the time dependent method (Von Neuman & Richtmyer 1950; Lax & Wendroff 1964; Crocco 1965; Moretti & Abbett 1966), and the strip integration method (Dorodnitsyn 1956; Chushkin 1957; Holt 1962). All this not only improved and enriched the analytic methods of the earlier days, but also provided a theoretical basis for the numerical methods characteristic of the period to come.

In the fifteen years since mid-sixties, the pendulum seems to have swung back. The problem of transonic flow has once again claimed the attention of many researchers.

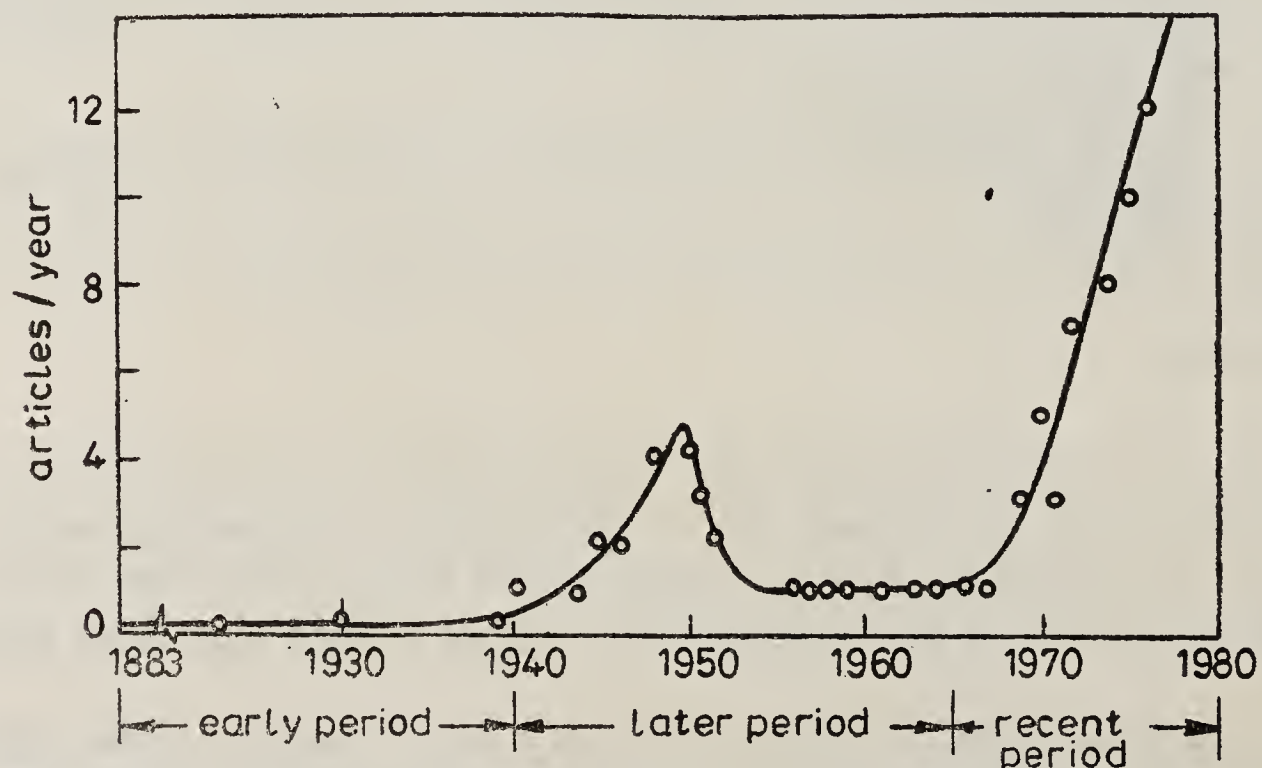


Figure 1. Development of transonic studies.

This second upsurge in transonic research has been necessitated by the urgent demand in air transport and space exploration for greater payloads, better cruising performance of large transport and shuttles, and higher efficiencies of jet engines, turbo-machines, and cascades. Flights in the transonic realm, once deliberately avoided, have become the object of intensive study with their inherent advantages being maximally exploited. This trend in research has been further accelerated by the recent energy crisis in the industrial world.

One of the dominant features of transonic flow study during this period is the rapid development and extensive application of numerical methods. Many of the transonic flow problems that used to be tackled with wind tunnels, are being solved with the aid of digital computers. The main numerical methods being developed are the hodograph method (Nieuwland 1967; Boerstoeel & Uijlennoel 1970; Boerstoeel 1974; Takanashi 1973; Garabedian & Lieberstein 1958; Swenson 1968; Korn 1969; Garabedian & Korn 1971; Bauer *et al* 1975; Sobieczky 1972), the relaxation method (Murman & Cole 1971; Murman 1973; Krupp 1971; Krupp & Murman 1972; Jameson 1971, 1974, 1975a, b; Hafez & Cheng 1977a, b; Cheng & Hafez 1976), the time-dependent method (Magnus *et al* 1968; Magnus & Yoshihara 1970; Moretti 1969, 1970; Grossman & Moretti 1973; Serra 1972; Cline 1974), the integral equation method (Nørstrud 1973; Hansen 1975; Nixon 1975, 1978; Chakrabarty 1978), the integral relation method (Holt & Masson 1971; Gross & Holt 1975; Klopfer & Holt 1975), and the finite element method (Chan & Brashears 1974; Shen 1975, 1977; Norrie & de Vries 1975; Chan *et al* 1975). These methods, though inherited from the previous period, have taken on a new character by the introduction of numerical procedures. This period, which might conveniently be called the third stage of transonic research, has made a promising start and has up to now shown no signs of abatement.

In fact, transonic flow research is currently in a state of fast development, with new findings appearing in rapid succession. However, along with the fruitful results achieved, a series of new problems, have also emerged. First of all, as the general line of attack has been the search for adequate computing schemes, based on the theories of the previous period, greater effort has been made from the viewpoint of numerical computation than from that of the physical characteristics of the flow. Besides, for the purpose of obtaining convergent solutions some man-made factors, such as artificial viscosity, are being introduced in numerical computation, and this tends to affect the accuracy of the results. Moreover, while notable success has been made with respect to thin wings, relatively little has been achieved for thick bodies. For example, in respect of transonic flow about a cylinder, the sonic lines and the iso-Mach lines for different free-stream Mach numbers, especially for free-stream Mach number equal to 1, have not been made clear, in spite of the many interesting papers published on the topic. In the case of transonic flow about a sphere, the situation also calls for further study. Another feature characteristic of current research is by and large the use of the potential function rather than the stream function as a means of solving transonic flow problems. One of the main reasons for this prevailing preference has been the difficulties in solving the many-valued function with the stream-function approach. But as a matter of fact the stream-function, with its more obvious physical property, may, when properly used, well prove to be a more efficient approach both in theoretical analysis and in numerical computation.

In view of all this, the present paper proposes to adopt the stream-function approach for the solution of transonic flow problems. A method has accordingly been developed for analysing transonic flow, based indeed on the simple but neglected physical fact that the angle made by the streamline of the transonic flow and that of the corresponding incompressible flow is usually small. By using curvilinear coordinates, the differential equation of the stream function of a compressible flow can be simplified and a general solution obtained.

As examples of the application of the method, a number of specific transonic flow problems are analysed and solutions, including sonic lines and iso-Mach lines of the flow fields, are given. In the case of internal flow, the flow fields through two-dimensional and axisymmetric Laval nozzles of different contraction ratios and different throat wall radii are analysed for various mass flow rates. In the case of external flow, the flow fields about a circular cylinder and about a sphere are analysed for free stream Mach number M_∞ varying from the subcritical to the supercritical including M_∞ equal to 1.

Some of the results obtained by the present method are compared with those available in current literature. It will be found that the present method has a much wider scope of application, requires far simpler computation and gives results of good accuracy.

The present method is being used to analyse supercritical wings and cascades, and we expect to extend its use to the study of transonic unsteady flow.

2. The basic equation and the solution

We shall confine our discussion to the study of the steady-state, irrotational, isentropic, two-dimensional or axisymmetric flow of an ideal gas. The non-dimensionalized quantities are signified by a bar placed over the corresponding symbols:

$$\left. \begin{aligned}
 \bar{x} &= x/b & \bar{p} &= p/p_* \\
 \bar{y} &= y/b & \rho &= \rho/\rho_* \\
 \bar{z} &= \bar{x} + i\bar{y} & \bar{T} &= T/T_* \\
 \bar{u} &= u/a_* & \bar{\phi} &= \phi/a_* b(\pi b)^\epsilon \\
 \bar{v} &= v/a_* & \bar{\psi} &= \psi/a_* \rho_* (\pi b)^\epsilon \\
 \bar{q} &= q/a_* & M &= \bar{q}/\bar{a} \\
 \bar{a} &= a/a_* & \bar{r} &= r/b
 \end{aligned} \right\} \quad (1)$$

Here b denotes characteristic length and the asterisk denotes sonic condition. As only non-dimensional quantities are to be used in this paper, the bar over the symbol is invariably left out.

For the two-dimensional or axisymmetric irrotational flow of ideal gas, the mass, momentum and energy conservation relations can be respectively represented in orthogonal curvilinear coordinates (Tsien 1958) as follows:

$$\left. \begin{aligned} (y^\epsilon H_2 \rho u)_\xi + (y^\epsilon H_1 \rho v)_\eta &= 0, \\ (H_2 v)_\xi - (H_1 u)_\eta &= 0, \\ T &= \frac{\gamma + 1}{2} - \frac{\gamma - 1}{2} q^2, \\ H_1 &= (x_\xi^2 + y_\xi^2)^{1/2}, \quad H_2 = (x_\eta^2 + y_\eta^2)^{1/2}. \end{aligned} \right\} \quad (2)$$

In the above equations H_1 and H_2 are the inverse of the Lamé coefficients (1934) for the transformation between the orthogonal curvilinear coordinates (ξ, η, θ) and the orthogonal coordinates (x, y, θ) ; u and v are the velocity components along ξ, η ; ρ and T express respectively the density and absolute temperature of the gas; $\epsilon = 0$ denotes plane motion, and $\epsilon = 1$ denotes axisymmetric motion.

The equation of state of a perfect gas, the adiabatic flow relation and the relation between temperature T and sonic velocity a under adiabatic conditions, when expressed in the non-dimensionalized variables chosen for this paper, may be written as follows:

$$p = \rho T, \quad p = \rho^\gamma, \quad a = T^{1/2}. \quad (3)$$

From (2) and (3), the relations between either density ρ or Mach number M and the velocity q are obtained respectively as

$$\left. \begin{aligned} \rho &= \left(\frac{\gamma + 1}{2} - \frac{\gamma - 1}{2} q^2 \right)^{\frac{1}{\gamma-1}}, \\ M &= q / \left(\frac{\gamma + 1}{2} - \frac{\gamma - 1}{2} q^2 \right)^{1/2}. \end{aligned} \right\} \quad (4)$$

From equations (2a, b)* one can define stream function ψ and potential function ϕ as follows:

$$\left. \begin{aligned} \psi_\xi &= -\rho y^\epsilon H_1 v, & \psi_\eta &= \rho v^\epsilon H_2 v, \\ \phi_\xi &= H_1 u, & \phi_\eta &= H_2 v. \end{aligned} \right\} \quad (5)$$

Using (3) and (4) and the definition given in (5), equation (2) gives the stream-function equation for two-dimensional or axisymmetric flow as

*The letters a, b etc. attached to the Arabic number indicate the sequential order of the formulas each equation.

$$\begin{aligned}
& (y^{2\epsilon} H_2^2 a^2 \rho^2 - \psi_\eta^2) \psi_{\xi\xi} + 2 \psi_\xi \psi_\eta \psi_{\xi\eta} + (y^{2\epsilon} H_1^2 a^2 \rho^2 - \psi_\xi^2) \psi_{\eta\eta} \\
& + H_1 \psi_\eta^2 \left[\frac{H_2}{H_1} \left(\frac{1}{y^\epsilon H_2} \right)_\xi \psi_\xi + \frac{H_1}{H_2} \left(\frac{1}{y^\epsilon H_2} \right)_\eta \psi_\eta \right] y^\epsilon \\
& + H_2 \psi_\xi^2 \left[\frac{H_2}{H_1} \left(\frac{1}{y^\epsilon H_1} \right)_\xi \psi_\xi + \frac{H_1}{H_2} \left(\frac{1}{y^\epsilon H_1} \right)_\eta \psi_\eta \right] y^\epsilon \\
& - \left(\frac{H_2}{H_1} \psi_\xi^2 + \frac{H_1}{H_2} \psi_\eta^2 - y^{2\epsilon} H_1 H_2 a^2 \rho^2 \right) \left[\left(\frac{H_2}{y^\epsilon H_1} \right)_\xi \psi_\xi \right. \\
& \left. + \left(\frac{H_1}{y^\epsilon H_2} \right)_\eta \psi_\eta \right] \eta^\epsilon = 0. \tag{6}
\end{aligned}$$

When $H_1 = H_2 = H$, this equation can be simplified. For axisymmetric flow, $\epsilon = 1$, equation (6) becomes

$$\begin{aligned}
& (y^2 H^2 a^2 \rho^2 - \psi_\eta^2) \psi_{\xi\xi} + 2 \psi_\xi \psi_\eta \psi_{\xi\eta} + (y^2 H^2 a^2 \rho^2 - \psi_\xi^2) \psi_{\eta\eta} \\
& - \frac{1}{H} (\psi_\xi^2 + \psi_\eta^2) (H_\xi \psi_\xi + H_\eta \psi_\eta) - y H^3 a^2 \rho^2 (y_\xi \psi_\xi + y_\eta \psi_\eta) = 0. \tag{7}
\end{aligned}$$

For two-dimensional flow $\epsilon = 0$, equation (6) becomes

$$\begin{aligned}
& (H^2 a^2 \rho^2 - \psi_\eta^2) \psi_{\xi\xi} + 2 \psi_\xi \psi_\eta \psi_{\xi\eta} + (H^2 a^2 \rho^2 - \psi_\xi^2) \psi_{\eta\eta} \\
& - \frac{1}{H} (\psi_\xi^2 + \psi_\eta^2) (H_\xi \psi_\xi + H_\eta \psi_\eta) = 0. \tag{8}
\end{aligned}$$

When $H_1 = H_2 = H$ one can utilize the conformal relations between the two coordinate systems (x, y) and (ξ, η) . According to the complex variable theory (Riemann 1851) the following relations are obtained:

$$\left. \begin{aligned}
z &= f(\zeta), \\
z &= x + iy, \\
\zeta &= \xi + i\eta, \\
H &= \left| \frac{dz}{d\zeta} \right|.
\end{aligned} \right\} \tag{9}$$

where $f(\zeta)$ is an analytic functions of ζ .

Equation (6) is valid for any orthogonal curvilinear coordinated system. It is obvious that to solve this equation mathematically is very difficult, especially under transonic conditions. For this reason, fluid dynamicists have often made use of the physical characteristics of the flow, simplified the flow equation through an order-of-magnitude analysis, and obtained approximate solutions with a certain degree of accuracy. For instance, Oswatitsch (1950) and Von Karman (1947), by making such

an analysis for transonic flow in rectangular coordinates, gave the small disturbance equation as

$$\phi_x \phi_{xx} - \frac{a_*}{\gamma + 1} \phi_{yy} = 0.$$

By employing a similar method in the velocity plane, Tricomi (1923) obtained a simplified transonic equation

$$\psi_a \psi_{aa} - (\gamma + 1) \psi_{\theta\theta} = 0.$$

Their efforts have contributed greatly to the solution of the transonic small disturbance problem. But as regards the flow in a nozzle with a comparatively large throat curvature (figure 2), or the flow past a comparatively thick body (figure 3), the simplified transonic flow equations described above are no longer valid. Some authors did solve the transonic problem by making one of the curvilinear coordinates coincide with the body surface. This, of course, helps tackle the boundary conditions in a convenient manner. But it fails to give a satisfactory and definite order-of-magnitude relation (figure 3a) between the velocity components in the whole flow field, and cannot provide a simplified flow equation.

It was against this background that we began to examine the problem of transonic flow through a nozzle (figure 2) and the flow past a circular cylinder (figure 3) and we note the important fact that the angle made by the stream lines of a compressible flow and those of the corresponding incompressible flow is usually small. In other

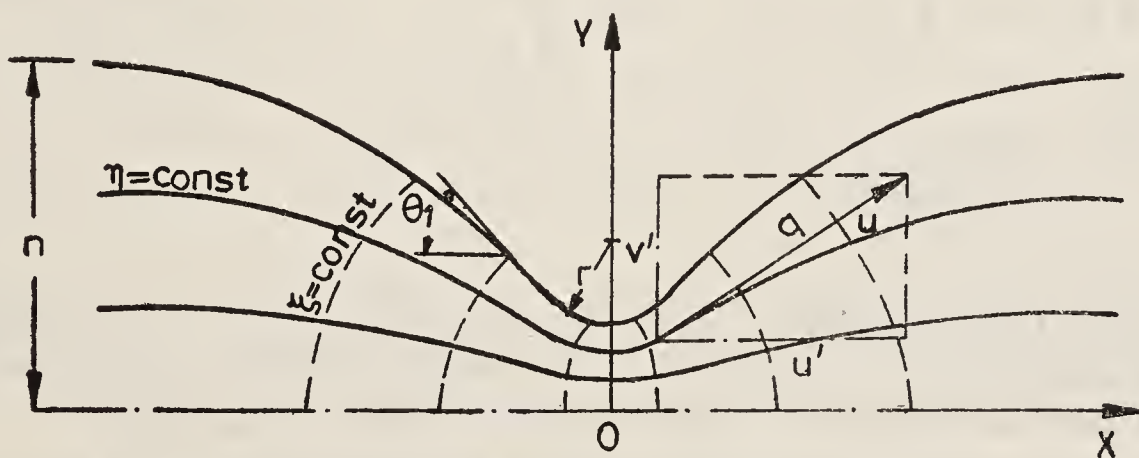


Figure 2. Laval-nozzle coordinates and the flow pattern.

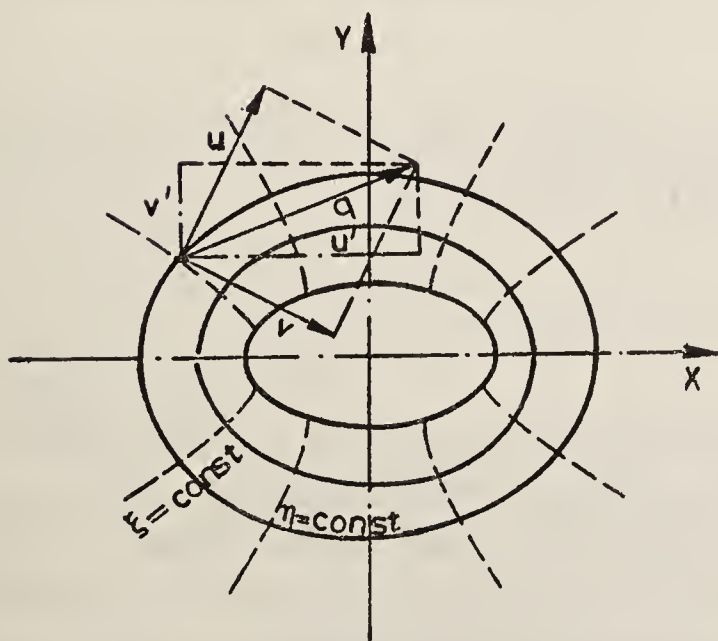


Figure 3(a). Elliptical coordinates.

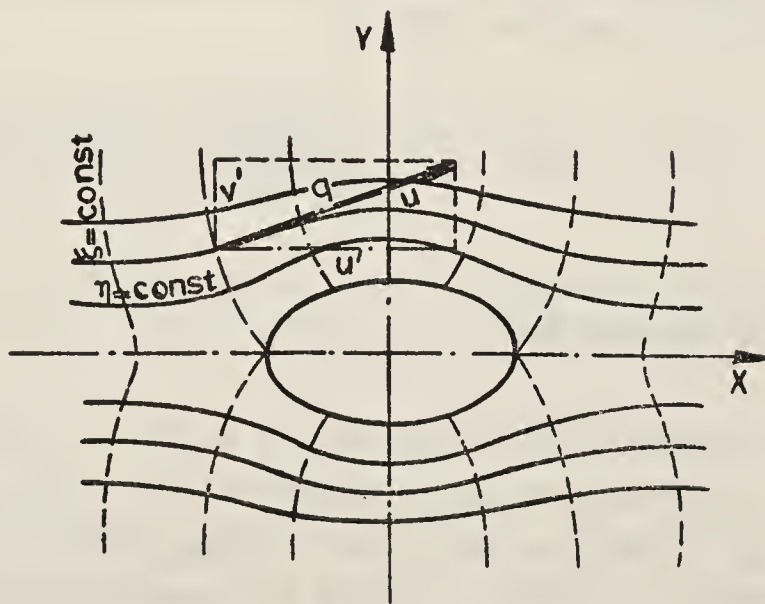


Figure 3(b). Incompressible-flow coordinates about an ellipse.

words, with u as the velocity component along η and v the one along ξ , u is far greater than v . Therefore, selecting the equipotential lines and the streamlines of an incompressible flow as the (ξ, η) coordinates, (6) can be successfully simplified. Assuming $u \gg v$, and using (5) we obtain $|\psi_\eta| \gg |\psi_\xi|$; by omitting ψ_ξ and its derivatives from (6), we obtain the simplified stream function equation,

$$y^{2\epsilon} H_1 a^2 \rho^2 \psi_{\eta\eta} - \frac{H_1 \eta}{y^\epsilon H_2^2} \psi_\eta^3 + y^{2\epsilon} H_2 a^2 \rho^2 \left(\frac{H_1}{y^\epsilon H_2} \right)_\eta \psi_\eta = 0. \quad (10)$$

This equation is a nonlinear ordinary differential equation in η , with ξ as a parameter. Utilizing (4a) after differentiating it with respect to η and substituting it in (10), we eliminate $\psi_{\eta\eta}$ and obtain the first integral of (10),

$$\psi_\eta = y^\epsilon (\xi, \eta) \rho (\xi, \eta) g (\xi) \frac{H_2 (\xi, \eta)}{H_1 (\xi, \eta)}. \quad (11)$$

Here $y^\epsilon (\xi, \eta)$ is a known function whereas $g (\xi)$ is a function to be determined. For flow through a nozzle, $g (\xi)$ is related to the mass discharge; for flow around a body, $g (\xi)$ is related to the free-stream Mach number. For convenience, $g (\xi)$ can be designated as a 'discharge function' with $\eta = \eta_1$ as the null stream line *i.e.* $\psi (\xi, \eta_1) = 0$. Substituting (4a) in (11), one obtains a general solution for $\psi (\xi, \eta)$:

$$\begin{aligned} \psi (\xi, \eta) = & \left(\frac{\gamma + 1}{2} \right)^{\frac{1}{\gamma-1}} g (\xi) \int_{\eta_1}^{\eta} \left[1 - \frac{\gamma - 1}{\gamma + 1} \frac{g^2 (\xi)}{H_1^2 (\xi, \eta)} \right]^{\frac{1}{\gamma-1}} \\ & \times \frac{H_2 (\xi, \eta)}{H_1 (\xi, \eta)} y^\epsilon (\xi, \eta) d\eta. \end{aligned} \quad (12)$$

Here $H_1 (\xi, \eta)$, $H_2 (\xi, \eta)$ and $y (\xi, \eta)$ are determined once the coordinate transformation is chosen, and only $g (\xi)$ is to be sought. The determination of $g (\xi)$ will be discussed later in this paper with reference to specific examples.

With $g (\xi)$ determined, the corresponding transonic flow field is established. In accordance with the stream function defined by (5), one obtains the velocity distribution in the flow field as

$$u(\xi, \eta) = \frac{g(\xi)}{H_1(\xi, \eta)}, \quad v(\xi, \eta) = \frac{-\psi^\xi}{p H_1(\xi, \eta) y^\xi(\xi, \eta)}. \quad (13)$$

3. Internal flow

In what follows, the above method is applied to transonic flow in a Laval nozzle. Given the nozzle coordinates, we analyse the maximum mass discharge and study the transition from the subsonic through the sonic to the supersonic regime in the throat region. A series of two-dimensional and axisymmetric sample flow fields in the throat region are presented, and the influence of the specific heat ratio γ is obtained.

3.1 Nozzle coordinates

In accordance with the incompressible potential flow and the complex variable theory, by selecting a slitted symmetrical biconvex wing section in the velocity plane, one obtains a symmetric nozzle in the physical plane. The mapping relation $f(\zeta)$ (Lin Tong Ji and Jia Zhen Hue 1978) between plane z and plane ζ is given as

$$z = \frac{n}{\eta_b} \left\{ \zeta - (1 - \sigma) \coth \lambda \ln \left[\frac{\cosh \frac{1}{2} (\lambda + \zeta)}{\cosh \frac{1}{2} (\lambda - \zeta)} \right] \right\}. \quad (14)$$

In this formula, λ , σ , η_b are nozzle shape factors and n is the nozzle contraction ratio. By separating the real and imaginary parts of (14), we obtain the relation between the (x, y) and the (ξ, η) coordinates as

$$\left. \begin{aligned} x(\xi, \eta) &= \frac{n}{\eta_b} \left\{ \xi - \frac{1}{2} (1 - \sigma) \coth \lambda \ln \left[\frac{\cosh (\lambda + \xi) + \cos \eta}{\cosh (\lambda - \xi) + \cos \eta} \right] \right\}, \\ y(\xi, \eta) &= \frac{n}{\eta_b} \left[\eta - (1 - \sigma) \coth \lambda \tan^{-1} \left(\frac{\sinh \lambda \sin \eta}{\cosh \xi + \cosh \lambda \cos \eta} \right) \right]. \end{aligned} \right\} \quad (15)$$

By selecting corresponding shape factors λ , σ , η_b according to the values of the throat wall radius r , contraction ratio n and contraction angle θ_1 of the nozzle, one obtains the required profile of the nozzle.

3.2 Maximum discharge

For the flow through a nozzle, the maximum discharge is one of the most significant parameters. It is essential in determining the transition of the flow field from the subsonic to the supersonic region in the throat. No satisfactory answer, however, has been given to the problem involved. As a solution to this problem an integral relation equation for determining the maximum discharge is presented below.

With the streamlines and equipotential lines of the corresponding incompressible flow as the coordinates, the boundary conditions can be expressed as follows:

$$\left. \begin{aligned} \eta = \eta_1: & \quad \psi(\xi, \eta_1) = 0 \\ \eta = \eta_b: & \quad \psi(\xi, \eta_b) = \psi_b \end{aligned} \right\}. \quad (16)$$

In these equations, ψ_b is the discharge through the nozzle; its value cannot be arbitrarily selected. For a given nozzle there exists a maximum value of ψ_b , namely the maximum discharge.

Given the throat section coordinates $\xi = \xi_*$ from equations (12) and (16), the maximum discharge ψ_s through the throat area is obtained as (Lin Tong Ji & Jiazhen Xue 1978)

$$\begin{aligned} \psi_s &= \left(\frac{\gamma+1}{2} \right)^{\frac{1}{\gamma-1}} g_s \int_{\eta_1}^{\eta_b} \left[1 - \frac{\gamma-1}{\gamma+1} \frac{g_s^2}{H_1^2(\xi_*, \eta)} \right]^{\frac{1}{\gamma-1}} \\ &\quad \times \frac{H_2(\xi_*, \eta)}{H_1(\xi_*, \eta)} y^\epsilon(\xi_*, \eta) d\eta, \end{aligned} \quad (17)$$

in which g_s satisfies the relation

$$\int_{\eta_1}^{\eta_b} \left[1 - \frac{g_s^2}{H_1^2(\xi_*, \eta)} \right] \left[1 - \frac{\gamma-1}{\gamma+1} \frac{g_s^2}{H_1^2(\xi_*, \eta)} \right]^{\frac{2-\gamma}{\gamma-1}} \times \frac{H_2(\xi_*, \eta)}{H_1(\xi_*, \eta)} y^\epsilon(\xi_*, \eta) d\eta = 0. \quad (18)$$

The roots of equation (17), g_s , are multi-valued, the smallest of which corresponds to the maximum discharge ψ_s . For the flow through the nozzle, ψ_b cannot be greater than ψ_s . For a given value of ψ_b , from the boundary condition (16), one obtains the integral relation that determines the discharge function $g(\xi)$ as follows:

$$\psi_b = \left(\frac{\gamma+1}{2} \right)^{\frac{1}{\gamma-1}} g(\xi) \int_{\eta_1}^{\eta_b} \left[1 - \frac{\gamma-1}{\gamma+1} \frac{g^2(\xi)}{H_1^2(\xi, \eta)} \right]^{\frac{1}{\gamma-1}} \times \frac{H_2(\xi, \eta)}{H_1(\xi, \eta)} y^\epsilon(\xi, \eta) d\eta. \quad (19)$$

Equation (18) is an integral relation equation for $g(\xi)$ with ξ as a variable parameter; for a given value of ξ , $g(\xi)$ is multivalued. In order to ensure the continuity and the non-occurrence of a negative density in the solution, $g(\xi)$ has to be selected as follows: for subsonic flow in the nozzle, $\psi_b < \psi_s$, the smallest positive root of $g(\xi)$ should be taken for the entire range of ξ ; for supersonic flow through the nozzle, $\psi_b = \psi_s$, the selection of $g(\xi)$ is dependent upon the range of ξ . When $\xi < \xi_*$, the smallest positive root of $g(\xi)$ should be taken, and this corresponds to the flow through the contracted portion. When $\xi = \xi_*$, the smallest positive repeated root should be taken, which corresponds to the flow in the throat section. When $\xi > \xi_*$, the second positive root of $g(\xi)$ should be taken, which corresponds to the flow through the expanded portion. Figure 4 gives the variation of $g(\xi)$ with ξ for various portions of the nozzle.

3.3 Transition of the nozzle throat flow field

For a given nozzle, there exists a maximum discharge. When the inlet discharge is smaller than the maximum discharge, *i.e.*, the discharge coefficient (factor) $k = \psi_b/\psi_s$ is smaller than 1, the flow through the nozzle is of a subsonic symmetric type. When $k = 1$, the flow is of a supersonic type. How the flow field in the throat region of a nozzle changes from the subsonic symmetric type to the supersonic type is one of the most significant problems of nozzle flow field investigations. Tomotika & Tamada (1950) applied the hodograph method to an artificial gas and explained qualitatively the relationship between the flow field transition and the discharge in the throat region. In this section the same problem is discussed quantitatively, and with reference to an ideal rather than artificial gas.

In accordance with the general solution of nozzle flow given above, proper selections can be made for the contraction ratio n of the nozzle, the maximum angle θ_1 of inclination of the wall surface, and the radius of curvature r of the throat wall. Our

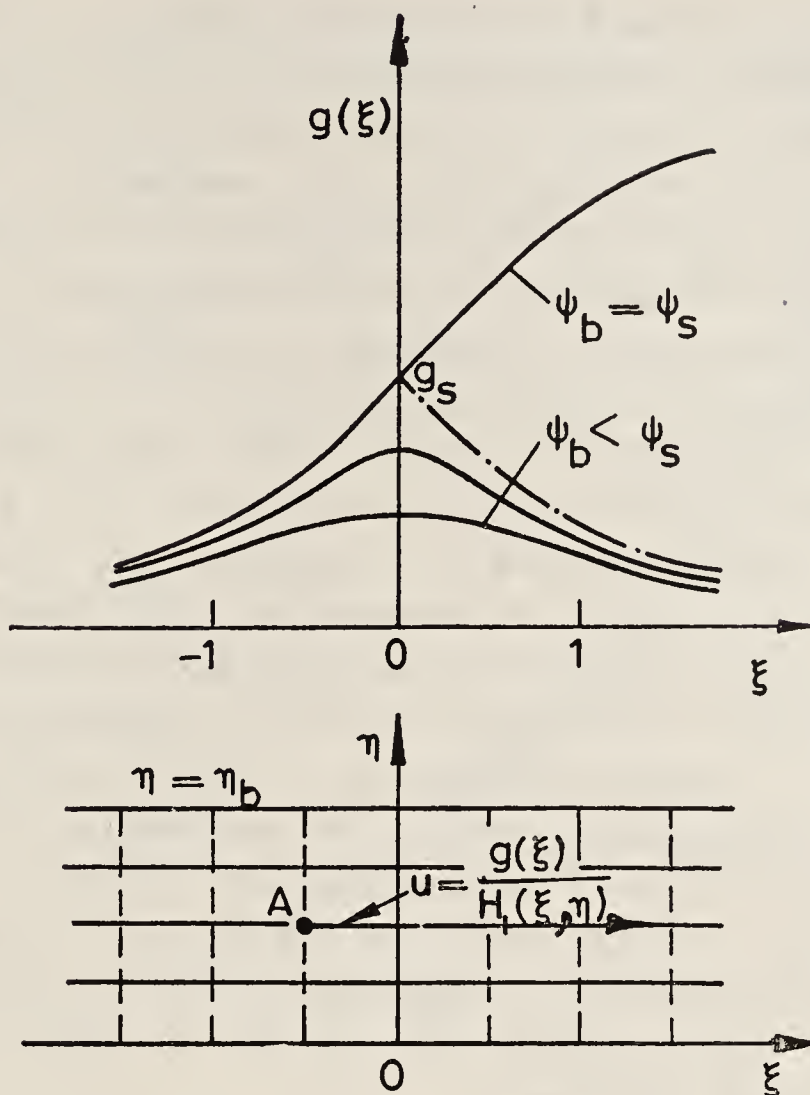


Figure 4. The "discharge correlation function" $g(\xi)$.

analysis demonstrates that the variation in the value of γ , the ratio of specific heats, hardly affects the flow field in the throat region. In view of the fact that when γ equals 2, the analytical expressions for the flow fields in the throat assume a simpler form and that water table tests also yield a flow condition with $\gamma = 2$, one can more conveniently explain the general properties of the throat flow field transition by making $\gamma = 2$. When $\gamma = 2$, the analytical solution (Lin Tong Ji & Jiazhen Xue 1978) of the throat flow field is

$$\begin{aligned}
 \psi(\xi, \eta) &= \frac{3}{2} \eta g(\xi) - \frac{1}{2} E_1(\xi, \eta) g^3(\xi), \\
 g(\xi) &= 2\eta_b^{1/2} E_1^{-1/2}(\xi, \eta) \cos \frac{1}{3} \left\{ \pi \pm \right. \\
 &\quad \left. \cos^{-1} [k E_1^{-1/2}(0, \eta_b) E_1^{1/2}(\xi, \eta_b)] \right\}, \\
 E_1(\xi, \eta) &= \left(\frac{\eta_b}{n} \right)^2 \eta + \frac{1 - \sigma}{\sigma} \left(\frac{\eta_b}{n} \right)^2 [B_{11}(\xi, a) N_1(\xi, \eta, a) \\
 &\quad + B_{11}(\xi, -a) N_1(\xi, \eta, -a)], \\
 B_{11}(\xi, a) &= 1 + \coth a \coth \xi \left(\tanh^2 \xi - \frac{1 - \sigma}{\sigma} \operatorname{sech}^2 \xi \right), \\
 N_1(\xi, \eta, a) &= \frac{2}{\tanh a + \tanh \xi} \operatorname{tg}^{-1} \left(\tanh \frac{\xi + a}{2} \tan \frac{\eta}{2} \right), \\
 k &= \psi_b / \psi_s, \quad \psi_s = \eta_b^{3/2} E_1^{-1/2}(0, \eta_b), \\
 \cosh a &= \sigma \cosh \lambda.
 \end{aligned} \tag{20}$$

When contraction ratio $n = 2$ and the throat wall radius $r = 2$, the relation between the throat flow field and the discharge coefficient k is worked out according to equations (19) and (20). Figure 5 gives the iso-Mach number line distribution in the throat with the values of $k = 0.5, 0.9, 0.98$ and 1.0 etc. respectively. For $k = 1.0$ sonic line AE, limiting characteristic line BE, dividing line DE and influence line CF are also given. From figures 5(a) and 5(b), one can see that when $k = 0.5$, the flow field as a whole can be approximately considered as incompressible, or low subsonic. When $k = 0.9$, the influence of compressibility has to be considered, but the nozzle flow field as a whole is still subsonic; when $k = 0.98$, local supersonic regions occur in the vicinity of either side of the throat wall; when $k = 1.0$, a breakoff occurs in the local supersonic region mentioned above and the sonic lines on the two sides extend until they meet on x -axis at the downstream of the throat. The throat flow is thus divided into two parts: the upstream subsonic flow and the downstream supersonic flow. This is the state of flow generally known as the supersonic nozzle flow.

For $\gamma = 1.5, 1.33 \dots$ equations (86) similar to equation (20) can be obtained; for any value of γ , a corresponding result can be obtained by using the integral relation equations (16)–(19). Figure 6 gives the relation between the Mach number at the throat wall and the discharge coefficient k with $\gamma = 1.40$ and the throat wall radius, 1, 2 and ∞ . From the figure, we can see that for any given throat wall radius, the throat wall Mach number steadily increases with k . The larger the value of k , the greater is the rate of the increase.

3.4 Nozzle flow field

In the study of transonic flow, the hyperbolic nozzle, being a typical example, is of great significance both in theory and in practice. It has been studied by many scholars

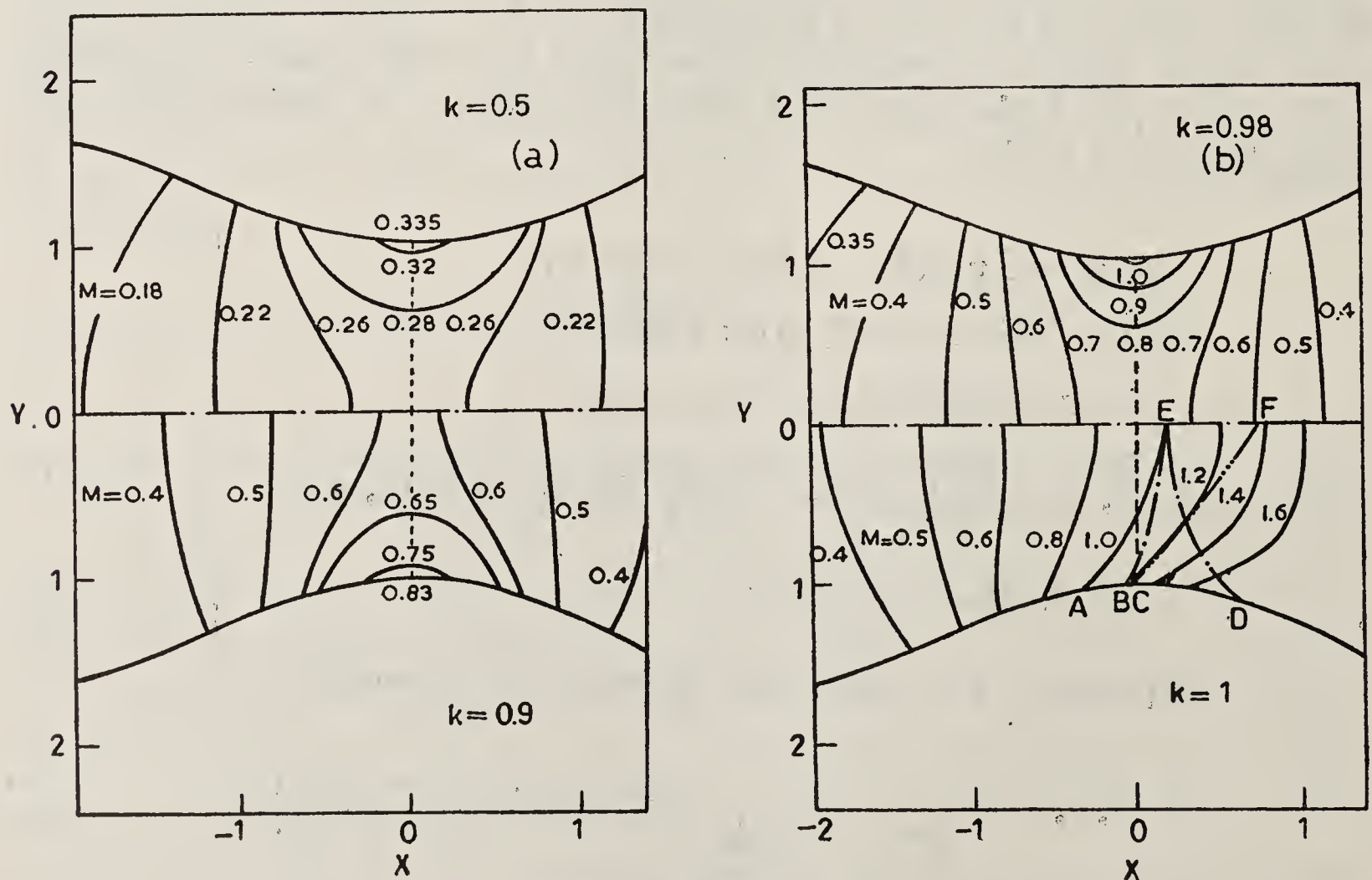


Figure 5. (a) Relation between the Mach number distribution and the discharge coefficient k (for $k = 0.5$ and 0.9). (b) Relation between the Mach number distribution and the discharge coefficient k (for $k = 0.98$ and 1.0).

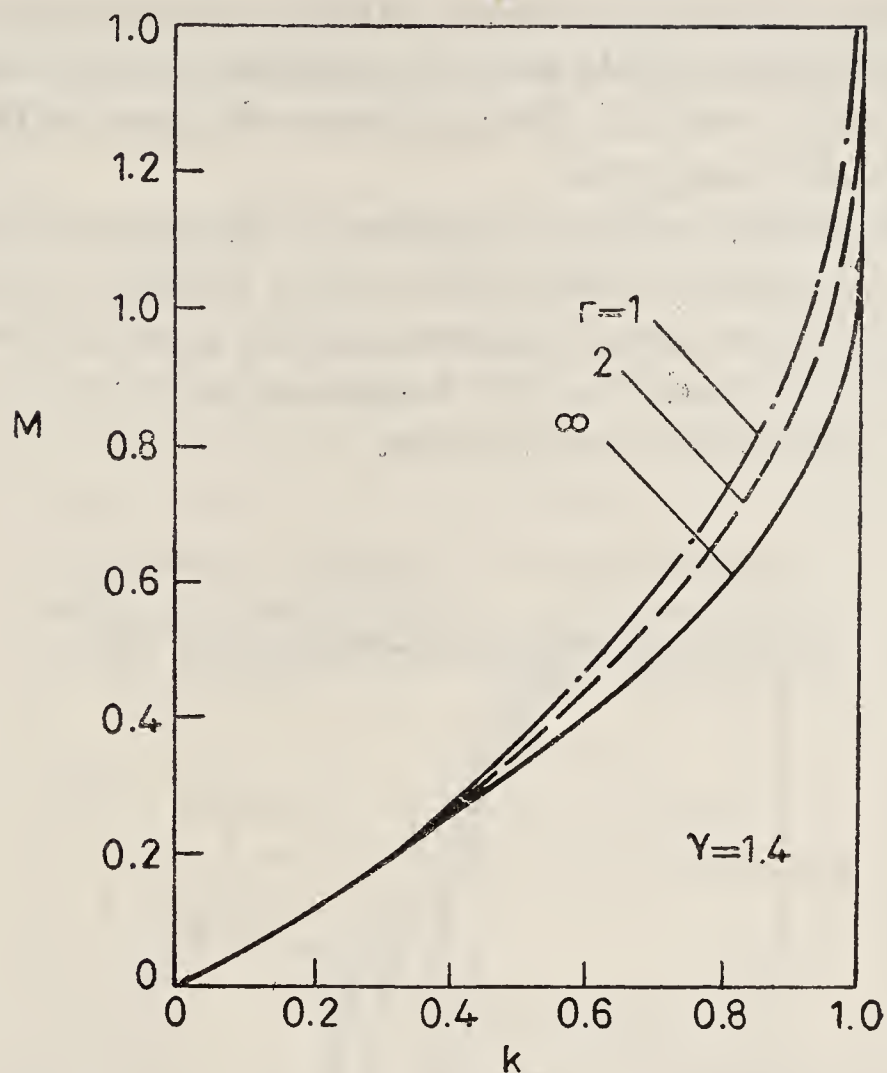


Figure 6. Relation between the maximum Mach number at the nozzle throat and the discharge coefficient k .

using various methods: Emmons (1946) used the relaxation method, Cherry (1959) the hodograph method (obtaining an accurate solution), Hall (1962) the small parameter method, and Seria (1972) the time-step correlation method. Most of these studies, however, only concentrated on one or two specific examples. Hall (1962) did discuss general conditions, but his method can only be applied to a nozzle with a relatively large wall radius of curvature. In what follows, we will apply the present method to the determination of the transonic flow (Jiazhen Hue and Lin Tong Ji 1979) in the throat region, taking the hyperbolic nozzle as an example.

By using the function of a complex variable, the hyperbolic nozzle coordinate relation between z and ζ , and the inverse of Lamé's coefficients H for the coordinate transformation, can be represented as

$$\left. \begin{aligned} z &= \operatorname{cosec} \eta_b \sinh \zeta, \quad z = x + iy, \quad \zeta = \xi + i\eta, \\ H(\xi, \eta) &= \operatorname{cosec} \eta_b (\sinh^2 \xi + \cos^2 \eta)^{1/2}, \end{aligned} \right\} \quad (21)$$

in which the constant $\operatorname{cosec} \eta_b$ involves the half-height of the throat. In this coordinate system, when the ratio of specific heats γ equals $1 + 1/\nu$ of and ν is a positive integer, the flow field at the throat has a simple analytical solution. For any value of γ , the computations can be carried out on the basis of formulae (16)–(19). Part of the typical results are given below.

Figure 7 gives the wall contours and the corresponding throat sonic lines for $\gamma = 1.40$ and wall radius $r = 10.6, 5, 1, 0.22$ respectively. The figure shows that for a comparatively large value of r , the sonic line has only one turning point located at its centre; when r is less than 1.1, an additional turning point occurs in the

vicinity of both sides of the wall surface. Within the range given in the figure, the distance between the centres of the sonic line and the throat section increases monotonically as r decreases, but with the continuous decrease in the value of r below 0.18, the distance begins to decrease.

Figure 8 gives the Mach number distribution on the central streamline for $\gamma = 1.4$ and $r = 10.6, 5, 1.0,$ and 0.22 respectively. It is evident from the figure that all Mach number distribution curves intersect at one point, whose location is given approximately as $x=0.37$ and $M=1.08$. Reduction in the value of r is accompanied by rapid variation in the airflow acceleration.

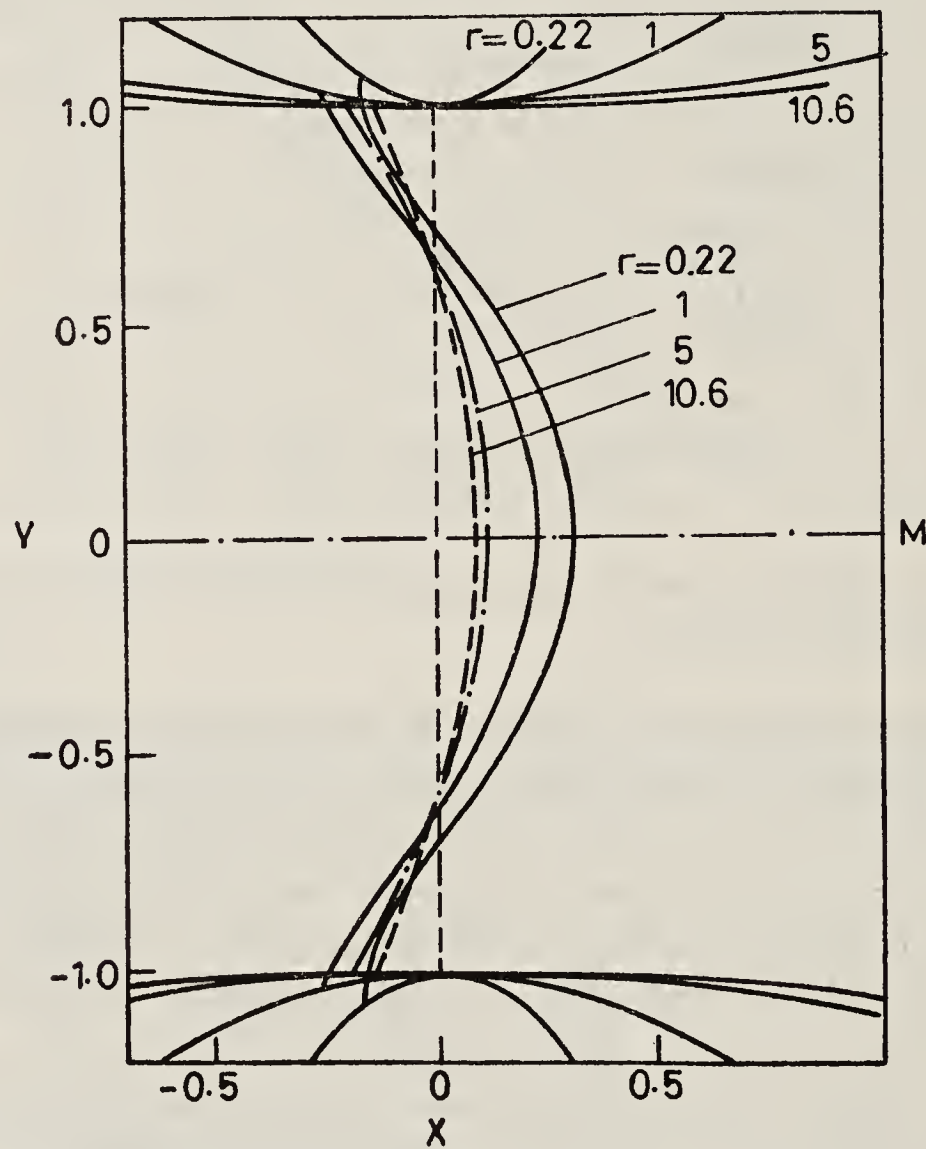


Figure 7. Sonic lines for hyperbolic nozzles.

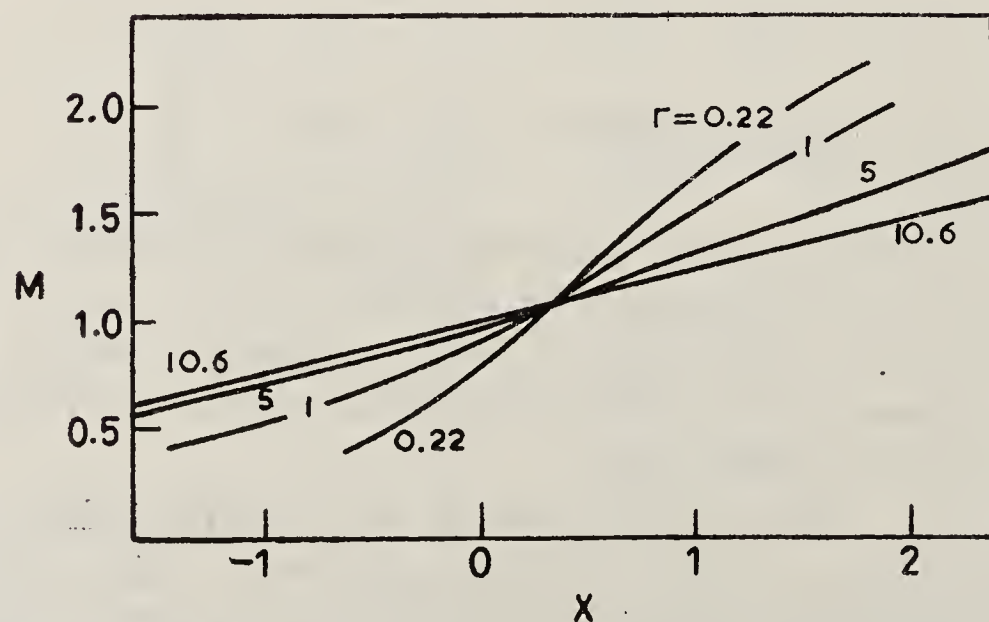


Figure 8. Mach number distribution along the axis of hyperbolic Laval nozzles.

Figure 9 demonstrates the influence of γ upon the iso-Mach number distribution in the throat flow. The dotted lines are for $\gamma = 1.2$ and the solid lines are for $\gamma = 1.667$. It is obvious from the figure that the larger the value of γ , the closer the iso-Mach line is to the throat.

Figure 10 gives the comparison between the results obtained by the present method and those obtained by Cherry (1959) and by Seria (1972) at $\gamma = 1.40$ and $r = 2$. Cherry, using the hodograph method, obtained the exact solution for the quasi-hyperbolic contour; Seria using the time step correlation method, carried out the calculations for the hyperbolic nozzle. The figure shows that the results obtained by the present method and those by Seria coincide for the iso-Mach lines when $M = 0.46$ and 1.90 . When $M = 0.75, 1.32$ and 1.68 our results lie between those obtained by Cherry and Seria, and our results for the sonic line coincide with those obtained by Cherry. But compared with both Cherry's and Seria's method, the

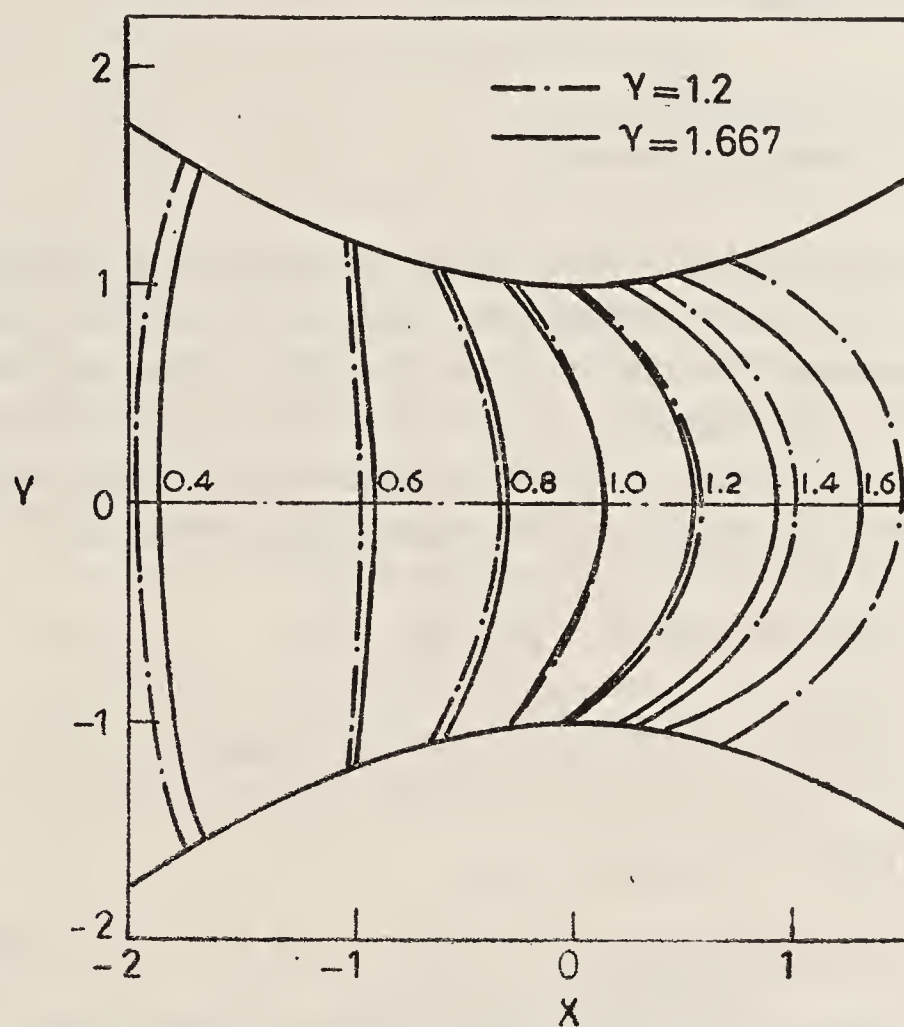


Figure 9. Influence of the ratio of specific heats upon the flow-field.

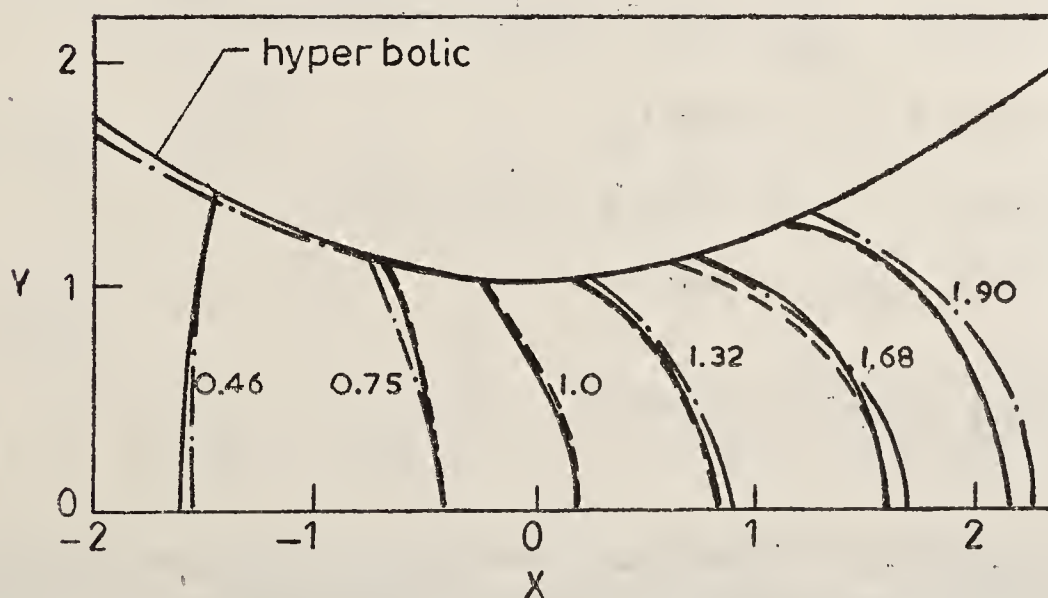


Figure 10. Iso-Mach line distribution for a hyperbolic nozzle. — Present results; — . — Cherry (1950); — — — Seria (1972).

present method is much simpler, and furthermore, the nozzle throat contours can be selected according to need.

3.5 Axisymmetric nozzle flow field

The method given in this paper is also applicable to the axisymmetric nozzle throat flow with any wall contour. In view of the extensive use of the circular arc throat, this section intends to analyse briefly the transonic flow for this type of nozzle.

For this purpose, the employment of double circular coordinates (Lamb 1932) will prove convenient. The coordinate relations, and $H(\xi, \eta)$, the inverse of Lamé's coefficients for the coordinate transformation, are respectively

$$\left. \begin{aligned} z = \coth \eta_b \tan \zeta, \quad z = x + iy, \quad \zeta = \xi + i\eta, \\ H(\xi, \eta) = \frac{2 \coth \eta_b}{\cosh 2\eta + \cos 2\xi} \end{aligned} \right\} \quad (22)$$

The constant $\coth \eta_b$ is so chosen that the throat radius is 1. Using the above-mentioned conformal curvilinear coordinates and applying the equations (16)–(19), one obtains the transonic flow field solution for the circular arc throat region. For some common ratios of specific heats, e.g. for $\gamma = 1.1, 1.667, 1.2$ etc., the throat flow field solution can be expressed by simple analytical equations (Jiazhen Hue and Lin Tong Ji). For instance when $\gamma = 1.4$, the resulting formulae are

$$\left. \begin{aligned} \psi(\xi, \eta) &= k_a g(\xi) [F(\lambda) - F(\mu\lambda)], \\ F(\lambda) &= \frac{2}{15} (23 - 11\lambda + 3\lambda^2) (1 - \lambda)^{1/2} - 2 \tanh^{-1} (1 - \lambda)^{1/2}, \\ k_a g(\xi) [F(\lambda_b) - F(\mu_b \lambda_b)] &= \mu_s, \\ \psi_s &= 4 \sqrt{6} k_a r (1 + 2r)^{-1/2} \lambda_s^{1/2} [(1 - \mu_s \lambda_s)^{5/2} - (1 - \lambda_s)^{5/2}], \\ F(\lambda_s) - F(\mu_s \lambda_s) + 2 (1 - \lambda_s)^{5/2} - 2 (1 - \mu_s \lambda_s)^{5/2} &= 0, \\ \lambda = \lambda(\xi, \eta) &= \frac{1}{24} (1 + 2r)^{-1} (\cosh 2\eta + \cos 2\xi)^2 g^2(\xi), \\ \lambda_b &= \lambda(\xi, \eta_b), \quad \lambda_s = \lambda(0, \eta_b), \\ \mu &= \mu(\xi, \eta) = \cos^4 \xi (\cosh 2\eta + \cos 2\xi)^{-2}, \\ \mu_b &= \mu(\xi, \eta_b), \quad \mu_s = \mu(0, \eta_b), \\ k_a &= \frac{1}{2} \left(\frac{r+1}{2} \right)^{r-1} (1+2r)^{1/2}. \end{aligned} \right\} \quad (23)$$

Using the above method, we obtain the following transonic flow field for the circular arc nozzle for different values of γ (Jia Zhen Hue and Lin Tong Ji, to be published).

Figure 11 gives the relationship between the maximum nozzle discharge ψ_s and the

wall radius r , for $\gamma = 1.40$. At the same time, results of some other theoretical and experimental studies are compared. It is evident from the figure that when r is comparatively large, the results obtained by the present method and those by Hall (1962) are basically the same, while the results given by Sauer (1944) are somewhat small; Kliegel & Levine's results (1969), on the contrary are somewhat large since they used the inverse of $(1 + r)$ as a small parameter, thus giving rise to a slowly convergent series. With the decrease in the value of r , Hall's solution becomes divergent, and Sauer's is no longer valid. The results given by Kliegel & Levine are evidently too large. Klopfer & Holt (1975), utilizing the integral relation method, obtained better results than those of Kliegel & Levine. The diagram shows that our results lie between those obtained by Klopfer & Holt on the one hand and Sauer on the other. Moreover, they match better with the experimental results (Back *et al* 1965; Durham 1955; Norton & Shelton 1969; Back & Cuffel 1971). At the same time, one must notice that when the entry portion is non-circular, *e.g.* when it is conical in shape, ψ_s is increased, especially when r is comparatively small.

Figure 12 gives the relation between the wall radius and the Mach numbers on the wall surface and on the axis at the throat section; at the same time, a comparison is made with the results of Sauer (1944), Hall (1962) and Kliegel & Levine (1969). It can be seen from the diagram that for relatively large values of r , the results given by the present method and those by the others are basically identical; when r is relatively small, the Mach numbers at the wall given by Kliegel & Levine are relatively high while those at the axis are relatively low. These results coincide with those presented in figure 7.

Figure 13 gives the contours and location of the sonic lines for $\gamma = 1.40$ and wall radius of curvature $r = 10, 5, 1$ and 0.50 respectively. The figure indicates that for relatively large r values, the sonic lines are nearly vertical; with the gradual reduction of the r value the curvature of the sonic line increases. When r is smaller than 0.5 , there appears a second turning point in the vicinity of each side of the wall surface, in addition to the original one at the centre of the sonic line.

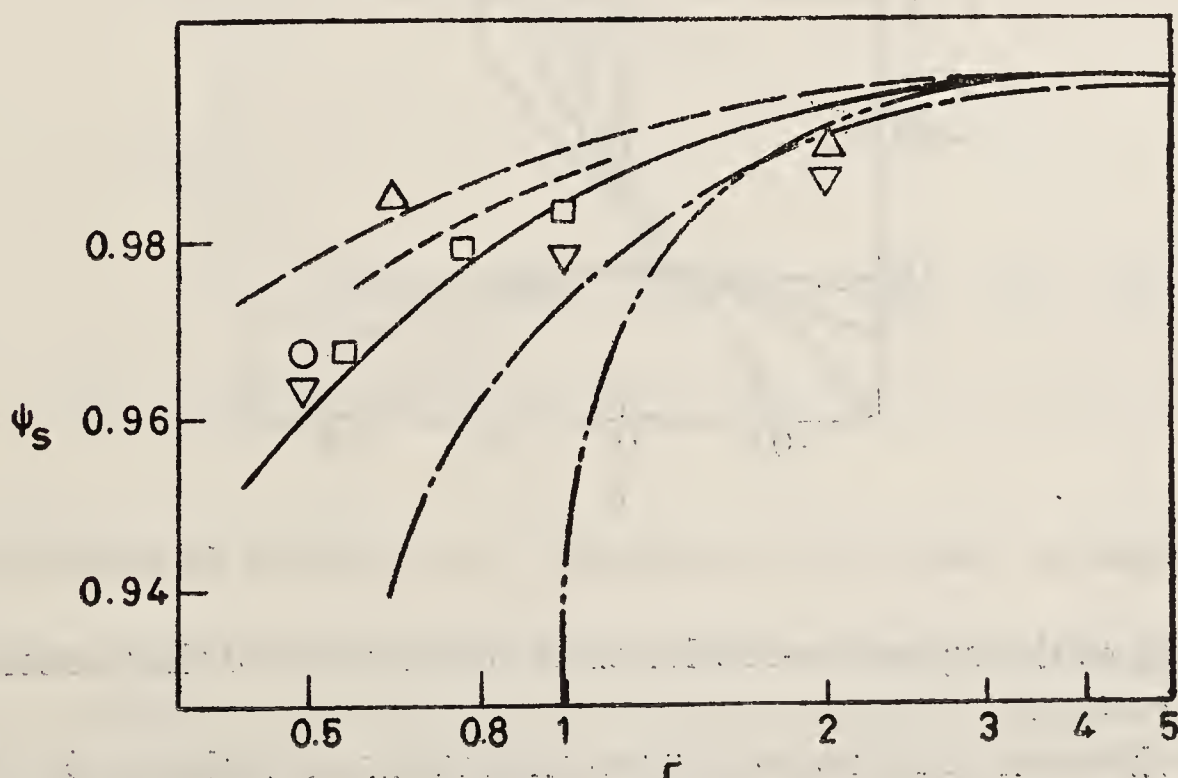


Figure 11. Maximum discharge for axisymmetric Laval nozzles. — Present method; - - - Sauer (1944); - · - Hall (1962); - - - Kliegel & Levine (1969); — Klopfer & Holt (1975); Δ Back *et al* (1965); ∇ Durham (1955); \square Norton & Shelton (1969); \circ Back & Cuffel (1971).

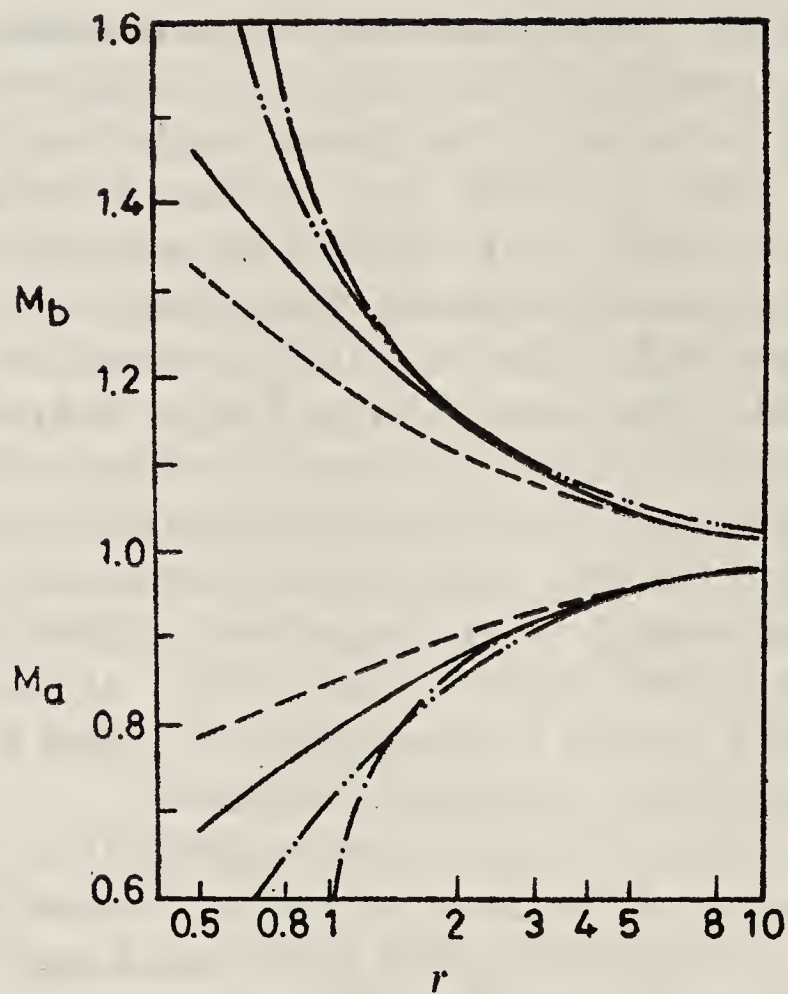


Figure 12. Throat wall and centre line Mach numbers for axisymmetric Laval nozzles. — Present results; --- Sauer (1944); - - - Hall (1962); - - - Kliegel & Levine (1969).

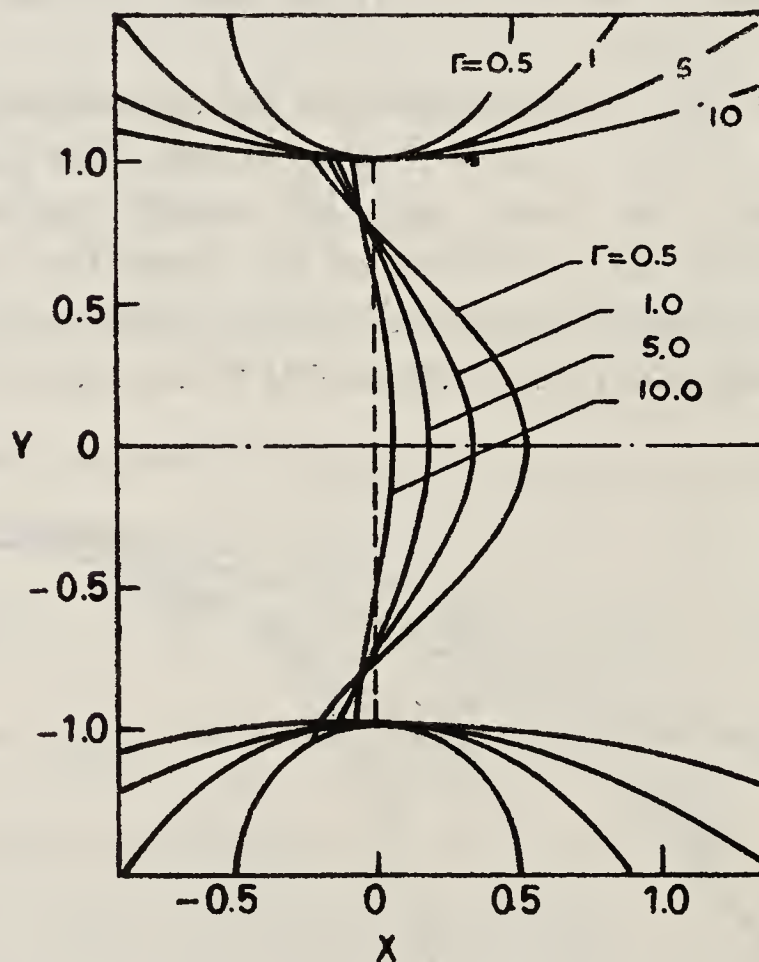


Figure 13. Sonic lines for axisymmetric Laval nozzles of the circular arc type.

Figure 14 gives the typical iso-Mach number distribution of the transonic flow in the throat for $r = 1$.

Figure 15 shows the influence of γ upon the maximum discharge ψ_s . It is clear that with the increase of the γ value the corresponding ψ_s value decreases.

It is to be noted that the present method, besides being simple in computation, is applicable to a small throat wall radius as well as to a large one.

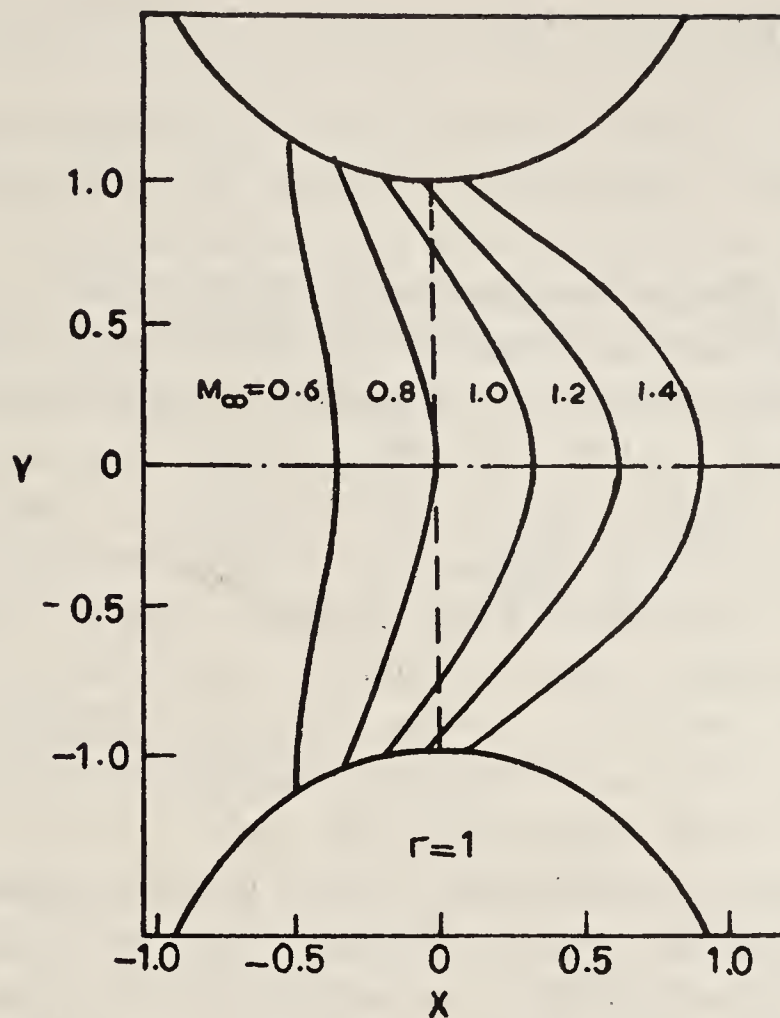


Figure 14. Transonic flow field for an axisymmetric Laval nozzle of the circular arc type.

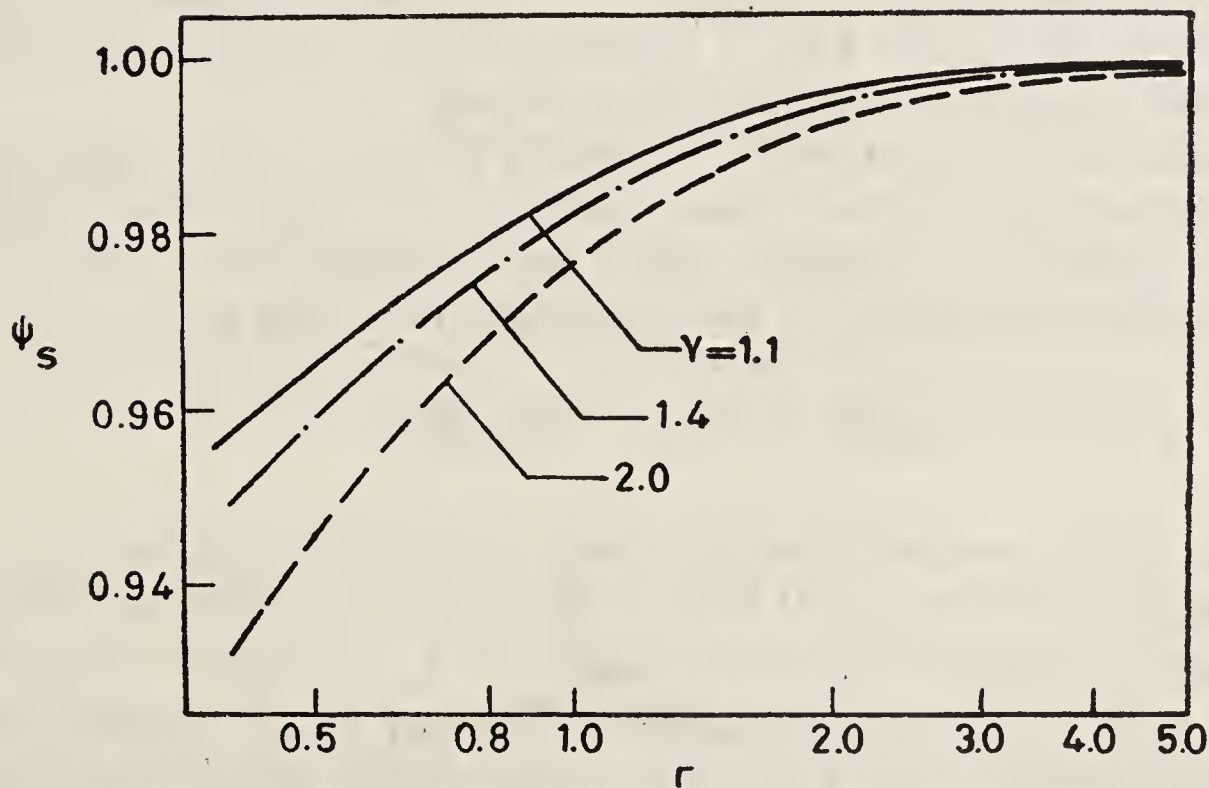


Figure 15. Effect of specific heat ratio on the maximum discharge of axisymmetric Laval nozzles.

4. External flow past bodies

In this section, the external flow past a body is studied in the light of the present method. A method of choosing the far field computation boundary is proposed; to overcome the difficulties associated with the small disturbance theory in dealing with thick bodies. As examples of the method, flow around a circular cylinder and a sphere are presented with free-stream Mach number M_∞ varying from subcritical to supercritical including M_∞ equal to 1.

4.1 Computation boundary

In tackling the problem of flow past a body, any numerical method, in general, can only provide solutions in a limited space (region). Therefore, how to select a distant computation boundary is a problem of great significance. In the case of a thin wing or a slender body, the disturbance generated in the flow field is usually small; so at a finite distance from the body the conditions at infinity can be applied. For example, for the flow field around a thin wing, Emmons (1948), Murman & Cole (1971) and others have replaced the boundary at infinity by one at a distance of a few chord lengths from the body. Chan *et al* (1974, 1975) divided the flow surrounding the body into the near region and the far region. A relatively fine mesh is used for the near region and a relatively coarse one for the far region. The two regions are matched at their junction. Disturbances to the flow field by thick bodies are usually large, especially under transonic conditions. It does not matter whether a straight line or a regional envelope line is selected as the outer computation boundary; they both need to be located at a very great distance from the body; this has brought about great difficulties in computation, as the region involved is greatly enlarged.

It is expected that the greater the distance from the body, the smaller is the difference between the streamlines of a compressible flow and the corresponding streamlines of an incompressible flow. Therefore, it would be a better approximation to select the streamlines of an incompressible flow at a certain distance from the body as the computation boundary. With the use of the conformal curvilinear coordinates in this paper, such a boundary then is the coordinate line $\eta = \eta_b$, which greatly facilitates the computations involved.

But it is to be noted that for flow around a body, there is a section between the computation boundary η_b and the body surface $\eta = 0$ which is the narrowest. Take the circular cylinder as an example; such a section occurs at $\xi = 0$, *i.e.* on the y axis. The mathematical expression for this relation can be written as

$$y(0, \eta) - y(0, 0) < y(\xi, \eta) - y(\xi, 0).$$

Moreover, for the oncoming uniform flow at an infinite distance, *i.e.* $\xi = -\infty$, the discharge ψ_b between $\eta = 0$ and $\eta = \eta_b$ is $(\rho u)_\infty \eta_b$. Therefore, the passage of the discharge ψ_b through the narrowest section on $\xi = 0$ serves as the necessary condition for η_b to be a possible computation boundary for the transonic flow. Using (7) and the condition $\xi = 0$, this relation can be written as (Lin Tong Ji & Jia Zhen Hue 1980)

$$\begin{aligned} & \left(\frac{\gamma+1}{2} \right)^{\frac{1}{\gamma-1}} g(0) \int_0^{\eta_b} \left[1 - \frac{\gamma-1}{\gamma+1} \frac{g^2(0)}{H_i^2(0, \eta)} \right]^{\frac{1}{\gamma-1}} \\ & \times \frac{H_2(0, \eta)}{H_1(0, \eta)} y'(0, \eta) d\eta = (\rho u)_\infty \eta_b. \end{aligned} \quad (24)$$

For (24) to be valid, there must exist a minimum value of η_b for a given supercritical free-stream condition $(\rho u)_\infty$ or M_∞ . Such a value is defined as the characteristic

boundary and is represented by η_c . From (24), one can see that η_c is only a function of $g(0)$; as a result of the above definition, η_c will satisfy the extremal relation

$$\partial \eta_b / \partial g(0) = 0.$$

With due note taken of the fact that the upper limit in the integral is a variable, and replacing the η_b in (24) by η_c and solving the equation, we obtain the following equation for η_c to satisfy the extremal relation mentioned above:

$$\int_0^{\eta_c} \left[\frac{g^2(0)}{H_1^2(0, \eta)} - 1 \right] \left[1 - \frac{\gamma-1}{\gamma+1} \frac{g^2(0)}{H_1^2(0, \eta)} \right]^{\frac{2-\gamma}{\gamma-1}} \times \frac{H_2(0, \eta)}{H_1(0, \eta)} y^\epsilon(0, \eta) d\eta = 0. \quad (25)$$

Now, the characteristic boundary η_c for a given oncoming flow Mach number can be obtained by replacing η_b in (24) by η_c and linking it with (25). When the oncoming flow Mach number $M_\infty \rightarrow 0$, the solution of the simplified equation (12) is accurate for the whole space; therefore, the corresponding computation boundary η_b should be ∞ . When $M_\infty = 1$, (24) and (25) yield η_c as ∞ . Since $\eta_b > \eta_c$, η_b is also ∞ . This shows that for $M_\infty = 1$, one gets the maximum value of the oncoming flow discharge and the effect of the body upon the flow field is to be shared by the whole flow field. This is precisely what is characteristic of a transonic flow. When the oncoming stream reaches the critical Mach number, the body-induced effect upon the flow field is mostly borne by the near region; η_c is then comparatively small in value.

To sum up, as M_∞ gradually increases from 0 to the critical Mach number and then to 1, the corresponding values of η_b first gradually decrease from ∞ to a minimum value and then gradually increase to ∞ . As a result, one can write

$$\eta_b = \eta_c + \sum_{k=1}^n a_k M_\infty^{-b_k k}, \quad 0 \leq M_\infty \leq 1. \quad (26)$$

A proper selection of η_b will raise the accuracy of the first order solution and reduce the number of iterations. For example, for the flow past a circular cylinder, with $n = a_1 = b_1 = 1$, (26) yields very good results. A detailed discussion of the topic will be given below.

4.2 Flow past a circular cylinder

The transonic flow past a circular cylinder is a longstanding problem that has engaged the attention of many researchers. For instance, Imai (1941) used the free stream Mach number as a small parameter to calculate the flow around a circular cylinder with $M_\infty < 0.4$; Cherry (1947, 1949 a, b) used the hodograph method, to simulate, by repeated additions of basic potentials, the approximate flow contours of a quasi-circular cylinder and to give a special solution for $M_\infty = 0.51$. Simanski (1956)

used a method similar to that of Imai (1941), and chose higher-order terms for calculations about subcritical flow past a circular cylinder. Dorodynitsyn (1956) and Chushkin (1957) used the strip integral method to calculate the flow past a circular cylinder for $M_\infty = 1$. Later, Holt & Masson (1970) used the integral relation method to calculate the critical flow past a circular cylinder. Moretti (1970) used the time-step correlation method for $M_\infty = 1.0$, and Norrie & Vries (1975) used the finite element method for $M_\infty = 0.3$ and 0.7 . Because of the inherent limitations of these methods, they could only provide results about the flow under certain specific conditions. The present paper, on the other hand, by using the method of conformal curvilinear coordinates, manages to provide an overall picture for the flow past a circular cylinder and gives systematic results ranging from subcritical to supercritical, including freestream Mach number $M_\infty = 1$.

Let us assume that the free stream at infinity and the x -axis are parallel and that the origin of the coordinate system is situated at the centroid of the cross section. Then, for a unit circle in the xy plane, the relations between the equipotential lines and the streamlines (ξ, η) for an incompressible potential flow and the coordinates (x, y) , and the related Lamé coefficient, are given respectively as (Lamb 1932; Lin Tong Ji & Jia Zhen Hue 1980)

$$\left. \begin{aligned} \zeta = z + \frac{1}{z}, \quad z = x + iy, \quad \zeta = \xi + i\eta, \\ h = \frac{1}{H} = \frac{1}{x^2 + y^2} [(x^2 + y^2)^2 - 2x^2 + 2y^2 + 1]^{1/2}. \end{aligned} \right\} \quad (27)$$

Substituting (27) into (24) and (25), (12) yields the first-order solution. Taking the streamlines thus obtained and their orthogonal lines as curvilinear coordinates, a second-order solution can be worked out by the same method, and so on to higher-order approximations. Generally speaking, the selection of the computation boundary η_b is not critical, but an appropriate selection can enhance the accuracy of the first-order solution and reduce the number of iterations necessary in the numerical operation. The results of computations based upon (26) show that for flow past a circular cylinder, with $n = a_1 = b_1 = 1$, *i.e.* $\eta_b = \eta_c + 1/M_\infty$, even the first-order approximation has a very good accuracy, as is shown in figures 17, 18 and 19.

The curves relating $g(\xi)$ to the free-stream Mach number M_∞ for different values of ξ are shown in figure 16. It can be seen that when $\xi \rightarrow -\infty$ the g value equals the corresponding free-stream velocity, *i.e.* $g(-\infty) = u_\infty$. This indicates that at infinite distance there is no body-induced disturbance and that the compressible and the incompressible flow are identical; with the increase in ξ , the influence of compressibility also grows. Departure from the free stream begins with $g < u_\infty$; this indicates that the influence of compressibility has reduced the flow velocity and made it lower than that in a corresponding incompressible flow. On approaching the forward stagnation point, which for a circular cylinder is at $\xi = -2$, the value of g is the smallest. With the continued increase in ξ , the value of g rises until it equals u_∞ at the location where $\xi = \xi_m$. It has to be noted, however, that the location of ξ_m varies with M_∞ . For still larger values of ξ , the values of g approach u_∞ . At $\xi = 0$, *i.e.* at the thickest section of the circular cylinder, the value of g , *i.e.* the influence of compressibility, is the largest.

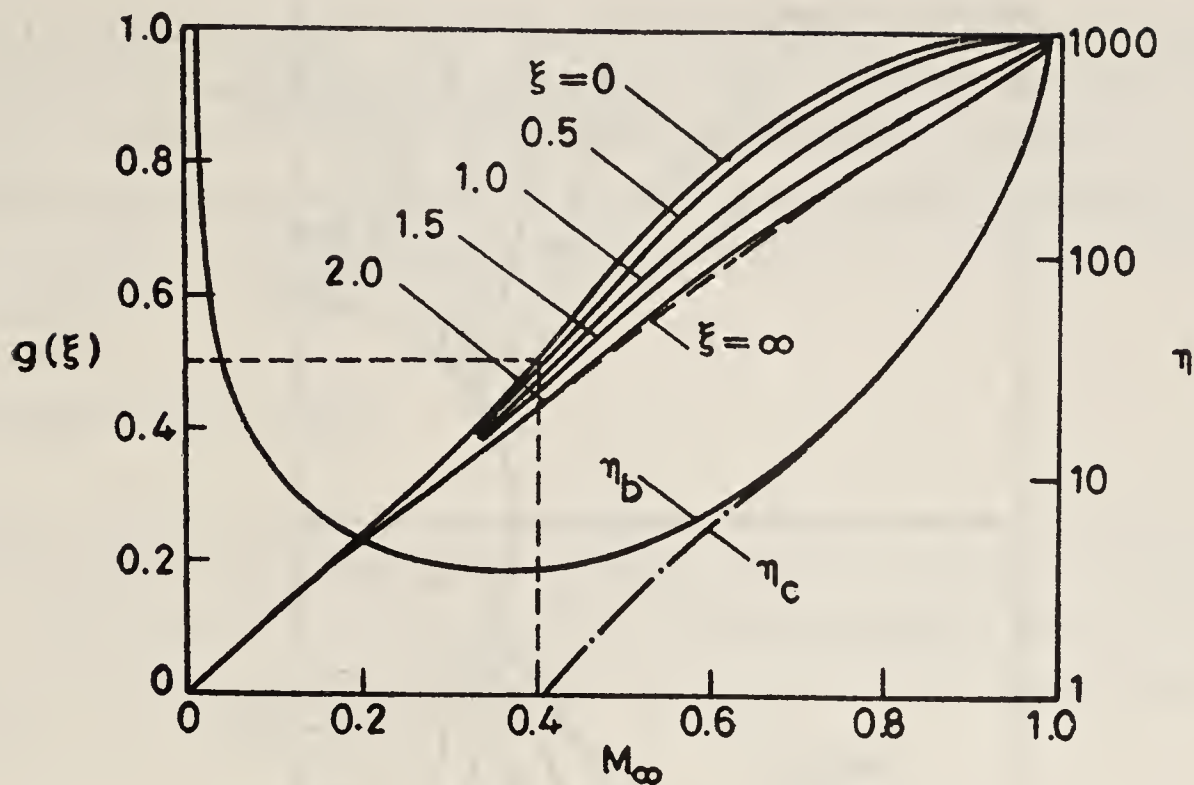


Figure 16. "Discharge functions" for a circular cylinder.

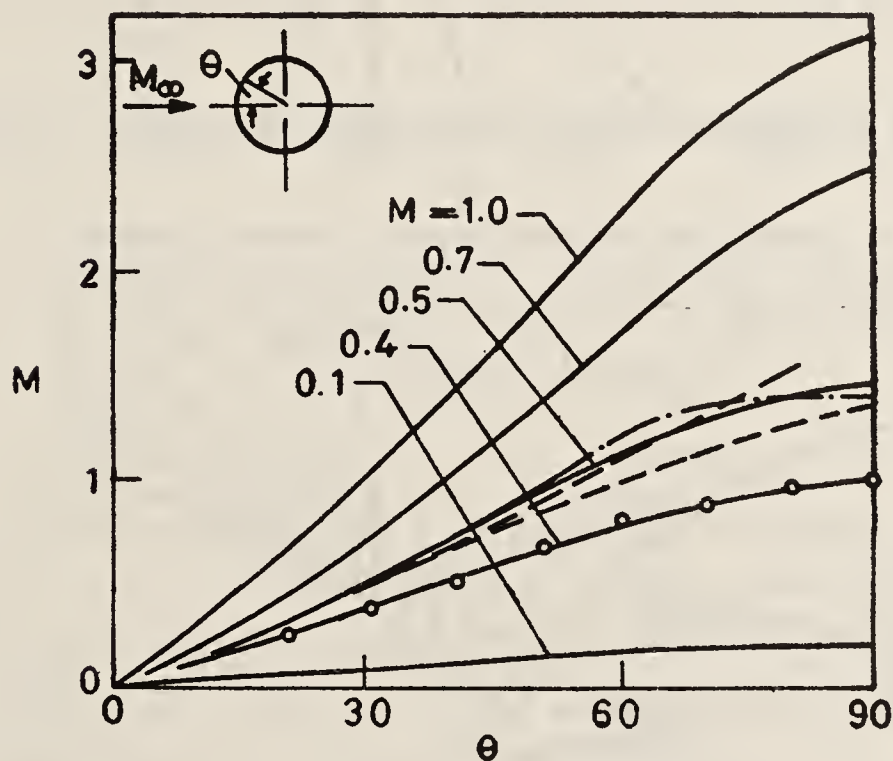


Figure 17. Mach-number distribution on the surface of a circular cylinder.
 — Present results; — — — Dorodnitsyn (1956); — · — · — Cherry (1949);
 ○ ○ Imai (1941); Hafez *et al* (1979).

From the results obtained in this paper, one can see that the values of g represent the effect of compressibility. Whether the body is thick or thin, the variation of $g(\xi)$ with ξ tends to follow a similar pattern. But, the difference between the maximum and the minimum value of g for a thin body is very small; therefore, one can go a step further towards approximation by using a single compressibility correction value for the entire flow field. For example, the Karman-Tsien method (Tsien 1939; Von Karman 1941) has yielded very good results for thin wings. As for thick bodies, from the results obtained by the present method, one can see that for different ξ values, it is necessary to use different compressibility corrections, namely compressibility corrections should be a function of the parameter ξ . Moreover, for different values of free stream Mach number M_∞ , the compressibility corrections are also different. Figure 16 shows that for very low M_∞ , the effect of compressibility is very small; with the increase in M_∞ , the compressibility correction also increases; at the critical Mach

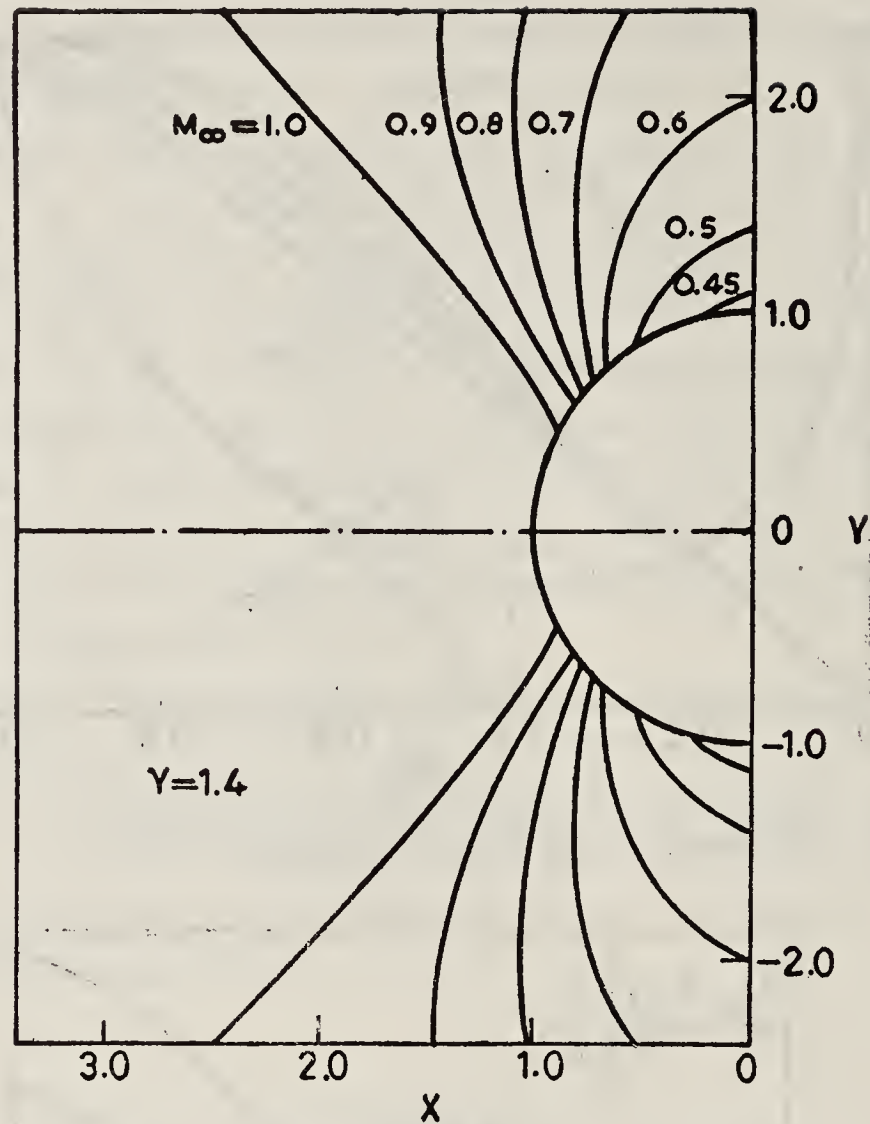


Figure 18. Sonic lines for the flow past a circular cylinder.

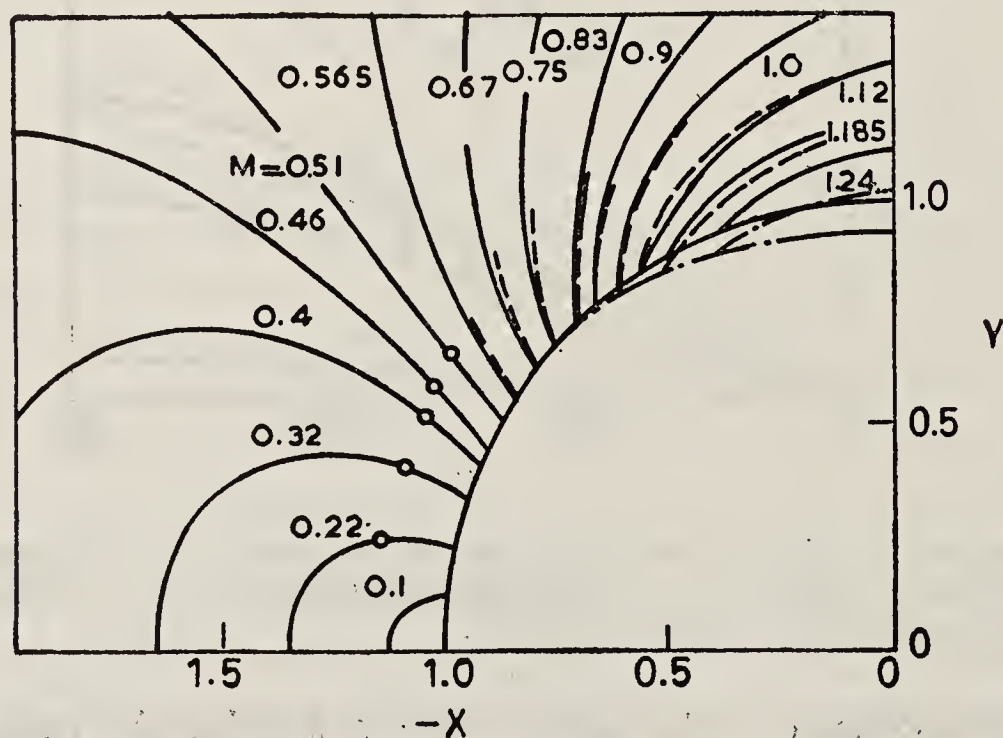


Figure 19. Iso-Mach lines for the flow past a circular cylinder at $M_\infty = 0.51$.
 — Present results; - - - Cherry (1949).

number, the correction reaches a maximum; further increase in M_∞ will cause, instead, a decrease in the values.

Figure 17 gives the Mach number distribution on a circular cylinder surface with free-stream Mach numbers ranging from 0.1 right up to 1. For the sake of comparison, the figure also gives Cherry's result (1949b) at $M_\infty = 0.51$; Chushkin's result (1957) at $M_\infty = 1$ and Imai's result (1941) at $M_\infty = 0.4$.

Figure 18 gives the sonic lines for flow past a circular cylinder with M_∞ varying from 0.45 up to 1.

Figure 19 gives the flow field past a circular cylinder at $M_\infty = 0.51$ and $\gamma = 1.405$. For comparison, the figure also gives Cherry's (1949b) quasi-circular cylinder results

(dotted lines). From the figure it can be seen that for $\theta \leq 45^\circ$, Cherry's quasi-circular cylinder contours coincide with those of a real circle and that his iso-Mach lines coincide with ours. When $\theta > 45^\circ$, the deviation between the quasi-circular and the real circular cylinder gradually increases. At $\theta = 90^\circ$, the corresponding deviation reaches a maximum of 7%; and the corresponding iso-Mach lines also gradually diverge, as may be expected.

4.3 Transonic flow past a sphere

Let us assume that the origin of the rectangular coordinates (x, y) is at the centre of the sphere with the x -axis parallel to the free stream at infinity. Because of axisymmetry, one need only consider the flow in the meridional plane (x, y) . For a unit sphere, the incompressible potential (ξ, η) in the meridional plane (x, y) is (Lamb 1932)

$$\xi = x \left[1 + \frac{1}{2(x^2 + y^2)^{3/2}} \right], \quad \eta = \frac{y^2}{2} \left[1 - \frac{1}{(x^2 + y^2)^{3/2}} \right]. \quad (28)$$

From (2) and (28) one obtains the inverse of Lamé's coefficients H_1 and H_2 as

$$\left. \begin{aligned} H_1 &= (x^2 + y^2)^{5/2} \left\{ \left[(x^2 + y^2)^{5/2} - x^2 + \frac{1}{2} y^2 \right]^2 + \frac{9}{4} x^2 y^2 \right\}^{-1/2}, \\ H_2 &= \frac{H_1}{y}. \end{aligned} \right\} \quad (29)$$

Now, by substituting (28) and (29) into (24) and (25), we obtain the corresponding characteristic boundary η_c for different values of M_∞ . As a first order approximation, we select the computation boundary to be equal to $\eta_c + (M_\infty)^{-1/2}$. According to (28), (29), (4), (12) and (13), one obtains the values of $g(\xi)$ and the flow fields for the corresponding free stream (see figures 20 and 21).

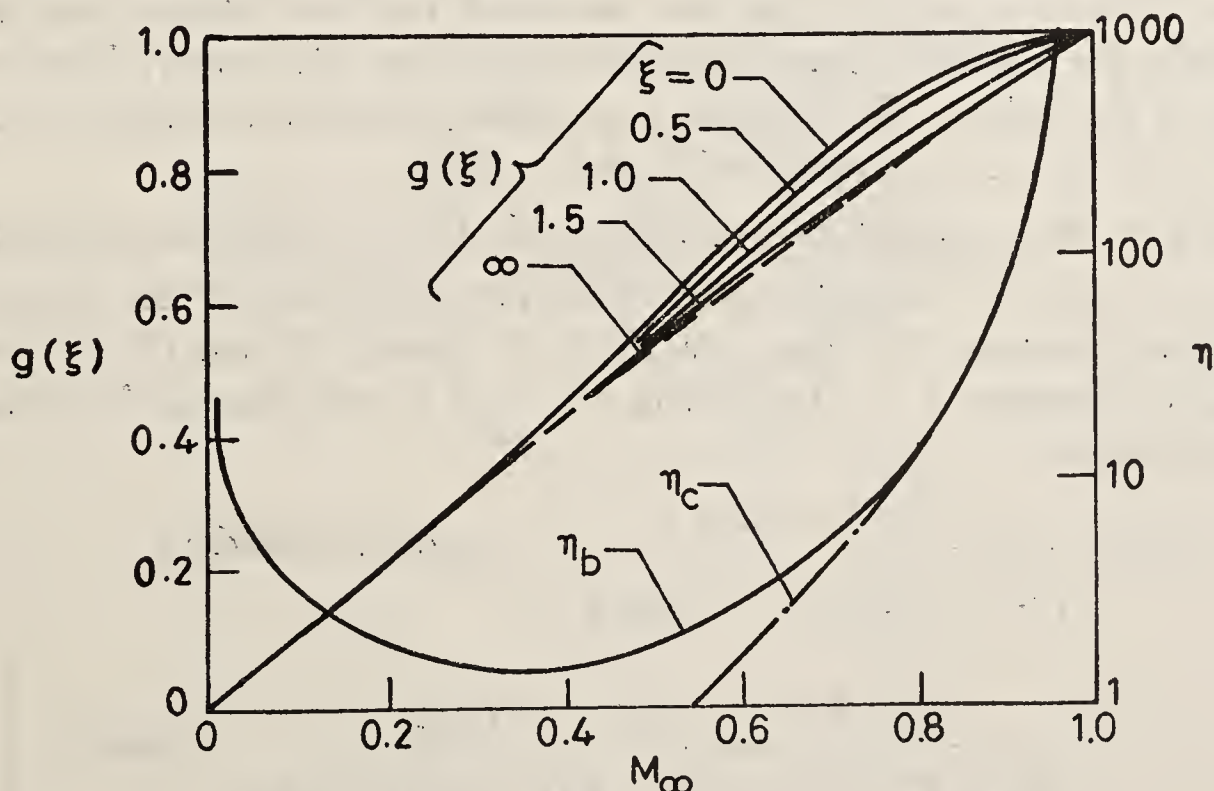


Figure 20. "Discharge function" for a sphere.

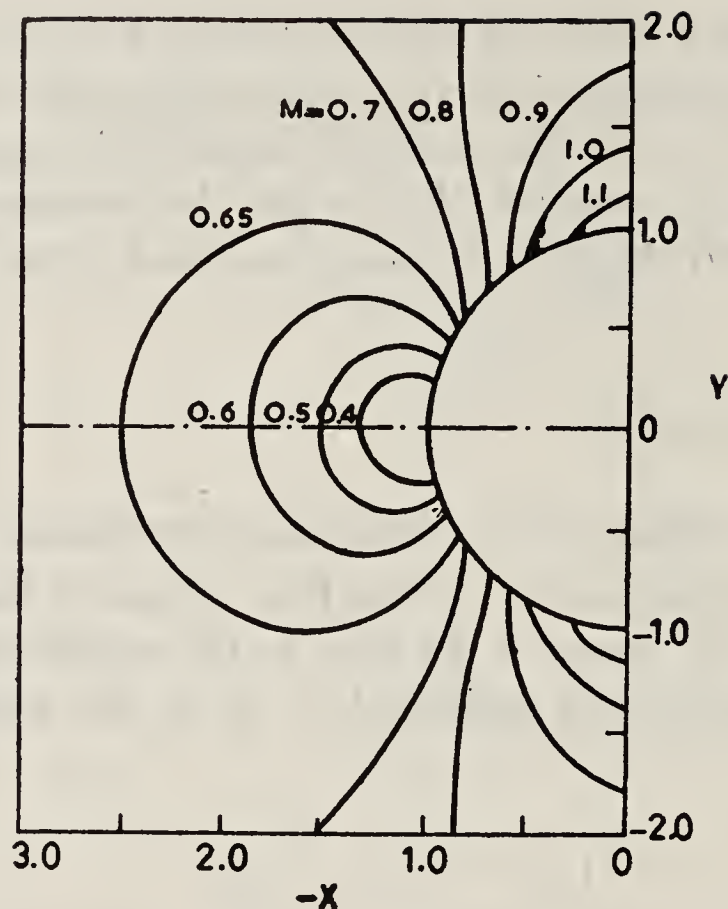


Figure 21. Iso-Mach lines for flow past a sphere at $M_\infty = 0.7$.

After comparing figure 16 with figure 20, one can see that the critical Mach number for a circular cylinder is 0.403, whereas for a sphere it is 0.58. As an example, figure 21 gives the transonic flow about a sphere at $M_\infty = 0.7$. It shows that the maximum Mach number in the flow field is 1.32, whereas figure 17 indicates that for a circular cylinder the maximum Mach number is 2.42. Moreover, the supersonic region for flow about a cylinder is much larger than that about a sphere.

4.4 Flow field at $M_\infty = 1$.

This is a crucial problem in transonic studies. As a result of the mixed nature of the flow equation, the scope of the body-induced flow disturbance is especially large, and this causes great difficulties in theoretical analysis, numerical computations and experimental studies. In the case of a circular cylinder, for example, at $M_\infty = 1.0$, neither the sonic line contours nor the iso-Mach line distribution, nor the characteristics of the far field flow, have yet been made clear. This paper, therefore, intends to discuss, in the light of the method it proposes, the characteristics of the flow at $M_\infty = 1.0$ for both a circular cylinder and a sphere.

According to the equations given earlier, with $M_\infty = 1$, (24) and (25) yield $\eta_c = \infty$, therefore η_b is also ∞ . Substituting the boundary conditions in the general solution for the stream-function (12), one gets $g(\xi) \equiv 1$. Using (4) and (13) as well as (27) and (28), and assuming $x = r \cos \theta$ and $y = r \sin \theta$, one obtains the Mach number at (r, θ) as follows:

$$\begin{aligned}
 M^2 &= \frac{r^4 - 2r^2 \cos 2\theta + 1}{r^4 - \frac{\gamma - 1}{2} (1 - 2r^2 \cos 2\theta)} \quad (\text{circular cylinder}), \\
 &= \frac{(1 + 2r^3)^2 + 3(1 - 4r^3) \cos^2 \theta}{4r^6 - \frac{\gamma - 1}{2} [1 + 4r^3 + 3(1 - 4r^3) \cos^2 \theta]} \quad (\text{sphere}).
 \end{aligned} \tag{30}$$

The flow fields calculated from (30) are given in figures 22 and 23 respectively. It can be seen that for $M > 1$, the iso-Mach lines intersect the y -axis, whereas for $M < 1$ they intersect the x -axis. The sonic lines extend to infinity. For a circular cylinder they are represented by that part of the hyperbolic curve which lies outside the cylinder, i.e., by the equation:

$$r^2 \cos 2\theta = \frac{1}{2}, r \geq 1.$$

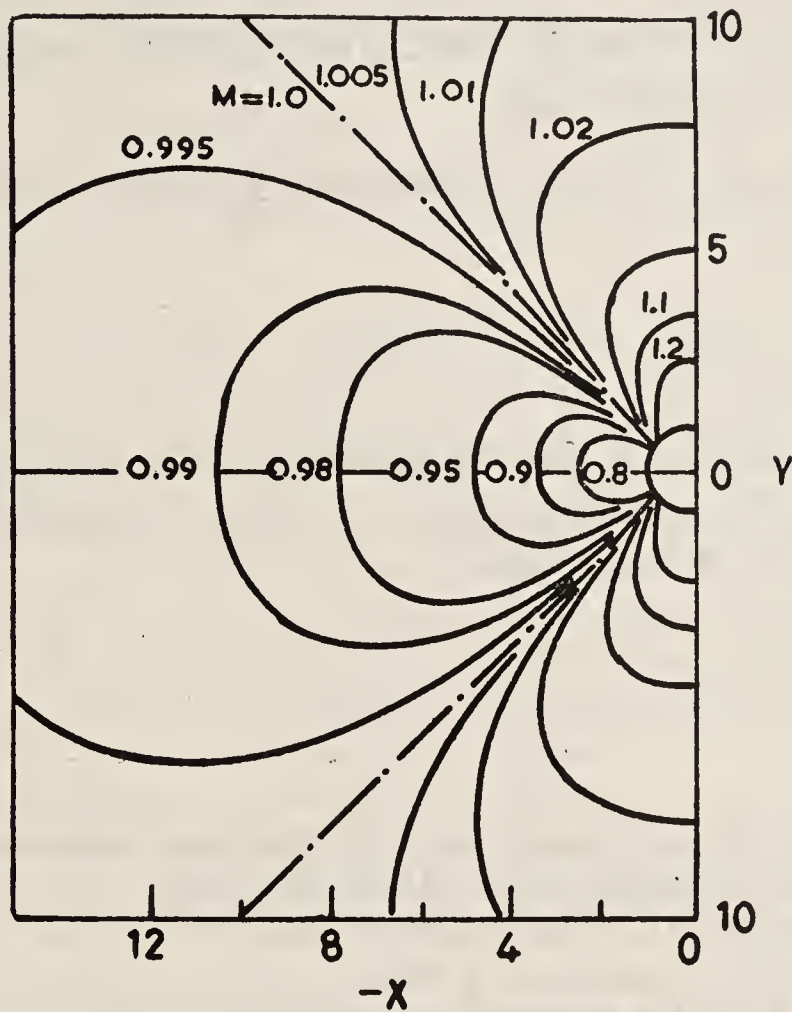


Figure 22. Iso-Mach lines for flow past a circular cylinder at $M_\infty = 1$.

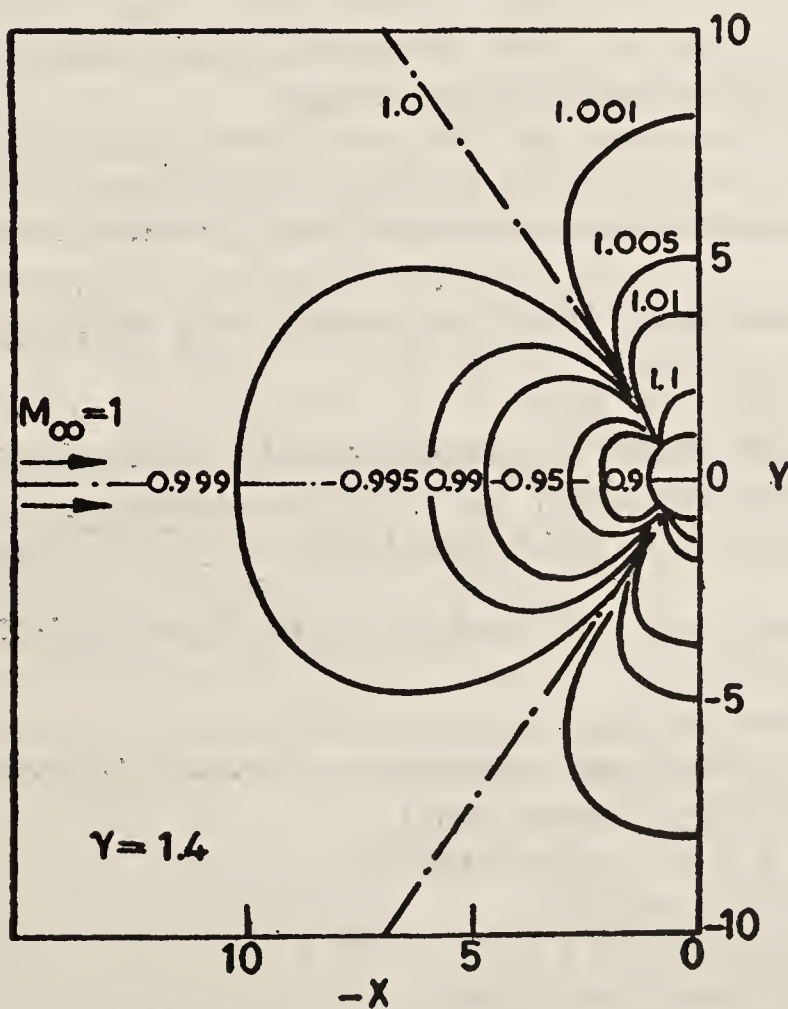


Figure 23. Iso-Mach lines for flow past a sphere at $M_\infty = 1$.

These sonic lines begin at $\theta = \pm 30^\circ$ on the surface of the cylinder and approach the lines $\theta = \pm 45^\circ$ asymptotically. In the case of a sphere, the sonic lines are given by the formula

$$\cos^2 \theta = \frac{4r^3 + 1}{3(4r^3 - 1)}.$$

They begin at $\theta = \pm 41^\circ 49'$ on the surface of the sphere and approach the conical surface $\theta = \pm 54^\circ 45'$ asymptotically.

From (30) or (22) and (23), one obtains the deviation of the Mach number on the x and y axis as

$$\Delta M = M - M_\infty = O(r^{-(2+\epsilon)}). \quad (31)$$

Thus the velocity disturbance in this transonic flow field varies as r^{-2} for the cylinder and r^{-3} for the sphere. For example, when $r = 10$, for a circular cylinder $M \approx 1 \pm 0.01$ whereas for a sphere $M \approx 1 \pm 0.001$.

References

- Aungier R H 1970 A computational method for exact, direct and unified solutions for axisymmetric flow over blunt bodies of arbitrary shape, AFWL-TR-70-16
- Back L H, Massier P H & Gier H L 1965 *AIAA J.* **3** 1606
- Back L H & Cuffel R F 1971 *J. Spacecraft.* **8** 196
- Barwell R W & Davis R M 1971 A computer program for calculating inviscid adiabatic flow about blunt bodies travelling at supersonic and hypersonic speeds at angle of attack, NASA TM X-2334.
- Bauer F, Garabedian P R & Korn D 1975 *Supercritical wing § 2 Lecture notes in economics and mathematical systems* (New York: Springer Verlag)
- Belotserkovskiy O M 1967 Supersonic gas flow around blunt bodies, NASA TT F-453
- Boerstoel J W 1974 A transonic hodograph theory for aerofoil design, IMA conference on computational methods and problems in aeronautical flow dynamics, Manchester, NLR Rep. MP 74024 U
- Boerstoel J W & Uijlenhoel R R 1970 Lifting aerofoils with supercritical shock-free flow, ICAS paper 70-15, NLR MP 70015U
- Chakrabarty S K 1978 *AIAA J.* **16** 1015.
- Chan S T K & Brashears M R 1974 Finite element analysis of transonic flow, AFFDL-TR-74-11
- Chan S T K, Brashears M R & Young V Y C 1975 Finite element analysis of transonic flow by the method of weighted residuals, AIAA 13th Aerospace Science Meeting, Pasadena, California, AIAA paper 75
- Chaplygin S A 1904 On gas flow. Scientific studies at the Moscow University, Physics—mathematical Sciences 21.
- Cheng H K and Hafez M M 1976 *Lecture notes in physics* 47 (ed. H Caléennes) 47 101
- Cherry T M 1947 *Proc. R. Soc. (London)* **A192** 45
- Cherry T M 1949a *Proc. R. Soc. (London)* **A196** 1
- Cherry T M 1949b *Proc. R. Soc. (London)* **A196** 32
- Cherry T M 1950 *Proc. R. Soc.* **A203** 551
- Cherry T M 1959 *J. Aust. Math. Soc.* **1** 80
- Chushkin N N 1957 *Appl. Math. Mech.* **21** 352
- Cline M C 1974 *AIAA J.* **12** 419

- Crocco L 1965 *AIAA J.* **3** 1824
- Dorodnitsyn A A 1956 On a method of numerical solution of some non-linear problems of aerodynamics, Work of 3rd All Union Mathematical Congress, Part III, (USSR Academy of Sciences) p. 447
- Durham F P 1955. The performance characteristics of small rocket-type nozzle, summary report 6. Contract N-123s-82337 T.O.1, Univ. of Colorado, Boulder, Colorado, U.S.A.
- Emmons H W 1946 The theoretical flow of a frictionless, adiabatic, perfect gas inside of a two-dimensional hyperbolic nozzle, NACA TN-10003
- Emmons H W 1948 Flow of a compressible fluid past a symmetrical airfoil in wind tunnel and in free air, NACA TN-1746
- Frankl F N 1945 *Proc. USSR Acad. Sci.* **5** 387
- Garabedian P R & Lieberstein H M 1958 *J. Aeronaut Sci.* **25** 109
- Garabedian P R & Korn D G 1971 *On numerical solutions of partial differential equations II* (New York: Academic Press)
- Goldstein S, Lighthill M J and Craggs J W 1948 *Q. J. Mech. Appl. Math.* **1** 344
- Gortler H 1939 *Z. Angew Math. Mech.* **19** 327
- Green J R & Southwell R V 1944 *Philos. Trans. R. Soc. (London)* **A239** 367
- Gross M B & Holt M 1975 in *Symposium Transsonicum II*, IUTAM Symposium Göttingen (Berlin: Springer-Verlag) p. 369
- Grossman B & Moretti G 1973 Development of analytical methods of predicting the pressure distribution about a nacelle at transonic speeds-exact solution, NASA CR-112271
- Gullstrand T R 1951a The flow over symmetrical aerofoils without incidence in the lower transonic range, Roy. Inst. Technol. (KTH) Tech. Note, AERD 20 Stockholm
- Gullstrand T R 1951b The flow over symmetrical aerofoils without incidence at sonic speed, Roy. Inst. Technol. (KTH) Tech. Note, AERD 24 Stockholm
- Hafez M M, South J & Murman E M 1979 *AIAA J.* **17** 838
- Hall I M 1962 *Q. J. Mech. Appl. Math.* **12** 487
- Hansen H 1975 in *Symposium Transsonicum II*, IUTAM Symposium Göttingen (Eds. K Oswatitsch & D Rues) (Berlin: Springer-Verlag) p. 183
- Hofez H M & Cheng H K 1977 *AIAA J.* **15** 1977
- Hofez H M & Cheng H K 1977 *AIAA J.* **15** 786
- Holt M 1962 in *Symposium Transsonicum*, IUTAM Symposium (Berlin: Springer-Verlag) p. 310
- Holt M & Masson B S 1971 *Lecture notes in Physics* **8** 243
- Imai I 1941 *Proc. Phys. Math. Soc. Jpn.* **23** 181
- Jameson A 1971 Transonic flow calculation for airfoils and bodies of revolution, Crumman aerodynamics Rept. 391-71-1
- Jameson A 1974 *Commun. Pure. Appl. Math.* **27** 283
- Jameson A 1975 Transonic potential flow calculations using conservation form, second AIAA conference on computational fluid dynamics, Hartford
- Jameson A 1975 Accelerated iteration schemes for transonic flow calculations using fast Poisson solves, New York Univ., ERDA Rept. COO-3072-82
- Jia Zhan Xue & Lin Tong Ji 1979 *Acta Mech. Sin.* **3** 199
- Jia Zhan Xue & Lin Tong Ji 1981 Transonic flow field in the throat region of axisymmetric nozzles (to be published)
- Jones D L & South Jr. J G 1975 A numerical determination of the bow shock wave in transonic axisymmetric flow about blunt bodies, NASA TM-X-72448
- Kliegel J R & Levine J N 1969 *AIAA J.* **7** 1375
- Klopfer G H & Holt M 1975 in *Symposium Transsonicum II*, Symposium Göttingen (Berlin: Springer-Verlag) p. 376
- Korn D G 1969 Computation of shock-free transonic flows for airfoil design, NYU Rep. NYU-480-125, Courant Inst. Math. Sci.
- Krupp J A 1971 The numerical calculation of plane steady transonic flow past thin lifting airfoils, Rep. D. 180-12958-1, Boeing, Seattle, Wash.
- Krupp J A & Murman E M 1972 *AIAA J.* **10** 880
- Kuo Y H 1948 Two-dimensional irrotational transonic flow, NACA TN-1445
- Kuo Y H 1951 Two-dimensional transonic flow airfoils, NACA TN-2356

- Lamb H 1932 *Hydrodynamics* (New York: Dover) sixth edition p. 70 123
- Lame G 1834 *J. Polytech. Sch.* **14** 191
- Laval D 1883 *Essentials of fluid dynamics* (ed. L Prandtl I) (New York: Hafner Publishing Company) p. 268
- Lax P D & Wendroff B 1964 *Commun. Pure. Appl. Math.* **17** 381
- Lightill M J 1947 *Proc. Roy. Soc. (London)* **A191** 323
- Lin C C, Reissner E & Tsien H S 1948 *J. Math. Phys.* **27** 220
- Lin Tong Ji & Jia Zhen Xue 1978 *Acta Mech. Sin.* **1** 1
- Lin Tong Ji & Jia Zhen Xue 1980 *Acta Mech. Sin.* **4** 327
- Magnus R, Grallaher W & Yoshihara H 1968 Inviscid supercritical airfoil theory, Trans. Aerodynam AGARD Conf. Proc. No. 35
- Magnus R & Yoshihara H 1970 *AIAA J.* **8** 2157
- Meyer T 1908 On the two-dimensional—forward motion in a gas moving at supersonic speed, Research No. 62
- Moretti G & Abbett M 1966 *AIAA J.* **4** 2136
- Moretti G 1969 The choice of a time-dependent technique in gas dynamics, Polytech. Inst. Brookly PIBAL Repl. 69-26, (von Karman Institute for Fluid Dynamics, Lecture Ser. 26 1970)
- Moretti G 1970 Transient and asymptotically steady flow of an inviscid, compressible gas past a circle, I. shockless flow, Brooklyn, Polytech. Inst. PIBAL Repl. 70-20, (von Karman Institute for Fluid Dynamics, Lecture Ser. 26)
- Murman E M & Cole J D 1971 *AIAA J.* **9** 114
- Murman E M 1973 Analysis of embedded shock waves calculated by relaxation methods, AIAA computational Fluid Mech. Conf. Palm. (Berlin: Springer-Verlag)
- Nieuwland G Y 1967 Transonic potential flow around a family of quasi-elliptical aerofoils section, NLR (Neth) Tech. Rept. T 172
- Nixon D 1975 *Aeronaut. Q.* **26** 56
- Nixon D 1978 *AIAA J.* **16** 976
- Norrie D H & de Vries G 1975 in *Finite element method in fluid problems* (ed. by Oden J T) (University of Alabama Press) p. 21
- Norton D L & Shelton S 1969 Performance of rocket nozzles with low radius of curvature, JPL space programs, summary No. 37-55, Vol. III, Pasadena, Calif. p. 167
- Nørstrud H 1973 *Aeronaut. Q.* **24** 129
- Oswatitsch K & Wieghendt K 1942 Theoretical investigations into the supersteady potential flow at higher velocities (unpublished)
- Oswatitsch K 1950 *Z. Angew. Math. Mech.* **30** 17
- Reynolds O 1886 *Philos. Mag.* **21** 185
- Riabouchinsky D 1932 *Fluid Mechanics Report* (Paris: Academy of Sciences) Vol. 195 p. 398
- Rieman B 1851 *Foundations of a general theory of functions of a complex variable*, Göttingen Mathematical Works, Leipzig, Vol. 187, p. 3
- Sauer R 1944 General characteristics of the flow through nozzles at near critical speeds, NACA TM-1147
- Seria R A 1972 *AIAA J.* **10** 603
- Shen S F 1975 *Finite element method in fluid problems* (ed. J T Oden), p. 189
- Shen S F 1977 *Annu. Rev. Fluid Mech.* **9** 440
- Simasalsi T 1956 *J. Math. Phys.* **34** 1
- Sobieczky H 1972 Analogue—analytical construction of supercritical profile flow. DGIR-symposium, aircraft aerodynamics at sonic flow
- Spreiter J R & Alksen A Y 1955 Theoretical prediction of pressure distributions on nonlifting airfoils at high subsonic speeds, NACA Rept. 1217
- Swenson E V 1968 *Commun. Pure. Appl. Math.* **21** 175
- Takanashi S 1973 *Trans. Jpn. Soc. Aeronaut. Space Sci.* **16** 34
- Taylor G I 1930 The flow of air at high speeds past curved surfaces, ARC RM 1831
- Tomotika S & Tamada K 1950 *Appl. Math.* **7** 381
- Tricomi F 1923 Sulle-equation lineari derivate parziali del secondo ordine, di tipo misto parts 1-7, memori Reale, Nazl. Linoei. Classe Scifis, mat. enat., (Ser. 5) 14, 133247, also see Brown Univ. Transl. A9-T-26

Tsien H S 1939 *J. Aeronaut. Soc.* **6** 399

Tsien H S & Kuo Y H 1946 Two-dimensional mixed subsonic and supersonic flow of a compressible fluid and the upper critical Mach number, NACA TN 995

Tsien H S 1958 in *Fundamentals of gas dynamics* (ed. by H W Emmons) (Princeton, New Jersey; Princeton University Press) p. 57

Von Karman 1941 *J. Aeronaut. Sci.* **8** 337

Von Karman 1947 *J. Math. Phys.* **26** 182

Von Neuman J & Richtmyer R 1950 *J. Appl. Phys.* **21** 232

Von Ringleb F 1940 *Z. Angew. Math. Mech.* **20** p. 185

Transonic flow past thin wings

PRADIP NIYOGI

Department of Mathematics, Indian Institute of Technology, Kharagpur 721 302

MS received 27 January 1981

Abstract. This paper is devoted to a discussion of steady inviscid transonic flow past thin wings, with subsonic free-stream Mach number $M_\infty < 1$, by the integral equation method. The integral equation formulation is developed for a thin unsymmetric wing at small incidence. A simple approximate analytical solution is presented for shock-free supercritical flow past a thin symmetric wing at zero incidence. The direct iteration scheme of Niyogi and Chakraborty is then extended to the three-dimensional zero incidence case, which may be used to obtain more accurate solutions for shock-free flows as well as for flows with shocks. The question of the existence and the uniqueness of a solution has been studied by means of the Banach contraction mapping principle in the space $L_2(E_3)$, which establishes the condition of convergence of the direct iteration scheme. Simultaneously it provides us with an error estimate for the solution.

Keywords. Transonic aerodynamics; high subsonic flow; thin wings; supercritical aerodynamics; three-dimensional transonic flow; integral equation method; direct iteration scheme; error estimate; shock-free supercritical flow.

1. Introduction

A flow field where both subsonic and supersonic regions are present and are significant in determining the overall character of the flow field is known as a transonic flow field. Such flow fields appear in nozzles, over propellers and turbine blades, around blunt bodies moving supersonically and near airplanes which fly close to the Mach number unity. Thus with the development of modern high-speed flight vehicles, the study of such flow fields has become important. Moreover, attention has been focussed in recent times, on the question of possible drag reduction in flight at transonic speed range.

Although a considerable amount of research has been done on transonic profile flow problems, the study of transonic flow past thin wings is only of recent origin (Bailey 1975). This study started with the breakthrough of Murman & Cole (1971), who gave for the first time a successful finite-difference relaxation procedure for studying steady inviscid irrotational transonic flow past a thin symmetric profile at zero incidence. During this time, Nørstrud (1973) extended the integral equation method of Oswatitsch (1950) to the three-dimensional case of flow past thin wings.

The present paper is devoted to a discussion of transonic flow past prescribed thin wings, with prescribed high subsonic free-stream Mach number $M_\infty < 1$, by the integral equation method. The flow field is such that a local supersonic region is formed near the maximum thickness of the wing, embedded in an otherwise subsonic flow. After a preliminary review of the integral equation formulation for a thin unsymmetric

wing at small incidence, it presents a simple approximate analytical solution for shock-free symmetrical supercritical flow, which is then improved by an iterative scheme. The convergence of the scheme is studied by the Banach contraction mapping principle, which simultaneously delivers a proof of existence and uniqueness of solution. The corresponding results for the two-dimensional case have been discussed in Niyogi (1980).

2. Basic equations in differential form

We consider steady inviscid transonic flow past a thin unsymmetric wing at small incidence ϵ , with free-stream Mach number $M_\infty < 1$. We choose a body-fixed rectangular Cartesian coordinate system, where the y -axis is in the direction of thickness, z -axis along the span and x -axis is aligned with the free-stream direction, as shown in figure 1. The wing is assumed to be thin and smooth with continuously turning tangents which are inclined at small angles with the free-stream direction. Let the upper and lower body surfaces be given by

$$y = \begin{cases} h_u(x, z) = f(x, z) + g(x, z), \\ -h_l(x, z) = f(x, z) - g(x, z), \end{cases} \quad (1)$$

so that the functions f and g give camber and thickness distributions respectively. The boundary conditions are as follows:

- (i) The resultant flow direction at the wing surface is tangential to the surface. In other words, the normal component of the velocity relative to the wing surface vanishes at it.
- (ii) The perturbation potential ϕ and its derivatives vanish at an infinite distance upstream of the wing. The Kutta condition, that the pressure is finite and continuous at the trailing edge, is necessary to ensure unique solution. For three-dimensional flow, in addition to satisfying the Kutta condition, provision

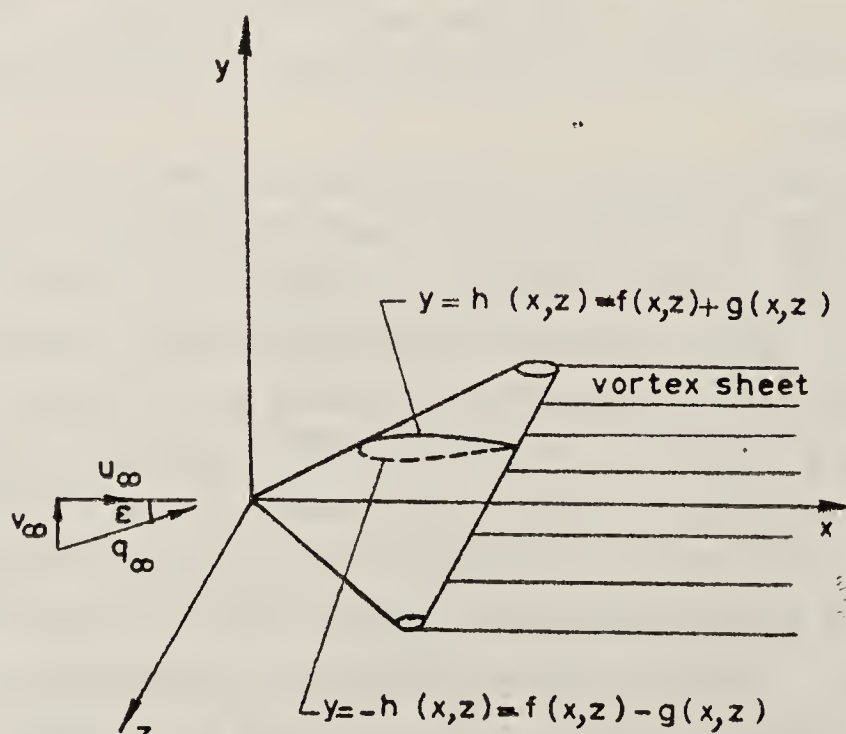


Figure 1. Thin unsymmetrical wing at small incidence.

must be made for a trailing vortex sheet downstream of the wing trailing edge. In accordance with the small-disturbance assumption, the vortex sheet is flat and lies in the plane $y=0$, with conditions that ϕ_x (pressure) and ϕ_y (flow angle) be continuous across it. The potential ϕ and its second derivative ϕ_{yy} , however, experience a jump across the sheet.

According to the transonic small-perturbation theory (Oswatitsch 1956; Cole 1969), the small-perturbation equations of continuity and irrotationality may be put in the following form, in reduced coordinates:

$$\Phi_{XX} + \Phi_{YY} + \Phi_{ZZ} = \Phi_X \Phi_{XX}, \quad (2)$$

where the reduced perturbation potential Φ is related to the true velocity potential φ by

$$\Phi(X, Y, Z) = \frac{\bar{K}}{(1 - M_\infty^2) u_\infty} [\varphi - u_\infty x - v_\infty y], \quad (3a)$$

and the reduced coordinates denoted by the corresponding capital letters by

$$X = x, \quad Y = y(1 - M_\infty^2)^{\frac{1}{2}}, \quad Z = z(1 - M_\infty^2)^{\frac{1}{2}}. \quad (3b)$$

From (3) we see that the reduced velocity components U, V, W are related to their true values denoted by the lower case letters by:

$$U = \Phi_X = \frac{\bar{K}}{1 - M_\infty^2} \cdot \frac{u - u_\infty}{u_\infty}, \quad V = \Phi_Y = \frac{\bar{K}}{(1 - M_\infty^2)^{3/2}} \cdot \frac{v - v_\infty}{u_\infty},$$

$$W = \Phi_Z = \frac{\bar{K}}{(1 - M_\infty^2)^{3/2}} \cdot \frac{W}{u_\infty}. \quad (3c)$$

The reduced quantities are not small in the transonic speed range and are of the order of unity. Further, it follows from the reduction equation (3c) that the flow at a point is subsonic for $U < 1$ and supersonic for $U > 1$, while the sonic surface is given by $U = 1$. The reduced pressure coefficient is given by (Oswatitsch 1956)

$$C_p(X, Y, Z) = -2U(X, Y, Z). \quad (4)$$

The quantity \bar{K} is a Mach number function, for which various alternative approximate forms exist. For example, Spreiter (1954) takes it as

$$\bar{K} = M_\infty^2(\gamma + 1), \quad (5a)$$

and Oswatitsch (1950) uses the value

$$\bar{K} = (1 - M_\infty^2) / \left(\frac{1}{M_\infty^*} - 1 \right), \quad (5b)$$

where M_∞^* denotes the critical free-stream Mach number, defined by $M_\infty^* = u_\infty/c^*$, c^* denoting the critical speed of sound.

Further, the tangency boundary condition may be shifted to the wing planform plane $y = 0$ and simplified as:

$$V(X, 0+, Z) = \frac{\bar{K}}{(1 - M_\infty^2)^{3/2}} \left[\frac{\partial h_u(X, Z)}{\partial X} - \frac{v_\infty}{u_\infty} \right], \quad (6a)$$

on the upper part $Y = 0+$,

$$V(X, 0-, Z) = - \frac{\bar{K}}{(1 - M_\infty^2)^{3/2}} \left[\frac{\partial h_l(X, Z)}{\partial X} + \frac{v_\infty}{u_\infty} \right],$$

on the lower part $Y = 0-$.

(6b)

3. Integral equation formulation

The small-perturbation differential formulation presented in the previous section, may be converted into an integro-differential equation for the velocity potential, by application of Green's theorem of potential theory, as shown by Klunker (1971), which on differentiation delivers the integral equations for the velocity components. Using the function Φ which is the reduced velocity potential, and the elementary solution Ψ of Laplace's equation

$$\Psi = 1/4\pi R, \quad (7a)$$

$$\text{where } R = [(X - \xi)^2 + (Y - \eta)^2 + (Z - \zeta)^2]^{1/2}, \quad (7b)$$

Green's theorem is applied to the region V outside the wing S_w , from which singularities of these functions have been excluded by suitable small indentations, as shown in figure 2.

The boundary surface S consists of (i) the surface at infinity chosen as a spherical surface of large radius, (ii) the spherical surface S_p of small radius R_0 around the pivotal point (X, Y, Z) which is a singularity of the function Ψ , (iii) any shock surfaces S_D on the upper and lower sides of the wing, which are surfaces

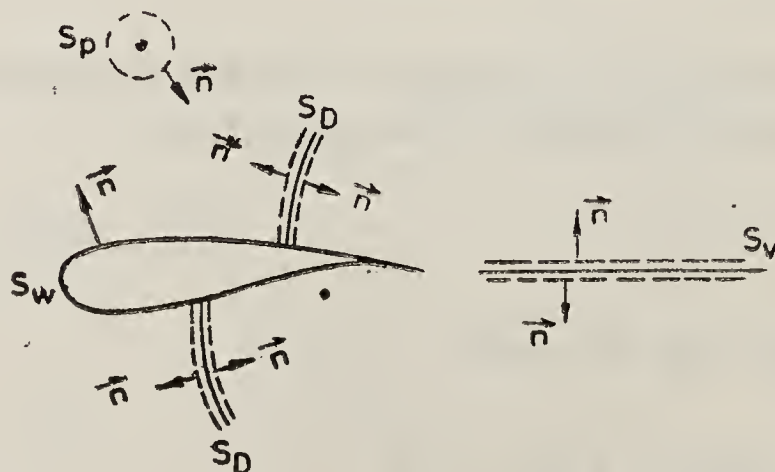


Figure 2. Region and surfaces of integration for applying Green's theorem.

of discontinuity for the normal derivative of Φ , (iv) the wing surface S_w and (v) the trailing vortex sheet S_V , leaving the trailing edge of the wing, assumed to lie in the XZ -plane in accordance with the small-perturbation theory.

As shown in detail by Klunker (1971), we obtain on simplification and reduction, the integro-differential equation:

$$\Phi(X, Y, Z) = \frac{Y}{4\pi} \int_{S_w} \frac{\Delta U}{Y^2 + (Z-\zeta)^2} \left[1 + \frac{X-\xi}{\{(X-\xi)^2 + Y^2 + (Z-\zeta)^2\}^{1/2}} \right] ds$$

$$- \int_{S_w} \Psi \Delta V ds + \int_V \frac{1}{2} U^2 \Psi_\xi dV, \quad (8)$$

where ΔU and ΔV denote respectively the values of U and V on the upper surface minus the value on the lower surface. It is to be noted that the contribution from the shock surfaces to the reduced potential Φ vanishes in this approximation.

The first term on the right of (8) corresponds to a vortex distribution and represents the lifting effect, the second term represents a source distribution, whereas the third term which originates from the nonlinearity of the gas dynamic equation (2), has the form of a doublet with its axis in the stream direction with a strength given by the local value of U^2 . This term influences the results for both lifting and non-lifting wings.

Although it is quite conceivable to solve (8) by straightforward numerical means on an electronic digital computer, no such attempts have been made so far. All the authors, on the other hand, find it convenient to work instead with the velocity components. The relevant integral equations may be derived from (8) through differentiation, taking appropriate care for the singularity in the integrand of the volume integral at the pivotal point (X, Y, Z) . A coupled pair of nonlinear singular integral equations results, whose form depends on the definition of the principal value of the singular integral.

Removing the singularity by means of two parallel planes perpendicular to the X -axis, at infinitesimal distance apart, it follows from (8) on differentiation with respect to X the integral equation derived by Heaslet & Spreiter (1957) that U obeys.

$$U(X, Y, Z) = U_H(X, Y, Z) + \frac{1}{2} U^2(X, Y, Z)$$

$$- \int_{-\infty}^{\infty} \int_{-\infty}^{\infty} \int_{-\infty}^{\infty} \frac{1}{2} U^2(\xi, \eta, \zeta) K_3(\xi-X, \eta-Y, \zeta-Z) d\xi d\eta d\zeta, \quad (9a)$$

where K_3 is the three-dimensional kernel having a dipole singularity at (X, Y, Z)

$$K_3(\xi-X, \eta-Y, \zeta-Z) = \frac{1}{4\pi} \frac{2(\xi-X)^2 - (\eta-Y)^2 - (\zeta-Z)^2}{[(\xi-X)^2 + (\eta-Y)^2 + (\zeta-Z)^2]^{5/2}}, \quad (9b)$$

and U_H is the harmonic function

$$U_H(X, Y, Z) = \frac{\partial}{\partial X} \left[\frac{Y}{4\pi} \int_{S_W} \frac{\Delta U}{Y^2 + (Z - \zeta)^2} \left\{ 1 + \frac{X - \xi}{[(X - \xi)^2 + Y^2 + (Z - \zeta)^2]^{1/2}} \right\} ds - \frac{1}{4\pi} \int_{S_W} \frac{\Delta V}{[(X - \xi)^2 + Y^2 + (Z - \zeta)^2]^{1/2}} ds \right]. \quad (9c)$$

The first integral on the right of (9c) contributes to the lifting effect, whereas the second contributes to the thickness effect. For the purely symmetrical problem of flow past a thin symmetrical wing at zero incidence, the first term vanishes identically, and ΔV is known by the tangency boundary condition, so that the harmonic function $U_H(X, Y, Z)$ may then be identified with the well-known Prandtl solution (Niyogi 1977), which we denote by $U_P(X, Y, Z)$. Thus, for a purely symmetrical problem, we obtain the following three-dimensional nonlinear singular integral equation, derived by Gullstrand (1951):

$$U(X, Y, Z) = U_P(X, Y, Z) + \frac{1}{2} U^2(X, Y, Z) - \int_{-\infty}^{\infty} \int_{-\infty}^{\infty} \int_{-\infty}^{\infty} \frac{1}{2} U^2(\xi, \eta, \zeta) K_3(\xi - X, \eta - Y, \zeta - Z) d\xi d\eta d\zeta, \quad (10)$$

|·|

where the kernel K_3 is given by (9b). The symbol $|\cdot|$ under the integral sign in (9a) and (10) is distinctive of the above principal value definition.

On the other hand, removing the singularity at (X, Y, Z) by means of a sphere of infinitesimal radius, it follows from (8) on differentiation with respect to X (Ogana 1979) for the lifting case

$$U(X, Y, Z) = U_H(X, Y, Z) + \frac{1}{6} U^2(X, Y, Z) - \int_{-\infty}^{\infty} \int_{-\infty}^{\infty} \int_{-\infty}^{\infty} \frac{1}{2} U^2(\xi, \eta, \zeta) K_3(\xi - X, \eta - Y, \zeta - Z) d\xi d\eta d\zeta, \quad (11)$$

⊙

and for the corresponding symmetrical problem

$$U(X, Y, Z) = U_P(X, Y, Z) + \frac{1}{6} U^2(X, Y, Z) - \int_{-\infty}^{\infty} \int_{-\infty}^{\infty} \int_{-\infty}^{\infty} \frac{1}{2} U^2(\xi, \eta, \zeta) K_3(\xi - X, \eta - Y, \zeta - Z) d\xi d\eta d\zeta, \quad (12)$$

⊙

where the symbol \odot under the integral sign refers to the above principal value definition.

We observe that (11) is an alternative form of the basic equation (9a) and similarly, for the particular case of a thin symmetric wing at zero incidence, (12) is an alternative form of (10). These equations were established first by Kluwick & Oswatitsch (1974). Nixon (1974) also derived (12) assuming shock-free flow. We would like to stress the fact that like the basic integro-differential equation (8), equations (9) to (12) are valid for shock-free flow as well as for flows with shocks, not necessarily straight and normal contrary to what has been stated by earlier authors like Ferrari & Tricomi (1968), for the corresponding two-dimensional case. If a shock is present, it is only required to have a small curvature. However, it is not difficult to see that across straight normal shocks, the volume integral in (10) is continuous, whereas across curved shocks, as shown in Kluwick & Oswatitsch (1974), it is no more continuous and delivers the requisite jump conditions for curved shocks. The validity of the system of equations (11) and (12), for curved shocks with small curvature, was shown first by Kluwick & Oswatitsch (1974), and independently for a system of equations equivalent to (9) by Chakraborty (1978).

In the present work we consider the mathematically simpler case of a thin symmetrical wing at zero incidence. Equation (10) or the alternative form (12) is the basic equation for our subsequent study.

4. An approximate analytical solution

The basic equation (10) or (12), describing steady inviscid irrotational transonic flow past a thin symmetric wing at zero incidence, is a three-dimensional nonlinear singular integral equation for the unknown reduced velocity component $U(X, Y, Z)$ parallel to the free-stream direction. Solving it, the pressure distribution may be determined from (4). No exact solution of these equations has been found so far. Approximate solutions have been computed by Nørstrud (1973) and Nixon (1974) by numerical means on an electronic digital computer. We present here a simple approximate analytical solution.

It is to be noted that due to the strong singularity of the kernel, the integrand of the volume integral in (12) decreases very rapidly away from the planform plane of the wing $Y=0$. Further, for subcritical flow and for low shock-free supercritical flow, the integral term is generally small compared to the known linearized solution U_P . Neglecting it, we get

$$U^2(X, Y, Z) - 6U(X, Y, Z) + 6U_P(X, Y, Z) = 0.$$

Solving it as a quadratic equation in U , and neglecting the purely supersonic solution, follows the transonic solution

$$U(X, 0, Z) = 3 [1 - \{1 - \frac{2}{3} U_P(X, Y, Z)\}^{1/2}]. \quad (13a)$$

which is a very simple expression. It expresses the unknown nonlinear solution $U(X, Y, Z)$ in terms of the known linearized solution $U_P(X, Y, Z)$. The reduced velocity distribution on the wing planform is of particular interest, which is obtained from (13a) by assuming $Y = 0$, as

$$U(X, 0, Z) = 3 [1 - \{1 - \frac{2}{3} U_P(X, 0, Z)\}^{1/2}]. \quad (13b)$$

Solution (13b) has been compared with the numerical solution of Nixon (1974) in figures 3 and 4, for a rectangular wing of aspect ratio 4 at $M_\infty = 0.75$ having a NACA 0012 section at two different spanwise stations. For these low supercritical cases, the agreements are quite satisfactory. For shock-free transonic flow, results of moderate accuracy may be obtained quickly by the simple solution (13b).

5. Iterative improvement

The encouraging results obtained from the simple approximate analytical solution (13b) suggests its iterative improvement. However, some caution is needed because most iteration schemes fail to converge in the transonic speed range (Oswatitsch 1956). We propose the following direct iteration scheme, which is an extension of the corresponding two-dimensional direct iteration scheme of Niyogi & Chakraborty (1979):

$$U_{n+1}(X, Y, Z) = U_P(X, Y, Z) + \frac{1}{6} U_n^2(X, Y, Z) - \int_{-\infty}^{\infty} \int_{-\infty}^{\infty} \int_{-\infty}^{\infty} \frac{1}{2} U_n^2(\xi, \eta, \zeta) K_3(\xi-X, \eta-Y, \zeta-Z) d\xi d\eta d\zeta, \quad n = 0, 1, 2, 3, \dots, \quad (14)$$

where the starting solution $U_0(X, Y, Z)$ may be conveniently taken as (13a).

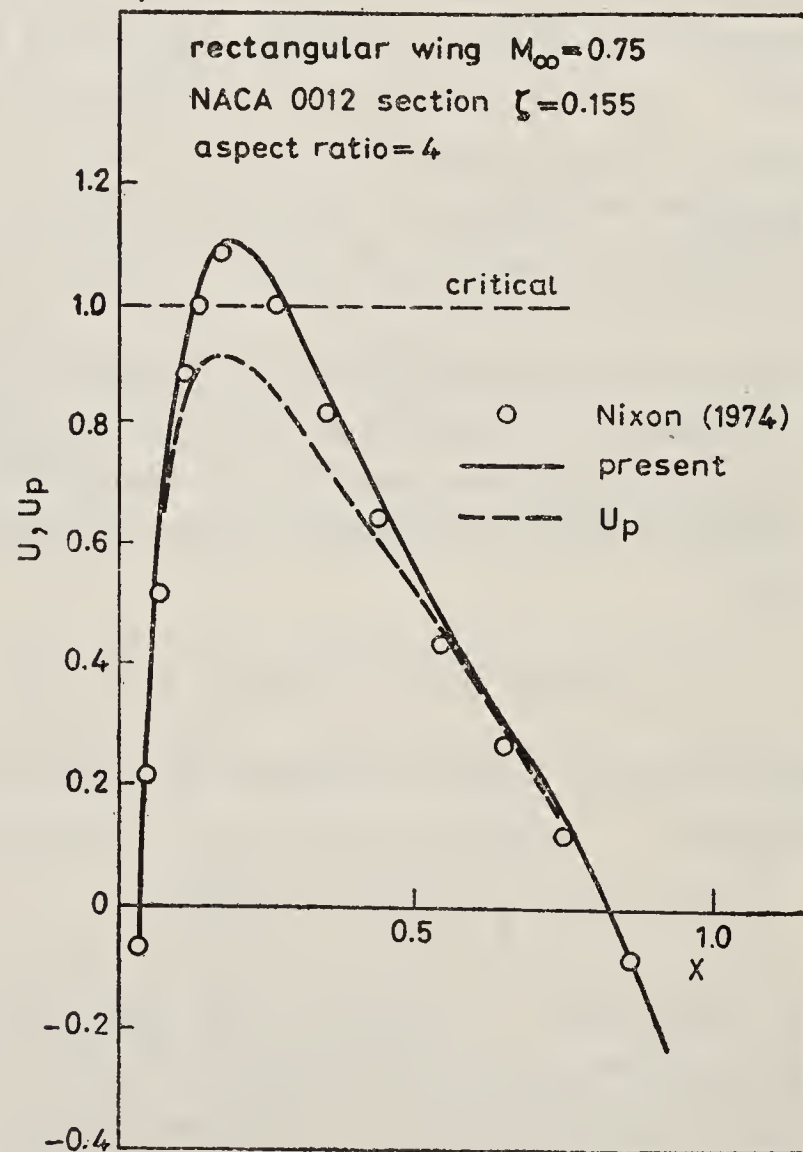


Figure 3. Pressure distribution on a rectangular wing of aspect ratio 4, with NACA 0012 section at zero incidence. $M_\infty = 0.75$, $\zeta = 0.155$. Comparison with the results of Nixon (1974).

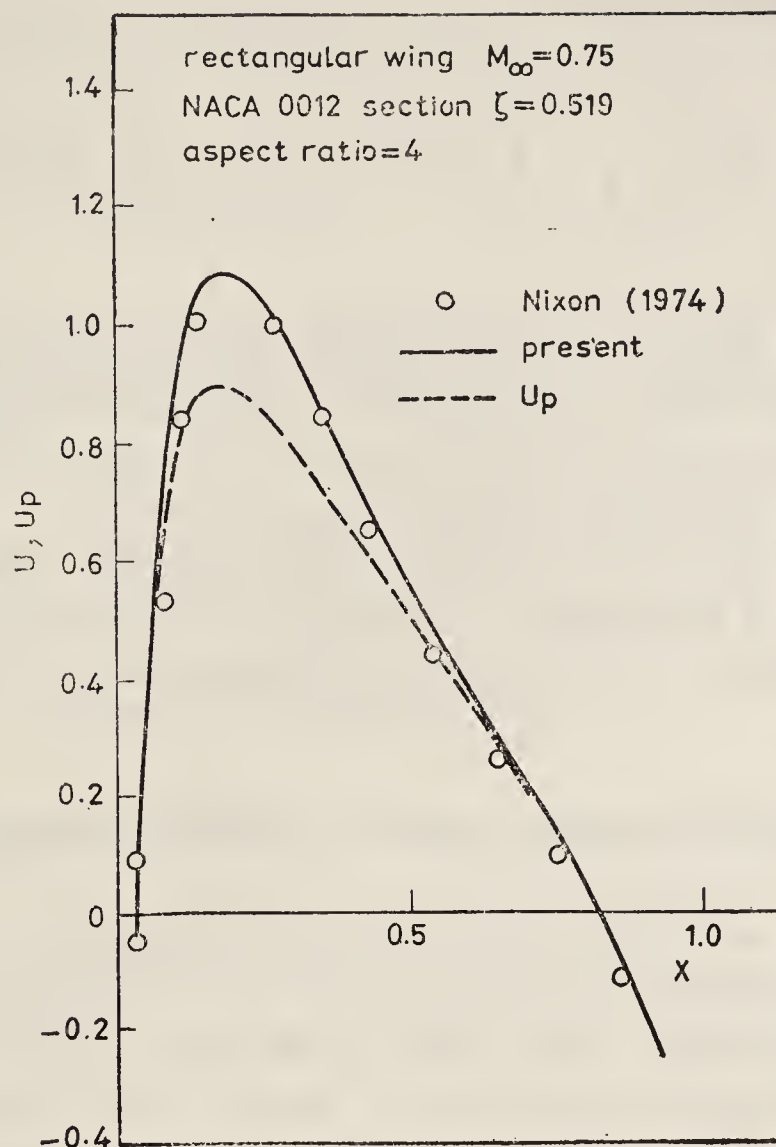


Figure 4. Pressure distribution on a rectangular wing of aspect ratio 4, with NACA 0012 section at zero incidence. $M_\infty = 0.75$, $\zeta = 0.519$. Comparison with the results of Nixon (1974).

The corresponding two-dimensional scheme is known to converge for supercritical shock-free transonic flow past a thin symmetric profile and it is expected that the corresponding three-dimensional scheme, (14), would also converge. In view of the strong singularity of the kernel and symmetry of the problem, the integrations in (14) need be carried out only in a finite domain D : $A \leq \xi \leq A'$, $-B \leq \eta \leq B$, $C \leq \zeta \leq C'$, where A , A' , B , C , C' are suitable finite constants such that contributions to the integral coming from a region outside D is negligibly small. Further, for numerical computations it appears convenient to rewrite the integral as:

$$\begin{aligned}
 & \int_{-\infty}^{\infty} \int_{-\infty}^{\infty} \int_{-\infty}^{\infty} U_n^2(\xi, \eta, \zeta) K_3(\xi-X, \eta-Y, \zeta-Z) d\xi d\eta d\zeta \\
 & = \int_{-\infty}^{\infty} \int_{-\infty}^{\infty} \int_{-\infty}^{\infty} [U_n^2(\xi, \eta, \zeta) - U_n^2(X, Y, Z)] K_3(\xi-X, \eta-Y, \zeta-Z) d\xi d\eta d\zeta \\
 & \approx \int_A^{A'} \int_{-B}^B \int_C^{C'} [U_n^2(\xi, \eta, \zeta) - U_n^2(X, Y, Z)] K_3(\xi-X, \eta-Y, \zeta-Z) d\xi d\eta d\zeta. \quad (15)
 \end{aligned}$$

It is to be noted that the free term

$$U_n^2(X, Y, Z) \int_{-\infty}^{\infty} \int_{-\infty}^{\infty} \int_{-\infty}^{\infty} K_3(\xi - X, \eta - Y, \zeta - Z) d\xi d\eta d\zeta,$$

vanishes identically. In this form, the singularity of the integrand has been weakened and the volume integral may be conveniently evaluated by numerical means.

Computations with the direct iteration scheme (14) where the volume integral has been approximated as in (15) are at present being carried out. Since the results are not yet ready, we cannot present any computational results. However, we give in the next section, a proof of convergence of the direct iteration scheme, which throws much light on the question of the existence and uniqueness of solutions.

6. Convergence of the direct iteration scheme: existence and uniqueness question

In the present section, we study analytically the convergence of the direct iteration scheme (14), with some suitable starting solution $U_0(X, Y, Z)$ by means of the Banach contraction mapping principle (Rall 1969), in the space $L_2(E_3)$.

For our purpose it appears convenient to rewrite (14) in spherical polar coordinates. With $\bar{X} = (X, Y, Z)$ as pole, let (r, θ, φ) denote the spherical polar coordinates of the point $\bar{Y} = (\xi, \eta, \zeta)$ of the Euclidian space E_3 . Then with $U = U(\bar{X})$, (12) may be stated in the form

$$U(\bar{X}) = U_P(\bar{X}) + \frac{1}{6} U^2(\bar{X}) - \frac{1}{4\pi} \int_{E_3} U^2(\bar{Y}) \frac{f(\theta)}{r^3} d\bar{Y}, \quad (16a)$$

$$\text{where } f(\theta) = \frac{1}{2} (3 \cos^2 \theta - 1). \quad (16b)$$

The iteration scheme (14), takes the form

$$U_{n+1}(\bar{X}) = U_P(\bar{X}) + \frac{1}{6} U_n^2(\bar{X}) - \frac{1}{4\pi} \int_{E_3} U_n^2(\bar{Y}) \frac{f(\theta)}{r^3} d\bar{Y},$$

$$n = 0, 1, 2, 3, \dots \quad (17)$$

Mikhlin (1965) considered operators in $L_2(E_3)$ of the form

$$P(Q) = a Q(\bar{X}) - \frac{1}{(2\pi)^{3/2}} \int_{E_3} \frac{\bar{f}(\theta)}{r^3} Q(\bar{Y}) d\bar{Y}, \quad (18)$$

where a is a constant and the characteristic $\bar{f}(\theta)$ satisfies the condition

$$\int_S \bar{f}(\theta) ds = 0, \quad (19)$$

where S is the unit sphere over which θ moves. Condition (19) holds in the present case for $f(\theta)$ defined by (16b). Mikhlin established that the operator $P(Q)$ is bounded in $L_2(E_3)$ and that its norm

$$\| P \| = \text{ess max } | \Phi_P(\theta) |, \quad (20)$$

where $\Phi_P(\theta)$ is the symbol of the singular operator P . The symbol is defined in terms of the Fourier transform (Calderon & Zygmund 1952) in E_3 of the kernel K of the integral operator:

$$FK \equiv \lim_{\substack{\epsilon \rightarrow 0 \\ N \rightarrow \infty}} \frac{1}{(2\pi)^{3/2}} \int_{\epsilon < |\bar{X}| < N} \exp[-i(\bar{X} \cdot \bar{Z})] K(\bar{X}) d\bar{X}, \quad (21)$$

and the symbol Φ_P is defined by (Mikhlin 1965)

$$\Phi_P = a - F[\tilde{f}(\theta)/r^3]. \quad (22)$$

Equation (16a) may be rewritten as an operator equation

$$U = A(U) \quad (23a)$$

where the operator

$$A(U) = U_P(\bar{X}) + (\pi/2)^{1/2} \left[\frac{U^2(\bar{X})}{3\sqrt{2\pi}} - \frac{1}{(2\pi)^{3/2}} \int_{E_3} \frac{f(\theta)}{r^3} U^2(\bar{Y}) d\bar{Y} \right]. \quad (23b)$$

The symbol of the singular operator P in (18) has been calculated by Niyogi (1976) for the characteristic function defined by (16b), as

$$\Phi_P = a - \frac{1}{\sqrt{2\pi}} \sin^2 \theta_1. \quad (24)$$

Consequently, in view of (20), the L_2 -norm of the operator in (23b) is

$$\| A \| = (\pi/2)^{1/2} \cdot \frac{1}{3\sqrt{2\pi}} = \frac{1}{6}. \quad (25)$$

We consider now two points U' and U'' in the closed ball $\bar{W}(U_0, R)$ in $L_2(E_3)$. Then noting that

$$\| U' + U'' \| \leq 2(\bar{U}_0 + R), \quad (26)$$

where \bar{U}_0 is the L_2 -norm of U_0 , we have

$$\| A(U') - A(U'') \| = (\pi/2)^{1/2} \left\| \frac{U'^2 - U''^2}{3\sqrt{2\pi}} - \frac{1}{(2\pi)^{3/2}} \int_{E_3} \frac{f(\theta)}{r^3} (U'^2 - U''^2) d\bar{Y} \right\| \leq \frac{1}{6} \cdot 2(\bar{U}_0 + R) \| U' - U'' \|. \quad (27)$$

Consequently, the operator A in $L_2(E_3)$ defined by (23b) is a contraction mapping of the closed ball $\bar{W}(U_0, R)$, provided the contraction factor $\bar{\theta}$ satisfies the condition

$$\bar{\theta} = \frac{1}{3} (\bar{U}_0 + R) < 1. \quad (28)$$

Further, choosing the starting solution as $U_0 = U_P$, we have from (17)

$$U_1 = U_P + \frac{1}{6} U_P^2 - \frac{1}{4\pi} \int_{E_3} U_P^2 \frac{f(\theta)}{r^3} d\bar{Y}.$$

Therefore,

$$\|U_1 - U_0\| = \left\| \frac{U_P^2}{6} - \frac{1}{4\pi} \int_{E_3} U_P^2 \frac{f(\theta)}{r^3} d\bar{Y} \right\| \leq \frac{1}{6} (\bar{U}_P)^2. \quad (29)$$

Thus, provided the condition (28) is satisfied, we have (Rall 1969)

$$R \geq \frac{1}{1 - \bar{\theta}} \|U_1 - U_0\|,$$

from which follows by conditions (28) and (29)

$$R \geq \frac{1}{1 - \frac{1}{3} (\bar{U}_P + R)} \cdot \frac{(\bar{U}_P)^2}{6}. \quad (30)$$

On simplification this yields

$$R^2 - (3 - \bar{U}_P) R + \frac{1}{2} (\bar{U}_P)^2 \leq 0. \quad (31)$$

Inequality (31) has the formal solution

$$\begin{aligned} \frac{1}{2} \{3 - \bar{U}_P - [(3 - \bar{U}_P)^2 - 2 (\bar{U}_P)^2]^{1/2}\} &\leq R \leq \\ \frac{1}{2} \{3 - \bar{U}_P + [(3 - \bar{U}_P)^2 - 2 (\bar{U}_P)^2]^{1/2}\}. & \end{aligned} \quad (32)$$

The maximum value of \bar{U} for which inequality (32) will be true is determined from

$$(3 - \bar{U}_P)^2 - 2 (\bar{U}_P)^2 = 0,$$

to be
$$\bar{U}_P = 3(\sqrt{2} - 1). \quad (33)$$

For this value of \bar{U}_P , inequality (32) delivers

$$R = 3 \left(1 - \frac{\sqrt{2}}{2} \right). \quad (34)$$

The corresponding value of the contraction factor $\bar{\theta}$ is

$$\bar{\theta} = \frac{1}{3} \left[3 (\sqrt{2} - 1) + 3 \left(1 - \frac{\sqrt{2}}{2} \right) \right] = \frac{\sqrt{2}}{2} < 1, \quad (35)$$

so that condition (28) is satisfied.

Thus, according to the Banach contraction mapping principle (Rall 1969), the direct iteration scheme (14) converges to the exact solution of (12) in the closed ball $\bar{W}(U_P, R)$ and the solution is unique there, provided the L_2 -norm of the known linearized solution \bar{U}_P satisfies the condition (33). Noting that \bar{U}_P may be expressed in terms of the transonic similarity parameter, (33) and (34) determine the maximum permissible value of the transonic similarity parameter for which a unique solution exists. The proof being a constructive one, allows us to construct solution of our problem. Simultaneously, it delivers a condition for the rate of convergence of the iterative scheme, and an error estimate.

7. Error estimate

An error estimate of the direct iteration scheme follows directly from the contraction mapping principle (Rall 1969) as

$$\| U_n - U \| \leq \frac{\bar{\theta}^n}{1 - \bar{\theta}} \| U_1 - U_0 \|, \quad (36)$$

where U denotes the exact solution. Using (28) and (29) we obtain from (36)

$$\| U_n - U \| \leq \frac{[\frac{1}{3} (\bar{U}_P + R)]^n}{1 - \frac{1}{3} (\bar{U}_P + R)} \cdot \frac{1}{6} (\bar{U}_P)^2, \quad (37)$$

which gives an estimate of the error in the n th step of iteration. Corresponding to the maximum permissible value of the norm \bar{U}_P , the error estimate is found from (36), (35) and (29) on simplification to be

$$\| U_n - U \| \leq 2^{-(n+1)/2}. \quad (38)$$

However, for lower values of the norm \bar{U}_P , the rate of convergence would be faster.

This paper is based on a talk delivered at the First Asian Congress of Fluid Mechanics held at Bangalore in December 1980.

List of symbols

c^*	critical speed of sound
E_3	three-dimensional Euclidean space
$f(x, y), g(x, y)$	camber and thickness distributions of the wing
h_u, h_l	upper and lower parts of wing geometry
\bar{K}	reduction factor, equations (5)
K_3	kernel with dipole singularity, equation (9b)
M_∞	free-stream Mach number
U, V, W	reduced velocity components
U_H	harmonic function
U_P	reduced linearized velocity component (Prandtl)
\bar{U}_P	L_2 -norm of U_P
$\bar{W}(U_0, R)$	closed ball in $L_2(E_3)$ with centre U_0 and radius R
X, Y, Z	reduced rectangular cartesian coordinates
$\Delta U, \Delta V$	difference of reduced velocity components on the upper part and lower part of the wing
Φ_P	symbol of the singular operator P , equations (21) and (22), used in § 6.
$\bar{\theta}$	contraction factor
Φ	reduced perturbation potential

References

- Bailey F R 1975 in *Progress in numerical fluid dynamics* (ed. H J Wirz) *Lecture Notes in Physics* (Berlin, New York, Heidelberg: Springer-Verlag) Vol. 41 p. 1
- Calderon A P & Zygmund A 1952 *Acta Math.* **88** 85
- Chakraborty S K 1978 *AIAA J.* **16** 1015
- Cole J D 1969 Twenty years of transonic flow, Boeing Scientific Research Laboratories U S A D1-82-0878
- Ferrari C & Tricomi F 1968 *Transonic aerodynamics* (New York: Academic Press) Ch. 5
- Gullstrand T R 1951 The flow over symmetrical aerofoils without incidence in the lower transonic range, KTH AERO TN 20
- Heaslet M A & Spreiter J R 1957 Three-dimensional transonic flow applied to slender wings and bodies, NACA Report 1318
- Klunker E B 1971 Contributions to the methods for calculating the flow about thin lifting wings at transonic speeds-analytical expressions for the far field, NASA TND-6530 U.S.A.
- Kluwick A & Oswatitsch K 1974 Unstetigkeitseigenschaften der Integralgleichung für stationäre räumliche Schallnahe strömungen. Ommagio a Carlo Ferrari. Libreria Editrice Universitaria Levrotto and Bella, 415 Torino.

- Mikhlin S G 1965 *Multidimensional singular integrals and integral equations* (London: Pergamon Press)
- Murman E M & Cole J D 1971 *AIAA J.* **9** 114
- Nixon D 1974 High subsonic flow past a steady finite wing, QMC EP 1015, London, Queen Mary College
- Niyogi A K 1976 *Z. Angew. Math. Mech.* **56** 173
- Niyogi P 1977 *Inviscid gas dynamics* (New Delhi: The Macmillan Company)
- Niyogi P 1980 *Proc. Indian Acad. Sci. (Engg. Sci.)* **3** 143
- Niyogi P & Chakraborty S K 1979 *Acta Mech.* **31** 173
- Nørstrud H 1973 High speed flow past wings, NASA CR 2246
- Ogana W 1979 *AIAA J.* **17** 305
- Oswatitsch K 1950 *Acta Phys. Austriaca* **4** 228
- Oswatitsch K 1956 *Gas dynamics* (New York: Academic Press) Ch. 9
- Oswatitsch K 1980 in *Contributions to the development of gas dynamics* (eds W Schneider & M Platzer) (Wiesbaden: Fieder Vieweg) p. 150
- Rall L D 1969 *Computational solution of nonlinear operator equations* (New York: John Wiley) Ch. 2
- Spreiter J R 1954 *J. Aeronaut. Sci.* **21** 71, 360

Thermal and fluid mechanical problems in space flight

KOICHI OSHIMA

Institute of Space and Aeronautical Science, University of Tokyo, Meguro, Tokyo, Japan

MS received 13 December 1980

Abstract. In this paper the basic research activities being carried out in the Institute of Space and Aeronautical Sciences, University of Tokyo and other establishments have been discussed. Four problems of space flight, namely, thermal design of spacecraft, thermal protection during planetary entry, surface contamination of spacecraft and microgravity effects in space have been specifically highlighted.

Keywords. Thermophysics; fluid mechanics; space flight.

1. Introduction

After the successful orbiting of Sputnik I around the earth in 1957, considerable efforts have gone into space exploration and its uses. This was also highlighted by the human footprint on the Moon in 1969 under the Apollo programme. Apart from the super powers some Asian countries have also been carrying out their own space exploration and development projects for the last 20 years.

The space exploration programme in Japan commenced around 1964 when the Institute of Space and Aeronautical Science, University of Tokyo, was organised to succeed the former Aeronautical Research Institute, University of Tokyo, and combining with a group of the Institute of Industrial Science, University of Tokyo, who had been previously carrying out a sounding rocket programme. Besides the development of the solid propellant rocket for satellite launching, design study of satellites and construction of space simulation facilities for satellite check-out test were started around that time as integral parts of this programme. In 1970, the first Japanese satellite *Ohsumi* (figure 1, plate 1) was launched by this Institute using the solid propellant rocket L4S developed at the Institute. Since then, the Institute has successfully launched various experimental and scientific satellites for space observation. Figure 2 (plate 2) shows one of them, ionospheric observation satellite *Shinsei*.

The National Space Development Agency of Japan (NASDA) was established around 1969, succeeding the former governmental space research and developmental agencies, so as to develop, launch and operate commercial satellites for Japan. Figure 3 (plate 3) illustrates one of the satellite testing facilities. NASDA launched its first test satellite in 1975, and has now been operating communication, weather and broadcasting satellites, which have hitherto been launched by Japanese liquid propellant rockets or by US launch vehicles. The activities of both ISAS and NASDA are controlled by the National Space Development Committee which is one of the

advisory committees to the Japanese Government. It now has quite ambitious plans to promote space exploration including planet exploration, advanced observation satellites and the use of the shuttle payload.

China launched its first satellite in April 1970 two months after the first Japanese satellite, and the second one in 1971. These were quite heavy, weighing about 200 kg. Around 1975, China launched many satellites each of several tons weight, and successfully recovered some of them. They now have plans to establish satellite communication with both foreign countries as well as within their own territory and using their own satellites under the international cooperation programme.

India established the Indian Space Research Organisation (ISRO) in 1969 for developing mass communications and educational systems in her widely dispersed rural communities as well as for timely survey and management of the country's natural resources. The first Indian-made satellite *Aryabhata* was launched in 1975 using a USSR launch vehicle. Following its success, a second one, *viz.*, Satellite for Earth Observations (SEO), went into orbit in 1979. After two more satellite communication experiments using foreign satellites, the Satellite Instructional Television Experiment (SITE) programme (1974–75) by ATS-6 and the Satellite Telecommunications Experiments Project (STEP) (1977–79) using the *Symphonie* satellite, India established its own satellite communication system, *viz.*, the Indian National Satellite (INSAT) programme using a US launch vehicle. India has also more ambitious plans to develop solid propellant rockets for satellite launching, and successfully fired the SLV-3 rocket and launched a small satellite into orbit in 1980. India has thus become the second Asian country having solid-propellant satellite-launching rocket facilities.

Independently, but closely related to these developmental efforts, basic research activities in all aspects of space science and technology have been taking place in various research institutes and universities all over the world. Various thermal and fluid mechanical problems have attracted the attention of basic research scientists; these problems have provided a strong impetus for our understanding of basic science. Some of these will be discussed in the present paper with emphasis on the basic research activities taking place in our Institute. Only those problems relating to launch vehicles and spacecraft will be considered while astrophysical and geophysical aspects will not be discussed.

2. Thermal design of spacecraft

The environmental control of spacecraft during sustained space flight or during the launch operation has been the most urgent task confronting the scientists from the beginning of the space exploration programme since there was no such previous experience at all in this area. The complete vacuum, the absolute radiation sink of the outer space and the solar irradiation are aspects of the environment that the satellite must endure.

2.1 *Thermal nodal analysis*

In order to analyse the temperature distribution and variation of each of the components of the satellite during space flight, a mathematical model has to be constructed

which simulates the temperature characteristics of the spacecraft and which is usually expressed as a network system of the various thermal nodal points assigned to the various places in the satellite (Oshima 1971; Mathanson *et al* 1969). In figure 4, an example of the nodal assignment of a small satellite is shown, in which the alphabetical symbols designate the sub-assemblies and the numeric symbols represent the nodal numbers. Thus, a thermal network with 19 nodal points is represented and the thermal balance equations applied to each nodal point provide the 19 simultaneous equations for the 19 unknown temperatures

$$C_i \frac{dT_i}{dt} = \sum_{j=1}^{19} \text{CND}_{ij} (T_i - T_j) + \sum_{j=1}^{19} \text{RAD}_{ij} (\sigma T_i^4 - \sigma T_j^4) + Q_i$$

$(i = 1 \text{ to } 19),$

where T_i , C_i and Q_i are the temperature, the heat capacity and the heat input respectively to the node i ; CND_{ij} is the thermal conductance between the nodes i and j , RAD_{ij} is the radiation exchange factor between the nodes i and j , and σ is the Stefan-Boltzmann constant. Computer programs to solve these non-linear simultaneous equations have been developed and used for every satellite design (Wood 1977). However, the nodal assignment method is more or less heuristic in

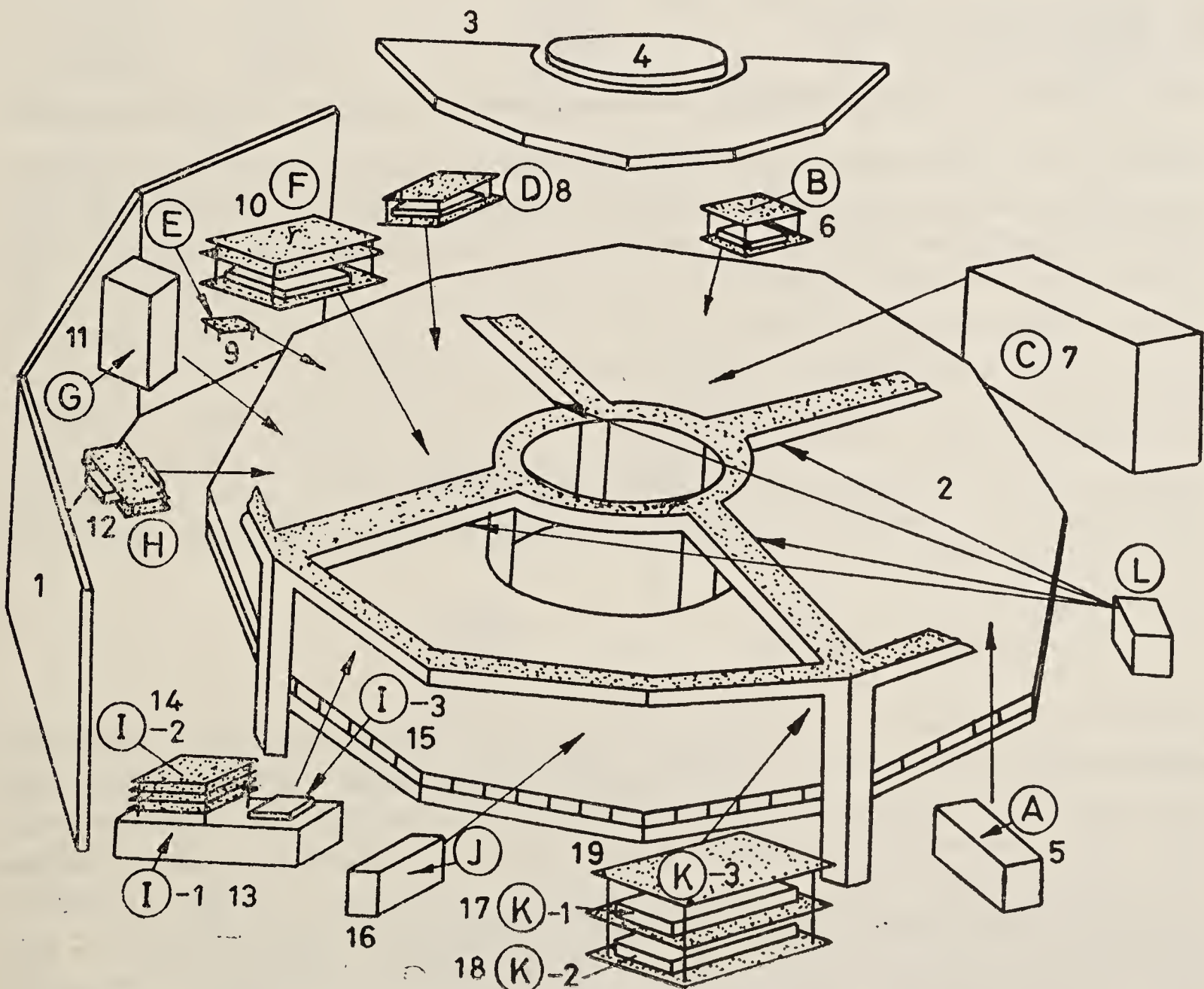


Figure 4. The thermal model analysed in Oshima (1971b). The functions of the assigned nodal points, the emissivities, the absorptivities and their areas are listed in the table below.

Name	Heat Capacity J/K	α	ϵ	Area cm ²
1 Outer side wall	1396.24	0.81	0.84	3570.00
1 Inner side wall, top	287.22	0.95	0.86	2120.04
1 Inner side wall, bottom	188.31	0.95	0.86	1389.96
2 Flat deck	835.94	0.95	0.86	1466.55
3 Outer side of top cover, outer part	226.04	0.31	0.12	1215.90
3 Inner side of top cover, outer part	648.83	0.95	0.86	1215.90
4 Outer side of top cover, inner part	378.83	0.31	0.12	290.90
4 Inner side of top cover, inner part	470.93	0.95	0.86	290.00
5 Telemeter transmitter	107.58		0.86	170.36
6 Subcarrier modulator	118.88		0.89	168.00
7 Battery	673.95		0.86	525.60
8 Commutator A and B	79.53		0.89	90.48
9 Commutator C	4.19		0.89	17.48
10 Logic controller	232.74		0.89	245.10
11 Sun sensor	91.67		0.86	97.20
12 House keeping unit	51.91		0.89	32.00
13 Command receiver	246.90		0.86	383.40
14 Command tone decoder	175.81		0.89	254.00
15 Command filter	119.30		0.89	182.50
16 Preselector	63.63		0.86	95.00
17 Regulator converter, middle	233.16		0.89	150.00
18 Regulator converter, bottom	233.58		0.89	150.00
19 Regulator convertor	232.32		0.89	150.00

practice. In order to give a more rigorous mathematical foundation to this phenomenological analysis, a systematic method of thermal design for spacecraft has been developed using the finite-element method. In this analysis, the conductive and radiative heat transfer equations for the spacecraft are discretized following the common finite element formulation, the lump approximation for the temperatures and the step approximation for the heat inputs are applied, and then the usual thermal network equations are derived based on a mathematically rigorous foundation (Oshima 1973). By this formulation the thermal network system is directly coupled with the structural nodal system, which is particularly useful for analysing the thermal deformation of large thin structures such as the dish antenna of broadcasting satellites.

2.2 Thermal vacuum testing

In order to measure the temperature characteristics of the spacecraft or its physical model, special kinds of testing facilities and thermal vacuum chambers have been constructed, in which are provided a sufficiently high vacuum to ensure minimization of the convection heat transfer, a cold, black surrounding wall which simulates the radiation sink of the space, and a simulated solar beam. In order to decrease convection heat transfer to a magnitude negligibly smaller than radiation or conduction heat transfer, a vacuum of 10^{-5} torr is sufficient, but since the outgassing rate of the test satellite is usually quite high, extraordinarily high pumping speed is required. Therefore cold surfaces for cryopumping are commonly provided within the chamber (Dawson 1966). The radiation sink of outer space is simulated by

a liquid nitrogen cooled shroud surrounding the space. The shroud surface has louvers or grooves which increase the absorption coefficients to the incident thermal radiation to about 0.98 or more, *i.e.* the testing space is surrounded by radiation sink at a temperature slightly higher than 77°K, which only slightly affect the model temperature, whose average values are about 300°K. The solar irradiation near the earth orbit has an intensity of about 1.4 kW/m², a subtense angle of 32 min and a spectrum close to the Johnson curve. The solar simulators now available have generally sufficient irradiation intensity, the subtense angle of 1.5 to 5°, a uniformity of 10% over the target area, and the spectrum distribution of xenon which is quite close to the Johnson curve with one peak in infrared which is correctable by a suitable interference filter. The solar simulators commonly use water-cooled high intensity xenon short arc lamps and off-axis collimated optics. The biggest chamber in our country is the NASDA large space chamber which is 25 m in height and 7.5 m in diameter, and has a solar simulator consisting of 19 × 30 kW xenon lamps and integrator and collimation mirrors of 5.5 m diameter (Ide *et al* 1977; Tsujimoto *et al* 1971).

2.3 Radiation interchange

The complete vacuum in space enhances the radiation heat transfer within the satellite; this requires a precise examination of the radiation heat transfer calculation between the satellite components and subsystems is needed. To determine the so-called script \mathcal{F} factor of the radiation interchange between the elements in complex surface system such as the thermal louvers, the Monte Carlo simulation of radiation heat transfer is one of the most useful methods. An example is the thermal louver element shown in figure 5, in which the solar irradiation incident

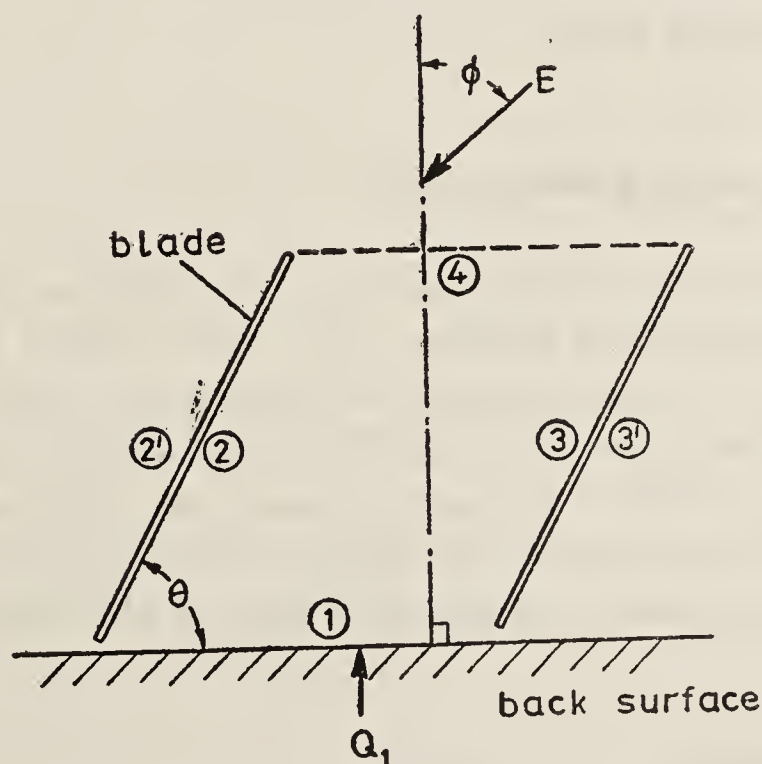


Figure 5. Radiation heat transfer within the louver system analysed by Monte Carlo method. In the figure, E is the solar radiation incident on the surface with an inclination angle of ϕ , Q_i is the heat input to the surface from the satellite, and θ is the opening angle of the louver which is automatically adjusted by sensing the surface temperature. The thermal nodal points were assigned to the satellite surface 1, the upper and the lower surfaces of the louver blades, 2, 3' and 2', 3 respectively, and the hypothetical surface 4 which closes the louver radiation cavity. The temperature characteristics of the louver system were obtained for the various solar incident angles, and the optimum surface coatings were determined.

with a skewed angle and the infrared radiation from the back surface and between the louver blades are traced using the Monte Carlo method, simulating the radiation transfer for each louver angle and each solar incident angle (Minning 1979). Diffuse as well as specular reflection are accounted for, and the complete thermal characteristics are obtained; this may not be easy with common analytical or experimental methods. Since radiation heat transfer is the only mode of dissipating satellite heat energy, radiation cooling devices of the onboard sensors and of the satellite thermal control systems have been analysed using these methods (Sekihara *et al* 1971; Furukawa 1979) and some of these have been applied in our satellites.

2.4 Prediction and optimization

In order to improve the predictability of this thermal-network mathematical model, network parameters such as the conductance between the nodes and the heat input to the nodes have to be corrected using physical simulation data or flight data. This is achieved by solving the least-square equations for the unknown parameters such as the conductances between the nodes using the measured temperature data. Usually, the number of unknown parameters is quite large, and the number of measured temperatures even larger; but the normal equations obtained are not necessarily full rank. Therefore, the statistical regression method has to be applied. This is a technique for extracting the best mathematical model of the thermal characteristics of the satellite from observational data using statistical regression. Using this improved mathematical model, the optimal design of the satellite can be chosen and the best operational procedure in flight can be determined by mathematical simulation. This technique originated independently at our Institute, at ESTEC and at NASA during the later part of the sixties, and has now become the standard procedure for satellite design and operation (Doenecke 1970; Ishimoto & Bevans 1971; Furukawa & Oshima 1973).

3. Thermal protection during planetary entry

When the mission calls for probe recovery or planetary soft landing, thermal protection against aerodynamic heating is the most critical aspect of the system. Because of the excessive speed of the probes during entry into the atmosphere, the gas in front of the probes is aerodynamically heated and dissociation and ionization take place. During entry into the outer planet, the radiation heat transfer from heated gas becomes comparable or dominant as against convective heat transfer. The heat protection commonly used in such cases is ablation cooling or transpiration.

3.1 Shock layer radiation

Since the radiation field may not influence the flow field, the latter is calculated by using the common gasdynamic theory but the physical properties of the gas at the raised temperature are accounted for. Such physical properties as the density, specific heats, internal energy, dissociation and ionization rates etc. of the various gases are now well documented in the literature (Biolsi 1980).

On the other hand, radiation heat transfer through an absorbing and scattering medium is one of the difficult problems in physics, and it is formulated as an integro-differential equation with nonlinear boundary conditions. Here again, Monte Carlo simulation is one of the most powerful and effective methods of solving this problem, and the program code was written and has been used for various problems in this category (Murakami 1971). The finite element formulation of this problem was also written and integrated into the thermal network mathematical model, both of the radiation shock layer and the ablating body (Spiga *et al* 1980). Based on the kernel expansion method, an approximate analytical solution of this problem was also found (Murakami & Oshima 1973).

3.2 Ablating body

In order to determine the temperature distribution and variation in the body, the unsteady heat conduction equation has to be treated under the varying boundary, *i.e.* the ablating front. In addition, the flow of the transpiring coolant or the melted gel layer along the surface has to be accounted for. Various numerical calculation schemes have been presented and now most of the characteristics of the field are fully understood at least for the one-dimensional case (Karashima *et al* 1978; Arai & Karashima 1979).

For the three-dimensional flow field, capability of the numerical code is rather limited, and the finite element formulation seems to be more effective owing to its flexibility.

4. Surface contamination of spacecraft

The spacecraft surface tends to get contaminated due to the deposition of contaminants emitted from rocket plumes and volatile surfaces. This problem is classified into (i) emission of outgas molecules from the satellite surfaces, (ii) the expansion of the rocket plume or the vented fluid into vacuum, (iii) the migration of the emitted or ejected molecules and their interaction with ambient molecules, and (iv) the deposition of contaminants or the impact of the particles on the surfaces, and their eventual control.

4.1 Outgassing from the satellite surface

Various organic compounds used in spacecraft such as electric insulators and surface coatings are volatile and emit the volatile mass to the outer space in vacuum. This kind of surface emission decreases with the duration of exposure to vacuum, and the decay law depends on the physical process taking place at the surface—decay is exponential for the strong evaporation from the absorbed and desorbed materials, and linear for diffusion-dominated evaporation across the surface potential barrier. Such analyses are necessarily phenomenological and rely heavily on experimental observations (Heslin 1977).

Considerable work on this problem has been carried out at the NASA Goddard Space Flight Centre and a standard testing procedure known as ASTM E 595-777 has been developed in which the sample material is placed in a preweighed aluminium

foil boat and is weighed. The samples are then loaded into individual compartments in a solid copper bar that can be heated. Each compartment is closed by a solid copper cover, to ensure that all the volatile material escapes through a 6.2 mm diameter exit port only. The copper heater bar and the samples are heated in a vacuum chamber, to 398°K for 24 hr. This heating causes the volatile materials to be driven out through the exit port. At a distance of 12.7 mm a chromium-plated collector is in the direct line of sight of the exit port and is maintained at 298°K. The escaping volatile compounds are collected if their condensation temperature is 298°K or above. The mass loss of the sample is determined from the weights before and after the 398°K exposure and the percentage loss is calculated to provide the total mass loss (TML) value. Similarly the difference between the weight of a clean collector and the collector having condensed materials will provide the mass of condensibles. This mass is calculated as a percentage of the starting mass of the sample and is stated as the collected volatile condensible materials (CVCM). Materials having a TML value of less than 1% and a CVCM value of less than 0.10% are considered to be spaceworthy (Campbell *et al* 1973, 1975, 1978, 1980). Such testing facilities have been widely constructed in our country and considerable data for the various spacecraft materials has been accumulating.

4.2 *Plume expansion*

The rocket plume fired in the vacuum of space expands as a free jet, and its flow field around the rocket nozzle is calculated by continuum gasdynamics, including chemical and molecular kinetic effects (Chatwani & Fiebig 1980). Various computer codes are now available for calculating the flow interaction with the high speed flow outside the rocket body (Guernsey & Hrubes 1980). After it expands sufficiently, rarefied gas dynamic calculations must be used. Several simplified numerical schemes are in use and the Monte Carlo simulation of such a flow field has been carried out for various cases, including the surrounding surface interaction effects. The contamination and the heating of satellite surfaces and the interaction of the electromagnetic wave due to the plumes are important problems for rocket operation (Dreaper & Sperlein 1980).

In order to simulate such a flow field in the space chamber the so-called mol-sink facilities are used, one of which is shown in figure 6. This has the test space completely surrounded by a cryo-cooled shroud having deep-groove plates on it, as seen in figure 7. Thus all the molecules hitting the shroud surface are absorbed on it, and it is thereby ensured that there are no return molecules. The mass flow rate of fired rockets is quite high and large facilities are required for testing them (Stephens 1966; Nelson & Chuan 1969; Oshima & Kobayashi 1969).

4.3 *Interaction of ejected molecules*

Orbiting satellites are intercepted by the cosmic molecules and particles as well as those emitted from the satellite itself. For a satellite at low altitude, the interaction with the ambient atmosphere becomes significant, and for one at higher altitudes, the solar wind interaction can be a problem. These phenomena have been widely analysed using rarefied gasdynamics and molecular kinetics (Scialdone 1972; Borucki *et al* 1972). Much data has been compiled by Scialdone and his colleagues

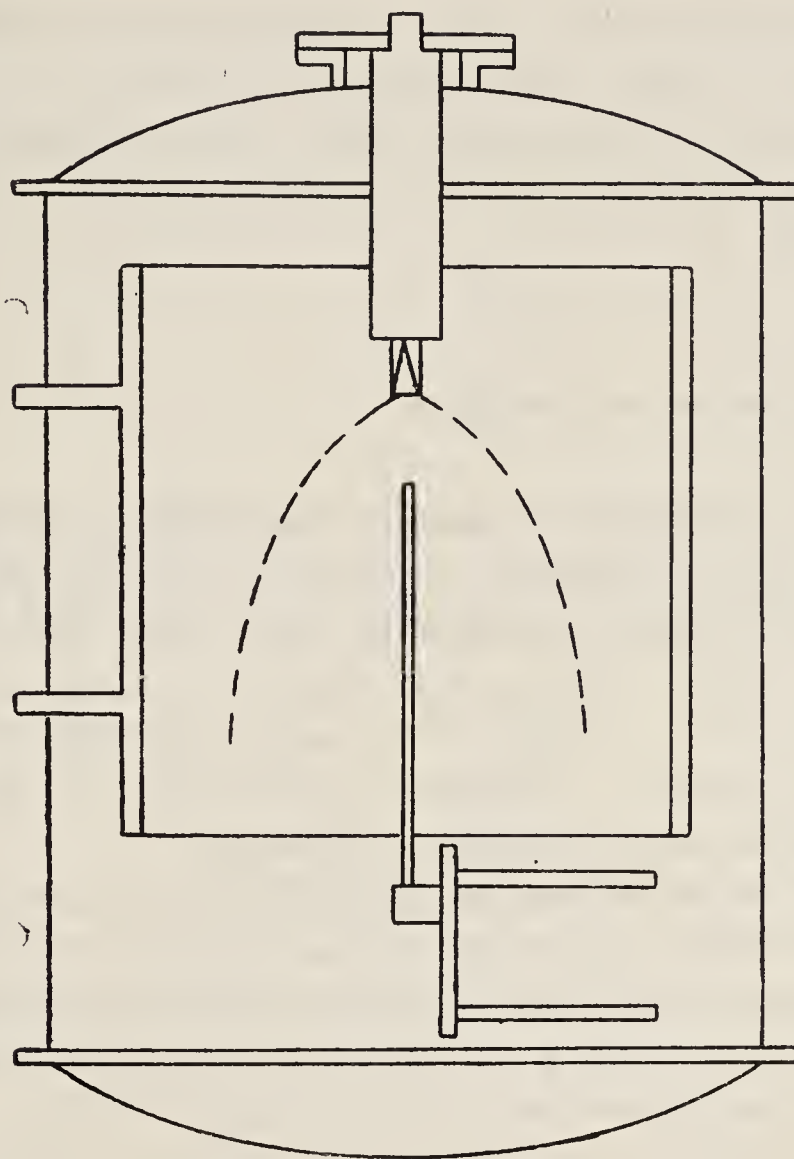


Figure 6. The mol-sink facility of ISAS. For the experiments of free jet expansion of water, this has a liquid nitrogen cooled shroud of 80 cm diameter and 80 cm length, placed within a vacuum chamber of 120 cm diameter and 120 cm length. The testing water jet of up to $0.5 \text{ cm}^3/\text{s}$ is expanded from the right side into the cooled shroud which has mol-sink capability. The flow field was surveyed by the traversing mechanism shown in the left side.

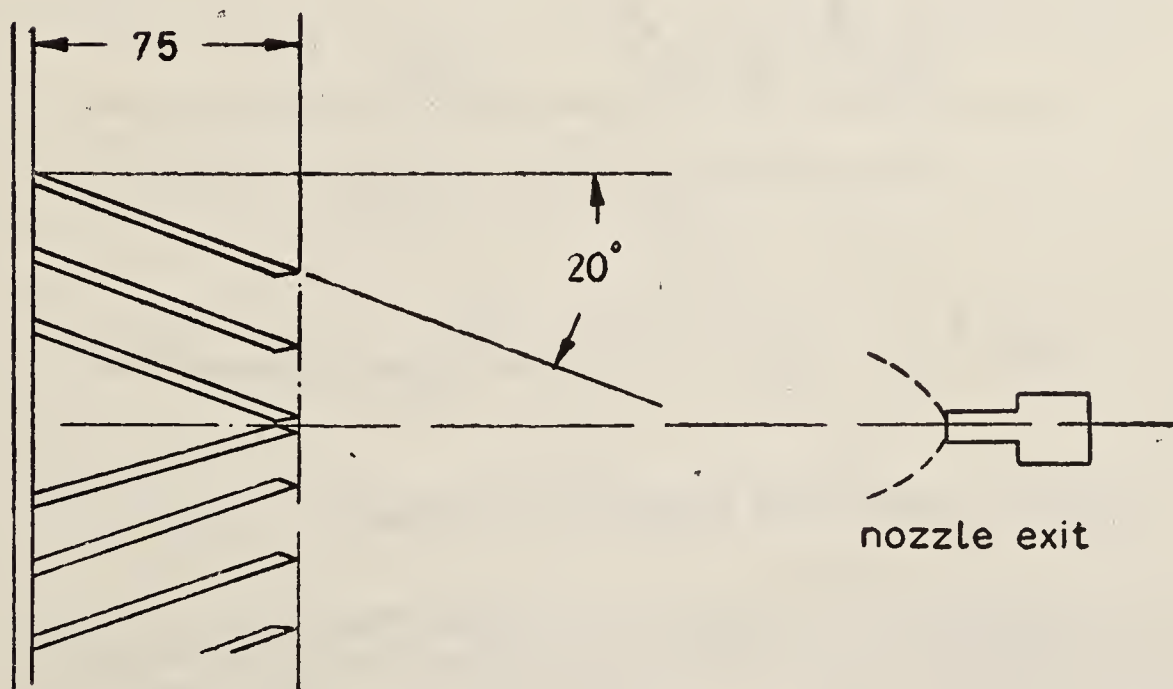


Figure 7. The detailed view of the cooled shroud. This has 7.5 cm deep fin with a uniform inclination angle of 20° to the normal, which ensures a very high capture coefficient to the incoming water molecule.

on this problem (Scialdone 1977). Since emitted particles increase the background noise of the telescope sight, several detailed analyses concerning this phenomenon have been carried out (Murakami 1979). The molecular distribution around the space shuttle has been analysed and enough precaution provided against contamination (Bareiss 1979).

4.4 Contaminant deposition and its effects

In order to measure the deposited mass on the surface, the quartz crystal microbalance (QCM) has been widely used, as shown in figure 8 (plate 4) (Wallace 1972, 1980). This is a quartz crystal oscillator in shear mode with the contaminant deposition surface on one side. The resonant frequency change is directly proportional to the mass deposited on it. In figure 9 the output signature of a QCM for various depositing materials is shown. Through the examination of these output signatures some information on the deposited mass is obtained.

The effects of the contamination are most critical for the optical surface and the solar cells. The degradation of the surface characteristics in the space environment is enhanced by the contamination and experience on these synergic and accumulating effects has been documented but a systematic physical understanding of this complicated phenomenon is not satisfactory yet (Roux *et al* 1979).

Besides those originated from the spacecraft itself, the spacecraft surfaces are hit by cosmic rays such as electrons, ions, or electromagnetic radiations and also by micrometeorites. When solar activity is high, or within the van Allen belt, these charged particles have quite a strong influence on the spacecraft surfaces. The charge-up of the orbiting satellites is also very important, especially for those in the geostationary orbit (Rosen 1976).

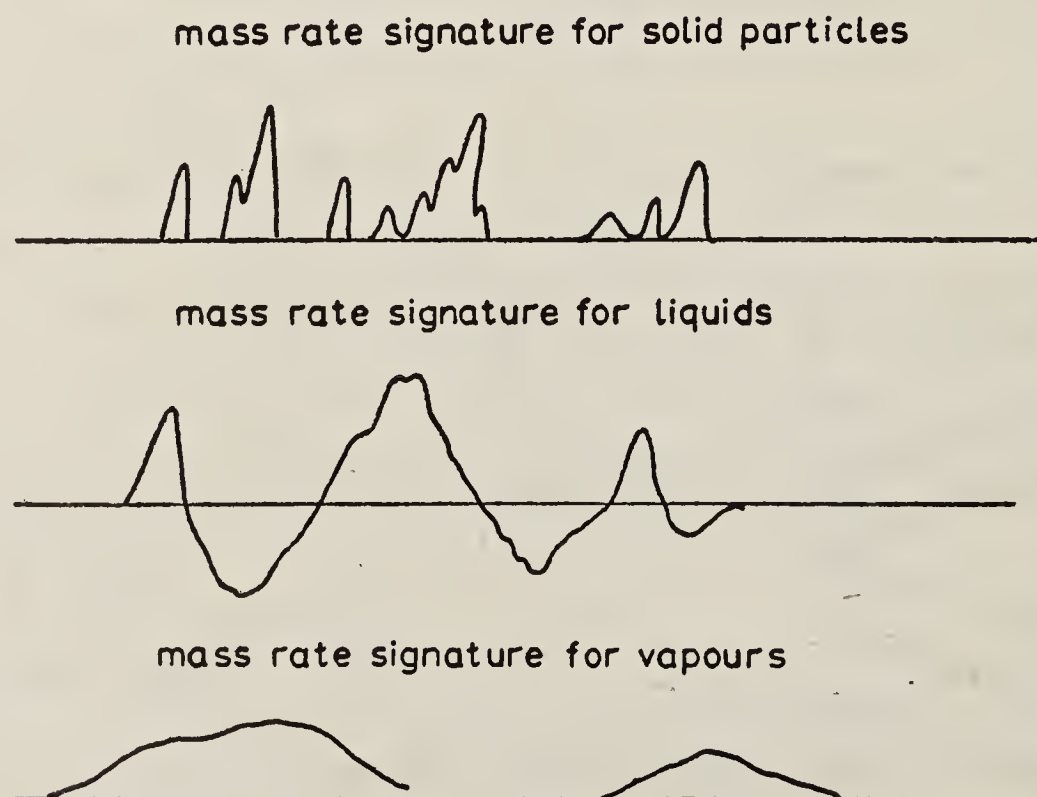


Figure 9. The QCM output signatures. This difference depends upon the physical state of the deposited contaminants. These signatures and the QCM temperature ranges which are controllable provide useful information to identify the contaminants and to find out their origin.

5. Microgravity effects

During sustained space flight, the spacecraft environment is under quite reduced gravity (microgravity). This is caused by the centrifugal force due to the satellite's spinning motion, the gravity gradient of the external gravity field, the fluid venting, the firing of control rockets of the satellite and the atmospheric drag. It is usually less than 0.01% of the gravity at the earth's surface: it is quite small, but changing. That is, the so-called g-jittering is caused by vibrations of the machines on board or movements of the crew. Thus, the behaviour of the fluid aboard the spacecraft is strongly influenced by the absence of gravity. The other forces which are minor in the terrestrial environment such as surface and interfacial tension, thermovolumetric expansion, molecular diffusion and electric and magnetic effects, become effective.

5.1 Material processing in space

The phenomena strongly influenced by these effects are the natural convection of the continuum fluid, the interfacial instability between different fluids and the behaviour of the free surface of a liquid. From a practical point of view, these phenomena are utilized quite successfully for processing of various materials in space. To do this, a product recovery system is needed, and the use of the space shuttle for this purpose may become common practice. At present preliminary experiments

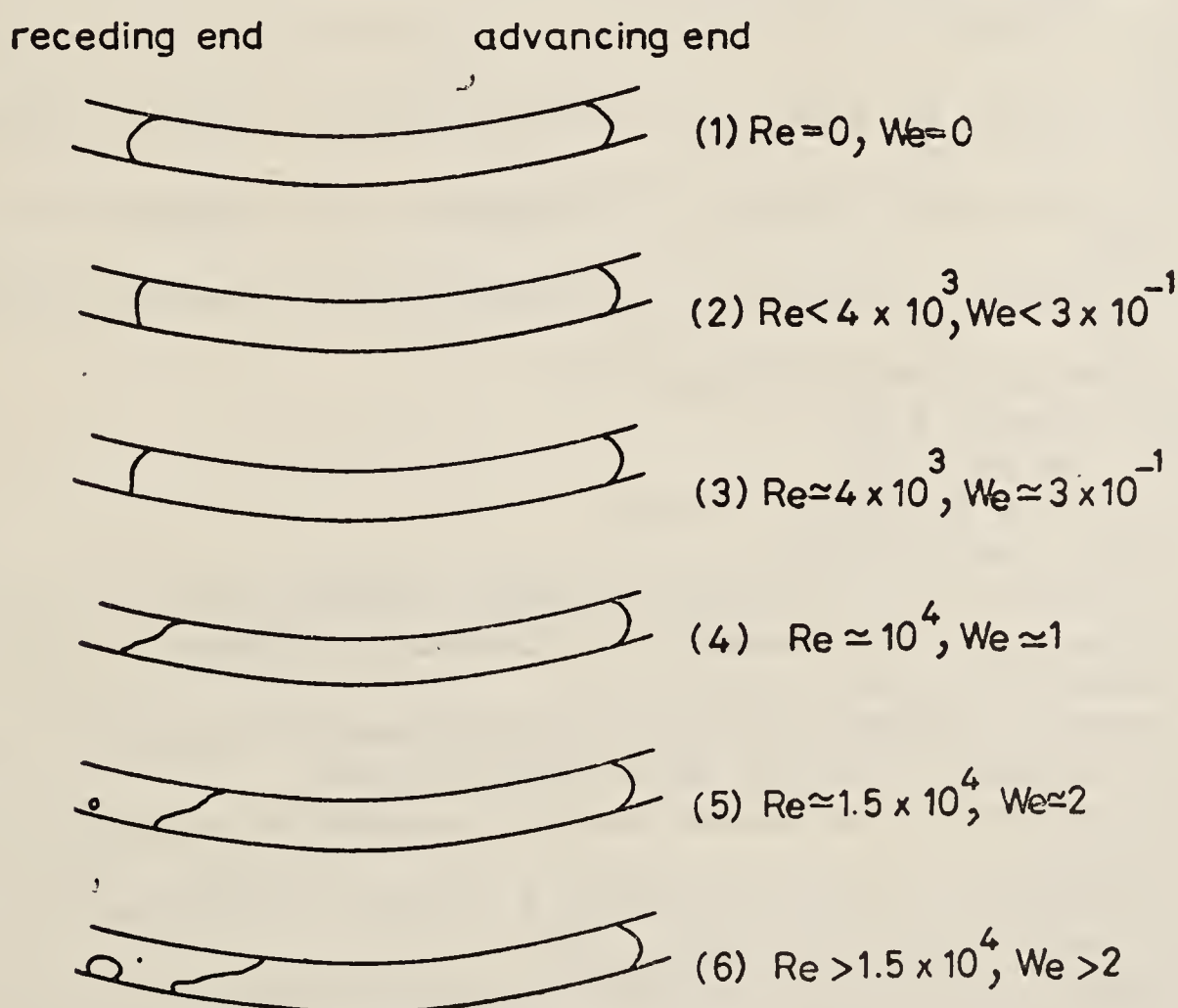


Figure 10. The liquid configuration observed in a nutation damper on ground. Here Re is the Reynolds number, Ur/ν , and We is the Weber number $\rho U^2 r/\sigma$, and U is the liquid velocity, r is the tube radius, and ρ , σ and ν are the density, the surface tension coefficient and the dynamic viscosity, respectively, of the liquid. The liquid container with annular ring shape with a ring radius of 20 to 30 cm and a tube radius of 1 to 2.5 mm was set on the gymbal stand, and the shape of the liquid contained in it was observed.

using sounding rockets with recovery systems have been in progress in our country (Steg 1977).

5.2 Heat pipes and nutation dampers in space

The attitude control system of spacecraft using liquid-containing wheels is also subject to this effect and therefore liquid-containing systems such as coolant heat exchangers and heat pipes have to be carefully designed to overcome these effects (Oshima *et al* 1978).

In this Institute, an analysis of liquid behaviour in the nutation damper, including an analysis of surface tension and microgravity effects, has been made and some ground simulation testing has been carried out. The liquid shape observed by this experiment is summarized in figure 10. Also the rocket-borne flight test of the heat pipe has been carried out by the Institute, and the effect of gravity has been identified and the successful operation of the heat pipe in the space environment has been confirmed.

References

- Arai N & Karashima K 1979 *AIAA J.* **27** 191
 Bareiss L E 1979 *J. Spacecr.* **16** 394
 Biolsi L 1980 *AIAA J.* **18** 596
 Borucki L, Lehmann V & Muller W J C 1972 *Ruckstreuung desorbierter Gasmolekule von Raumflugkorpern* (Raumfahrtforschung heft 4) p. 166
 Campbell W A Jr, Marriott R S & Park J J 1973 Outgassing data for spacecraft materials, NASA TN D-7362
 Campbell W A Jr, Marriott R S & Park J J 1975 Outgassing data for spacecraft materials, NASA TN D-8008
 Campbell W A Jr, Marriott R S & Park J J 1978 Outgassing data for spacecraft materials, NASA Ref. Pub. 1014
 Campbell W A Jr, Marriott R S & Park J J 1980 Outgassing data for spacecraft materials, NASA Ref. Pub. 1061
 Chatwani A U & Fiebig M 1980 *Phys. Fluids* **23** 646
 Dawson J P 1966 *J. Spacecr.* **3** 218
 Doenecke J 1970 *J. Spacecr.* **7** 720
 Dreaper J S & Sperlein R F 1980 *AIAA J.* **18** 712
 Furukawa M 1979 *J. Spacecr.* **116** 412
 Furukawa M & Oshima K 1973 An application of multiple regression analysis to determination of thermal mathematical model of spacecraft, 10th International Symposium on Space Technology and Science (ISSTS) Tokyo, p. 603
 Guernsey C S & Hrubes J D 1980 Comparison of quick-look plume heating calculations and Monte Carlo direct simulation, AIAA Paper No. AIAA-80-1516, p. 80
 Heslin T M 1977 An equation that describes materials outgassing for contamination modelling, NASA TN D-8471
 Ide S, Itagaki H, Kanamori Y, Aoki D, Kawakami A, Tashiro T & Sakakibara S 1977 NASDA large space chamber, 12th ISSTS, Tokyo p. 739
 Ishimoto T & Bevans J T 1971 Sensitivity analysis in thermal design, 9th ISSTS, Tokyo p. 451
 Karashima K, Arai N & Sato K 1978 *J. Jpn. Soc. Aeronaut. Space Sci.* **20** 191
 Mathanson D, Gabron F & Almgren D W 1969 *J. Spacecr.* **5** 876
 Minning C P 1979 *AIAA J.* **17** 1406
 Murakami M 1979 Direct Monte Carlo simulation of two dimensional radiative heat transfer in absorbing emitting medium bounded by the non-isothermal gray walls, 9th ISSTS, Tokyo p. 407
 Murakami M 1979 *J. Spacecr.* **16** 193

- Murakami M & Oshima K 1972 An exact solution of the propagation of small disturbances in a radiating grey gas with isotropic scattering, 10th ISSTS, Tokyo p. 553
- Nelson L A & Chuan R L 1969 *J. Environ. Sci.* 12
- Oshima K 1971a Thermal design method of spacecraft, 9th ISSTS, Tokyo, p. 463
- Oshima K 1971b An experimental critique to the thermal nodal analysis ISAS Report 468
- Oshima K 1973 A unified thermal structural design analysis of spacecraft, 10th ISSTS, Tokyo p. 617
- Oshima K, Matsushita T & Murakami M 1978 *Heat pipe engineering* (Tokyo : Asakura Publ. Co.)
- Oshima K & Kobayashi Y 1969 Experimental study of underexpanded jet expanding into vacuum, 8th ISSTS, Tokyo, p. 477
- Rosen A 1976 *Progr. Astronaut. Aeronaut.* 47
- Roux J A, Wood B E, Alt R E, Frazine D F, Smith A M & Scott H E 1979 *J. Spacecr.* 16 373
- Scialdone J J 1972 *J. Vacuum Sci. Technol.* 9 1007
- Scialdone J J 1977 Correlation of self-contamination experiments in orbit and scattering return flux calculation, NASA TN D-8438
- Sekihara K, Kano M, Yeta A, Iwanaga M & Nakasuji M 1971 Two-stage radiant cooler, 9th ISSTS, Tokyo, p. 509
- Spiga G, Santarelli F & Stramigioli C 1980 *Int. J. Heat Mass Transfer* 23 841
- Steg L 1977 *Progr. Astronaut. Aeronaut. AIAA* 52 52
- Stephens J B 1966 *J. Spacecr.* 3 844
- Tsujimoto K, Nakamura Y, Amoh H & Mihara T 1971 A solar simulator using water-cooled 30kW xenon arc lamp, 9th ISSTS, Tokyo p. 495
- Wallace D A 1972 *J. Vacuum Sci. Technol.* 9 462
- Wallace D A 1980 *J. Spacecr.* 17 153
- Wood W L 1977 *J. Number Methods Engg.* 11 1059

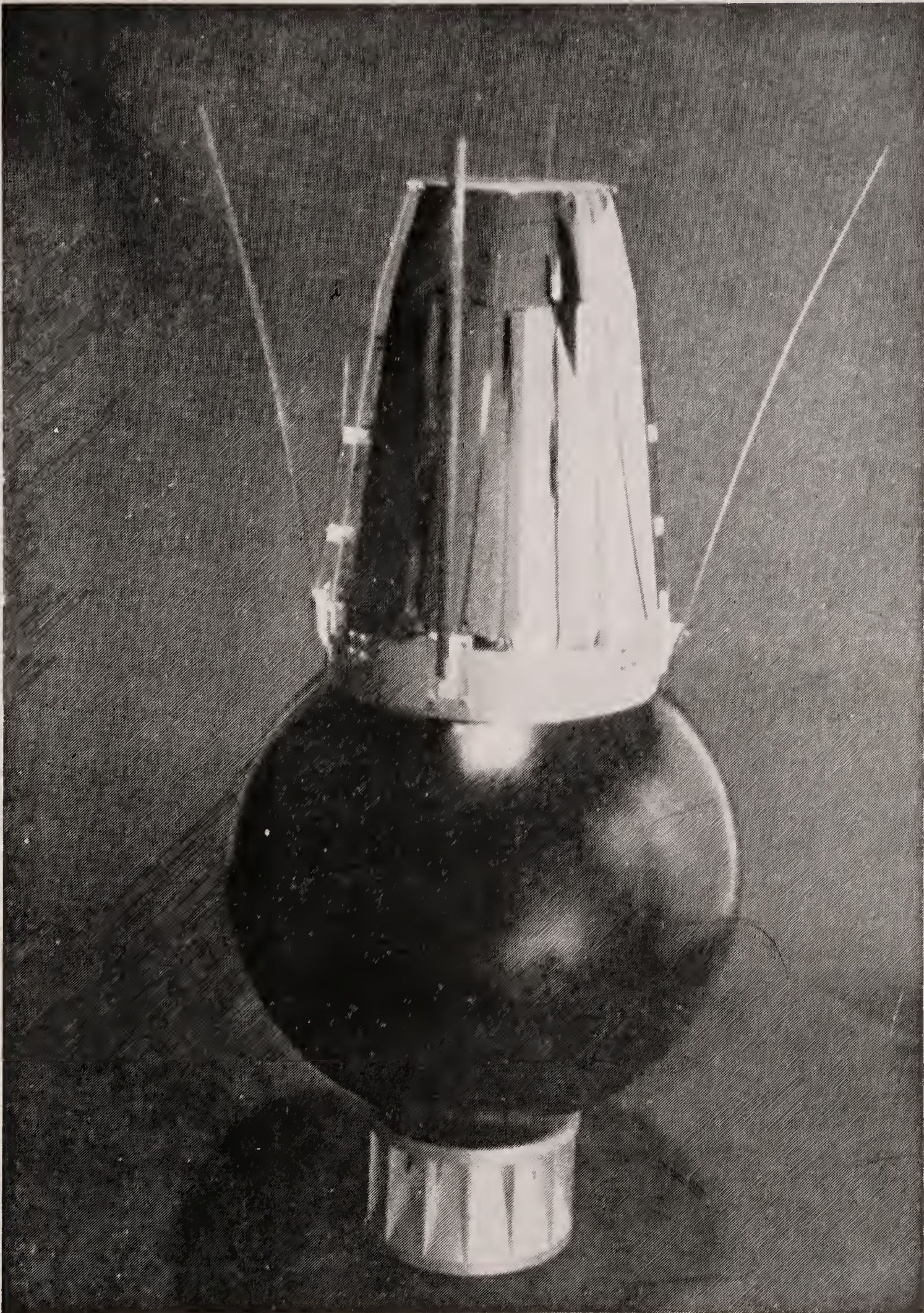


Figure 1. The first Japanese satellite *Ohsumi* launched on 11 February 1970 by a solid propellant rocket L-4S. It is 23.8 kg in weight and a highly elliptic orbit with a period of 144.2 min.

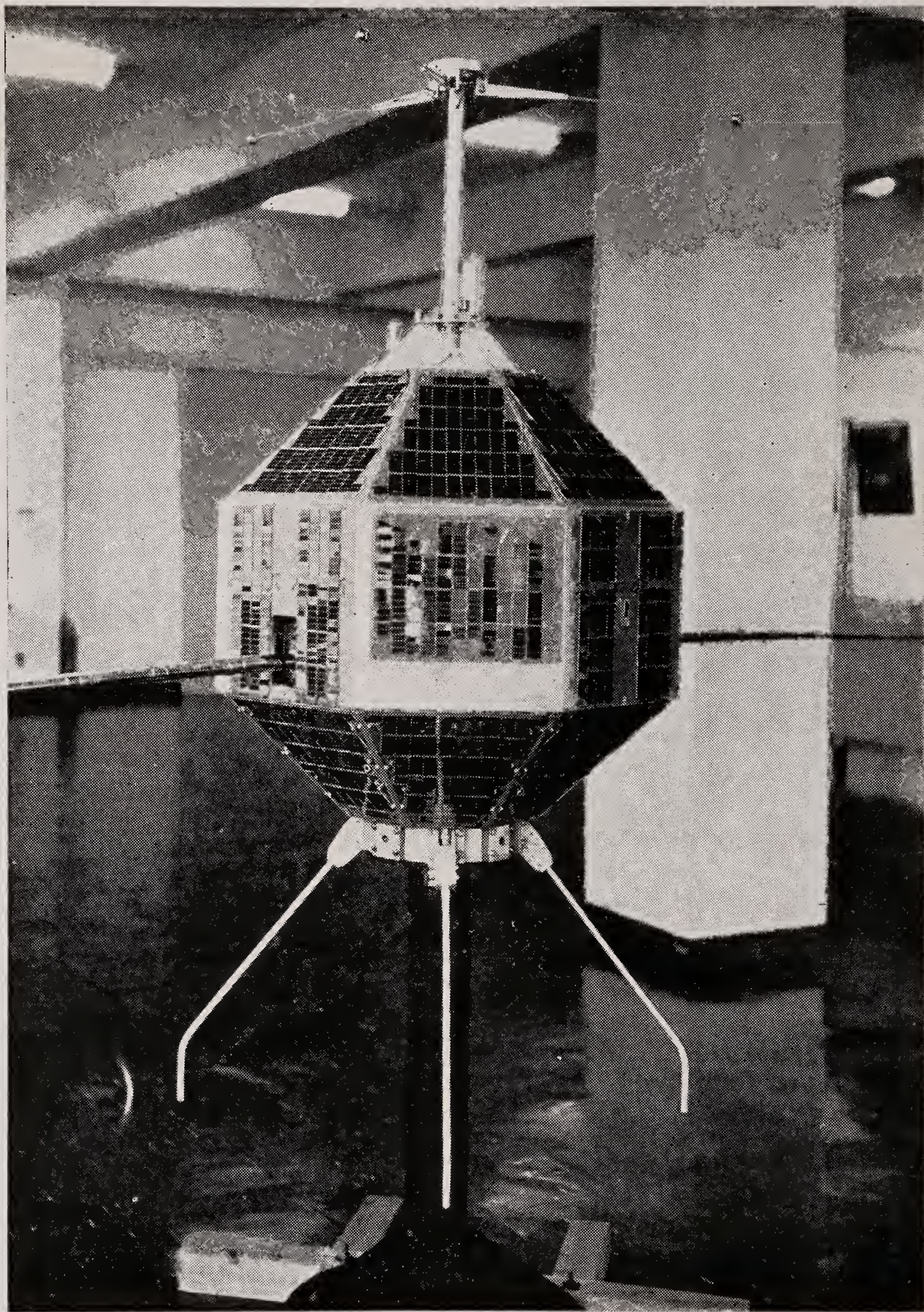


Figure 2. The first scientific satellite *Shinsei* of ISAS. Launched on 28 September 1971 by the M-4S launch vehicle for investigation of ionospheric plasma, cosmic ray and solar radio waves.

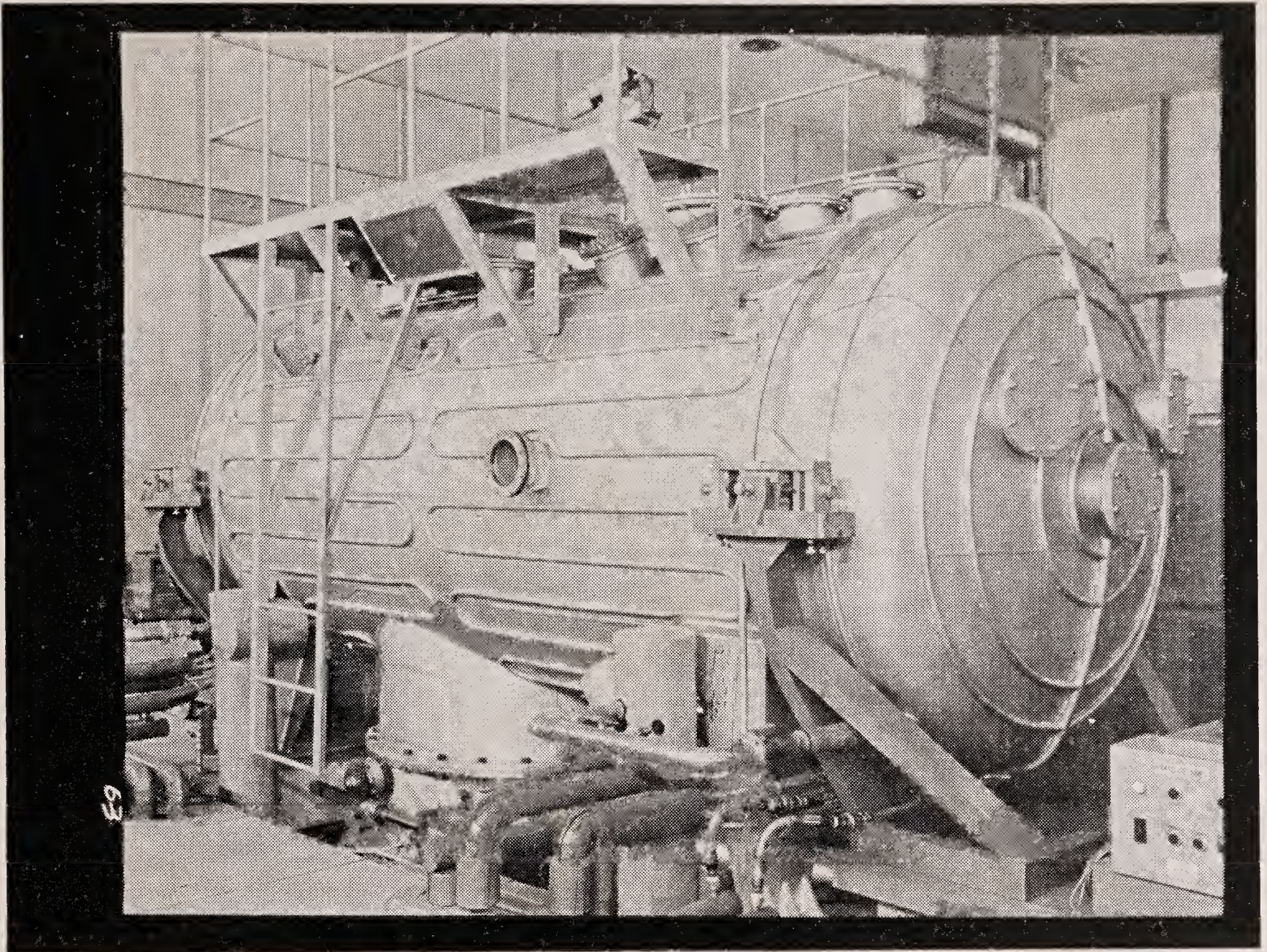


Figure 3. The first operational space simulation chamber of NASDA. It was constructed in 1964 and is 180 cm in diameter, 490 cm long and is able to pump down to 10^{-8} torr within 2 hr. The solar simulator is provided with the intensity of 1.5 kW/m^2 .

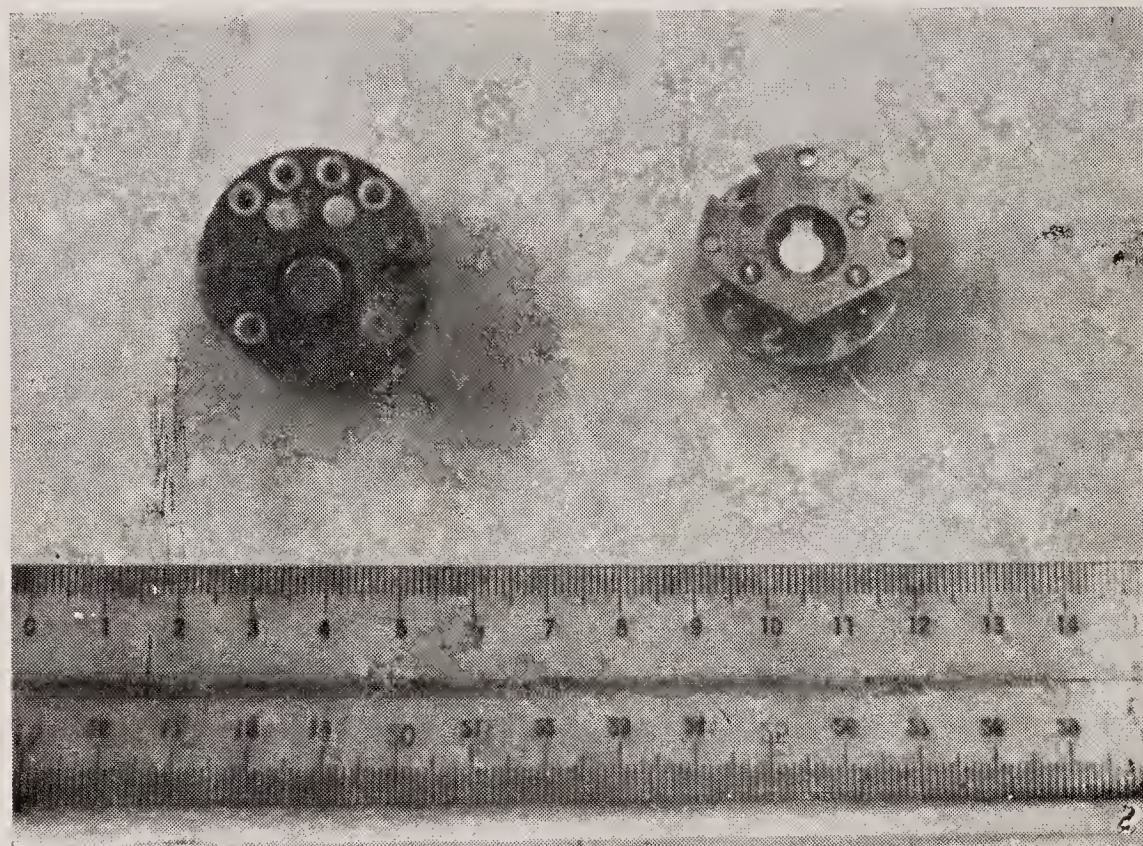


Figure 8. An assembly of quartz crystal microbalance sensor made by Celesco Industries. This has a sensing area of 0.316 cm^2 and can be cooled down to 77° K .

Real-fluid effects in flow cavitation

VIJAY H ARAKERI

Department of Mechanical Engineering, Indian Institute of Science, Bangalore 560 012

MS received 9 June 1981

Abstract. The possible role of real fluid effects in two aspects of flow cavitation namely inception and separation is discussed. This is primarily qualitative in the case of inception whereas some quantitative results are presented in the case of separation. Existing evidence clearly indicates that in particular viscous effects can play a significant role in determining the conditions for cavitation inception and in determining the location of cavitation separation from smooth bodies.

Keywords. Flow cavitation; inception; separation; real fluid effects.

1. Introduction

One definition of "cavitation" may be taken to be the formation of a new surface in an otherwise homogeneous body of liquid. This broad definition would include such other phenomena as boiling and evolution. However, at present, we restrict ourselves to cavitation in "cold" liquids. A liquid may be said to be cold if due to vaporization at the new surface the local temperature drop is insignificant compared to the bulk temperature of the liquid. Thus, in a cold liquid, cavities are formed as a result of the liquid being subjected to tensile stresses (or negative absolute pressures). One would expect that if the cavities once formed are subjected to compressive stresses (or positive absolute pressures) they would tend to disappear or collapse. In general, then, cavitation is a physical phenomenon which involves the appearance, development and disappearance of cavities in a body of liquid.

The cavity may contain either permanent gas or vapour, and, depending upon which dominates, we may distinguish between two different types of cavitation, namely (i) gaseous cavitation and (ii) vaporous cavitation. In addition, either type of cavity may be generated in a stagnant or in a flowing liquid. In the former case, normally termed "acoustic cavitation", the liquid is subjected to a time-varying pressure field by external means (for example, using a magnetostrictive device), whereas in the latter case, which may be termed "flow cavitation", the liquid is subjected to a time-varying pressure field due to the dynamic action of the flow. The subject of acoustic cavitation has recently been reviewed comprehensively by Neppiras (1980). In the present paper we consider two aspects of flow cavitation, namely inception and separation. Since review articles on the subject of inception have recently appeared (Acosta & Parkin 1975; Arakeri 1979; Arakeri & Acosta 1979) only its qualitative aspects are covered here. However, on the subject of separation, some earlier results, which are contained in a report (Arakeri 1971) of limited availability, have also been included.

2. Cavitation inception

2.1 Nuclei and thresholds

Theoretical predictions (see for example Flynn 1964) indicate that pure homogeneous liquids can withstand considerable tensile stresses, of the order of thousands of atmospheres. However, even carefully treated liquid samples are known to withstand only a moderate tensile stress, of the order of hundreds of atmospheres. This discrepancy has led to the postulation of the presence of weak spots in the liquid samples, commonly known as 'nuclei'. One of the simplest models of a nucleus is the so-called 'free nucleus', which is a spherical bubble containing the vapour of the liquid and some permanent gas. To understand the role of nuclei in cavitation inception it is helpful to consider the static stability of such a free nucleus. With this analysis (see for example Knapp *et al* 1970) it is easily shown that the critical condition for cavitation inception is given by

$$p_v - p_c = 4S/3R, \quad (1)$$

where p_c is the critical pressure, p_v is the vapour pressure of the liquid at its bulk temperature, S the coefficient of surface tension and R the radius of the bubble. From equation (1) it should be apparent that the critical pressure for cavitation inception is always less than p_v but will approach it for sufficiently large values of R . Therefore, from equation (1) it is possible to calculate the threshold pressure required to initiate cavitation from a bubble of radius R . Another interpretation of equation (1) is that there is a critical radius R_c for a given liquid pressure p_L such that nuclei of radius $R_n < R_c$ are stable; whereas, nuclei of radius $R_n > R_c$ are unstable. It follows from (1) that the magnitude of R_c is given by

$$R_c = \frac{4S}{3(p_v - p_L)}. \quad (2)$$

It is interesting to extend the above analysis to include pressure fields having a mean component p_{L_0} and a time-varying sinusoidal component of an amplitude p_A . Such pressure fields are the source of acoustically generated cavitation and as will be discussed later, they could be the source of flow cavitation as well. It is of significance here to determine the threshold magnitude of p_A such that a nucleus of initial radius R_n grows to a critical radius R_c . Under the conditions considered, the minimum value of p_L is

$$p_L = p_{L_0} - p_A, \quad (3)$$

and substituting the above in (2) we find that

$$R_c = \frac{4S}{3(p_A - p_{L_0} + p_v)}. \quad (4)$$

Now an alternate expression for R_c can be arrived at by considering the condition required for expanding a nucleus of initial radius R_n to the critical size R_c . This is given by

$$p_n (R_n/R_c)^3 + p_v = -p_A + p_{L_0} + (2S/R_c), \quad (5)$$

where p_n is the initial gas pressure in the bubble. If the critical radius R_c is eliminated from (5) using (4) we find a relationship between the threshold pressure p_A denoted by $p_t^{(1)}$ first derived by Blake (see Flynn 1964) given by:

$$p_t^{(1)} = p_{L_0} - p_v + \frac{4S}{3\sqrt{3} R_n} \left[1 + (p_{L_0} - p_v) \frac{R_n}{2S} \right]^{-1/2}. \quad (6)$$

Thus equilibrium theory predicts that a nucleus of radius R_n will grow explosively when the acoustic pressure amplitude is increased to the threshold value $p_t^{(1)}$. However, so far we have considered only vaporous growth. There is possibly another mechanism of bubble growth, namely by gaseous diffusion. In particular, as Hsieh & Plesset (1961) have shown, a small bubble which would normally disappear under steady pressure fields can grow by a phenomenon known as rectified diffusion under unsteady pressure fields. Thus, there exists a second threshold pressure amplitude $p_t^{(2)}$ at which a nucleus will start to grow by rectified diffusion. The expression for $p_t^{(2)}$ derived by Hsieh & Plesset is:

$$p_t^{(2)} = \frac{\sqrt{2}}{3} p_{L_0} \left[1 + \frac{2S}{R_n p_{L_0}} - \frac{C_\infty}{C_0} \right]^{1/2}. \quad (7)$$

Here C_0 is the saturation concentration of gas at an ambient pressure p_{L_0} , and C_∞ is the actual concentration of the gas in the liquid at a great distance from the nucleus. The above equation is limited to small values of (p_A/p_{L_0}) but computations without this restriction have been provided by Eller & Flynn (1965). A comparison of the two threshold pressures for a fixed value of p_{L_0} and various values of C_∞/C_0 is provided in figure 1. It is to be noted that for nuclei with radii (R_n) between $0.2 \mu\text{m}$

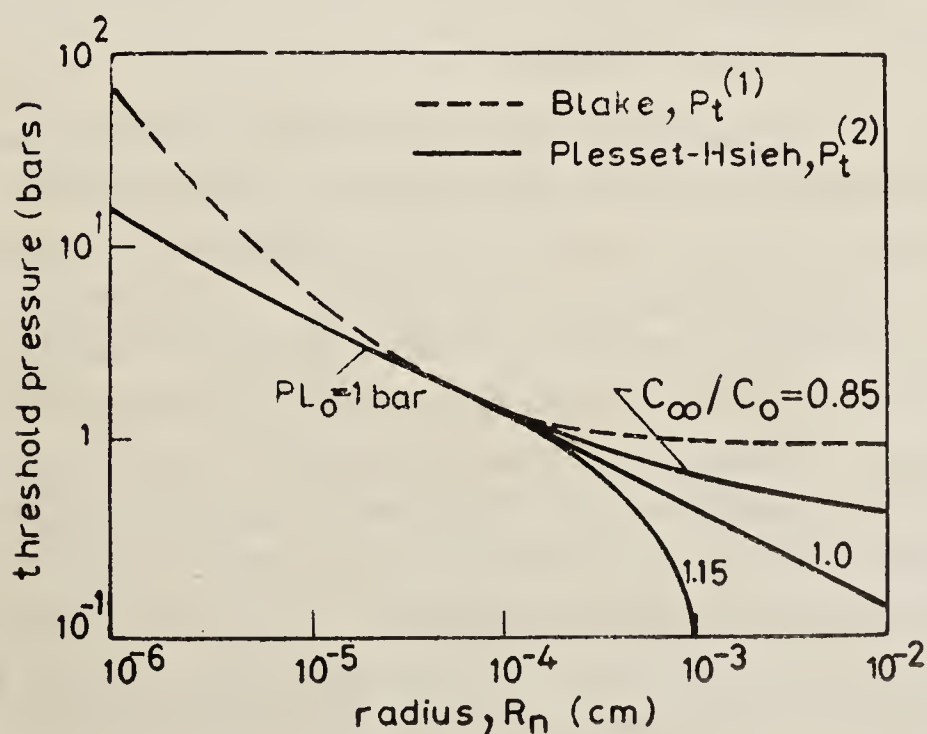


Figure 1. Theoretical thresholds for vaporous and gaseous cavitation.

and $1\ \mu\text{m}$ the two threshold amplitudes are almost equal. However, for nuclei with radii greater than $1\ \mu\text{m}$, which are found to be plentiful in a flowing liquid (see for example Keller 1972), the threshold amplitude for rectified diffusion can be an order of magnitude smaller than that for vaporous cavitation. Therefore, these observations certainly suggest the possibility that a nucleus initially having a size below the critical size for vaporous cavitation could grow to the critical size by rectified diffusion provided sufficient time is allowed for bubble growth.

2.2 Bubble trajectory and pressure fields

As has been indicated previously (Arakeri 1979), bubble growth leading to cavitation is primarily determined by two factors; namely, the magnitude and the duration of low pressures experienced by the nuclei. The bubble growth, of course, is expected only if the magnitude is greater than the threshold value predicted on the basis of static stability considerations indicated in the previous section. The crucial information required then for predicting bubble growth is the knowledge of the magnitude of low pressures as well as the residence time of the bubbles in these low pressure regions. This information can be obtained based on certain assumptions which may not be valid under all conditions of flow cavitation. One example of such calculations where good agreement was found with experiments is due to Plesset (1949). The assumption involved here was that the bubble travels following a streamline at the local liquid velocity ignoring any boundary layer effects. Thus, the bubble follows a trajectory determined by these assumptions. It is conceivable that the bubble may follow a different trajectory if boundary layer effects are included. In order to elaborate further it is worthwhile to note that several different flow regimes can be identified for flow past a solid body. Some of these are listed below:

- (i) laminar boundary layer in the region of interest,
- (ii) laminar boundary layer followed by turbulent transition in the region of interest,
- (iii) laminar boundary layer followed by separation with turbulent transition in the free shear layer leading to reattachment,
- (iv) laminar boundary layer followed by separation with turbulent transition in the free shear layer without reattachment, and
- (v) turbulent boundary layer in the region of interest.

Observations, for example by Arakeri & Acosta (1973), have indicated the importance of different flow regimes in the mechanism of cavitation inception including bubble growth patterns. Subsequent investigations (see recent review by Arakeri & Acosta 1979) have clearly established that the bubble growth calculations must take into account the modification of the pressure field as well as possible changes in the residence time due to viscous effects. In view of these observations, one can define several classes of trajectories following which bubbles in different trajectories would experience differing pressure fields as well as residence times. The several classes of trajectories possible including the one analyzed by Plesset (1949) are summarized in figure 2. The class I trajectory is essentially the one analyzed by Plesset. It may be noted that if the boundary layer remains laminar, then even if the bubble gets entrained within the boundary layer, the pressure field experienced by the bubbles will be

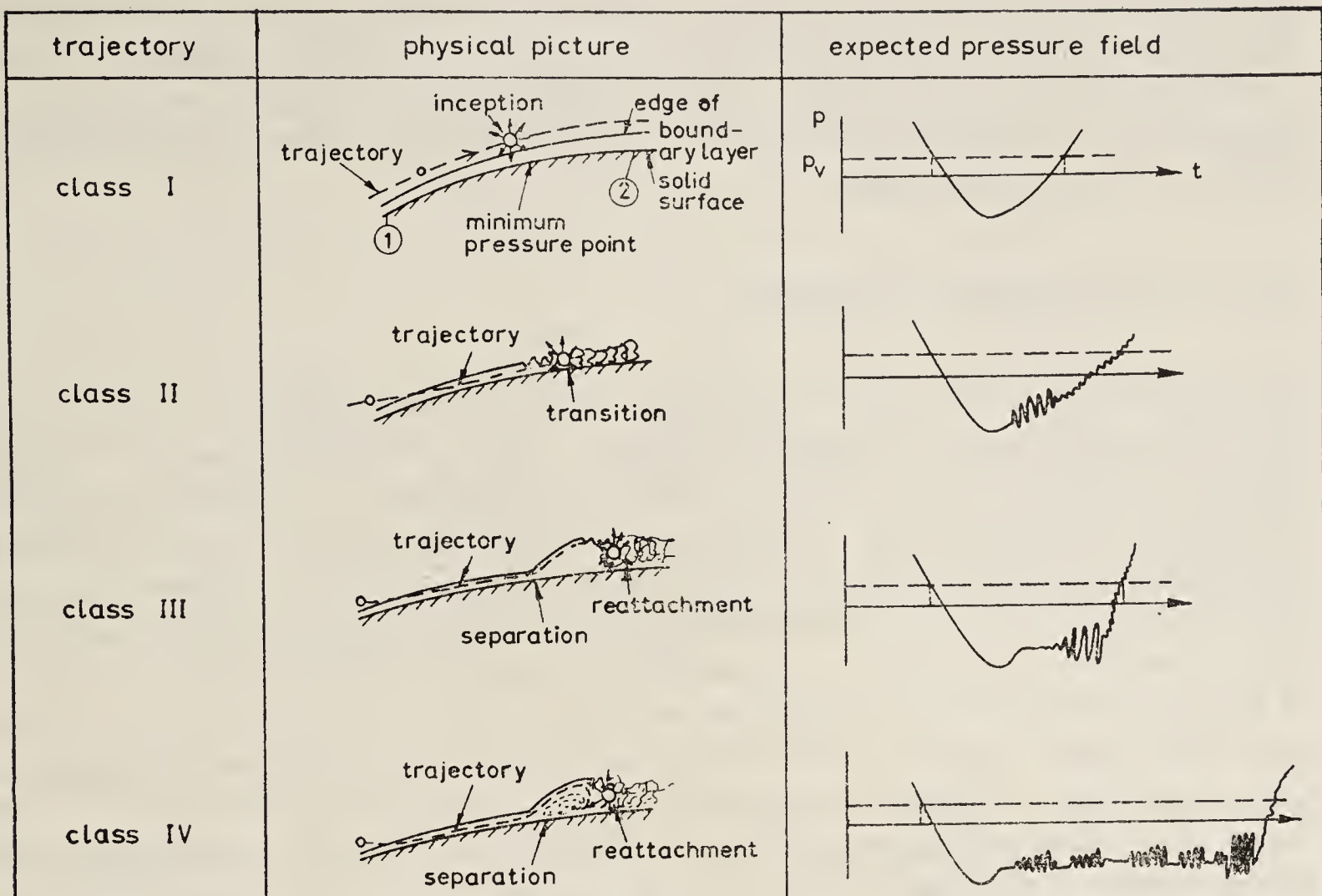


Figure 2. Expected pressure field and physical picture of a nucleus following various trajectories.

similar to the class I trajectory except that the residence time in low pressure regions is likely to be greater. However, if boundary layer transition does occur within the region of interest then the pressure field is modified as shown for the class II trajectory. The primary difference is the addition of unsteady pressures to the existing static pressure distribution. The class III trajectory is the one experienced by a bubble following the free shear layer of a short laminar separation bubble. Again the presence of unsteady pressures is to be noted. Measurements by Arakeri (1974) and Huang & Hannan (1975) have shown that the magnitude of unsteady pressures, particularly in the transition region, can be quite significant. The class IV trajectory is the one in which a bubble spends some time in the recirculating region of a short separation bubble and eventually gets entrained in the free shear layer to be carried into the reattachment region. Thus, the bubble experiences intermittent steady pressures when near separation, and intermittent unsteady pressures when near reattachment. It is expected that the pressure field experienced by a bubble entrained in the free shear layer of long separation *i.e.* without the reattachment bubble would be similar to the one for the class III trajectory. Finally, if the boundary layer is turbulent in the region of interest then the pressure field would be expected to be similar to the class I trajectory apart from the addition of turbulent pressure fluctuations. However, measurements (see for example Huang & Hannan 1975) have shown these to be significantly smaller than those existing in the transition region.

In the foregoing discussion nothing was said about how a bubble comes into the region of low pressures. The initial source of the bubble is likely to be a nucleus existing in the liquid upstream of the body. Thus the complete calculations of bubble growth leading to cavitation inception should include the trajectory analysis starting

from a point far upstream of the body. Trajectory analysis upstream of the body was first made by Johnson & Hsieh (1966). In particular, they showed that there exists a "screening effect" where larger, easily cavitable nuclei are pushed away from the boundary layer regions of a body due to pressure gradient effects in the neighbourhood of the stagnation point.

2.3 *Viscous interactions in inception*

As noted earlier, recent observations have clearly indicated that viscous effects do play an important role in cavitation inception. These observations have also led to useful correlations (Arakeri 1979) to predict the conditions for cavitation inception dominated by viscous effects. The correlations have been found to work; however, the reasons behind the success are not entirely clear. From the discussion in the previous section, we expect the amplitude of unsteady pressures to be at least partially responsible for the viscous interactions in inception. However, here we will try to find out whether these unsteady pressures may also be responsible for modification of the nuclei content of the liquid in the region of separation and/or transition. One observation of Gates & Acosta (1978) is of particular relevance here. They found that bodies which possess laminar separation are relatively insensitive to the nuclei content of the liquid. This strongly suggests that if nuclei content measurements were carried out upstream of a body and within the laminar separated region of the same body near inception conditions, these are likely to be different. Recently, Parkin (1979) has proposed a theoretical explanation for the possible role of laminar separated regions in nucleation. It is suggested that nuclei initially of very small diameter possessing relatively high tensile threshold values grow first by vaporous means in the minimum pressure area and subsequently by gaseous diffusion while entrapped in the separated region. However, the possible role of unsteady pressures in the growth while in the separated region was not considered.

Our considerations of pressure fields encountered by a nucleus trapped in the separated region suggest that growth may be controlled both by the magnitude of the mean or static pressure and the magnitude of unsteady pressures. In particular, we have seen from § 2.1 that the possibility of bubble growth by rectified diffusion in the presence of unsteady pressure fields exists. Further, the threshold amplitude required for bubble growth by rectified diffusion is lower than that predicted for vapour growth in the size range one to ten microns. It is to be noted that measurements by Keller (1972) indicate that nuclei in this range are likely to be available in plenty and at the same time they are not subject to the screening effect described earlier. Therefore, the possibility of bubble growth by rectified diffusion must be considered in the presence of unsteady pressure fields. It is to be granted that growth by this mechanism is relatively slow, but at the same time faster than static diffusion considered by Parkin. Thus, though at first, bubble growth by rectified diffusion was thought to be important only for the class IV trajectory, its importance for other trajectories should not be completely ruled out at this juncture. It must also be pointed out here that rectified diffusion is likely to be an important mechanism for bubble growth only in the transition region of flow, where large amplitude of pressure fluctuations exists within a narrow band of frequencies, as compared to smaller amplitude pressure fluctuations over a wide band of frequencies existing in the turbulent region of flow.

Thus, the above arguments lead to a possible explanation for the observations of Gates & Acosta (1978) that bodies with laminar separation are relatively insensitive to the free-stream nuclei content of the liquid. In addition, the significance of small separated regions in the inception of cavitation is further strengthened. In this regard it is to be pointed out that small laminar separated regions can persist on certain bodies even upto Reynolds numbers exceeding five million. In addition, the measurements of Klebanoff & Tidstrom (1972) indicate that the flow downstream of a small roughness element has similar properties as small laminar separated regions. Therefore, isolated roughness elements buried in a thin laminar boundary layer may be a ready source for cavitation inception. An example of such cavitation commonly termed "spot cavitation" is shown in figure 3 (plate 1) taken from Acosta & Hamaguchi (1967). It is expected that such cavities may be prevalent at higher Reynolds numbers typical of prototype situations. It would then be interesting to investigate whether the appearance of spot-type cavities is also relatively insensitive to the free-stream nuclei content of the liquid.

3. Cavitation separation

3.1 Background

We saw in the previous section how viscous effects can play an important role in determining the conditions for the onset of cavitation. If conditions are made favourable beyond onset for additional cavitation growth then subsequently a large vapour cavity will envelope some portion of the body. This condition is normally known as supercavitating flow. In most applications involving supercavitating flows the prediction of the various forces, generated by the device is of utmost importance. It is to be expected that the force coefficients would be dependent not only on such physical parameters like angle of attack, body shape, etc., but also on the starting position of the developed cavity which we may call the position of cavitation separation.

Bodies with sharp corners (such as disks, wedges and sharp-edged hydrofoils at moderately large angles of attack) possess cavitation separation points whose position is known *a priori*; and force coefficients for such bodies can be predicted quite accurately within the potential flow approximations (Wu 1968). But for smooth bodies, the position is not known *a priori* and the condition of smooth separation (Armstrong 1953) is normally invoked to predict the position of cavitation separation. However, this condition does not take into account such real fluid effects as viscosity, surface tension, etc., on the position of cavitation separation. However, as will be seen later, there is now substantial evidence that the position of cavitation separation is in fact influenced by real fluid effects.

3.2 Cavitation separation from axisymmetric bodies

Extensive observations of the physical features of supercavitating flows past spheres have been conducted by Brennen (1969a, 1970). Among other things the position of cavitation separation was measured for spheres of various sizes, covering a wide range of Reynolds numbers. The results shown in figure 4 for one value of cavitation number, $\sigma = 0.1$, clearly indicate that the position of cavitation separation is a strong

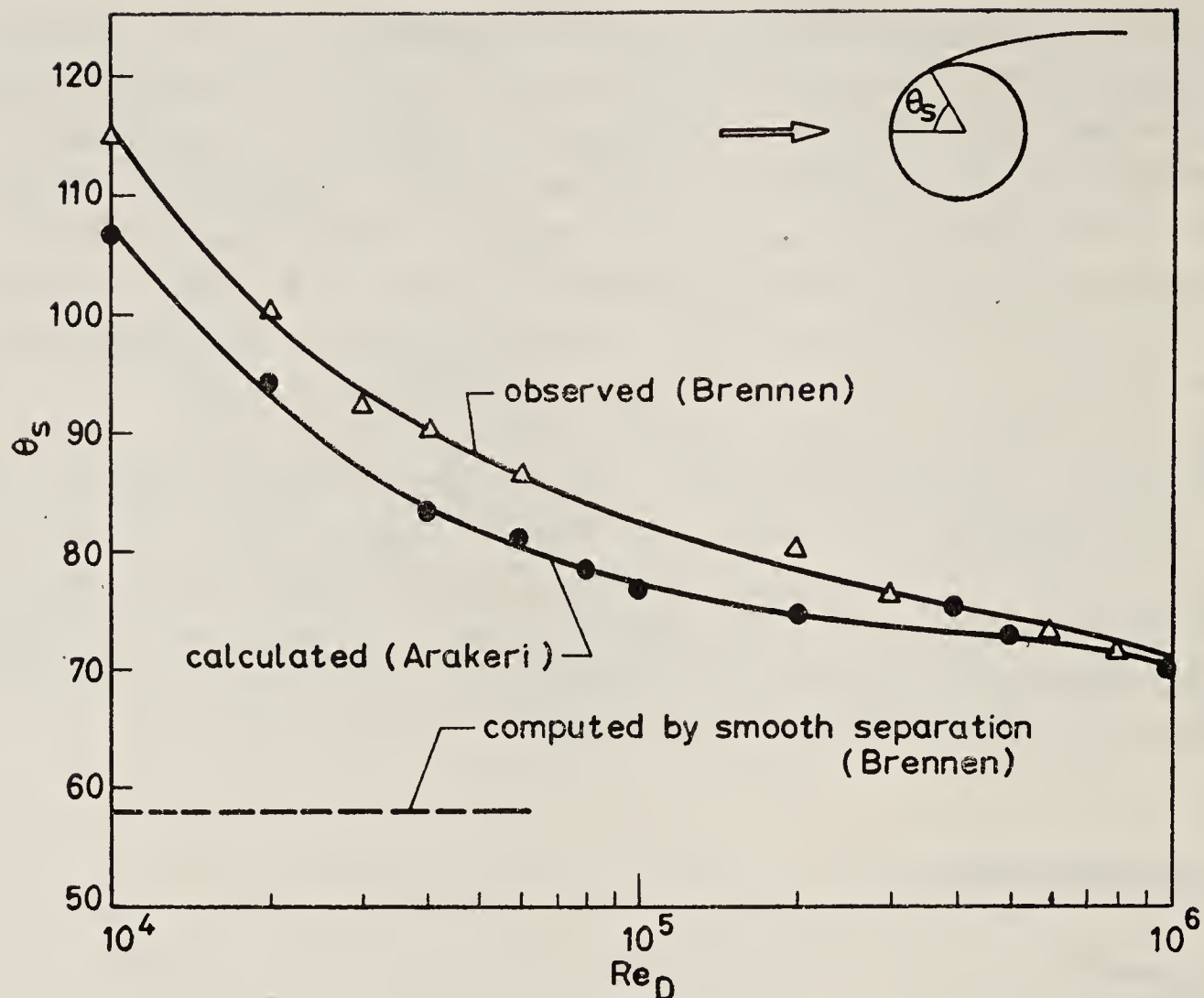


Figure 4. Position of cavitation separation from sphere at $\sigma=0.1$. θ_s is in degrees.

function of the Reynolds number. The observed Reynolds number dependence was first explained by Arakeri (1975) based on flow visualization studies of the real fluid flow in the neighbourhood of cavitation separation. It was noted that cavitation separation is preceded by laminar boundary layer separation and the distance between the two is a strong function of Reynolds number. Based on these findings a correlation was suggested (figure 4) which predicted the observed values by Brennen on spheres quite well.

3.3 Cavitation separation from slender two-dimensional hydrofoils

The measured position of cavitation separation from two different sized 8.32% bi-convex hydrofoils at zero angle of attack is shown in figure 5. The trend with Reynolds number is found to be similar to that observed in figure 4 for spheres. At zero angle of attack, cavitation separation from the hydrofoils was symmetric on the top and bottom surfaces; the physical appearance of cavitation was in the form of streaks consisting of large cavitation bubbles. Following a suggestion by Brennen (1969b), this type of cavitation separation has been termed 'nucleate cavitation separation'. At small positive angles of attack, the nucleate type of cavitation separation was observed on the top or suction side surface; however, on the bottom or pressure side surface the physical appearance of cavitation was quite different. This latter type had a smooth glassy appearance at separation and has been termed 'viscous laminar cavitation separation' (Arakeri 1975). We might note that this type of cavitation separation was also observed by Brennen on spheres and by Arakeri on two axisymmetric bodies. A few measurements of the position of cavitation separation of the two types noted above with hydrofoil at small positive angles of attack are presented in table 1.

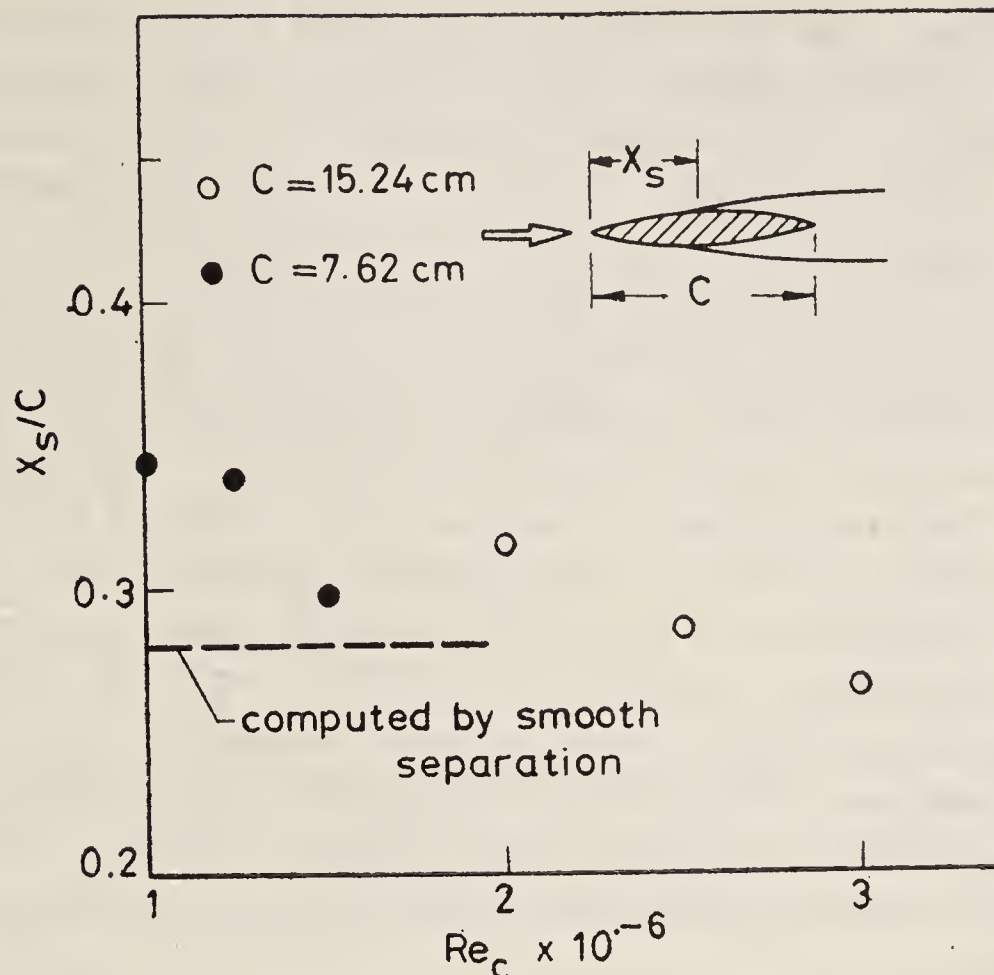


Figure 5. Position of cavitation separation from bi-convex hydrofoil with $\alpha=0$ and $\sigma=0.1$ (After Arakeri 1971.)

3.4 Comparison with theory

Brennen (1969a) modelled the cavitating flow past a disk and a sphere using one of the nonlinear free streamline theories. His numerical computations included the prediction of the drag coefficient, C_D for both the disk and the sphere as well as of the position of cavitation separation on the sphere using the smooth separation criterion. For the disk, the separation position is fixed and in this case the computed values of the drag coefficient were within about 5% of the measured values. For the sphere in the Re_D range of 3×10^5 to 8×10^5 , the agreement was within 10% despite the fact that the position of cavitation separation was predicted (figure 4) quite erroneously based on the smooth separation criterion.

Arakeri (1971) used the linearized theory to predict the position of cavitation separation as well as the force coefficients on a bi-convex hydrofoil at zero and small positive angles of attack. As shown in figure 5, the predicted position of cavitation separation using the smooth separation criterion agrees well with the measurements, in particular at the higher values of Reynolds numbers. Similar agreement on the suction side was found with hydrofoil at small positive angles of attack. However,

Table 1. Cavitation separation position from a hydrofoil at small positive angles of attack and $\sigma = 0.1$.

α	Experiment		Theory	
	Suction side	Pressure side	Suction side	Pressure side
1°	0.32	0.75	0.22	0.31
2°	0.25	0.73	0.17	0.35

as indicated in table 1, the difference for the pressure side was quite significant. The observed values were substantially more downstream than those predicted. Even with these differences, good agreement was found between the predicted and observed values of C_D . For the lift coefficient C_L , however, as shown in figure 6 the magnitude was predicted erroneously and even the sign was in disagreement. This may be explained as follows. On the suction side, the cavity separates very near the leading edge and hence the pressure is essentially uniform and equal to vapour pressure. On the pressure side, the cavity is predicted to separate at about 30% of the chord; however, it is observed to separate beyond the minimum pressure point at about 75% of the chord. Thus, the surface between the two is subjected to pressures at least below vapour pressure or even to a small negative pressure. Thus, the net effect is that the average pressure on the suction side is higher than the average pressure on the pressure side resulting in negative C_L at positive angles of attack! This in fact was found to be the case if the observed values of separation were introduced in the theoretical computations. This phenomenon is primarily due to viscous effects which lead to delay in separation; and to the lack of sufficient "nuclei", which leads to the liquid being able to sustain pressures below vapour pressure or even negative pressures without cavitating.

4. Conclusions

There is overwhelming evidence now that real fluid effects do influence the mechanism of cavitation inception and separation strongly. With regard to inception, it was anticipated that the strong pressure fluctuations which exist within the boundary

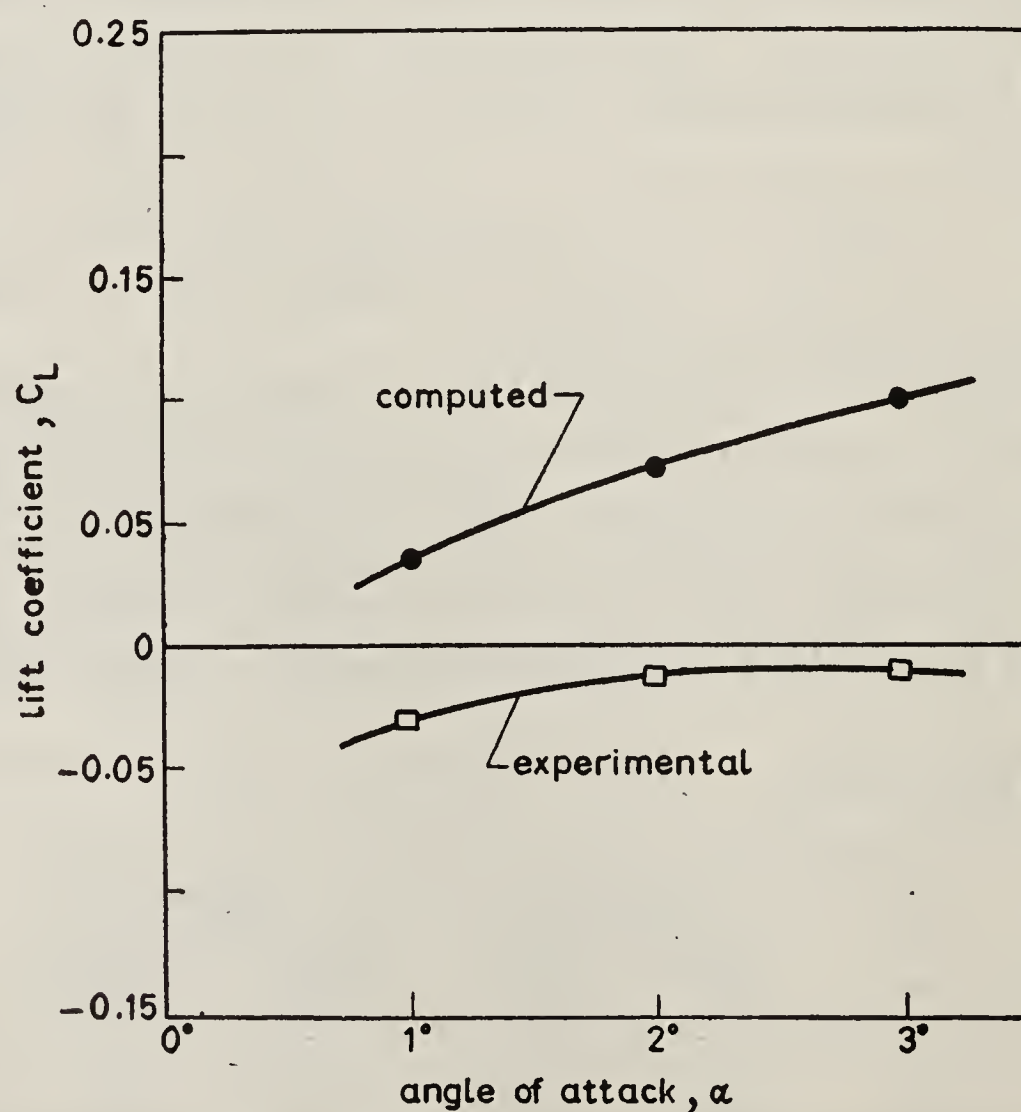


Figure 6. Comparison of experimental and computed lift coefficients on a bi-convex hydrofoil with $\sigma=0.1$ (Arakeri 1971).

layer transition region could account for the observed viscous effects. However, it is argued here that these same pressure fluctuations in particular with laminar separation may also be responsible for modification of the nuclei content of the liquid locally. With regard to separation, it is found that cavitation detachment from smooth bodies is strongly dependent on Reynolds number and weakly dependent on Weber number. It is also found that even though the cavitation separation position is predicted quite erroneously using the smooth separation criterion, the drag forces are predicted reasonably well. However, this is not necessarily the case with prediction of lift forces on slender hydrofoils.

List of symbols

A	cross-sectional area, $A = \pi D^2/4$ for sphere and $A = C \times S_p$ for hydrofoil
C	chord of hydrofoil
C_D	drag coefficient, $2D_f/\rho U^2 A$
C_L	lift coefficient, $2L/\rho U^2 A$
C_0	saturation concentration of gas
C_∞	actual concentration of gas
D	diameter
D_f	drag force
L	lift force
p_A	amplitude of the unsteady pressure
p_c	critical pressure given by equation (1)
p_{L_0}	ambient or mean liquid pressure
p_L	liquid pressure
p_n	initial gas pressure
$P_t^{(1)}$	threshold pressure given by equation (6)
$P_t^{(2)}$	threshold pressure given by equation (7)
p_v	vapour pressure of the liquid
p_∞	reference static pressure
R	bubble radius
R_c	critical bubble radius given by equation (2)
R_n	initial bubble radius
Re_C	Reynolds number, UC/ν
Re_D	Reynolds number, UD/ν
S	coefficient of surface tension
S_p	span of hydrofoil
U	reference velocity
X_s	axial location of cavitation separation
α	angle of attack
ρ	liquid density

- σ cavitation number, $(p_{\infty} - p_v) \frac{1}{2} \rho U^2$
 θ_s angular location of cavitation separation

References

- Acosta A J & Hamaguchi H 1967 Cavitation inception on the ITTC standard headform. Rep. No. E-149-1 (Pasadena: California Institute of Technology)
- Acosta A J & Parkin B R 1975 *J. Ship. Res.* **19** 193
- Arakeri V H 1971 Water tunnel investigations of scale effects in cavitation detachment from smooth slender bodies and characteristics of flow past a bi-convex hydrofoil. Rep. No. E-79 A. 12 (Pasadena: California Institute of Technology)
- Arakeri V H 1974 *J. Fluids Engg.* **97** 82
- Arakeri V H 1975 *J. Fluid Mech.* **68** 779
- Arakeri V H 1979 *Proc. Indian Acad. Sci.* **C2** 149
- Arakeri V H & Acosta A J 1973 *J. Fluids Engg.* **95** 519
- Arakeri V H & Acosta A J 1979 International Symposium on Cavitation Inception (New York ASME), p. 1
- Armstrong A H 1953 Abrupt and smooth separation in plane and axisymmetric flow. Mem. Arm Res. Est. 6. B. No. 22/63
- Brennen C 1969a *J. Fluid Mech.* **37** 671
- Brennen C 1969b *Cavitation state of knowledge* (New York: ASME) p. 141
- Brennen C 1970 *J. Fluid Mech.* **44** 51
- Eller A I & Flynn H G 1965 *J. Acoust. Soc. Am.* **37** 493
- Flynn H G 1964 *Physical acoustics* ed. W P Mason (New York: Academic Press) **1** (Part B) p. 127
- Gates E M & Acosta A J 1978 Twelfth symposium on naval hydrodynamics, Washington, Office of Naval Res., US Dept. of Navy
- Hsieh D Y & Plesset M S 1961 *J. Acoust. Soc. Am.* **33** 206.
- Huang T T & Hannan D E 1975 Pressure fluctuations in the regions of flow transition. Rep. No. 4723, Naval Ship Res. and Dev. Centre, Washington, DC.
- Johnson V E & Hsieh T 1966 Sixth symposium in naval hydrodynamics, Washington, Office of Naval Res. US Dept. of Navy.
- Keller A P 1972 *J. Basic Engg* **94** 917
- Klebanoff R S and Tidstrom K D 1972 *Phys. Fluids* **15** 1173
- Knapp R T, Daily J W & Hammitt F G 1970 *Cavitation* (New York: McGraw Hill) Ch. 3
- Neppiras E A 1980 *Phys. Rep.* **61**
- Parkin B R 1979 A theory for cavitation inception in a flow having laminar separation, ARL RM No. 79-198, AD A082 851, The Pennsylvania State University.
- Plesset M S 1949 *J. Appl. Mech.* **16** 277
- Wu TY 1968 *Basic developments in fluid dynamics* (New York: Academic Press)

Plate 1

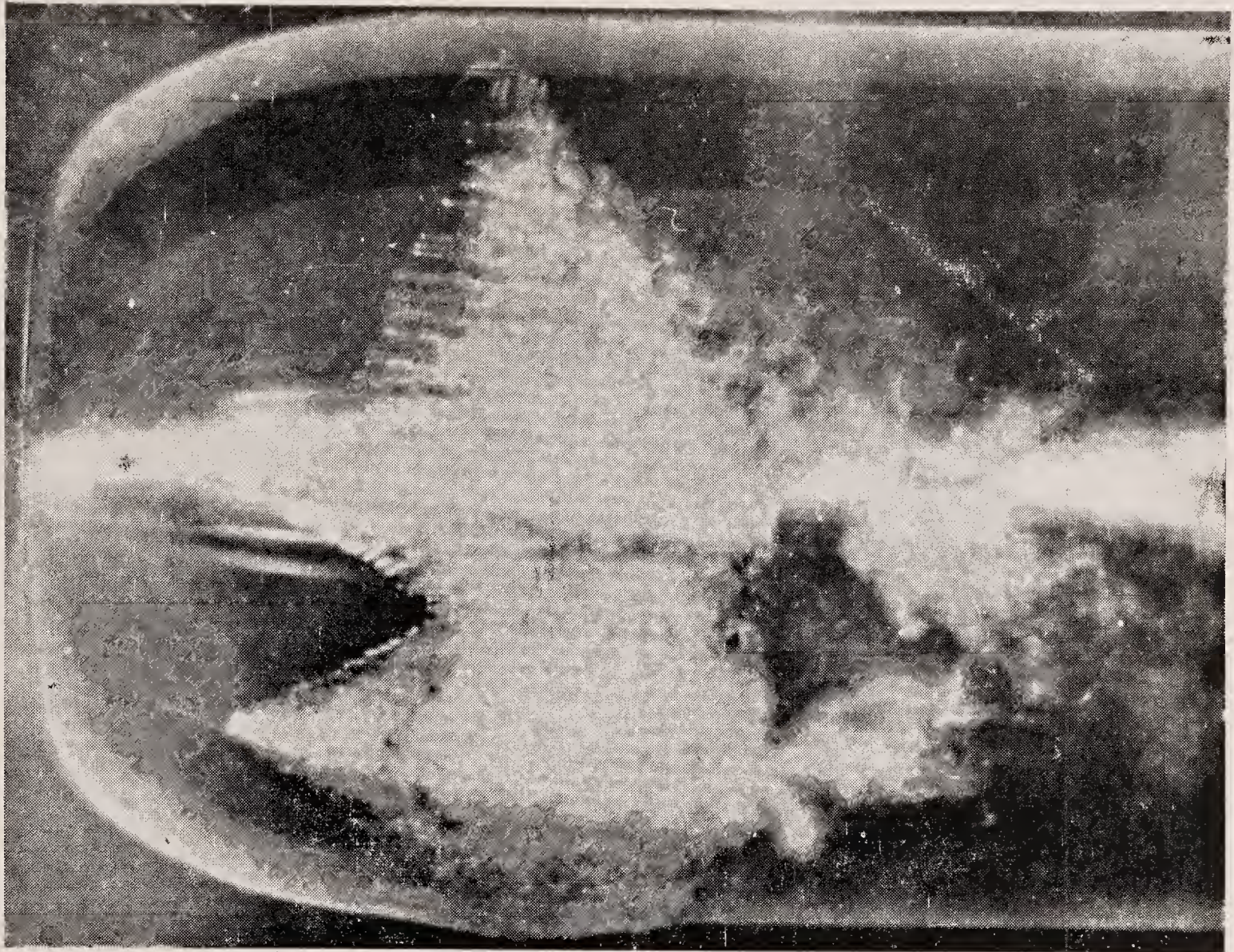


Figure 3. Photograph illustrating spot cavitation. The flow is from left to right. (After Acosta & Hamaguchi 1967.)

Wind tunnel tests on slow-running vertical-axis wind-rotors

S SIVASEGARAM

Department of Mechanical Engineering, University of Peradeniya, Peradeniya,
Sri Lanka

MS received 8 January 1981

Abstract. This paper summarises the results of investigations on the Savonius-type, slow-running, vertical-axis wind-rotors as well as on rotor designs of different subclasses under comparable design and test conditions. It is seen that the performance of the conventional Savonius rotor could be considerably improved upon and the best results are achieved by using two-bladed rotors with a more sophisticated sectional profile than in the conventional design. Rotors with several blades, although capable of considerably higher performance than the Savonius rotor, do not appear to be as good as those with two blades and improved sectional geometry.

Keywords. Wind power; vertical-axis wind-rotors; model tests on wind-rotors; fluid mechanics.

1. Introduction

The oldest known windmills are of the resistance-type operating about a vertical axis. Some refined versions of these ancient windmill designs are still in operation in parts of Asia. Although several attempts were made over the centuries to improve them, the performance (measured in terms of the power coefficient C_P) remained poor compared to that of even the less refined versions of horizontal-axis wind-rotors. The design of Savonius, now well known as the Savonius rotor (figure 1), showed considerable improvement on the performance of earlier designs. Nevertheless, the performance of the Savonius rotor was still low (C_P around 0.15) compared to its horizontal-axis rivals. Bach (1931) modified the sectional profile (figure 2) of the rotor blade which resulted in a considerable increase in the power coefficient. Savonius-type rotors, despite their low power coefficients, have certain advantages namely, their direction-independent operation, simple geometry and high starting torque, which make them suitable for certain applications such as rural water pumping (see Bodek 1965; Govindaraju & Narasimha 1978; Makhijani 1976; and Lysen *et al* 1978). However, since the work of Bach no attempt was made until the mid-seventies to improve the performance of the conventional Savonius rotor. This lack of interest was not confined to the Savonius-type rotors but extended to wind rotors in general, with isolated exceptions.

Interest in wind power was revived in the post-war period particularly with the recognition that fossil fuels were being depleted and oil prices were increasing. Newman (1974), Shankar (1976) and Sheldahl *et al* (1978) are among those who investigated the performance of a limited variety of two- and three-bladed rotors of the Savonius type. Khan *et al* (1975) tested a rotor design which was a further

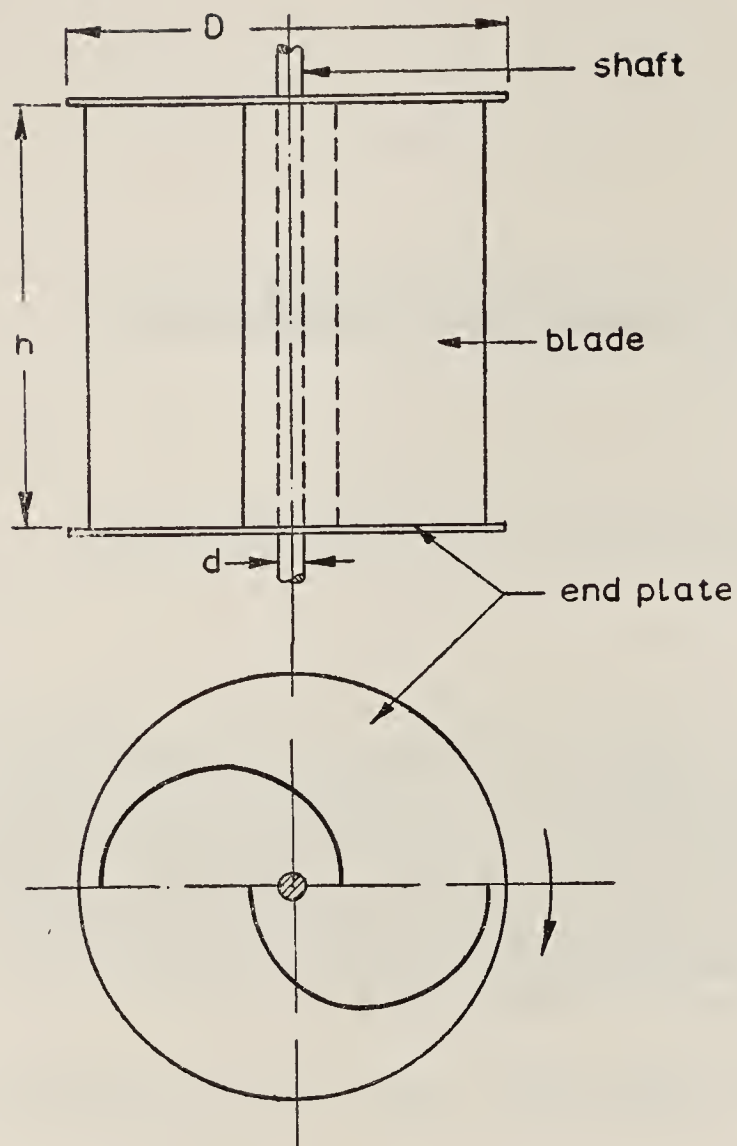


Figure 1. The Savonius rotor in elevation and in sectional plan.

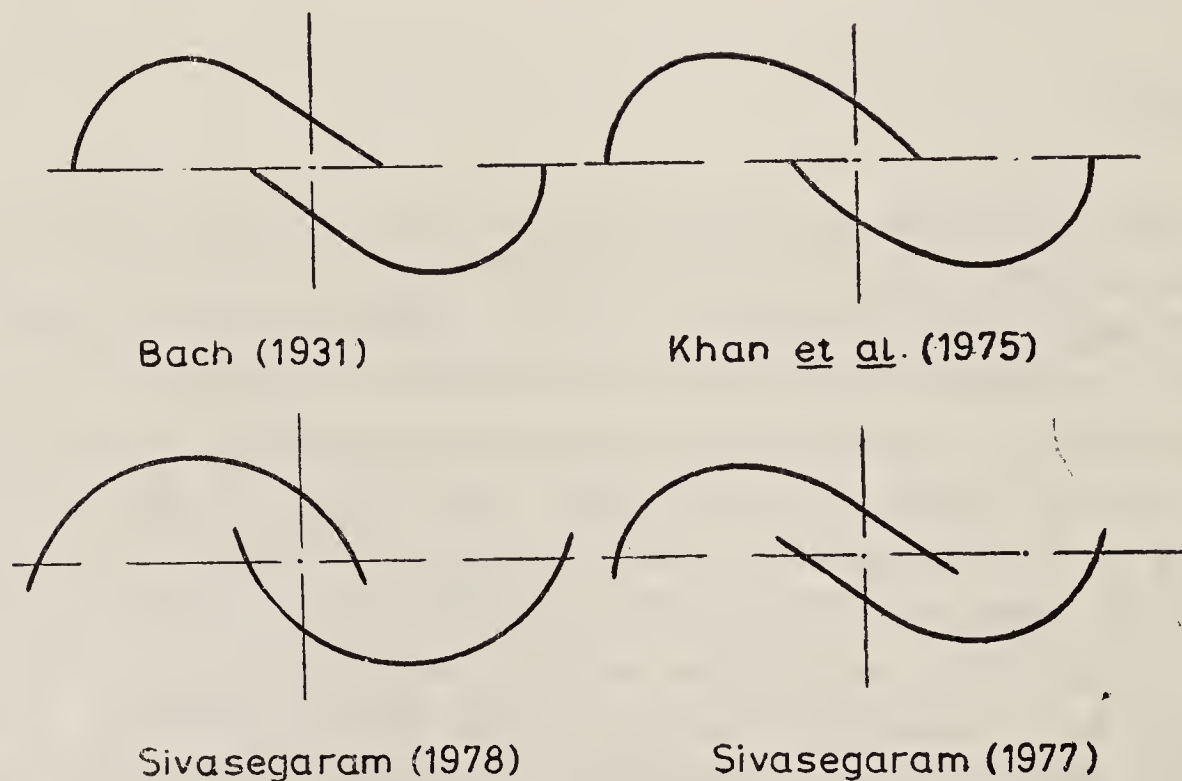


Figure 2. Sectional geometries of some two-bladed rotors.

modification of the design of Bach (1931); they claimed a large increase in power coefficient compared to the conventional Savonius rotor, but their experimental technique had major errors and the improvement, although real and considerable, was, perhaps, more modest than the authors claimed. Besides these, there were other tests done on the Savonius rotor, but none of these constituted a systematic experimental investigation of the rotor, so as to improve its performance (see Steyn 1975; Meel & Hengeveld 1977).

The difficulty of carrying out a detailed experimental study is not hard to recognize. The rotor section itself involves several design parameters and it would also be necessary to investigate the effects of several other parameters such as the Reynolds

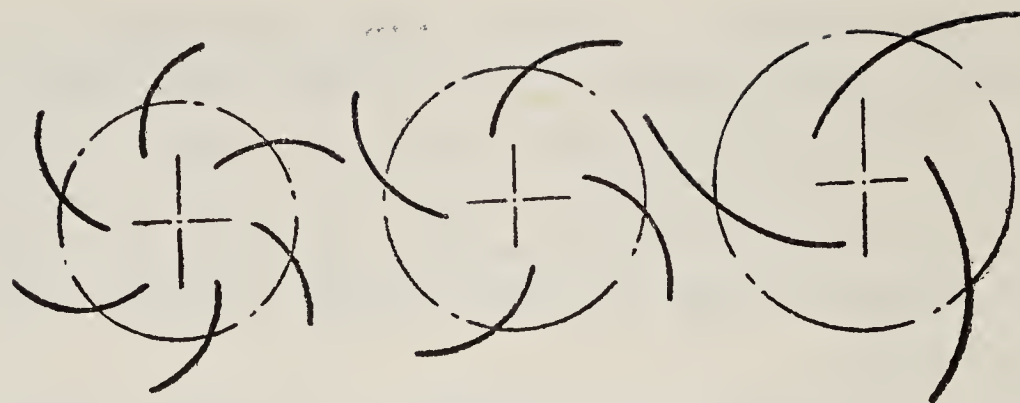
number, the wake aspect ratio ($r_a =$ the ratio of the rotor height h_1 to twice the rotor tip radius R_t), the rotor shaft diameter d , in the event of the shaft passing through the rotor section, and the rotor end plate diameter D . No theoretical method seems possible, at present or in the near future, to predict the performance of this class of rotors. The only theoretical predictions which could be made concern the qualitative nature of the influence of the Reynolds number and that of the wake aspect ratio (see Lissaman 1976).

Another problem confronting the investigator is the large disparity between the experimental findings of different workers who have studied the performance of effectively the same design of rotors. The effect of wind-tunnel blockage appears to be a major contributor to the observed differences. Tests carried out on rotor models placed inside wind tunnels appear to give increased power coefficient values whereas tests done on models placed outside a wind-tunnel in the jet issuing from the wind-tunnel tend to give smaller power coefficient values. The reliability of the results of field tests is hampered by large uncertainties in the measurements. Jansen (1976) who tested a horizontal-axis wind-rotor in the jet issuing from a wind-tunnel observed that the 'blockage' effect was negligibly small for the rotor (whose size was about half that of the tunnel exit) placed in the core of the jet, about one half of the tunnel diameter away from the exit. The error due to blockage effects in tests done outside wind tunnels, although likely to be small and substantially lower than for tests inside wind-tunnels, should not be ignored, especially where there is no reliable way of quantifying the error and ensuring that the final uncertainty is insignificant.

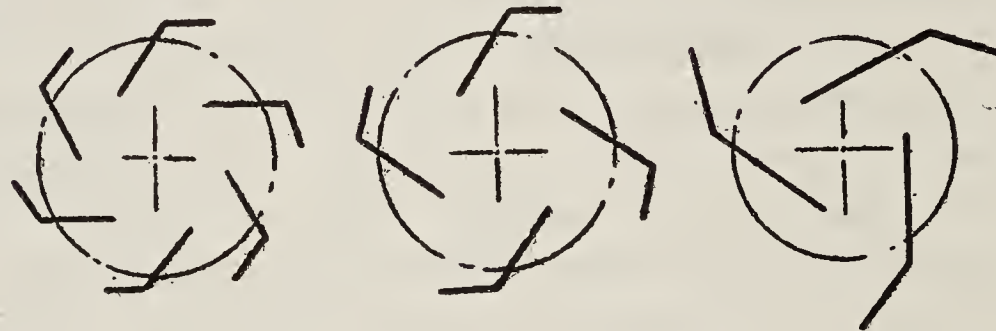
One economical and valid approach will be to construct the models to comparable dimensions and carry out the tests under matching test conditions. Placing the models of more or less the same overall dimensions at the same location relative to the wind tunnel exit and carrying out tests at the same wind speed would certainly permit a valid comparison of the performance of the different models under these conditions. Comparisons between different sources may be possible provided that the sources have at least one identical rotor configuration in common and all tests within the same source are done under comparable test conditions.

2. The present work

An investigation of Savonius-type rotors with blades of circular arc section, numbering from two to six (see figure 3) revealed the existence of certain optimum design parameters (Sivasegaram 1978a). In this study four parameters relating to the sectional geometry, namely, number of blades, arc angle of blade, size of blade (expressed nondimensionally as a fraction of the blade pitch circle radius or of the rotor tip radius) and the angle of setting of the blade, were considered. The rotor performance, however, was not excessively sensitive to the geometric parameters. This investigation was followed by an investigation of the performance of rotors with angled blades, which could be fabricated out of timber relatively easily (Sivasegaram 1976). One more geometric parameter was taken into account, namely, the angle between the two arms and the ratio of the lengths. The performance of the rotors with two or three blades was poor irrespective of blade geometry. Six-bladed rotors with asymmetric blades of 60° angle gave performances comparable with those of rotors of circular arc section. On the basis of these findings, an extensive investigation



Sivasegaram, 1978



Sivasegaram, 1976



Sivasegaram, 1977

Figure 3. Sectional geometries of rotors with several blades.

of rotors with a blade section composed of a circular arc and a straight line, and the blades numbering two to six again, was carried out (Sivasegaram 1977).

It will be clear that rotor configurations with blades of circular arc section are only a special case of the more complex configuration referred to above. (The circular arc section of figure 4 will correspond to the section shown in figure 5 with $\theta = S/R_B$.) The tests carried out at a wind speed of around 16 m/s on rotors with blades of circular arc section indicated that rotors with three, four or six blades could give 10% more power than a conventional Savonius rotor of the same size, and that the two-bladed rotor with optimum sectional configuration gives an even larger power output (see figures 6 and 7). The investigations on rotors with blades of more complex geometry, carried out at a nominal wind speed of around 18 m/s, indicated that modifications to the geometry of the blades did not result in significant improvement in the performance of the rotors with several blades; however, the performance of the rotors with two blades showed a marked improvement in performance over that for the optimum sectional profile with circular arc blades (see figure 8).

Although there was no major reason to doubt the validity of the conclusions of the model studies, the comparisons were not adequately precise for the following reasons: the model tests were not always carried out at the same wind speed; the rotors, although of the same height throughout, had varying lateral dimensions

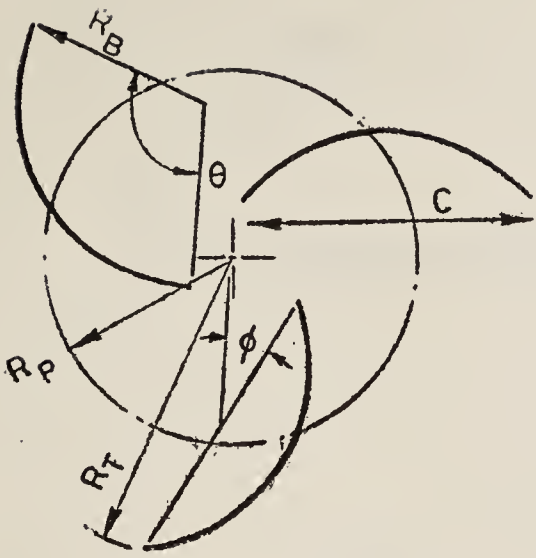


Figure 4. Geometric parameters of rotors with circular arc blades.

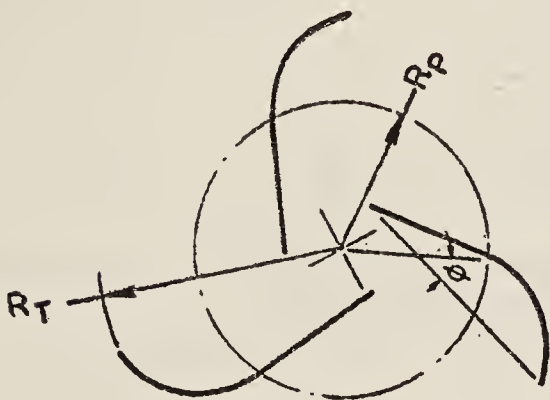


Figure 5. Geometric parameters of rotor with more complex blades.

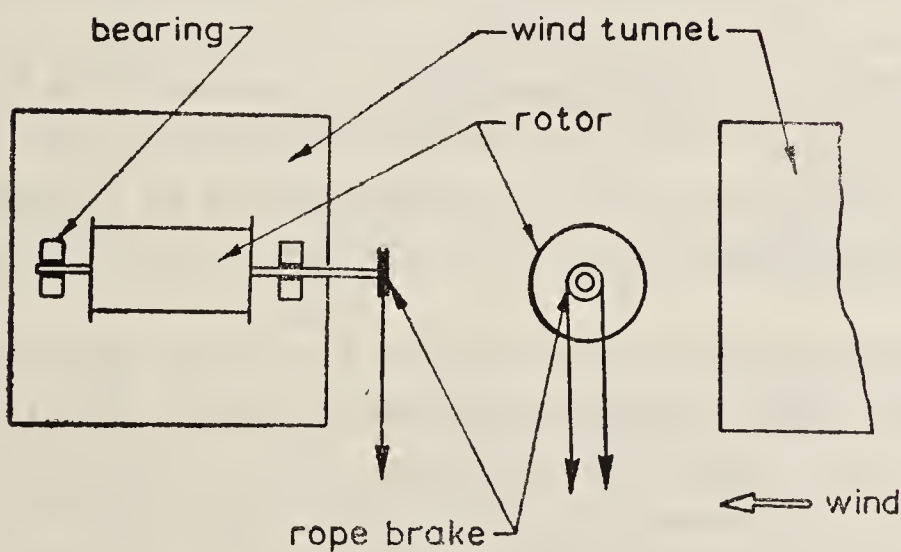
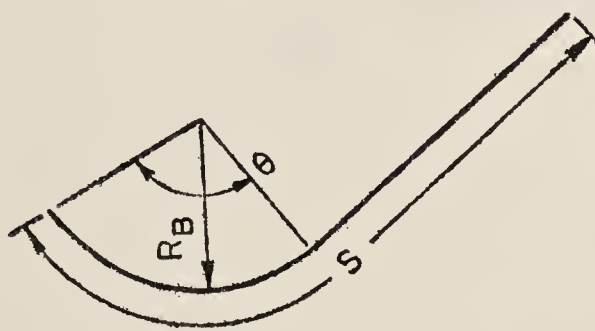


Figure 6. The experimental set-up.

resulting from the need to vary both the blade width and the angle of setting of the blade; the rotor end plate was selected so that it completely covered the blade tips and the influence of the dimension of the end plate was not known; and the extent of the influence of the rotor shaft, which ran through the working section of the rotor, could be of particular importance in rotors with two blades.

The influence of secondary parameters such as the Reynolds number, the wake aspect ratio, the diameter of the end plate and the shaft radius was studied by Sivasegaram (1978b) (see figures 9, 10 and 11). These observations are in qualitative

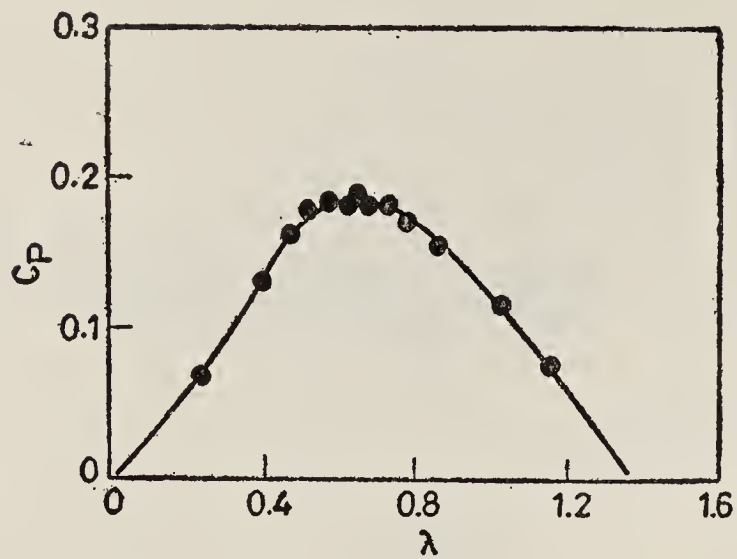


Figure 7. A typical power-speed curve.

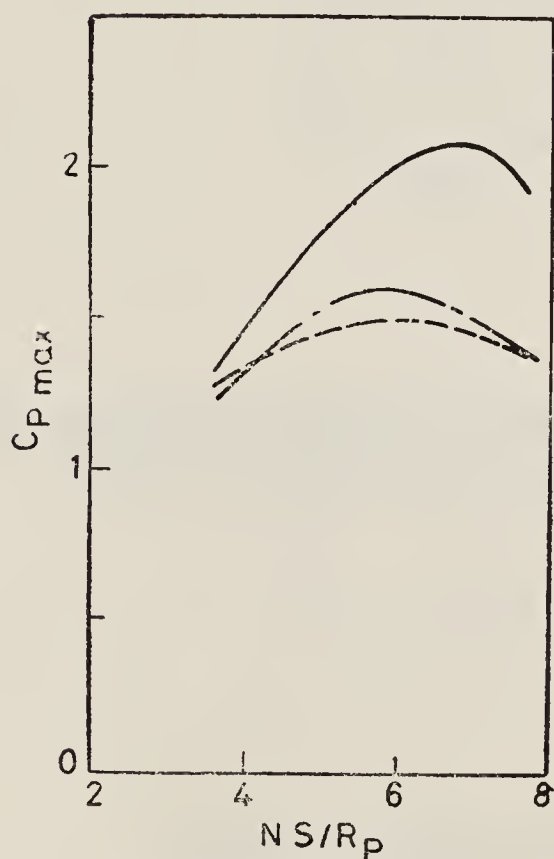


Figure 8. Dependence of maximum power coefficient on blade area parameter.

- $n = 2, S/R_B = 3.11, \theta = 127^\circ;$
- · - $n = 3, S/R_B = 2.83, \theta = 99^\circ;$
- - - $n = 6, S/R_B = 1.11, \theta = 66.$

agreement with those of Newman (1974), Bach (1931) and Lissaman (1976) in the case of the Reynolds number. The only available experimental studies of the influence of wake aspect ratio by Sivasegaram (1978b) are again in qualitative agreement with the predictions of Lissaman (1976), who suggests that the influence of wake aspect ratio is marked for values of $r_a < 2$. The experiments seem to confirm this and an r_a value close to 1.5 appears to be both realistic for design and for not having a large deviation from the performance at $r_a = 2$.

The findings about the size of the end plate indicated that as long as its diameter was not far in excess of the rotor wake width or was not significantly smaller than the rotor wake width the performance was not significantly affected. The end plate diameters in the investigations referred to in Sivasegaram (1976, 1977 and 1978a) were well within this safe margin. The influence of shaft diameter was found to be insignificant as long as the shaft diameter was small compared to the space available for air flow. None of the models tested, or for that matter no full-scale rotor, had 'air-gaps' which were narrow enough to permit interference by the shaft.

The effect of Reynolds number and wake aspect ratio could be quantified. As mentioned earlier, the heights of the models were kept equal while the lateral dimensions were subject to a small variation from model to model. The influence of this variation is two-fold: an increase in the wake width implies a reduction in the wake aspect ratio; it also means an increase in the Reynolds number based on the lateral

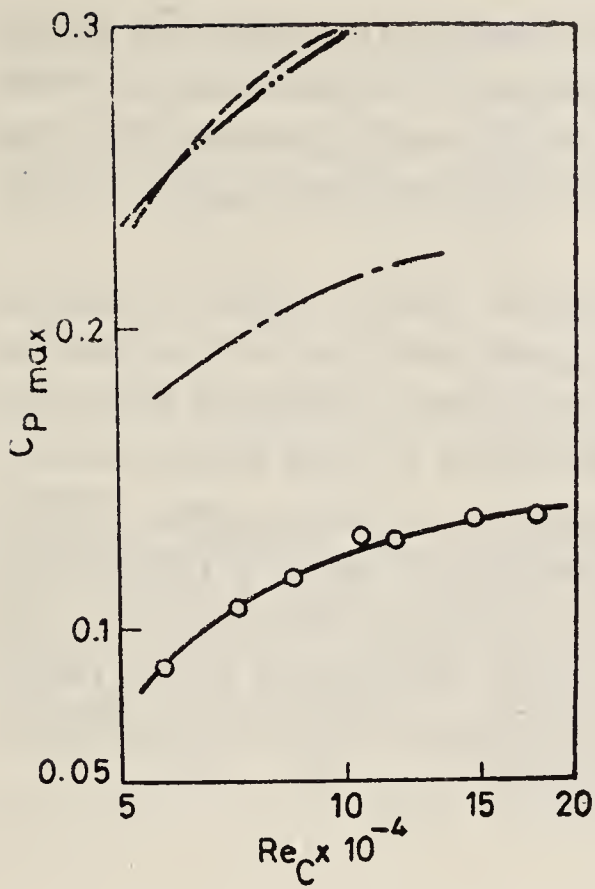


Figure 9. The influence of Reynolds number on performance.

○—○ Sivasegaram, three-bladed rotor;
 - · - Bach;
 - - - Newman.

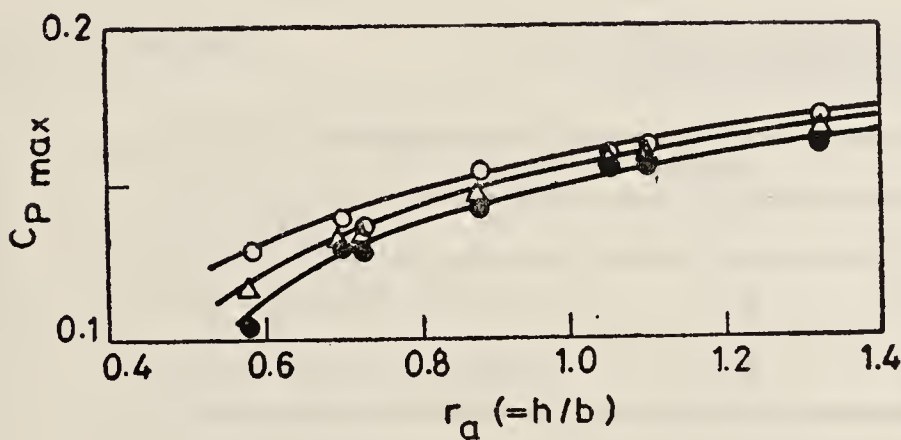


Figure 10. The influence of wake aspect ratio on performance of a three-bladed rotor.

● Re = 85,700; △, 105,500;
 ○, 117,000.

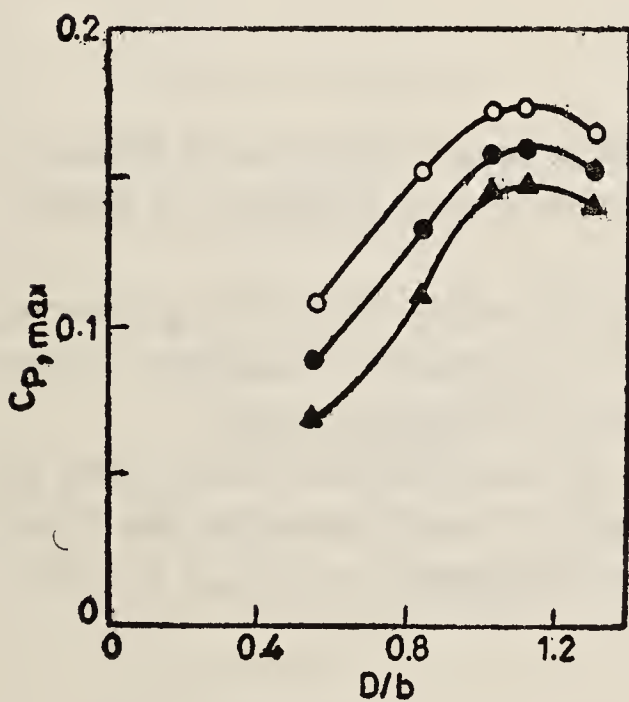


Figure 11. Influence of diameter of end plate on performance. ○, $h/b=1.24$; ●, 1.04 ; △, 0.83 .

dimension of the rotor (but not in the one based on the chord length of the blade). In comparing performances of rotors, one may either use the overall dimensions of the rotors or the total area of blading as the criterion. The former is more consistent with the use of the power coefficient C_P as the criterion of performance. The latter is more related to power output per unit mass of rotor and has also been used in the model studies of Sivasegaram (1977, 1978b). In the case of the former the effects of an increase in Reynolds number and of a decrease in wake aspect ratio tend to

oppose each other, and the net effect will be small if the fractional change in the lateral dimension is small (of the order of 10% or so). In the case of the latter, comparisons between the performances of rotors of equal height will be valid, provided that the wake aspect ratios are not too small ($\ll 1$) and the Reynolds numbers based on blade chord remain essentially the same.

The comparisons of the models tested by Sivasegaram (1977, 1978b) could be considered valid in the main for models with sectional geometry close to the optimum for the given blade section, had due corrections been made for the effect of Reynolds number. It was therefore decided that models with sectional profiles corresponding to the optimum profiles determined by the investigations of Sivasegaram (1977, 1978b) would be made to have the same overall dimensions and tested at equal wind speeds, and the results compared with those for a conventional Savonius rotor of optimum sectional geometry and having the same overall dimensions as the other models. Tests were carried out on models of 200 mm height and 150 mm wake width placed in 18 m/s wind. The results are presented in table 1.

Table 1. Values of ratio

$\frac{\text{maximum achievable power coefficient for class of rotor}}{\text{maximum power coefficient for Savonius rotor}}$

Blade section	Number of blades			
	2	3	4	6
Figure 4	1.25	1.1	1.1	1.1
Figure 5	1.45	1.15	1.1	1.1

3. Conclusions

(i) The maximum achievable power coefficient from a rotor with several blades is not highly sensitive to blade geometry. The achievable power coefficient is slightly more than that for a conventional Savonius rotor.

(ii) The performance of rotors with two blades is highly sensitive to blade geometry, and by proper design of blade and rotor geometries it is possible to achieve a large improvement over the performance of the conventional Savonius rotor.

(iii) Even simple modifications to the geometry of the Savonius rotor, such as using blades with arc angles smaller than the usual 180° and increasing the blade overlap without very much altering the gap between the blades, can result in a substantial increase in output.

4. Recommendations

(i) In designing full-scale rotors the wake aspect ratio should be such that the operating Reynolds number is adequately large while at the same time the wake aspect ratio is not too small.

(ii) The possibility of further improving the performance of two-bladed rotors deserves to be investigated. A thorough survey of the performance of rotors with

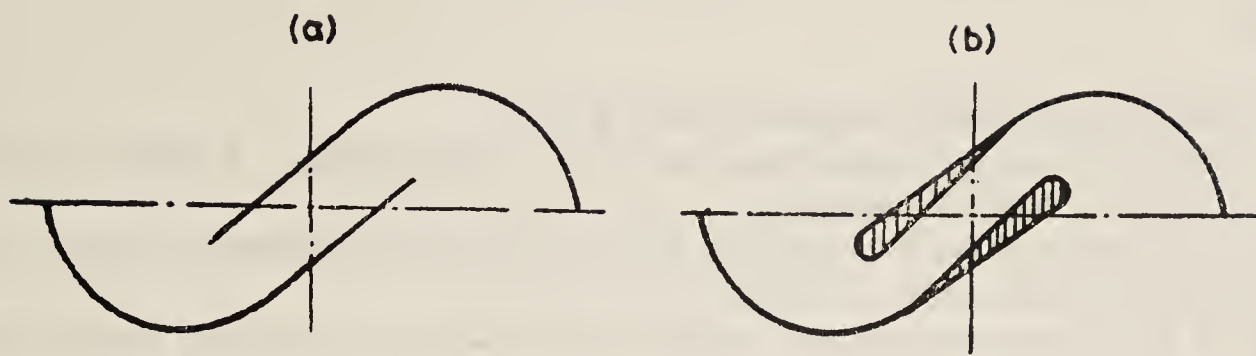


Figure 12. Sectional profiles of high performance rotors. a. rotor (Sivasegaram 1977), $N = 2$, $\theta = 127^\circ$, $S/R_B = 3.11$, $S/R_p = 2.8$, $\phi = 10^\circ$. b. Suggested profile.

complex blades of spiral section or with blades of section made of two arcs of different radii (see Khan *et al* 1975, figure 2) may be worthwhile, even if further improvements are likely to be relatively small. Blade geometries of the type shown in figure 12b are likely to improve rotor performance.

(iii) Other means of improving performance, such as the use of concentrators and diffusers, also deserve to be investigated.

List of symbols

b	rotor wake width
C	blade chord
C_p	power coefficient
D	diameter of end plate
d	shaft diameter
h	height of rotor
N	number of blades
P	power output from rotor
r_a	wake aspect ratio
Re	Reynolds number
R_B	radius of curvature
R_p	pitch circle radius
R_t	blade tip radius
S	blade sectional length
V	wind speed
λ	tip speed ratio
ω	angular velocity of rotor
ϕ	angle of setting
ρ	density
θ	blade angle

References

- Bach von G 1931 *Forsch. Gebeite. Ingenieurwesens* 2 218
- Bodek A 1965 *How to construct a cheap wind machine for water pumping*. Leaflet 5, Brace Research Institute (Canada: McGill University)
- Govindaraju S P & Narasimha R 1978 Paper 0117, *Proc. Int. Solar Energy Congress*, New Delhi, also 1979 *Proc. Indian Acad. Sci.* C2 67
- Jansen W A M 1976 *Horizontal axis fast running wind turbines for developing countries*. SWD 76-3, (Amersfoort, Netherlands, SWD)
- Khan A U, Duff B, Keuther D O & McMennamy J A 1975 *Rice machinery development and mechanisation research* (Phillippines: IRRI) Report 21
- Lissaman P B S 1976 *Wind energy systems* (Cranfield, U K: BHRA) Paper C-2
- Lysen E H, Bos H G & Cordes E H 1978 *Savonius rotors for water pumping*, SWD 78-2 (Amersfoort, Netherlands: SWD)
- Makhijani A 1976 *Bull. Atomic Scientists* June 14
- Meel J V & Hengeveld D 1977 *Wind energy, a bibliography*, Parts 3 & 4 (Netherlands: Eindhoven University)
- Newman B G 1974 *Wind energy*, Proc. Symp., Sherbrooke, Canada (Canada: McGill University) p. 116
- Shankar P N 1976 *The effect of geometry and Reynolds number on Savonius-type rotors*. AE-TM 3-76 (Bangalore: Natl. Aero. Lab.)
- Sheldahl R E, Blackwell B F & Feltz L V 1978 *J. Energy* 2 160
- Sivasegaram S 1976 *Engineer (Sri Lanka)* 4 26
- Sivasegaram S 1977 *Wind Engg.* 1 207
- Sivasegaram S 1978a *Energy* 3 23
- Sivasegaram S 1978b *Wind Engg.* 2 49
- Steyn R V 1975 *Wind energy, a bibliography*, Parts 1 & 2 (Netherlands: Eindhoven University)

AUTHOR INDEX

A		Betchov R	129
Abbett M	222	Bevans J T	274
Abramowitz M	87	Biolsi L	274
Acharya M	56	Bippes H	131
Acosta A J	287, 290, 292, 293, 299	Birch S F	78
Acton E	18, 37	Bjerknes J	213
Adrian R J	32	Black T J	55
Alksen A Y	222	Blackwelder R F	31, 54, 55, 140
Almgren D W	280	Bodek A	301
Alt R E	281	Boerstoeel J W	223
Amoh H	281	Bogar T J	56
Ananthakrishnan R	202	Borucki L	276
Antonia R A	55, 59, 75	Bos H G	310
Aoki D	280	Bouthier M	133
Arai N	275	Bradshaw P	36, 39, 111, 113
Arakeri V H	287, 290-292, 294-296	Brashears M R	223
Ardanuy P	215	Brennen C	293-295
Aref H	37	Brodkey R S	36, 55
Armstrong A H	293	Browand F K	37, 40, 50, 51, 58
Asai M	140	Brown G	17, 18, 28, 36, 37, 51, 53, 55
Asaka S	27	Brown G L	78
Ashurst W T	37	Brunn H H	67
Atwell N P	123	Buckley F T	80
Augstein E	204	Buneman O	78
Azad R S	32	Bushnell D M	31, 79, 113
		Busse F H	183
B		C	
Bach von G	301, 302, 306	Cain A B	37
Back L H	221, 237	Calderon A P	263
Badrinarayanan M A	2, 4, 55	Campbell W A Jr	276
Bailey F R	253	Cantwell B	138
Baker C B	76	Cantwell F J	23, 24, 26-28, 37, 55, 75
Balasubramanyam	182	Carr L W	56
Bandyopadhyay P	37, 55	Cebeci T	111, 112, 133
Banerjee S	32	Chakrabarty S K	223, 259, 260
Bareiss L E	278	Champagne F H	19-21, 31, 36, 37, 53, 54, 57, 63, 76
Barker S J	23, 49, 51	Chambers A J	78
Barnett T P	213	Chan S T K	223, 240
Barsoum M L	28	Chandrsuda C	37, 50, 51, 53
Batchelor G K	95-98, 100, 152	Chaplygin S A	222
Batt R G	50	Charney J G	80, 209, 210, 215
Bauer F	223	Charters A C	137
Baxter D R J	62	Chatwani A U	278
Beatty K O	30	Chen W Y	93
Beckwith I E	113	Cheng H K	223
Belotserkovskiy O M	248	Cherry T M	221, 222, 233, 235, 241, 243, 244
Benney D J	126, 129		

- | | | | |
|-----------------|--|---------------------|--------------------|
| Chew Y T | 80 | E | |
| Chin D T | 133 | | |
| Chin S C | 140 | Eckelmann H | 55 |
| Chou L | 114, 215 | Elder J W | 23, 24 |
| Chou Pei-Yuan | 83 | Eliassen A | 209 |
| Chow S | 215 | Eller A I | 289 |
| Chuan R L | 276 | Emmons H W | 22, 222, 233, 240 |
| Chushkin N N | 222, 242, 244, | | |
| Clark A R | 37, 40, 51-53, 65, 67, 74, 76, 77 | F | |
| Clarkson M H | 133 | | |
| Claus H H | 152 | Falco R | 37, 55 |
| Clifford S F | 75 | Falco R E | 24 |
| Cochran W G | 134 | Favre A | 93, 94 |
| Cockrell D J | 32, 123 | Feigenbaum M J | 195 |
| Colak-Antic P | 150 | Ferrari C | 259 |
| Cole J D | 223, 240, 253, 255 | Ferrel W | 203 |
| Coles D | 17, 21, 23-26, 30, 37, 49, 51, 53, 109, 110, 140 | Ferriss D H | 78, 123 |
| Comte-Bellot G | 22, 55 | Ferziger J H | 78 |
| Corcos G M | 37, 59 | Feshbach H | 181 |
| Cordes E H | 310 | Ffowcs-Williams J E | 36 |
| Corke T | 27 | Fiebig M | 276 |
| Corke T C | 56 | Fiedler H E | 37, 53, 76, 77 |
| Corrsin S | 103 | Findlater J | 211 |
| Couët B | 37 | Fisher M J | 79 |
| Craggs J W | 249 | Flynn H G | 288, 289 |
| Craik A D D | 128 | Fohl T | 27 |
| Crichton D G | 78 | Foss J F | 77 |
| Crocco L | 222 | Frankignoul C | 213 |
| Crow S C | 31, 36, 37, 54, 57, 63, 76 | Frankl F N | 222 |
| Cuffel R F | 237 | Frazine D F | 281 |
| Curry J H | 190 | Frenkiel F N | 55 |
| | | Friedman D | 33, 81 |
| | | Fujita H | 32 |
| | | Furukawa M | 264 |
| D | | | |
| | | G | |
| Daily J W | 298 | | |
| Daly B | 117 | Gabron F | 280 |
| Damms S M | 18 | Gad el Hak M | 24, 139 |
| Danel F | 80 | Gadgil S | 201, 207, 213, 220 |
| Das P K | 175, 177 | Garabedian P R | 223 |
| Davies P O A L | 62, 75 | Gartshore I S | 50 |
| Davis R E | 213 | Gates E M | 292, 293 |
| Dawson J P | 272 | Gaviglio J | 79, 103 |
| Deardorff J W | 120, 183, 185 | George W K | 79 |
| de Vries G | 223, 242 | Gier H L | 248 |
| Dhawan Satish | 1, 23, 55 | Ginevskiy A S | 76 |
| Dimotakis P | 36, 140 | Gilbrech D A | 20 |
| Dinkelacker A | 37, 56 | Goldschmidt V W | 74 |
| Doenecke J | 274 | Goldstein S | 222 |
| Dorodnitsyn A A | 221, 222, 242, 243 | Görtler H | 131, 222 |
| Dreaper J S | 276 | Govindaraju S P | 301 |
| Dryden H L | 22 | Gradshteyn I S | 86 |
| Duff B | 310 | Grallaher W | 250 |
| Dumas R | 79, 103 | Grant H L | 36, 55 |
| Durham F P | 221, 237 | Gray W M | 205 |
| Dziomba B | 79 | Green J R | 222 |

Greenspan H P	129	I	
Gregory N	131-133, 135-137	Ide S	273
Grigg H R	26	Iida S	140
Gross M B	223	Imai I	221, 222, 241-244
Grossman B	223	Ishida Y	110, 111
Guckenheimer J	195	Ishimoto T	274
Guernsey C S	276	Itagaki H	280
Guezennec Y	78	Ito A	131
Gullstrand T R	222, 258	Itoh N	127, 130
Gupta A K	137	Iuchi M	141
H		J	
Hafez M M	223, 243	Jameson A	223
Hale J C	20	Jansen W A M	303
Hall I M	221, 222, 233, 237, 238	Jayaraman R	80
Hama F R	129	Jia Zhan Xue	229, 231, 233, 236, 240, 242
Hamaguchi H	293, 299	Jimenez J	28, 37
Hammitt F G	298	Johnson D A	27
Handa N	138, 139	Johnson G M	26
Hanjalic K	117	Johnson R F	78
Hannan D E	291	Johnson V E	292
Hanratty T J	55	Jones B G	32
Hansen H	223	Jones W P	114
Haritonidis J H	23, 24, 55		
Harlow F H	114, 117	K	
Hasan M A Z	22, 65	Takehi Y	154
Hasan Y A	32	Kambe T	27
Hassler H	150	Kanamori Y	280
Hasegawa K	154	Kaplan R E	31, 80
Hasselmann K	213	Karashima K	275
Head M R	37, 55, 109	Kawakami A	280
Heaslet M A	257	Kawamura H	114, 115
Hefner J N	56	Kawall J G	31
Heidrick T R	32	Keffer J F	31, 36
Helland K N	24	Keller H B	133, 290, 292
Hengeveld D	302	Kells L C	128
Hernan M A	28, 37, 51	Kempton A J	36
Herring H J	120	Keuther D O	310
Heskestad G	75	Khan A U	301, 309
Heslin T M	275	Kibens V	57
Hessel M	78	Kida S	103
Hinze J O	52	Kim J	37
Hirst E A	109, 110	Kistler A L	103
Ho C M	51	Kita Y	77
Hofez H M	223	Kitamura O	133, 134
Holt M	221-223, 237, 242	Klebanoff P S	2, 23, 24, 53, 55, 126, 128-130, 135
Howard L N	184, 185	Klebanoff R S	293
Hrubes J D	276	Kliegel J R	221, 222, 237, 238
Hsieh D Y	289, 292	Klies S J	71, 73, 77
Hubert L F	204	Kline S J	17, 30, 36, 37, 55, 108, 110
Huang Yung-Nien	83	Klopfer G H	221, 237
Huang T T	291	Kluwick A	259
Husain Z D	74, 76	Klunker E B	257
Hussain A K M F	35-38, 40, 41, 46, 47, 49-54, 57-59, 62, 65-68, 73-77	Knapp R T	288

- | | | | |
|---------------------|-----------------------------------|---------------------|----------------------------|
| Knight D D | 371 | Masson B S | 223, 242 |
| Kobayashi Y | 132, 133, 276 | Mathanson D | 271 |
| Kohama Y | 140 | Matsui T | 24, 27, 145, 149, 150, 153 |
| Komoda H | 140 | Matsushita T | 280 |
| Komatsu Y | 141 | Mattioli E | 21 |
| Korn D G | 223 | McMennamy J A | 310 |
| Kornfield J | 215 | Meel J V | 302 |
| Kovaszny L S G | 26, 55, 112, 128 | Mehta R D | 78 |
| Krishnamurti R | 183-185, 210 | Meier G A E | 78 |
| Krueger A F | 215 | Melinand J P | 80 |
| Krupp J A | 223 | Mensing P | 79 |
| Kuchemann D | 18 | Meseth J | 20 |
| Kuo Y H | 222 | Metcalfe R | 37 |
| | | Meyer T | 316 |
| L | | Michalke A | 39, 49 |
| | | Mihara T | 281 |
| Lamb H | 237, 242, 245 | Mikhlin S G | 262, 263 |
| Lan K M W | 215 | Mills R R | 96 |
| Landahl M T | 130 | Minami K | 154 |
| Landau L D | 152 | Minning C P | 264 |
| Lau J C | 77 | Mizushima J | 103 |
| Laufer J | 36, 37, 55, 58, 115 | Mizushina T | 22, 56 |
| Lauder B E | 113, 114, 117 | Mochizuki M | 135 |
| Laval D | 221 | Moin P | 37 |
| Lax P D | 222 | Mollo-Christensen E | 36 |
| Lee R L | 32 | Moore C J | 37 |
| Lehmann V | 280 | Moretti G | 222, 223, 242 |
| Leonard A | 37, 120 | Morkovin M | 123 |
| Levine J N | 221, 222, 237, 238 | Morkovin M M | 32 |
| Lieberstein H M | 223 | Morse P M | 181 |
| Liepmann H W | 37 | Muller W J C | 280 |
| Lifshitz E M | 152 | Mumford J C | 51, 74 |
| Lighthill M J | 36, 222 | Murakami M | 275, 278 |
| Lilly D K | 120 | Murata Y | 154 |
| Lim T T | 37 | Murman E M | 221, 223, 240, 253 |
| Lin C C | 126 | Murray B T | 37 |
| Lin Tong Ji | 222, 229, 231, 233, 236, 240, 242 | | |
| Lindgren E R | 19, 20, 22 | N | |
| Lindzen R S | 208 | | |
| Lissaman P B S | 303, 306 | Nagata H | 152 |
| Litt M | 133 | Nagib H M | 56 |
| Longuet-Higgins M S | 174 | Nakamura Y | 281 |
| Lorenz E N | 190 | Namias J | 213 |
| Lugovtsov B A | 26 | Narasimha R | 2, 5, 23, 55, 301 |
| Lumley J L | 36, 37, 40, 75 | Nayfeh A H | 133 |
| Lysen E H | 301 | Nee V W | 112 |
| | | Nelson L A | 276 |
| M | | Neppiras E A | 287 |
| | | Newman B G | 301, 306 |
| Magnus R | 223 | Ng K H | 114 |
| Makhijani A | 301 | Nielsen K T W | 27 |
| Malkus W V R | 183 | Nieuwland G Y | 223 |
| Marriott R S | 280 | Nishioka M | 129 |
| Marumo E | 123 | Nixon D | 259-261 |
| Maruyama T | 32, 80 | Nixton D | 223 |
| Maseev L M | 128 | Niyogi A K | 263 |
| Massier P H | 248 | Niyogi P | 253, 254, 258, 260 |

Norrie D H	223, 242	Rao G N V	4, 55
Nørstrud H	223, 253, 259	Reece G J	123
Norton D L	221, 237	Reid W J	100
Nutant J	129	Reissner E	250
O		Reiter E R	213
Obrien V	103	Reshotko E	20
Offen G R	37, 55	Rey C	80
Ogana W	258	Reynolds O	41, 221
Ohji M	105	Reynolds W C	32, 78
Ojha S K	7	Richards J M	26
Okude M	27, 149	Richardson F M	30
Oldaker D K	56	Richtmyer R	222
Oler J W	74	Riehl H	205, 213, 217-219
Olivari D	31	Riemann B	226
Orszag S A	121, 128	Riley J	78
Oshima K	269, 271, 272, 274-276	Riley J J	31, 140
Oshima Y	27	Rockwell D	80
Oster D	61, 77	Rockwell D O	74, 76
Oswatitsch K	222, 226, 253, 255, 259, 260	Rodi W	114
Owen F K	27	Rosen A	278
P		Rosgen T	79
Pantulu P V	3	Roshko A	17, 18, 28, 36, 37, 53
Pao Y H	78	Roux J A	278
Parikh P G	56	Rubin Y	22
Park J J	280	Runstadler P W	32, 79
Parkin B R	287, 292	Ryan L F	27
Parthasarathy S P	7	Ryzhik I M	86
Pasch R	215	S	
Patterson G S Jr	121	Sabot J	22, 55
Payne F R	36	Saffman P G	62, 114
Perry A E	37, 55	Sakakibars S	280
Petersen R A	76	Santarelli F	281
Pfizenmaier E	76	Sargent L M	79, 140
Phan-Thien N	78	Saric W S	133
Plesset M S	289, 290	Sarpkaya T	20
Prabhu A	9	Sato H	135
Prandtl L	20, 113, 129	Sato K	280
Praturi A K	37, 55	Sato T	123
Proudman I	98, 100	Sauer R	221, 222, 237, 238
Pui N K	50	Savas O	23, 24
Purtell L P	52	Schachenmann A	76
Q		Schneider P	208
Quirk W J	215	Schon J P	37
R		Schraub F A	32, 79
Rajagopalan S	55	Schubauer G B	2, 23, 24, 126
Rall L D	262, 264, 265	Schumann U	117
Ramage C S	201, 202, 212	Scialdone J J	276, 278
Ramanathan Y	215	Scott H E	281
Ramaprian B R	76	Sekihara K	274
		Serra R A	221, 223, 233, 235
		Sforza P M	27
		Shacter P	140
		Shankar P N	301
		Sharkovsky A N	195
		Sharma L K	55

- | | | | |
|-----------------|------------------------|------------------|-------------------------------|
| Sheldahl R E | 301 | Teh E W | 80 |
| Shelton S | 221, 237 | Teitgen R | 20 |
| Shen S F | 223 | Theodorsen T | 55 |
| Sherman F S | 59 | Tennekes H | 40 |
| Shiozaki Y | 32, 80 | Thaper R | 195 |
| Shivaprasad B G | 80 | Thies H J | 77 |
| Siggia E D | 37 | Thomann H | 27 |
| Sikka D R | 207, 210, 213, 220 | Thomas A S W | 51, 55 |
| Simasalsi T | 222, 241 | Thompson C A | 74 |
| Simmons J E L | 19 | Tidstrom K D | 79, 126, 128, 129, 135, 293 |
| Simpson R L | 56 | Tiederman W G | 80 |
| Sinha M C | 177-179 | Tobak M | 132, 133, 137 |
| Sirkar K K | 55 | Tomotika S | 222 |
| Sivasegaram S | 301, 303-309 | Townsend A A | 36, 37, 40, 51, 91, 92, 95-98 |
| Smagorinsky J | 120 | Traci R M | 114 |
| Smith A M | 281 | Tricomi F | 222, 227, 259 |
| Smith A M O | 112 | Troutt T R | 50 |
| Smith C R | 55 | Tsien H S | 222, 225, 243 |
| Snyder H | 25 | Tso J | 40, 51, 74 |
| Sobieczky H | 223 | Tsujimoto K | 273 |
| Sokolov M | 68, 71, 75 | Tsunekawa M | 154 |
| South J G Jr | 249 | Turner J S | 26, 27 |
| South J | 221 | | |
| Southwell R V | 222 | U | |
| Sovran G | 32, 123 | | |
| Spalding D B | 113, 114, 117 | Uijlenhoel R R | 223 |
| Sperlein R F | 276 | | |
| Spreiter J R | 222, 255, 257 | V | |
| Sreenivasan K R | 5, 55 | | |
| Starr V P | 170 | Vallerani E | 19, 20, 31 |
| Steg L | 280 | Van Atta C | 24, 25, 30, 93 |
| Stegun I A | 87 | Van Maanen H R E | 22 |
| Stephens J B | 276 | Vasudeva B R | 80, 140 |
| Stern E | 20 | Viets H | 27 |
| Stewart R W | 26, 91, 92, 95, 97, 98 | Viswanath P R | 5 |
| Stewartson K | 130, 133 | Vivekanandan R | 4 |
| Steyn R V | 302 | Vlasov Y V | 76 |
| Stone P H | 208 | Von Karman | 222, 226, 243 |
| Stramigioli C | 281 | Von Neumann J | 121, 222 |
| Stuart J T | 126, 128 | Von Ringleb F | 222 |
| Suzuki K | 117, 118 | | |
| Swenson E V | 223 | W | |
| | | | |
| T | | Walker W S | 135, 136, 137 |
| | | Wallace D A | 278 |
| Takaki R | 28 | Watson J | 126 |
| Takamadate Ch | 140 | Webster P J | 215 |
| Takanashi S | 223 | Weidman P D | 77 |
| Takao T | 27 | Weinstein L M | 79 |
| Takematsu M | 132, 133 | Weir R A D | 78 |
| Tamada K | 222 | Wendroff B | 222 |
| Tanaka J | 123 | Whitehead J A | 183 |
| Taneda S | 27 | Whitham G B | 130, 165 |
| Tani I | 125, 126, 128, 135 | Widnall S | 62 |
| Tashiro T | 280 | Wilcox D C | 114 |
| Tatsumi T | 91 | Willis G E | 183, 185 |
| Taylor G I | 22, 75, 222 | Willmarth W W | 55, 56 |

Author Index

317

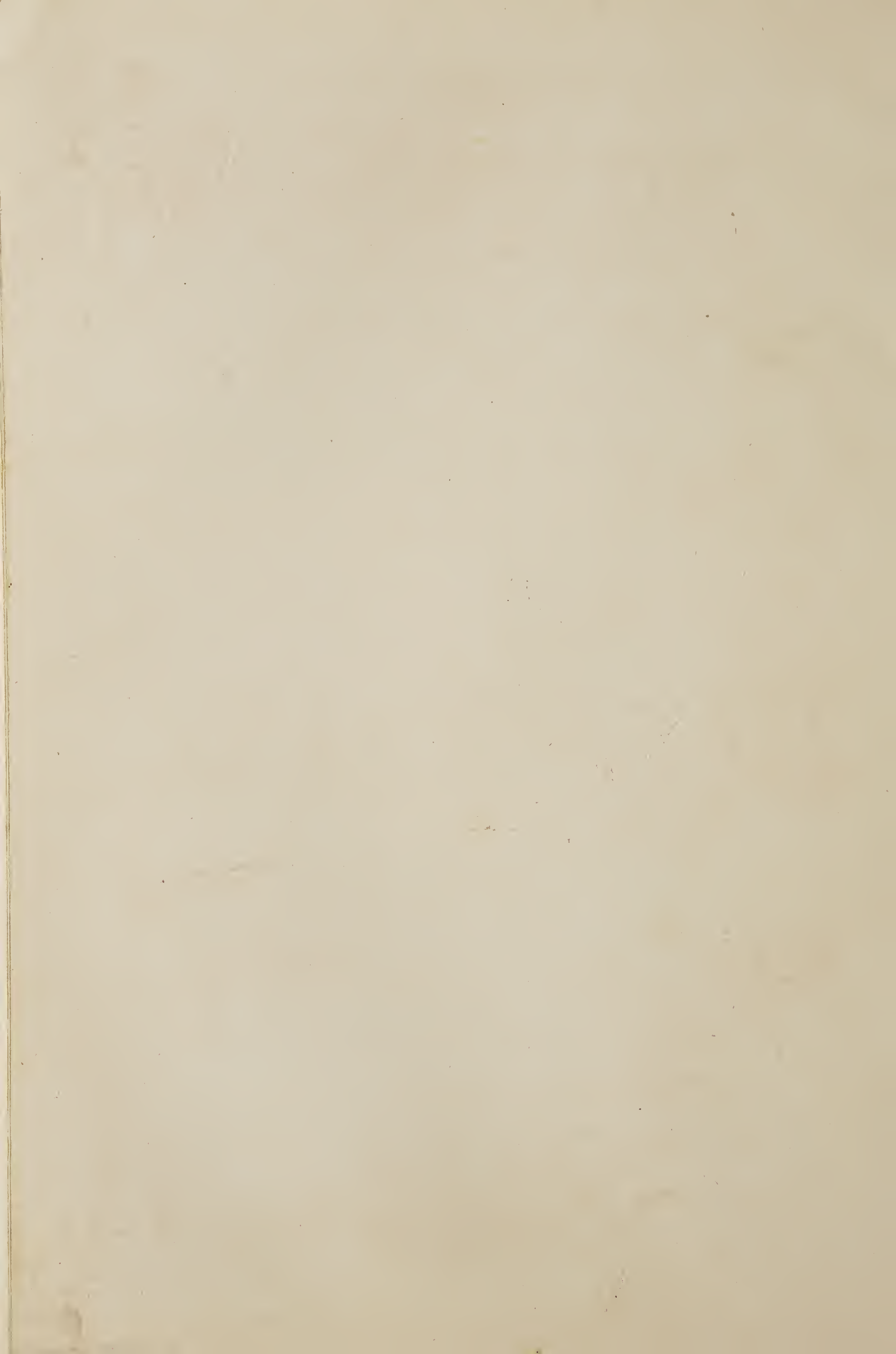
Winant C D	40, 51	Yellin E L	21
Winston J S	215	Yoshihara H	250
Wood B E	281	Young V Y C	248
Wood W L	271	Yule A	37, 40, 54, 67
Wu T Y	293		
Wynanski I	19-21, 23, 24, 49, 51, 53, 55, 61, 76, 77	Z	
Wyngaard J C	75	Zaman K B M Q	36, 50-52, 54, 57-59, 61-63, 65-67, 73, 75-77
		Zdravkovich M M	27
Y		Zedan M F	52, 76
Yajnik K	56	Zhenxue J	221
Yamada H	153	Zilberman M	23, 24, 75
Yamashita I	132, 133	Zito G	21
Yeh T T	93	Zygmund A	263

SUBJECT INDEX

- | | | | |
|--|-----|--|--|
| Atmospheric instabilities | | | |
| Fluid dynamics of the monsoon | 201 | | |
| Axisymmetric jets | | | |
| Role of coherent structures in turbulent shear flows | 35 | | |
| Base flows | | | |
| A glimpse of fluid mechanics research in Bangalore 25 years ago | 1 | | |
| Basin response | | | |
| Storm surges in the Bay of Bengal | 175 | | |
| Bay of Bengal | | | |
| Storm surges in the Bay of Bengal | 175 | | |
| Boundary layer | | | |
| Prospects for useful research on coherent structure in turbulent shear flow | 17 | | |
| Boundary-layer transition | | | |
| Three-dimensional aspects of boundary-layer transitions | 125 | | |
| Circulation of a vortex | | | |
| Flow visualization studies of vortices | 145 | | |
| Coherent structure | | | |
| Prospects for useful research on coherent structure in turbulent shear flow | 17 | | |
| Role of coherent structures in turbulent shear flows | 35 | | |
| Conditional sampling | | | |
| Role of coherent structures in turbulent shear flows | 35 | | |
| Core of a vortex | | | |
| Flow visualization studies of vortices | 145 | | |
| Couette flow | | | |
| Prospects for useful research on coherent structure in turbulent shear flow | 17 | | |
| Direct iteration scheme | | | |
| Transonic flow past thin wings | 253 | | |
| Eduction of large-scale structures | | | |
| Role of coherent structures in turbulent shear flows | 35 | | |
| Effects of initial condition | | | |
| Role of coherent structures in turbulent shear flows | 35 | | |
| Electrolysis method | | | |
| Flow visualization studies of vortices | 145 | | |
| Energy spectrum | | | |
| On the solutions of Navier-Stokes equations and the theory of homogeneous isotropic turbulence | 83 | | |
| Error estimate | | | |
| Transonic flow past thin wings | 253 | | |
| Flow cavitation | | | |
| Real-fluid effects in flow cavitation | 287 | | |
| Flow field computations | | | |
| Inviscid transonic flow field analysis | 221 | | |
| Flow past circular cylinder | | | |
| Inviscid transonic flow field analysis | 221 | | |
| Flow visualization | | | |
| Flow visualization studies of vortices | 145 | | |
| Fluid mechanics | | | |
| A glimpse of fluid mechanics research in Bangalore 25 years ago | 1 | | |
| Thermal and fluid mechanical problems in space flight | 269 | | |
| Görtler vortex | | | |
| Flow visualization studies of vortices | 145 | | |
| High subsonic flow | | | |
| Transonic flow past thin wings | 253 | | |
| Homogeneous isotropic turbulence | | | |
| On the solutions of Navier-Stokes equations and the theory of homogeneous isotropic turbulence | 83 | | |
| Hydrogen bubble technique | | | |
| Flow visualization studies of vortices | 145 | | |
| Importance of coherent structures | | | |
| Role of coherent structures in turbulent shear flows | 35 | | |
| Inception | | | |
| Real-fluid effects in flow cavitation | 287 | | |
| Instability | | | |
| Generation of large scale circulation in turbulent convection | 183 | | |
| Integral equation method | | | |
| Transonic flow past thin wings | 253 | | |
| Intertropical convergence zone | | | |
| Fluid dynamics of the monsoon | 201 | | |
| Kármán vortex street | | | |
| Flow visualization studies of vortices | 145 | | |
| Large-scale order | | | |
| Generation of large scale circulation in turbulent convection | 183 | | |
| Large scale organised motions | | | |
| Role of coherent structures in turbulent shear flows | 35 | | |
| Laval nozzles | | | |
| Inviscid transonic flow field analysis | 221 | | |
| Mixing layer | | | |
| Prospects for useful research on coherent structure in turbulent shear flow | 17 | | |

- Role of coherent structures in turbulent shear flows 35
 Modelling
 Mathematical modelling of turbulent shear flows 105
 Monsoon
 Fluid dynamics of the monsoon 201
 Navier-Stokes equations
 On the solutions of Navier-Stokes equations and the theory of homogeneous isotropic turbulence 83
 Nonlinear waves
 On finite amplitude water waves 165
 Phase average
 Role of coherent structures in turbulent shear flows 35
 Pipe flow
 Prospects for useful research on coherent structure in turbulent shear flow 17
 Prediction
 Mathematical modelling of turbulent shear flows 105
 Real fluid effects
 Real-fluid effects in flow cavitation 287
 Rebound of a vortex ring
 Flow visualization studies of vortices 145
 Roughness element
 Three-dimensional aspects of boundary-layer transition 125
 Separation
 Flow visualization studies of vortices 145
 Real-fluid effects in flow cavitation 287
 Separation bubbles
 A glimpse of fluid mechanics research in Bangalore 25 years ago 1
 Shear
 Mathematical modelling of turbulent shear flows 105
 Shock-free supercritical flow
 Transonic flow past thin wings 253
 Slip-through of a pair of vortex rings
 Flow visualization studies of vortices 145
 Smoke-wire technique
 Flow visualization studies of vortices 145
 Space flight
 Thermal and fluid mechanical problems in space flight 269
 Supercritical aerodynamics
 Transonic flow past thin wings 253
 Surges
 Storm surges in the Bay of Bengal 175
 Taylor hypothesis
 Role of coherent structures in turbulent shear flows 35
 Taylor vortex
 Flow visualization studies of vortices 145
 Thermophysics
 Thermal and fluid mechanical problems in space flight 269
 Thin wings
 Transonic flow past thin wings 253
 Three-dimensional aspects
 Three-dimensional aspects of boundary-layer transition 125
 Three-dimensional transonic flow
 Transonic flow past thin wings 253
 Time line
 Flow visualization studies of vortices 145
 Transition
 A glimpse of fluid mechanics research in Bangalore 25 years ago 1
 Prospects for useful research on coherent structure in turbulent shear flow 17
 Generation of large scale circulation in turbulent convection 183
 Transonic aerodynamics
 Transonic flow past thin wings 253
 Transonic flow
 Inviscid transonic flow field analysis 221
 Transport
 Mathematical modelling of turbulent shear flows 105
 Tropical circulation
 Fluid dynamics of the monsoon 201
 Turbulence
 Prospects for useful research on coherent structure in turbulent shear flow 17
 Mathematical modelling of turbulent shear flows 105
 Generation of large scale circulation in turbulent convection 183
 Turbulent shear flows
 Role of coherent structures in turbulent shear flows 35
 Turbulent spots
 A glimpse of fluid mechanics research in Bangalore 25 years ago 1
 Three-dimensional aspects of boundary-layer transition 125
 Twin vortices
 Flow visualization studies of vortices 145
 Unsteady turbulent flows
 Role of coherent structures in turbulent shear flows 35
 Variational methods
 On finite amplitude water waves 165
 Vortex pairing
 Role of coherent structures in turbulent shear flows 35
 Vortex ring
 Prospects for useful research on coherent structure in turbulent shear flow 17

Flow visualization studies of vortices	145	Wall vortex	
Vortex street		Flow visualization studies of vortices	145
Prospects for useful research on coherent structure in turbulent shear flow	17	Water waves	
Wall jets		On finite amplitude water waves	165
A glimpse of fluid mechanics research in Bangalore 25 years ago	1	Wave motion	
		Three-dimensional aspects of boundary-layer transition	125



ACADEMY PUBLICATIONS IN
ENGINEERING SCIENCES

General Editor : R. Narasimha

- Volume 1. The Arayabhata Project
Edited by U. R. Rao, K. Kasturirangan
- Volume 2. Computer Simulation
Edited by N. Seshagiri, R. Narasimha
- Volume 3. Rural Technology
Edited by A. K. N. Reddy
- Volume 4. Alloy Design
Edited by S. Ranganathan, V. S. Arunachalam, R. W. Cahn
- Volume 5. Surveys in Fluid Mechanics
Edited by R. Narasimha, S. M. Deshpande

The cover shows a flow visualization photograph from the paper by T. Matsui.